Lecture Notes in Applied and Computational Mechanics Vol. 41

Fred Browand
Rose McCallen
James Ross (Eds.)

The Aerodynamics of Heavy Vehicles II: Trucks, Buses, and Trains

EXTRA MATERIALS
extras.springer.com

Springer

Lecture Notes in Applied and Computational Mechanics

Volume 41

Series Editors

Prof. Dr.-Ing. Friedrich Pfeiffer
Prof. Dr.-Ing. Peter Wriggers

Lecture Notes in Applied and Computational Mechanics

Edited by F. Pfeiffer and P. Wriggers

Further volumes of this series found on our homepage: springer.com

Vol. 41: Browand F., Ross J., McCallen R. (Eds.)
Aerodynamics of Heavy Vehicles II: Trucks, Buses, and Trains
486 p. 2009 [978-3-540-85069-4]

Vol. 40: Pfeiffer F.
Mechanical System Dynamics
578 p. 2008 [978-3-540-79435-6]

Vol. 39: Lucchesi, M.; Padovani, C.; Pasquinelli, G.; Zani, N.
Masonry Constructions: Mechanical Models and Numerical Applications
176 p. 2008 [978-3-540-79110-2]

Vol. 38: Marynowski, K.
Dynamics of the Axially Moving Orthotropic Web
140 p. 2008 [978-3-540-78988-8]

Vol. 37: Chaudhary, H.; Saha, S.K.
Dynamics and Balancing of Multibody Systems
200 p. 2008 [978-3-540-78178-3]

Vol. 36: Leine, R.I.; van de Wouw, N.
Stability and Convergence of Mechanical Systems with Unilateral Constraints
250 p. 2008 [978-3-540-76974-3]

Vol. 35: Acary, V.; Brogliato, B.
Numerical Methods for Nonsmooth Dynamical Systems: Applications in Mechanics and Electronics
545 p. 2008 [978-3-540-75391-9]

Vol. 34: Flores, P.; Ambrósio, J.; Pimenta Claro, J.C.; Lankarani Hamid M.
Kinematics and Dynamics of Multibody Systems with Imperfect Joints: Models and Case Studies
186 p. 2008 [978-3-540-74359-0]

Vol. 33: Niesłony, A.; Macha, E.
Spectral Method in Multiaxial Random Fatigue
146 p. 2007 [978-3-540-73822-0]

Vol. 32: Bardzokas, D.I.; Filshtinsky, M.L.; Filshtinsky, L.A. (Eds.)
Mathematical Methods in Electro-Magneto-Elasticity
530 p. 2007 [978-3-540-71030-1]

Vol. 31: Lehmann, L. (Ed.)
Wave Propagation in Infinite Domains
186 p. 2007 [978-3-540-71108-7]

Vol. 30: Stupkiewicz, S. (Ed.)
Micromechanics of Contact and Interphase Layers
206 p. 2006 [978-3-540-49716-5]

Vol. 29: Schanz, M.; Steinbach, O. (Eds.)
Boundary Element Analysis
571 p. 2006 [978-3-540-47465-4]

Vol. 28: Helmig, R.; Mielke, A.; Wohlmuth, B.I. (Eds.)
Multifield Problems in Solid and Fluid Mechanics
571 p. 2006 [978-3-540-34959-4]

Vol. 27: Wriggers P., Nackenhorst U. (Eds.)
Analysis and Simulation of Contact Problems
395 p. 2006 [978-3-540-31760-9]

Vol. 26: Nowacki, J.P.
Static and Dynamic Coupled Fields in Bodies with Piezoeffects or Polarization Gradient
209 p. 2006 [978-3-540-31668-8]

Vol. 25: Chen C.-N.
Discrete Element Analysis Methods of Generic Differential Quadratures
282 p. 2006 [978-3-540-28947-0]

Vol. 24: Schenk, C.A., Schuëller. G
Uncertainty Assessment of Large Finite Element Systems
165 p. 2006 [978-3-540-25343-3]

Vol. 23: Frémond M., Maceri F. (Eds.)
Mechanical Modelling and Computational Issues in Civil Engineering
400 p. 2005 [978-3-540-25567-3]

Vol. 22: Chang C.H.
Mechanics of Elastic Structures with Inclined Members: Analysis of Vibration, Buckling and Bending of X-Braced Frames and Conical Shells
190 p. 2004 [978-3-540-24384-7]

Vol. 21: Hinkelmann R.
Efficient Numerical Methods and Information-Processing Techniques for Modeling Hydro- and Environmental Systems
305 p. 2005 [978-3-540-24146-1]

Vol. 20: Zohdi T.I., Wriggers P.
Introduction to Computational Micromechanics
196 p. 2005 [978-3-540-22820-2]

Vol. 19: McCallen R., Browand F., Ross J. (Eds.)
The Aerodynamics of Heavy Vehicles: Trucks, Buses, and Trains
567 p. 2004 [978-3-540-22088-6]

Vol. 18: Leine, R.I., Nijmeijer, H.
Dynamics and Bifurcations of Non-Smooth Mechanical Systems
236 p. 2004 [978-3-540-21987-3]

Vol. 17: Hurtado, J.E.
Structural Reliability: Statistical Learning Perspectives
257 p. 2004 [978-3-540-21963-7]

Vol. 16: Kienzler R., Altenbach H., Ott I. (Eds.)
Theories of Plates and Shells: Critical Review and New Applications
238 p. 2004 [978-3-540-20997-3]

Vol. 15: Dyszlewicz, J.
Micropolar Theory of Elasticity
356 p. 2004 [978-3-540-41835-1]

The Aerodynamics of Heavy Vehicles II: Trucks, Buses, and Trains

Fred Browand
Rose McCallen
James Ross (Eds.)

With 308 Figures and 52 Tables

Springer

Fred Browand, Ph.D.
Department of Aerospace
and Mechanical Engineering
University of Southern California
Los Angeles, CA 90089-1191
USA

Rose McCallen, Ph.D.
Center for Advanced
Fluid Dynamics
Applications (CAFDA)
Lawrence Livermore
National Laboratory
P.O.Box 808, L-098
Livermore CA 94551
USA

James Ross, Ph.D.
NASA Ames Research Center
Experimental Physics Branch
MS 260-1
Moffett Field CA 94035
USA

ISBN: 978-3-540-85069-4 e-ISBN: 978-3-540-85070-0

Lecture Notes in Applied and Computational Mechanics ISSN 1613-7736
e-ISSN 1860-0816

Library of Congress Control Number: 2008934051

© Springer-Verlag Berlin Heidelberg 2009

This work is subject to copyright. All rights are reserved, whether the whole or part of the material is concerned, specifically the rights of translation, reprinting, reuse of illustrations, recitation, broadcasting, reproduction on microfilm or in any other ways, and storage in data banks. Duplication of this publication or parts thereof is permitted only under the provisions of the German Copyright Law of September 9, 1965, in its current version, and permission for use must always be obtained from Springer. Violations are liable for prosecution under the German Copyright Law.

The use of general descriptive names, registered names, trademarks, etc. in this publication does not imply, even in the absence of a specific statement, that such names are exempt from the relevant protective laws and regulations and therefore free for general use.

Cover design: WMXDesign GmbH, Heidelberg

Printed on acid-free paper

9 8 7 6 5 4 3 2 1 0

springer.com

Engineering Conferences International

Engineering Conferences International (ECI) is a not-for-profit global engineering conferences program, originally established in 1962, that provides opportunities for the exploration of problems and issues of concern to engineers and scientists from many disciplines. The organization sponsors leading edge, interdisciplinary, international scientific/engineering conferences.

Executive Director:
Barbara K. Hickernell
Engineering Conferences International
32 Broadway, Suite 314
New York, NY 10004
USA
Tel: 1-212-514-6760
Email: info@engconfintl.org
www.engconfintl.org

Introduction

It is our pleasure to present these proceedings for "The Aerodynamics of Heavy Vehicles II: Trucks, Buses and Trains" International Conference held in Lake Tahoe, California, August 26-31, 2007 by Engineering Conferences International (ECI). Brought together were the world's leading scientists and engineers from industry, universities, and research laboratories, including truck and high-speed train manufacturers and operators. All were gathered to discuss computer simulation and experimental techniques to be applied for the design of the more efficient trucks, buses and high-speed trains required in future years.

This was the second conference in the series. The focus of the first conference in 2002 was the interplay between computations and experiment in minimizing aerodynamic drag. The present proceedings, from the 2007 conference, address the development and application of advanced aerodynamic simulation and experimental methods for state-of-the-art analysis and design, as well as the development of new ideas and trends holding promise for the coming 10-year time span. Also included, are studies of heavy vehicle aerodynamic tractor and trailer add-on devices, studies of schemes to delay undesirable flow separation, and studies of underhood thermal management.

We would like to thank the ECI organizers for their efficient organization of the meeting. In addition, we would like to express our appreciation to all session chairs, the scientific advisory committee, authors, and reviewers for their many hours of dedicated effort that contributed to a successful conference, and that are manifest in this proceeding. We also gratefully acknowledge the financial support received from ECI, the United State's Truck Manufacturers Association, International Truck and Engine Corporation, Lawrence Livermore National Laboratory, and CD Adapco.

Conference Co-Chairs:

Professor Fred Browand, Ph.D.
Aerospace & Mechanical Engineering Department
University of Southern California
Los Angeles, CA

Rose McCallen, Ph.D.
Lawrence Livermore National Laboratory
Livermore, CA

Jim Ross, Ph.D.
NASA Ames Research Center
Moffett Field, CA

Contents

Keynote Papers

Flow Field Characteristics

Separation Control for Drag Reduction

Design Optimization Techniques Related to Vehicle Aerodynamics

Train Aerodynamics

Poster Session

CFD, Numerical Methods and Application

Vehicle and Tire Spray and Vehicle Interaction

Drag Reduction

Keynote Papers

Bluff Body Flow Research with Application to Road Vehicles

Peter Bearman

Department of Aeronautics, Imperial College, London, SW7 2AZ, UK
p.bearman@imperial.ac.uk

Abstract This paper explores a number of aspects of bluff body research that may help in the understanding and advancement of the aerodynamics of heavy vehicles. The relationship between the lift and drag of bodies moving close to the ground is discussed and the unsteady trailing vortex structure of a vehicle is illustrated. The importance of the ground boundary condition and the flow structure around wheels rotating in contact with the ground are also described. Methods for the reduction of forebody and base drag are discussed and the possibilities for using flow control techniques to modify free shear layer development as a means of reducing drag are addressed. Finally the role of the natural wind, particular atmospheric turbulence, in affecting vehicle flows is examined.

Introduction

Road vehicles are subject to design constraints which severely limit aerodynamic efficiency and practical vehicles operate with regions of separated flow. While much of our understanding of road vehicle aerodynamics has developed through the application of techniques used in the aerospace industry, vehicles fall into a category of bodies that are aerodynamically bluff. For streamlined bodies considerable advances are being made in using flow control methods to reduce skin friction drag but with bluff bodies the emphasis needs to be on minimising pressure drag. This means keeping flow attached over as much of the body surface as possible and raising the pressure in the large separated region at the rear of a vehicle. For economic, environmental and political reasons, drag reduction is a prime goal but it should be kept in mind that aerodynamics affects other important aspects of vehicle operations including: cooling, handling and noise. However, in this paper the main emphasis is placed on the processes of drag generation and drag reduction of road vehicles.

Aerodynamics is a key technology in motor racing, particularly for the open-wheeled vehicles used, for example, in Formula 1. Here significant advances have been made in wind tunnel test techniques and in the appreciation of the importance of the correct simulation of the ground boundary condition. This has led to improved understanding of lift generating mechanisms and the complex problem of wheel flow, which in one form or another affects all road vehicles. A further consideration is that vehicles are exposed to the natural wind and as a result can experience yawed flow and aerodynamic loading influenced by turbulence. Here there is an obvious connection with the study of wind loading on buildings and structures. Hence in addressing the aerodynamics of heavy road vehicle, ideas will be drawn from aerospace, wind engineering, motor racing, as well as from basic research on bluff bodies. In summary, some of the important aerodynamic considerations for road vehicles are:

- Large areas of separated flow leading to high drag
- Close proximity to the ground which influences both lift and drag
- The presence of wheels
- The effects of the natural wind introducing yawed flow and turbulence
- Interference due to the close proximity of other vehicles

The Relation between Lift and Drag

For an aircraft, lift is accompanied by the generation of trailing vortices and these vortices contribute to induced or lift-related drag. Total drag is then the summation of profile drag and induced drag. However, for road vehicles the relationship between lift and drag is more complex because even in an ideal, or inviscid, flow lift can be generated on a body moving close to a boundary. This manifests itself as an attractive force between the body and its imaginary image in the boundary. For example, a sphere moving near the ground through an ideal fluid generates a force towards the ground and the associated lift coefficient can rise to nearly -0.4 when the gap between the sphere surface and the ground is very small. This force is generated without the shedding of trailing vortices and without drag. For a road vehicle the lift will be a combination of this component and the more familiar one experienced by lifting bodies in a real fluid. It is the latter component that is related to trailing vortices and drag generation.

Most vehicles generate lift but the associated trailing vortices are unsteady and rapidly dissipate since they are influenced by the large separated region at the rear of a vehicle. Figure 1 shows two velocity maps measured in the near wake of a passenger car model using particle image velocimetry and reported by Wang et al (1996). They were measured a short time apart and it is clear that there are substantial differences in the two plots. However, if a small number of these maps are averaged then the time-average picture that appears is quite different. Figure 2 shows the result of averaging just 10 plots and now we see the emergence of a pair

of trailing vortices but it is clear that the vortex structure in the instantaneous flow is very different to the time-average one. Such observations give strength to the argument that LES methods are likely to be more appropriate for computing vehicles flows than using the RANS equations coupled with a turbulence model.

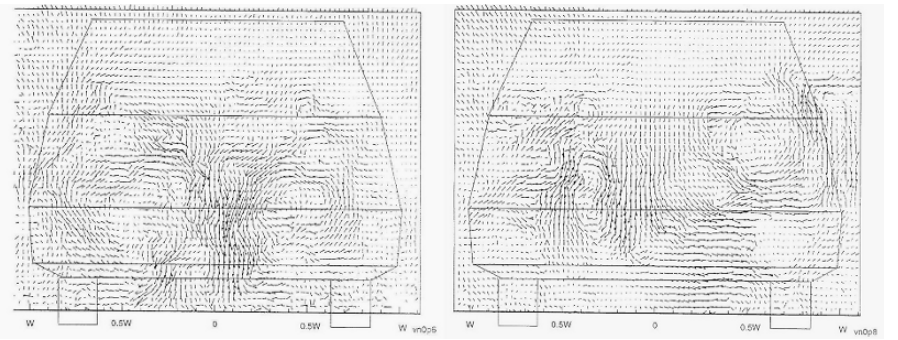

Fig. 1 Instantaneous cross-flow velocity maps measured in the near wake of a passenger car model at a vertical plane 20% of the car length from the rear bumper

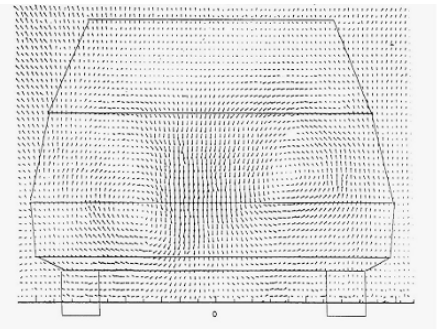

Fig. 2 The velocity field obtained from the average of only 10 instantaneous velocity maps

The Ground Boundary Condition and Wheels

Wind tunnel testing using a rolling road has become standard practice for many racing car applications where an important feature is the low ground clearance. As well as generating the correct ground boundary condition, a further advantage of using a rolling road is that wheels and their effect on aerodynamic performance can be correctly simulated. Although at first sight there may not appear to be too many similarities between a Formula 1 racing car and a tractor-trailer vehicle, when ground clearance is expressed as a fraction of vehicle length the values for the two are not so different. Also for both vehicles the wheel flows are important,

particularly for a trailer where wheels are often very exposed. If vehicle flow is considered in a wind tunnel frame of reference where the ground is correctly simulated, an obvious observation is that the relative flow speeds beneath and over a vehicle are similar. This has an important implication for drag reduction since there are many potential drag generating components under a vehicle and designers need to pay as much attention to the design of the underbody as they do to the more visible parts of a vehicle.

Obtaining a full understanding of the flow around a rotating road wheel presents a challenging problem. Working in a wind tunnel frame of reference, the flow travelling along the ground meets flow driven by the no slip condition at the tyre surface, which is a thin layer of flow rotating with the wheel, in the region of contact between the wheel and the ground. The result of these flows coming together is the sideways jetting flow that can be seen in the instantaneous PIV velocity field plotted in Fig. 3. Here the measurement plane is very close to the ground and parallel to it and the free stream flow is from left to right. The jet and resulting large region of locally disturbed flow are clearly visible in this plot from a study of a racing car wheel by Pegrum (2006). The investigation of this problem is made even more complex because contact with the road occurs over a patch of tyre and the contact area may change in response to varying driving conditions.

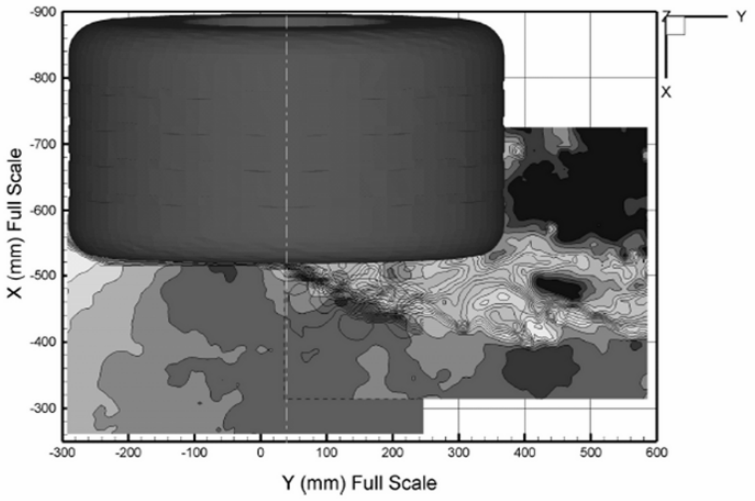

Fig. 3 An instantaneous velocity field measured in a horizontal plane just above the contact patch of a rotating wheel (Pegrum (2006))

As discussed by Fackrell and Harvey (1975) in their pioneering work on wheel flow, separation from the circumferential tyre surface is affected strongly by wheel rotation. Again working in a stationary frame of reference, at the top of the wheel the flow at the surface is moving in opposition to the free stream flow. For a rotating wheel flow separation is brought forward compared to that for a non-rotating

one. Reynolds number effects on the flow about a rotating wheel are far less than those for the classic problem of a fixed circular cylinder where a large drop in drag coefficient occurs in the critical Reynolds number regime. Zdravkovich et al (1998) have termed small aspect ratio circular cylinders “coin-like” bodies where separation from the front edges is as important, or perhaps more important, than separation from the curved boundary. Wheel flows fall into a similar category and they give rise to the shedding of a vortex system that is quite different to that for a two-dimensional cylinder. Figure 4 shows a plot of vorticity passing through a vertical plane placed 20% of the wheel diameter behind the back of a wheel. This data, obtained by Pegrum (2006) using PIV, shows two pairs of counter-rotating vortices, one pair emanating from the upper edges of the tyre and

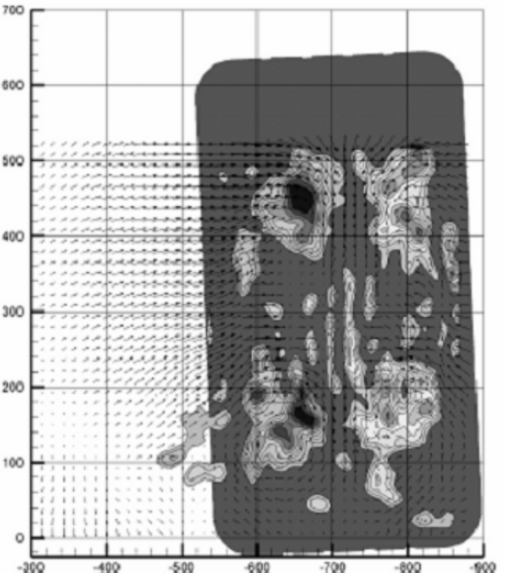

Fig. 4 Vorticity field showing the wake structure at 20% of a diameter behind a wheel (Pegrum (2006))

the other forming lower down in the near wake. The self-induced velocity on the upper pair drives the vortices down and they merge with the lower pair. Hence further downstream only one pair of vortices can be found. Figure 5, due to Saddington et al(2007), shows how the vortex configuration changes with distance behind an isolated wheel. It should be noted that wheel wake flows are highly unsteady and the sketches in Fig. 5 present a time-average picture.

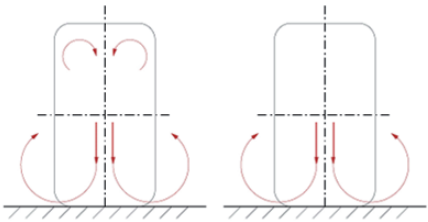

Fig. 5 Vortex Structure behind a Rotating Wheel, left 0.5 diameters downstream and right 2 diameters downstream (Saddington et al (2007))

Drag Reduction of Heavy Vehicles

As mentioned earlier, possibilities for drag reduction of heavy vehicles are limited by the requirement that the basic function of the vehicle should not be compromised. This puts a serious constraint on what might be done to reduce the base drag of a trailer, for example. The aerodynamic drag of a heavy vehicle results primarily from differences in pressure acting on forward and rearward facing surfaces and for the simplified vehicle shape shown in Fig. 6 the drag can be conveniently split into forebody and base drag components. The techniques for reducing these two components differ. To reduce the forebody drag, regions of flow separation need to be minimised. For the basic body shown in Fig. 6 this might be done by increasing corner radii and by enhancing the mixing in the separated shear layer to encourage earlier reattachment. The more difficult problem is to reduce base drag because the practical constraints are much more severe here. To increase the pressure in the base region some form of mild boat-tailing might be used to raise the pressure ahead of separation. Alternatively, since the base pressure is related to the entrainment of fluid into the surrounding separated shear layers, the base pressure would increase if the mixing in the separated shear layers could be reduced. Modern developments in flow control technology are providing interesting possibilities for achieving this.

Techniques that have been used, and also those that might be used in the future, to reduce the drag of heavy road vehicles include:

- Shielding, incorporating the strategy of driving in close platoons
- The long established method of fitting cab-top deflectors to reduce forebody drag
- Surface treatments to delay separation, possibly including the use of dimples
- Base cavities and boat-tailing to reduce base drag
- Active and passive methods applied to the control of separation
- Active and passive methods applied to the control of separated shear layer development

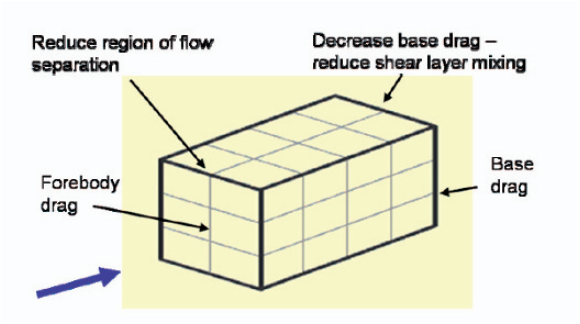

Fig. 6 A highly simplified heavy road vehicle

Considerable success can be achieved in reducing drag by attention to a large number of small details on a vehicle. This is sometimes referred to as aerodynamic tuning but it can only be taken so far and a significant region of separated flow is always likely to remain at the rear of a vehicle. For a bluff body with fixed separation, say from sharp edges, the higher the base suction then the smaller the time-average recirculation region in the near wake. Hence, to reduce drag the recirculation region must be made larger, not smaller. This can be achieved by reducing stresses in the free layers so as to reduce entrainment from the near wake and hence raise the base pressure. The challenging problem this poses is how can the structure of separated shear layers be controlled in such a way as to reduce stresses?

Chun and Sung(1996) have carried out an experimental study of flow over a backward-facing step where the separating shear layer has been excited by an oscillating jet. The experimental set up is shown in Fig.7 and it can be seen from the detail that the massless jet issues from a small slit at the corner of the step. Some of the results from this experiment are reproduced in Fig. 8 where the mean flow reattachment distance behind the step, X_r, non-dimensionalised by the reattachment distance with no blowing, is plotted against non-dimensional forcing frequency. Here the frequency of forcing is non-dimensionalised by using the step height and the approaching flow velocity to form the parameter St_H. The results for three jet velocity amplitudes are plotted and they all show similar features. As frequency is increased the reattachment length shortens, a minimum is reached and for high values of frequency the reattachment length extends beyond that for no jet. An interpretation of these results is that the Kelvin-Helmholtz type instability in the shear layer is enhanced at low values of the frequency parameter leading to increased entrainment, higher base suction and a shorter reattachment length. From the viewpoint of drag reduction, the significant result is the increase in reattachment length for high forcing frequencies where presumably the high frequency massless jet interferes in a beneficial way with the shear layer instability mechanism leading to reduced stresses. This will result in a lower base drag on the step.

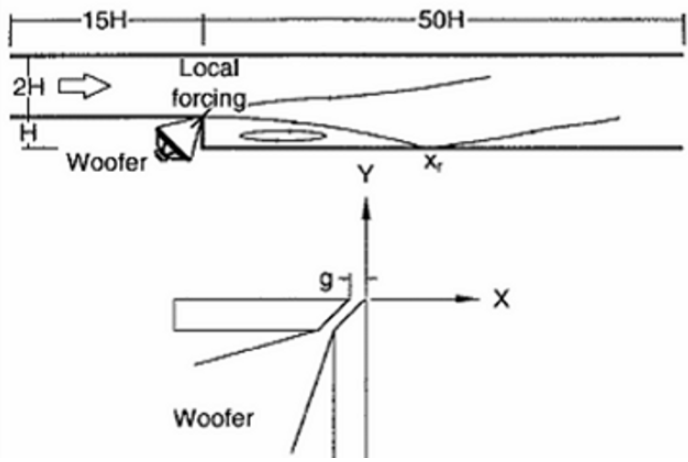

Fig. 7 Control of flow over a backward-facing step (Chun and Sung (1996))

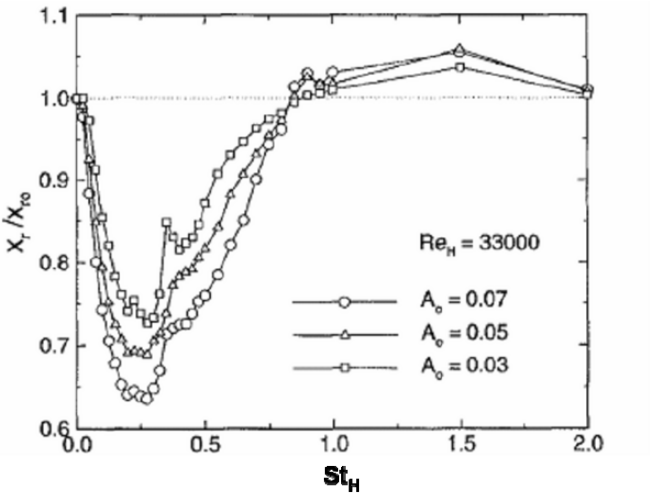

Fig. 8 Reattachment length behind a backward-facing step versus non-dimensional forcing frequency (Chun and Sung (1996))

A further example of the effectiveness of a massless jet can be found in the numerical simulations of Dandois et al (2007). Figure 9 shows examples of their direct numerical simulations of flow over a rounded two-dimensional, backward-facing ramp. The upper plot shows the mean flow without control, the middle one is with low frequency forcing and the effect of high frequency forcing is shown in the lower plot. Again enhanced entrainment occurs for low frequency forcing and some suppression takes place for high frequency forcing leading to a substantial

increase in reattachment length. The application of such techniques to reduce the drag of road vehicles appears possible but further research is required to determine the overall efficiency of such a control method, its optimisation and practicality. Nevertheless, it presents an interesting new direction.

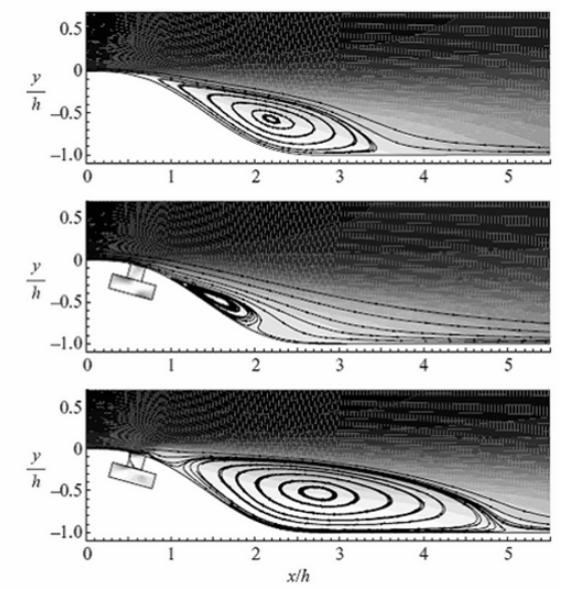

Fig. 9 Numerical simulations of flow control over a two-dimensional ramp using a massless jet: upper no control, middle low frequency forcing, lower high frequency forcing (Danois et al (2007))

The Influence of the Natural Wind on Road Vehicle Flows

Road vehicles are subjected to strong flow disturbances generated by other vehicles and by the natural wind. The influence of the wind can be summarised as follows:

- Changes occur in the magnitude and direction of the relative approaching flow
- Small angles of yaw can lead to increases in aerodynamic drag and the generation of side forces that may give rise to handling problems
- Turbulence produced by the wind generates unsteady aerodynamic forces
- The presence of turbulence may change mean force coefficients

Bearman and Morel (1983) reviewed the effects of free stream turbulence on the flow around bluff bodies and identified two mechanisms by which turbulence can influence the mean flow about a body. These are shown in diagrammatic form in Fig. 10 for an attached boundary layer and a free shear layer. For vehicles, turbulence can affect separation, reattachment and the pressure in a separated region.

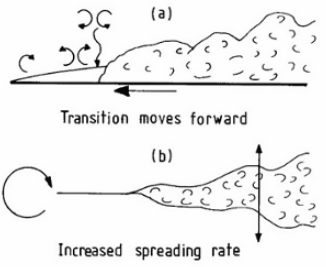

Fig. 10 Two mechanisms by which free stream turbulence affects flows (Bearman and Morel (1983))

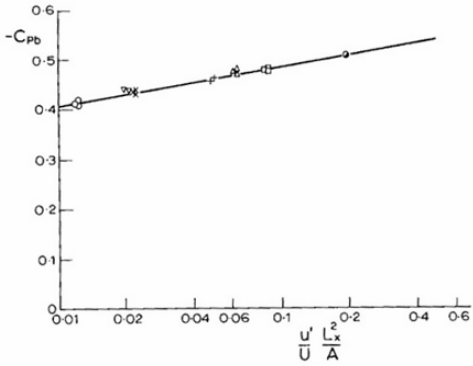

Fig. 11 Base pressure coefficients acting on square and circular thin plates set normal to turbulent flow

Figure 11 shows the effect of turbulence on the base pressure acting on thin plates mounted normal to a flow. Base pressure coefficient is seen plotted against a turbulence parameter involving the product of the free stream turbulence intensity and the ratio of turbulence scale length squared to plate area. This parameter is discussed by Bearman (1971) and has been devised on the assumption that the main effect of turbulence for the plates is to enhance mixing in their near wakes. While buildings may be exposed to turbulence levels of 20% or more, vehicles that are moving in the presence of wind see substantially lower relative intensities under conditions of high vehicle speeds. A practical range for the turbulence

parameter used in Fig.11 may be up to 0.06 but as can be seen from the results this can still lead to a significant increase in base suction.

The interaction between a turbulent approaching flow and a road vehicle is complex and gives rise to a number of different effects that are too varied to go into further detail here. However, let it suffice to say that turbulence gives rise to uncertainties when comparing on road measurements of aerodynamic quantities with measurements made in a conventional smooth flow wind tunnel.

References

Bearman P (1971) Investigation of forces on flat plates normal to a turbulent flow. J Fluid Mech 46:177-198

Bearman P, Morel T (1983) Effect of free stream turbulence on the flow around bluff bodies. Prog. Aerospace Sci 20:97-123

Chun K, Sung H (1996) Control of turbulent separated flow over a backward-facing step by local forcing. Exp Fluids 21:417-426

Danois J, Garnier E, Sagaut P (2007) Numerical simulation of active separation control by a synthetic jet. J Fluid Mech 574:25-58

Fackrell J, Harvey J (1974) The aerodynamics of an isolated road wheel. Proc 2nd AIAA Symp. of Aerodynamics of Sports and Competition Automobiles, 16:119-125

Pegrum J (2006) Experimental study of the vortex system generated by a Formula 1 front wing. PhD thesis, University of London

Saddington A, Knowles R, Knowles K (2007) Laser Doppler anemometry measurements in the near-wake of an isolated Formula One wheel. Exp Fluids 42:671-681

Wang Q, Bearman P, Harvey J (1996) A study of the instantaneous flow structure behind a car by particle image velocimetry. International Seminar on Optical Methods and Data Processing in Heat and Fluid Flow, 1996:179-188, IMechE, London

Zdravkovich M, Flaherty A, Pahle M, Skelhorne I (1998) Some aerodynamic aspects of coin-like cylinders. J Fluid Mech 360:73-84

Climate Change and the Energy Economy

David Schimel

The National Center for Atmospheric Research (NCAR), USA
schimel@ucar.edu

Abstract There is a robust scientific consensus that human-induced climate change is occurring. The recently released Fourth Assessment Report of the IPCC states with "very high confidence," that human activity has caused the global climate to warm. Many well-documented observations show that fossil fuel burning, deforestation, and other industrial processes are rapidly increasing the atmospheric concentrations of CO_2 and other greenhouse gases. An increasing body of observations and modeling results shows that these changes in atmospheric composition are changing the global climate and beginning to affect terrestrial and marine ecosystems. In this talk, I'll review observed and projected changes to the US climate, discuss the sectoral contributions to US greenhouse gas emissions and speculate about the future of the US carbon economy.

Flow Field Characteristics

Large Eddy Simulations and Acoustic Predictions in Automotive Applications

G. Iaccarino[1], F. Ham[1], Y. Khalighi[1], D. Bodony[1], P. Moin[1], B. Khalighi[2]

[1] Stanford University, USA
[2] General Motors R&D Center, USA
jops@stanford.edu (G. Iaccarino)

Abstract The emergence of the computational tools capable of accurately predicting the flow properties around complex geometries has opened new opportunities in the design of automotive components and their integrations. In particular, one may now be able to predict the acoustic noise produced by the unsteady fluid motion induced by the individual parts and quantitatively evaluate their loudness and spectral (i.e. frequency content) without relying on semi-empirical models. To demonstrate this capability the flow noise produced by two configurations typical of automotive applications – namely the outside rear view mirrors and the rain gutters – are examined quantitatively. Relevant details regarding the prediction methods as well as a selection of results are discussed.

Validation of the Immersed Boundary CFD Approach for Complex Aerodynamic Flows

B. Khalighi[1], S. Jindal[1], J.P. Johnson[1], K.H. Chen[1], G. Iaccarino[2]

[1] General Motors, USA
[2] Stanford University, USA
bahram.khalighi@gm.com

Abstract Standard CFD methods require a mesh that fits the boundaries of the computational domain. For a complex geometry the generation of such a grid is time-consuming and often requires modifications to the model geometry. This paper evaluates the Immersed Boundary (IB) approach which does not require a boundary-conforming mesh and thus would speed up the process of the grid generation. In the IB approach the CAD surfaces (in Stereo Lithography –STL- format) are used directly and this eliminates the surface meshing phase and also mitigates the process of the CAD cleanup. A volume mesh, consisting of regular, locally refined, hexahedrals is generated in the computational domain, including inside the body. The cells are then classified as fluid, solid and interface cells using a simple ray-tracing scheme. Interface cells, correspond to regions that are partially fluid and are intersected by the boundary surfaces. In those cells, the Navier-Stokes equations are not solved, and the fluxes are computed using geometrical reconstructions. The solid cells are discarded, whereas in the fluid cells no modifications are necessary. The present IB method consists of two main components: 1) TOMMIE which is a fast and robust mesh generation tool which requires minimum user intervention and, 2) a library of User Defined Functions for the FLUENT CFD code to compute the fluxes in the interface cells. This study evaluates the IB approach, starting from simple geometries (flat plate at 90 degrees, backward facing step) to more complex external aerodynamics of full-scale fully-dressed production vehicles. The vehicles considered in this investigation are a sedan (1997 Grand-Prix) and an SUV (2006 Tahoe). IB results for the flat plate and the backward-step are in very good agreement with measurements. Results for the Grand-Prix and Tahoe are compared to experiments (performed at GM wind tunnel) and typical body-fitted calculations performed using Fluent in terms of surface pressures and drag coefficients. The IB simulations predicted the drag coefficient for the Grand-Prix and the Tahoe within 5% of the body-fitted calculations and are closer to the wind-tunnel measurements.

Introduction

Numerical simulations allow the analysis of complex phenomena without resorting to expensive prototypes and difficult experimental measurements. This trend, to bring CFD to bear on vehicle aerodynamics design issues, is appropriate and timely in view of the increasing competitive and regulative pressures being faced by the automotive industry [1].

The industrially relevant geometries are usually defined in the CAD environment and must be *cleaned* (small details are usually eliminated and overlapping surface patches are trimmed- before it can be used for computational analysis). A smooth water-tight surface mesh is then generated to serve as a boundary condition for the volume mesh. There are mainly two types of approaches in volume meshing, structured and unstructured meshing. In structured mesh, the governing equations are transformed into the curvilinear coordinate system aligned with the surface. It is trivial for simple shapes, however, becomes extremely inefficient and time consuming for complex geometries. In the unstructured approach, there is no transformation involved for governing equations. The integral form of governing equations is discretized and either a finite-volume or finite-element scheme is used. The information regarding the grid is directly incorporated into the discretization. Unstructured grids are in general successful for complex geometries. However, the quality of these grids deteriorates with complex shapes. In addition, there is large computational overhead owing to a large number of operations per node and low accuracy in combination with the low-order dissipative spatial discretization.

The Immersed Boundary (IB) method [2] is an alternative procedure that can handle the geometric complexity, and at the same time retains the accuracy and high efficiency of the simulations performed on regular grids. This represents a significant advance in the application of CFD to realistic flows. It uses Cartesian-like meshes in a simple, fictitious computational domain obtained by eliminating the object of interest (i.e. the road vehicles in the present application).

The main objective of this study is to evaluate the IB method to assess the accuracy, robustness, and the speed for routine aerodynamics simulations in the automotive industry. The IB flow simulations are presented for two simple geometries as well as for two production vehicles. The vehicles considered in this investigation are a sedan (1997 Pontiac Grand-Prix) and an SUV (2006 Chevy Tahoe).

The IB Method

The IB method is an alternative procedure in which a non-body conformal grid is used. The method “immersed boundary” was first developed by [3] to simulate

cardiac mechanics and the associated blood flows. In the present approach, the boundary surfaces are still present but the volume mesh is generated independently. Because the volume grid does not conform to the solid boundary, enforcing the physical boundary conditions requires a modification of the equations in the vicinity of boundary. Consider the Navier-Stokes equations below,

$$\pounds(\underline{U}) = 0 \text{ in } \Omega_f \text{ (volume)} \tag{1}$$

$$\text{with} \qquad \underline{U} = \underline{U}_\Gamma \text{ on } \Gamma_b \text{ (surface)} \tag{2}$$

Where $\underline{U} = (u,p)$ and $\pounds$ are the operators representing the Navier-Stokes equations. u and p refer to the velocity components and the pressure, respectively. Conventional methods proceed by developing a discretization of equation (1) on a body-conformal grid where the boundary condition (equation 2) on the immersed surface Γ_b is enforced directly. For IB, a forcing function is used in the governing equations that reproduce the effect of the boundary.

$$\pounds(\underline{U}) = f_b \quad \text{(volume + surface)} \tag{3}$$

The above system of equations is solved in the entire fluid domain. The forcing function f_b can be defined before and after the discretization step which leads to a dichotomy among different IB methods. A detailed discussion is provided in [4]. In the present approach, the forcing is defined after the discretization step and is applied in all the cells cut by the immersed surfaces (interface cells). The forcing is computed such that the desired boundary value is recovered at the location of the immersed boundary. In finite volume methods, source terms can be interpreted as flux imbalances and, in the current implementation of the IB method, the forcing is actually replaced by a modified flux applied at the faces connecting fluid and interface cells. No modification (f_b =0) is applied at the fluid cells.

In the IB approach, the ramifications of the boundary treatment on the accuracy and the conservation properties of the numerical scheme are not trivial. In the body-fitted method the conformal grid aligns the gridlines and the body surface and allows better control of the grid resolution in the vicinity of the body. However the same is not true for the IB methodology and this results in an increase in the grid size with the Reynolds number for the IB. As described by [4], the grid size ratio would scale to $(Re)^{1.5}$ for a 3D body.

A schematic diagram depicting the CAD to the CFD solution in the IB framework is shown in Fig. 1. The IB approach in this study consists of two main parts; 1) TOMMIE, a mesh generation tool, and 2) IBLIB, a set of User Defined Functions (UDFs) for the FLUENT CFD code which are described briefly in the following sections.

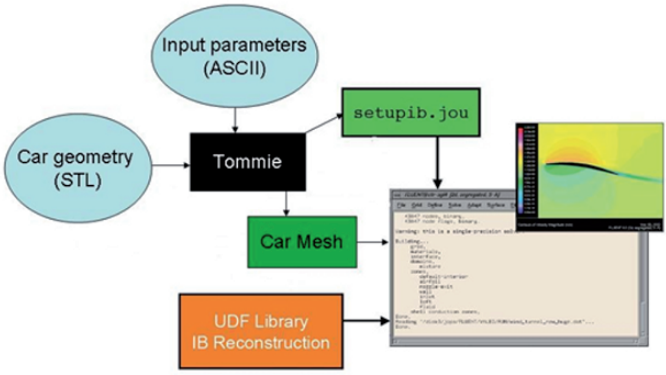

Fig. 1 Schematic diagram for the CAD to CFD solution in the IB approach.

1. TOMMIE

TOMMIE is the immersed boundary grid generator written in ANSI C++. It performs four main functions, namely the grid generation, the interface and the interior cell determination, wall-distance calculation and the evaluation of the weighting coefficients for the immersed boundary interpolation.

Geometries are imported in ASCII Stereo-Lithography format (STL). The STL representation of a surface is a collection of unconnected triangles of sizes inversely proportional to the local curvature of the original surface. The format is standard for the Rapid Prototyping community and all the CAD systems have the ability to export a given surface in the STL format automatically. This allows the treatment of any complex geometry without the need to generate an intermediate CFD surface mesh.

The geometry is placed on a structured background Cartesian mesh. This mesh covers the entire computational domain which includes the region inside the body. The generation of this grid is extremely simple and automatic. The mesh stretching is based on the location of the immersed boundary, and the cells are clustered near the object surface in accordance to the normal and tangential resolution as specified by the user. Several window refinements (rectangular, spherical and cylindrical) can be introduced to cluster the cells in the regions of interest such as the wake, underbody and the stagnation regions. The geometrical module then performs the separation (tagging) of the computational cells as shown in Fig. 2. The tagging procedure is based on a simple Ray Tracing (RT) technique. A random ray which originates from the location to be checked (grid nodes) is considered and the intersections between this ray and the given surface are computed. If the total number is even the point is outside the object. Similarly, if the total number is odd

the point is inside the object. The intersection between a ray (a 3D segment) and the surface (a collection of triangles) is carried out using the geometrical algorithms reported in [5]. In some cases, the RT could fail due to incorrect surface representations (e.g. unintentional missing triangles in the STL file). These gaps might be present in the original raw CAD representation or might arise while generating the STL representation of the CAD surfaces. To overcome this difficulty, before tagging any locations, three perpendicular rays are cast. In this case if the corresponding results are the same, the point is tagged, otherwise up to 20 additional random rays are traced and the most probable result is accepted. Alternatively, the STL file might be checked for inconsistency.

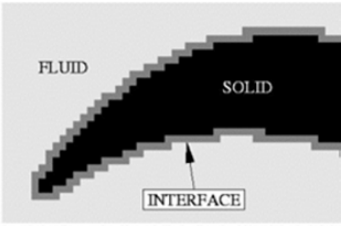

Fig. 2 Immersed Boundary tagging By Ray Tracing.

In the context of the IB technique, very refined grids are often required close to the highly curved immersed surfaces in order to properly represent the details of the geometry. Here a Local Grid Refinement (LGR) algorithm is used which allows an efficient clustering of cells. The present implementation is an extension of the classical Adaptive Mesh Refinement (AMR) technique for non-isotropic refinements. This requires a modification of the solution algorithm in order to handle grids with the hanging nodes. A detailed discussion of the implementation and the accuracy issues related to the present LGR method is given in [2, 6, and 7]. Another important aspect of the application of the LGR is the selection of the refinement/coarsening criteria. In the present implementation, the LGR is used to increase the resolution in the surroundings of the immersed boundary and, therefore, the only criterion used is the geometrical distance between each cell and the boundary. A Heavy-side tag function (using RT technique mentioned earlier) is used to mark the cells inside and outside the immersed body. An illustration of this procedure is shown in Fig. 3 for a geometry representing the letter F. Top row shows TOMMIE mesh, where a) to d) represents successive levels of refinement. The corresponding tagging function T is shown in the middle row, the dark area corresponds to the internal cells (T = -1) whereas the white area corresponds to the fluid cells (T = 1). The bottom row represents the numerical gradient of the Tagging function. Starting from a background mesh (Fig. 3a) and successively halving the cells until this gradient exceeds a prescribed value, the grid and the corresponding sharper representation in Fig. 3d is obtained. More detail about the LGR is available in [6, 7].

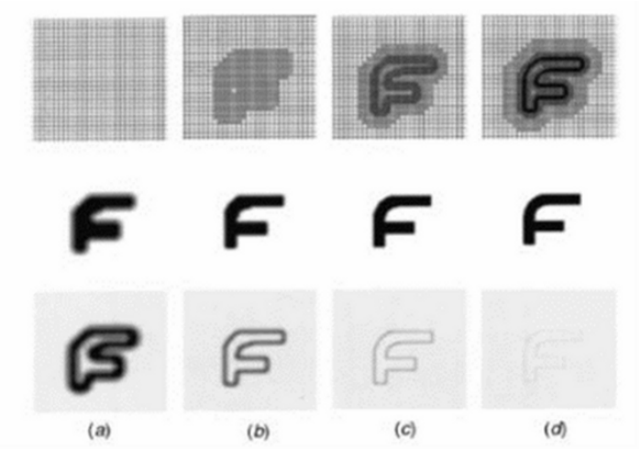

Fig. 3 Example of the automatic grid refinement strategy for immersed boundaries.

TOMMIE executes in batch mode and is extremely easy to use. A typical TOMMIE input file with its main features is reported in Appendix A.

The STLs can be added or deleted easily for the individual parts. Since there is no surface mesh associated with the volume cells, it amounts to saving time for the design/parametric studies. The surface mesh nodes need not to be aligned with one another and the neighboring surfaces need not have similar mesh sizes.

2. FLOW SOLVER

The flow solver used in this study is FLUENT V6.2. A user defined library (IBLIB) is used to handle the forcing functions in FLUENT. This library provides function hooks for reading/writing case files, initializing mesh, and implementing/updating wall boundary conditions.

The transport equations are solved only in the fluid cells, the solid cells are not considered and the values for interface cell values are obtained through interpolations. The steady incompressible 3D Reynolds-Averaged Navier-Stokes (RANS) equations are solved using a second-order implicit, cell-centered, finite volume scheme on Cartesian non-uniform grids. SIMPLE (Semi-Implicit Method for Pressure-Linked Equations) procedure is used to obtain an intermediate velocity field that is corrected to divergence-free conditions using the solution of a Poisson's equation for the pressure.

Imposition of boundary conditions on the immersed surfaces is the key factor in developing an IB algorithm. It is also what distinguishes one IB method from other. Here a derivative of direct discrete forcing algorithm based on the ghost cell

approach is used [7, 8]. Local reconstructions of the solution in the vicinity of the immersed boundary are built for the interface cells (Fig. 4). Assuming nodal solution is available directly or through interpolation from cell-centers, Figs. 4b and 4c show the linear and quadratic 2D stencils. In the linear case, two exterior values (2 and 3) are used together with the wall value (0) to evaluate the solution close to the interface (1). For a quadratic interpolation (Fig. 4c), a generic flow variable Φ can be expressed as:

$$\Phi = C_1 n^2 + C_2 t^2 + C_3 nt + C_4 t + C_5 n + C_6 \tag{4}$$

where n and t are the local coordinates normal and tangential to the IB, respectively. The six coefficients then can be determined by using the five exterior points (2, 3, 4, 5 and 6) and the boundary condition point (0) which is the normal intercept from the node 1 to the IB. The word exterior here refers to the fluid side; therefore at node 1, the velocity is reversed in order to prevent the flow from penetrating and slipping on the immersed boundary. This approach can be considered as a generalization of the ghost cell approach where the boundary conditions are imposed by fixing suitable values of the solution outside the computational domain. Since polynomial interpolations are keen to introduce wiggles and spurious oscillations, an inverse distance weighted method is employed in the present study. A detailed treatment of the interface cells is described in [8]. Without IBLIB, Fluent would not have access to the velocity reconstruction for interface cells, and it would only obtain the solution over the stair-step approximation of geometry as prescribed by Tommie mesh.

Eddy viscosity is obtained through realizable k-ε turbulence model with enhanced wall treatment [9, 10]. Information needed for turbulence modeling and enhanced wall treatment, such as wall distances, is contained in Tommie mesh file and used through IBLIB. Currently only k- ε class of turbulence models is available for solving IB mesh in FLUENT.

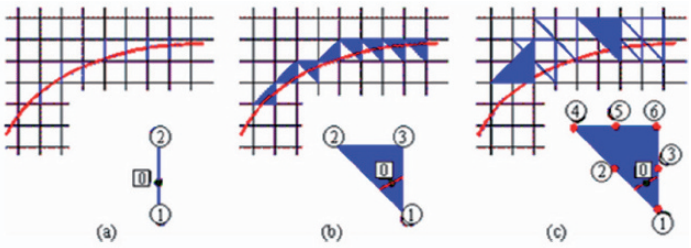

Fig. 4 Reconstruction stencils in the vicinity of the immersed boundary: (a) Linear 1D- scheme; (b) Linear 2D-scheme; (c) Quadratic 2D-scheme.

3. POST-PROCESSING

In the IB approach the immersed surface is disconnected from the computational grid and, therefore, it is not trivial to represent surface solution. Pressure values are projected from the stair-step grid onto the original body surfaces (STLs) using least-square interpolations.

The procedure used is shown in Fig. 5 schematically. Given a boundary node B and the surface normal in that location, the point P is defined at a certain distance δ from the surface. A least-square interpolation is used to obtain the velocity and the pressure at point P. The surface pressure at B is then obtained using the zero-normal gradient condition, $P_P = P_B$.

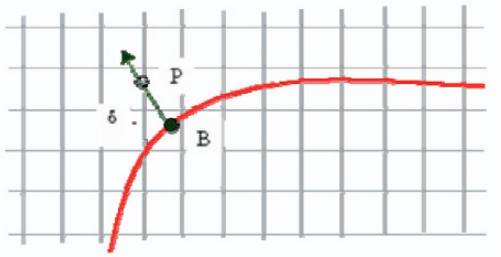

Fig. 5 Evaluation of surface quantities on the immersed body (Post-processing).

After each iteration, pressure is projected to the original STL surfaces automatically (transparent to the user) using the DEFINE_ADJUST function available in IBLIB. For a baffle (zero-thickness) surface, a shadow-copy is automatically made and pressure from one side of baffle is projected onto the shadow surface. The projected pressure is then integrated over the desired surfaces (original STLs) and resultant forces and moments could be calculated inside FLUENT framework as usual.

Similarly, calculation of the skin friction is not available directly in FLUENT. The cell-centered velocity gradients at wall surfaces are provided to FLUENT through IBLIB in order to calculate the skin friction.

TEST CASES AND RESULTS

1. FLAT PLATE

The plate dimensions considered for this investigation are 2mx2m. The plate is placed perpendicular to the flow as shown in Figure 6a. The flat plate is specified with just two surface triangles in STL file. The surface mesh resolution does not matter as the volume mesh is made irrespective of the surface refinement. This case is important in the IB framework because it illustrates the IB support for baffle (zero-thickness) surfaces.

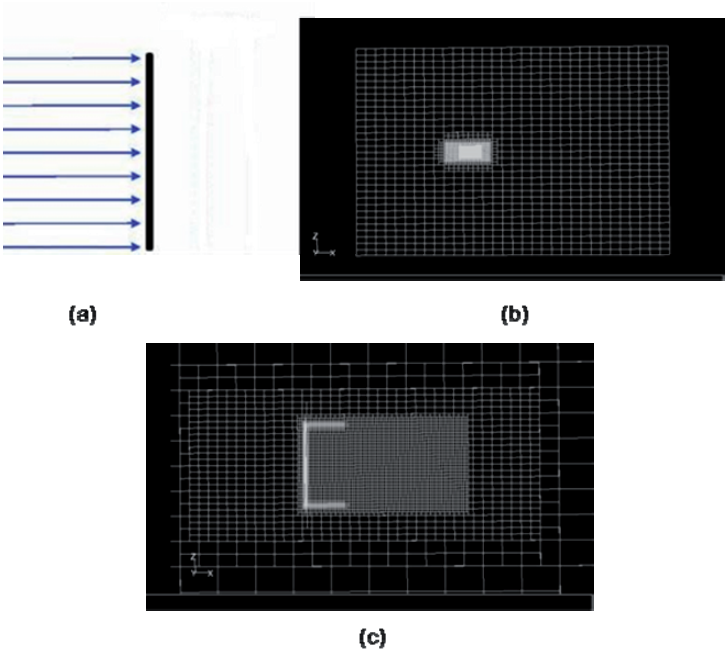

Fig. 6 (a) Schematic diagram of flow impinging on a squared flat-plate at 90^o to the flow; (b) Symmetry plane view showing computational domain for flow over a perpendicular flat-plate; (c) Zoomed-in view of mesh near flat-plate.

The Reynolds numbers based on the frontal area ($4m^2$) and the free stream velocity (30m/s) is 8.2×10^6. Mesh comprising of 150,000 cells is made with clustering around the wake and the stagnation regions. Figure 6b shows the symmetry plane for computational domain. A zoomed-in view near the plate and its wake is presented in Fig. 6c. Figure 7 shows the computed streamlines in the symmetry plane.

For the flat plate the experiments have shown that the separation points are fixed and the drag coefficient is 1.17 which is independent of Reynolds number [10]. The simulation result from the IB method is 1.18, which is in very good agreement with the experiments.

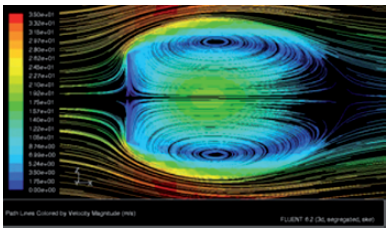

Fig. 7 Streamlines for flow over flat-plate perpendicular to flow direction.

2. BACKWARD STEP

Often the turbulent flow over a backward facing step is used to evaluate the accuracy of various numerical schemes. The main feature is a recirculation region just downstream of the step. The prediction of the reattachment length has proven to be challenging for numerical techniques. A brief review of incompressible flow over backward step can be found in [11, 12].

The step height (H) is 38.1 mm (1.5”), and the height of the inlet channel is 76.2 mm (3”). The uniform inlet velocity of 18.2 m/s is specified eight step heights (8H) upstream of the smaller inlet channel. The computational domain is extended about 29.3H downstream of the larger expansion channel.

A side-view of the computational domain is shown in Fig. 8. It is well known that the grid resolution in the near-wall and the high gradient regions is crucial for turbulent flow calculations. Two grids were tested for grid convergence study. The coarse grid is about ~ $200x10^3$ cells, and the fine mesh is about ~ $1x10^6$ cells. Both grids are generated with a y^+~10, but the fine grid is more refined in the recirculation region.

Fig. 8. Outline of the computational domain for backward step.

Figure 9 shows both the meshes and their respective recirculation regions. The experimental data for the length of recirculation zone is 7.1±0.5H [11, 12]. The simulations reveal a recirculation zone length of approximately 7.03H for the

coarse mesh and 7.11H for the fine mesh. It is clear that, both meshes capture the essential features of the flow in terms of recirculation bubble length and are in very good agreement with the experiment.

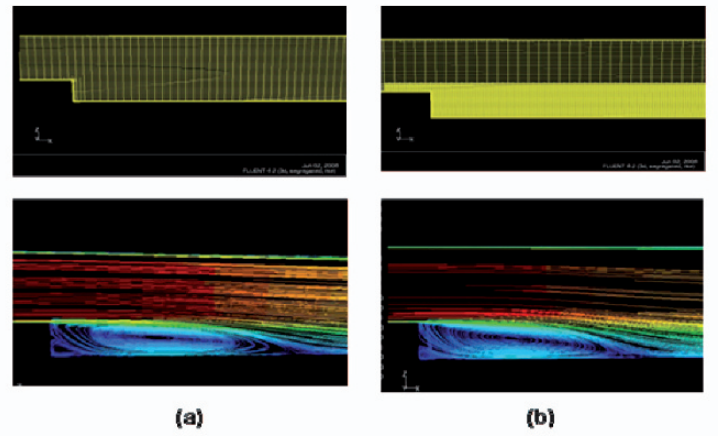

Fig. 9 Side-view of the mesh (top) and the streamlines (bottom). The colors represent the velocity magnitudes: (a) Coarse mesh; (b) Fine mesh

3. THE SEDAN

A picture of a sedan (97 Pontiac Grand-Prix) used in this study is shown in Figure 10. The length of the model is ~ 5m (x axis), the width is ~2m (y-axis) and the height is ~ 1.4m (z-axis). A coordinate system is attached to the front tip of the vehicle in the symmetry plane. The water-tight car surface was exported in STL format from HYPERMESH with overall 270,800 surface triangles. The geometry was distributed over 84 STLs including 18 baffles. Four fluid zones were generated in TOMMIE, one each for the outer body, the radiator, the condenser, and the fan.

Fig. 10 1997 Pontiac Grand-Prix

The model is placed in a wind tunnel test-section with a cross-section of 2.1Lx1.1L, where L is the length of the vehicle. The length of the test section is about 4.3L. Figure 11 shows the symmetry plane of the computational domain depicting the location of the car with respect to the wind-tunnel. A free-stream velocity of 22.352 m/s is specified at the inlet with a low turbulence intensity of 0.6%. The Reynolds number based on the vehicle length and the free stream velocity is 7.6 x 10^6. The outlet is specified as pressure outlet and the wind-tunnel walls are treated as no-slip walls. Heat exchangers are treated as porous media and the fan-outlet surface is specified as momentum-jump based on the normal velocity (Fan BC in FLUENT).

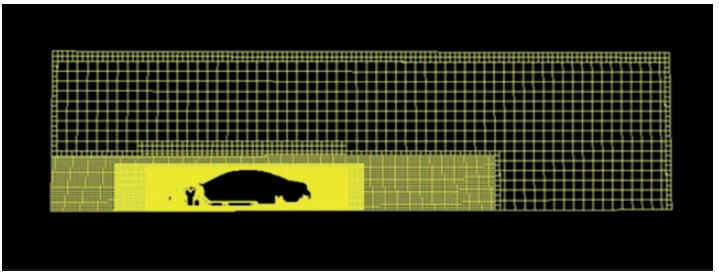

Fig. 11 Symmetry-plane view of the wind-tunnel test section for the sedan.

Three different IB meshes are considered for investigating the effect of grid refinements. These meshes, referred to henceforth as "IB1", "IB2", and "IB3", respectively, differed only in the number of cells used for the simulations. Case IB1 contains about 12 million cells, IB2 has about 16 million cells, and IB3 is about 17 million cells. TOMMIE requires about 4 CPU hours and 7 GB of RAM for IB1 case (12 million) on an IBM p655 workstation. The IB simulations were compared to the conventional body-fitted approach. For the body-fitted approach two different simulations of 7 (BF1) and 10 million (BF2) cells were carried out. TGRID was used for the volume meshing in the body-fitted cases. An image of the mesh in the symmetry plane for cases IB3 and BF2 (body-fitted) are shown in Fig. 12.

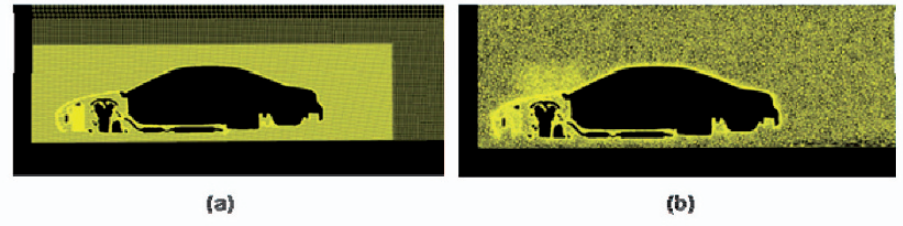

Fig. 12 Side-view showing mesh density near the sedan and its wake: (a) IB1; (b) BF2

The residuals for each of the flow variables were monitored and solution convergence was achieved when the residuals were down to approximately 10^{-5}. Figure 13 shows the convergence pattern for both simulations. Convergence of IB meshes per iteration seems to be similar to that of the regular body-fitted meshes.

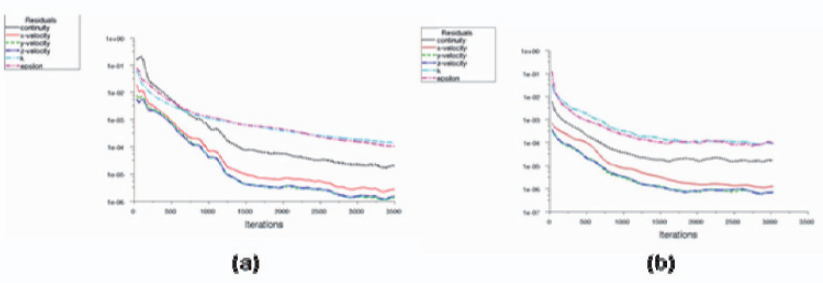

Fig. 13 Relative FLUENT residuals for flow variables depicting convergence: (a) IB3; (b) BF2

Figure 14 shows the velocity contours for IB (IB3) and body-fitted (BF2) meshes in the symmetry plane. Both simulations show similar qualitative features. There is a stagnation region in front of the vehicle, the flow then accelerates on the hood and stagnates at the wind-shield bottom. It then strongly accelerates on the front wind-shield. There is some pressure recovery on the top of the cabin. The flow then separates at the edge of trunk. The underbody flow also accelerates which is due to less area caused by wheels and the underbody components. There is a small wake at the rear end characterized with a strong downwash.

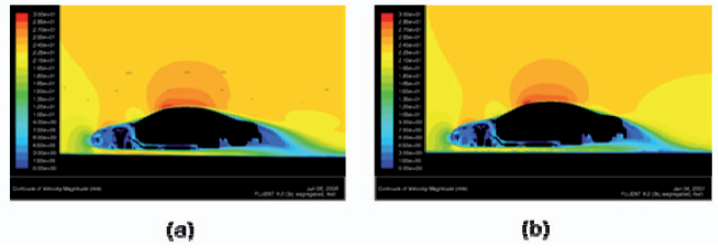

Fig. 14 Velocity contours near the sedan and its wake: (a) IB3; (b) BF2

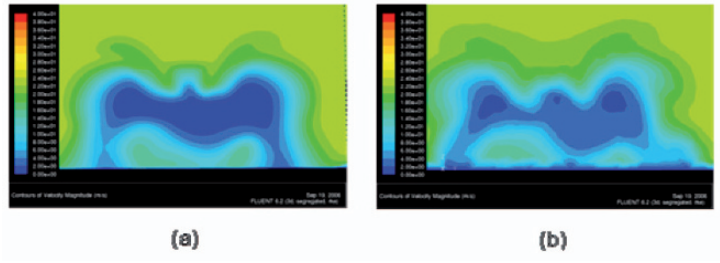

Fig. 15 Cross plane velocity contours in the sedans near wake at x = 6m: (a) IB3; (b) BF2

Figure 15, shows the velocity contour plots in the near wake at an axial plane of x = 6m. The flow looks symmetric which is expected. Also both simulations seem to have a similar flow structure in the near wake.
Pressure coefficients (C_p) are calculated using the equation,

$$C_p = (P-P_{ref})/(0.5\times\rho\times U_\infty^2) \quad (5)$$

where P_{ref} is the reference static pressure measured at the inlet of the computational domain (wind-tunnel), P is the surface pressure, ρ is the air density and U_∞ is the free-stream velocity.

Figure 16 shows the comparisons between the two simulated pressure distributions (C_p) on the symmetry plane. The overall agreement between the body-fitted and the IB simulations is very good. However, peaks in the separation region are somewhat different. This could be due to the absence of prism layers or the sufficient grid resolution near the wall surfaces in IB meshes. Experimental pressure measurement for this vehicle is not available.

Table 1 summarizes the experimental and the computed drag coefficients for this vehicle. The values are normalized by the experimental value. The result for IB3 simulation case is in very good agreement with the experimental results.

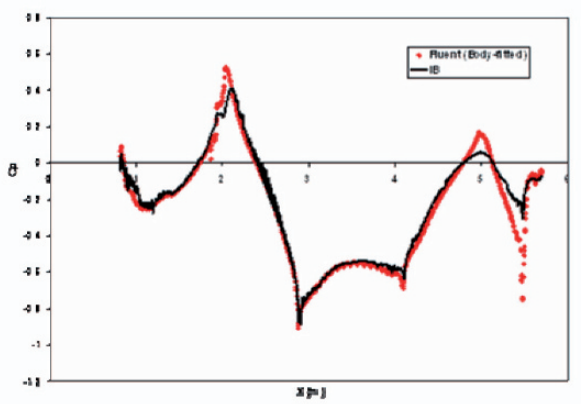

Fig. 16 Pressure distribution comparison on the top of the sedan (symmetry plane).

Table 1 Drag coefficient comparison for the sedan.(Drag coefficients are normalized by the experimental value)

Sedan	Case	Drag Coefficient
Experiment	-	100
IB Simulation	IB1 – 12M cells	101
	IB2 – 16M cells	99
	IB3 – 17M cells	100
Body-fitted Simulations	BF1 – 7M cells	95.3
	BF2 – 10M cells	94.4

4. THE SUV

A picture of the Chevy Tahoe SUV is shown in Fig. 17. The water-tight geometry was exported from ANSA comprising of 923,409 STL facets. A free stream velocity of 31.11 m/s is specified at the inlet of wind-tunnel. All other boundary conditions are similar to the sedan case.

Fig. 17 2006 Tahoe SUV.

The IB mesh consists of 13 million cells, and grid generation took about 4 hours on an IBM workstation. Results are compared to a body-fitted solution-adapted (based on pressure gradient) mesh of 8 million cells. A view of both grids in the symmetry plane is shown in Fig. 18.

Figure 19 shows the velocity contour plots for both the IB and the body-fitted cases. The qualitative features of the flow are similar in both simulations. The recirculation region is slightly larger in the IB case which could be due to the less resolved grid in the wake.

Figure 20 shows the wake streamlines in the symmetry plane. The main features of the flow are the shear layers originating at the upper and lower edges of the model. A strong reversed flow region is formed behind the model which is bounded by these two shear layers. There is a rapid upward deflection of the underbody flow and a strong upsweep in both the computed fields. The upper shear layer in the body-fitted seems to be somewhat thicker than the IB simulations.

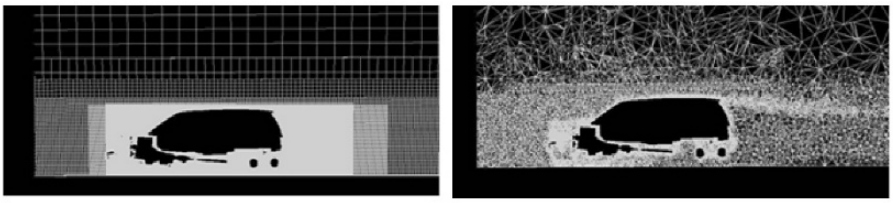

Fig. 18 Side-view showing mesh density near the SUV and its wake: (a) IB; (b) Body-fitted

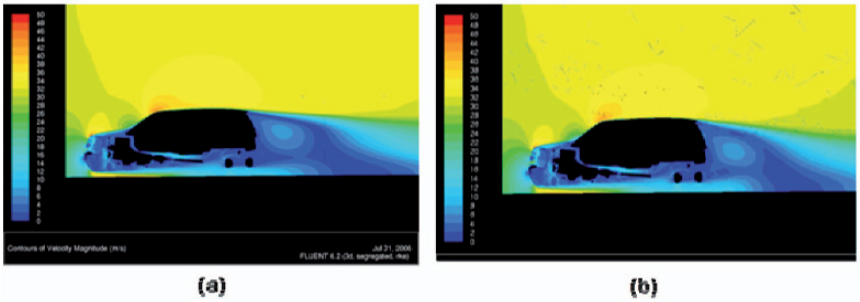

Fig. 19 Side-view showing velocity contours near the SUV and its wake: (a) IB; (b) Body-fitted

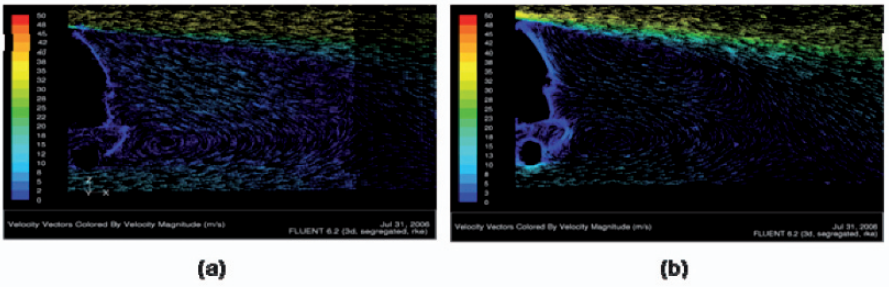

Figure 20. Side-view showing velocity vectors for the SUV in its wake: (a) IB; (b) Body-fitted

Pressure coefficient distributions are presented in Fig. 21. The overall agreement between the two simulations (IB and body-fitted) is very good.

Comparison of drag coefficients for the SUV is summarized in Table 2. The results show that the IB method does a very good job in predicting the drag coefficient.

Table 2 Drag coefficient comparison for the SUV. (Drag coefficients are normalized by the experimental value)

SUV	Drag Coefficient
Experiment	100
IB simulation	97.3
Body-fitted simulation	93.5

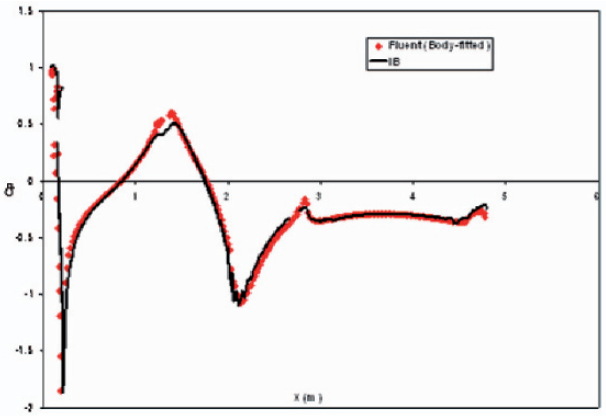

Fig. 21 Pressure distribution comparison on the top of the SUV (symmetry plane).

Conclusions and Future Work

The IB method was successfully validated for flat-plate and backward step geometries. Further, to test its applicability for standard aerodynamics applications in automotive industry, it has been applied to the simulation of the flow past a sedan and an SUV. For the sedan and SUV applications the STL surfaces were obtained from the CAD geometry that had already undergone clean up operations in preparation for the FLUENT body-fitted solutions. These STL files therefore represented "water-tight" surfaces prior to their input to TOMMIE. This was done to compare solver accuracy when the identical surfaces are used for both the IB and body-fitted utilization of the FLUENT solver. The results are in good comparison. Convergence per iteration is similar to traditional body-fitted methods. However, for similar accuracy IB results requires more number of cells. This is due to IB's inability to generate high aspect-ratio cells near angled wall surfaces. The worst case being a surface at 45 degrees to horizontal, for which IB refines in tangential

directions as much as it does in normal direction, thereby increasing the overall number of cells [4].

Future work will study the usage of STL files exported directly from a vehicle program's CAD database with no or minimal CAD clean up operations, sometimes referred to as "raw" STL files. Since CAD clean up operations comprise the majority of time spent executing a typical body-fitted aerodynamics CAE study, a successful validation of the IB method's capability to calculate accurate results using raw STL files will be a significant milestone in reducing project execution times. This in turn will improve the capability of aerodynamic CAE to impact vehicle design decisions.

It is also intended to investigate the IB method for solving coupled flow and thermal problems.

References

1. Ahmed S, "Computational Fluid Dynamics," in *Aerodynamics of Road Vehicles*, 4th ed., Editor: Hucho, W.-H., 1998.
2. Jindal S, Khalighi B and Iaccarino G, "Numerical Investigation of Road Vehicle Aerodynamics Using Immersed Boundary Approach", SAE paper no. 2005-01-0546.
3. Peskin C, "The Fluid Dynamics of Heart Valves: Experimental, Theoretical and Computational Methods," *Annual Review of Fluid Mech*., 14:235-59.
4. Mittal R and Iaccarino G, "Immersed Boundary Methods," *Annual Review of Fluid Mech.* 2005, 37:239-61.
5. O'Rourke J, Computational geometry in C, *Cambridge university press*, 1998.Durbin P and Iaccarino G, "An approach for local grid refinement of structured grids," *Journal of Computational Physics*," pp. 639-653, 2002.
6. Iaccarino G, Kalitzin G, Moin P and Khalighi B, "Local Grid Refinement for an Immersed Boundary RANS Solver", AIAA paper No. 2004-0586, 2004.
7. Iaccarino G and Verzicco R, "Immersed Boundary Technique for Turbulent Flow Simulations," A*pplied Mechanical Review*, pp. 331-347, 2003.
8. Kalitzin G and Iaccarino G, "Turbulence Modeling in an Immersed Boundary RANS Method", C*TR Annual Briefs*, 2002.
9. Iaccarino G, Kalitzin G and Khalighi B, "Towards an Immersed Boundary RANS Flow Solver", AIAA paper No. 2003-0770, 2003.
10. Aerodynamic Drag, Data for Airfoils, Wings, Aircraft, Automobiles, http://www.aerodyn.org/Drag/tables.html
11. Kim J, Kline S and Johnson J, "Investigation of a Reattaching Turbulent Shear Layer: Flow Over a Backward-Facing Step," *Journal of Fluid Engineering*, 102, pp. 302-308, 1980.
12. Chen K and Liu N, "Evaluation of a Non-Linear Turbulence Model Using Mixed Volume Unstructured Grids," AIAA paper No. 98-0233, 1998.

Experimental Characterization of the Unsteady Flow Field behind Two Outside Rear-View Mirrors

Bahram Khalighi[1], James P. Johnson[1], Kuo-Huey Chen[1], Richard G. Lee[2]

[1] General Motors, Warren, Michigan, USA
[2] NRC Institute for the Aerospace Research, Ottawa, Ontario, Canada
bahram.khalighi@gm.com

Abstract The unsteady flow field behind two outside rear-view automobile mirrors was examined experimentally in order to compile a comprehensive database for the validation of the ongoing computational investigation effort to predict the aero-acoustic noise to the outside rear-view mirrors. This study is part of a larger scheme to predict the aero-acoustic noise due to various external components on automobiles. To aid with the characterization of this complex flow field, mean and unsteady surface pressure measurements were undertaken in the wake of two mirror models. Velocity measurements with particle image velocimetry were also conducted to develop the mean velocity field of the wake. Two full-scale mirror models with distinctive geometrical features were investigated.

1 Introduction

The unsteady flow field in the wake of external rear-view mirrors of a typical production car is known to be a significant source of aerodynamic noise inside and outside of a vehicle in motion. The shape of the mirror assembly, its attitude in relation to the flow and the adjacent windowpane, the details of its installation on the car, and the relative airspeed are all factors that can influence the aero-acoustics of automobiles. Because the wake and the adjacent shear layers around a mirror are an important source of noise, a numerical study of the flow field around and in the wake of typical external side-view mirrors was initiated as a collaborative project between General Motors and the Center of Turbulence Research, Stanford University. Experimental validation of the predictions is necessary and it is intended to include the characterization of the steady and unsteady pressures in the wake of two mirrors, as well as direct measurements of acoustic radiation in a well-controlled experiment that could be reproduced easily in the computational domain. These validation measurements were organized in a two-phase wind-tunnel test program: The first phase focused on mean pressure and unsteady

pressure measurements and mean flow field measurements of the mirror wake; the second phase will concentrate on the measurement of the acoustic radiation. This paper describes the first phase of the validation program.

2 Experimental Details

The characterization of the unsteady flow field in the wake of the rear-view mirrors was performed in the 0.9m Pilot Wind Tunnel at the NRC Institute for Aerospace Research (NRC-IAR) in Canada. Each mirror model was mounted at zero-yaw angle on a ground plane model near the nozzle inlet of the test section (Fig. 1). An array of static pressure taps and fast-response pressure transducers (microphones) were located on the ground plane in the wake of the mirrors; additional pressure taps were located on the floor upstream of the mirror and on the reflective surface of the mirror. A two-dimensional particle image velocimetry (PIV) system captured the streamwise (u) and the lateral (v), or vertical (w) velocity components in the wake. The mean or time-average velocity field was determined for three horizontal planes (u- and v-components of velocity and three vertical planes (u- and w-components).

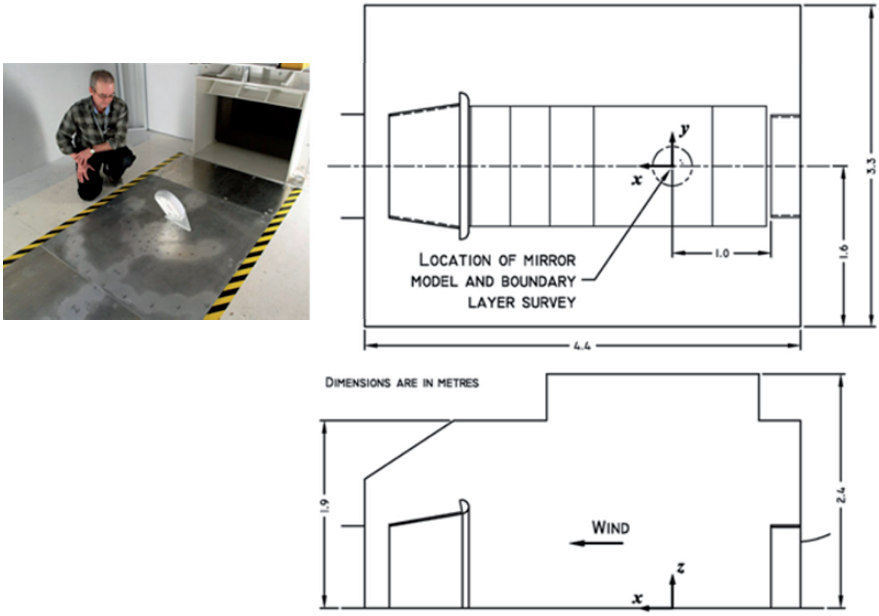

Fig. 1 The layout of a mirror model on the ground plane in the Pilot Wind Tunnel and a schematic of the plenum.

0.9m Pilot Wind Tunnel

The 0.9m Pilot Wind Tunnel at the NRC-IAR is a closed-return facility featuring a ¾- open-jet test section enclosed within a large plenum that is 4 m long, 3 m wide, and 2 m high (Fig. 1). The cross-sectional dimensions of the nozzle exit are 1 m wide by 0.6 m high, and the highest velocity attainable in the test section is approximately 50 m/s. The freestream flow has longitudinal and vertical turbulence intensities of 0.8% and 1.3%, respectively; the displacement thickness of the boundary layer is estimated to be 4 mm at a velocity of 30 m/s.

Measurements of the background noise level for an empty test section were acquired with a microphone placed outside the flow of the test section in a quiescent corner of the plenum enclosure. The sound pressure level reaches a level of approximately 98 dB at 30 m/s, the speed at which the majority of testing was performed. No steps were taken in this experiment to insulate the test section against the noise emanating from the fan and the drive motor. An acoustic resonance in the proximity of 14.5 Hz was known to persist in the plenum. Because the resonance was found to be especially significant at a velocity of 35 m/s, the decision was made to conduct the pressure and PIV measurements at 30 m/s

The coordinate system referred to in this paper is defined in Fig. 1. The x-axis is aligned with the freestream flow, the y-axis is normal to the flow in the lateral direction, and the z-axis is normal to the floor of the plenum.

Mirror Models

The full-scale mirror models that were used in the tests are shown in Fig. 2.

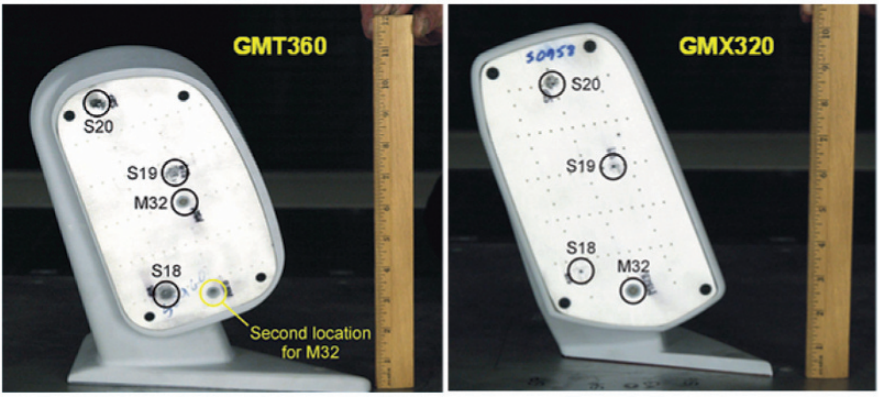

Fig. 2 The mirror models and the layout of static pressure taps and an unsteady pressure transducer on the reflective surface of each model.

The model of the GMT360 mirror is generally found on sport-utility vehicles, features distinctly rounded edges on its windward surface, and is the largest of the mirrors. In contrast, the smaller GMX320 mirror is typically found on the Cadillac brand and has sharper edges on the windward surface of its body. Each body features a cavity that is covered by a model of the reflective surface. For pressure measurements, this reflective-surface model was a thick plastic plate perforated with an array static pressure taps, from which only a few were actually used. For PIV measurements, the reflective-surface model was a simple imperforated aluminum sheet; moreover, the entire surface of each mirror model was painted flat black to avoid undesirable reflections of laser light. The mirrors were mounted on the ground plane model (e.g., the floor of the plenum), which represents the adjacent door window of an automobile.

The location of each mirror model on the ground plane corresponded with the origin of the *x*-*y* coordinate system shown in Fig. 1. This particular model location – being 1 m from the nozzle exit – was selected because it falls within a certain range of longitudinal positions for which blockage corrections to the dynamic pressure are known to be unnecessary.

Mean Pressure Measurements

Measurements from twenty static pressure taps were acquired. Fifteen static pressure taps were laid on the ground plane along the centerline of the test section – three taps were located upstream of the mirror model and twelve taps were placed in its wake (Fig. 3).

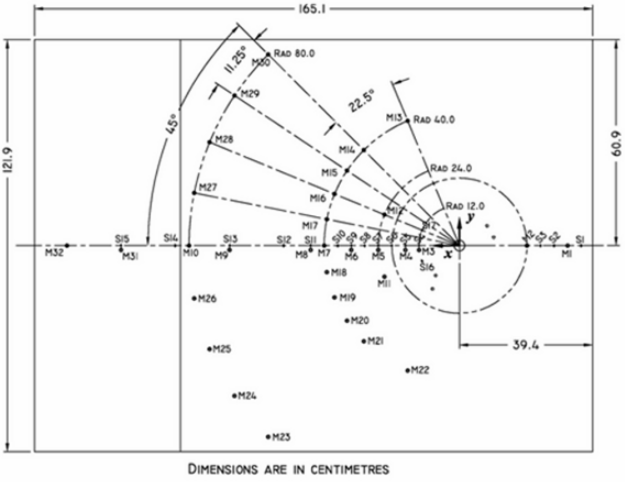

Fig. 3 The layout of fourteen static pressure taps (S) and thirty-one unsteady pressure transducers (M) on the ground plane

Two additional static pressure taps were placed in the wake off the centerline and a further three were installed on the reflective-surface model of the mirror (Fig. 2).

Static pressures were measured with two Scanivalve electronic scanning pressure modules, which have a differential pressure range of 2.5 kPa (10 inches of water) and an accuracy of 5 Pa. Mean pressures were derived from static pressure data acquired at a rate of 100 samples/second for a period of 10 seconds.

Unsteady Pressure Measurements

Measurements of unsteady pressure with sensitive microphones in the wake of a bluff body have been successfully demonstrated, for example, in the case of a two-dimensional backward-step (Lee and Sung, 2002). In the investigation at the NRC-IAR, Brüel & Kjær Delta Tron pressure-field ¼-inch pre-polarized microphones (Type 4944A) were employed to measure the unsteady surface pressures in the wake of the mirror models. The microphones are vented for pressure equalization, have a flat pressure-field response from 4 Hz to 70 kHz, and a dynamic range of 30 to 170 dB(A). With protective nose cones removed, thirty-one microphones were flush-mounted with custom fittings in the ground plane (Fig. 3). Of the microphones mounted along the streamwise centerline of the ground plane, some were collocated with static pressure taps. An additional microphone was installed in the reflective face of the mirror model. Because of the depth of its cavity, two locations on the reflective surface of the GMT360 mirror were possible (Fig. 2); however, only one location was feasible on the GMX320 mirror because of its shallower cavity. Unsteady pressure data was sampled at a rate of 44 kHz for a period of 70 seconds, yielding a frequency bandwidth of at least 20 kHz.

Particle Image Velocimetry

Three measurement planes were selected for each view. Two overlapping image segments of the measurement plane covered the near-wake and the far-wake (a distance of approximately 550 mm in the streamwise direction) and were adequate to resolve most of the recirculation zone, the freestream, and the shear layer in between. The elevation of the views was concentrated on the wake of the main body of the mirror; the wake of the neck was not surveyed. Two hundred double-frame images (the limit that could be stored in the random access memory of the PIV computer) were typically acquired for each segment of the wake. Details of the PIV recording parameters are listed in Table 1. INSIGHT^{TM}, the software package developed by TSI, was used to acquire and analyze the PIV image data. The *deformation grid* scheme – a particle-displacement analysis algorithm developed by TSI for application to high shear flows – was employed to compute the particle displacements in the images. Although it was general practice to acquire the maximum number of images possible, not all were required

by the particle-displacement analysis algorithm to render a satisfactory mean flow field. The number of images processed varied. In the first segment, which covered the near-wake, only seventy-five images were necessary to yield a satisfactory mean flow. In the second segment farther downstream, where high shear flow features were less predominant, twenty-five images were processed instead. Within the total observed flow field, approximately 8,500 velocity vectors were resolved at a nominal spatial resolution of 3.5 mm.

Table 1 PIV recording parameters for mirror wake measurements

Flow geometry	V_∞ = 30 m/s parallel to the light sheet
Maximum in-plane velocity	V_∞ = 35 m/s
Field of view	355 mm × 267 mm (W × H)
Interrogation volume	7 mm × 7 mm ×1.5 mm (W × H × D)
Observation distance	*x-y* plane: 859 mm
	x-z plane: 804 mm (GMT360), 940 mm (GMX320)
Recording method	15 Hz double frame/single exposure
Recording medium	2-megapixel, full frame CCD (1600 × 1200 pixels)
Recording lens	f = 28 mm, f-stop = 1.4
Illumination	Nd:YAG laser, 120 mJ/pulse
Pulse delay	*x-y* plane: Δt = 12.5 μs
	x-z plane: Δt = 12.5 μs
Seeding material	olive oil

3 Results and Discussion

Results for mean pressure, unsteady pressure, and the mean velocity field are presented for 30 m/s. Further results for mean pressure are presented for 14, 22, and 39 m/s.

Mean Pressure

The variation of static pressure coefficient (C_P) on the centerline of the ground plane against streamwise distance is plotted in Fig. 4 for both mirror models and the baseline case (i.e., with no model in place) over four wind speeds. The results reflect the typical streamwise mean pressure distribution fore and aft of a bluff body. Upstream of the models, the increase of positive C_P reflects increasing stagnant flow due to the presence of the mirror. Downstream of the models, the results show two distinct features of the flow field, namely a wake and the attachment of the local flow. The presence of significant negative C_P downstream of the leeward face of each mirror reflects the wake of the model. At the streamwise distance where $C_P = 0$, the flow attaches to the ground plane and the recirculation region

closes. By this indication, the wake of the GMT360 mirror is slightly longer than that of the GMX320, although the latter generally has a higher negative peak in C_P. The fact that GMT360 is taller by 24 mm may partly account for its longer wake. The results for the wake of GMX320 collapse very well over the four wind speeds; for GMT360, however, the variations in C_P suggest a Reynolds number dependence, which may be attributed to the rounded features of its windward surface. Over the reflective surface of GMT360 the base pressure is reasonably constant, whereas for the GMX320 the base pressure varies significantly over the face.

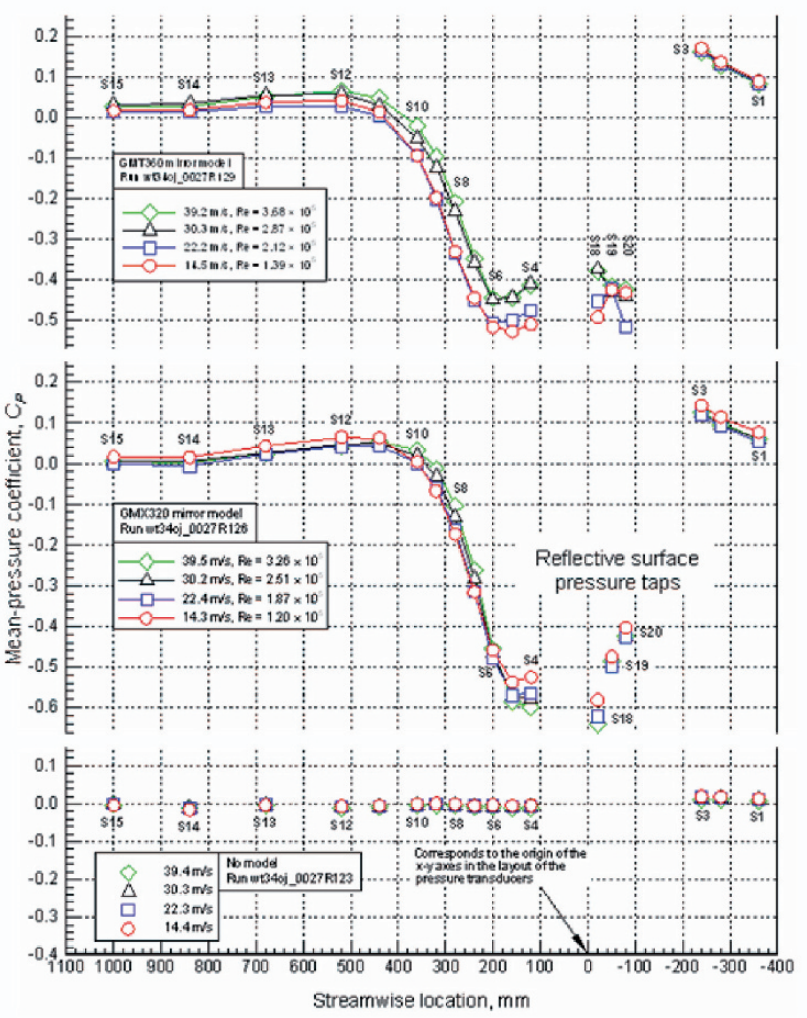

Fig. 4 Mean-pressure coefficient on the surface of the ground plane plotted against streamwise-centerline location for both mirror models and the baseline case.

Unsteady Pressure

Figures 5 and 6 present typical examples of mean-square spectral distributions (S_{Cp}) and coherence functions for both mirror models at a wind speed of 30 m/s. The spectra were derived from data acquired with the microphones embedded in the ground plane and were computed from an average of ninety-four 32,768-point fast-Fourier transforms of the unbiased time-histories of pressure. All plots of spectra and coherence have a frequency resolution of 1.3 Hz. For the coherence plots, correlations were developed with respect to the farthest downstream microphone, e.g., microphone M31 from the line of microphones that parallels the streamwise centerline (Fig. 3).

The mean-square spectral distributions and coherence functions for the GMT360 mirror model are shown in Fig. 5. In Fig. 5a, the results presented are for microphones that are located on the streamwise centerline of the ground plane with the exception of microphone M32, which was located on the reflective surface of the mirror (Fig. 2). In Fig. 5b, the microphones are located off the centerline. In both sets of results, the mean-square spectral distributions are dominated by relatively low-frequency turbulent excitation and sharp peaks are clearly evident in the spectra at a frequency of 45.6 Hz (with the exception of microphones M1 and M3). These features are also reflected in the spectra of the corresponding microphones on the opposite side of the centerline. The corresponding Strouhal number (St) is 0.212, based on the width of the mirror body. The results suggest the presence of an alternating trailing vortex system. The case for trailing vortices is substantiated in Fig. 7c, which shows that a good correlation exists between the centerline microphone M31 and M10/M9/M8/M6

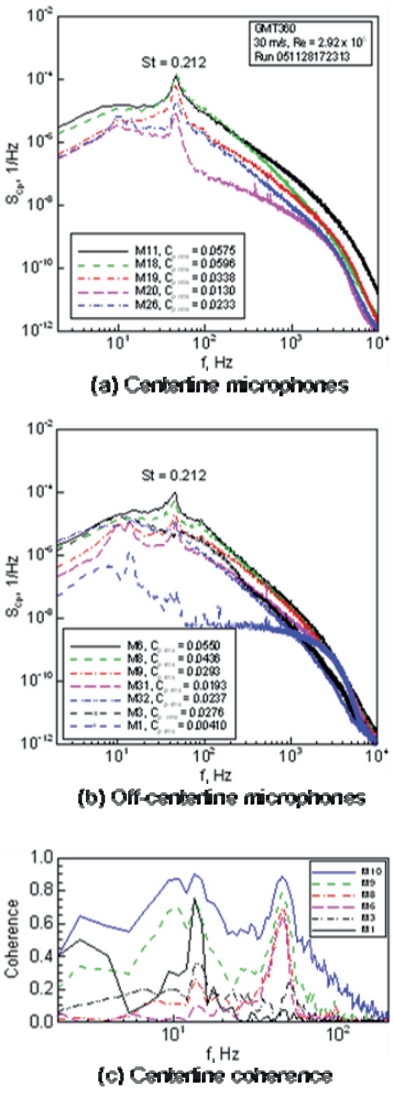

Fig. 5 The mean-square spectral distributions of C_P and coherence functions for the GMT360.

at a frequency of 45.6 Hz, whereas the correlation between M31 and M1 (located upstream of the model) at the same frequency is weak. The fact that centerline microphones in the wake of the mirror are registering the alternating trailing vortices serves as an indication of the size of these flow structures, which emanate from the sides of the mirror. On another note, a reasonable coherence is observed between M31 and M10/M9/M1 at 13.4 Hz, suggesting that these microphones registered the acoustic resonance in the plenum. In contrast, the coherences between M31 and M8/M6/M3 at 13.4 Hz are relatively weak, an indication perhaps that M8/M6/M3 either lie inside or are in close proximity to the recirculation zone of the wake. If so, then the energy of the turbulent excitation within the recirculation zone dominates the energy of the acoustic resonance.

The mean-square spectral distributions and coherence functions for the GMX320 mirror model are illustrated in Fig. 6. The spectra shown in this figure are for the same microphones appearing in Fig. 5. In Fig. 6a the 45-Hz peak identified previously in the GMT360 results, is conspicuously absent in the spectra for the centerline microphones in the wake of GMX320. However, the spectra for the off-centerline microphones, appearing in Fig. 6b, reveal broad shallow peaks in the proximity of 45 Hz. Again, there exists a degree of symmetry in the spectra for corresponding microphones on both sides of the centerline. It is suggested that these results may be the signature of an *Arch*-type trailing vortex, which sheds as one feature from the GMX320 unlike alternating trailing vortices (Okuda and Taniike, 1988). If in fact a trailing vortex sheds from GMX320, then the reasonable correlation between M26 and M19/M20 in Fig. 6c could be an indicator of its track.

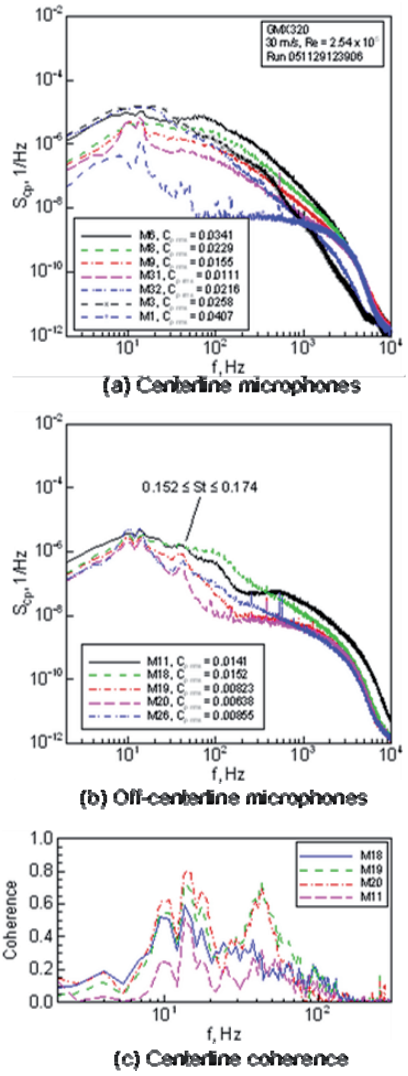

Fig. 6 The mean-square spectral distributions of C_P and coherence functions for the GMX320.

Mean Velocity Field

Typical contour plots of the mean velocity field captured by the PIV measurements in the *x*-*z* and *x*-*y* planes are shown in Figs. 7 and 8 for the GMT360 mirror, and in Figs. 9 and 10 for the GMX320 mirror. The velocity contour plots are compositions of two overlapping segments that captured an adequate length of the main-body wake in the measurement plane. It should be noted that the contour plots are not blended at the juncture of the overlapping segments, nor have the data sets of the segments been integrated. Instead, a composite was formed by overlaying the segments after transforming the local coordinate system of each segment to a common system for the measurement plane (the x_2-y_2 and x_2-z_2 coordinate systems) with its origin located on the reflective surface of the mirror. Each contour plot is accompanied by a series of *u*-component velocity profiles that exemplify the development of the streamwise velocity component within the wake of the main body. The profiles were extracted from the mean velocity field at intervals of equal distance.

In Fig. 7, a number of key features of the mean flow field can be seen in the *x*-*z* plane of the GMT360. These features are the region of local flow acceleration on the top of the mirror, the high-gradient shear layer that emanates from the top of the mirror, and the recirculation zone over the reflective surface of the mirror. Of particular note is the strong tendency for the shear layer and the freestream to be deflected towards the ground plane. The *u*-component profile closest to the reflective surface (x_2 = 75 mm) depicts a large velocity deficit and also a high-gradient shear layer at the top of the mirror. By x_2 = 224 mm the shear layer has diminished and the profiles farther downstream reflect a significant degree of recovery of the velocity deficit.

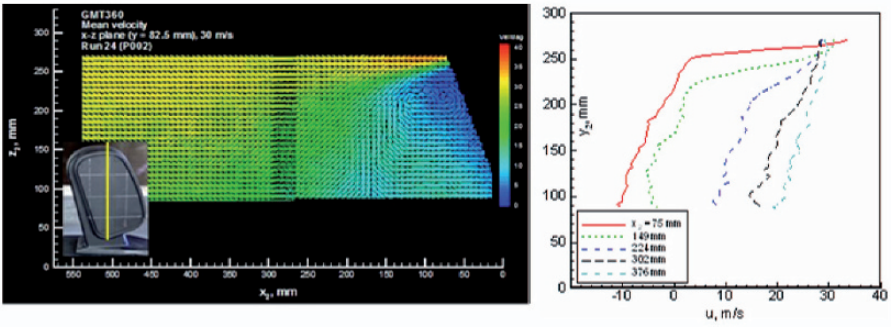

Fig. 7 A typical mean velocity field in the *x*-*z* plane and corresponding *u*-component profiles for the GMT360 mirror model. In the velocity field, the magnitude of mean velocity is represented by colored contours, and arrows indicate the local flow direction; the inset identifies the measurement plane.

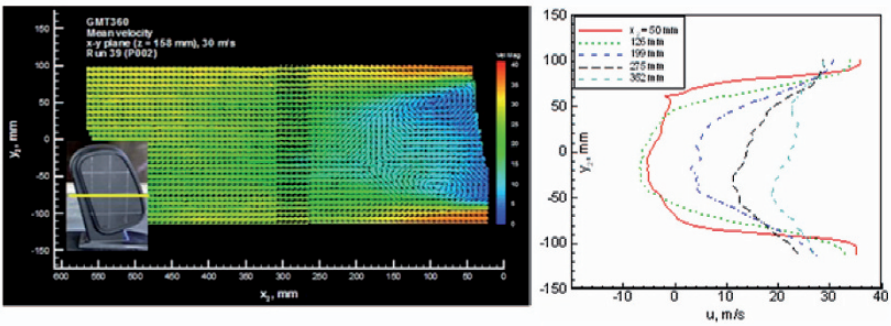

Fig. 8 A typical mean velocity field in the *x*-*y* plane and corresponding *u*- component profiles for the GMT360 mirror model.

In Fig. 8, the recirculation zone, as viewed in the *x*-*y* plane, features two distinct regions of near-stagnant velocity across the face of the reflective surface. Corresponding with these areas are asymmetrical time-averaged vortex structures that alludes to the presence of an alternating trailing vortex. The sequence of *u*-component profiles in Fig. 8 reveals a velocity recovery comparable to that seen in the *x*-*z* plane.

The PIV results for GMX320 reveal a different wake structure. In the *x*-*z* plane, Fig. 9, the shear layer at the top of the mirror is not deflected downward and appears, instead, to remain inline with the freestream flow. In addition, a vortex structure appears near the bottom of the reflective surface, and, at the bottom of the view, there is a significant degree of upward flow, which seems to originate from the region of the neck and the base. In the *x*-*y* plane, Fig. 10, the hint of a vortex structure on the border of the recirculation zone is insufficient evidence to confirm the presence of *Arch*-type vortices trailing the GMX320, as suggested earlier.

In Figs. 9 and 10, the selections of the velocity profiles taken from the wake of the GMX320 mirror are reasonably consistent, in the respective planes,

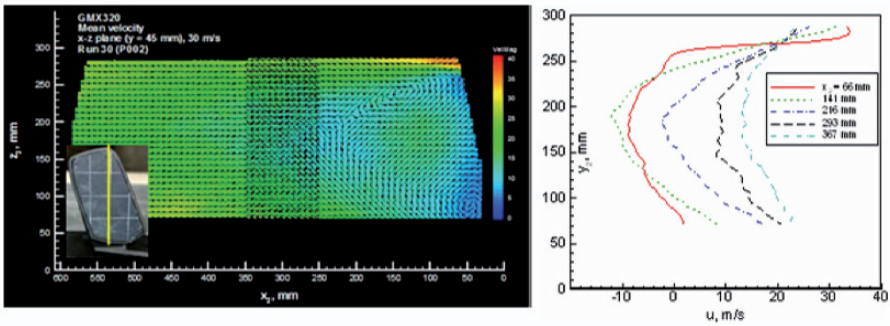

Fig. 9 A typical mean velocity field in the *x*-*z* plane and corresponding *u*-component profiles for the GMX320 mirror model.

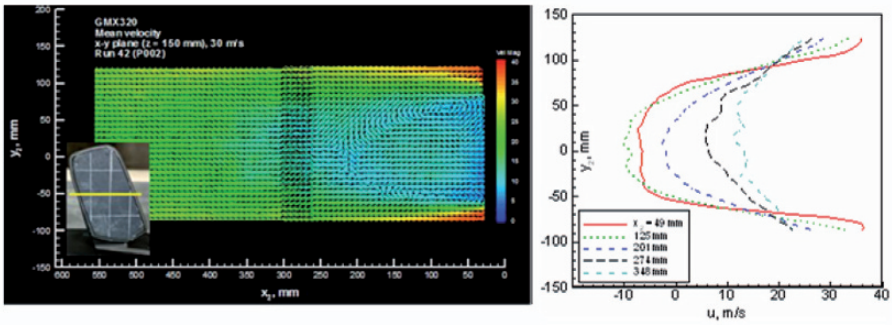

Fig. 10 A typical mean velocity field in the *x*-*y* plane and corresponding *u*-component profiles for the GMX320 mirror model.

beyond 125 mm from the reflective surface. When compared to the wake of GMT360, however, the recovery of the velocity deficit in the wake of GMX320 has a spatial lag. This observation can be readily confirmed by a direct comparison of the mean flow fields in the *x*-*y* plane of both mirrors, shown in Figs. 8 and 10.

4 Closing Remarks

Tests in an open-jet wind tunnel were undertaken to examine experimentally the unsteady flow fields behind automobile side-view mirrors. The tests were conducted to characterize the mean and unsteady surface pressures in the wake of two full-scale side-view mirror models, and also to describe the mean velocity field of each wake with PIV measurements. The distinctive geometric of the mirror models may be responsible for significant differences in the makeup of the respective wakes. The results of the mean pressure measurements, for instance, show that the wake of the GMT360 mirror appears to be sensitive to Reynolds number. Meanwhile, unsteady pressure measurements appear to reveal a difference in the character of the trailing vortices in the wake of each mirror. Moreover, PIV measurements depicted wake structures that are as distinctive as the geometry of the mirrors. The experimental data arising from these tests will be used to validate a computational fluid dynamics code that is a component of a larger scheme to predict aero-acoustic noise numerically

References

Lee I, Sung HJ (2002) Multiple-Arrayed Pressure Measurement for Investigation of the Unsteady Flow Structure of a Reattaching Shear Layer. Journal of Fluid Mechanics 463: 377–402

Okuda Y, Taniike Y (1988) Flow Visualization Around a Three Dimensional Square Prism. Journal of Wind Engineering, No. 37, October. Presented at he International Colloquium on Bluff Body Aerodynamics and Its Applications, Kyoto

Investigation of Buoyancy Driven Flow in a Simplified Full Scale Underhood – PIV and Temperature Measurements

P. Merati[1], C.H. Leong[1], K.H. Chen[2], J.P. Johnson[2]

[1] Department of Mechanical and Aeronautical Engineering,College of Engineering and Applied Sciences, 4601 Campus Drive, Western Michigan University, Michigan, USA
[2] General Motors Corporation, 30200 Mound Rd., Warren, Michigan, USA
parviz.merati@wmich.edu

Abstract Results of the detailed flow measurements for an underhood buoyancy driven flow using a simplified full scale model of an engine compartment, engine block, and exhaust heaters are presented. The engine block surface temperature and exhaust heaters are kept at about 100 ºC and 600 ºC, respectively. This investigation reveals the complex dominant flow structures and thermal behavior of a vehicle underhood under steady state and transient states.

1 Introduction

The objective of this project was to measure the magnitudes of the flow velocity components, temperature values on the engine block and the enclosure, and airflow temperatures under the hood. These measurements were conducted for a full scale simplified underhood configuration without openings under steady state conditions. In addition, feasibility studies were conducted to observe the thermal-flow behavior of this underhood flow for a transient condition as the system goes through its cooling cycle. The simplified underhood geometry that is used for this study is a modified version from an earlier GM R&D's underhood model [1]. The data provided can be used to validate the available and future computational codes for this complicated flow. Buoyancy convection heat transfer plays a dominant role in a vehicle underhood environment during "soaking". The "soak" condition occurs after the vehicle endures high thermal loads due to performing a sequence of operating conditions such as highway driving and trailer grade loads in hot ambient environment (>38 ºC). The vehicle is then parked in a windbreak, and power is shut down. Due to the absence of any underhood airflow from the fans or the ambient surroundings, the underhood begins a thermal process that is dominated by buoyancy driven flow. During this soak process, the temperature of the engine

compartment components can rise in a tightly packed underhood before they start the cooling process.

The work published by Franchetta, et al [2] concentrated on experimental and computational investigation of a half-scaled underhood compartment using PIV, thermocouples, and commercial software VECTIS. These studies [2] were carried out for the transient natural convection condition with openings on the engine compartment model. Franchetta, et al [3] used the data obtained in [2] to validate a developed procedure within VECTIS predicting the "soak" condition with substantially reduced CPU time compared with standard fully transient CFD codes. The PIV and thermal measurement experiments carried out by Merati, et al [4] were conducted for a ¼ scale model resulting in basic understanding of the flow and thermal behavior of this buoyant flow. These experiments were carried out for a closed enclosure under steady-state condition. Three dominant 3-D laminar coherent structures were found to exist at the top of the engine compartment that agree strongly with flow visualization animations and measured air temperature: two counter rotating vortices on the top right corner and over the engine surface and one on the top left corner. The numerical results presented by Chen, et al [5] used the boundary conditions generated in [4] and computed the thermal and flow structure within the enclosure. The numerical results were in good agreement with the experimental results.

The geometry used for the current investigation consists of a glass engine compartment, trapezoidal shaped aluminum engine block and two exhaust pipes. This geometry allows for a simple experimental testing and computational modeling while retaining the general shape and main components of the engine compartment. Additionally, it is interesting to note that the geometry investigated here is a combination of several classical buoyancy driven flow experiments. They include the heated inclined and horizontal surfaces, and heated horizontal cylinders in the proximity of flat inclined surfaces.

This study is a first detailed investigation of this buoyant flow for a full scale model under steady and transient conditions. The detailed fluid flow and thermal results and the physical phenomena obtained from these measurements are valuable information for verification of the computational results and automotive engineers. Future study will concentrate on similar measurements for open enclosure under steady state and transient conditions.

2 Experimental Setup and Procedure

A simulated underhood environment was constructed for the study of buoyancy driven underhood air flow and heat transfer. The experiment was designed to give optical visibility to obtain PIV measurements of airflow and access for measurement of local air temperatures. The geometry used was kept simple, and close control of the temperature of important boundaries was made to aid in computer modeling. The underhood environment consists of the enclosure, the block, and the exhaust heaters. The complete underhood environment is shown in Fig. 1. A scale drawing of the experimental setup with overall dimensions is shown in Fig. 2.

Fig. 1 Complete simulated underhood environment

The enclosure consists of the base, back wall, glass cover, PIV calibration grid, and seeding mechanisms. The back wall contains patterns of holes that provide access for thermocouple measurements of air temperatures. The layout of these holes is shown in Fig. 3. The PIV calibration grid is a 0.125″ sheet of aluminum cut out to fit around the block and exhaust heaters. The grid is mounted to two rods that allows it to be moved forward to the plane of interest. An image is taken of the grid before any PIV measurements are made to allow for scaling of the image and stitching of many images into a composite velocity profile. The seeding consists of injection through a small tube in the back wall.

The block, representing the engine block, oil pan, engine heads, and intake manifold, consists of a sealed chamber for holding the water that maintains the temperature of the block, and a shroud that locates and hides the thermocouples used to map temperature profiles along the block surface. A spray manifold is located inside the sealed chamber to maintain a constant film of water on all the inner walls of the sealed chamber. An immersion heater is placed inside the sealed chamber for heating of the water and block.

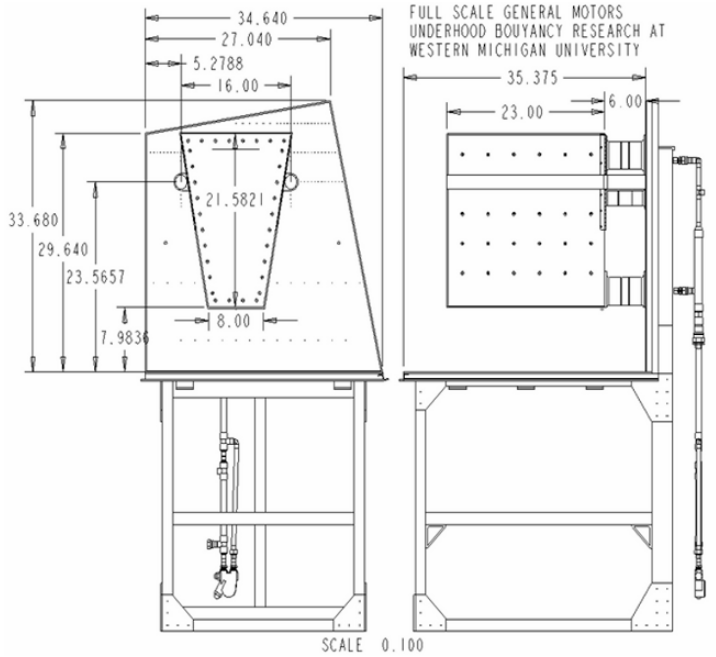

Fig. 2 Overall dimensions of the experimental underhood environment (dimensions in inches)

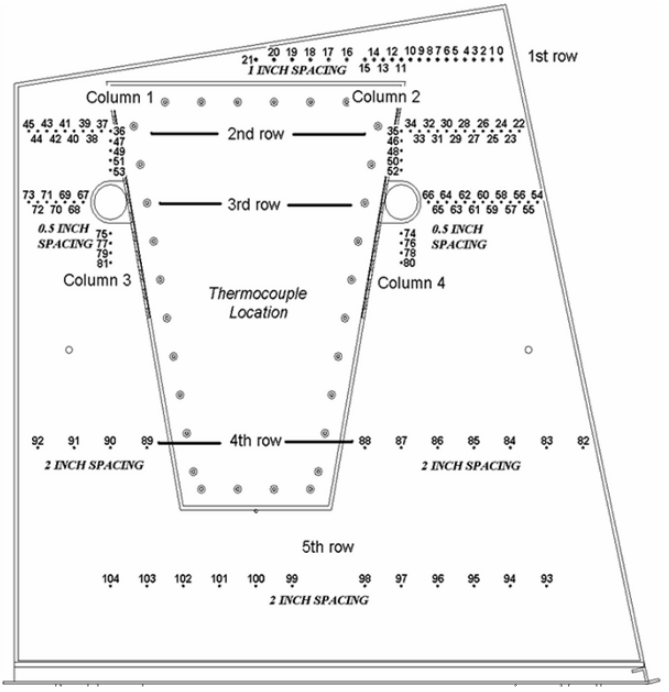

Fig. 3 Locations for air temperature measurements

The shroud was constructed of 0.250″ aluminum plate on the back and 0.125″ aluminum plate on the sides, top, and bottom. The shroud allows for thermocouples to be located at many points on the block without disturbing airflow, which will allow for validation of consistency from one run to the next. The thermocouples are placed in groves machined into the shroud plates as shown in Fig. 4. The majority of thermocouples are located on the sides near the exhaust heaters as this is where the largest temperature gradients are expected.

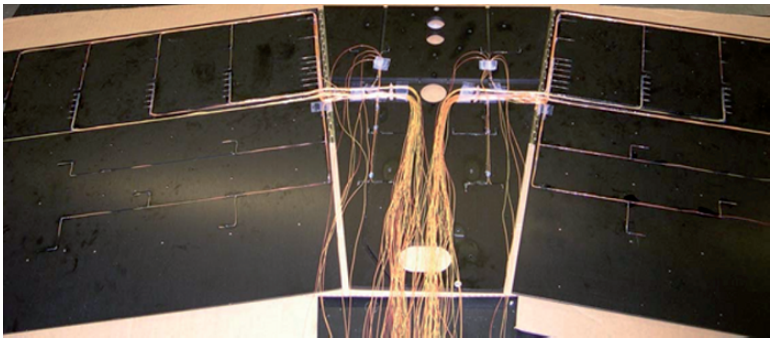

Fig. 4 Thermocouple routing in block shroud

The exhaust heaters, representing the exhaust manifold, consist of a cartridge heater, a steel shroud, a ceramic insulator, and a standoff. The control of temperature for the simulated underhood environment required a water circulation loop and a relay bank control of power. The relay bank consists of four relays that are controlled by the data acquisition system. Two are used to control the power to the two exhaust heaters, one is used to control power to the immersion heater in the sealed chamber, and the last one switches the power to the circulation pump on and off. The control of exhaust heater surface temperature relies on a feedback control loop written into the LabView software, and the surface temperature of the block is controlled through the use of the heat pipe concept. The heat pipe allows for control of surface temperature without a control loop, and the use of embedded cartridge heaters in the exhaust heaters allows for the 600 ºC. The control of the exhaust heater temperature is obtained by using relays to turn the cartridge heaters on and off. Maintaining the surface temperature of the block at 100 ºC is achieved by relying on the fact that for a pure fluid, the temperature of the liquid vapor interface is a function of pressure only. This is maintained by the evaporation with a slight increase in temperature, and condensation with a slight decrease in temperature. The effect is the strongest when a chamber is filled entirely with a single fluid. In this case, water is used as the working fluid. By allowing the chamber inside the block to vent to atmosphere, the evaporation of water inside the chamber displaces the air, and the action of boiling on the heater element also serves to drive dissolved gasses in the water out of solution. This allows for the chamber to be filled completely with water and water vapor after the system has been operating for a length of time. The system is then operated at saturation temperature under the atmospheric condition inside the engine block.

A reservoir of water is maintained in the bottom of the block, and water is circulated through a bank of atomizing nozzles to maintain a thin layer of water on all surfaces inside the block. This thin layer of water creates the liquid-vapor interface needed for this design to function properly. Although the reservoir of water insulates the bottom four inches of the block, the low heat transfer rate on the outside of the block allows the forced convection of the water to remove or add heat as necessary.

Thermal Measurements

Each engine block surface, except front surface, is embedded with thermocouples. External thermocouples are attached to the engine block front surface and enclosure surfaces. The temperature measurements are taken by four-32 channel temperature data conditioning modules and a National Instrument data acquisition card. Furthermore, these measurements are monitored and recorded by a LabView code developed at WMU. The results are then converted to the Tecplot format (FE Block, cell-centered). The thermocouple mesh size and associated areas for each of the engine block and enclosure surfaces are shown in Table 1. The temperature values are obtained at the center of the cells. The temperature mesh distribution and chosen coordinate system located at the point where the inner surfaces of the vertical, bottom, and back enclosure walls intersect are shown in Fig. 5. The temperature of the twelve thermocouples embedded in the two exhaust heater shrouds and the three thermocouples in the water circulation loop are monitored to assure that the system has reached steady state condition.

Table 1 Thermocouple grid

	Location, Side (s)	Thermocouple Grid	Average TC Cell Area (cm^2)
Engine Block	Front (I)	4 × 9	48.1
	Back (II)	4 × 3	150.3
	Right (III)	5 × 11	82.9
	Left (IV)	5 × 11	82.9
	Top (V)	2 × 3	390.3
	Bottom (VI)	2 × 3	196.9
Glass Enclosure	Front (VII)	7 × 9	102.7
	Right (VIII)	9 × 11	123.6
	Left (IX)	9 × 11	107.3
	Top (X)	9 × 11	99.4
	Back (XI)	7 × 9	102.7
	Bottom (XII)	4 × 7	283.3

The engine block is heated internally by water near saturation and externally by the exhaust heaters. The enclosure and the space within the enclosure are heated by the engine block and exhaust heaters. The exhaust heaters are heated to 600 °C, and water spray temperature inside the block is kept at 95 °C. The exhaust heaters, water temperature inside the block, and the average block surface temperature reach their desired steady state temperature after 3,600 sec. All tests are then conducted at this steady state condition except for transient experiments where the system is allowed to reach the steady state and then all heating is turned off for the cool down period.

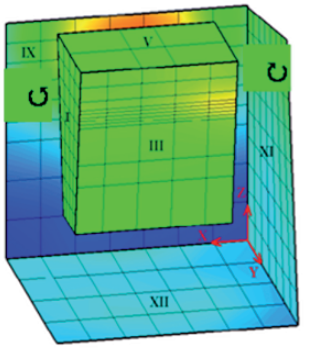

Fig. 5 The chosen coordinate system

Particle Image Velocimetry

The simulated engine compartment and measurement setup for 2D PIV measurements are shown in Fig. 6. Paths A and B are the two orientations used to measure the flow velocities on the left and right sides of the engine block. PIV is conducted on three vertical front, middle and back planes corresponding to X = 317 mm, 444 mm, and 571 mm, respectively. This configuration allowed most of the regions on the sectioned planes to be captured. The exception was the small gap between the cylinder and the engine block side wall where the CCD camera sensor saturated from the reflections on the neighboring surfaces, labeled shadow regions in Fig. 6.

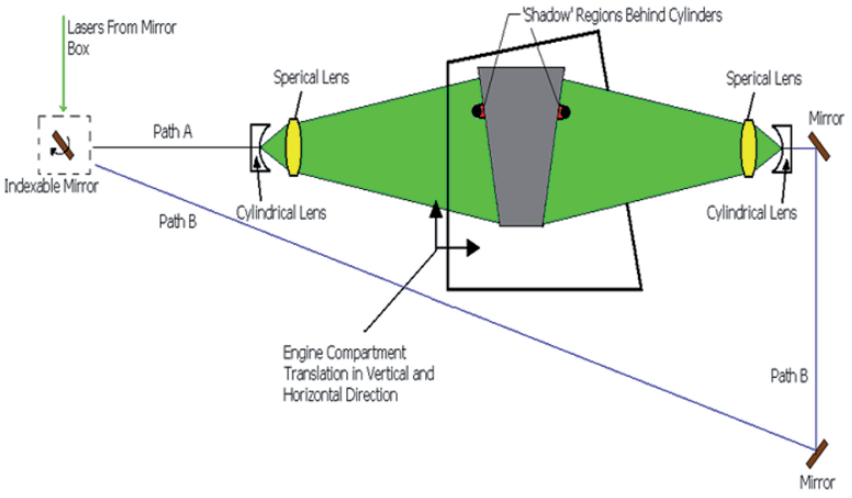

Fig. 6 The simulated engine compartment and 2D PIV setup

The camera field of view for these PIV tests was 12 cm by 12 cm in size. An interrogation area size of 32 X 32 pixels corresponding to physical size of approximately 4 mm X 4 mm provided adequate signal to noise ratio for repeatable results. Thus, to capture velocity field one region at a time, each vertical plane was broken up into 49 separate regions. With this limited field of view, the measurement regions are overlapped to increase vector density and avoid discontinuities near the regions' borders.

Particle Seeding

For seeding, chalk particles are used since they can sustain the high temperature environment around the hot exhaust heaters unlike the commonly used olive oil aerosol. Chalk particles are adequately small in size and weight to capture the flow details within this mostly low speed buoyant flow. A new fluidized bed solid aerosol generator was developed for PIV seeding. Using this seeder, chalk particles are injected into the engine compartment from the back plate holes once the system reaches steady state conditions. Flow disturbances due to particle injection damps out approximately 45 seconds after seeding as observed on the PIV camera. Thus, after 45 seconds, PIV recording sequence was started to capture 200 image pairs at 15 Hz.

3 Results

Engine Block Surface Temperatures

The temperature contours for the top (V), bottom (VI), right (III), left (IV), back (II), and front (I) faces of the engine block are presented in Fig. 7 and the corresponding statistics are presented in Table 2.

The discontinuity of the temperature magnitudes at some of the corners, especially between the right (III) and back (II) faces is due to the large mesh size for the temperature measurements.

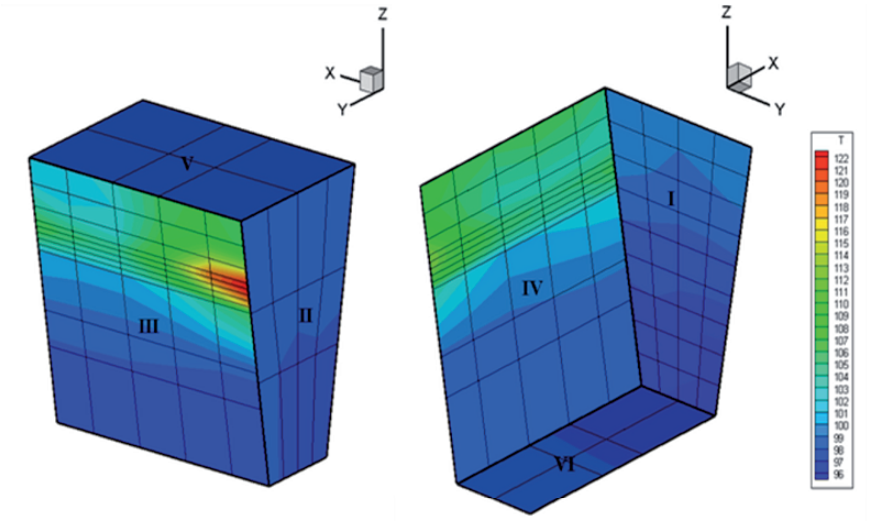

Fig.7 Engine block surface temperature contours

Table 2 Engine block surface temperature statistics

Engine Block Surface Temperature C°						
	Front (I)	Back (II)	Right (III)	Left (IV)	Top (V)	Bottom (VI)
Mean	97.6	98.2	105.1	103.8	98.6	97.9
Std Dev	1.4	0.5	7.0	4.2	0.1	0.5
Max	99.7	98.9	123.2	113.6	98.8	98.2
Min	94.3	97.2	97.6	98.2	98.4	97.1
Range	5.3	1.7	25.6	15.4	0.4	1.2

The thermal contours presented assume constant temperature over a cell area and does not take into account its thermal gradient. This is because temperatures were only obtained at the center of cells. Measurement of thermal gradients over the cells requires extensive time and effort.

There are small temperature gradients at the front (I), back (II), top (V), and bottom (VI) surfaces. The temperature is slightly higher at the top corners and becomes lower as the distance of Z-axis decreases for the front face. The highest temperature value is found at the right (III) surface closest to the exhaust heater. At the right (III) and left (IV) surfaces, the temperature is high along the axis of the exhaust heaters and becomes lower as the distance from the heaters increases. In addition, the temperature is lower at the bottom of each surface. Temperature gradients exist along the X-axis at the right (III) and left (IV) surfaces.

In the upper back corner of the left and right faces, the temperature is high near the back face, more noticeable on the right (III) surface. In order to verify that this is a real effect and not due to the design of the engine heating system, the engine block was heated to the desired temperature without turning on the heaters for the exhausts. Under this condition, a uniform surface temperature for the engine block is expected. Any deviation from this is most likely due to the errors caused by the thermocouple measurements and the engine block heating system. The surface temperature gradients are found to be much smaller than what were observed with the exhaust heaters at 600 °C. Thus, the observed thermal behavior of the engine block surfaces is caused by the radiated and convected heat from the exhausts and not due to the experimental errors.

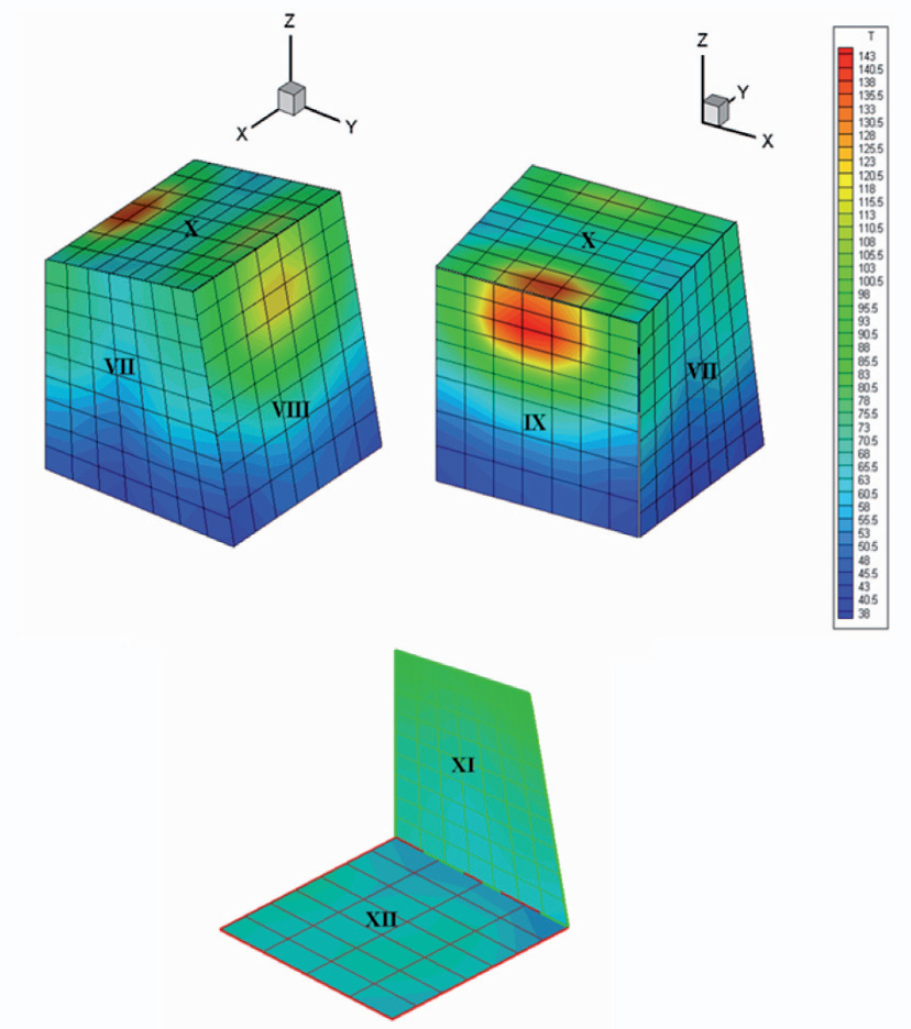

Fig. 8 Enclosure surface temperature contours

Based on the computational results for a ¼ scale geometry by Leong[7] (engine block surface temperature of 120 °C, enclosure wall temperature of 100 °C, and exhaust surface temperature of 600 °C), two large secondary flows shown schematically in Fig. 5 were observed. If the existence of these flow structures could be validated by future experimental work, the larger temperature regions observed on the engine block side surfaces toward the end faces are justified. The vortex structures squeezed between the end faces of the engine block and the front and back sides of the enclosure are the main cause of three dimensionality of the flow near the end faces of the engine block. Thus, the heat of the exhausts at these locations are not mostly carried away toward the top face of the enclosure wall similar to the middle region of the exhaust (reason for higher temperatures observed near the midplane of the enclosure walls, Fig. 8). Instead, near the ends, heat of the exhaust and thermal boundary layers on the engine block surface is constantly convected along the exhaust axis by the end region secondary flows. This effect generates higher temperature on the engine block surface and lower temperature on the enclosure walls near the front and back sides of the engine block. There are less thermal gradients on the enclosure walls on the right side relative to the left side due to existence of turbulent flow observed over the plume near the top regions of the enclosure walls on the right half of the enclosure.

Enclosure Surface Temperatures

The temperature magnitudes are measured on the outside surfaces to prevent the thermocouple wires from disturbing the flow inside the enclosure. Because of the design constraints, the temperatures on the back (XI) and bottom (XII) faces had to be measured on the inside. The enclosure surface temperature contours and statistics are shown in Fig. 8, Tables 3 and 4, respectively.

The high temperature regions are located directly above the exhaust heaters on the top face and closest to the exhaust heaters on the right (VIII) and left (IX) faces.

Table 3 Enclosure inner surface temperature statistics

	Enclosure Inner Surface Temperature ºC	
	Back (XI)	Bottom (XII)
Mean	72.9	59.7
Std Dev	7.3	10.4
Max	89.3	77.7
Min	61.3	40.4
Range	28.1	37.3

The high temperature of these regions is mostly caused by radiation from the exhaust heaters as described in the following section. Temperature distributions on the front surface (VII) show similar characteristics as the engine block front surface. The temperature is highest at the top two corners with thermal gradients along the Y and Z axes. The back face is warmer than the bottom surface with an obvious rise in temperature approaching the exhaust heaters.

Table 4 Enclosure outer surface temperature statistics

	Glass Outer Surface Temperature °C			
	Front (VII)	Right (VIII)	Left (IX)	Top (X)
Mean	59.7	80.6	84.4	83.8
Std Dev	10.4	24.7	32.6	24.0
Max	77.7	124.4	147.2	146.4
Min	40.4	41.2	39.1	58.8
Range	37.3	83.2	108.0	87.6

Temperature Difference across the Wall Thickness of the Enclosure at the Middle Plane

The outside and inside wall temperatures for the right (VIII), top (X), and left (IX) surfaces are measured at the middle plane of the enclosure. The inside and outside wall temperatures for the enclosure wall are shown in Fig. 9. ΔT is the temperature difference across the wall thickness of 3/16″, and r is the distance of the outer thermocouple location from the center of the exhaust heaters

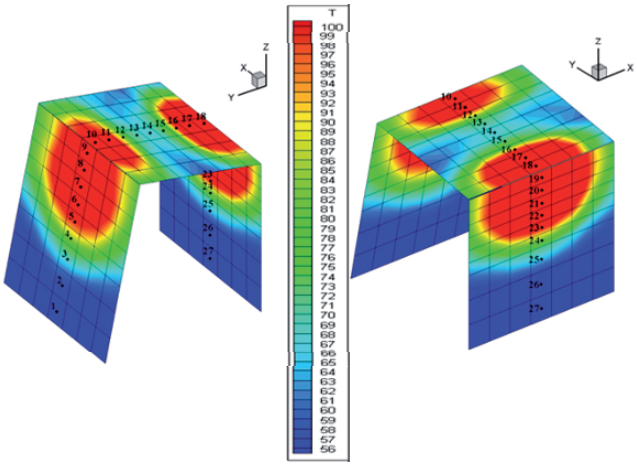

Fig. 9 Middle plane thermocouple locations

As the magnitude of the local temperature becomes higher, ΔT increases, representing larger heat flux across the enclosure wall. The largest temperature difference is observed at thermocouple 17 which is located directly above the left exhaust heater. In addition, on the side walls (VIII and IX), the highest temperature magnitudes occur at thermocouples 7 and 20 with the smallest distance from the neighboring exhaust heaters. Since the highest temperatures occur where the enclosure walls are exposed to the exhaust heaters, it is suspected that most of heat in the hottest regions of the enclosure wall is transferred through radiation. Since heat flux due to radiation is proportional to $1/r^2$, for the hottest regions, the dominance of radiation heat transfer is validated by the correct predicted trend of the $1/r^2$ curves in Fig. 10. On a section of the top surface, the $1/r^2$ curves are not plotted because view of the exhaust heaters is blocked by the engine block. In this region, the radiation is assumed to be significantly smaller consistent with the observed lower temperatures.

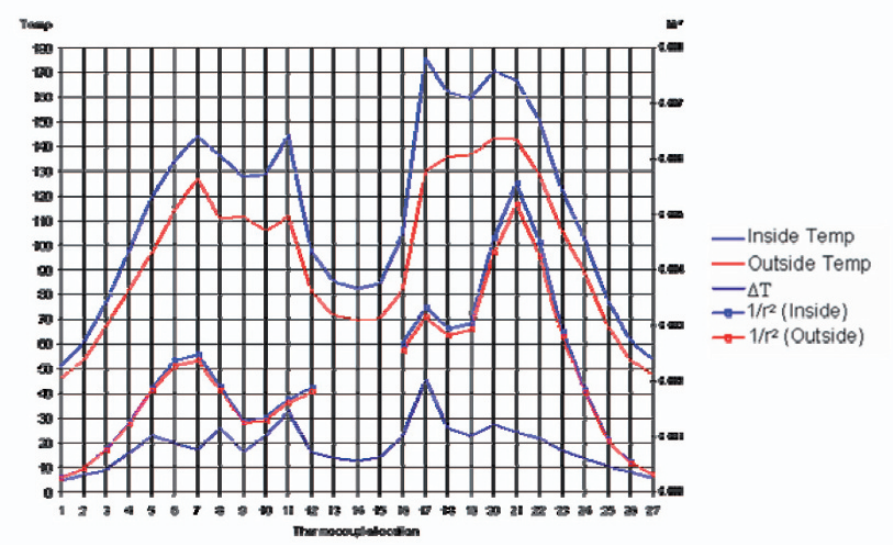

Fig. 10 Inside and outside wall temperatures for the enclosure wall at the middle plane

Air Temperature

Air temperature measurements are obtained on the middle plane with the location labeled in Fig. 3. Since active flow structures in the quarter scale are concentrated in the upper portion of the enclosure, most of the temperature measurements were conducted here. Due to structural integrity of the back plate as part of the support for the engine block, extensive access holes were not implemented. Response characteristics of the thermocouple used for air temperature measurements showed that a 5 seconds cut off and a 45 seconds recording time for actual air temperature

are acceptable. The data shows a general slow increase in temperature since the thermocouple is exposed to not only hot fluid but also radiation from the heated cylinders. Therefore, a cut off time is required.

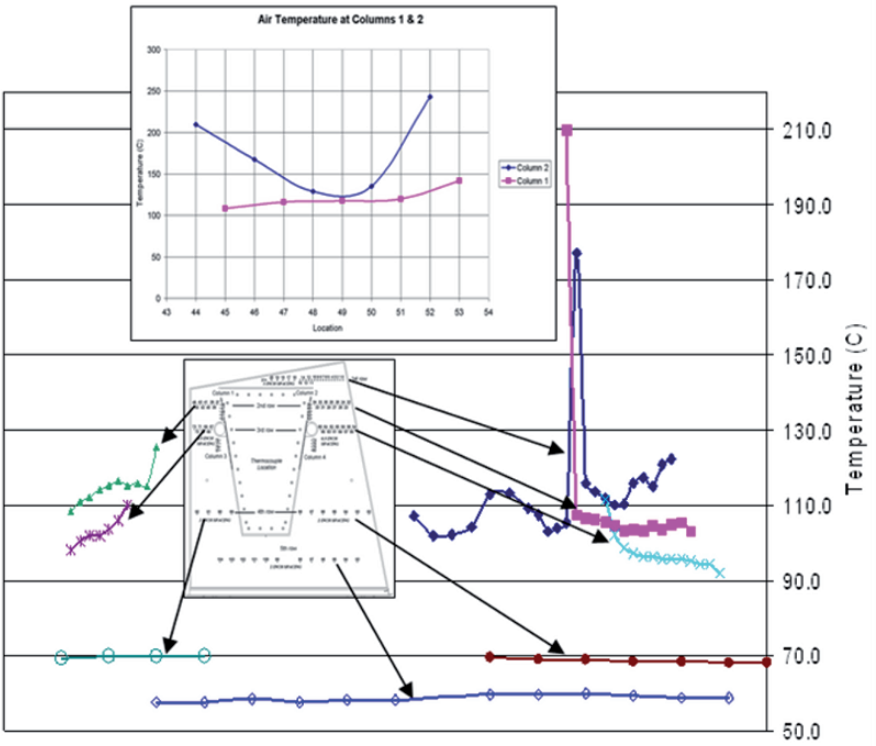

Fig. 11 Air temperature profiles

Figure 11 shows the results of the air temperature measurements using unshielded thermocouples starting from top row. Air temperature on the left side is consistently higher than the right side. The temperature profile for the first row shows the presence of the hot plume and the lobes on the side are consistent with the mixing due to the secondary flows observed by the PIV measurements. Air temperatures of the column 2 thermocouples presented in Fig. 11 are higher than column 1. This is an indication of a hotter thermal layer around the right exhaust heater and the upper right engine block surface. This can only be verified with extensive thermal boundary layer measurements with accurate traversing thermocouple measurements to resolve the large temperature gradients in these regions. The bottom regions, rows 4 and 5 are much colder than the top regions as expected.

Velocity Measurements

Contours of velocity magnitude and standard deviations and their close up views for vertical middle plane are shown in Figs. 12, 13, and 14, respectively.

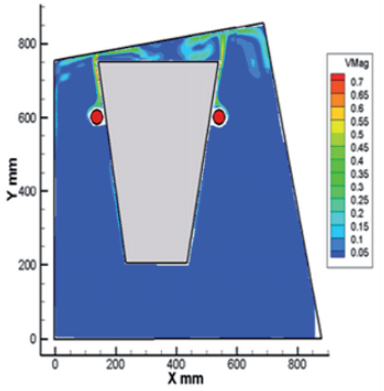

Fig. 12 Contours of velocity magnitudes

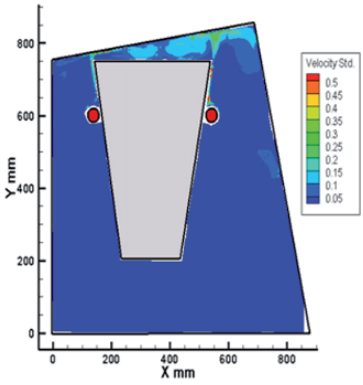

Fig. 13 Contours of velocity standard deviations

Visualized flow with stream traces is shown in Fig. 15. Most of the flow activity within this buoyant flow occurs near the top of the compartment above the exhaust heaters and in the region between the top of the engine surface and the top enclosure wall. The maximum measured velocity magnitude is about 0.72 m/sec above the exhaust heaters. Large flow standard deviations are seen over the engine block and the right top side of the compartment. Two large counter-rotating vortices are observed in Fig. 14.

The flow within this region is turbulent as demonstrated by animation movie created from the instantaneous velocity vector fields above the right exhaust heater. Since the distance from the top of the exhaust heater from the top enclosure wall is larger for the right side compared with the left side, the hot plume on the right has more time to go through flow transition and turbulent stages. The turbulent jet finally impinges on the top surface of the enclosure wall. This phenomenon is clearly shown by six instantaneous realizations of the flow structures in Fig. 16 as the plume cycles through one period of overall flow oscillation. Since PIV was conducted with the laser pulse frequency of 15 Hz, the interval between consecutive images is 0.0667 sec. With six images contributing to a full cycle, the overall frequency of this sweeping turbulent impinging jet is about 2.5 Hz. The entrainment due to the plume shear layer is clearly shown by the ensemble average of velocity traces above the right exhaust heater in Fig. 17.

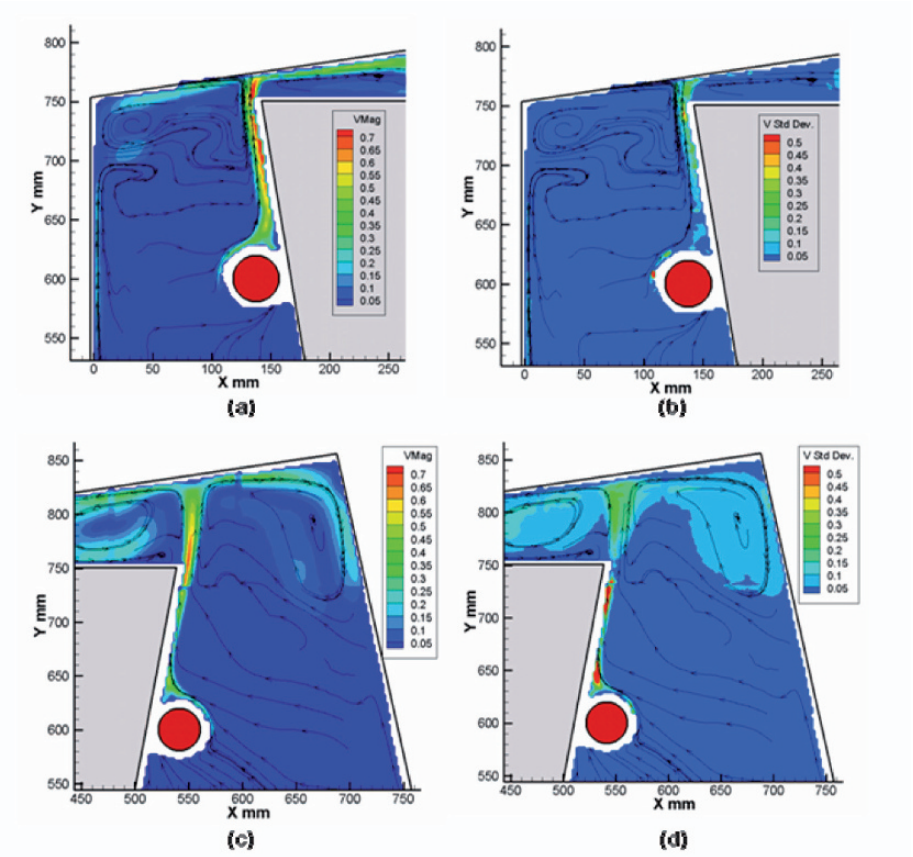

Fig. 14 Regional close up display of velocity contours with stream tracers

The temperature profiles on the enclosure inner surface at middle plane (Fig. 18) show that the wall temperatures are hotter on the left side. In addition, due to the turbulent flow of the top right side, thermal gradients are smaller on the top right side of the enclosure wall relative to the left side

The onset of instability waves and transition to turbulence is clearly observed by visualizing a long candle flame behavior

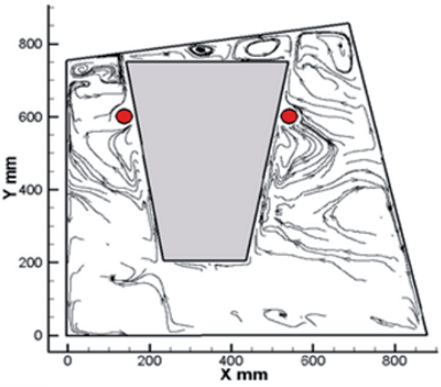

Fig. 15 Stream traces on middle plane

Although flame propagation is not exactly the same as the buoyant flow around a heated cylinder, the hot flame and smoke downstream of the candle flame shows a phenomenon very similar to the hot plume of the exhaust in this experiment. These findings are also consistent with the results of tests performed by T. Maxworthy[6] who generated a hot thermal plume from propane diffusion flames and observed oscillations similar to the ones that are observed here. Extensive studies have been made on forced and cross flow convection of buoyancy driven flow over a cylinder at very low Reynolds numbers. Unfortunately, the authors have not found any work on pure natural convection buoyant flow over a cylinder.

The critical Grashof numbers for flow around a vertical flat plate and around a cylinder are about 10^9. The Grashof number is the ratio of buoyancy force to viscous force as defined by the following equation

$$Gr_{L_c} = \frac{g\beta\,(T_s - T_\infty)\,L_c^{\,3}}{\nu^2} \tag{1}$$

where $\beta = 1/T$ is the volume expansion coefficient
T_s is the surface temperature of the object
T_∞ is the fluid temperature far from the surface
L_c is a characteristic length of the geometry and
ν is the kinematics viscosity of the fluid at $T_f=(T_s+T_\infty)/2$

Calculated Grashof numbers for different geometrical shapes that make this full scale model result in values less than the critical value. However, downstream of the right heated exhaust, flow transitions from laminar to turbulent flow. Thus this flow is composed of different flow regimes, laminar, transition, and turbulent flows depending on the flow location relative to the underhood components.

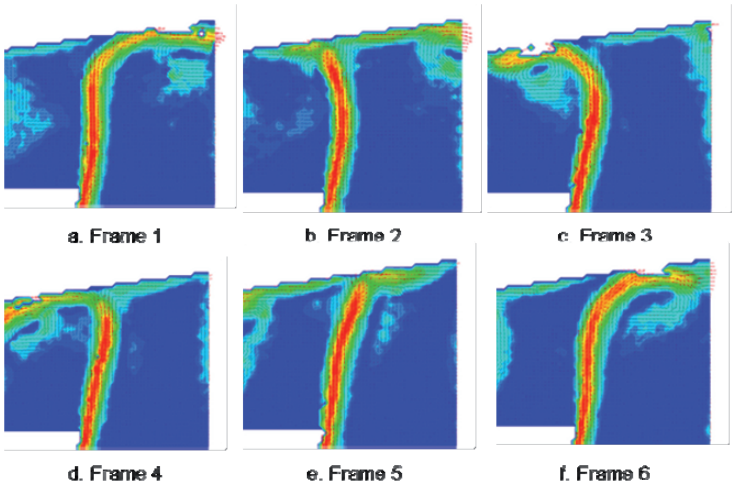

Fig. 16 Full cycle of instantaneous unsteady thermal plume on top of the right exhaust heater

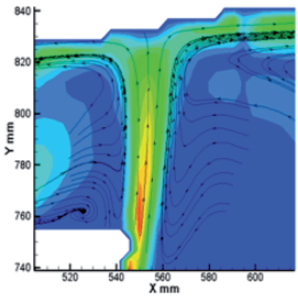

Fig. 17 Velocity traces above the right exhaust heater

Although in the lower regions of the enclosure, velocity magnitudes are in the range of 0.0001 to 0.02 m/sec, stream traces show the details of the flow. Buoyancy generated as the result of hot surfaces of the inclined engine block are the cause of higher speeds in the proximity of these surfaces. The shape of the stream traces near the inclined engine block surfaces indicates the presence of thermal boundary layers caused by hot engine block surfaces observed by a PIV animation video created for the region below the right exhaust heater. At y ~ 400 mm, flow diverts toward the hotter sections of the enclosure surfaces and then it is drawn toward the hotter exhaust heater. This is due to the low pressure region generated around the exhaust as a result of the buoyancy. Plots similar to those of the middle plane are obtained for the front and back vertical planes. Discussion of the flow behavior on these planes is not presented here since flow on these planes is similar in nature to the flow of the middle vertical plane described in previous section.

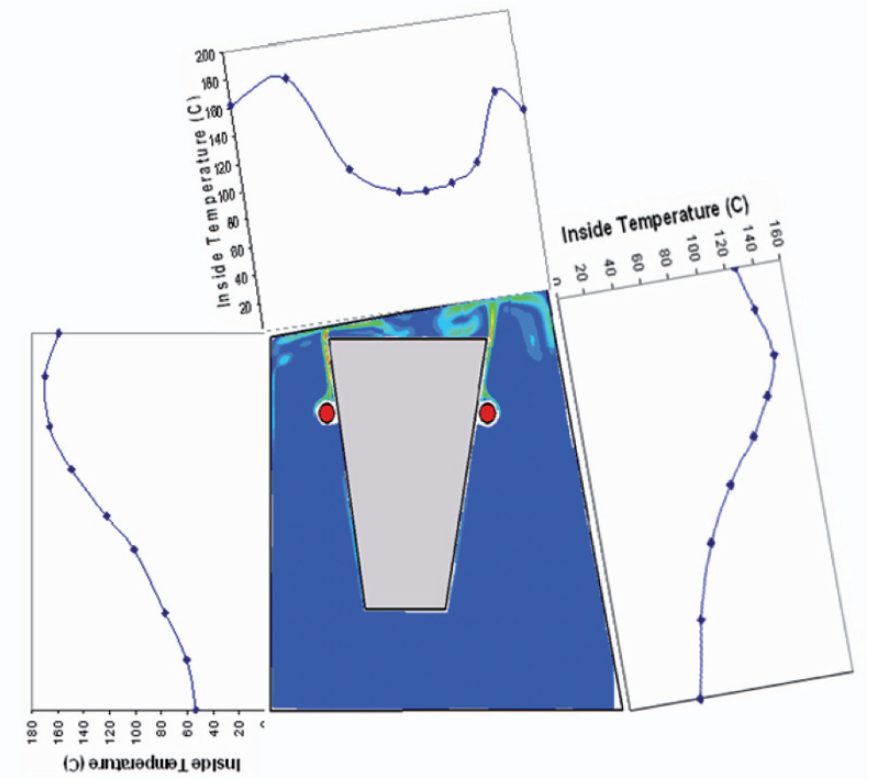

Fig. 18 Enclosure inner surface temperature profiles at the middle plane

Transient Velocity and Temperature Measurements-Feasibility Study

Final part of this project was to assess the feasibility of conducting transient PIV and temperature measurements. The challenge for PIV measurements under transient conditions is that seeding particles at very low speeds drop out of the flow field and no longer follow the flow field. At high speeds, the particles attach to the surfaces of the enclosure and the engine block due to moisture and surface roughness. As a result, seeding density has a dramatic effect on data density. However, by initial heavy seeding of the flow, high quality measurements for up to 45 minutes in the region above the right exhaust heater could be obtained without reseeding. PIV measurements were taken every 5 minutes at 15 Hz, recording 200 frames for averaging. This region is chosen since it is over the plume and is expected to be directly affected by thermal changes during transient period of cooling down. Flow in the rest of the enclosure is also changing during transition. However, for transient capture of the flow behavior, PIV is only possible for one region at a time due to large field of view of the entire engine compartment. The sequence of velocity magnitude contour plots in Fig. 19 displays gradual change in the flow characteristics and velocity magnitude. As the hot plume weakens, its centerline is tilted toward the right corner of the enclosure. The small vortex on top of the right corner of the engine block starts to disappear and the large vortex on the left side of the plume migrates toward the right side accompanying the plume. This overall migration might be due to a clockwise mean velocity field throughout the engine compartment due to the slant angles on the top and right surfaces. The animated videos obtained from the velocity fields show that the large oscillation of hot plume begins to die down and eventually disappear as the system cools down. Disappearing of the large oscillatory motion observed under steady state condition can be seen from decreasing magnitudes in velocity standard deviation. Although, low frequency oscillations with small amplitudes on the hot plume still exists, at about 15 minutes from the start of the transition period, large flow fluctuations are completely vanished.

Air temperature at a point in this region was measured, and block temperature was recorded throughout the process. Air temperature was measured at 2.5 minutes interval and block temperature data were obtained every 10 seconds. The data show the temperature change during transient cooling up to 45 minutes. Once all power is shut off, temperature of the exhaust heaters drops and the heat transferred to the engine block is no longer cooled to saturation by the jet sprays inside the engine block. Therefore, the right and left side of the engine block surface temperatures spike immediately after power shut down.

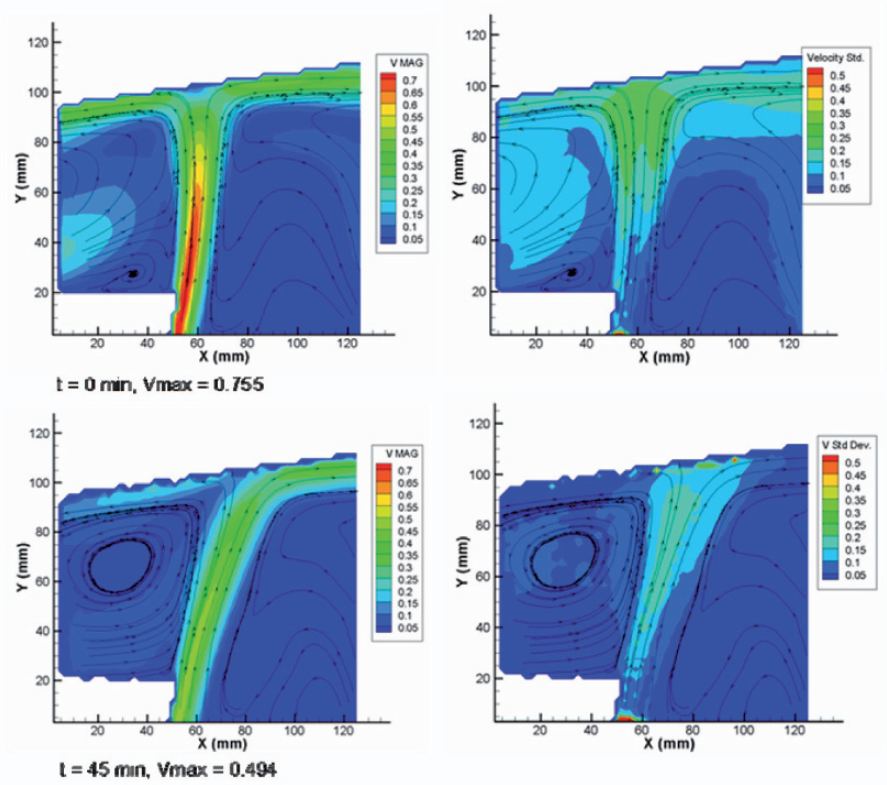

Fig. 19 Ensemble average of velocity fields for the region above the right exhaust heater under transient cooling down process

4 Conclusions

- We have found some differences between the flows for ¼ and the full scale models. This is because the driving force in this flow is the buoyancy that is created by the temperature difference between the hot surfaces and the surrounding flow. The important non-dimensionalized number is Grashof number, a measure of the relative magnitudes of the buoyancy force and the opposing viscous force acting on the fluid. Under the same thermal boundary conditions, the full scale model's Grashof number is 64 times larger than the ¼ scale model. The dominant difference between the two model flows is the transition from laminar to turbulent flow over the right cylinder which was not observed in the ¼ scale model

- For steady state condition, PIV measurements on three vertical planes at X = 317, 444, and 571 mm have shown that flow is turbulent on the right top portion of the enclosure contributing to enhanced thermal convection relative to the top left side. Radiation from the exhaust heaters plays a dominant role in raising the temperature of the enclosure walls in the vicinity of the exhaust heaters.

- The measured dominant structures are two larger counter rotating vortices over the top right side of the engine block and two counter rotating vortices over the top left side. In addition, there exist two dominant smaller secondary flows, one over the top surface of the engine block near its right corner, and one in the top right corner of the enclosure.

- Entrainment of the flow contributes to thick thermal boundary layers on the exhaust heater and slant surfaces of the engine block. Three dimensional computational results conducted for ¼ scale model exhibit secondary flows between the end faces of the engine block and the enclosure walls. These secondary flows are the main cause of the three dimensionality of the flow near the end faces of the engine block. The heat of the exhausts at these locations is not mostly carried upward toward the top face of the enclosure wall similar to what is observed in the middle region of the heater. Instead, near the ends, heat of the exhaust and thermal boundary layers on the engine block surface is constantly convected along the exhaust axis by the end region secondary flows. This effect generates higher temperatures on the engine block surface and lower temperatures near the top regions of the front and back sides of the enclosure walls.

- Air temperature results under steady state condition show that generally the right side is cooler than the left. The temperature profile for the first row show the presence of the hot plume and the lobes on the side are consistent with the mixing occurring due to the secondary flows observed by the PIV measurements. Large temperature gradients over the narrow regions of the plume require a more accurate traversing mechanism for temperature measurements with higher resolution.

- PIV and thermal measurements were conducted during the first 45 minutes after the power to the entire system was turned off to investigate the feasibility of the transient cooling. PIV was only obtained for the region of the enclosure above the right exhaust heater in the middle plane. Air temperature was also measured at a point in this region. However, the entire engine block surface temperature and the exhaust heater temperatures were measured. Once transient cooling starts, the hot plume weakens and its centerline is tilted toward the right corner of the enclosure. The small vortex on top of the right corner of the engine block disappears and the large vortex on the left side of the plume migrates toward the right side accompanying the plume. The turbulent flow observed under steady state condition weakens drastically and the intensity of the

flow structures and in general flow activity begins to slow down with time. The temperature of the block surfaces start to rise for the first 7.5 minutes and then the cooling process begins. This effect is because the heat pipe mechanism of the engine block ceases to function and thus for the first few minutes, the heat of the exhausts is not removed properly.

References

[1] *GMR report, General Motors Research and Development* 1990.
[2] Franchetta M, Suen K, Williams P and Bancroft T, Investigation into Natural Convection in an Underhood Model Under Heat Soak Condition, *SAE Technical Paper Series,* 2005, 2005-01-1384.
[3] Franchetta M, Bancroft T, Suen K, Fast Transient Simulation of Vehicle Underhood in Heat Soak, *SAE Technical Paper*, 2006, 2006-01-1606.
[4] Merati P, Cooper N, Leong C, Chen K and Johnson J, Investigation of the Buoyancy Driven Flow in a Simplified Underhood-Part I, PIV and Temperature Measurements, *SAE Technical Paper Series*, 2006, 2006-01-1698.
[5] Chen K, Johnson J, Merati P, Cooper N and Leong C, Investigation of the Buoyancy Driven Flow in a Simplified Underhood-Part II, Numerical Study, *SAE Technical Paper Series*, 2006, 2006-01-1607.
[6] Maxworthy T, The Flickering Candle: Transition to a Global Oscillation in Thermal Plume, *J. Fluid Mech.,* 1999, Vol. 390, pp. 297-323.
[7] Leong C, Computational Analysis of Heat Convection Buoyancy Pattern using Fluent Simulation Software, *WMU-ME 595 Project Report*, June 26, 2006.

Investigation of Buoyancy Driven Flow in a Simplified Full-Scale Underhood – Numerical Study

K.H. Chen[1], J.P. Johnson[1], P. Merati[2] and C.H. Leong[2]

[1] General Motors Corporation, 30200 Mound Rd., Warren, Michigan, USA
[2] Department of Mechanical and Aeronautical Engineering,College of Engineering and Applied Sciences, 4601 Campus Drive, Western Michigan University, Michigan, USA
kuo-huey.chen@gm.com

Abstract Transient numerical results are presented for simulating buoyancy driven flow in a simplified full-scale underhood in automobile. The flow condition is set up in such a way that it mimics the underhood soak condition, when the vehicle is parked in a windbreak with power shut-down, after enduring high thermal loads due to performing a sequence of operating conditions, such as highway driving and trailer grade loads in a hot ambient environment. For validation, several experiments were conducted to measure the temperature and velocity fields. The simplified underhood geometry, although simplified, consists of the essential components in a typical automobile underhood undergoing the buoyancy driven flow condition. It includes an enclosure, an engine block and two exhaust cylinders mounted along the sides of the engine block. The calculated temperature and velocity were compared with the measured data at different locations near and away from the hot exhaust plumes. The numerical predictions reveal a complex, transient flow structure under the buoyancy condition, and the results show very favorable comparisons with the experimental velocity and temperature measurements. The transient numerical procedure developed for the current study would pave the way for the future numerical simulations of the practical real underhood soaking.

1 Introduction

Buoyancy convection heat transfer plays a dominant role in a vehicle underhood environment during “soaking”. The underhood thermal soaking, or “soak”, condition occurs after the vehicle endures high thermal loads due to performing a sequence of operating conditions such as highway driving and trailer grade loads in a hot ambient environment (>38 degrees C). The vehicle is then parked in a

windbreak, and the power is shut down. Due to the absence of any underhood airflow from the fans or the ambient surroundings, the underhood begins a thermal process that is dominated by buoyancy driven flow. During the soaking, the temperature can rise even higher in a tightly packed underhood environment.

To numerically simulate the underhood soak condition in a full size vehicle, required is a significant amount of computer resources and computational techniques. The soak process is inherently transient and involves a small scale flow motion (usually less than 1 m/s) in a very complex 3D underhood layout. Before this thermal process can be confidently analyzed in a production analysis environment, it is necessary to evaluate the numerical approaches step by step using an idealized geometry that captures the essential features of the flow physics but avoids undue complexity.

A previous experimental and numerical study of similar flow configuration with quarter-scale was conducted [1] [2]. Several numerical issues, including mesh type and size, spatial and temporal accuracy have been discussed [2]. For the quarter- scale case, both experimental measurement and numerical simulation exhibit steady state flow pattern [1] [2] and the agreement between the prediction and the experiment is very favorable in both temperature and velocity. As mentioned previously, the current study using the simplified model is to develop a viable numerical procedure to predict such buoyancy driven flow in an automobile underhood undergoing a soak condition. This development was designed to capture all the essential flow physics with the help of the experiment without involving details of the complication in the real underhood geometries. With this in mind, the quarter-scale study in [1] and [2] might not provide the correct flow physics due to size difference. Nonetheless, the experiences learned, both in simulation and experiment, from the quarter-scale study are very helpful in providing directions in devising a more sophisticated full-scale study. The full-scale configuration is almost identical to the quarter-scale. However, due to the significant increase in size, a new Particle Image Velocimetry (PIV) measuring technique, new type of seeding for the laser and lots more thermocouples for temperature fields are required. The full-scale simplified underhood geometry consists of an enclosure, an engine block and two exhaust cylinders mounted along the sides of the engine block (Fig. 1). The flow condition is set up in such a way that it mimics the soak condition in the underhood. The geometry size difference for the current full-scale study produces quite different flow and temperature fields than the quarter-scale does with a similar temperature boundary condition. Among others, the most significant difference is that both experimental and numerical predictions for the full-scale case reveal a complex, transient flow structure which does not exist for the quarter-scale case. This indicates that the thermal plume driven by the strong buoyancy force above the cylinder becomes unstable at the full-scale configuration. For the full-scale test, in addition to the constant boundary temperature condition measurement, a 45-minute transient cool-down temperature boundary condition and a limited number of temperature and velocity data above the hot thermal plume were taken during the cool-down period.

This paper is organized as follows. A brief overview of the experimental setup and measurement is presented first. Following that, the numerical study using Fluent [3] and the comparison with the measurements are discussed. The plan for further investigation is laid out as well.

2 Experimental Setup

The details of the experimental work were documented well in [4, 5]. In the current paper, the experimental data and experimental setup will be described briefly so that the numerical study can be easily explained. The flow configuration is shown in Fig. 1 in which depicted an outer enclosure, an engine block and two exhaust cylinders mounted along the sides of the engine block. The size of the outer enclosure in the simplified underhood shown in Fig. 1 is roughly 1m x 1m x 1m and it has a slanted hood and sloped dash which mimic the underhood compartment in a production vehicle. The two exhaust cylinders are identical in length and size and they are 584.2 mm long and 45.7 mm in diameter. A brief sketch with dimensions for the experimental setup is shown in Fig. 2. The detailed geometry with dimensions is documented in [4, 5].

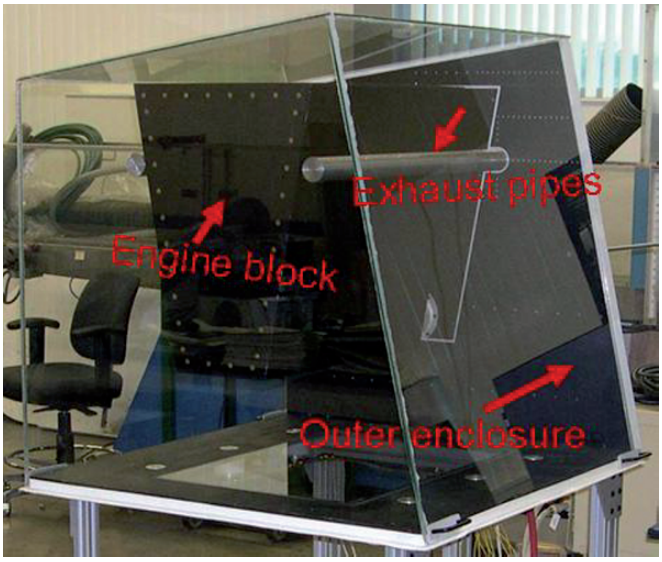

Fig. 1 Experimental setup

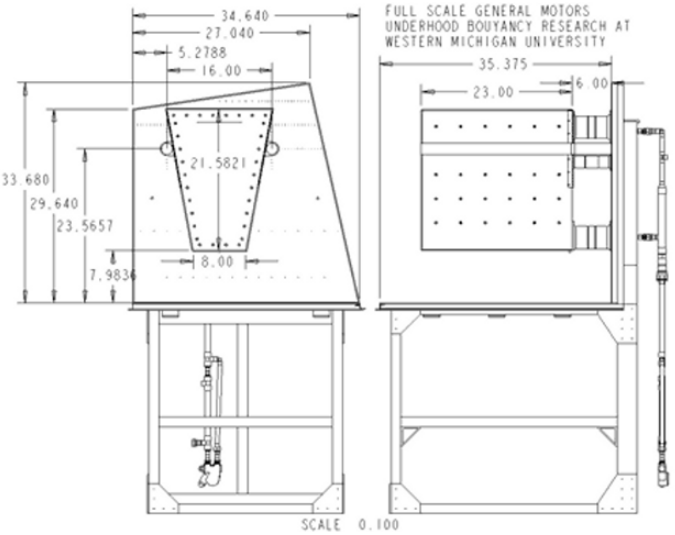

Fig. 2 Overall dimensions of the experimental underhood (units in inches)

2.1 Wall Boundary Temperature conditions

Two sets of boundary temperatures were recorded for the numerical validation purpose. The first is a fixed temperature boundary condition and the second is a time varying cool down temperature boundary condition. They are described as follows.

Fixed boundary temperature

There are three types of boundary surfaces in which temperature distributions need to be experimentally controlled. These three surface types are: exhaust cylinders, engine block and the outer enclosure. The surface temperature of each exhaust cylinders is kept at 600 ºC by inserting a 3500 W cartridge heater into the core of the cylinder. The surface temperature of the engine block is kept at a nominal temperature of 100 ºC by a specially designed water spray circulating system inside the engine block. A total of 116 thermocouples were buried under the skin of the engine block to monitor and record the actual temperature distribution on the engine block surfaces. As can be seen later, some surface areas, due to the proximity to the two exhaust cylinders, are inevitably hotter than 100 °C. This design is much simpler and more effective than that used in the quarter-scale setup [1]. No special device was used to keep the surface temperatures of the outer

enclosure constant. Instead, thermocouples were directly placed on the enclosure surfaces to record the final equilibrium temperature. The total number of thermocouple measuring points on the outer enclosure to map the temperature distribution is 451.

Time varying cool-down boundary temperature

When the vehicle is in thermal soaking condition, the surface temperature in each underhood component is changing with time. To model this cool-down thermal environment, a second set of temperature boundary conditions were recorded. Following the previously described fixed temperature boundary condition, the power used to maintain the temperatures for the exhaust cylinders and the engine block was shut off and the temperature readings were recorded for all the boundary surfaces for 45 minutes. The time history of the temperature cool-down data will provide time varying boundary conditions for another set of numerical validation and calibration. The experimental data of the transient cool-down boundary condition are documented in [4, 5] and are not presented here.

2.2 Air temperature and flow measurements

Air temperature measurement

The air temperatures are measured by thermocouples at 104 locations inside the engine compartment. These locations are on the mid-plane (at y=0) and their locations can be seen in Fig. 3.

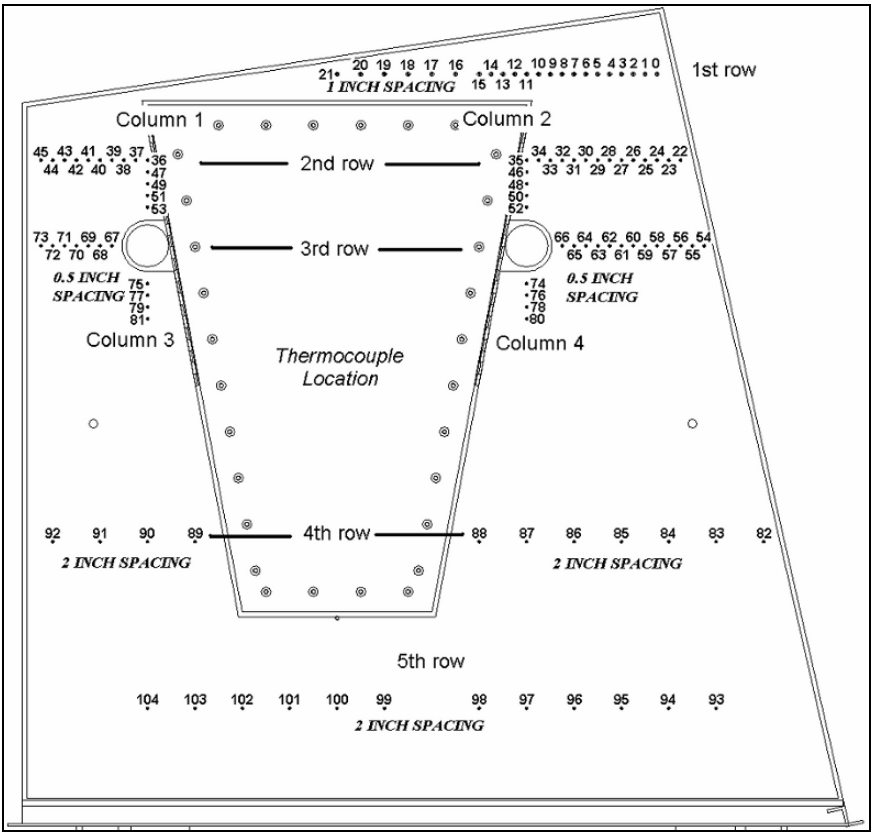

Fig. 3 Locations of the air temperature measurements

PIV flow measurement

The air velocity was measured by a conventional 2D PIV (Particle Image Velocimetry) system. The PIV setup can be seen in Fig. 4. There are three PIV test planes that correspond to mid-plane (y=0), front quarter plane (y=-127 mm) and back quarter plane (y=+127 mm). The camera field of view for these PIV tests was 12 cm by 12 cm in size. An interrogation area size of 32 x 32 pixels corresponding to physical size of approximately 4 mm x 4 mm provided adequate signal to noise ratio for repeatable results. Thus, to capture velocity field one region at a time, each vertical plane was broken up into 49 separate regions shown in Fig. 5. With this limited field of view, the measurement regions are overlapped to increase vector density and avoid discontinuities near the regions' borders. The regions are combined to show the flow statistics on an entire vertical plane.

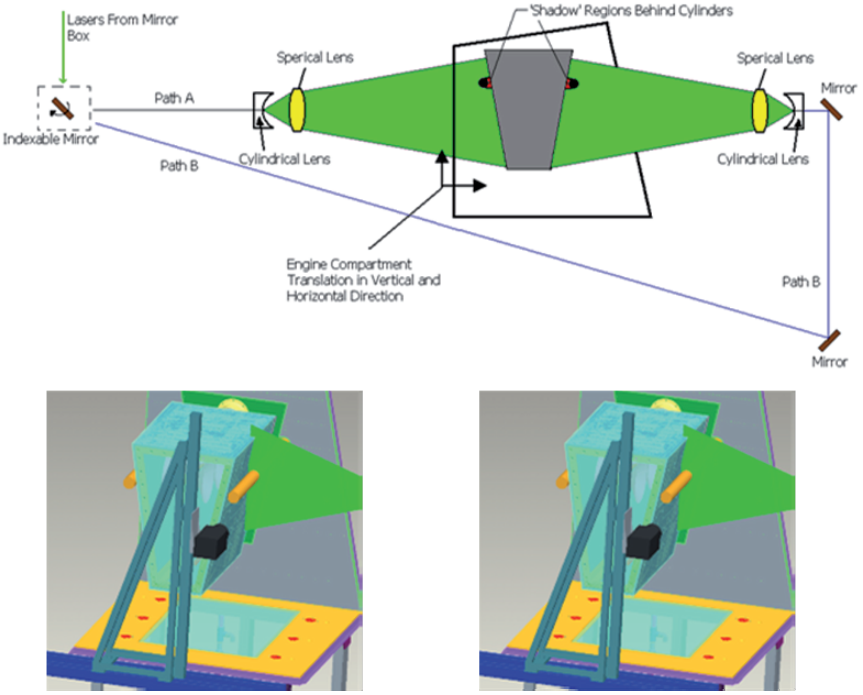

Fig. 4 PIV test setup

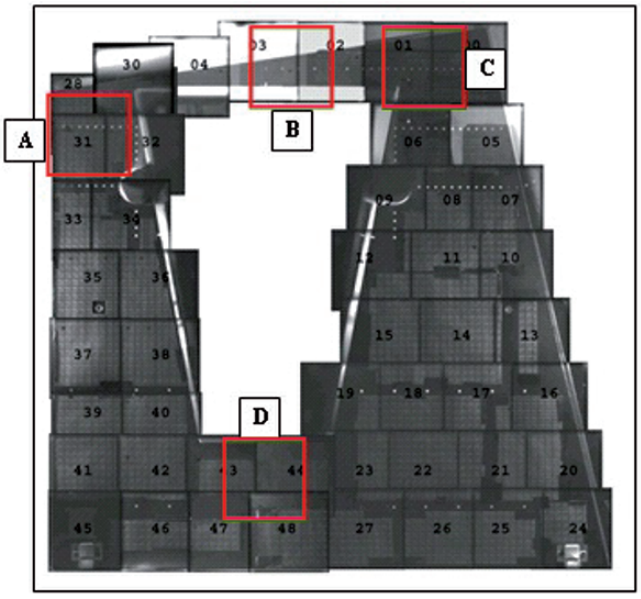

Fig. 5 Stitched overlapping region for PIV.

3 Experimental Results

The experimental results were categorized into three parts: (1). the surface temperature maps on the engine block and outer enclosure, (2). air velocity at the mid-plane, and (3). air temperature at the mid-plane. The surface temperature data are to be used as boundary conditions for numerical validation. The air temperature and velocity from the measurement at the mid-plane are the data to be used for numerical validation and comparison. Again the transient boundary temperature cool-down data described above are in large quantity and are not reported here. It is described in detail in [4, 5].

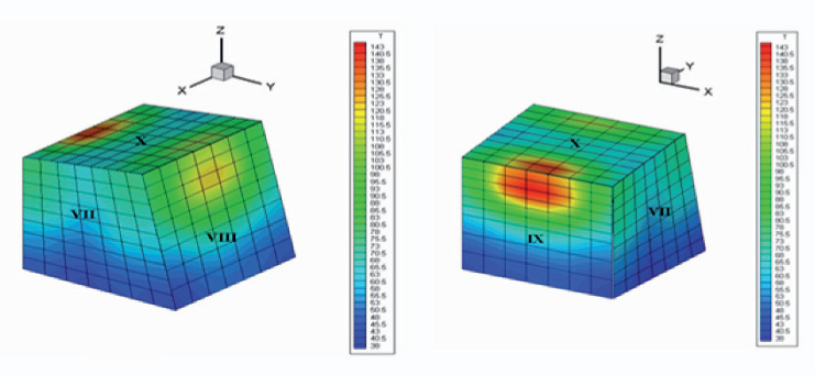

Fig. 6 Temperature maps for the outer enclosure

Table 1 Outer enclosure temperature statistics

	Glass Outer Surface Temperature ºC			
	Front (VII)	**Right (VIII)**	**Left (IX)**	**Top (X)**
Mean	59.7	80.6	84.4	83.8
Std Dev	10.4	24.7	32.6	24.0
Max	77.7	124.4	147.2	146.4
Min	40.4	41.2	39.1	58.8
Range	37.3	83.2	108.0	87.6

3.1 Surface temperatures

The temperature maps on all the surfaces are recorded. These include exhaust cylinders, engine block, outer enclosures and the three pipes which provide the heating and cooling fluids and the thermocouple wiring in and out of the engine block. Figure 6 shows the surface temperature distribution of the outer enclosure. The temperature distribution is quite non-uniform with strong influence from the exhaust cylinders on both sides. Table 1 lists the temperature statistics of the outer enclosure. Figure 7 shows the temperature distribution for the surfaces of the engine block and Table 2 lists the temperature statistics. Again, the surface temperatures on the engine block are much higher than 100 °C due to the proximity to the hot exhaust cylinders. The average surface temperatures of the three pipes at the back of the engine block as seen in Fig. 2 are 95.7 °C for the upper pipe, 92.8 °C for the middle pipe and 74.8 °C for the lower pipe respectively.

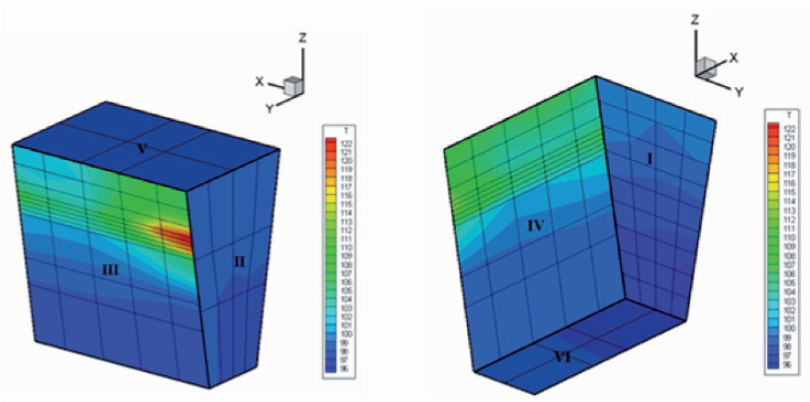

Fig. 7 Temperature maps for the engine block.

3.2 Air velocity at the mid plane

Figure 8 shows a time-averaged velocity contours at the mid-plane with close-up views from the upper left and right corners. Most of the flow activity occurs near the top of the compartment above the exhaust heaters and in the region between the top of the engine surface and the top enclosure wall. The maximum measured velocity magnitude is about 0.72 m/sec above the exhaust heaters. The flow field under the current flow configuration eventually evolves into an oscillating thermal plume above the exhaust cylinders. Figure 9 shows six thermal plume pictures in a cycle which has a frequency of 2.5 Hz. More discussions about the

transient behavior of the thermal plumes will be given when the numerical results are presented.

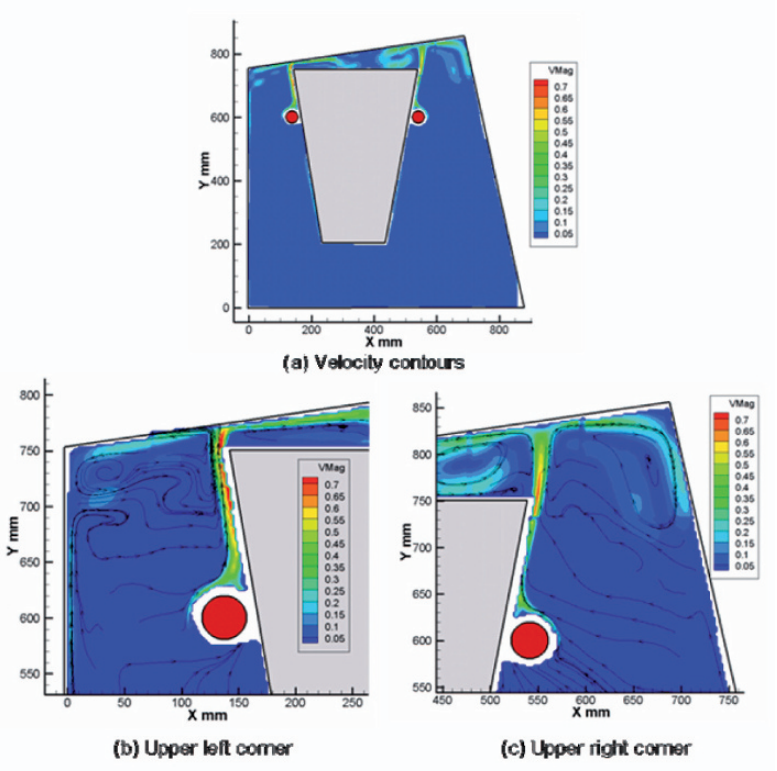

Fig. 8 Time-averaged velocity contours at mid-plane

Table 2 Engine block temperature statistics

	Front (I)	Back (II)	Right (III)	Left (IV)	Top (V)	Bottom (VI)
Mean	97.6	98.2	105.1	103.8	98.6	97.9
Std dev	1.4	0.5	7.0	4.2	0.1	0.5
Max	99.7	98.9	123.2	113.6	98.8	98.2
Min	94.3	97.2	97.6	98.2	98.4	97.1
Range	5.3	1.7	25.6	15.4	0.4	1.2

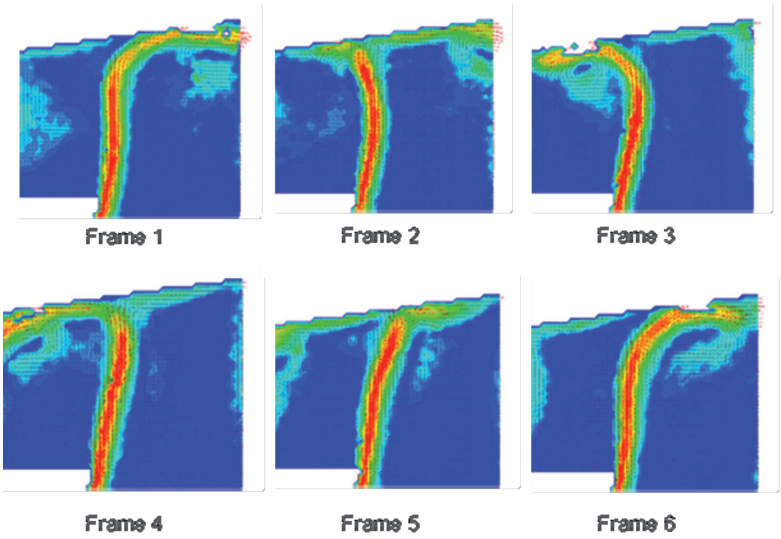

Fig. 9 Experimental instantaneous unsteady thermal plume on top of the right exhaust cylinder in a cycle

3.3 Air temperature at the mid plane

The location of the thermocouples at the mid-plane is shown in Fig. 3. There are 104 thermocouples used at the mid-plane with more distributed near and above the exhaust cylinders and the gap between the top engine block surface and the upper surface of the outer enclosure. The measured temperature distributions for rows 1 to 5 are shown in Fig. 10. These temperatures are to be compared with the numerical predictions and will be discussed later in the paper.

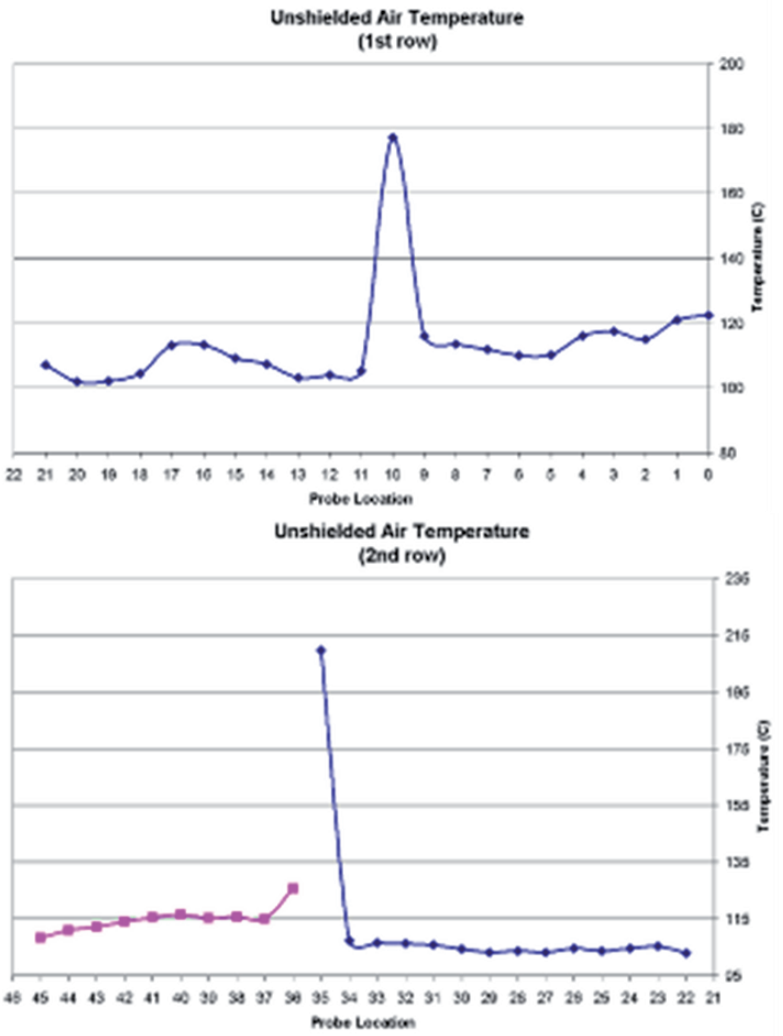

Fig. 10 Temperature profiles at various lines defined at the mid-plane.

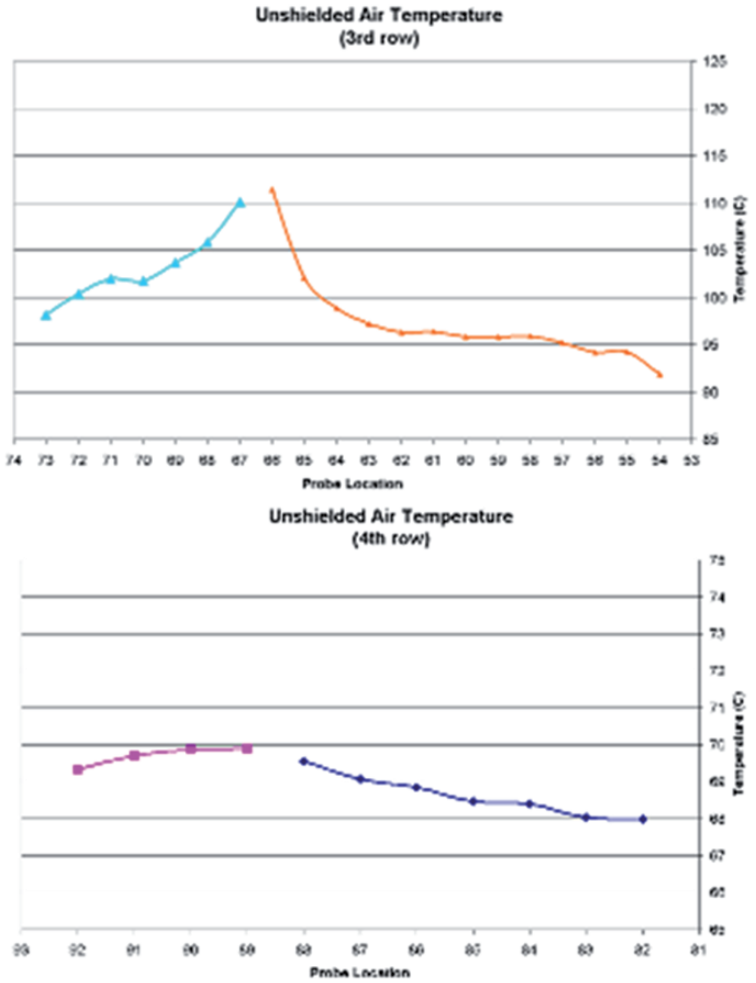

Fig. 10 (Continue)

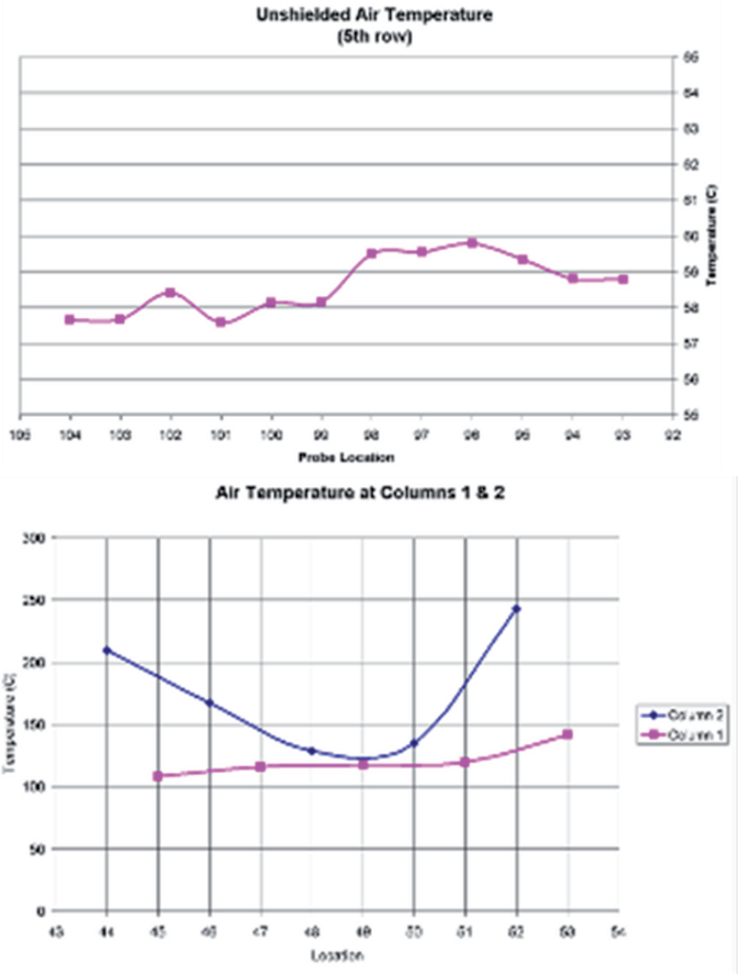

Fig. 10 (Continue)

4 Numerical Results

Numerical simulations were carried out with Fluent version 6.3.26 [3]. From the previous quarter-scale study [2], it was concluded that the 2nd order accuracy in both space and time is best suitable for the present simulation. It also demonstrates that a well prepared tetrahedral mesh can achieve a comparable accuracy with a prism layer mesh. The experiences gained from the detailed numerical study from the quarter-scale study [2] lead to the following mesh size arrange-

ment. The mesh size on the surface of the exhaust cylinders and engine block are 2 mm and 5 mm respectively. The total number of cells is 4.7 million tetrahedral cells. Much more cells were placed near the exhaust cylinders and the upper portion of the engine block to resolve the high temperature gradient and buoyancy induced flow field. The temperature boundary conditions on the surfaces of the engine block and the enclosure are directly obtained from the experimental data shown in Figs. 6 and 7, respectively (see also data in [4, 5]). The temperature on the surface of the exhaust cylinders was kept constant at 600 °C. A no-slip condition is used on all the wall surfaces. The RNG $\kappa-\varepsilon$ turbulence model with a non-equilibrium wall function is chosen to model the turbulence. The air dynamic viscosity and thermal conductivity vary with temperature by Sutherland law [3]. The range of air density variation in the domain was very significant due to the large temperature difference (~500 °C) and therefore the compressible ideal gas law was used to ensure the validity of the solution. A 2nd order implicit time marching scheme with sub-iterations was used to solve the flow and temperature fields from an initially quiescent flow field with a uniform temperature of 60 °C. The size of the time step reduced sequentially along the transient simulation process from 0.01 to 5×10^{-4} second to help obtain fast initial transient flow development and ensure capturing the accuracy of the fine scale flow motion toward the end of the simulation. The sensitivity of the time step to the accuracy of the transient motion will be discussed later in the paper.

The computational domain and the mesh in the mid-plane are shown in Fig. 11. The domain was set up exactly according to the experimental configuration which also includes the two bigger pipes used to support the engine block and to provide the plumbing supply to maintain the desired temperature of the engine block and the middle small pipe for thermocouple wires. The measured temperature maps on the wall boundaries were used to specify as the boundary conditions in the numerical simulation.

The simulation was carried out from a steady state run for 1000 iterations and then switched to the transient mode. The flow quantities were monitored for transient behavior at points 10 and 39 at the mid-plane as indicated in Fig. 12 (see also Fig. 3).

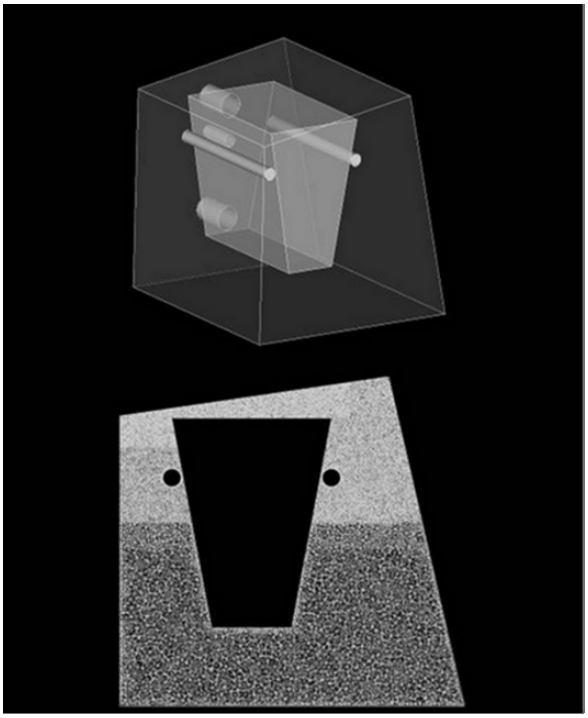

Fig. 11 The computational domain and the mesh at mid-plane.

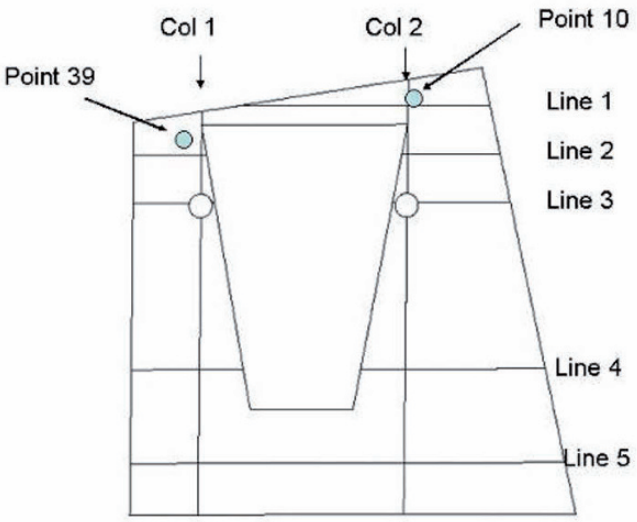

Fig. 12 Velocity and temperature profiles recorded for comparison.

4.1 Transient behavior of the flow

Figure 13 shows the time histories of the velocity magnitude at points 10 and 39. Due to the slope of the upper outer enclosure, the upper right corner has more room for the flow to develop. This can be seen in Fig. 13. It shows that the velocity magnitude at point 10 is much higher values than that at point 39. The time history also shows that the flow fields in the two monitor points are relatively quite for the first 10 seconds. The region at and around the point 39 starts to respond to the effect of the thermal plume originated from the left exhaust cylinder between t = 5 and 15 seconds. The velocity at point 39 stays flat at lower than 0.1 m/s for the next 30 seconds before it turns violent and exhibits a very regular periodic motion with a amplitude of around 0.1 m/s. The time history of the velocity magnitude at point 10 behaves similar to point 39 except that the velocity magnitude at point 10 is much larger than that at point 39.

To gain more insights of the final oscillating pattern, the time histories of the velocity and temperature at these two points for the last 5 seconds are shown in Fig. 14(a) and Fig. 14(b). They are clearly developing into a periodic motion as suggested by the experiment [4, 5] shown above. Figure 15 shows the power spectral density of the velocity at point 10. It clearly reveals a dominant frequency at about 2.53 Hz (the time period T=0.395 s). The frequency recorded in the experiment shown in Fig. 9 is 2.5 Hz. The agreement with the current numerical prediction is very satisfactory. This comparison is also listed in Table 3. The ability to capture the transient accuracy during system integration is extremely important in predicting the correct peak temperature during the soaking stage to prevent part failure due to inadequate heat protection.

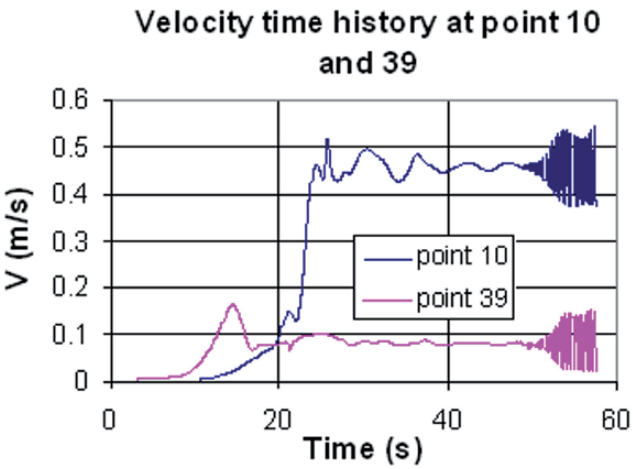

Fig. 13 Time histories of the velocity magnitude at points 10 and 39

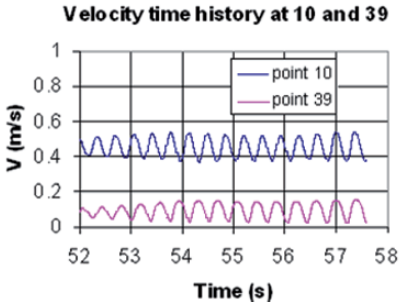

Fig. 14a Close-up view of the oscillating pattern for velocity at points 10 and 39

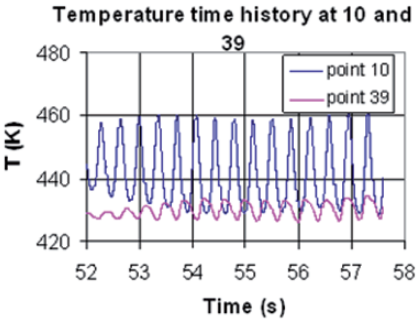

Fig. 14b Close-up view of the oscillating pattern for temperature at points 10 and 39

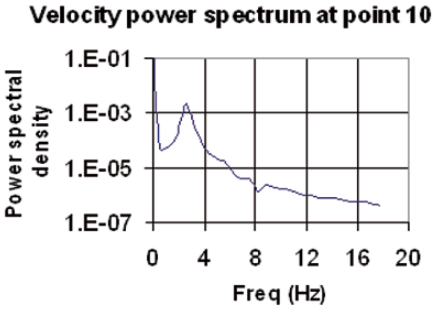

Fig. 15 Velocity power spectrum at point 10.

Table 3 Comparison of the oscillating frequency of the hot thermal plume

	Frequency (Hz)	Period (second)
exp	2.5	0.4
Fluent	2.53	0.395

4.2 Sensitivity of the time step size

As mentioned earlier, the size of the time step reduced sequentially along the transient simulation process from 0.01 to 5×10^{-4} second to help obtain fast initial transient flow development and ensure capturing the accuracy of the fine scale flow motion toward the end of the simulation. A separate study was conducted to investigate sensitivity of the time step size to the solution accuracy. Figure 16 shows the results of this study. It was found that for the current flow, if a constant large time step of 0.01 second was used, the thermal plume never developed a correct periodic motion as indicated by the velocity time history at point 10. When compared to Fig. 13 which shows a correct velocity time history using time step of 5×10^{-4} second, the velocity curve at point 10 begins to show development of periodic motion as early as around 50 seconds, the velocity time history at the same point in Fig. 16 never develops a periodic motion up to 67 seconds when the time step of 0.01 second is used. It was found that the reduction in time step at least by a factor of 10 (time step of 0.001 second) would allow the flow to establish a converged flow behavior. The velocity time history for a time step of 0.001 second is shown in Fig. 16 by restarting the simulation from the solution of 0.01 second obtained at time=65 seconds. It is very clear that a converged (in a transient sense) periodic motion begins to develop right after using the time step of 0.001 second.

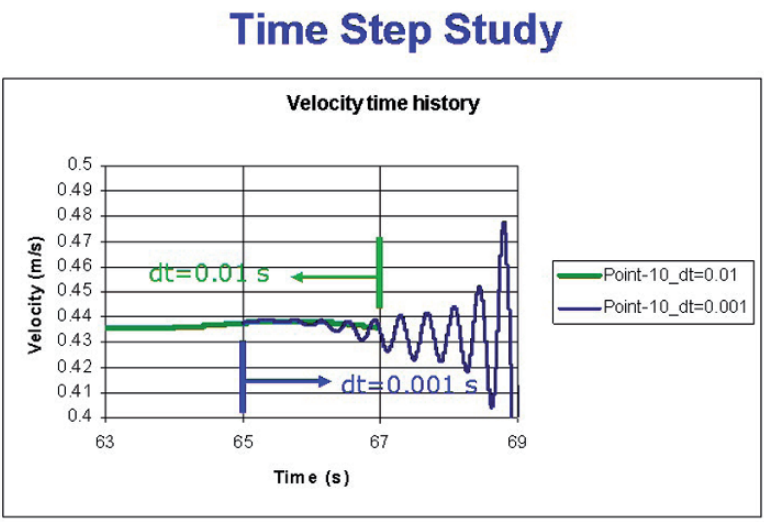

Fig. 16 Time history plot for the velocity at point 10 with two time step sizes during the final stage of simulation.

4.3 Buoyancy flow characteristics

The Grashof number, Gr_L , is usually used to characterize the buoyancy flow. The definition of the Grashof number is expressed as follows:

$$Gr_L = \frac{g\beta\,(T_s - T_\infty)\,L^3}{\nu^2}$$

where g is the gravity, β is the thermal expansion coefficient, v is the kinematic viscosity, L is the length scale, T_s is the surface temperature, and T_∞ is the temperature in the flow-field. Due to the complexity of the geometry, two Grashof numbers are identified. As shown in Table 4, the two Grashof numbers are based on two length scales, one with the slanted engine block wall and the other with the exhaust cylinder. T_∞ is based on the average flow temperature close to the heat sources as indicated in Table 4. The estimated range of the Grashof numbers indicates that it is very close to the turbulent regime according to the classic cylinder flow analysis [6].

Table 4 Buoyancy flow characteristics

	Right engine block	Right exhaust
g (m/s²)	9.81	9.81
β(1/K)	0.0026	0.0026
Ts (C)	123	600
T∞ (C)	104.3	104.3
L (m)	0.557	0.0457
v (m²/s) @Tf=0.5(Ts+ T∞)	2.77×10^{-5}	5.4925×10^{-5}
Gr=	1.0569×10^{8}	4.0×10^{5}

4.4 Time-averaged temperature and velocity

Figure 17 shows snapshots of both temperature and velocity contours at midplane. The velocity contours shown in Fig. 17 qualitatively resemble the experimental data shown in Fig. 8. As mentioned earlier, the flow exhibits a periodic pattern as both suggested by the test and numerical simulation. Therefore to compare with the experimental data for both the temperature and velocity components, the flow results from the numerical simulation over many cycles into the oscillating

periods are time-averaged. The time-averaged temperature and velocity components are compared with the measurements in five rows and two columns defined in Fig. 12. Figure 18 shows the temperature profiles from the current simulation for 5 horizontal rows. The symbols represent the measured data reported in [4, 5].

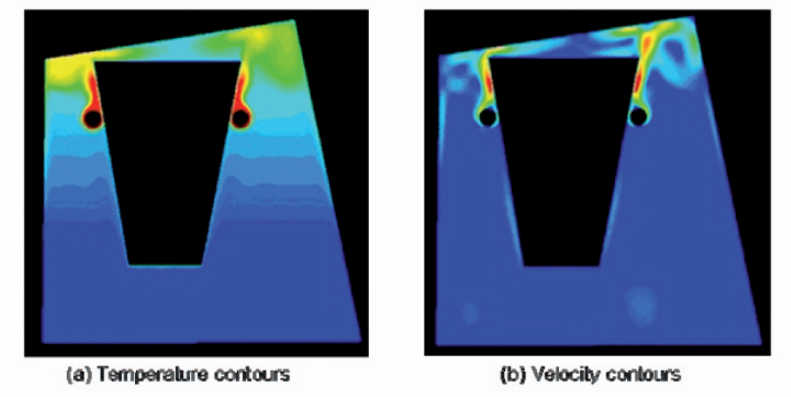

Fig. 17 Snap shots of the temperature and velocity contours at the mid-plane

The temperature profiles are shown in Fig. 18. The predicted temperature profile in line L1 which is in the gap between the upper surface of the engine block and the outer enclosure follows the trend quite well with the test data except that it under-predicts the peak value near the right enclosure surface. Similarly the profile in line L2 on the right part shows the correct trend with the test data but misses the peak by about he same amount. The temperature discrepancy around this small region close to the engine block was thought to come from the under-resolved boundary temperature mapping from the experimental data where only finite number of thermocouples was installed. More thermocouples in the future measurement should provide better boundary conditions for numerical validations. Figure 19 shows the temperature profiles along two vertical columns. The figure shows very clearly that the temperature gradient near the exhaust cylinders is very high.

The velocity components are compared with the PIV measurements along the same five horizontal rows and two vertical columns. Figure 20 shows the W (vertical) velocity component on those five rows. The trend in the velocity profiles is well captured. It should be noted that the velocity magnitude is very small and is in the order of 0.7 m/s. Figure 21 shows the U (horizontal) velocity component along the two vertical columns. The trend of the profiles is also very well predicted. However, it can be seen in Figs. 20 and 21 that the numerical results under-predict the peak values for both U and W components. This under-prediction is very consistent to the temperature profiles discussed in the previous paragraph. A higher degree of boundary temperature mapping from the measurement with more thermocouples should be able to improve the prediction accuracy.

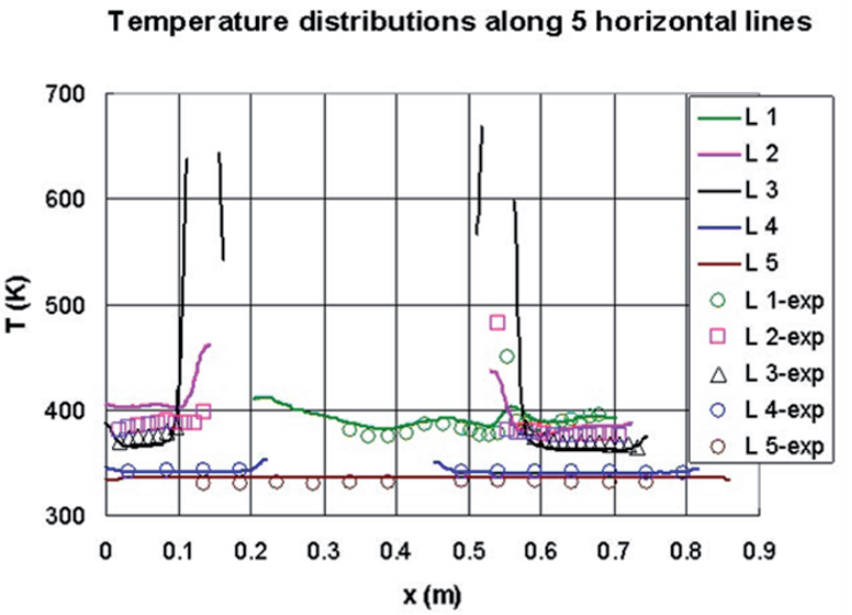

Fig. 18 Temperature profiles comparison with the measured data in five rows.

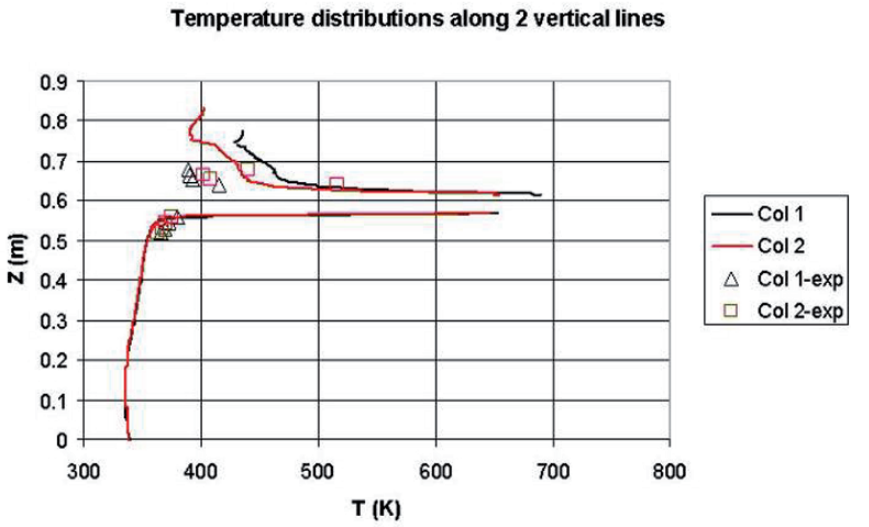

Fig. 19 Temperature profiles comparison with the measured data in two columns.

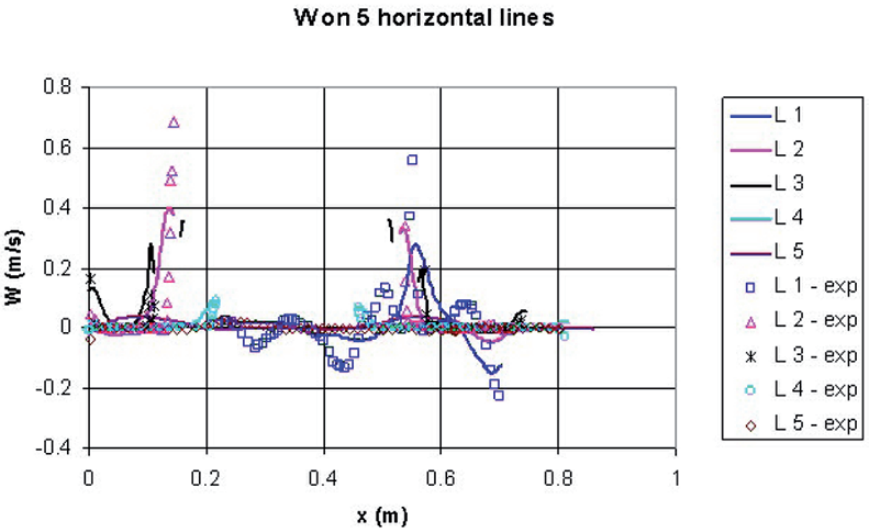

Fig. 20 W velocity component profile comparison with the measured data in five rows

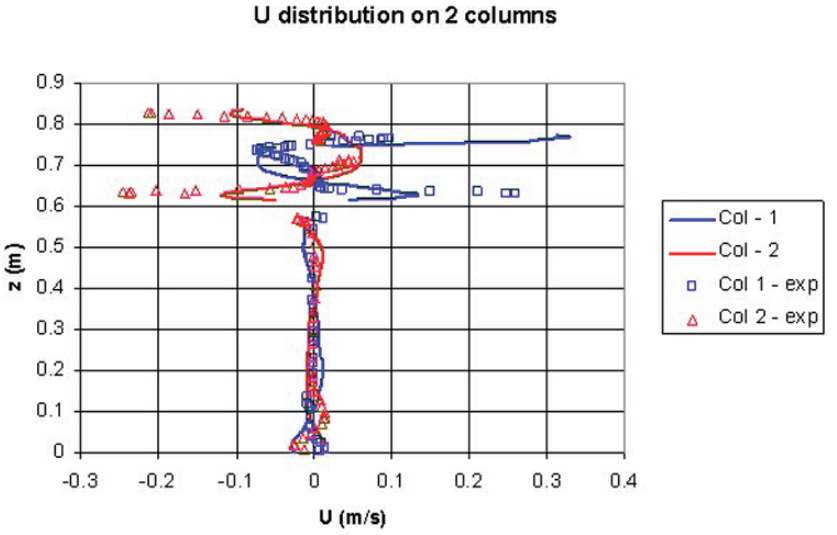

Fig. 21 U velocity component profile comparison with the measured data in two columns

5 Conclusions

Both experimental and numerical approaches are used to study the buoyancy driven flow in a simplified underhood. The simplified underhood geometry consists of an enclosure, an engine block and two exhaust cylinders mounted along the sides of the engine block. The experiment measures both temperature at the mid-plane and PIV velocity field at the mid-plane and 2 off-center planes. The wall temperature distributions along all the boundary surfaces are also recorded to be used for numerical validation. The numerical simulation predicts the transient thermal plume right above the exhaust cylinders very well with the predicted oscillating frequency at 2.53 Hz which is very close to the test data of 2.5 Hz. The contours of the flow and temperature fields show well-captured thermal plumes right above the exhaust cylinders, recirculation vortices around two upper corners and the gap between the engine block and the upper enclosure surface. The time-averaged air temperature and velocity profiles at the mid-plane for five horizontal rows and two vertical columns are compared to the measured data. The temperature values, in general, are in close agreement with the test data except the numerical results under-predict the peak temperature in the gap region between the top surface of the engine block and the outer enclosure. The under-predicted temperature and velocity near the engine block are believed to come from the under-resolved boundary temperature distributions. A more detailed boundary temperature mapping from the measurement can improve the current accuracy. The predicted maximum air velocity scale is in the order of 0.7 m/s which is extremely small and very hard to obtain accurately in the measurement. Nonetheless, the numerical predictions capture the flow motion quite well when compared to the measured velocity profiles.

A transient cool-down air flow and temperature measurement was also conducted in the experiment. The time history of the 45-minute temperature boundary condition was recorded to be used later as transient boundary conditions for future numerical simulations. A limited number of air temperature and velocity data above the thermal plume are recorded for 45 minutes for later comparison. The numerical study of the transient cool-down test condition will be presented in a separate paper.

Acknowledgments

The authors would like to express gratitude for the funding support by Jim Welton at GM Global Engineering. Additional thanks to Rose McCallen, Fred Browand, Jim Ross and ECI for the organization of The Aerodynamics of Heavy Vehicles II conference.

References

[1] Merati P, Cooper N, Leong C, Chen K-H and Johnson J, "Investigation of the Buoyancy Driven Flow in A Simplified Underhood - Part I,PIV and temperature Measurements", SAE Paper 2006-01-1608, *SAE Congress 2006*, Detroit, MI.

[1] Merati P, Cooper N, Leong C, Chen, K-H and Johnson J, "Investigation of the Buoyancy Driven Flow in A Simplified Underhood – Part I, PIV and Temperature Measurements", SAE Paper 2006-01-1608, SAE Congress 2006, Detroit, MI.

[2] Chen K-H, Johnson J, Merati P, Cooper N and Leong C, "Investigation of the Buoyancy Driven Flow in A Simplified Underhood - Part II, Numerical Study", SAE Paper 2006-01-1607, *SAE Congress 2006*, Detroit, MI.

[3] Fluent 6.3.26, Fluent Inc. 2007

[4] Merati P, Leong C and Sakuma Y, "Investigation of the Buoyancy Driven Flow in a Simplified Full-Scale Underhood – PIV and Temperature Measurements", Mechanical and Aerospace Engineering, Western Michigan University, MI. July 13, 2006.

[5] Merati P, Leong C, Chen K-H and Johnson J, "Investigation of the Buoyancy Driven Flow in a Simplified Full-Scale Underhood – PIV and Temperature Measurements", to be published in Springer-Verlag Lecture Notes in Applied and Computational Mechanics :*The Aerodynamics of Heavy Vehicles II: Trucks, Buses and Trains*, July, 2008.

[6] Holman J *Heat Transfer* fourth edition, 1976, McGraw-Hill, Inc.

The Flow Environment of Road Vehicles in Winds and Traffic

Simon Watkins, Riccardo Pagliarella

RMIT University, Melbourne, Australia
simon@rmit.edu.au

Abstract The aerodynamic development of a new vehicle is usually performed in smooth flow EFD or CFD domains with the vehicle in isolation. However the flow environment on-road is complex due to the presence of atmospheric winds, the wakes of nearby stationary objects and, depending upon driving conditions, the wakes of other vehicles. Winds and traffic generate a turbulent flow environment and can augment or reduce the mean velocity experienced by the moving vehicle. Recent work on turbulence arising from vehicles traversing the atmospheric boundary layer is reviewed and the consequence of upstream vehicle wakes is considered. The influence of distance and rear slant angle is examined, via wind-tunnel measurements of wakes of Ahmed bodies using dynamically calibrated multi-hole probes. The effect on very closely coupled vehicles (such as may occur in future platoons) is investigated via force and surface pressure measurements on two and three vehicle Ahmed bodies of varying rear slant angle. It is argued that the typical turbulence intensity for current highway driving is about 5%, but this can be significantly augmented when in the close proximity of other vehicles and/or during high winds. Further it is shown that for some vehicle forms, close coupling can increase the total platoon drag.

Separation Control for Drag Reduction

Preliminary Experiments Applying Active Flow Control to a 1/24th Scale Model of a Semi-Trailer Truck

L. Taubert and I. Wygnanski

The University of Arizona, Dept. of Aerospace and Mechanical Engineering
taubert@u.arizona.edu, wygy@email.arizona.edu

Abstract Preliminary experiments were carried out to investigate possible benefits of using a relatively new type of fluidic actuators (Raman & Raghu [1]) in combination with attached aft bodies to reduce the drag on a standard semi-trailer truck. The actuators generate oscillating jets that cause the formation of streamwise vortices that enhance the entrainment of the shear layer significantly. Taking into account the potential feasibility of any add-ons to a trailer, seven different bodies with simple geometries were chosen for this investigation.

Nomenclature

A_a	total open area of actuator nozzles
A_{cs}	cross section of trailer, based on total height
L_c	circumference of trailer
U_j	actuators jet velocity, based on flow rate
U_∞	free stream velocity
ρ	density of air
$C_\mu = 2*A_a/A_{cs}*(U_j/U_\infty)^2$	momentum coefficient
F_t	measured thrust force
F_d	measured drag force
$C_t = F_t/(1/2*\rho*U_\infty^2*A_{cs})$	thrust coefficient
$C_d = F_d/(1/2*\rho*U_\infty^2*A_{cs})$	drag coefficient
C_{d0}	C_d of baseline configuration (no actuation)
$D_{hydr} = 4*A_{cs}/L_c$	hydraulic diameter
Re	Reynolds number, based on D_{hydr}

Introduction

Significant improvements have been made in the last decades to reduce the drag of commercial vehicles (Cooper [2]), especially heavy trucks. Experiments were carried out in a wide range of Reynolds numbers (Cooper [2], Storms et al. [3]), up to on-the-road tests (Englar [4]) to check the validity of smaller-scale studies. The potential of further reducing fuel consumption and emissions led to numerous research projects applying active flow on heavy vehicles. Steady blowing was investigated (Coon and Visser [5]) as well as oscillatory forcing (Hsu et al. [6]) in combination with different configurations of added aft-bodies. All these approaches focus mainly on altering the spanwise structures of the flow. In contrast to this the type of actuation investigated preliminarily in this study is targeted at generating streamwise structures.

Experimental Setup

A 1/24th scale model of a Kenworth T-600 B with Great Dane trailer (Fig. 1a), was modified for this investigation. Main alterations were the addition of a pressurized chamber containing 20 actuators at the rear end of the trailer (Fig. 2a) and an aluminum rail connecting tractor and trailer, providing balance mount points of the model and a connection for the pressurized air, as shown in Fig. 1b.

The experiments were carried out in the open-return, suction wind tunnel at the AME Department of the University of Arizona. The test section is 122 cm wide, 85.5 cm high and 355 cm long. The model was mounted on a six-component balance using the standard pylon to which a pressurized air tube was attached and a separate pitch rod. A stationary false floor (Fig. 1a), 51 cm wide and 182.5 cm long was positioned approximately 2mm below the wheels of the model, 39 cm above the tunnel floor and starting approximately 30 cm upstream of the model.

Fig. 1a Truck model in wind tunnel

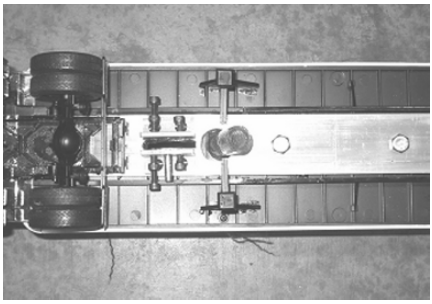

Fig. 1b Details: mount point and lines

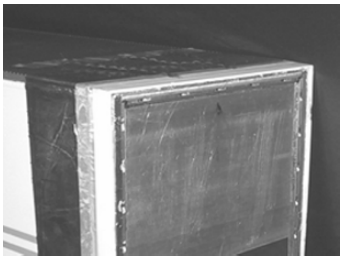

Fig. 2a Mounted actuators

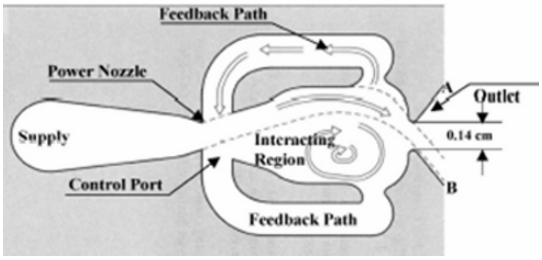

Fig. 2b Principle of actuator [1]

Active flow control was applied through fluidic actuators shown schematically in Fig. 2b. They were driven by pressurized air source and emitted oscillatory jets in the direction of streaming. For these actuators the frequency of the oscillations depends on the supplied flow rate and cannot be changed independently. It varied approximately between 1 and 2.5 kHz for the investigated range of C_μ.

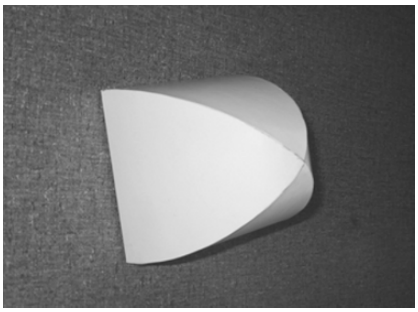

Fig. 3a Ellipsoid

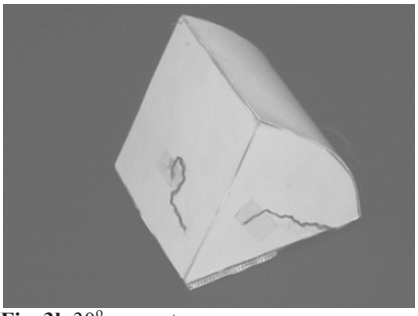

Fig. 3b 30° arc sector

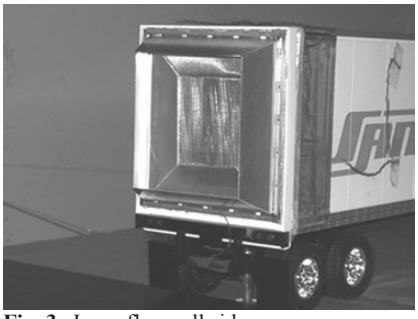

Fig. 3c Inner flaps, all sides

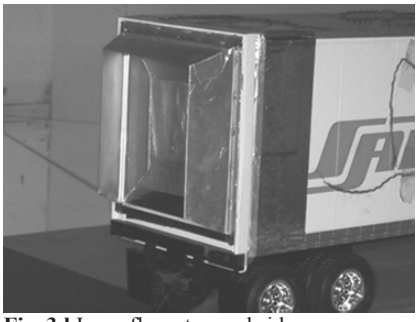

Fig. 3d Inner flaps, top and sides

Fig. 3e Outer flaps, top and sides

Fig. 3e Long flap

The main attraction of these actuators is their simplicity because they do not require moving parts and they proved themselves in laboratory tests associated with aeronautical applications. Five equally spaced actuators were mounted on each side at the very end of the trailer. The distance between the outer surface of the trailer and the center plane at which the jets oscillated, was approximately 6% of the width of the trailer, as shown in Fig. 2a.

In the first series of experiments various simple modifications to the trailer were investigated with the focus being on additions that will not impede the utility of the fundamental trailer design. Two different solid (closed) bodies were attached to the model. A three-dimensional ellipsoid of 100mm length with rectangular base (Fig. 3a), and a two-dimensional body formed by a 30° circular arc sector with its radius equal the vertical distance between the actuators (Fig. 3b). Both bodies filled the entire area between the actuators.

Five different types of flaps mounted onto the trailer's aft surface were investigated. A single long flap was formed by a sheet metal, 100mm long (the vertical distance between the actuators) and attached right below the top actuators at an angle of 20° to the horizontal, filling the entire horizontal space between the actuators shown in Fig. 3f. The other four configurations consisted of flaps either mounted flush with the outside surfaces, thus surrounding the actuators on the outside, or being mounted onto the trailer's aft surface and being surrounded by the actuators (Fig. 3d & e). The inclination of these flaps to the trailer's walls was 20°.

Two variations of these flap configurations were tested: first with flaps and active actuators on all four sides of the trailer and second with the bottom flaps removed and bottom actuators inactive (Fig. 3f). All configurations were investigated at three different Reynolds numbers and at four different momentum coefficients. The model was aligned parallel to the free stream in all cases.

Results

The drag coefficient of the basic configuration (without aft bodies) was approximately, C_D=0.62. This value varied little with Reynolds numbers over the range of Re considered. The various additions to the baseline configuration reduced the drag by 2-4% at the higher Re range, with the exception of the long flap that was suspended from the roof of the trailer and pulled air upward from the ground region into the wake of the trailer increasing the drag in that fashion by approximately 1-1.5% as shown in Fig 4.

The drag measured at different levels of actuation emanating from the entire circumference of the trailer's base is shown in figure 5. The jet momentum, or rather *the thrust that was measured in the absence of external stream was added to the drag* and the result was normalized by the particular baseline configuration of the appropriate geometrical addition at the Reynolds number at which the experiments were carried out. This normalization presumes that the same amount of compressed air could be used for jet propulsion and in the absence of deleterious interference one should recover the input momentum as thrust. Such thrust is also dependent on the velocity of the vehicle but this was not considered presently and thus the results may be somewhat pessimistic. Nevertheless any value that is lower than unity in Fig. 5 represents a net benefit to the system. Unfortunately the specific installation of the actuators around the periphery of the trailer's aft did not reduce the drag sufficiently to justify the momentum input.

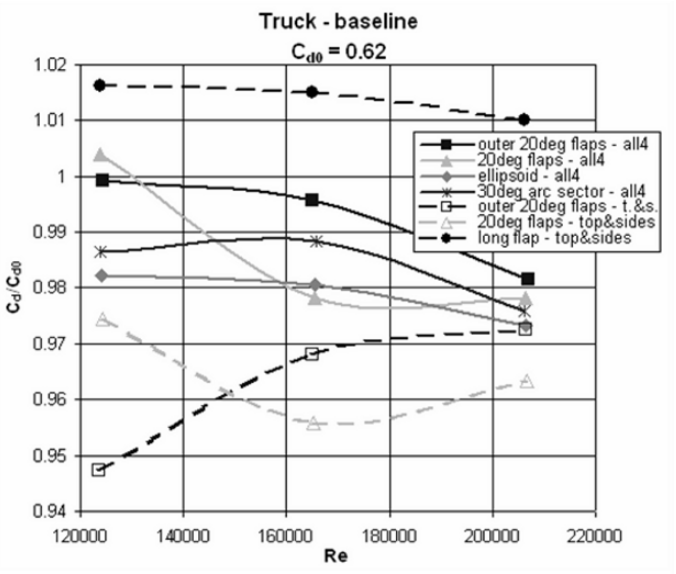

Fig. 4 The drag of a modified trailer relative to its basic configuration

In order to affect the base flow, the flaps or center-bodies were surrounded by the actuators generating a substantial discontinuity in the surface (backward facing step) around the circumference of the trailer's base. This arrangement was not conducive to drag reduction. For this reason one set of flaps was set flush with the trailer's sidewalls (see Fig. 3e) and although the actuation could only affect the external stream downstream of the flap's trailing edge its presence was somewhat beneficial provided the momentum coefficient, $C_\mu < 2\%$. In fact relative to the truck's original drag the reduction is in excess of 4% provided the alternative use of the momentum coefficient is not considered.

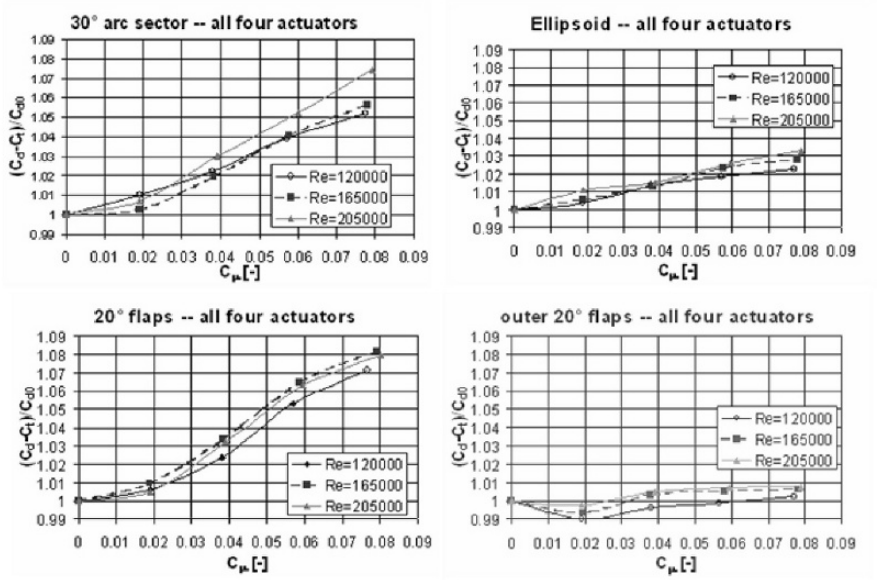

Fig. 5 The effect of four-sided actuation on the drag

The thrust was measured in the absence of an external stream and thus the penalty of considering it that way is too high and the results presented are overly pessimistic. Additional evidence for this pessimism is provided below in Fig. 7. Large differences in momentum recovered as thrust were observed for the different configurations shown in Figs. 5 and 6. A simple flow visualization study using tufts revealed that close to the center span or mid height of the trailer, the flow is deflected clearly inwards (Figs. 7b and d). This is caused by the entrainment of ambient fluid by the oscillating jets and is most visible in the absence of an external flow. In contrast, next to the corners of the trailer, the flow is jetting outwards (Figs 7a & c). This is easily explained by the oscillating jets from the top and one of the sides that intercept one another near the corner at an approximate angle of 90^o. This forces the flow away from the trailer, widening its wake and increasing the drag. This effect was also observed in the presence of the external flow at

different Re with different values of C_μ used. It is caused solely by the non-optimized positions of the actuators in combination with the direction of oscillation of the emitted jets.

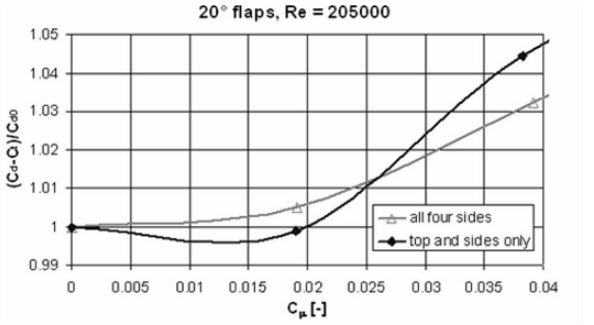

Fig. 6 Effect of actuator location

In order to test if the outflow from the corner has any effect on the drag the bottom flap that was interior to the actuators had been removed and the actuation was limited to the three remaining sides. At low momentum coefficient some benefit was drawn from the removal but it disappeared at higher C_μ (see Fig. 6).

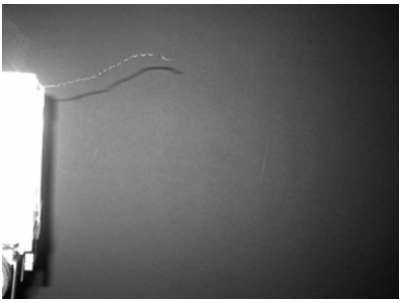

Fig. 7a Top right corner, side view

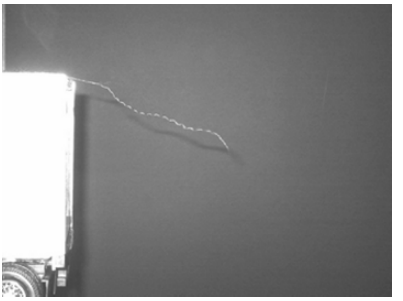

Fig. 7b Top center, side view

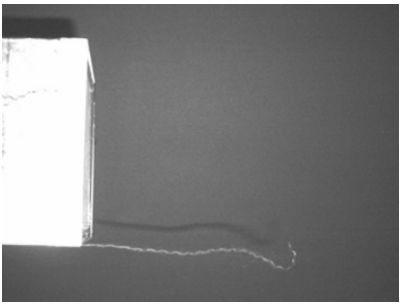

Fig. 7c Top left corner, top view

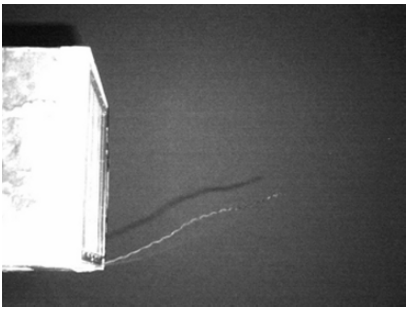

Fig. 7d Left center, top view

Concluding Remarks

The drag of a semi-trailer truck model was reduced by added aft bodies by up to 5.5% depending on the shape and size of the added body and the Re. When active flow control was added, its contribution to this reduction was minor. The maximum reduction obtained by active flow control was approximately 1% for the short flaps that were inclined at 20^o to the sidewalls and the top of the trailer.

One important factor of the low effectiveness of the actuation is due to the fact that the actuators close to the corners are interfering with one another, forcing the jets away from the truck into the free stream and thus increasing the (local) drag.

Another, possibly more important, factor is the orientation of the jets. An inclination of the jets towards the axis of the truck should in every case be beneficial. This was impossible to implement using them as add-ons on a small-scale model. Additionally, the length of the attached bodies/flaps should be optimized with respect to the formation of the streamwise vortices.

It seems that the structure of the wake behind the lower part of the trailer has a significant impact on the overall performance of the drag-reduction system. The investigated flap configurations generated significantly different results concerning effectiveness. Therefore detailed visualization studies of any modification are necessary for better understanding of the near wake and optimization of added bodies and active flow control.

In general, actuators providing streamwise vortices in the wake of a truck by oscillatory jets seem to be promising for reducing its drag, especially when the simplicity and robustness of the investigated actuators is considered.

In view of the preliminary nature of this experiment and the lack of any optimization, these results are quite promising. The interaction with the stationary "ground" surface has to be considered, proper flow diagnostics have to be used and finally the construction of actuators that are embedded conformally in the surface should be undertaken.

References

[1] Raman G and Raghu S **(2004) Cavity Resonance Suppression Using Miniature Fluidic Oscillators.** AAIA Journal ,Vol. 42, No. 11

[2] Cooper K (1985) The Effect of Front-Edge Rounding and Rear-Edge Shaping on the Aerodynamic Drag of Bluff Vehicles in Ground Proximity. SAE paper No. 850288

[3] Storms B, Satran D, Heineck J and Walker S (2004) A Study of Reynolds Number Effects and Drag-Reduction Concepts on a Generic Tractor-Trailer. AIAA paper No. 2004-2251

[4] Englar RJ (2004) Pneumatic Heavy Vehicle Aerodynamic Drag Reduction, Safety Enhancement, and Performance Improvement. In: McCallen R, Browand F, Ross J (eds.) The Aerodynamics of Heavy Vehicles:Trucks, Buses and Trains, Lecture Notes in Applied and Computational Mechanics, Springer-Verlag, Heidelberg

[5] Coon J and Visser K. (2004) Drag Reduction of a Tractor-Trailer Using Planar, Non-Ventilated Cavities. In: McCallen R, Browand F, Ross J (eds.) The Aerodynamics of Heavy Vehicles:Trucks, Buses and Trains, Lecture Notes in Applied and Computational Mechanics, Springer-Verlag, Heidelberg

[6] Hsu T-Y, Hammache M and Browand F (2004) Base Flaps and Oscillatory Perturbations to Decrease Base Drag. In: McCallen R, Browand F, Ross J (eds.) The Aerodynamics of Heavy Vehicles:Trucks, Buses and Trains, Lecture Notes in Applied and Computational Mechanics, Springer-Verlag, Heidelberg

Large Trucks Drag Reduction using Active Flow Control

Seifert A., Stalnov O., Sperber D., Arwatz G., Palei V., David S., Dayan I. and Fono I.

The Meadow Aerodynamics laboratory, School of Mech. Eng., Faculty of Engineering, Tel Aviv University, ISRAEL

Abstract Aerodynamic drag is the cause for more than two-thirds of the fuel consumption of large trucks at highway speeds. Due to functionality considerations, the aerodynamic efficiency of the aft-regions of large trucks was traditionally sacrificed. This leads to massively separated flow at the lee-side of truck-trailers, with an associated drag penalty of at least a third of the total aerodynamic drag. Active Flow Control (AFC), the capability to alter the flow behavior using unsteady, localized energy injection, can very effectively delay boundary layer separation. By attaching a compact and relatively inexpensive "add-on" AFC device to the back side of truck-trailers (or by modifying it when possible) the flow separating from it could be redirected to turn into the lee-side of the truck, increasing the back pressure, thus significantly reducing drag. A comprehensive and aggressive research plan that combines actuator development, computational fluid dynamics and bench-top as well as wind tunnel experiments was performed. The research uses an array of 15 newly developed Suction and Oscillatory Blowing actuators housed inside a circular cylinder attached to the aft edges of a generic 2D truck model. Preliminary results indicate a net drag reduction of 10% or more.

1. Scientific background

Active flow control (AFC) is a fast-growing, multidisciplinary science and technology thrust aimed at altering a natural flow state into a more desired flow state (or path). Flow control was simultaneously introduced with the boundary layer concept by Prandtl [1] at the turn of the 20th century. In the period leading to and during WW II, as well as in the Cold War era, flow control was extensively studied and applied mainly to military fluid related systems. Though the fluid mechanics aspect can be robust, steady-state flow control methods were proven to be of inherently marginal power efficiency, and therefore limited the implementation

of the resulting systems. Unsteady flow control using periodic excitation and utilizing flow instability phenomena (such as the control of flow separation [2]) has the potential of overcoming the efficiency barrier. Separation control using periodic excitation at a reduced frequency of the same order, but higher than the natural vortex shedding frequency of bluff bodies (such as an airfoil in post-stall or a circular cylinder), can save 90% to 99% of the momentum required to obtain similar gains in performance compared to the classical method of steady tangential blowing [2]. The feasibility of increasing the efficiency and simplifying fluid related systems (e.g., for high-lift, [3-4]) is very appealing. This becomes even more appealing if one considers that *1% saving* in the fuel consumption of the US fleet of large trucks (about 8 million trucks in 2004, [5]) is worth about *$1.5 Billion per year*, while the environmental and political effects are difficult to quantify. The progress in miniaturization, actuators, sensors, simulation techniques and system integration enables the utilization of wide bandwidth unsteady flow control methods in a closed-loop AFC (CLAFC) manner. See Collis et al. [6] for a comprehensive review of the subject. Experimental demonstrations are required to close the gap between the current theoretical understanding, the computational capabilities and real-world problems. The described study brings together AFC expertise, specifically actuator development and implementation for separation control, closer to real-life industrial applications.

The essential ingredients of an active separation control system, packaged as an "add-on" device that will be attached to the rear-end of large truck trailers, in order to reduce the aerodynamic drag by about 20-30% were recently completed and will be presented in the following sections. At highway speeds, the aerodynamic drag is responsible for roughly 65% of the fuel consumption, making the potential fuel saving about 15-20%. There has been considerable effort in the US to reduce the fuel consumption of trucks using shape changes, simple add-on devices and steady state AFC methods [7], but those have inherent limitations and can lead to only half the expected benefit of our suggested method. Hsu et al. [7] cite several research efforts focused on truck-trailer drag reduction. Adjustable inclination flat plates could be attached at the truck lee-side. These could reduce drag but are rather large, heavy and expensive. Their size raises functionality and compatibility issues. Periodic excitation was also mentioned in [7] but that research effort did not progress far. Steady blowing [8] was also applied to a modified aft-region of a truck-trailer and resulted in significant aerodynamic drag reduction, but at a marginal to zero or mostly negative energy efficiency due to reasons identified already by our research group [2]. It is expected, and substantiated by preliminary CFD analysis and experimental efforts already performed [9, 10], that the combination of steady suction and pulsed blowing could overcome the above identified efficiency barrier.

The current study is aimed at applying active flow control (AFC) technology as an "add-on" device attached to the aft-body of heavy-trucks and tractor-trailer configurations. The TAU-developed Suction and Oscillatory Blowing (SaOB) AFC actuators are used for drag reduction of heavy ground transportation systems. The above fluidic device is a combination of an ejector (jet-pump) and a bi-stable fluidic amplifier that was recently thoroughly studied and published [11, 12]. The

study is assisted by computational fluid dynamics (CFD) effort to narrow the huge parameter space. After completing the actuator development and adaptation to the speed range relevant to trucks, three stages of experiments were performed on a circular cylinder, the generic bluff-body [9, 10]. These studies resulted in a significant reduction of drag due to delay of boundary layer separation. A wide range of boundary conditions were tested and only the common results to all conditions were considered as valid. Successful wind tunnel demonstration on a two-dimensional (2D) equivalent of a blunt truck-trailer model was subsequently performed and is the main subject of the current paper. This stage is to be followed by a complete, small-scale, truck model with drag reducing devices and a full scale prototype of the "add-on" device for road testing will follow. The technology could lead to a revolutionary aerodynamic drag reduction of heavy road vehicles and could lead to new efficiency levels of aeronautical systems as well. The current research is especially appealing since it provides a valuable contribution to a slower production of "Green house" gases.

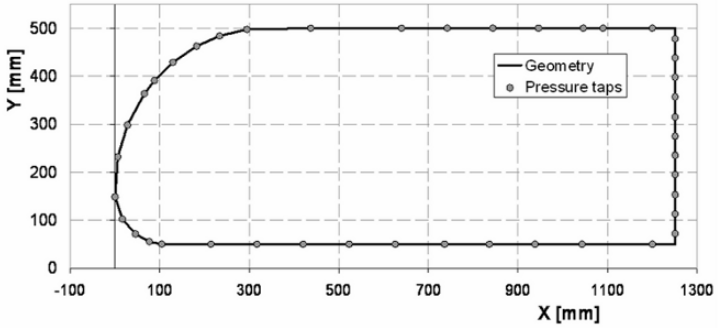

Fig. 1 A cross section of the 2D "truck" model, H=450mm, L=1250mm and its width, b=609mm. No control cylinders. Y=0 is the simulated road level, when present.

2. Description of the experiment

The experiments were performed on a generic 2D equivalent model of a large truck, along the lines of the GTS model [13]. Figure 1 shows a cross section of the model, showing also the location of the 43 pressure taps. The model height (H) is 450mm and its length is 1250mm. It spans the entire width of the wind tunnel test section, b=609mm. The model is made of aluminum beams and ribs and a skin of 2mm thick aluminum plates. The significant interference with the wind tunnel has not been taken into account in any manner. However, during the 2D truck experiments the ceiling static pressures were measured and could be used for evaluation of the wind tunnel interference with the use of future CFD effort. It is argued that since the flow accelerates more around our model, with respect to free flow conditions, the AFC results are conservative since the AFC effects are proportional to the flow linear momentum at the separation points. For control purposes, one or

two circular cylinders were attached to the aft region of the truck model. The cylinders were 76.2mm diameter and spanned the 609mm of the wind tunnel. The cylinders were installed such that were tangent to the aft body corners and extended one radius behind the aft plate line, their centers one radius below the upper cover plate or above the lower cover plate (see Fig. 7a with only the upper control cylinder sketched). The upper control cylinder was installed with an array of 15 SaOB actuators, as described in [9, 10]. An array of 96 suction holes with diameter of 2mm and spacing of 6mm were drilled in the cylinder. The wall thickness was close to 10mm, so the flow resistance was high. The flow was sucked into the cylinder by the ejector that is part of the SaOB actuator. The entire flow rate (the sum of the inlet and entrained-sucked flow) was ejected alternately out of two tangential, 1.7mm high, pulsed blowing slots connected to each actuator. Each actuator was 28mm wide and it controlled about 40 mm of the span of the cylinder. The lower control cylinder was used only for steady suction and was connected to an external suction pump. It had two staggered rows of 96 holes 2mm diameter each, spaced 7.5 deg apart along the cylinder arc (Figs. 10a and 10b).

A simulated road was placed under the 2D truck in some of the tests. The plate, with rounded leading edge positioned 67 cm upstream of the model, was 280 cm long, 4 mm thick, and extended 90 cm behind the model. A 3D wake rake was positioned 120 cm downstream of the model. It measured 29 total pressures and 2 static pressures, one close to each side-wall. The wake rake was mounted on a Y-axis traverse allowing vertical motion, with typical grid resolution or 20-25mm in the wake scans.

The experiments were performed in the Meadow-Knapp low-speed wind tunnel. The speed range is 4-60m/s, the turbulence level is about 0.1% and the test section dimensions are 1.5m (high) by 0.61m (wide) and 4.25m long. Pressures were measured by a PSI Inc. pressure scanner with 128 ports at a resolution of 0.001psi. Tunnel dynamic pressure was measured by a Pitot-Prandtl tube, positioned 110cm upstream of the model leading edge on the tunnel ceiling, connected to a Mensor pressure transducer (10” water full scale and resolution of 0.06%). The Reynolds number was monitored to 1% tolerance and dynamic pressures were also measured on the model aft region, to identify unsteady effects. The tunnel temperature was 24±2ºC. Air density and viscosity were calculated using standard formulae and the ambient temperature and pressure.

3. A brief review of recent related work

3.1 Suction and Oscillatory Blowing (SaOB) Actuator

The development of the SaOB actuator [11, 12] and its utilization for drag reduction on the circular cylinder (currently used as the aft-upper control device), were reported elsewhere [9, 10]. However, for the sake of completeness and due to the time-lag until these studies would become publicly available, some of the results are cited and discussed here.

The Tel Aviv University (TAU) suction and oscillatory blowing (SaOB) actuator was invented in October 2003, patented [14] and recently completed a two year study. Several size actuators were developed. A theoretical model for the valve operation was validated [11, 12]. Small size devices, suited for the current application with minor adjustments, were also developed and validated [9, 10]. A cross-section of the actuator can be seen in Fig. 2a and a sketch explaining the principle of operation is shown in Figs. 2b and 2c. The actuator is a combination of a bi-stable fluidic oscillator connected downstream of an ejector ("jet pump"). The purpose of the ejector is to create a suction flow, by increasing the flow entrained into the valve. Suction is probably the most efficient flow separation control method [15], but is difficult to generate efficiently. It has been shown that the ejector is indeed increasing the flow rate by a factor up to three with its entrances unrestricted. To create self-oscillations, the two control ports (Figs. 2a and 2c) were connected by a short tube, without any moving part or energy expenditure. The tube was later replaced by an S-shaped channel machined in a plate on which all the actuators were installed (referred hereafter as "mounting plate"). The SaOB actuator has a wide and appropriate frequency range (0.1 to 1.4 kHz) depending on the nozzle shape, the length of the feedback tube and the inlet flow-rate [11, 12]. Near-sonic actuator exit velocities have been measured, but currently the exit velocities are of the same order as the free-stream velocities. The inlet flow rate is controlled by a pressure regulator connected to shop air supply, to be replaced by the truck pneumatic system, by flow extracted from the truck turbocharger or by an auxiliary system connected electrically or mechanically to the rear wheels. The valve operation is insensitive to rain or dust conditions.

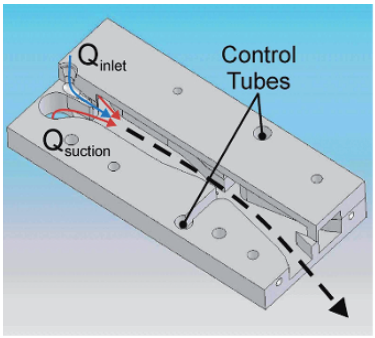

Fig. 2a Small size suction and oscillatory blowing actuator. Overall length is about 60mm

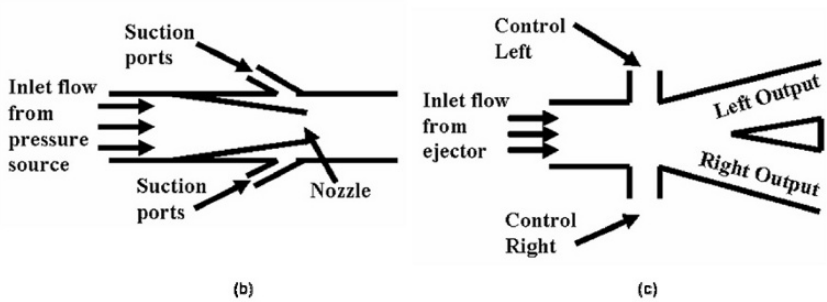

Fig. 2b,c A schematic rendering of the SaOB actuator: (b) ejector (c)

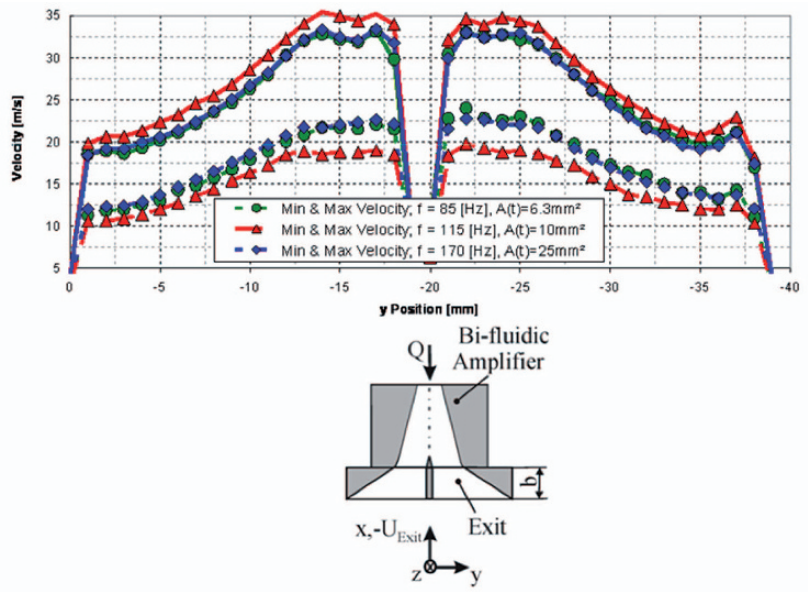

Fig. 3 Valve exit velocity profiles for three different tube diameters (maximum velocity = solid lines; minimum velocity = dashed lines; $p_{(inlet)}$=6 [psi]) measured with Hot-Wire-Anemometry; (right) Slot configuration drafted. Length of control tube, 80mm

During the course of the study reported in [9, 10], there were several cycles of modifications to the valve design. The main objective was to fit the valve into the cylinder while minimizing the pressure drop across it. This was achieved by redesigning the ejector nozzle to have a short converging-straight geometry and shortening the mixing chamber between the ejector and the oscillator to the minimum possible (Fig. 2a).

Following these modifications the valve was bench-top tested, initially only with exit restrictions, simulating the assembly in the control cylinder. Figure 3 shows the maximum and minimum flow velocity out of a single SaOB actuator with an exit assembly simulating the conditions that will prevail in the "add-on" device as well as in the control cylinder at half scale. The exit velocities were measured by a hot wire that was traversed along the exit slot. The cross section of the feedback tubes (all with L=80mm) was altered during those tests. It can be seen that the cross section of the feedback tube has a strong effect on the oscillation frequency. It has a weaker effect on the switching quality, defined as: $\kappa = \frac{U_{\max} - U_{\min}}{U_{average}}$.

3.2 Circular Cylinder with the SaOB Actuator Array

The 15 valve array was mounted on a plate, providing inlet pressure to all the valves, feedback for each valve self-oscillation and synchronization tubes between the valves. The cross section of the feedback tubes was 5.7mm^2 and their length was maintained at 80mm. The reader is referred to [9, 10] for more details. Figure 4 shows the velocity (a) and frequency (b) of oscillation of an actuator array installed in the circular cylinder and tested on the bench-top set-up. The valves were not all synchronized, the frequencies of the central 13 valves deviated by no more than 10% and the peak velocities deviated by a maximum of 20%. These results deemed sufficient to go ahead and test the valve array for the purpose of the cylinder and later the 2D truck model drag reduction while it is planned to continue improving the uniformity of the magnitude and frequency and the synchronization between the different valves.

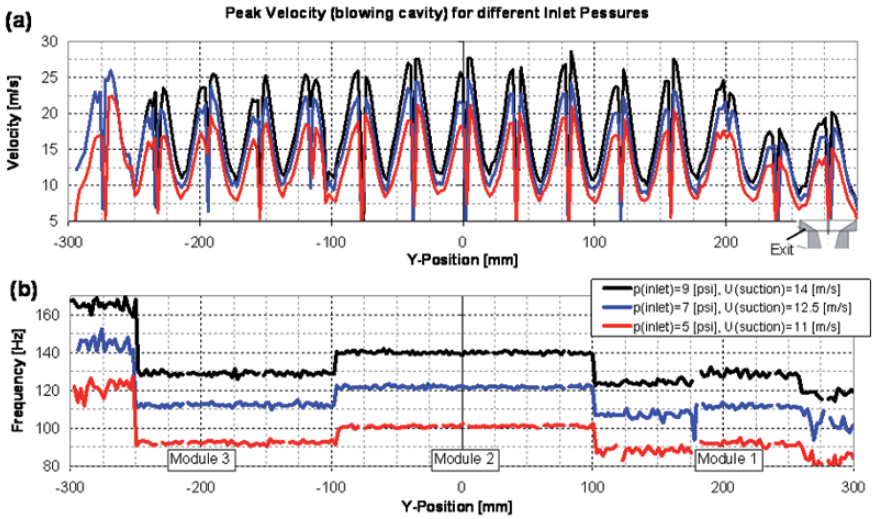

Fig. 4 Measurement of the output of a 14-valves array installed in a circular cylinder. (a) velocity, (b) frequency

The combination of oscillatory blowing and steady suction has never been tested before this project, but both methods are known to be very effective for the control of boundary layer separation [15]. A significant body of knowledge has been acquired by [9, 10]. These experiments established the drag reducing capability of steady suction through a 2D slot and later an array of holes in a wide range of boundary conditions. The data set also established that a 15 deg delay in separation region on the circular cylinder at Re=100,000 and Re=150,000 (associated with the target highway driving speeds) is possible with suction magnitude of about half the free-stream velocity. This enabled the definition of the configuration shown on the right side of Fig. 5. The suction holes are located 15 deg upstream of the pulsed blowing slot. The array of 15 SaOB actuators is mounted inside the 76.2mm diameter cylinder. Inlet flow is provided via common channel feeding all the ejectors' jets. These create low pressure in the half cylinder to the left of the valve-array, sucking flow through the holes. The entire flow is then ejected through the pulsed-blowing exit slots. The oscillation frequencies are in most cases larger than the natural vortex shedding frequencies on a circular cylinder at the current velocity range and significantly higher than the truck vortex shedding frequency.

Three series of wind tunnel experiments were performed on the circular cylinder (shown in Fig. 5, [9, 10]).

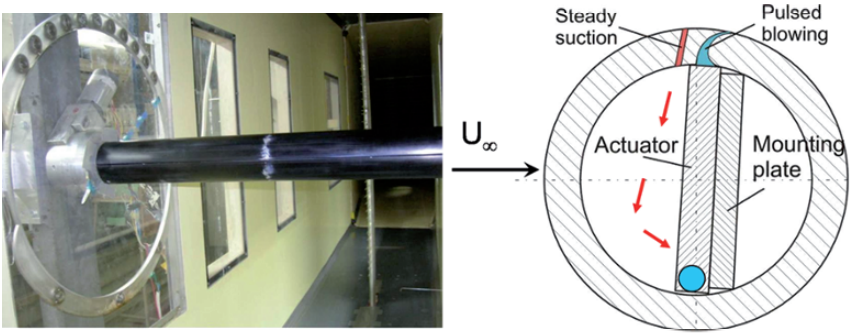

Fig. 5 The cylinder Setup with the suction holes (red) and the tangential slot (light blue) installed at the Meadow-Knapp Wind Tunnel (left), and a sketch of the experimental setup with the array of 15 SaOB actuators installed in the cylinder, the mounting plate for synchronization and pressure supply (right, light blue circle). The arrows indicate the path of the suction flow.

Figure 5 shows the experimental set-up of the cylinder in the Meadow-Knapp wind tunnel and a cross section of the 15-valves actuator array as installed inside the cylinder.

The cylinder was tested and a sample of the drag reduction data is presented in Figure 6 below.

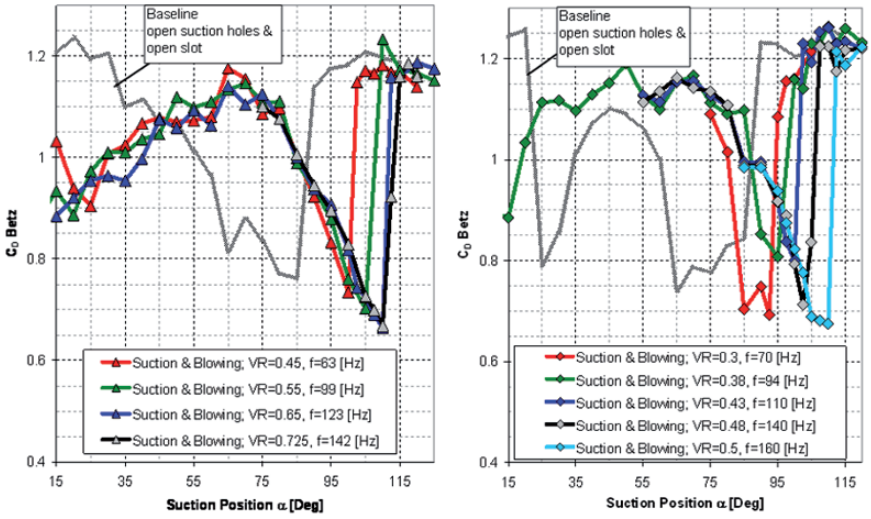

Fig. 6 Cylinder drag coefficient (C_D Betz – wake rake survey with static pressure correction) versus Suction Position (0 deg is the summit of the cylinder) in "free" (no truck model) laminar flow conditions; measured with Steady Suction and Oscillatory Blowing Actuation for two Reynolds numbers and different amplitudes (left) Re_d=100k (right) Re_d=150, blowing cavity is located $\Delta\alpha$=15 Deg downstream to the suction holes. VR is the velocity ratio between the suction and free-stream velocities.

The data shown in Fig. 6 indicates a drag reduction from about 1.1 to about 0.7, or a relative drag reduction of about 35%. This is obtained when the suction holes

are located at about 110 deg (relative to the free-stream direction) on the cylinder and the pulsed blowing slot at are positioned 15 deg downstream (at about 125 deg), where 90 deg is the summit of the cylinder. The energy efficiency of this drag saving, which was measured at flow velocity comparable to the highway speed of trucks indicates net positive energetic efficiency [9, 10]. For the acquisition of all the data presented below, net energy efficiency was the prime consideration. As shown in Fig. 7a, the add-on device will have a shape that resembles a -semi- to quarter-cylinder attached to the back side of truck-trailer. The advantage of having a complete cylinder at this stage of the study is the capability to conveniently alter the actuation location, which is shown to be very sensitive on the "free" cylinder (Fig. 6) and also in the "truck" results to be presented later in the paper.

3. Two dimensional (2D) truck experiments

3.1 Two dimensional (2D) truck with SaOB cylinder at upper- aft corner

Figure 7a shows a schematic cross-section of the 2D truck model, with the SaOB cylinder installed on its back-upper corner. Figures 7b and 7c present pictures of the model installed in the Meadow-Knapp wind tunnel, above a simulated road. The vertical distance between the model and the floor was allowed to increase from 50 to 55mm in order to compensate for boundary layer growth. It was validated that the boundary layers did not restrict the free-flow under the model. Wheels or moving floor were not used. These effects seem secondary since most of the effort was spent on the upper aft corner, least effected by the wheels or simulated road, moving or stationary. However, the mere presence of the simulated road is essential for simulating a side-view of the truck driving on a road. Several 50mm wide roughness strips (grit #60) were placed on the top and bottom plates of the truck model, to reduce Reynolds number effects. Figure 7d presents a close-up view of the cylinder. An array of 96 holes with 2mm diameter was positioned 15 deg upstream of a 1.7 mm (nominally) wide slot. The slots allowed almost tangential-downstream directed introduction of the pulsed blowing excitation. Each actuator controlled a span of about 40mm with two exits, as shown schematically in Fig. 3 (insert). The trailing-edge of the top and bottom cover plates were machined to create a back-step no thicker than 0.5mm, allowing a smooth transition of the flow from the covers to the cylinders.

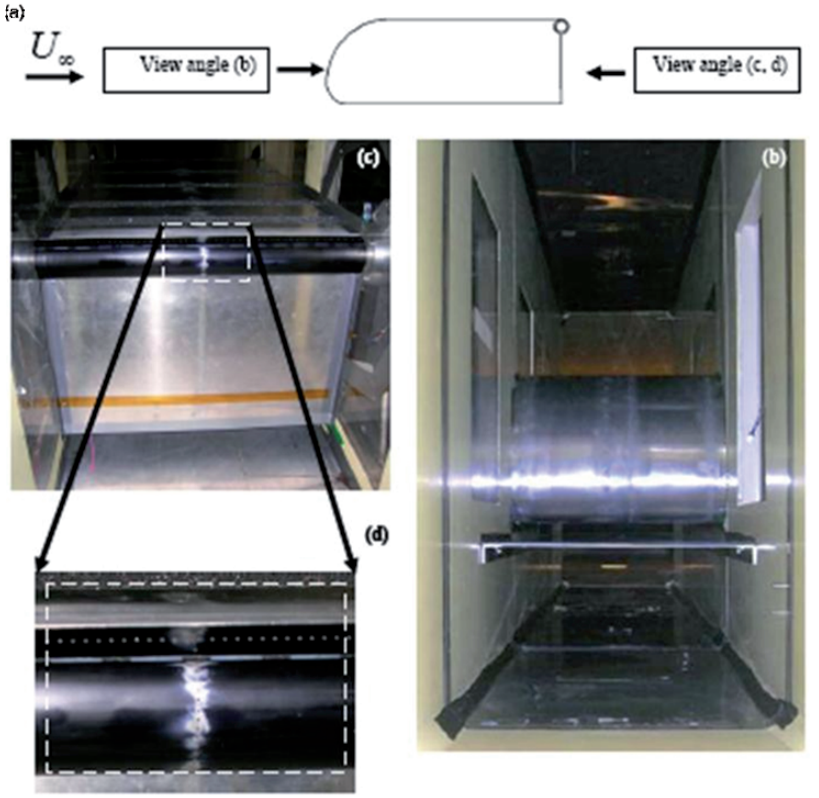

Fig. 7 The 2D truck model: (a) cross section (flow is coming from left to right); (b) front view showing the model installed in the tunnel 50-55mm above the simulated road; (c) a rear view showing the back plate and SaOB instrumented cylinder on the top-rear edge; and (d) close-up of the row of 96, 2mm suction holes and 1.7mm wide pulsed blowing slot on the cylinder (that was allowed to rotate for optimal actuation locations).

Of major importance was the determination of the optimal holes/slot location. Note that at this stage of the investigation the angular distance between the suction holes and pulsed blowing slots was fixed, 15 deg, based on the results of [9, 10].

The drag of the 2D truck model was calculated from the integration of the pressures around the model and from a 3D wake survey performed 1.2m behind the model. The wake flow was found to be quite 2D and the agreement between the two methods of drag evaluation was better than 2%, in most cases and in the absence of the simulated road. The drag reduction magnitudes were similar when evaluated either with the wake integration method or from the pressure drag. The aft-body "add-on" device was tested as a circular cylinder, due to the larger size and ease of installation of the 15 SaOB valve array inside it. A secondary major consideration was the capability to rotate the cylinder, bringing the holes/slot to an optimal location.

Figure 8a shows the form-drag of the 2D truck model with the SaOB cylinder installed at the upper-aft corner. The addition of the passive control cylinder at the aft-upper corner had a drag reducing effect of about 5% with respect to the baseline configuration shown in Fig. 1. The slot was just exposed when its location was 90 deg. With the control cylinder present but when the slot was hidden, Cdp=0.99±0.01. The passive effect of the slot, and its associated discontinuity, can be seen by the drag increase between 85 and 105 deg. At larger slot locations the drag returns to its undisturbed value, with a possible drag penalty of 0.01-0.02. At slot positions greater than 105 deg both slot and suction holes are open. Also shown on Fig. 8a are results of different levels of control applied by the array of SaOB actuators, with increasing level of input pressures, as indicated in the legend. A significant drag reduction develops in the range of tested pressures, up to 0.5Bar. An optimal holes/slot location can be identified around 130-132.5 deg, slightly increasing with the magnitude of the control authority. These results were obtained with a simulated road, similar to a truck with control applied only from the top-aft edge. It was later found that adding a second control cylinder at the lower-aft edge, *with simulated road* did not provide additional drag-reducing effect.

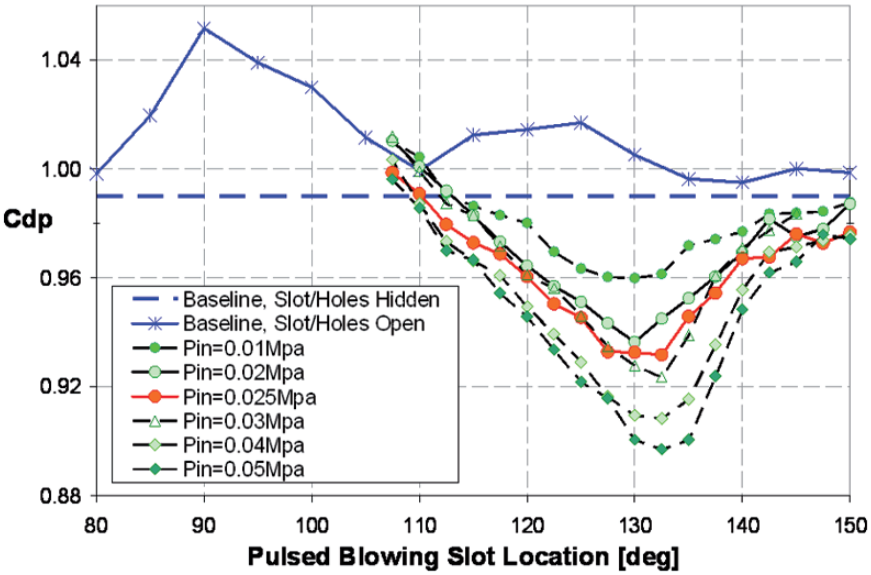

Fig. 8a The effect of the SaOB actuation on the drag of the 2D truck model at U=25m/s for different actuation levels indicated by the inlet pressures. The actuation location is altered via cylinder rotation, where 90 deg is the cylinder – upper plate junction.

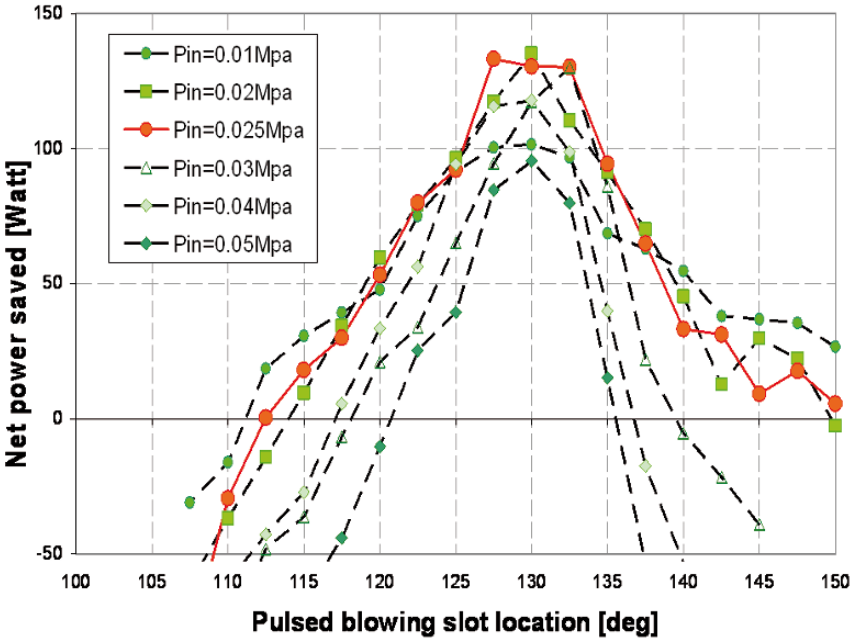

Fig. 8b The effect of the SaOB actuation on the required power to propel the 2D truck model at U=25m/s for different actuation levels indicated by the inlet pressures. The actuation location is altered via cylinder rotation, where 90 deg is the cylinder – upper plate junction. Reference power is about 2.57kWatt.

Despite the apparent capability of increased levels of inlet pressure to provide further drag reduction, one should consider the energy cost of the control input, since our aim is a reduction in *fuel consumption* and therefore total invested power should be a prime consideration. The net power saving was calculated according to: $Power\ saved = 0.5\rho U_\infty^3 S\Delta C_d - P_i Q_i/\eta$. Where ρ is the air density, U_∞=25m/s is the free-stream velocity, S=0.61x0.45m^2 is the 2D truck cross-section area, ΔC_d is the drag reduction at the same holes/slot position with respect to the baseline uncontrolled condition. The control power was taken as the product of the inlet pressure (*Pi*, measured at the supply line) and the inlet flow rate (*Qi*, measured by an orifice flow meter at the pressure regulator and neglecting the effect of the larger static pressure on the flow rate, making the actual flow rates smaller by 5-20% than those currently cited depending on the excess pressure). The pumping efficiency, η, was taken as 75%, as is in many common low-pressure compressors. In reality the control flow was provided by the lab shop air through a computer controlled pressure regulator. The data presented in Fig. 8b shows a rather insensitive (to the inlet pressure) peak power saving of around 130 watts for inlet pressures of 0.02-0.025MPa. With either lower or higher pressure levels, the power efficiency decreases.

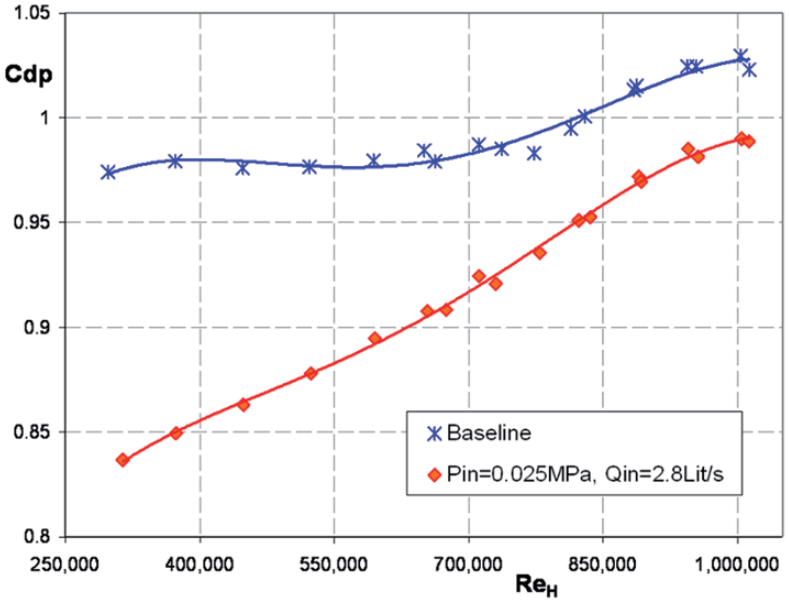

Fig. 9a The effect of the SaOB actuation on the baseline and controlled drag of the 2D truck model vs. the height Reynolds numbers for fixed actuation level. The actuation location is: pulsed blowing slot at α=130°, suction holes at α=115°, Pin=0.025 MPa, Qin=2.8 Lit/s where 90 deg is the cylinder – upper plate junction.

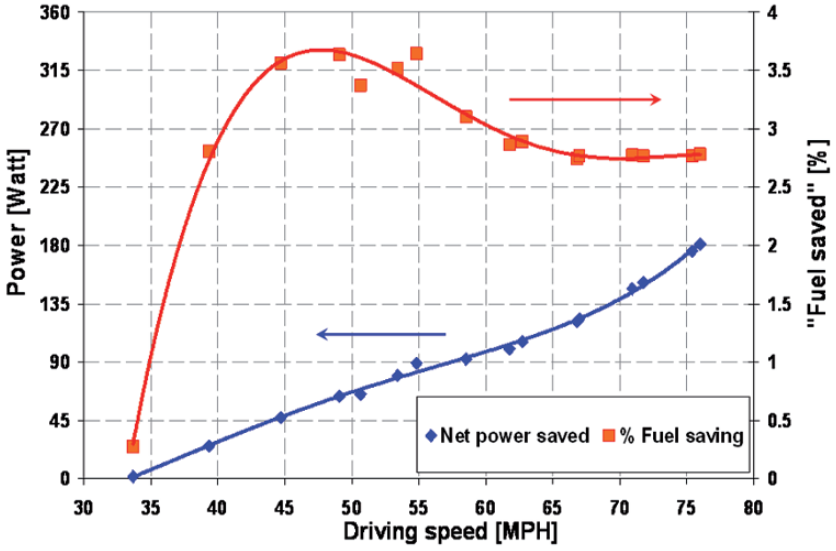

Fig. 9b The net flow power saved and equivalent "fuel" saving of the controlled 2D truck model vs. the driving speed for fixed actuation level. The actuation location is: pulsed blowing slot at α=130°, suction holes at α=115°, Pin=0.025MPa, Qin=2.8 Lit/s where 90 deg is the cylinder – upper plate junction. Same Re range as Fig. 9a.

While the data presented in Figs. 8a & b was obtained at a fixed free-stream velocity of 25m/s, it is important to evaluate the effectiveness of the drag reducing technology over the entire range of free-stream velocities, or driving speeds. Furthermore, this was done with one actuation condition, allowing the system just to be turned-on or off with no proportional control, for simplicity. Figure 9a presents form-drag data for the 2D truck model, with one upper control cylinder, the SaOB array installed on the upper-aft edge of the 2D truck model (as shown in Fig. 7a). Simulated road was present in this experiment. The drag slightly increases, from 0.98 to 1.02 with Re (based on the model height and the free-stream velocity) increasing from about 200,000 to about 1,000,000. Note that at the larger Re range the drag reaches a plateau. This Re, based on the height of the model, is considered minimal for Reynolds number free results. With fixed level of inlet pressure and fixed actuation locations, as indicated in the legend and caption of Fig. 9a, one can clearly note a significant drag reduction over the entire Re range. It is only natural to expect that the magnitude of the drag reduction will decrease as Re increases, due to the relative decrease between both the suction and pulsed blowing magnitudes when normalized by the free-stream velocity. Clearly aerodynamic drag reduction of about 20% is possible at low speeds, decreasing to about 5% at the highest speeds considered operational and legal for large trucks in the US highway system.

While the drag reduction is of interest, the power efficiency is our prime motivation. Figure 9b shows the net power saved and the percentage of net power saving. The latter is equivalent to about twice the expected fuel saving after considering friction resistance and wind averaged performance.

One can note a 45Watts power saving at 45MPH increasing to 180 watts saved at 75MPH. These power savings translate to more than 3.5% power saving at speeds between 45 and 55 MPH. At larger speeds the aerodynamic power saving (taking into account the invested power in the actuation system) saturates at about 2.8%. Considering that at these speeds (above 60 MPH) two thirds of the power is invested in overcoming aerodynamic drag, the equivalent net fuel savings is about 1.9%. While these numbers might appear small, they are still significant. The inlet pressure was optimal at about 50 MPH, so larger control authority would shift that peak to higher speeds, depending on the target speed range. Furthermore, the obtainable drag reduction due to the application of the control on the upper-aft edge with the simulated road present is smaller compared to its application on the sides of the truck, as will become clear from the subsequent discussion.

3.2 Two-dimensional truck with two control cylinders

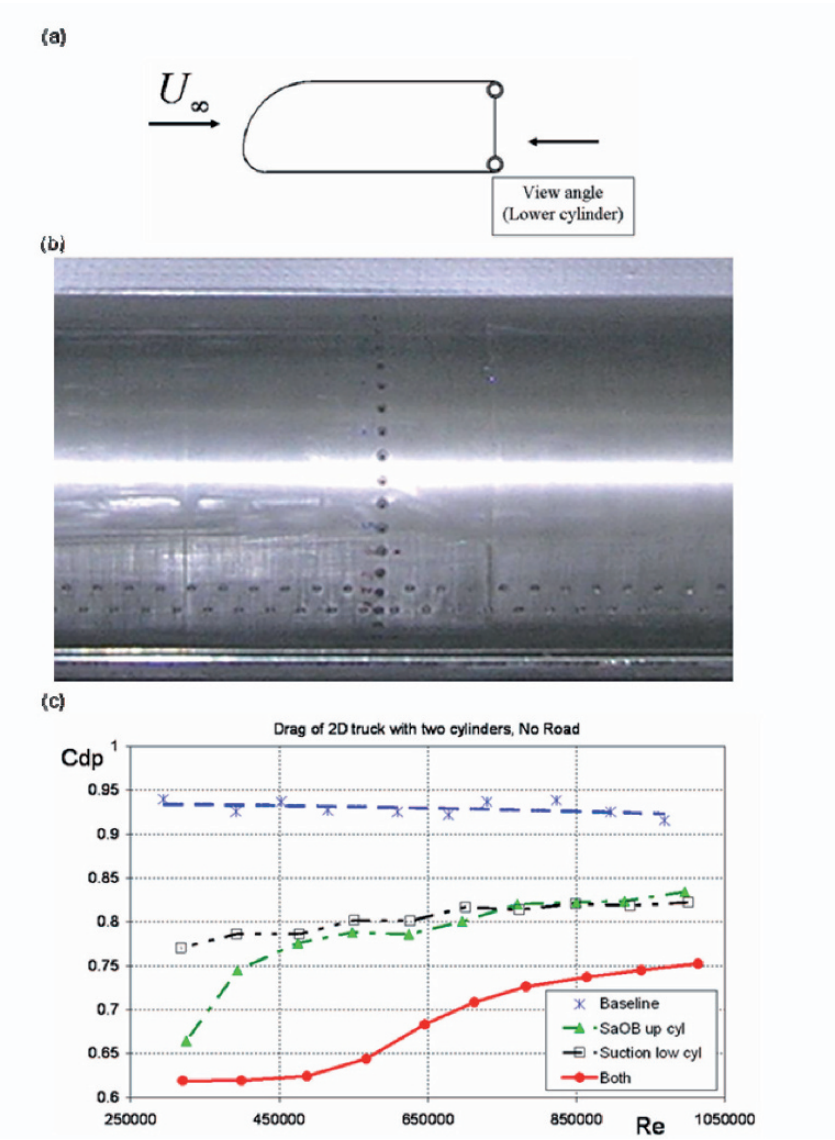

Fig. 10 (a) A sketch of the 2D truck model with two control cylinders, (b) a close-up rear-view of the lower aft-corner control cylinder, and (c) drag reduction due to SaOB array on top aft, Suction cylinder on bottom aft corners.(c) The actuation location is: pulsed blowing slot at α=130°, suction holes at α=115°, Pin=0.04 MPa, where 90 deg is the cylinder summit. Lower cylinder: two rows of suction holes, the 1st at α=-121°, the second at α=128.5°. Lower cylinder suction provides the same drag reduction as the SaOB array alone at Re~800,000. (c) Form drag coefficient vs. Reynolds number for four states: baseline, only the upper SaOB cylinder is turn on, only the lower suction cylinder is on, and both the cylinders are on.

To asses the effectiveness of controlling both vertical sides of the aft truck trailer, the simulated road was removed and a second control cylinder was mounted on the lower-aft edge of the 2D truck model, as shown in Fig. 10a. The lower control cylinder was also mounted on a rotary system to allow optimal control locations. However, for simplicity, cost and time considerations only steady suction was applied for the lower control cylinder. It should be noted that suction only (lower cylinder) is not as effective as SaOB valves (upper cylinder). Detailed comparison of the effectiveness of the two control methods (with suction only and with the SaOB valve array) can be found in [9, 10]. The suction was applied from two rows of staggered 2mm diameter holes, each containing 96 holes and spaced 7.5 deg in their angular locations (seen in Fig. 10b). The lower suction holes were just exposed for holes location of -90 deg. The same optimization procedure was applied to the lower cylinder in order to identify a condition which provides the same level of drag reduction that the upper SaOB control cylinder is capable of with inlet pressure of 0.04 MPa. This higher pressure level was selected based on the results shown in Figs. 8 and 9 and discussed above.

The data presented in Fig. 10c shows that the baseline-drag of the 2D truck model, with two control cylinders and without the simulated road is 0.93±0.01 regardless of the Reynolds number. The two control cylinders, when operated alone, can provide significant and similar drag reduction over the entire Re range, with the exception of the SaOB control that is more effective at low speeds. This difference might be associated with the oscillation frequency being somewhat low, and therefore optimal for low speeds. When the two control cylinders operate together, a very encouraging trend can be noted, i.e., that the drag reducing effects sum up. The data presented in Fig. 10c demonstrates about 20% aerodynamic drag reduction at highway speeds, translated to about 10% net fuel savings on large trucks, busses and tractor-trailer configurations.

A smaller 3D truck model with an array of SaOB actuators is currently being tested. Road tests will hopefully be conducted during the second quarter of 2008.

4. Conclusions and Recommendations

A comprehensive set of experiments were conducted with the aim of reducing the aerodynamic drag of large trucks by 20%. This effort included: (1) development, modeling and adjustment of the SaOB actuator to low-speed operation, (2) installation of a 15-valve actuator array in a circular cylinder, (3) comprehensive wind tunnel testing of the drag reduction effects on the circular cylinder under the effect of various boundary conditions, (4) the design and testing of a 2D truck model with and without simulated road, with and without control cylinders and finally (5) evaluation of the energy efficiency of control cylinder(s) drag reducing capability. Only stages (4-5) are currently discussed. Two related publications [9, 10] discuss stages (1-3).

It was found that the optimal location for introducing the suction through holes is about 15-20 deg downstream of the plate-cylinder junction. During the

cylinder alone tests it was found that suction with half the free-stream magnitude is capable of 15 deg separation delay. Therefore, the pulsed blowing was introduced 15 deg further downstream of the suction holes. One control cylinder positioned at the upper aft edge of the simulated trailer is capable of about 10% drag reduction and more. But if the power invested in the actuation is considered, the optimum is obtained at lower fluidic power input, where the aerodynamic drag reduction is roughly 6-7%. When two control cylinders were applied in a situation simulating a control applied to the two vertical edges of the aft-trailer region, 20% drag reduction is possible. This should lead to at least 10% net fuel savings.

Significant enhancement in power efficiency is expected when scale-up of the small-size model will be performed. This should originate from lower resistance of the suction holes (due to smaller wall thickness and rounded edges) and a factor of 2-4 power saving on the actuators' ejector due to the larger ejector-nozzle cross section.

Acknowledgment

The authors would like to thank S. Pastuer, E. Ben-Hamou, A. Blas, A. Kronish, S. Balvis, S. Moshel and M. Vaserman for the great technical support.
The research was funded by the Yeshaya Horowitz Fund and managed by RAMOT of Tel Aviv University. Three patents (one approved and two pending) exist.

References

[1] Prandtl L, "Motion of Fluids with Very Little Viscosity", Third International Congress of Mathematicians at Heidelberg, 1904, from Vier Abhandlungen zur Hydro-dynamik und Aerodynamik", pp. 1-8, Gottingen, 1927, NACA TM-452, March 1928.

[2] Seifert A, Darabi A and Wygnanski I, 1996, "Delay of Airfoil Stall by Periodic Excitation", J. of Aircraft. Vol. 33, No. 4, pp. 691-699.

[3] Pack Melton L, Schaeffler N, Yao C and Seifert A, "Active Control of Flow Separation from the Slat Shoulder of a Supercritical Airfoil", J. of Aircraft, 42 (5): 1142-1149 SEP-OCT 2005 (previously AIAA Paper 2002-3156).

[4] Pack Melton L, Yao C and Seifert A, "Active Control of Flow Separation from the Flap of a Supercritical Airfoil", AIAA J., 44 (1): 34-41 JAN 2006 (previously AIAA Paper 2003-4005).

[5] Traffic safety facts: large trucks, DOT HS 810 619.

[6] Collis S, Joslin R, Seifert A and Theofilis V, "Issues in active flow control: theory, simulation and experiment", Prog. Aero Sci., V40, N4-5, May-July 2004 (previously AIAA paper 2002-3277).

[7] Hsu T-Y, Hammache M & Browand F, "Base Flaps and Oscillatory Perturbations to Decrease Base Drag," Proceedings of the UEF Conference on The Aerodynamics of Heavy Vehicles:Trucks, Buses and Trains, Lecture Notes in Applied and Computational Mechanics Springer-Verlag, Heidelberg, September, 2004.

[8] Englar R, Advanced aerodynamic device to improve the performance, economics, handling and safety of heavy vehicles, SAE paper 2001-01-2072

[9] Sperber D, Dipl. Eng. Thesis, Technical University of Berlin, 2007.

[10] Sperber et al., "Drag reduction of a circular cylinder at transitional Reynolds numbers", in preparation.

[11] Arwatz G, Fono I and Seifert A, "Suction and Oscillatory Blowing Actuator", in "Proceedings of IUTAM Symposium on Flow Control and MEMS", London, Sep. 2006, Eds. Morrison, J.E., Birch, D.M. and Lavioe, P., p. 33-44, Springer 2008.

[12] Arwatz G, Fono I and Seifert A, "Suction and Oscillatory Blowing Actuator", accepted for publication, AIAA J., Nov. 2007.

[13] R McCallen, K Salari, J Ortega, L DeChant, B Hassan, C Roy, W Pointer, F Browand, M Hammache, T Hsu, A Leonard, M Rubel, P Chatalain, R Englar, J Ross, D Satran, J Heineck, S Walker, D Yaste, B Storms, "DOE's Effort to Reduce Truck Aerodynamic Drag-Joint Experiments and Computations Lead to Smart Design" AIAA paper June 2004.

[14] Seifert A, Pastuer S, "Method and mechanism for producing suction and periodic flow", US Patent 2006-0048829-A1, Granted 2005.

[15] Seifert A and Pack L, "Active Control of Separated Flow on a Wall-mounted "Hump" at High Reynolds Numbers", AIAA J., V. 40, No. 7, July, 2002, pp. 1363-1372. (Part of AIAA paper 99-3430).

Flow Separation Control on Trailing Edge Radii using Single Dielectric Barrier Discharge Plasma Actuators: An Application to Vehicle Drag Control

R. Spivey[1], R. Hewitt[2], H. Othman[2] and T. Corke[2]

[1] Mach Zero Associates, USA
[2] Center for Flow Physics and Control Aerospace and Mechanical Engineering Department, University of Notre Dame, USA

machzero@sbcglobal.net

Abstract As cruise speeds of ground vehicles has risen to as high as 70 miles per hour, overcoming the aerodynamic drag has become a significant percentage of the total power required. Engines have been increased in power and fuel tanks made larger to provide reasonable range between fuel stops. Heavy truck data in particular indicate that 2/3rds of the cruise power is needed to overcome drag. This paper focuses on reducing drag on class-8 trucks, but the principles can be applied to lighter trucks, busses, pick-ups, SUVs, and many other ground vehicles. The University of Notre Dame has developed unique actuators that have shown potential to maintain unseparated airflow around corners. This technology promises to reduce drag on ground vehicles thus increase fuel efficiency and gas mileage. This paper discusses these actuators and the preliminary wind tunnel tests that have been conducted at Notre Dame in 2007. The cost of fuel has risen so rapidly in the past few years that drag is now a major contributor to the cost of moving freight and consumer goods around the country. The use of these actuators can be applied to passenger cars and as well as many other types of ground vehicles.

Introduction

Over the past decade and a half much work has been conducted by the aerospace industry to control airflow in an effort to reduce the drag, improve handling qualities and lower the noise of aircraft. This paper applies that technology to ground vehicles. While the speed of ground vehicles is much less than that of aircraft, aerodynamics has become an important issue in today's energy-conscious world. The amount of fuel needed to move goods across the nation has risen sharply, just as the cost of that fuel has exploded. Data generated by the Department of Energy, show that 65% of the power required by a class-8 truck when cruising at 70 miles per hour is used to overcome aerodynamic drag. A significant amount of that drag is caused by (1) base drag, the air separation that occurs around the rear of the trailer; (2) gap drag, the drag associated with the area between the tractor and the trailer; and (3) the under-carriage, the area beneath the rig including the tires, the drive system and the structure that is needed to support the weight and utility of the rig.

Reducing the flow separation and momentum losses in these three areas will increase the truck's efficiency, resulting in a reduction of cruise power, fuel consumption and emissions. Figure 1 shows the truck locations where the application of Single-Dielectric Barrier Discharge Plasma Flow Control (PFC) could reduce drag.

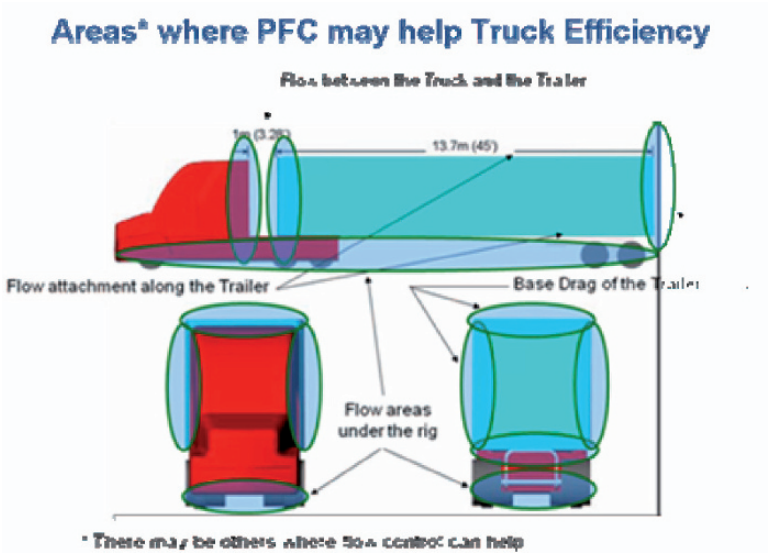

Fig. 1 Possible locations for PFC application to reduce flow separations and aerodynamic drag losses

Mach Zero Associates, a Fort Worth, Texas based, Small Business, has been working with the Department of Energy, truck and trailer manufacturing firms, truck leasing and operating companies, after-market businesses and the University

of Notre Dame to lay the groundwork to reduce this aerodynamic drag and improve the efficiency of long haul trucks. Class-8 Trucks are the large, 18-wheel vehicles that move freight around the country, fueling our commerce and providing an essential service to our nation's economy.

The University of Notre Dame's Center for Flow Physics and Control (FlowPAC) has developed the PDF actuator that has the capability of delaying flow separation around blunt objects. Test results show a 75-90% reduction in drag by incorporating two actuators on a cylindrical object causing the flow to remain attached far longer than expected (Thomas et al. [1]). These actuators use Single Dielectric Barrier Discharge (SDBD) plasma flow effects to maintain boundary layer stability, keeping the airflow attached around the cylinder, reducing the size of the wake and significantly decreasing the drag.

Figure 2 illustrates the flow around a four-inch cylinder with and without PFC application. The large wake fluctuations shown in the top photo are associated with the Von Karman vortex street that is the standard condition for cylinder wakes. In the lower photo, PFC actuators were located at the top and bottom (90° and 270° locations relative to the upstream stagnation line) of the cylinder at the flow separation locations. These effectively caused the flow over the cylinder to remain attached so that the flow pattern appears like that of an airfoil-shaped body. As expected, this transformation led to a significant drag reduction.

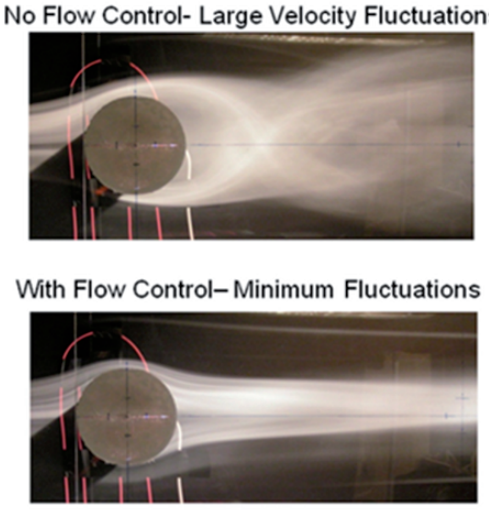

Fig. 2 Visualization records of the flow over a 4 in. cylinder at Re_D = 30,000 without (top) and with (bottom) PFC. (From Thomas et al.[1])

This paper will discuss early analyses and wind tunnel testing that was performed in an effort to determine the extent to which these actuators can reduce truck drag, thereby reducing the power required and fuel needed to move cargo throughout the country. The results are expected to lead to practical application of SDBD Plasma Actuator Flow Control (PFC) technology that is aimed at lowering the energy, emissions, power, fuel and turbulent airflow behind a class-8 truck.

Much work needs to be done, but the potential of reducing the enormous amount of carbon-based fuel that is consumed moving goods across the United States is well worth the effort.

SDBD Plasma Actuator Background

Based on the work at the University of Notre Dame Center for Flow Physics and Control (FlowPAC) over the last 15 years, much is known about the method of operation and capability of (SDBD) Plasma Flow Control (PFC). This flow control approach has been successful in a number of applications ranging from separation control, lift enhancement, drag reduction and flight control without moving surfaces [2-10]. A recent review of SDBD plasma actuators was given by Corke et al.[11].

Figure 3 illustrates the PFC actuator. It consists of two electrodes, one exposed to the air and one covered by a dielectric layer. The electrodes are supplied with an a.c. voltage that at high enough levels causes the air over the covered electrode to ionize. In the classic description, the ionized air is a "plasma", which is why these are referred to as "plasma actuators". The dielectric layer is very important to the design. The charge build-up on the dielectric prevents the discharge from collapsing into a constricted arc.

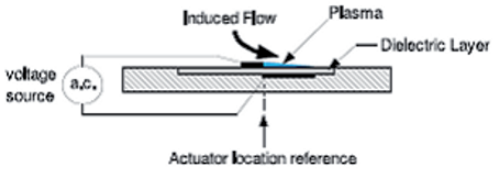

Fig.3 Plasma Flow Control actuator

The ionized air, in the presence of the electric field produced by the electrode geometry, results in a body force vector that acts on the ambient (neutrally charged) air [12, 13]. The body force is the mechanism for active aerodynamic control. If operated properly, there is very little heating of the air.

The asymmetric plasma actuator design in Fig. 3 produces a body force vector that induces a flow that is similar to that produced by a tangential wall jet. The mean velocity profile of the flow generated by this plasma actuator design is shown in Fig. 4. This accelerates the flow immediately adjacent to the wall. If applied to a separating boundary layer, it can cause the boundary layer to stabilize keeping the flow attached. Because the plasma actuator mechanism is through a body force, its effect is additive, namely N-actuators produce N-times the effect. Therefore additional actuators placed at stations downstream of a flow separation have the potential to maintain an attached flow over large distanced and sharp curvatures.

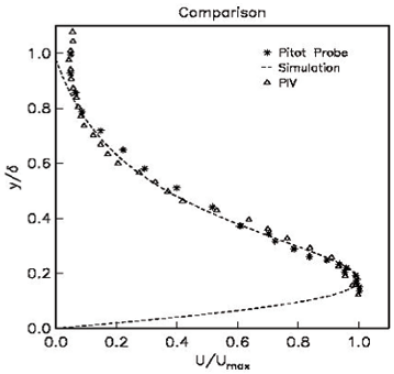

Fig. 4 Mean velocity profiles of the velocity component parallel to the wall (U) of flow induced by an asymmetric-electrode SDBD plasma actuator like that illustrated in Fig. 3 in still air. (from Post and Corke[6])

Motivation

Early analyses of using PFC on blunt bodies and airfoils have shown great promise in delaying airflow separation and reducing drag. While automobile gas mileage has increased over the years, class-8 truck mileage remains basically unchanged for almost 25 years. Much work has been done by the 21st Century Truck initiative that began in 2000, but the use of PFC has not been applied before. Most of the efforts that have been incorporated into production are passive shaping. These have been applied on the tractor but not on the trailer. There appears to be many locations on the tractor and trailer where the use of PFC can help reduce drag. In fact, if these actuators contribute as expected, redesign of both tractor and trailer may be in order. At this point in the research, most of the attention is being placed on after-market additions to existing designs to make them more fuel efficient.

From DOE documents, [14, 15] in the year 2003 the average class-8 truck used 4700 gallons of fuel while driving approximately 30,000 miles. However long haul rigs operating on the nation's freeway system averaged well over 100,000 miles. If two-thirds of that fuel was used to overcome aerodynamic drag, and based on an average diesel fuel cost of $2.50 per gallon, the fuel cost used to overcome the drag alone is approximately $30,000 per long haul truck per year. If the aft end of the truck trailer accounts for one-third of the total drag, then that drag itself contributes approximately $10,000 to the fuel cost per year per truck. The same can be said for the drag in the truck-trailer gap and the undercarriage. Any decrease in the aerodynamic drag of the tractors and trailers has the potential to greatly reduce the cost of operation, and the level of harmful emissions of the

trucks on our highways. The question at this point it is how much drag reduction can the achieved without impacting the utility of the rig.

This effort will utilize the approaches for plasma-based flow control from past experiments to design a combination of fairings and PFC actuators in strategic locations on the tractor and trailer to create more effective flow attachment and drag reduction. The overall plan is to determine the design parameters for the fairings, and the locations and strength of the actuators. Prototypes of these designs will then be built and tested in a wind tunnel at the University of Notre Dame. The most promising designs will ultimately be selected for tests at full-scale on trucks in over-the-road conditions to determine their ultimate impact and practicality.

Experimental Approach

The experiments were designed to determine the effectiveness of SDBD plasma actuators for turning flow around corners that would be representative of the aft edges of a tractor or trailer. Based on the results of the circular cylinder tests, [1] significant reduction in drag is possible if flow separations can be reduced or eliminated to allow the flow to negotiate sharp corners and fill the wake deficit region. The objective was to investigate the use of the plasma actuators to turn the flow around different radii. In order to simulate possible conditions on trucks, it was important that the boundary layer approaching the radius was turbulent. Therefore the test model consisted of a suspended flat plate of sufficient length, with a circular radius at the downstream edge. A schematic of the experimental setup is shown in Fig. 5. The flat plate setup was placed in an open return wind tunnel with a 2 foot square cross-section by 6 foot long test section.

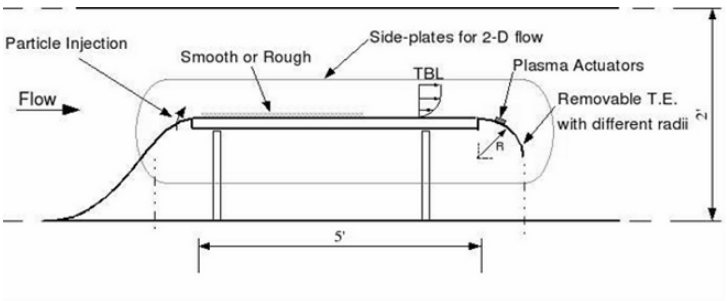

Fig. 5 Experimental setup for trailing-edge radius plasma actuator flow control.

The flat plate leading edge was located at the entrance to the test section, which was just downstream of the wind tunnel contraction. A second contraction was added to the leading edge of the plate to prevent flow from going under the plate. This was intended to better simulate a larger bluff body (like the aft end of a truck trailer). Side plates were used to limit 3-D side effects and maintain a 2-D mean flow across the spanwise direction of the flat plate. Two different types of

surface roughness were applied to the plate. One was course (No. 8) sand paper that was designed to trip the boundary layer to a turbulent state. The other was uniformly spaced 0.25 inch high wooden slats that both tripped the flow and produced rapid thickening of the boundary layer.

The trailing-edge radii were removable on the flat plate. Three radii were examined: 2.5 in (6.35 cm), 4.1 in (10.4 cm) and 5.0 in (12.7 cm). These were examined for three free-stream velocities of 6.6, 16.6 and 33 ft/s (2, 5 and 10m/s). The relatively low free-stream speeds were dictated by the ability to perform flow visualization, which gave a quick assessment of the degree to which the flow was turned by the plasma actuator, as well as the large blockage produced by the plate assembly in the test section.

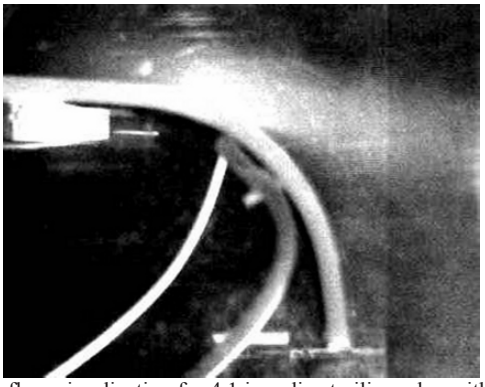

Fig. 6 Sample particle flow visualization for 4.1 in radius trailing edge without plasma flow control. Flow direction is from left to right.

The trailing edges were made by forming 0.25 inch thick Teflon sheets around circular mandrels. Teflon was chosen because it has excellent electrical properties to act as the dielectric layer between the electrodes in the SDBD plasma actuator. By using the whole radius material as the dielectric, the electrodes for the actuator could be located anywhere on the radius. The electrodes were made of 0.001 in (0.0254mm) thick copper foil tape. Generally, the downstream edge of the exposed electrode (flow side of the radius) was located just upstream of the separation location. The covered electrode dimension in the flow direction was 1 in (2.54 cm). The spanwise dimension of the electrodes corresponded to two-thirds of the width of the plate, and was centered in the spanwise direction.

The flow was made visible by introducing particles from a PIV particle generator part of the way up the second contraction ahead of the leading edge of the flat plate. The flow at the leading edge was carefully examined to insure that the particle injection did not cause the flow to separate on the second contraction or at the plate leading edge. An example of the particle flow visualization is shown in Fig. 6 for a 4.1 inch (10.4 cm) radius trailing edge. Here the flow is from left to right. It was illuminated by a sheet of light that was projected from the top at the spanwise centerline. This is a case without a plasma actuator. The flow is observed to naturally turn part way over the radius. Although there was a systematic

pattern to the degree with which the flow would turn as a function of the various parameters, the interpretation was felt to be too subjective. Therefore a surface flow visualization approach was also used.

A technique that visualized the flow on the surface of the trailing-edge radius was used to quantitatively determine the angle at which the flow separated. This technique involved applying a thin layer of an oil and china-white particle mixture that evaporated over time. The mixture was applied with the wind tunnel off. The tunnel was then quickly brought up to the set velocity. The liquid mixture was transported over the surface in response to the local surface shear stress vectors. After some time the liquid evaporated leaving the white particles in their final locations. The separation line was clearly visible from this technique. It was recorded by measuring around the circumference from the junction of the trailing-edge radius and the flat plate to the line of flow separation.

The approaching boundary layer was documented using a pitot-static probe attached to a motorized traversing mechanism. Examples of the mean profiles are shown in Fig. 7. These profiles were taken at the junction between the flat plate and the trailing-edge radius. The profiles are for the sand paper tripped boundary layer labeled "smooth", and the wall that was covered with the 0.25 inch wood slats, labeled "rough", at the highest free-stream speed of 33 ft/s (10 m/s). The boundary layer thickness for the "smooth" case is approximately 1.6 inches (4 cm). The "rough" wall increases the boundary layer thickness by approximately 60 percent at the downstream location. This is sufficient to investigate any influence of the boundary layer thickness on the ability of the plasma actuator to turn the flow around a radius.

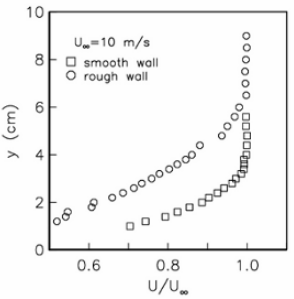

Fig. 7 Mean velocity profiles take at the junction between the flat plate and the trailing- edge radius for the two roughness conditions (sand-paper trip labeled "smooth") and the 0.25 inch wood slats (labeled "rough").

The effect of the plasma actuator voltage on the flow turning angle was investigated for the different parameters including the three radii and three velocities. An example of particle flow visualization images is shown in Fig. 8. This corresponds to the 4.1 in (10.4 cm) radius at the free-stream speed of 33 ft/sec (10m/s). The baseline (0 volts) indicates that there is a small amount of turning of the flow that occurs naturally. The plasma actuator was then located just upstream of that location. With the plasma actuator operating, the images clearly show an increase

in the angle of turning of the flow over the trailing edge radius as the voltage input to the actuator increases.

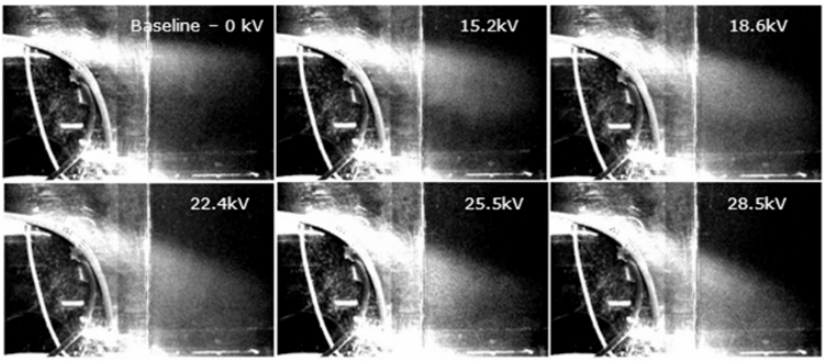

Fig. 8 Particle flow visualization showing the effect of plasma actuator voltage on the flow turning angle with 4.1 inch trailing edge radius

As previously mentioned, it was felt that the particle visualization was not sufficient to quantitatively indicate the turning angle of the flow. This was especially true at the higher velocity where there was considerable mixing of the separated shear layer. Therefore the surface flow visualization was used.

The surface visualization left a clear impression of the separation line on the trailing edge radius. Based on this, we defined a separation length, xs, as the distance along the circumference from the junction of the flat plate and the start of the radius to the separation location. Figure 9 illustrates this separation length.

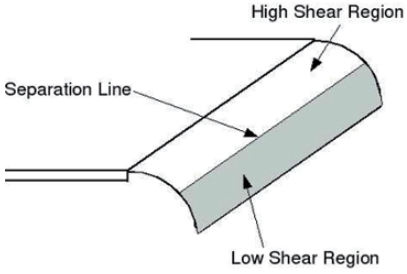

Fig. 9 Schematic showing the method of measuring the separation length, xs

The separation distances, xs, for the three radii as a function of the plasma actuator input voltage at the three free-stream speeds are shown in Fig. 10. The different freestream speeds are indicated by the different symbols. For any given radius, the change in xs is more a function of the plasma actuator voltage than the free-stream speed. Therefore we chose to fit a curve through the average of the values of the three free-stream speeds. For all three radii, the best fit curve relating the separation length to the actuator voltage was a straight line. Extrapolating the straight lines to the 0 kV actuator voltage gives the natural separation lengths for the three radii.

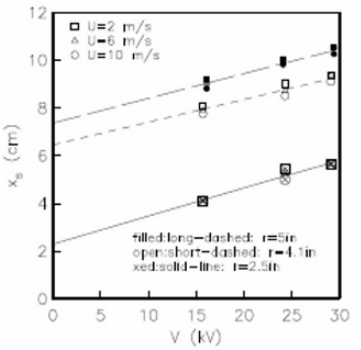

Fig. 10 Separation length, xs, for three radii as a function of the actuator voltage for three free-stream speeds

The separation lengths can be converted into turning angles of the flow by incorporating the trailing-edge radius, namely, $\theta = xs/r$. The flow turning angles, θ, that were converted from the xs values plotted in Fig. 10 are shown in Fig. 11. Again the effect of the different free-stream speeds is minimal, and the same straight-line fits that were used in Fig. 10 are again applied here. Extrapolating the straight lines to the 0 kV actuator voltage in this case gives the natural turning angle for the three radii.

We can observe a number of characteristics about the flow turning angle:

1. The natural flow turning angle decreases with increasing velocity
2. The response of the flow turning to the actuator input voltage increases with decreasing radius

In order to better illustrate these observations, we wished to subtract off the natural (actuator off) turning angles for the three radii. Figure 12 shows a comparison of the directly measured natural flow turning angles and the values obtained by extrapolating the straight- line fits to 0 kV in Fig. 11. These are observed to agree well, which substantiates the fit used in the previous figures.

We refer to the angle that the flow turns naturally for a given radius, as θ_0. These values have been subtracted from the turning angles produced by the plasma actuator previously shown in Fig. 11 to obtain the results plotted in Fig. 13. This figure indicates the flow turning increment. That is, it represents the added flow turning, above the natural amount that occurs without flow control that is actually produced by the plasma actuator. This representation clearly shows that the plasma actuator was more effective (larger slope) as the radius decreased.

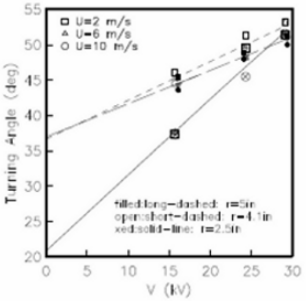

Fig. 11 Flow turning angle, θ, for three radii as a function of the actuator voltage for three free-stream speeds.

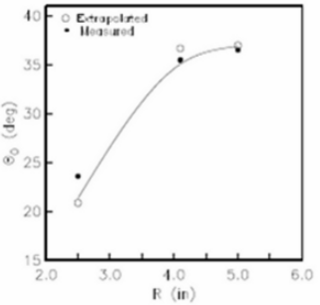

Fig. 12 Natural flow turning angle, θ, for three radii directly measured, and found by extrapolating values in Fig. 11 to a 0 kV actuator input.

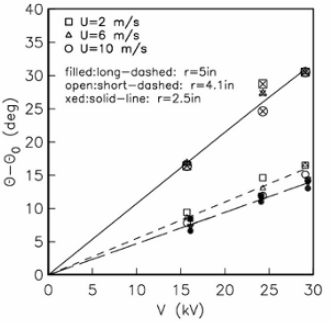

Fig. 13 Flow turning angle increment, $\theta-\theta_0$, for three radii as a function of the actuator voltage for three free-stream speeds.

The effect of the boundary layer thickness on the flow turning angle produced by the plasma actuator was found to be minimal. This is documented in Fig. 14 for the intermediate radius case.

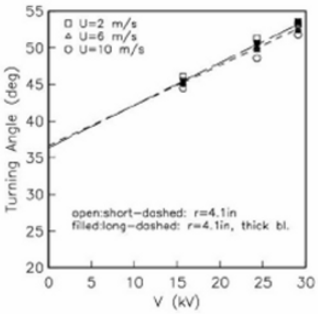

Fig. 14 Effect of the boundary layer thickness on the flow turning angle, θ, for an intermediate radius as a function of the actuator voltage for three free-stream speeds

Flat-plate Cylinder

One of the original objectives was to determine the effect that turning the flow around the trailing-edge radius had on the momentum recovery of the flow in the wake. The original setup was not sufficient to estimate this. Therefore a different setup was used that consisted of a suspended flat plate with a 2.5 in (6.35 cm) radius cylinder at the trailing edge. A schematic of the setup is shown in Fig. 15. Sand paper roughness like that used in the previous setup was used to trip the boundary layer to turbulence. Because the approach boundary layer to the cylinder was turbulent, it could be thought of as representing a super-critical Reynolds number condition for a circular cylinder. Under such as condition, the separation locations move from the top and bottoms of the cylinders, to positions approximately 23° further downstream. The lower blockage of this setup also allowed the measurements to be performed at higher free-stream speeds.

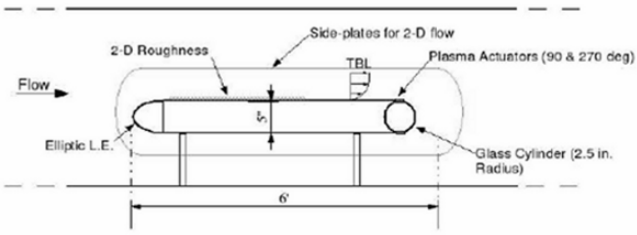

Fig. 15 Schematic of plate-cylinder setup used to measure mean velocity profiles resulting

Mean velocity profiles were measured in the wake of the plate-cylinder at a downstream location corresponding to 3 cylinder diameters. This was done at four free-stream speeds corresponding to 15, 20, 25, and 30 m/s. For these, the Reynolds number based on the cylinder diameter ranged from $128K \leq Re_D \leq 256K$, and the Reynolds number based on the x-length of the plate ranged from $1.5M \leq$

Rex ≤ 3.1M. Figure 16 shows mean velocity profiles for the four speeds for three conditions: (1) with the plasma actuator off, (2) with plasma actuators on at the 90° and 270° positions, and (3) with plasma actuators on at the 112° and 248° positions. In general the plasma actuator reduces the wake deficit compared to the base condition. In addition, the actuator is more effective when it is placed closer to the separation location (112° and 248°) than at the sub-critical cylinder separation locations from plasma flow control designed to turn the flow around the trailing edge radius.(90° and 270°). Finally for the fixed power applied to all of the free-stream conditions, the improvement of the wake deficit was less at the higher speeds.

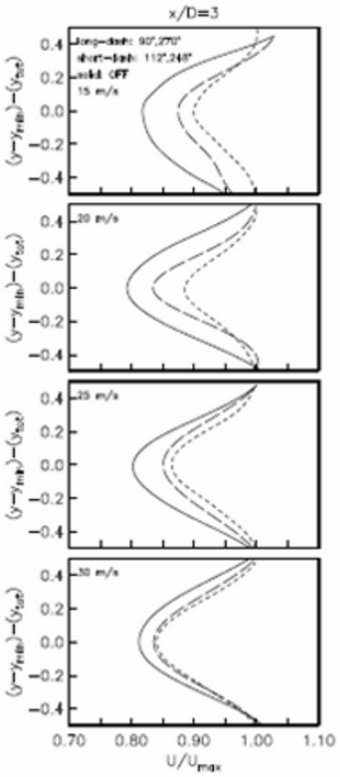

Fig. 16 Mean velocity profiles measured 3 trailing-edge cylinder diameters downstream of the plate-cylinder with the plasma actuator off (solid curve), and with it on in two arrangements (dashed curves). (128K ≤ ReD ≤ 256K, 1.5M ≤ Rex . ≤ 3.1M)

The results are further quantified by integrating the mean velocity profiles to obtain the momentum in the wake. This is shown in Fig. 17. In this figure, the momentum in the wake with the plasma actuator on (Momact) is normalized by the momentum with the actuator off (Mom0) as Momact/Mom0. The smaller the ratio, the larger the amount of recovered momentum and, presumably, the lower the drag.

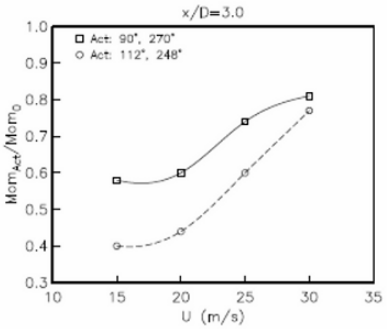

Fig. 17 Normalized momentum based on the mean velocity profiles in Fig. 16 for the two plasma actuator arrangements. ($128K \leq Re_D \leq 256K$, $1.5M \leq Rex \leq 3.1M$)

As expected based on the mean velocity profiles, the plasma actuators located closer to the separation location performed better and thereby recovered a larger amount of the momentum in the wake of the cylinder. Also as indicated by the mean velocity profiles, the effect is reduced at the higher velocity. However at 30m/s, which corresponds to 67mph, (a respectable truck interstate speed), 25 percent of the momentum in the wake is recovered. Further measurements are needed to determine the drag improvement and the relative improvement after accounting for the power supplied to the plasma actuators. However, at this stage, the results are encouraging.

Summary

The SDBD plasma actuators were effective in controlling flow separation around a trailing- edge radius in which the approaching flow is a turbulent boundary layer. The baseline separation location moves upstream with decreasing radius. A linear dependence of the separation location, and thereby the flow turning angle, on the plasma actuator voltage was found. For this, there was a minimum sensitivity to the free-stream velocity and approaching turbulent boundary layer thickness.

The response of the flow to turn a prescribed radius as a result of the plasma actuator was found to increase with decreasing radius. Using a plate-cylinder setup, up to a 50 percent recovery of wake momentum was measured. At the highest free-stream speed of 30 m/s (67mph) there still remained a 25 percent recovery in momentum.

While much more work is needed to determine the total impact of this technology to reduce the drag and fuel consumption of trucks and other ground vehicles, the research thus far is very promising. Additional tests are planned for later in 2008 based on the results obtained in this effort. Additional baseline tests are planned along with different placement of actuators and the use of several actua-

tors operating in tandem to build on the technology such that further, more representative testing can be done over the road on actual rigs.

References

1. Thomas FO, Kozlov A and Corke TC 2005, Plasma actuators for landing gear noise control, AIAA Paper 2005-3010, 11th AIAA/CEAS Aeroacoustics Conference, To appear AIAA J., 2008.
2. Corke T, Jumper E, Post M, Orlov D, and McLaughlin T 2002, Application of weakly-ionized plasmas as wing flow-control devices. AIAA Paper 2002-0350.
3. Huang J, Corke T and Thomas F 2003, Plasma actuators for separation control of low pressure turbine blades. AIAA Paper 2003-1027. also AIAA J., Jan. 2006.
4. Post M and Corke T 2003, Separation control on high angle of attack airfoil using plasma actuators. AIAA Paper 2003-1024, also AIAA J., 42, 11, p. 2177.
5. Post M 2004, Plasma actuators for separation control on stationary and oscillating wings. Ph.D Dissertation, University of Notre Dame.
6. Post M and Corke T 2004, Separation control using plasma actuators – stationary and oscillating airfoils. AIAA Paper 2004-0841.
7. Corke T, He C and Patel M 2004, Plasma flaps and slats: an application of weakly- ionized plasma actuators. AIAA Paper 2004-2127.
8. Corke T and Post M 2005, Overview of plasma flow control: concepts, optimization, and applications. AIAA Paper 2005-0563.
9. Huang J 2005, Documentation and control of flow separation on a linear cascade of Pak-B blades using plasma actuators. Ph.D., University of Notre Dame, Notre Dame, Indiana.
10. Huang J, Corke T and Thomas F 2005, Unsteady Plasma actuators for separation control of low pressure turbine blades. To appear AIAA J..
11. Corke T, Post M and Orlov D 2007, SDBD Plasma Enhanced Aerodynamics: Concepts, Optimization and Applications. J. Progress in Aerospace Sci., Vol 43, No. 7-8, Oct-Nov.
12. Enloe L, McLaughlin T, VanDyken, Kachner, Jumper E, and Corke T 2004, Mechanisms and Response of a single dielectric barrier plasma actuator: Plasma morphology. AIAA J., 42, 3, p. 589. Also AIAA 2003-1021.
13. Enloe L, McLaughlin T, VanDyken, Kachner, Jumper E, Corke T, Post M, Haddad O 2004, Mechanisms and Response of a single dielectric barrier plasma actuator: Geometric effects. AIAA J., 42, 3, p 585.
14. Bradley R et al, Technology Roadmap for the 21st Century Truck Program. http://www.doe.gov/bridge, December, 2000.
15. DOE Annual Report, Annual Energy Review 2004. DOE/EIA-0384(2004), www.eia.doe.gov/aer, August, 2005

Adaptive Control of Post-Stall Separated Flow Application to Heavy Vehicles

L. Cattafesta[1], Y. Tian[1] and R. Mittal[2]

[1] Interdisciplinary Microsystems Group, Department of Mechanical and Aerospace Engineering, Gainesville, FL 32611-6250, USA
cattafes@ufl.edu
[2] Department of Mechanical and Aerospace Engineering
The George Washington University
Washington D.C. 20052

Abstract This paper discusses two adaptive feedback control approaches designed to reattach a massively separated flow over a NACA airfoil with minimal control effort using piezoelectric synthetic jet actuators and various sensors for feedback. One approach uses an adaptive feedback disturbance rejection algorithm in conjunction with a system identification algorithm to develop a reduced-order dynamical systems model between the actuator voltage and unsteady surface pressure signals. The objective of this feedback control scheme is to suppress the pressure fluctuations on the upper surface of the airfoil model, which results in reduced flow separation, increased lift, and reduced drag. A second approach leverages various flow instabilities in a nonlinear fashion to maximize the lift-to-drag ratio using a constrained optimization scheme – in this case using a static lift/drag balance for feedback. The potential application of these adaptive flow control techniques to heavy vehicles is discussed.

Introduction

Flow separation incurs a large amount of energy loss and limits the performance of many flow-related devices (e.g., airfoils, automobiles, trucks etc.). Researchers have been trying to mitigate or eliminate flow separation for over a century because of its large potential payoff in practical applications. Numerous passive and active separation control strategies have been attempted with varying degrees of success. Passive techniques involve geometric modifications to alter the flow characteristics, while active methods involve the use of flow actuators to modify the flow and therefore require external energy addition.

Passive techniques are desirable because of their simplicity and, if properly designed, their effectiveness at design conditions. However, the performance of a passive control system usually degrades at off-design conditions. In the context of

heavy vehicles, "off-design" encompasses speed deviations and poor weather (e.g., wind, snow, or rain).

The main benefit of active techniques is their ability to "adapt" to off-design conditions. However, most of the active control approaches are open-loop in nature and, hence, are not really adaptive. Feedback control uses sensors to feed back information about the flow and/or vehicle states, and a controller automatically adjusts the actuator input to achieve a desired control objective. If the controller is adjusted or redesigned automatically during this process, it is called "adaptive." The primary disadvantage of this approach is its complexity, and its use thus represents a paradigm shift from conventional passive and active control. Nonetheless, the potential performance benefits and improved robustness warrants research.

This paper addresses a model problem that is representative of the separated flow behind a heavy vehicle. In particular, two adaptive feedback control approaches are discussed that seek to reattach a massively separated flow over a NACA 0025 airfoil with minimal control effort using piezoelectric zero-net mass-flux actuators and various sensors for feedback. One approach uses an adaptive feedback disturbance rejection algorithm in conjunction with a system identification algorithm to develop a reduced-order dynamical systems model between the actuator voltage and unsteady surface pressure signals. Its objective is to suppress the pressure fluctuations on the upper surface of the airfoil model, which results in reduced flow separation, increased lift, and reduced drag. A second approach leverages various convective and global flow instabilities in a nonlinear fashion to maximize the lift-to-drag ratio using a constrained optimization scheme – in this case using a static lift/drag balance for feedback. Experiments are described to elucidate the baseline uncontrolled and controlled flow physics, and the potential application of these approaches to heavy vehicles is discussed.

Experimental Configuration

As shown in Fig. 1, separation control experiments are conducted on a two-dimensional, $c = 15.24$ cm chord NACA 0025 airfoil mounted in an open-return, low-speed wind tunnel with a 30.48 cm by 30.48 cm by 60.96 cm test section. Six unsteady pressure transducers (Kulite LQ125-5A) are mounted beneath 2.2 mm diameter pinhole apertures at the mid-span location located at approximately 44.0%, 52.5%, 61.0%, 69.5%, 77.9% and 86.4% chord. A strain-gauge balance integrated into the model mount is used to measure the total lift and drag forces of the airfoil for varying angles of attack.

The airfoil contains four piezoelectric zero-net mass-flux (ZNMF) actuators with $h = 0.5$ mm wide slots located in the central 1/3rd spanwise region of the airfoil. Here we describe control experiments that only use actuator #1 located at the 3% chord location; the other unused actuators slots are covered. Details on the

synthetic jet actuators used in this research can be found in Gallas et al. (2003), Holman et al. (2003), and Gallas (2005).

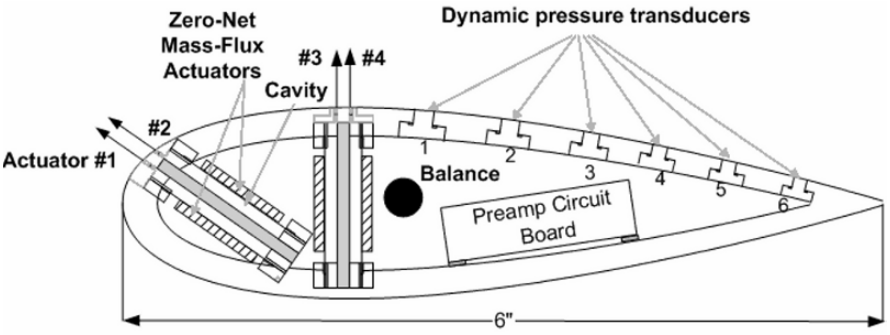

Fig. 1 Experimental setup of NACA 0025 airfoil showing four ZNMF actuators, a strain gage balance, and six dynamic surface pressure transducers.

The control system for the separation control experiments is implemented using a dSPACE (Model DS1005) DSP system with a 466 MHz PowerPC CPU. The dSPACE system has a 5-channel 16-bit A/D board (DS2001) and a 6-channel 16-bit D/A board (DS2102). The control algorithms are first programmed in Matlab/Simulink and C programs (C code S-functions) and then compiled and loaded on the dSPACE DSP processor.

The angle of attack (AoA) was greater than 10° for these experiments, corresponding to massive leading-edge separation or post-stall separated flow, as shown in Fig. 2. The chord Reynolds number, $\mathrm{Re}_c = \rho U_\infty c/\mu$, was 1E5 to 1.2E5. The BL is tripped in the leading edge region using 100 sand grit.

Problem Definition and Background

The objective of the control is to reattach the flow to the airfoil surface with minimal actuator power expenditure. A ZNMF actuator is a popular device for active flow control that requires no external flow source and works by alternately expelling and ingesting fluid through the actuator slot via a vibrating diaphragm (Glezer and Amitay 2002). Input sinusoidal oscillations are characterized by a dimensionless frequency $F^+ = fc/U_\infty$ and oscillatory momentum coefficient, $< C_\mu >= \left(\rho u_{j,rms}^2 h\right) \Big/ \left(0.5\rho U_\infty^2 c\right)$, where $u_{j,rms}$ is the rms jet velocity in the slot.

Although numerous studies are reported in the literature to determine the optimal forcing frequencies for effective separation control, the observed values of optimal F^+ vary over a wide range. For example, Greenblatt and Wygnanski (2000) concluded that the optimal range is $2 < F^+ < 4$. Seifert and Pack (1999) found

that the excitation frequency should be chosen such that $0.5 < F^+ < 1.5$ over a wide range of high Reynolds numbers. Conversely, Amitay et al. (2001) found that when the excitation frequency $F^+ > 10$, the lift-to-pressure-drag ratio was larger than when the excitation frequency $F^+ < 4$ for their unconventional airfoil.

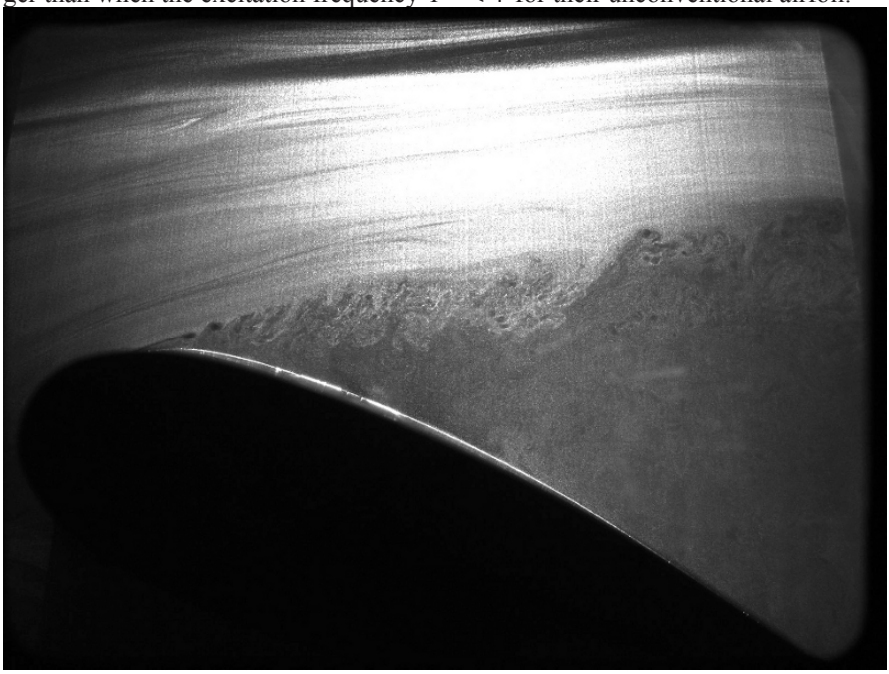

Fig. 2 Instantaneous laser light sheet visualization of the baseline uncontrolled post-stall separated flow on the airfoil at Re_c = 1E5 and angle-of-attack (AoA) = 20°.

For the case shown in Fig. 2, the optimal open-loop sinusoidal forcing for the present experiment is $F^+ = 15$ with $< C_\mu >= 3.16 \times 10^{-4}$, resulting in partial reattachment with an increase in lift-to-drag ratio from 1.1 for the baseline uncontrolled case to 1.76 (Tian 2007). Thus, it may appear that the present results are more in line with the findings of Amitay et al. However, this result is misleading since the optimal value of F^+ depends not only on the flow dynamics but also on the actuator. Figure 3 shows the normalized frequency response (i.e., the ratio of output rms jet velocity to input sinusoidal voltage) of actuator 1. Note that the actuator output is negligible below 500 Hz and peaks around 1100 Hz. So the optimal result of $F^+ = 15$, which corresponds to ~1000 Hz excitation, is at least partially explained by the fact that the actuator "works best" near this frequency. Nonetheless, the goal of the closed-loop control schemes is to at least match the performance of this optimal open-loop result, preferably with reduced actuator output, by relaxing the restriction to sinusoidal excitation.

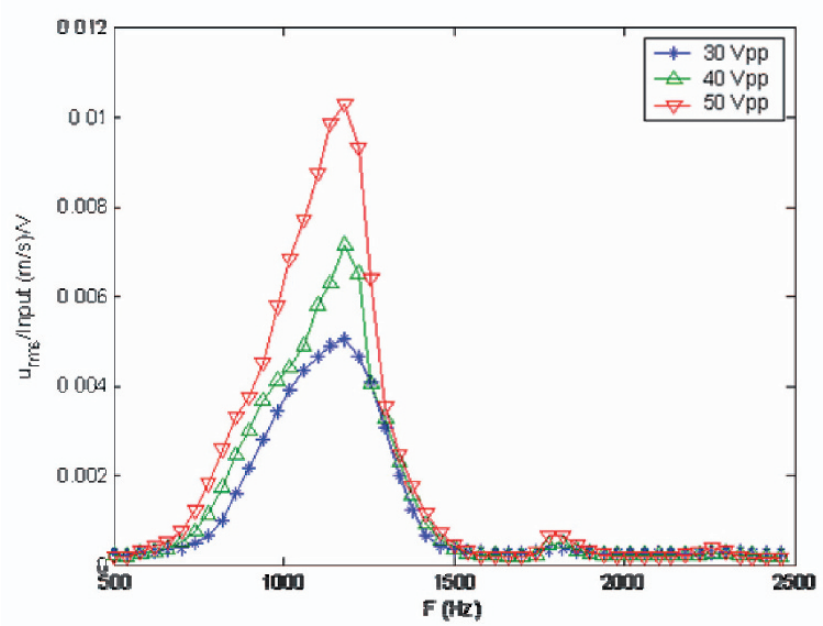

Fig. 3 Frequency response of ZNMF actuator 1. Note the actuator produces non-negligible output to sinusoidal inputs only in the range from 500-1500 Hz.

Results and Discussion

In this section we summarize the results for two algorithms used for real-time adaptive flow control. The first is a conventional adaptive disturbance rejection algorithm that includes an adaptive linear system identification model. The second approach uses a nonlinear constrained optimization strategy to adjust the parameters of a multi-frequency waveform to maximize the lift-to-drag ratio.

ARMARKOV Disturbance Rejection

As mentioned above, this algorithm contains two parts: system identification (ID) and control. The ID portion produces a low-order dynamical system model between the actuator voltage and the unsteady pressure signals, while the control algorithm seeks to suppress the power or mean-square value of the unsteady pressure fluctuations from one of the transducers. This approach is based on an inherent assumption that the unsteady pressure fluctuations are larger when the flow is

separated due to the passage of vortical structures over the surface of the model, the validity of which is demonstrated in Kumar and Alvi (2005).

A block diagram of the simultaneous ID and control algorithm is shown in Fig. 4. Here, both ID and control signals are input into the flow system, comprised of the actuator and airfoil, and the outputs of the system are assumed to be unsteady surface pressure measured by the transducers. The ID algorithm uses a band-limited input signal to the actuator with the performance pressure signal to develop an ARMARKOV system ID model (Akers and Bernstein 1997). The adaptive disturbance rejection algorithm uses the parameters identified in the system model combined with the measured airfoil surface pressures to tune or adjust the controller (Venugopal and Bernstein 2000). The ID and disturbance rejection algorithms are described in detail in the above references and in Tian et al. (2006b) and Tian (2007) for this problem.

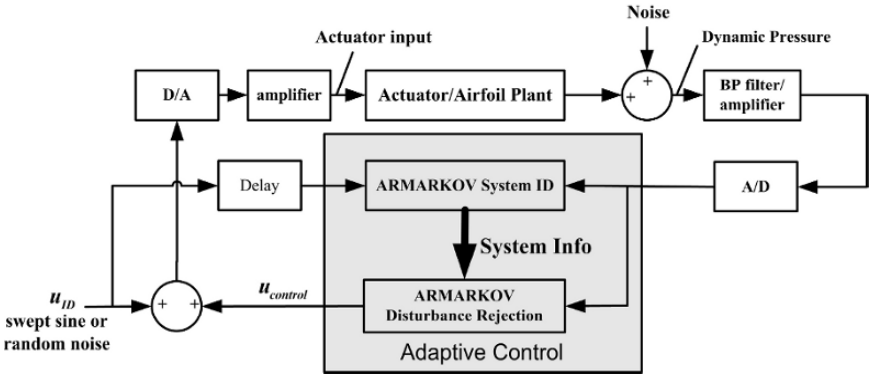

Fig. 4 Block diagram of adaptive system identification and disturbance rejection algorithm.

Constrained Nonlinear Optimization

Various optimization strategies are discussed in the literature (Press et al. 1992). After some experimentation with several extremum-seeking algorithms (Artiyur and Krstic 2003; Banaszuk et al. 2003), the downhill simplex method described in Press et al. was implemented to minimize the drag-to-lift ratio.

The benefits of the algorithm are its simplicity and applicability to multi-parameter constrained optimization and its faster convergence rate compared to extremum-seeking control for the present problem. The key steps of the algorithm are summarized as follows: 1) evaluate the cost function at chosen initial conditions, 2) use the lowest value as a reference and search for a lower value of the cost function, 3) move only in the downhill direction, and 4) terminate when some convergence criteria are met. The method thus finds a local minimum. To improve

the probability of finding the global minimum, multiple experiments are performed starting from different initial conditions. Again, the details of this algorithm are described in Tian et al. (2006a) and Tian (2007).

As explained in Tian (2007), the separated flow exhibits two dominant flow instabilities. The separated shear layer is characterized by convective Kelvin-Helmholtz (K-H) instabilities, which manifest themselves as the large-scale vortical structures with frequency $f_{SL} \sim U_\infty / \theta_0$, where θ_0 is the initial momentum thickness of the boundary layer just prior to separation (see Fig. 2). The large wake is characterized by a global instability, which manifests itself as a vortex street with frequency $f_{wake} \sim U_\infty / \theta_{wake}$, where θ_{wake} is the momentum thickness of the wake. The global wake instability interacts in a nonlinear fashion with the K-H instability. Since $\theta_{wake} >> \theta_0$, then $f_{wake} << f_{SL}$ so these two frequencies are widely separated in the post-stall case. This fact emphasizes the need for an actuator with sufficient bandwidth to excite both instabilities. The key assumption is that control will be more effective if both of these instabilities are excited, and this can only be achieved via a mult-frequency waveform.

Tian et al. (2006a) and Tian (2007) describe three such waveforms: amplitude modulation (AM), burst modulation (BM), and pulse modulation (PM). Each of these represents the product of a high-frequency carrier signal and a low-frequency modulation signal. For example, an AM signal is

$$e(t) = A \sin\left(2\pi f_c t\right) \frac{1 + \sin\left(2\pi f_m t\right)}{2},$$

which is characterized by three parameters: the amplitude A, carrier frequency f_c, and modulation frequency f_m. The use of such a complex waveform produces a rich spectrum of input disturbances due to flow nonlinearities, which in turn excites the K-H and wake instabilities. The goal of the simplex algorithm is to adjust these three parameters to minimize the drag-to-lift ratio.

Finally, to negate the preferential actuator output over a certain frequency range described above, the ZNMF actuator output jet rms velocity is "calibrated" using a constant-temperature hot-wire anemometer and current probes for each waveform type (AM, BM, or PM) to provide a look-up table that relates $< C_\mu >$ and actuator electrical power to the waveform parameters. In this manner, the optimization can be constrained to fix either $< C_\mu >$ or electrical power while A, f_c, and f_m are adjusted. This permits a fair comparison between different actuator waveforms.

Both adaptive controllers are able to completely reattach the separated flow at AoA=12°, as shown in Fig. 5, and L/D is increased to 7.0 ± 0.4. As the AoA is increased above 12°, the performance of the adaptive disturbance rejection controller, which is inherently linear, gradually deteriorates. Finally at AoA=20°, the

lift-to-drag ratio is essentially identical to that of the uncontrolled case ($L/D = 1.1 \pm 0.04$). In contrast, the nonlinear controller is more robust at higher angles of attack. In particular, at AoA=20°, $L/D = 2.18 \pm 0.07$ for AM with $< C_\mu >= 7.15 \times 10^{-6}$, $f_m = 61$ Hz and $f_c = 2405$ Hz. Optimal sinusoidal control was achieved with $< C_\mu >= 3.16 \times 10^{-4}$, resulting in $L/D = 1.76 \pm 0.03$. Note that slightly superior performance is achieved via nonlinear feedback vs. sinusoidal control but with a reduction in $< C_\mu >$ by a factor of 44! More details on these experiments are provided in Tian (2007).

Conclusions

The results of these experiments on a model post-stall airfoil problem show the potential of adaptive control of separated flow. In particular, the nonlinear controller appears most promising due to its ability to leverage multiple flow instabilities and therefore achieve control with very low energy expenditure.

The above closed-loop methodology appears to be applicable to heavy vehicles and would be a natural extension of previous open-loop control approaches (Hsu et al. 2004; Englar 2004). In particular, the massive wake behind a truck will likely exhibit similar flow instabilities as that of a post-stall airfoil, namely the K-H shear layer and global wake instabilities. Of course, the three-dimensional nature of the bluff body wake will be more complex. In addition, the objective function for control will differ from the lift-to-drag ratio. Since drag reduction is the main objective for a heavy vehicle, maximizing the average base pressure is perhaps a reasonable objective. Unsteady actuation around the rear perimeter of the vehicle appears to be a logical location for the actuators. In summary, it seems clear that further research on this topic is both warranted and required to understand the benefits and limitations of adaptive feedback flow control as applied to heavy vehicles.

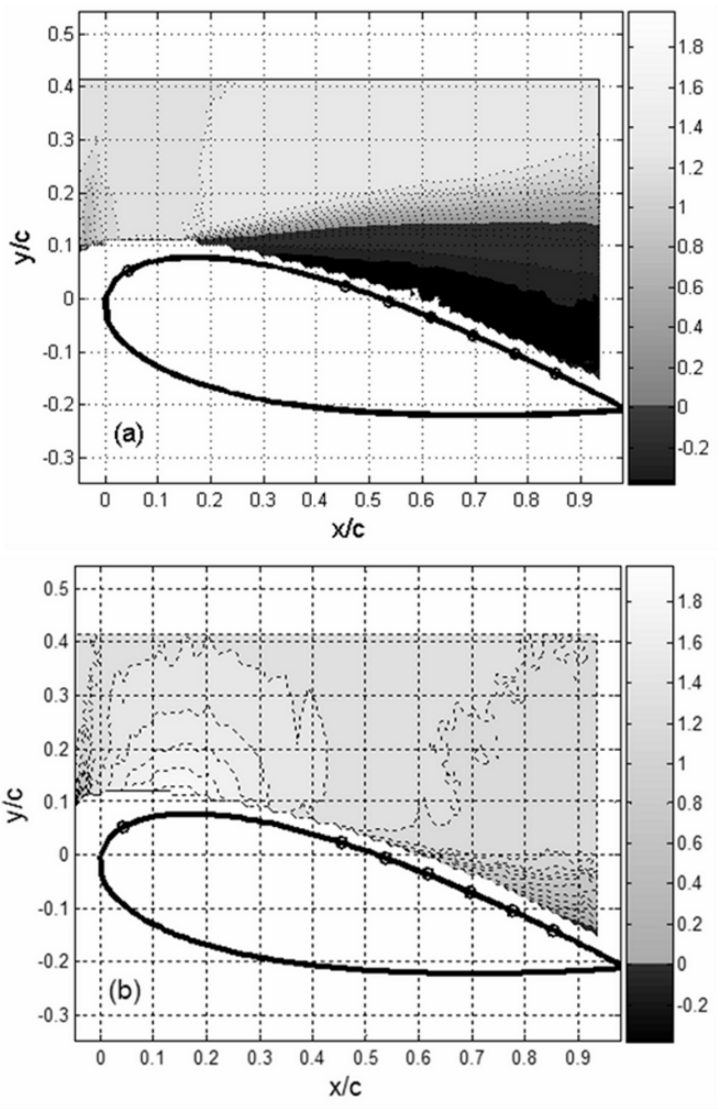

Fig. 5 Contours of streamwise velocity u/U_∞ for (a) baseline and (b) closed-loop control at AoA = 12° and Re_c =120,000.

References

Akers J and Bernstein D, "Time-Domain Identification Using ARMARKOV/Toeplitz Models", Proceedings of the American Control Conference, pp. 191-195, June 1997.

Amitay M, Smith D, Kibens V, Rarekh D and Glezer A, "Aerodynamic Flow Control over an Unconventional Airfoil Using Synthetic Jet Actuators," *AIAA Journal,* Vol. 39, No. 3, pp. 361-370, March 2001.

Artiyur K and Krstic M, Real-Time Optimization by Extremum-Seeking Control, Wiley-Interscience, 2003.

Banaszuk A, Narayanan S and Zhang Y, "Adaptive Control of Flow Separation in a Planar Diffuser," AIAA paper 2003-0617, January 2003.

Englar R, "Pneumatic Heavy Vehicle Aerodynamic Drag Reduction, Safety Enhancement and Performance Improvement," Proceedings of the UEF Conference on The Aerodynamics of Heavy Vehicles:Trucks, Buses and Trains, Lecture Notes in Applied and Computational Mechanics Springer-Verlag, Heidelberg, September, 2004.

Gallas Q, "On the Modeling and Design of Zero-Net Mass Flux Actuators," Ph.D. Thesis, Department of Mechanical and Aerospace Engineering, University of Florida, May 2005.

Gallas Q, Holman R, Nishida T, Carroll B, Sheplak M, and Cattafesta L, "Lumped Element Modeling of Piezoelectric-Driven Synthetic Jet Actuators," *AIAA Journal*, Vol. 41, No. 2, pp. 240-247, 2003.

Glezer A and Amitay M, "Synthetic Jets," *Annual Review of Fluid Mechanics*, Volume 34, pp. 503-529, January 2002.

Greenblatt D and Wygnanski I, "The control of flow separation by periodic excitation," *Progress in Aerospace Sciences*, Vol. 36, pp. 487-545, 2000.

Holman R, Quentin G, Carroll B and Cattafesta L, "Interaction of Adjacent Synthetic Jets in an Airfoil Separation Control Application", AIAA Paper 2003-3709, June 2003.

Hsu T-Y, Hammache M & Browand F, "Base Flaps and Oscillatory Perturbations to Decrease Base Drag," Proceedings of the UEF Conference on The Aerodynamics of Heavy Vehicles:Trucks, Buses and Trains, Lecture Notes in Applied and Computational Mechanics Springer-Verlag, Heidelberg, September, 2004.

Kumar V and Alvi F, "Efficient Control of Separation Using Microjets," AIAA Paper 2005-4879, June 2005.

Press W, Flannery B, Teukolsky S and Vetterling W, Numerical Recipes in Fortran, 2nd edition, Cambridge University Press, January 1992.

Seifert A, Pack L, "Oscillatory Control of Separation at High Reynolds Numbers," *AIAA Journal,* Vol. 37, No. 9, pp. 1062-1071, September 1999.

Tian Y, "Adaptive Control of Separated Flow," Ph.D. Thesis, Department of Mechanical and Aerospace Engineering, University of Florida, Gainesville, FL, August 2007.

Tian Y, Cattafesta L, and Mittal R "Adaptive Control of Separated Flow," AIAA Paper 2006-1401, January 2006a.

Tian Y, Song Q and Cattafesta L, "Adaptive Feedback Control of Flow Separation," AIAA Paper 2006-3016, June 2006b.

Venugopal R and Bernstein D , "Adaptive Disturbance Rejection Using ARMARKOV/Toeplitz Models," IEEE Transactions on Control Systems Technology, Vol. 8, No. 2, pp. 257-269, March 2000.

Investigation of Tractor Base Bleeding for Heavy Vehicle Aerodynamic Drag Reduction

Jason Ortega[1], Kambiz Salari[1], Bruce Storms[2]

[1] Lawrence Livermore National Laboratory, USA
[2] NASA Ames Research Center, USA
ortega17@llnl.gov

Abstract The drag reduction capability of tractor base bleeding is investigated using a combination of experiments and numerical simulations. Wind tunnel measurements are made on a 1:20 scale heavy vehicle model at a vehicle width-based Reynolds number of 420,000. The tractor bleeding flow, which is delivered through a porous material embedded within the tractor base, is introduced into the tractor-trailer gap at bleeding coefficients ranging from 0.0-0.018 for two different gap sizes with and without side extenders. At the largest bleeding coefficient with no side extenders, the wind-averaged drag coefficient is reduced by a maximum value of 0.015 or 0.024, depending upon the gap size. To determine the performance of tractor base bleeding under more realistic operating conditions, computational fluid dynamics simulations are performed on a full-scale heavy vehicle traveling within a crosswind for bleeding coefficients ranging from 0.0-0.13. At the largest bleeding coefficient, the drag coefficient of the vehicle is reduced by 0.146. Examination of the tractor-trailer gap flow physics reveals that tractor base bleeding reduces the drag by both decreasing the amount of free-stream flow entrained into the gap and by increasing the pressure of the tractor base relative to that of the trailer frontal surface.

1 Introduction

During the 1970s and 1980s, a number of first-generation drag reduction devices were designed to reduce the aerodynamic losses of heavy vehicles [5]. The result of this effort led to the development of a number of devices (front-end rounding, tractor aero-shields, body molding, and cabin side extenders) that improved the aerodynamics of heavy vehicle tractors. Additionally, a number of second-generation devices (tractor-trailer gap sealers, trailer side skirts, and boat-tails) were developed. Unfortunately, these devices did not enter into the market on a wide-scale basis, which was due not to their ineffectiveness in reducing drag,

but rather to operational, maintenance, and, ultimately, economic concerns. However, with rising fuel costs and potentially unstable fuel supplies, there is a renewed objective to further reduce heavy vehicle aerodynamic drag.

On a modern heavy vehicle, one of the main sources of aerodynamic drag is tractor-trailer gap drag, which occurs when the vehicle is operating in a crosswind and free-stream flow is entrained into the tractor-trailer gap. This flow entrainment imparts a momentum exchange to the heavy vehicle in the direction opposite of travel, resulting in a drag increase. Presently, cabin side extenders, which are 0.46-0.51 m wide vertical plates attached to the tractor base, are routinely utilized on modern heavy vehicles to mitigate flow entrainment into the gap. Wind tunnel measurements have shown that side extenders, when used in conjunction with a rooftop aero-shield and tractor side skirts, reduce the wind-averaged drag coefficient, C_{dwavg}, by about 0.15 [6]. Other devices, such as gap sealers and fillers are also effective in reducing tractor-trailer gap drag and provide additional reductions in the wind-averaged drag coefficient ranging from about 0.03-0.06 [6]. However, due to maintenance and operational issues, these devices are not commonly installed on modern heavy vehicles.

Despite their widespread use, side extenders are often damaged during routine shipping operations. Commercial fleets frequently comment that the large structural surfaces comprising the side extenders are easily bent or crushed when the tractor pivots too sharply relative to the trailer during loading maneuvers. When such damage occurs, the commercial fleets are forced to take the tractor out of operation for service and either remove or replace the side extenders, a task which can become extremely costly when such repairs are required for several thousand tractors in the larger shipping fleets. Consequently, there is a need to devise alternate drag reduction concepts that can both alleviate flow entrainment into the tractor-trailer gap and be less prone to damage during vehicle articulation. One such concept recently developed are side extenders that are about 38% shorter than those presently used and still provide nearly the same aerodynamic benefit [7].

Another proposed concept is tractor base bleed, in which a stream of low-speed flow is injected into the tractor-trailer gap at a velocity, U_b, over a large surface area, A_b, on the tractor base. Base bleed has been previously studied as a means of reducing the drag of bluff bodies, such as ballistic shells [18], blunt-base airfoils [28], backward facing steps [16], and circular cylinders [23]. The typical values of bleeding flow, defined by the bleeding coefficient, $C_\mu = U_b A_b / U_o A_o$, range from 0.0-0.28, where U_o is the free-stream velocity and A_o the characteristic area of the body. Bearman [3], Michel & Kost [20], and Wood [28, 29] showed that base bleed increases the pressure over the bleeding surface, thereby reducing the overall drag of the bluff body. When sufficient bleeding flow is injected into the separated wake, Bearman [3], Schumm, *et al.* [23], and Wood [28, 29] demonstrated that the strength of the shed vortex street can be reduced. In addition, base bleeding displaces the separated wake in the downstream direction [3, 24, 29, 30]. Further increases in bleeding can suppress vortex shedding entirely. Yao & Sandham [30] showed that bleeding over a large area at a low velocity is more effective in

reducing the drag than bleeding over a small area at a high velocity. Base bleed has also been shown to influence the stability characteristics of the separated wake [11]. Arcas & Redekopp [1], Hammond & Redekopp [10], Huerre & Monkewitz [11], and Sevilla & Martinez-Bazan [24] observed that, at a critical bleed rate, the wake transitions from being absolutely unstable to convectively unstable. And, Koch [14,15] showed that the transition from absolute to convectively unstable flow occurs slightly downstream of the region of reverse flow in the separated wake.

Although the previous studies elucidated the flow physics and drag reduction capability of base bleeding, the types of bluff bodies used were either two-dimensional or axisymmetric. In addition, the bluff bodies were isolated from the influence of other bodies and were oriented at zero degrees yaw with respect to the free-stream flow. It is therefore difficult to determine from these previously published results as to whether or not base bleeding is an effective means of reducing the drag of a tractor-trailer gap, which is surrounded by both a highly asymmetric, three-dimensional geometry and a moving ground plane and which is typically oriented at a finite yaw angle. Thus, the purpose of this study is to investigate base bleeding as means of reducing tractor-trailer gap drag. In particular, we wish to answer the following questions. Does tractor base bleeding reduce the drag of a heavy vehicle? How much bleeding flow is required to produce a modest drag reduction? How is the flow within the tractor-trailer gap altered as a result of base bleeding? How do the gap flow physics and the reductions, if any, in drag due to tractor base bleeding compare to those of traditional side extenders?

2 Wind Tunnel Measurements

As a first step in providing answers to these questions, we perform wind tunnel measurements on a 1:20 scale heavy vehicle model that employs tractor base bleeding. The model tractor, which is a detailed representation [27] of a Freightliner Columbia [8], is fabricated using a rapid prototyping technique (Fig. 1a) [25]. The engine grill and the air inlets on the bumper are sealed since Leuschen & Cooper [17] measured very little difference in the drag coefficient when the cooling airflow through these two regions was blocked. To prevent laminar flow separation, several lengths of 4×10^{-4} m diameter wire are laid over the leading edges of the tractor and 4.6×10^{-4} m diameter glass beads are bonded to the tractor nose, visor, aero-shield, window pillars, door columns, and engine grill. The tractor is attached to a 0.69 m long model freight van that includes cross members and a landing gear on the trailer underside. The trailer body is constructed from 0.006 m thick sheets of acrylic, while the trailer wheels are fabricated in the same manner as that of the tractor. The tractor-trailer gap is adjustable and, for this study, is set to 0.038 and 0.076 m. Force measurements are made by suspending the entire tractor-trailer model on a six-component force balance (Northrop MK XVA 0.75")

that is positioned near the upstream end of the trailer. The signals from the force balance are digitized and stored on a computer using BDAS 9.3 data acquisition software [4]. The resulting drag coefficients, $C_d = D / \frac{1}{2}\rho U_o^2 A_o$, are obtained to within $\pm 1.69 \times 10^{-3}$, which includes both the balance accuracy and the average measurement repeatability, where D is the drag force along the body axis, x_a, of the model, ρ the density of air, and $A_o = 2.47 \times 10^{-2}$ m^2 the characteristic area of the model.

Tractor base bleeding is provided by directing a compressed air supply into two 0.019 m NPT air supply lines that are connected to two smaller 0.006 m internal diameter tubes, which enter the model through the trailer underside (Fig. 1b). The bleeding flowrate is measured with a pneumatic in-line flowmeter (Omega FL7722A). Since the 0.006 m internal diameter tubes pass from the non-metric to the metric portions of the force balance, a service loop is incorporated into the tubing before it exits the upstream end of the trailer underside and is attached to two ports on the tractor underside. These ports direct the airflow into a plenum that comprises the entire model tractor cabin. On the base of the tractor cabin are threaded holes to which several different rapid-prototyped pieces can be affixed. For base bleeding configurations, perforated tractor bases with and without 0.02 m wide side extenders are employed. On these pieces, the bleeding surface area is about 19% of the characteristic area, A_o, of the model tractor. For cases in which there is no bleeding flow, aluminum duct tape is placed over the perforated holes or a separate non-perforated tractor base piece with or without side extenders is fixed to the tractor base. Within the plenum, 0.051 m thick packing foam is positioned against the perforated tractor base to provide a pressure drop for the bleeding flow as it exits the plenum, thereby ensuring a more uniform bleeding velocity profile. Four bleeding flowrates, corresponding to base bleeding coefficients of 0.0, 0.008, 0.013, and 0.018, are used in this wind tunnel study. Velocity measurements made in the gap using a multi-hole pressure probe (Cobra, Turbulent Flow Instrumentation) with no tunnel velocity demonstrate fairly uniform bleeding velocity (Fig. 2).

The drag coefficient measurements are made within the NASA Ames Fluid Mechanics Laboratory open-circuit wind tunnel, which has a contraction ratio of 9:1, a test section size of 0.813 m × 1.219 m, and a free-stream turbulence level of 0.15%. The wind tunnel is operated at a nominal dynamic pressure and tunnel speed of 1420 N/m^2 and 48.95 m/s, respectively. The resulting width-based

a)

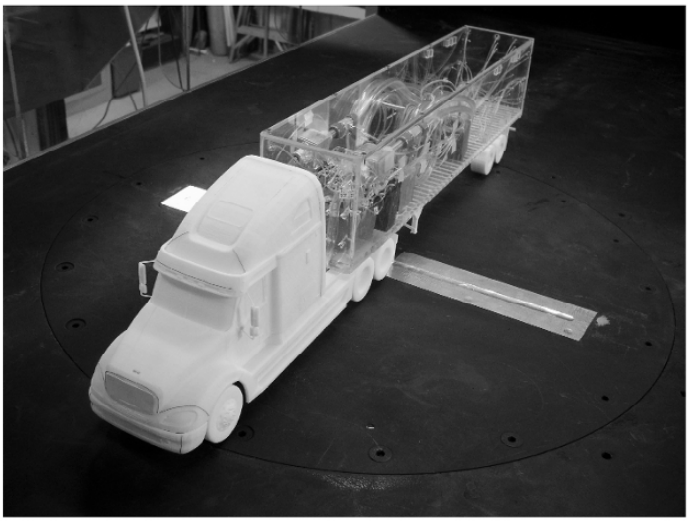

b)

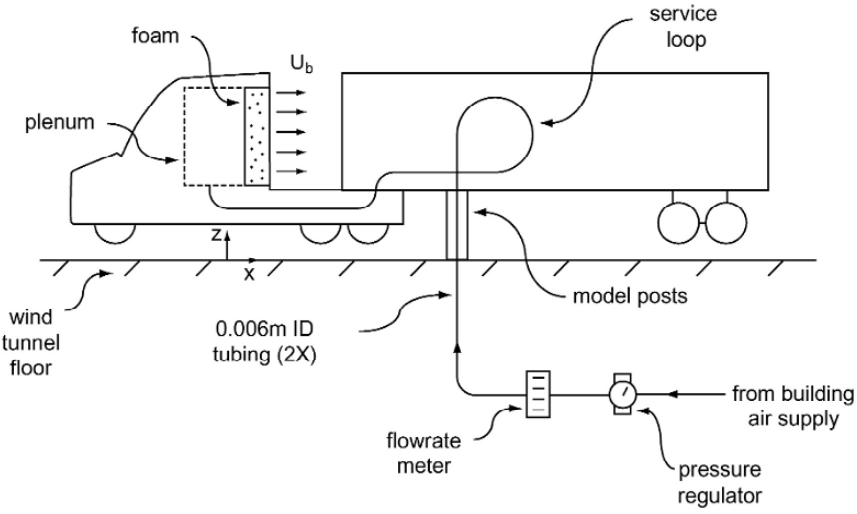

Fig. 1 a) 1:20 scale heavy vehicle model in the low-speed NASA Ames wind tunnel. b) Details of the tractor base bleeding system.

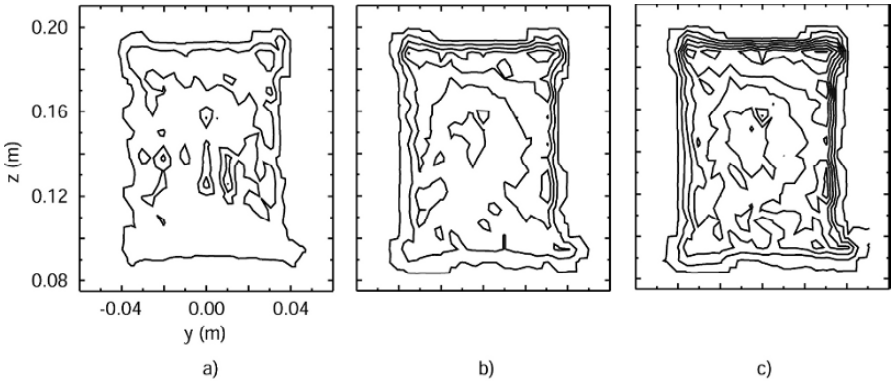

Fig. 2 Bleeding velocity contours in the x-direction made 0.019m downstream of the tractor base for C_μ equal to a) 0.008, b) 0.013, and c) 0.018 for a tractor-trailer gap distance of 0.076 m with no tunnel velocity.

Reynolds number, $Re_w = U_o w/\nu$, of the model is 420,000, where $w = 0.13$ m is the model width, and ν the kinematic viscosity of air. The percentage of blockage of the model in the tunnel test section is 2.5% at 0° yaw. The model is mounted at a height about equal to the boundary layer displacement thickness ($\approx 5.0 \times 10^{-3}$ m) above the tunnel floor on a turntable that is driven by a computer-controlled servo motor (Parker Compumotor), which can rotate the model to within ±0.05°. For each model configuration, force measurements are made at yaw angles ranging from ±8°. To assess the repeatability of the measurements, as well as hysteresis in the flow patterns over the model, the data are acquired on selective configurations for both increasing and decreasing yaw angle directions and are observed to show negligible hysteresis effects. Since the tractor bleeding flow generates forces on the model due to the effects of thrust and the expansion of the 0.006 m internal diameter tubing within the trailer, force measurements are first made at a zero tunnel velocity at each non-zero bleeding coefficient value. These forces are then subtracted from the subsequent measurements made at the corresponding bleeding coefficient values.

While the C_d data at each yaw angle is useful for evaluating the tractor base bleeding concept, it is somewhat cumbersome since the C_d distribution does not summarize the drag reduction performance into a single quantity that can be easily compared with that of other devices, such as side extenders. Taking the mean value of C_d over all measured yaw angles is also insufficient since it does not account for the fact that the crosswind velocities cause a vehicle traveling at a particular speed to experience certain yaw angles more than others. A quantity that resolves both of these issues is the wind-averaged drag coefficient, C_{dwavg} [12], which is computed for each base bleeding configuration (Fig. 3). It is apparent that the drag coefficient decreases as the bleeding coefficient is increased for both gap distances. However, a greater reduction in drag is observed for the larger gap distance both with and without side extenders. When $C_\mu > 0.006$, tractor base bleeding

with no side extenders at the larger gap distance yields a greater reduction in drag than that of side extenders alone with no bleeding flow. It should also be noted that the wind-averaged drag coefficients for the larger gap are greater than those of the smaller gap, indicating the presence of a larger amount of entrained flow into the tractor-trailer gap. Similar trends in the dependence of the drag coefficient upon gap distance, d_{gap}, were observed by Hammache & Browand [9], who investigated tractor-trailer gap flow dynamics on a simplified tractor-trailer geometry at a comparable Re_w of 270,000. At a critical gap distance of $d_{gap}/A_o \approx 0.5$, Hammache & Browand showed that the total vehicle drag increases sharply. In the present study, the values of $d_{gap} = 0.038$ and 0.076 m are below and about equal to the critical gap distance, respectively.

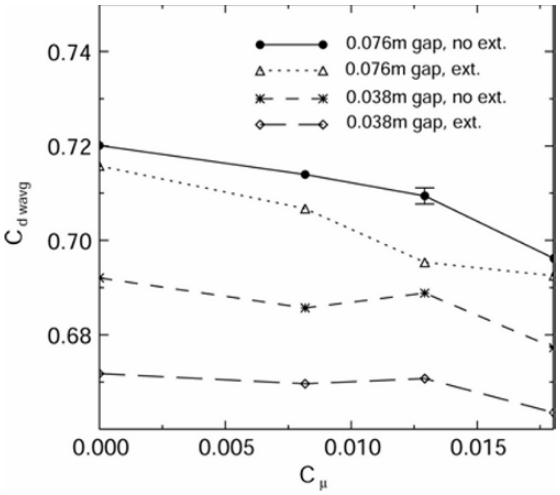

Fig. 3 Wind-averaged drag coefficient, C_{dwavg}, as a function of the tractor base bleeding coefficient, C_μ, for two tractor-trailer gap distances with and without side extenders

3 CFD Simulations

While the wind tunnel measurements demonstrate that tractor base bleeding can indeed reduce the drag of the heavy vehicle model, further investigation is needed both to demonstrate the effectiveness of this concept at a full-scale Reynolds number and to understand the changes in the gap flow physics arising from the base bleeding. For these reasons, we perform computational fluid dynamics (CFD) simulations on a full-scale Freightliner Columbia operating at highway conditions within a crosswind. The tractor-trailer gap distance is set to 1.02 m and a 13.6 m long freight van is attached to the tractor.

The simulations are performed within a computational domain that is 98m × 49m × 128m (Fig. 4), such that the heavy-vehicle cross-sectional area is 0.2% of that of the domain. To model the crosswind velocity, U_w , which is typically 3.1 m/s at vehicle mid-height [22], while the vehicle travels at a ground speed of U_g = U_o = 29.1 m/s, the vehicle is yawed to θ = $\tan^{-1}$ (U_w/U_g) = 6.1° and a velocity of $\sqrt{U_g{}^2 + U_w{}^2}$ = 29.3 m/s is specified at the inlet to the computational domain (Fig. 4). The resulting width-based Reynolds number is 5,000,000. Beneath the vehicle, a no-slip, moving ground plane boundary condition is prescribed at a velocity of U_g and a yaw angle of 6.1°. The no-slip surfaces of the tractor and trailer tires, which have a surface angular velocity boundary condition of 53 s^{-1}, intersect the ground plane, producing a tire contact patch that has a swept angle of 20° [2]. A slip boundary condition and a zero gradient boundary condition are specified along the walls and outlet, respectively, of the computational domain. To produce the tractor base bleeding flow, an inlet velocity boundary condition (U_b = 0.0-0.2U_o, v_c = 0, w_c = 0) is defined across the tractor base, which has an area that is 65% of that of the vehicle cross-section, A_o = 9.87 m^2. The corresponding bleeding coefficients range from 0.0-0.13. The other variables on the bleeding inlet boundary are computed by assuming a zero gradient normal to the inlet, such that the variables on the inlet nodes are extrapolated from the values of the interior nodes. To provide a performance comparison for the base bleeding concept, side extenders, which have a length of 0.38 m, are modeled in one vehicle configuration and compared with the baseline case. A finite-volume code [26] is used to solve the steady Reynolds averaged Navier-Stokes (RANS) equations for the flow about the heavy vehicle. The k−ω SST turbulence model [19] with a wall function is employed since a previous study by Pointer [21] demonstrated that this approach can adequately capture the value of C_d at a Re_w on the order of 10^6. The cell height adjacent to the vehicle is chosen to be 3.3 × 10^{-3} m, yielding a nominal value for y^+ [13] of 90 over the entire tractor-trailer surface. Meshes with about 25 × 10^6 cells are used in this study. The drag coefficient, which is typically averaged over 10,000-20,000 iterations, tends to oscillate by approximately ±0.007 about the average value, an effect possibly due to a lack of local mesh resolution.

A plot of the drag coefficient as function of the bleeding coefficient (Fig. 5) reveals that, in much the same manner as that of the wind tunnel measurements,

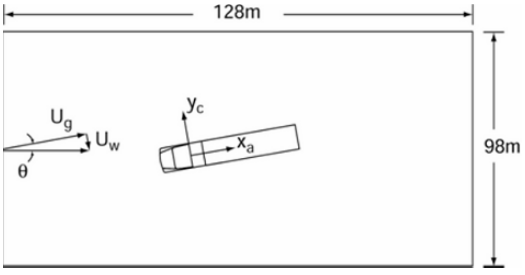

Fig. 4 Computational domain used for the full-scale CFD simulations

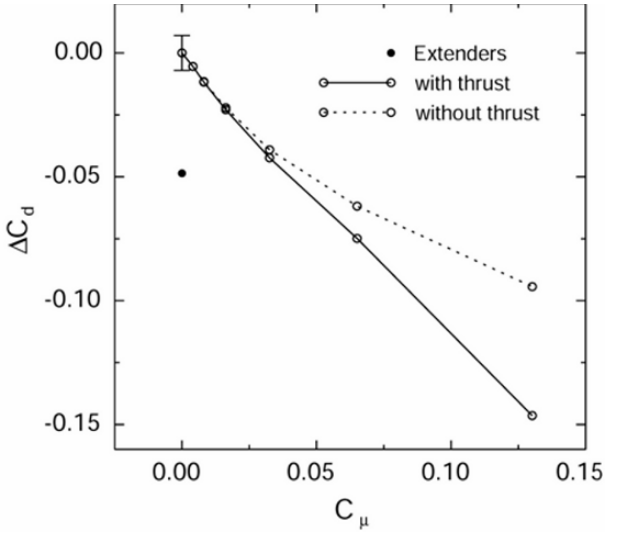

Fig. 5 Change in the drag coefficient as function of the bleeding coefficient for the CFD simulations

increases in bleeding flow decrease the drag coefficient. In addition, the drag reduction of $\Delta C_d \approx 0.025$ observed for $C_\mu \approx 0.018$ is about equal to that seen experimentally ($\Delta C_d \approx 0.02$) at 6° yaw for the larger gap distance despite the relatively large difference in Re_w. For the computational results, the drag coefficient decreases in a nearly linear fashion for the largest bleeding coefficients, values of which were not attainable in the wind tunnel measurements. The largest reduction in drag ($\Delta C_d = 0.146$) occurs at the maximum bleeding coefficient of 0.13. It is also evident that bleeding coefficients greater than 0.04 provide a larger reduction in drag than that of the side extenders ($\Delta C_d = 0.049$).

Obviously, a portion of the drag reduction produced by base bleeding is due to the thrust,

$$T = \int_{A_b} \rho U_b \mathbf{u} \cdot \mathbf{n} dA, \tag{1}$$

of the bleeding flow and not to modifications of the tractor-trailer gap flow physics, where **u** is the fluid velocity vector and **n** the unit normal vector of the vehicle surface. Removing this thrust contribution from the data in Fig. 5 demonstrates that, for the bleeding coefficients evaluated in this study, a significant drag reduction occurs solely due to changes in the gap flow physics.

One of the changes to occur is in the amount of free-stream fluid entrained into the tractor-trailer gap. The entrainment rate is computed by defining a rectangular control surface that encompasses the volume of the entire tractor-trailer gap (Fig. 6), but not the bleeding area over the tractor base. The entrainment flowrate,

$$Q_e = \int_{A_{in}} \mathbf{u} \cdot \mathbf{n}_{cs} dA, \tag{2}$$

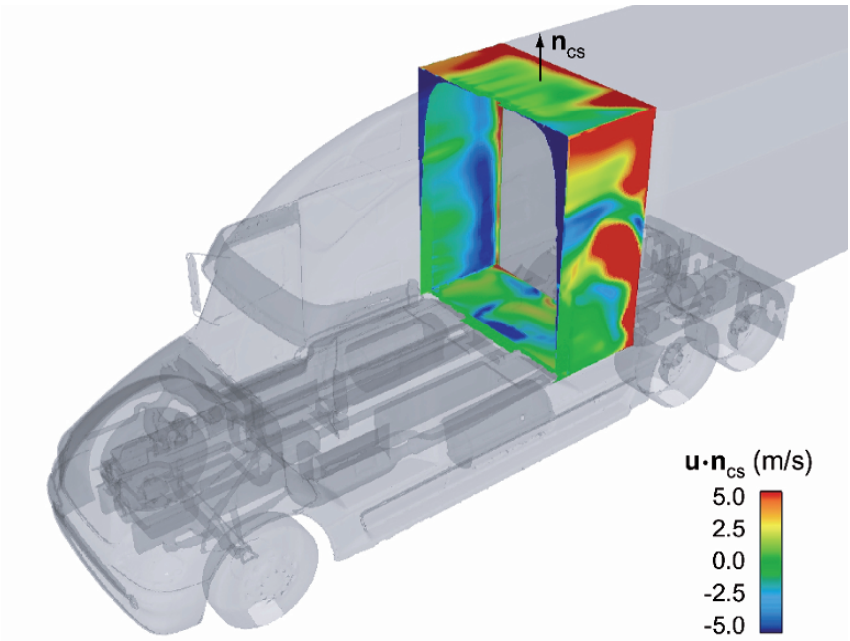

Fig. 6 Control surface defined for computing the flow entrainment rate, Q_e, into the tractor-trailer gap. The color contours on the surface denote the values of $\mathbf{u} \cdot \mathbf{n}_{cs}$ for $C_\mu = 0.0$.

is calculated over the control surface to determine the amount of fluid entering the gap from the free-stream, where $\mathbf{n}_{cs}$ is the normal vector of the control surface and the integration area, A_{in}, indicates that the integral is computed over those portions of the control surface in which $\mathbf{u} \cdot \mathbf{n}_{cs} < 0$. Without any base bleeding, the gap entrains free-stream fluid at a rate of $0.085 U_o A_o$, where a large portion of the entrainment occurs on the windward-downstream and bottom-upstream areas (Fig. 6) of the control surface. When side extenders are placed on the tractor base, $Q_e = 0.072 U_o A_o$. Due to the highly three-dimensional nature of the velocity field in the gap, the flow exits through distinct patches spread over the leeward and upper areas of the control surface. When $C_\mu > 0$, the bleeding flow reduces the amount of free-stream fluid entrained into the tractor-trailer gap (Fig. 7). (Note that the asymptotic decay of Q_e to what appears to be a value greater than zero is a result of the manner in which the control surface geometry is defined. The value of Q_e will likely be greater than zero for all C_μ because free-stream fluid will continue to enter the control surface through the upstream, vertical face.) A comparison of the contour plots of $\mathbf{u} \cdot \mathbf{n}_{cs}$ (Fig. 8) reveals that base bleeding significantly reduces the entrainment of free-stream fluid on the windward and bottom areas of the control

surface and produces an exit flow pattern that is more uniformly distributed over the downstream areas of the control surface.

The specific manner in which fluid entrainment is altered as a result of base bleeding can be understood by investigating the velocity field within the tractor-trailer gap. Prior to base bleeding, the windward shear layer separating from the tractor base impinges upon the trailer frontal face, producing a cross-stream flow in the form of a wall jet that spans the entire gap width (Fig. 9a,c). At the centerline of the gap, this wall jet has a maximum magnitude that is about $0.75U_o$ (Fig. 10). Since the flow re-circulates within the gap, a positive cross-stream velocity is present near the tractor base. As the amount of base bleeding is increased, the strength of the wall jet decreases. In addition, the cross-stream velocity profile becomes linear with the gap distance near the tractor base and the peak velocity of the positive-valued re-circulating flow diminishes. At a bleeding coefficient of C_μ = 0.13, the cross-stream velocity profile is linear throughout the entire tractor-trailer gap centerline, except within a thin boundary layer on the trailer frontal surface. Plots of the velocity field (Fig. 9b,d) show a relatively uniform gap flow, where the regions of large cross-stream flow are confined to the outer extents of the gap. It should also be noted that side extenders reduce the strength of the cross-stream flow, such that the maximum magnitude of the wall-jet is reduced to a value about equal to that which occurs when $C_\mu \approx 0.033$ (Fig. 10).

The shear layer that produces the wall jet within the gap leaves a distinct high pressure signature as it impinges upon the trailer frontal face (Fig. 11a). Away from this impingement zone, the pressure is considerably lower in magnitude, except for a region on the leeward side of the gap. When bleeding flow (C_μ = 0.13)

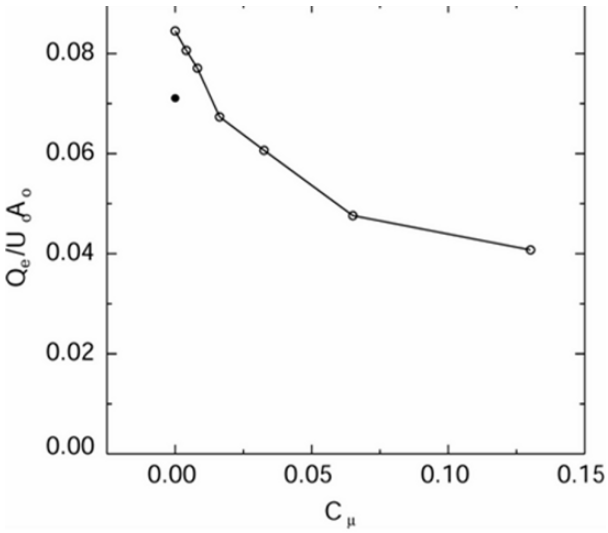

Fig. 7 Non-dimensional flow entrainment rate into the tractor-trailer gap as function of the bleeding coefficient. The symbol • denotes the configuration with side extenders (C_μ = 0.0).

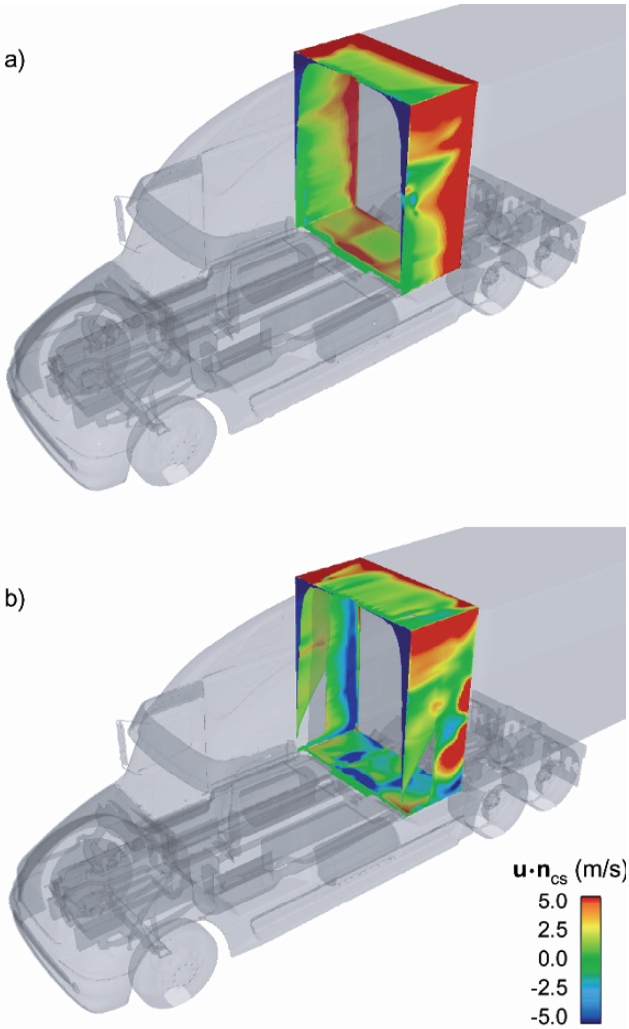

Fig. 8 Contours of $\mathbf{u} \bullet \mathbf{n}_{cs}$ over the control surface for a) a bleeding coefficient of $C_\mu = 0.13$ and b) for side extenders ($C_\mu = 0.0$).

is applied to the tractor base, this high pressure signature is diminished (Fig. 11b) and replaced with a more uniform pressure distribution that extends over nearly the entire trailer frontal face. The application of side extenders also reduces the pressure signature from the windward shear layer (Fig. 11c), though not to the extent seen for $C_\mu = 0.13$.

Plots of the pressure coefficient acting in the body axis-direction, $C_{pa} = |\mathbf{n} \bullet \mathbf{n}_a|(P - P_o)/ \frac{1}{2}\rho U_o^2$, (Fig. 12) along the vertical centerline of the tractor base and trailer frontal face demonstrate that the pressure increases on both surfaces as the bleeding coefficient is increased, where P is the fluid pressure, P_o the free-stream

pressure, and $\mathbf{n}_a$ is the unit body-axis direction vector. Calculating the average value of C_{pa} over the tractor base, trailer frontal face, and trailer base shows that the average pressure coefficient acting in the body-axis direction on the tractor base increases more rapidly than that on the trailer frontal face as C_μ is increased (Fig. 13). This subsequently reduces the difference between the average pressure coefficients on the tractor base and trailer frontal face, which is, in turn, responsible for the reduction in drag on the entire vehicle. In fact, for $C_\mu > 0.053$, the average pressure coefficient on the tractor base is greater than that of the trailer frontal face. The side extenders reduce the difference between average pressure coefficients over the tractor base and trailer frontal face, as well. However, the average pressure coefficient on the trailer base exhibits little sensitivity to either the bleeding flow or the side extenders.

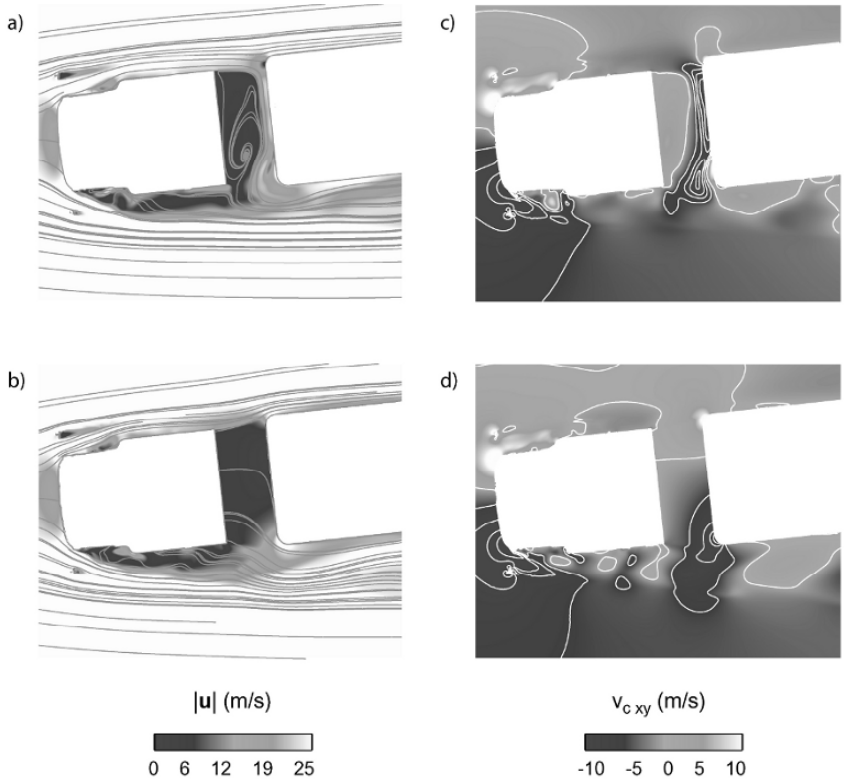

Fig. 9 a-b) Velocity magnitude and streamlines and c-d) cross-stream velocity at the mid-height of the tractor-trailer gap for C_μ equal to a,c) 0.0 and b,d) 0.13. Note that additional negative-valued contours are applied in c-d) to highlight the cross-stream gap flow.

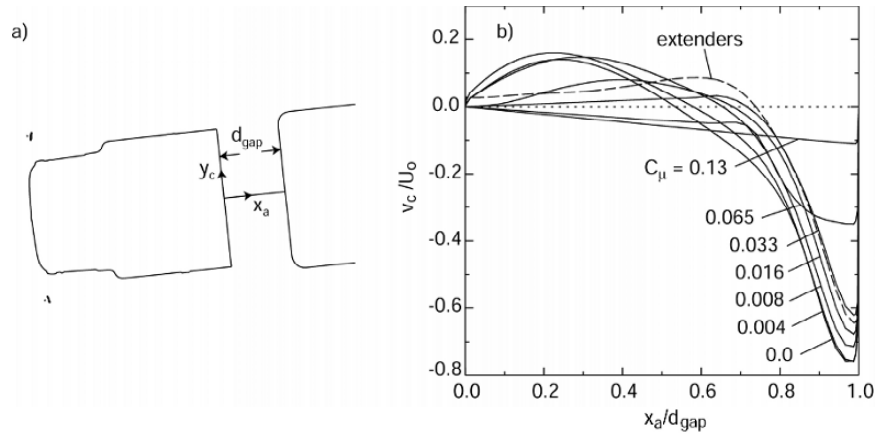

Fig. 10 a) Horizontal cross-section at the mid-height of the tractor-trailer gap. b) Non-dimensional cross-stream velocity through the gap as function of the bleeding coefficient.

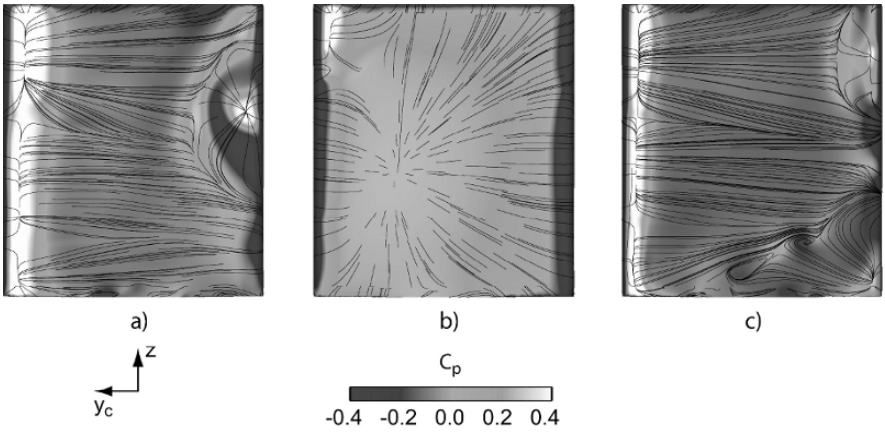

Fig. 11 Pressure coefficient and surface streamlines on the trailer frontal face for C_μ equal to a) 0.0 and b) 0.13 and for c) side extenders.

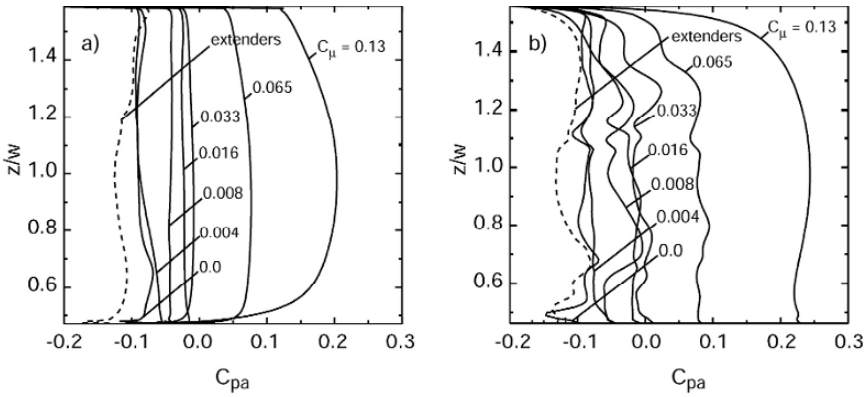

Fig. 12 Pressure coefficient in the body-axis direction on the a) tractor base and b) trailer frontal face centerlines as a function of the bleeding coefficient.

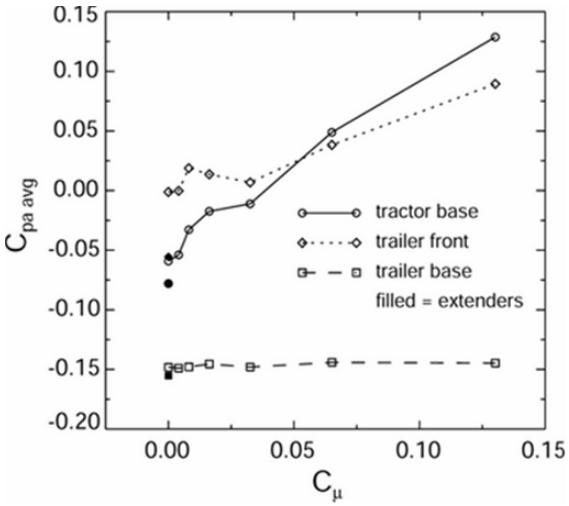

Fig. 13 Average pressure coefficient in the body-axis direction over the tractor base and trailer frontal surface and base as a function of the bleeding coefficient.

4 Conclusions

Through this investigation, we have studied the drag reduction capability of tractor base bleeding. Both the 1:20 scale wind tunnel measurements and the full-scale CFD simulations demonstrate that tractor base bleeding reduces the drag coefficient of a heavy vehicle. For bleeding coefficients greater than 0.04, the simulations show a reduction in the drag coefficient that is larger than that of side extenders. The simulation results also highlight the flow physics within the tractor-trailer gap that contribute to this drag reduction. As the bleeding coefficient increases, the rate of fluid entrainment from the free-stream into the gap decreases, which reduces both the pressure signature of the impinging windward shear layer on the trailer frontal face and the strength of the cross-stream wall jet within the gap. Lastly, tractor base bleeding reduces the difference between the average pressure coefficients on the tractor base and trailer frontal face, which is the mechanism responsible for the drag reduction.

The reason for selecting tractor base bleeding as a drag reduction concept is to alleviate the maintenance and operational issues that often arise with conventional side extenders. It is evident through the results of this investigation that tractor base bleeding may, in fact, offer an alternative means to side extenders in reducing tractor-trailer gap drag. However, the base bleeding concept is not without its own set of concerns and a number of questions remain unanswered regarding its feasibility, some of which are: how much power is required to produce the bleeding flow? Would it be more efficient to utilize solar energy or energy stored from regenerative braking to produce the bleeding flow? Can a base bleeding system be designed robustly enough so as to require a minimum level of maintenance? Under normal operating conditions, does tractor base bleeding provide a net reduction in fuel usage? Lastly, how much would a bleeding system add to the price of a tractor? Obviously, we are not in the position to answer these important questions at the present time. However, if these questions can be adequately and cost-effectively addressed, tractor base bleeding may, in the future, offer commercial fleets a viable drag reduction alternative.

Acknowledgments

The authors would like to thank Dennis Acosta and Kurt Long of NASA Ames Research Center for their assistance in performing the wind tunnel measurements. This work was performed under the auspices of the U.S. Department of Energy by Lawrence Livermore National Laboratory under Contract DE-AC52-07NA27344. UCRL-PROC-235892.

References

[1] Arcas D, Redekopp L, Aspects of wake vortex control through base blowing/suction. Phys. Fluids 16(2), 452-456 (2004)

[2] Axon L, Garry K, Howell J, An evaluation of CFD for modelling the flow around stationary and rotating isolated wheels. SAE 980032, SAE International Congress and Exhibition, Detroit, Michigan, February 23-26 (1998)

[3] Bearman P, The effect of base bleed on the flow behind a two-dimensional model with a blunt trailing edge. Aero. Quart. 18, 207-224 (1967)

[4] BDAS 9.3 Software Package, Aerospace Computing, Inc. (2006)

[5] Cooper K, Truck aerodynamics reborn: lessons from the past. SAE 2003-01-3376, SAE International Truck and Bus Meeting and Exhibition, Fort Worth, Texas, November 10-12 (2003)

[6] Cooper K, Commercial vehicle aerodynamic drag reduction: historical perspective as a guide. In: McCallen, R.C., Browand, F., Ross, J. (eds.) The Aerodynamics of Heavy Vehicles: Trucks, Buses, and Trains, pp. 9-28. Springer, Heidelberg (2004)

[7] Gill R, Freightliner, LLC, private communication (2007)

[8] Freightliner, http://www.freightlinertrucks.com/trucks/find-by-model/columbia/ (2007)

[9] Hammache M, Browand F, On the aerodynamics of tractor-trailers. In: McCallen R, Browand F, Ross J (eds.), The Aerodynamics of Heavy Vehicles: Trucks, Buses, and Trains, pp. 185-205. Springer, Heidelberg (2004)

[10] Hammond D, Redekopp L, Global dynamics of symmetric and asymmetric wakes. JFM 331, 231-260 (1997)

[11] Huerre P, Monkewitz P, Local and global instabilities in spatially developing flows. Ann. Rev. Fluid Mech. **22**, 473-537 (1990)

[12] Ingram K, The wind-averaged drag coefficient applied to heavy goods vehicles. Transport and Road Research Laboratory Supplementary Report 392 (1978)

[13] Kays W, Crawford M, Convective heat and mass transfer. McGraw-Hill, Inc., New York (1993)

[14] Koch W, Organized structures in wakes and jets—an aerodynamic resonance phenomenon? In: Bradbury L, Durst F, Launder B, Schmidt F, Whitelaw J (eds.), Turbulent Shear Flows 4, Springer (1983)

[15] Koch W, Local instability characteristics and frequency determination of self-excited wake flows. J. Sound Vib. 99, 53-83 (1985)

[16] Leal L, Acrivos A, The effect of base bleed on the steady separated flow past bluff bodies. JFM 39(4), 735-752 (1969)

[17] Leuschen J, Cooper K, Full-scale wind tunnel tests of production and prototype, second-generation aerodynamic drag-reducing devices for tractor-trailers. SAE Paper 06CV-222, (2006)

[18] MacAllister L, The aerodynamic properties and related dispersion characteristics of a hemispherical-base shell, 90-mm, HE, T91, with and without tracer element. BRL Memo. Report 990, Aberdeen Proving Ground, MD (1956)

[19] Menter F, Zonal two equation k-ω turbulence models for aerodynamic flows. Paper No. AIAA 93-2906, Proc. 24th Fluid Dynamics Conf., Orlando, Florida, USA, 6-9 July (1993)

[20] Michel G, Kost F, The effect of coolant flow on the efficiency of a transonic HP turbine profile suitable for a small engine. ASME 82-GT-86 (1982)

[21] Pointer W, Evaluation of commercial CFD code capabilities for prediction of heavy vehicle drag coefficients. Paper No. AIAA-2004-2254, 34th AIAA Fluid Dynamics Conference and Exhibit, Portland, Oregon, 28 June-1 July (2004)

[22] SAE wind tunnel test procedure for trucks and buses. SAE J1252, SAE Recommended Practice (1979)

[23] Schumm M, Berger E, Monkewitz P, Self-excited oscillations in the wake of two-dimensional bluff bodies and their control. JFM 271, 17-53 (1994)
[24] Sevilla A, Martínez-Bazán C, Vortex shedding in high Reynolds number axisymmetric bluff-body wakes: local linear instability and global bleed control. Phys. Fluids 16(9), 3460-3469 (2004)
[25] Solid Concepts, Inc., www.solidconcepts.com (2006)
[26] STAR-CD v. 3.24-3.26. CD-Adapco Group, www.cd-adapco.com (2007)
[27] Turbo Squid, www.turbosquid.com (2006)
[28] Wood C, The effect of base bleed on a periodic wake. J. Roy. Aero. Soc. 68(2), 477-482 (1964)
[29] Wood C, Visualization of an incompressible wake with base bleed. JFM 29(2), 259-272 (1967)
[30] Yao Y, Sandham N, Direct numerical simulation of turbulent trailing-edge flow with base flow control. AIAA J. 40(9), 1708-1716 (2002)

Drag Reduction on a Generic Tractor-Trailer using Active Flow Control in Combination with Solid Flaps

Christian Navid Nayeri[1], Johannes Haff[1], David Greenblatt[2], Lennart Loefdahl[3] and Christian Oliver Paschereit[1]

[1] Berlin Institute of Technology, Herrmann-Föttinger-Institut, De-10623 Berlin, Germany, christian.nayeri@tu-berlin.de, johannes.haff@gmx.de, oliver.paschereit@tu-berlin.de,

[2] Faculty of Mechanical Engineering, Technion - Israel Institute of Technology, Technion City - Haifa 32000, Israel, davidg@technion.ac.il

[3] Chalmers University of Technology, SE-41296 Göteborg, Sweden, lennart.lofdahl@chalmers.se

Abstract An experimental investigation was carried out to assess the drag reducing potential of active flow control in conjunction with flat panel flaps attached to the trailer of a generic tractor–trailer model. The experiments were carried out in a wind tunnel with a $1/10^{th}$ scale generic tractor-trailer model at Reynolds numbers up to 640,000 based on the model width. Active flow control was achieved by means of constant blowing, constant suction and oscillatory blowing and suction. A secondary objective was to make short base flaps with active flow control as effective as long flaps with no active flow control. Measurement techniques such as flow visualizations, loads by means of a 6-component balance, LDA and PIV were employed. The results show that constant blowing at a momentum coefficient of 11.13% is able to achieve higher drag reduction than long flaps with no active flow control. The analysis of the flow field in the wake showed that constant blowing deflects the shear layer between the free stream and the wake region downward and hence reduces the size of the wake. The flaps at the side of the truck did not appear to have any substantial drag reducing effect.

1 Introduction

In recent years the economy of tractor-trailer configurations has improved significantly. After the implementation of drag-reducing devices on the tractor, further investigations were aimed at drag reduction by optimisations of the trailer. In

addition to the development of side skirts and components which close the gap between the tractor and trailer it was recognized that, in particular, the trailer end contains a high drag-reducing potential.

Therefore additional components were installed at the trailer end to reduce the area thereby reducing the dead air region and hence pressure losses. In the past, the influence of several different components (e.g. boat-tailing, boat tail plates, base flaps) was investigated with respect to the drag reduction and the application to in-service trucks.

Several studies showed the drag reducing potential of flaps and that longer flaps can reduce the drag more than short flaps [1, 3, 4, 6]. Some authors attempted to increase the drag reducing effect through combination with active flow control (AFC). Englar [2] showed that Coanda blowing can be applied on trailers to reduce trailer drag. Hammache and Browand [5] investigated the effect of oscillatory forcing and found that additional drag reduction is only achieved at flap tilt angles higher than 9-10 degrees. Seifert [8] applied constant suction and oscillatory blowing to a two dimensional truck model with a fluidic device integrated in the rounded trailing corner.

The main objective of this paper is to investigate combinations of active flow control with short flat flaps with the goal of obtaining additional drag reduction. The results are compared to a passive baseline configuration with short flaps. The experiments were performed with a generic tractor-trailer model using constant suction (CS), constant blowing (CB), zero mass flux forcing (ZMF) and oscillating blowing (OB). Detailed information about the flow behaviour in the trailer wake is given by using LDA and PIV techniques for the CB configuration.

2 Experimental Setup

The experiments were performed in a closed loop 500kW-powered wind tunnel at the Hermann-Föttinger Institute. In the closed test section of 2m x 1.4m x 10m (W x H x L) a maximum velocity of U_{max}=40m/s can be achieved. The turbulence level is below 1 %. The corresponding Reynolds number is 640,000 based on the model width of $W_{trailer}$ = 0.25m at U_{max}. A six component external balance was used to determine the drag. The distance between the model wheels and the wind tunnel floor was 3mm. The floor of the wind tunnel was stationary.

Additionally, LDA and PIV-measurements were used to gain insight into the structure of the flow field in the wake of the trailer.

A $1/10^{th}$ scaled model corresponding to the longest legal European tractor-trailers was designed and constructed of medium density fibreboard. The edge radius at the front of the truck is 80mm on the roof and 40mm on the remaining edges. The dimensions of the model and the coordinate system are shown in Fig. 2.1. The model was mounted on a turntable such that yaw angles between ±30°

could be realized. The back of the model was equipped with a 1mm slot at the base of the trailer that was used for active flow control. The internal trailer volume was used as a plenum and air entered through a flexible tubing system in the bottom of the trailer. Any additional forces which were generated through blowing or suction (e.g. forces through the tubing, jet blowing) were accounted for in the drag measurements. To reduce the effect of the boundary layer thickening on the wind tunnel floor, the truck was mounted at the beginning of the test section near the contraction.

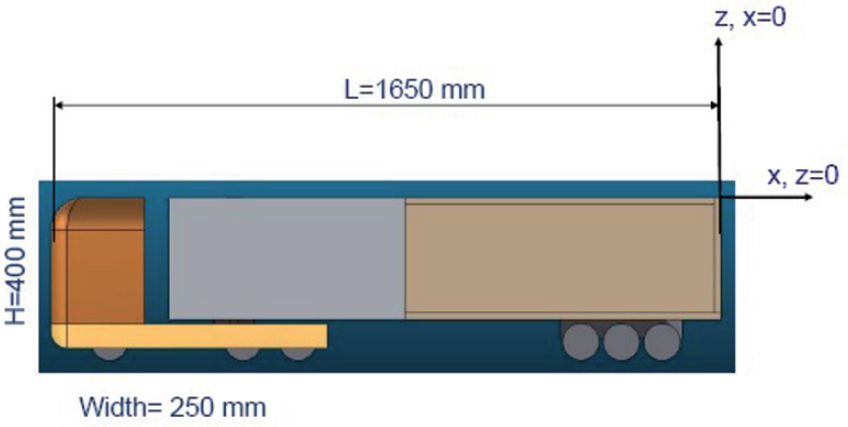

Fig. 2.1 Schematic representation of the generic tractor-trailer model

3 Baseline Configuration

As a baseline configuration the model was used without any drag reduction devices. Drag measurements were performed with different yaw angles between $\psi = \pm 30°$ to simulate side wind effects (not shown here).

The only differences between the baseline configuration and those described in the sections below, were the modifications to the base of the trailer. The gap between the tractor and trailer was always kept constant and was typical for European tractor-trailers. The drag of this configuration at $\psi = 0°$ was measured at $C_D = 0.477$.

4 Long Base Flap Configuration without AFC

The drag reduction geometry and generic model used here were designed and investigated by Zühlke [10]. In his studies the base flaps were attached to all 4 sides of the trailer without any gap or step and no AFC was applied. The flap length of 63mm corresponded to one quarter of the trailer width. This length was chosen as it is a good compromise between length and drag reduction [1]. However, it was also shown by Cooper [1] and Göring [3] that longer flaps can provide more drag reduction. The test program carried out by Zühlke [10] consisted of several configurations with different deflection angles between 10° and 20°. The maximum drag reduction was achieved with flaps deflected by 12°. All results presented in this paper were compared with this configuration in order to quantify the benefit of additional AFC. For the sake of convenience this configuration is referred to as "passive long flaps" (PLF) for the remainder of this paper. This passive configuration showed a drag reduction of $\Delta C_D = 8.22\%$ compared to the baseline. Zühlke [10] showed that for deflection angles larger than 12° the drag increased again. It is assumed that at higher deflection angles the flow is not able to stay attached to the flap resulting in a larger wake. Flow visualisation, performed with china clay and tufts provided some details about the flow behaviour. Based on tuft visualization, it was observed that the flow is attached to the whole flap surface whereas only the lower part of the side-flaps exhibited a separated flow. The visualisations with china clay confirmed these results. The flow is fully attached up to the trailing edge of the flap over the whole flap surface. A surprising observation was that the flow did not separate at the corners where the side flaps adjoin the top flap.

5 Short Base Flap Configuration with AFC

For the configuration with AFC short flaps of 40mm length with a deflection angle of 20° were applied. The motivation for these modifications compared to the PLF-configuration was to achieve more drag reduction with shorter flaps. The combination of a short flap, a higher deflection angle and AFC was intended to reduce the wake size. Shorter flaps increase the acceptance of drag-reducing components from an industrial viewpoint as the overall truck length is limited in Europe. In contrast to the PLF-case the flaps were not directly attached to the trailer but rather formed a small slot so that blowing or suction could be employed (Fig. 5.1). The trailing edge of the trailer was formed by an aluminium skirt with a thickness of 1mm. This arrangement resulted in a slot width of b_{slot}=1mm between the skirt and the flap surface. The slot extended over the top and both sides of the

trailer whereas the bottom side was only equipped with a flap without any gap. At the upper corners of the trailer where the side flaps adjoin the upper flap no slot was implemented along a length of 20mm as this area was needed to fasten the base to the back of the trailer. This reduced the total length of the effective slots.

Within the test program four different AFC methods were applied: constant suction, constant blowing, zero mass flux and oscillating blowing. The intention was to investigate their drag reducing effect in combination with the short base flap configuration. However, only the CB results are discussed here in detail, as the other methods did not produce meaningful drag reduction.

Equation 5.1 defines volumetric suction rates (Q) as a dimensionless parameter C_Q, where b_{slot} is the slot height, l_{slot} the total effective slot length, b_{flap} the length of the flap, l_{flap} the total length of all flaps and U_j is either the amplitude of the oscillatory jet fluctuation or the velocity of the constant blowing or suction.

$$C_Q = \frac{Q}{A_{flap} \cdot U_\infty} = \frac{U_{slot} \cdot A_{slot}}{A_{flap} \cdot U_\infty} = \frac{U_{slot} \cdot l_{slot} \cdot b_{slot}}{U_\infty \cdot l_{flap} \cdot b_{flap}} \cong \frac{U_{slot} \cdot b_{slot}}{U_\infty \cdot b_{flap}} \tag{5.1}$$

Equation 5.2 defines a dimensionless momentum parameter C_μ.

$$C_\mu = \frac{U_{slot}^2 \cdot A_{slot}}{0.5 \cdot U_\infty^2 \cdot A_{flap}} \cong \frac{U_{slot}^2 \cdot b_{slot}}{0.5 \cdot U_\infty^2 \cdot l_{flap}} \tag{5.2}$$

The first method tested was constant suction using the slot configuration described above. The underlying mechanism of suction is generally to remove low momentum fluid from the boundary layer in order to attach the flow to the flap surface. However, CS did not yield any drag reduction for this configuration. Therefore further tests were performed with two other orientations of the suction slots: suction orthogonal to the trailer surface and suction orthogonal to the flap surface. For these two cases longer flaps of the baseline were used. The suction rate was increased up to a maximum C_μ of more than 20%. However, these CS-cases even increased the drag (see Table 5.1). This failure is believed to be caused by the rather thick boundary layer at the trailing edge of the trailer which was measured to be δ_{99}=40mm.

The remaining three AFC methods (CB, ZMF and OB) were only applied to the short base flap configuration. The ZMF method was realised by using actuators developed at the Illinois Institute of Technology [7] which produces a sinusoidal signal. OB means that in addition to the sinusoidal signal produced by the actuators a constant blowing volume flow is superimposed. The application of ZMF provided only a small drag reduction of $\Delta C_D = 2.52\%$. Slightly more reduction was achieved with OB: $\Delta C_D = 3.35\%$. The best results were achieved with CB which was even better than the PLF-case. This confirms the idea of using a short and more deflected flap in combination with AFC. However the necessary

blowing corresponded to a very high value of C_μ = 11.13%. The jet blowing effect, which was accounted for in the drag values, was in this case 0.75% of the drag coefficient.

Table 5.1 Drag values and AFC parameters, $\psi = 0°$ (* C_D-value without AFC, ** $\Delta C_D = (C_D - C_{D,BL})/C_{D,BL}$ with $C_{D,BL} = 0.477$)

Configuration	C_D [ ]	ΔC_D **	C_μ [%]	C_Q [%]
CS parallel to the trailer surface	0.487	2.10 %	-	1.76
CS orthogonal to the trailer surface	0.496	3.98 %	-	1.76
CS orthogonal to the flap surface	0.489	2.52 %	-	1.76
Baseline Configuration (BL)	0.477	-	0	-
Long Base Flap Configuration without AFC	0.438	-8.22 %	0	-
Short Base Flap Configuration with AFC (CB)	0.435 (0.470*)	-8.81 %	11.13	-

In Table 5.1 the drag values obtained for $\psi = 0°$ are summarized for the different methods investigated. To get a better understanding of how the short flaps with CB influence the wake of the trailer, visualizations with china clay, LDV and PIV measurements were performed. With the results a comparison of the flow behaviour with and without blowing is discussed in the following. Measurements were made at C_μ = 0% (no blowing) and at C_μ = 11.13%, which provided the highest drag reduction

At first visualisations with china clay were carried out to see if the flow attached to the flap surface. The free stream velocity was U_∞=38m/s and the yaw angle was ψ=0°. For the case with no blowing Fig. 5.1 shows that the flow is not attached. It seems that the flow separates right at the trailing edge of the trailer where there is a gap similar to the baseline configuration (not shown here). Although the flow is not attached a small reduction in drag of ΔC_D= -1.47% was measured.

The visualization in Fig. 5.2 shows clearly how the flow field is affected when constant blowing is applied. The flow attaches for approximately 2/3 of the flap length. The surface streamlines visualized with china clay indicated an axial flow on the flap except at the corners. At the corners, where the top and side flaps adjoin, the streamlines indicate a vortex. This is attributed to the lack of slots for blowing at the corners.

Fig. 5.1 No blowing

Fig. 5.2 Blowing with C_μ = 11.13%

The vortex at the left corner rotates in clockwise direction. Further testing should be performed with an improved blowing slot, which allows AFC also at the corners to avoid the development of these vortices because they generate a low pressure area near the base. Low base pressures leads to an increased pressure drag. These vortices were only observed on the short flaps as flow visualization with china clay on the long flaps with no AFC (not shown here) indicated that no vortices were generated. In that case the flow was fully attached also at the corners.

It is worth noting that the flow even reattaches on the flap directly behind the slot at the beginning of the flap surface although there is a gap of 2mm between the surface of the trailer (aluminum skirt) and the surface of the flap. Fig. 5.2 was obtained at the optimum blowing rate. Higher blowing rates led to an increase in drag. It is not clear if a lower deflection angle leads to a fully attached boundary layer with better results than the 20°-configuration. Therefore further parameter studies have should be performed.

Quantitative results obtained with a 2D-LDA-System are presented below. The coordinate system used here is equal to that in Fig 2.1. The LDA-Probe was positioned underneath the wind tunnel and allowed measurements through a piecewise transparent floor for a $y/H > -0.05$ (y=0 corresponds to the centre line of the model).

LDA contour plots of the mean and fluctuation axial-velocity components (Fig. 5.3) are shown for $x/H = 0.825$ behind the trailer with view towards the rear end of the trailer. Because of the symmetric flow field, data for only one half of the trailer is shown. The black marking lines inside the plots define the right half of the trailer contour. Note that in the range of $0.325 < y/H < 0.45$ and $0.7 < z/H < 0.75$ the data is erroneous due to an increase of scattered laser light resulting in a poor signal-to-noise ratio, and therefore should be ignored.

The contour plots of the non-dimensionalized mean axial velocity U/U_∞ in Fig. 5.3 show that CB entrains high speed fluid from above the trailer down into the wake region. Thereby the dead air is moved down which leads to decreasing velocities in the lower regions.

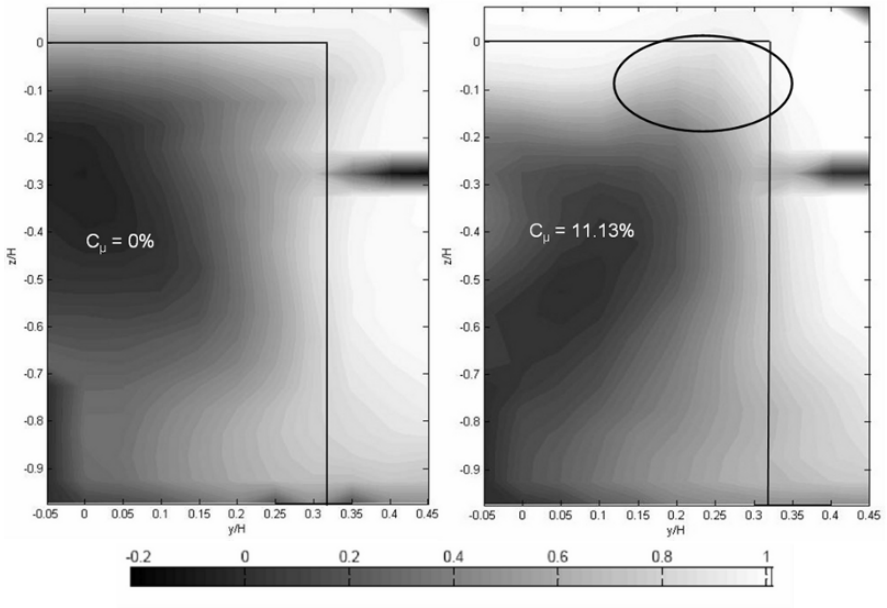

Fig. 5.3 Non-dimensionalized mean axial velocity distribution, U/U_∞, in the wake of the trailer at $x/H = 0.825$. The trailer is indicated by the solid line.

The different flow behaviour on the upper corner (see black ellipse) is due to the fact that no CB was applied there. It seems that the vortices, which were observed with the china clay visualization, influenced this part of the separation area strongly.

Additionally, CB leads to an increase of the wake extension in *y*-direction which is expected to have a negative effect with regard to the drag. The investigations of the long base flap configuration with no AFC also showed a flow separation on the bottom of the side flaps. Perhaps the ground flow influences the remaining flow field behind the trailer in a negative manner. It is speculated that the only reason why CB in combination with the short flaps has a drag reducing effect only because of the reduced wake in the upper region of the flow field.

The analysis of the contour plots of the axial fluctuations, U_{rms}, shown in Fig. 5.4 underlines the above interpretations. The upper region of the trailer wake is the most influenced area, where the turbulence level is significantly decreased, i.e. free stream fluid is moving downwards. The whole upper region, $y/H \approx 0.9\text{-}1.1$, of the trailer wake shows low turbulence levels whereas the corner region contains higher turbulence levels (see white ellipse in Fig. 5.4).

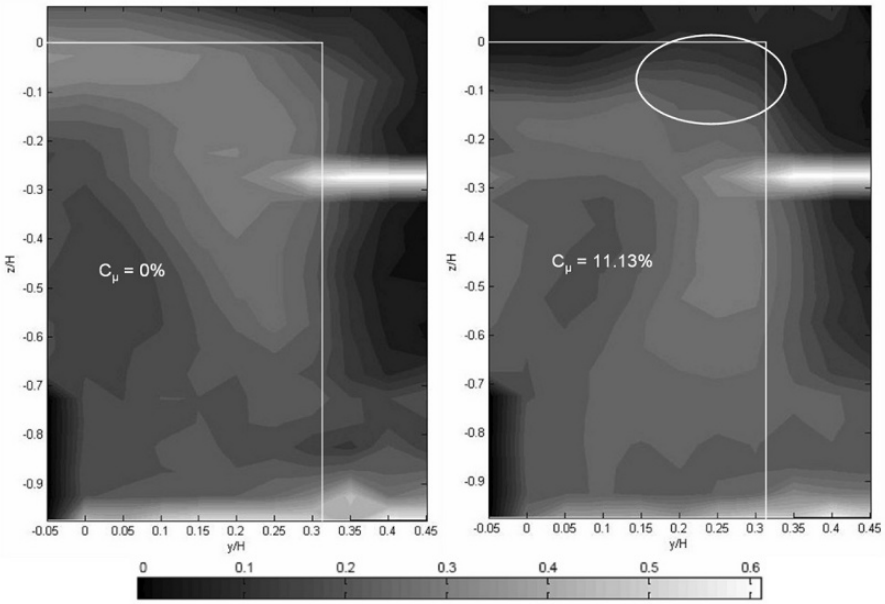

Fig. 5.4 Non-dimensionalized fluctuating axial velocity component, U_{rms}/U_{∞}, in the wake of the trailer at $x/H = 0.825$

The LDA data of Fig. 5.3 and 5.4 were made with 11x22=242 measurement points whereas Fig. 5.5 consists of 12x12=144 measurement points.
Fig. 5.5 shows the results of other LDA measurements take from the side of the wind tunnel. The figures show an *x*-*z*-plane at y/H= 0.05. The range was limited to the upper part of the trailer.

Without CB the flow seems not to be influenced by the flap. The contours of the axial velocity are essentially parallel to the upper trailer surface. The increasing velocity field at higher *x/H*-values is due to the mixing within the shear layer. Surprisingly, without control there region with a relatively high axial velocity somewhat below the flap at z/H≈-0.15. In the LDA results of Figs. 5.3 and 5.4 this region was not captured as the measurement were made further downstream at x/H=0.825. When control is applied, this region is eliminated. In combination with CB the separation area behind the trailer shows a different flow behaviour. The flow seems to be attached to the flap surface and high speed flow is deflected downwards into the wake.

However, Fig. 5.5 gives no definitive information about the flow behaviour directly on the flap surface because the resolution of the measurement grid was not fine enough.

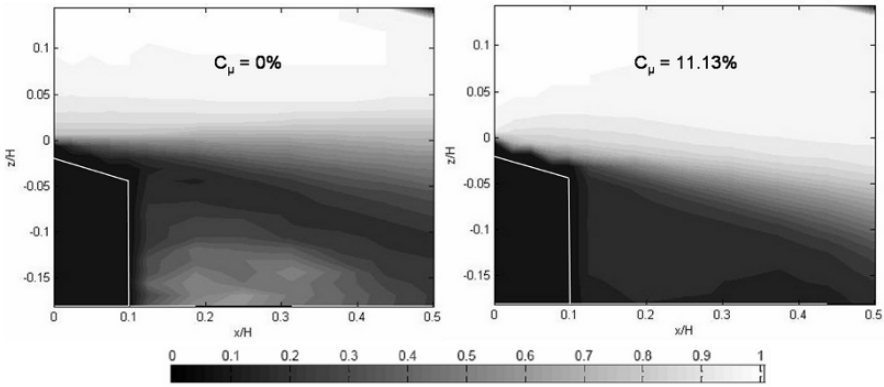

Fig. 5.5 Contours of the non-dimensionalized mean axial velocity component, U/U_∞, in the *x*-*z*-plane at y/H=0.05

The vector field and the mean spanwise vorticity (ω_y) field are plotted in Fig. 5.6. The data is based on PIV measurements and is averaged over 200 samples. The plots show that when no AFC is applied the shear layer between the free stream (indicated by the vorticity) and the wake region is orientated parallel to the axial direction. The vectors indicated a large area with recirculation. When constant blowing is activated a strong deflection of shear layer downwards takes places. This is consistent with the results of the LDA-measurements (in the PIV case the measurement grid is much finer). Moreover, the size of the recirculation area is decreased. The strong reverse flow which existed in the passive case disappears with CB activated.

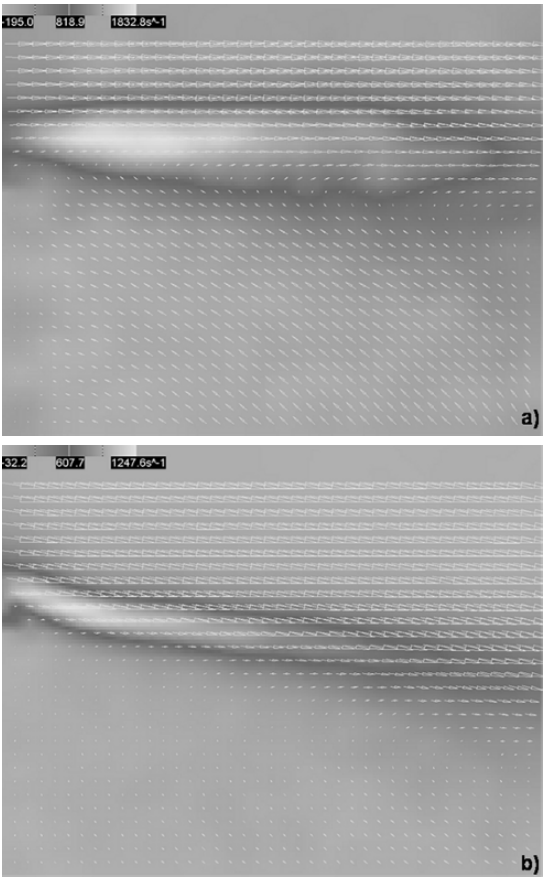

Fig. 5.6 Mean vector and spanwise vorticity field. The axial extension of the area shown corresponds to 0.4 *y/H*. a) $C_\mu = 0\%$; b) $C_\mu = 11.13\%$

6 Concluding Remarks

The present study considered the combined effect of passive and active drag reducing methods applied to a generic model of European tractor-trailer. It was shown that short base flaps combined with constant blowing through a slot at the trailing edge of the trailer could achieve a higher drag reduction than 36% longer flaps without active flow control. However, it appears that there is more potential for drag reduction as the effective slot length for blowing was not optimal. Further investigations should address this point. It is believed that the necessary momentum coefficient $C_\mu = 11.13\%$ can be reduced this way. The results also showed

that the flaps at the sides of the trailer were not as efficient as the flap at the top as they did not reduce the size of the wake in the spanwise direction. This could be attributed to the combination of two adverse effects: the vicinity of the ground (wind tunnel floor without a moving belt) with its boundary layer and the short effective length of the blowing slot. Both effects can reduce the effectiveness of the blowing as they disturb the flow.

The flow region at the lower region of the wake where the interaction between the boundary layer of the ground and the wake takes place needs also to be studied.

References

[1] Cooper K (1985) The Effect of Front-Edge Rounding and Rear-Edge Shaping on the Aerodynamic Drag of Bluff Vehicles in Ground Proximity. SAE paper No. 850288, Detroit Michigan

[2] Englar R (2004) Pneumatic Heavy Vehicle Aerodynamic Drag Reduction, Safety Enhancement and Performance Improvement. Proceedings of the UEF Conference on The Aerodynamic of Heavy Vehicles:Trucks, Buses and Trains, Lecture Notes in Applied and Computational Mechanics Springer-Verlag, Heidelberg

[3] Göhring E, Krämer W (1991) Fahrwiderstandsreduzierende Maßnahmen zur weiteren Optimierung der Wirtschaftlichkeit von Sattelzügen – Teil 1. ATZ Automobiltechnische Zeitschrift 93, pp. 434-439

[4] Gustavsson T (2006) Alternative approaches to rear end drag reduction. KTH, Department of Aeronautical and Vehicle Engineering, Royal Institute of Technology, Stockholm

[5] Hsu T-Y, Hammache M & Browand F (2004) Base Flaps and Oscillatory Perturbations to Decrease Base Drag. Proceedings of the UEF Conference on the Aerodynamic of Heavy Vehicles: Trucks, Buses and Trains, Lecture Notes in Applied and Computational Mechanics Springer-Verlag, Heidelberg

[6] McCallen R C, Salari K, Ortega J et al (2004) DOE's Effort to Reduce Truck Aerodynamic Drag – Joint Experiments and Computations Lead to Smart Design, Portland, Oregon

[7] Nagib H, Kiedaisch J, Wygnanski I et al (2003) First-In-Flight Full-Scale Application of Active Flow Control: The XV-15 Tiltrotor Download Reduction. RTO-MP-AVT-111

[8] Seifert A, Arwatz G, Palei V et al (2007) Heavy Trucks Base-Drag Reduction Using Active Flow Control. Tel Aviv, Heavy Vehicle-Aerodynamics II Conference, 2007, Lake Taho, USA

[9] Storms B, Ortega J, Salari K et al (2007) An Experimental Study of Tractor Base Bleed for Heavy Vehicle Aerodynamic Drag Reduction. Lawrence Livermore National Labority

[10] Zühlke O (2008) Investigation of aerodynamic devices to reduce aerodynamic drag of a generic tractor trailer. , Diplomathesis, ISTA (HFI), TU-Berlin

Design Optimization Techniques Related to Vehicle Aerodynamics

Advanced Aerodynamics and Cooling System Solutions for Higher Fuel Efficiency and Decreased Emissions

Ilhan Bayraktar

Oshkosh Truck Corp., USA
ibayraktar@oshtruck.com

Abstract Auxiliary load systems, fuel and lubrication systems, and cooling systems are an integral part of any truck, and contribute to the overall design and energy use/management. Research and development appropriate to this topic include advanced aerodynamics, heat exchanger technologies, heat pipe/two-phase flow systems, advanced pumps and compressors, and other advanced thermal and fluid management concepts to improve electric powertrain cooling, enhance drivetrain performance, reduce energy usage, improve system energy management, and reduce component and system weight, volume, and aerodynamic drag in hybrid power trains and hybrid vehicle systems. The current study presents a cooling system and vehicle aerodynamics integration through the substitution of more efficient hardware and better integration with existing vehicle systems. Several aerodynamic add-on devices are tested for drag reduction. Practical vehicle designs are developed and software simulations are conducted to determine improvements in aerodynamic efficiency. Coastdown testing is conducted to determine the drag reduction achieved with aerodynamic modifications. Weight reduction and energy consumption improvements projected for a practical aerodynamic refuse vehicle are calculated. Improved aerodynamics and cooling system designs are integrated into the current vehicle technology and tested to quantify the benefits.

Optimization of Aerodynamic Properties of High-Speed Trains with CFD and Response Surface Models

Siniša Krajnović

Chalmers University of Technology, Department of Applied Mechanics, Göteborg, Sweden, e-mail: sinisa@chalmers.se

Abstract A new procedure for optimization of aerodynamic properties of trains is presented. Instead of large number of evaluations of Navier-Stokes solver, simple polynomial response surface models are used as a basis for optimization. The suggested optimization strategy is demonstrated on two flow optimization cases: optimization of the train's front for the crosswind stability and optimization of vortex generators for purpose of drag reduction. Besides finding global minimum for each aerodynamic objective, a strategy for finding a set of optimal solution is demonstrated. This is based on usage of generic algorithms onto response surface models. The resulting solutions called Pareto-optimal help to explore the extreme designs and to find tradeoffs between design objectives. The paper shows that accuracy of the polynomial response surfaces is good and suitable for optimization of train aerodynamics.

1 Introduction

The Swedish national rail administration Banverket has in 2004 launched a new research program called "Gröna Tåget" (Eng. Green Train). One of the aims of this program is to develop a new high-speed train for Nordic conditions (meaning strong winter, large temperature differences during the year and sparsely populated region). Although the maximal speed of the new train will be 250 [km/h] compared with 200 [km/h] for the existing Swedish high-speed train X2000, the energy consumption for propelling the train should decrease by $20-30\%$. Besides, the aero-acoustic noise generated by the new train must not increase or even better should decrease. However, the aerodynamic drag increases with speed by power of two and aero-acoustic noise by power of six. The new train needs also to be lighter in order to reduce energy requirement. Although trains in past were probably unnecessary heavy, cutting in weight must be done with largest possible care in order to retain train's stability. This cannot be done without careful

consideration of crosswind stability. Another way to achieve drag reduction is to use some form of flow control, active or passive, ones the shape optimization has reached its limitation due to practical constrains. Design and placing of devices for flow control can be done in almost infinite number of ways and even here an intelligent optimization strategy is required. External aerodynamic consideration of modern high-speed trains is not constrained to drag, stability and noise but includes also upraise of ballast, slipstreams, design of air-conditioning inlets etc. This makes optimization of aerodynamic properties of trains a true multi-objective optimization problem (MOP). The present paper describes the efforts of the author to develop a numerical technique that is capable of finding one or even better a set of optimal designs of trains or its parts (e.g. train's front or flow control devices). Several aerodynamic objectives are known to be in conflict. For example, a shape of a vehicle with low drag produces often high lift. Well rounded fronts of trains which are beneficial for drag reduction can deteriorate lateral stability. The reason for this is that the rear of the train is identical with its front and rounded rear produces position of separation that varies in time and as such produces oscillating lateral forces [1,4].

2 Optimization Approach

The optimization strategy suggested in the present paper is based on construction of simplified models called metamodels or surrogate-based models. The idea is to investigate the behaviour of the aerodynamic objective functions in the design domain using evaluation of Navier-Stokes solver (denoted NS in the following text) in small sequence of design points. The design points chosen for NS simulations are not chosen in random but using special strategy called design of experiments (DOE). Ones the results from NS simulations are available the construction of metamodels can begin using regression technique. There are several different metamodels but the present paper deals only with so called polynomial response surfaces (PRS) which are low order polynomial functions. Finally, the optimization itself is now based on the resulting PRS models and not on actual NS evaluations. This results in a radical simplification of the optimization procedure as the global behaviour of aerodynamic properties is represented with simple polynomials instead of complex evaluations of non-linear differential equations. A metamodel is model of a model and the natural question is if the simplification made in such a model has filtered to much information making it unsuitable for aerodynamic optimization applications. The aim of the present paper is to investigate this.

2.1 Choice of design variables

Greatest care should be given to the choice of design variables that will be varied in the optimization procedure as their number defines the number of required NS evaluations and thus computer effort required. There are today two competing approaches for description of designs. The first one is based on prescribing limited number of points on the surface of the body controlling the geometry and than prescribing rules for change of their coordinates in space. This is implemented in a CAD toll which than provides required number of designs. Ones the geometries are available they are transferred into a meshing tool that produces numerical grids for NS solver. The second approach is using so called morphing tools directly on the grids used for NS simulations. In this approach changes in the grid are governed by rules defined in the morphing tool. Again, the user prescribes these changes in the grid using limited number of points that in turn govern changes in larger sets of computational cells. Although there is large activity in development of these tools there is yet no tool that is sufficiently robust and that provides necessary flexibility in the design process or accuracy in the resulting computational grids. Therefore the present paper uses simple description of designs in terms of physical design variables such as lengths, angles and radiuses.

In the present work two shapes are optimized, train's front and vortex generators.

2.1.1 Crosswind stability

The aim of the first case is to optimize the shape of the front of a generic train for the crosswind stability. The shape of the train is the one studied in experiments by Chiu and Squire [2] and numerical studies by Hemida and Krajnović [6] and [7] .The profile of the cross section of this model is defined by the equation

$$|y|^n + |z|^n = c^n \tag{1}$$

The coefficient of curvature, n , varies linearly along the front of the train according to the equation:

$$n = \frac{2-q}{b} z + q \tag{2}$$

where q is the value of n at the body of the train, far from the front and b is the length of the front. The second equation that describes the shape of the front from a lateral side is

$$\frac{z^2}{b^2} + \frac{y^2}{c^2} = 1 \tag{3}$$

Here, b is the length of the front, $c = h/2$ and $h = 3.0$ [m] is the height of the train (see Fig. 1b). The length of the train excluding the front and the rear (which are identical) is 30 [m].

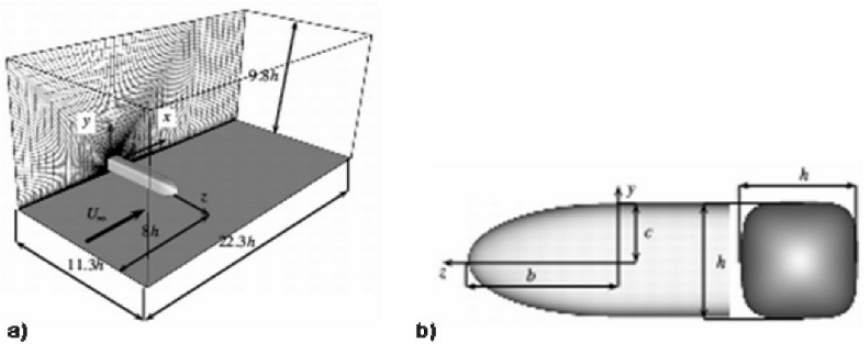

Fig. 1 a) Computational domain for the case of train influenced by a crosswind at 90^o yaw angle. b) Shape of the front of the train from a side and from in front of the train.

The design constraints were $0.64h \le b \le 1.28h$ and $4 \le n \le 6$. Such constrains were chosen in order to represent realistic length of the nose and the roundedness of the cross section of the train. The choice of the length of the train's front was in particular chosen to represent different rail vehicles from a commuter train to a high-speed train. The flow at 90^o yaw angle of the crosswind is studied in the present paper. The computational domain and the train are shown in Fig.1. A constant velocity U_∞ of 25 [m/s] is used at the inlet of the computational domain. Wall functions are used at tunnel walls and on the surface of the train while the outlet velocity condition was homogeneous Neumann.

The origin of the coordinate system is located in the centre of the cross section of the train body and on the later wall where the train was mounted. Objective functions in the present paper are drag force coefficient C_D, rolling moment coefficient C_{MR} and yawing moment coefficient C_{MY}. Drag force is the force in the z direction while rolling and yawing moments are moments acting around z and y axis, respectively. The moment canter is chosen to be at $x = 1.26$, $y = -1.95$ and $z = 0$ which is approximate position of the contact of one wheal with the track. When computing the moment coefficients the reference length and cross-sectional area of the train are chosen as $l = 3$ [m] and $A = 10$ [m/s], respectively, following the practice in train aerodynamics. However the exact cross-sectional area of the train normal to z direction was used for computation of drag coefficients.

2.1.2 Flow control

The second shape that is optimized in the present work is that of vortex generators (VG) placed on the rear of an ICE 2 high-speed train with the purpose of decrease of pressure drag (Fig. 2). Vortex generators act as small wings producing longitudinal tip vortices shown in Fig. 2b. The function of these longitudinal vortices is to sweep the high energy air from the inviscid portion of the flow-field or higher portion of the boundary layer to the inner parts of the boundary layer. As the energy is added from the high-energy air to the retarded air inside the boundary layer, the separation is delayed leading to an increased base pressure and lower drag of the train. In the present study a relatively short train is used containing only 1.25 car lengths of a real ICE2 train. Due to such a short train, the aerodynamic drag is dominated by the pressure drag and we expect the vortex generating devices to decrease the total drag.

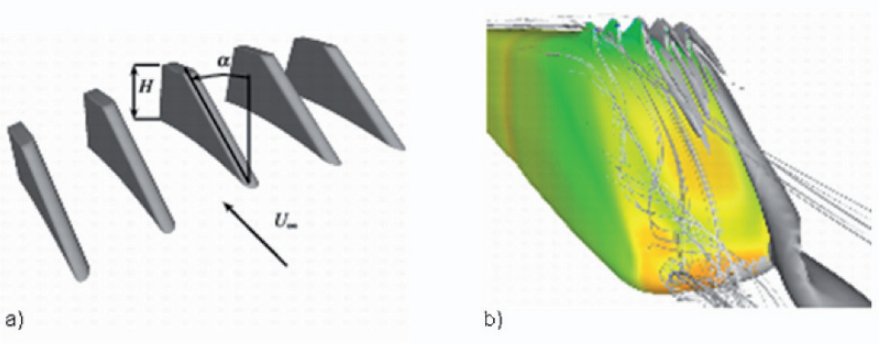

Fig 2 a) An example of VGs used in the present study with two design variables, α and H. b) The resulting flow over the rear of the train. An isosurface of streamwise vorticity component ω_x and streamlines produced from the cores of vortices behind the vortex generators are shown on the right and the left side of the figure, respectively. The body of the train is coloured with the surface pressure.

The shape of VGs is shown in Fig. 2a and in the present study two design variables: the height, H, of the VG and the angle, α, of the upstream slanted surface of VGs were varied. The design constraints were at first set as 6 [cm] $\leq H \leq$ 30 [cm] and $24^o \leq \alpha \leq 46^o$. However, later two additional designs were added with the height $H = 38$ [cm], to original six designs. The inlet and the floor boundary condition was 56 [m/s] corresponding to 200 [km/h]. The roof and the lateral walls were treated as slip surfaces while the outlet was homogeneous Neumann boundary condition for the velocities. Wall functions were used as boundary condition on the surface of the train.

The objective functions for VG case were drag and lift coefficients. Although the aim is to reduce drag the lift force should not become to large to deteriorate the

train's stability. Thus the problem was treated as a multi-objective optimization problem.

2.2 Exploration of the design space

In the present study center composite design (CCD) was used as DOE. The two DOEs are presented in Figs. 3 and 4, for the optimization of the front of the train and the VGs, respectively. Nine designs were first used for optimization in both cases. However, the number of designs for VGs was later increased to eleven. Here x_1 and x_2 are design variables normalized between -1 and 1 and between -1 and 1.67 in case of optimization of train's front and VGs, respectively.

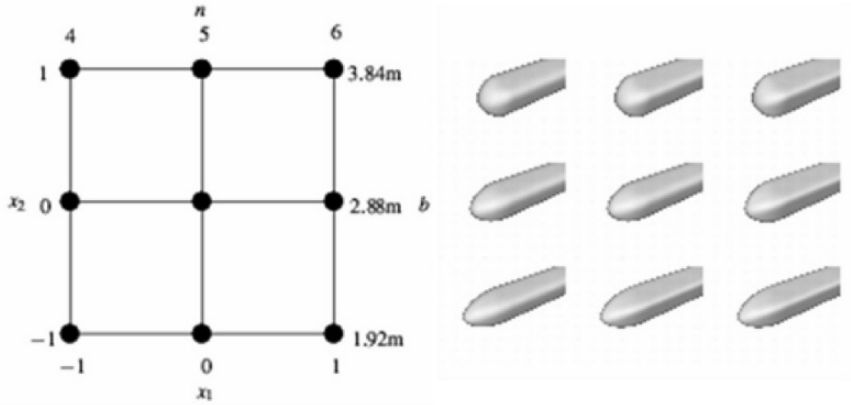

Fig 3. Canter composite design for the optimization of the front of the generic train.

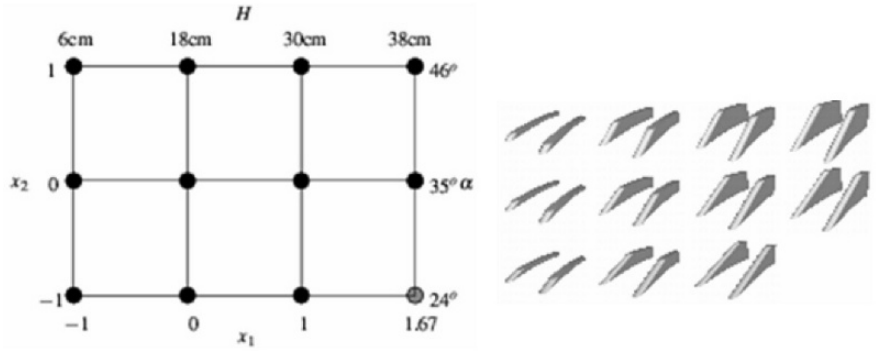

Fig 4. Canter composite design for the optimization of the VGs.

Reynolds-Averaged Navier Stokes (RANS) simulations were performed using the standard $k-$ model in optimization of train's front. However, four different

turbulence models were used for optimization of VGs. These are the standard $k-\varepsilon$ model, the RNG $k-\varepsilon$ model, the realizable $k-\varepsilon$ model and the Reynolds Stress Model (RSM) and tehy were all implemented in commercial solver Fluent 6.3. The standard $k-\varepsilon$ model was found to produce poor results for VG case. On the other hand the RNG $k-\varepsilon$ and the RSM model produced too much numerical noise due to incomplete convergence which prevented construction of a reasonable fit of RSs in the DOE points. Thus, only the results of simulations using the realizable $k-\varepsilon$ are presented in the present paper for VG case.

2.3 Polynomial response surface approximation

The approximation of the true response in a PRS is represented by low order polynomials which in the present paper are quadratic. A quadratic RS model reads

$$\hat{C} = \beta_0 + \sum_{i=1}^{n} \beta_i x_i + \sum_{j=1}^{n} \sum_{i<j}^{n} \beta_{ij} x_i x_j + \sum_{i=1}^{n} \beta_{ii} x_i^{\,2} \tag{4}$$

where n is the number of design variables and $\beta_i, \beta_{ii}, \beta_{ij}$ are the regression coefficients. The regression coefficients are determined by a least square regression. The RS can be expressed in matrix notation as $\hat{C}=\mathbf{x}^T\mathbf{b}$ where $\mathbf{b} = (\mathbf{X}^T\mathbf{X})^{-1}\mathbf{X}^T\mathbf{y}$ and $\mathbf{X}$ is the matrix containing the experimental designs.

In order to measure the goodness of fit both the coefficient of multiple determination R^2 and R-square adjusted (R_a^2) were used in the present work. The coefficient of multiple determination R^2 measures the fraction of variation in data captured by response surface.

$$R^2 = SS_R/SS_T = 1 - SS_E/SS_T \tag{5}$$

where SS_E is the sum of squared approximation errors at the n_p sampling points, SS_T is the true response's sum of squared variations from the mean $\overline{C}$, and SS_R is the approximation's sum of squared variations from the mean, i.e.

$$SS_E = \sum_{i=1}^{n_p} (C_i - \hat{C}_i)^2, \quad SS_T = \sum_{i=1}^{n_p} (C_i - \overline{C}_i)^2, \quad SS_R = SS_T - SS_E = \sum_{i=1}^{n_p} (\hat{C}_i - \overline{C}_i)^2 \tag{6}$$

A better suited measure for assessing predictive accuracy is the R-square adjusted (R_a^2) defined as

$$R_a^2 = 1 - \frac{SS_E/(n_p - n_\beta)}{SS_T/(n_p - 1)} \tag{7}$$

where n_β is the number of regression coefficients. Both R^2 and R_a^2 range between zero and one, and the higher value indicate better predicting accuracy of the response surface.

Although the full model was fitted at first, it is possible that this is not an appropriate model, i.e. it is possible that a model based on a subset of regressors in the full model may be superior. In the present work, a backward elimination procedure based on the t statistic is used to discard terms and improve the prediction accuracy. The t statistics of the fitting coefficient is defined as its value divided by an estimate of the standard error of the coefficient.

In the backward elimination we begin with a model that includes all candidate regressors (i.e. full quadratic model in the present work) and than the partial t statistics are computed for all regressors as if they were last to enter the model. The smallest of these partial t-statistics is compared with preselected value, t_{out} and if it is less than t_{out}, that regressor is removed from the model. A rule of thumb saying that regressor terms with absolute value of t larger than 2 are significant at a 95% confidence interval, was used in the present paper. Thus the regressor terms are removed from the model if regressor's t is smaller than 2 and if R_a^2 increases after regressor's removal.

2.4 Variable selection and backward elimination

This chapter demonstrates improvement of models (in form of PRS) using backward elimination procedure.

According to Table 1, the full quadratic response surface model for the drag coefficient has R_a^2 of 0.9850. Determination of the mixed-term regressor β_{12} involves a large standard error (exposed by $t = 0$ in Table 1). Discarding this term leads to an increase of R_a^2 to 0.9888. Thus elimination of this term improves the fit. The quadratic-term regressor β_{11} has also $t < 2$. However, discarding this term leads to reduction of R_a^2 to 0.9865 and the regressor β_{11} is not removed from the model. Thus the best quadratic PRS of the drag coefficient is

$$\hat{C}_D = 1.33 + 0.06x_1 - 0.02x_2 - 0.01x_1^2 - 0.05x_2^2 \tag{8}$$

2.4.1 Improvement of the model for the case of the train's front

Table 1 Backward elimination procedure for response surface approximation of the drag coefficient. Optimization of the train's front at 90^o yaw angle.

Coefficient	t (full)	t $(-\beta_{12})$	t $(-\beta_{11})$
β_0	231.41	267.21	313.86
β_1	20.15	23.27	21.24
β_2	-5.83	-6.74	-6.15
β_{12}	0	–	–
β_{11}	-1.22	-1.41	–
β_{22}	-9.49	-10.96	-10.00
Removed regressors	R^2	R_a^2	
—-	0.9944	0.9850	
β_{12}	0.9944	0.9888	
β_{11}	0.9916	0.9865	

Similar procedure of backward elimination is made for the rolling and the yawing moment coefficients. The results of the procedure are presented in Tables 2 and 3 and the resulting PRS model are

$$\hat{C}_{MR} = 1.75 + 0.11x_1 + 0.04x_2 - 0.04x_1^2 + 0.1x_2^2 \tag{9}$$

$$\hat{C}_{MY} = 7.75 + 0.76x_1 + 0.3x_2 - 0.05x_1^2 + 0.87x_2^2 \tag{10}$$

Contour plots of PRS in Eqs. 8,9 and 10 together with their global minima are presented in Fig. 5.

Minimization of PRSs was performed using constrained nonlinear optimization in MATLAB. The $\hat{C}_D$ obtains its minimal value of 1.188 at $n = 4$ and $b = 3.84$ [m], i.e. for the longest and most rounded train. On the other hand the optimal $\hat{C}_{MR}$ and $\hat{C}_{MY}$ are obtained for the most rounded train with an intermediate length of $b = 2.70$ [m] and $b = 2.71$ [m], respectively. The minimal $\hat{C}_{MR}$ and $\hat{C}_{MY}$ found for these designs are 1.6 and 6.92, respectively.

Table 2 Backward elimination procedure for response surface approximation of the rolling moment coefficient.

Coefficient	t (full)	$t\ (-\beta_{12})$	$t\ (-\beta_{11})$
β_0	85.42	98.63	97.37
β_1	9.95	11.49	8.91
β_2	3.27	3.77	2.92
β_{12}	0	–	–
β_{11}	-1.80	-2.08	–
β_{22}	5.15	5.94	4.60
Removed regressors	R^2	R_a^2	
—-	0.9789	0.9438	
β_{12}	0.9789	0.9579	
β_{11}	0.9562	0.9299	

Table 3 Backward elimination procedure for response surface approximation of the yawing moment coefficient.

Coefficient	t (full)	$t\ (-\beta_{12})$	$t\ (-\beta_{11})$
β_0	183.17	195.92	234.33
β_1	32.65	34.92	32.50
β_2	13.02	13.92	12.96
β_{12}	0.71	–	–
β_{11}	-1.25	-1.33	–
β_{22}	21.55	23.05	21.45
Removed regressors	R^2	R_a^2	
—-	0.9982	0.9953	
β_{12}	0.9979	0.9959	
β_{11}	0.9970	0.9953	

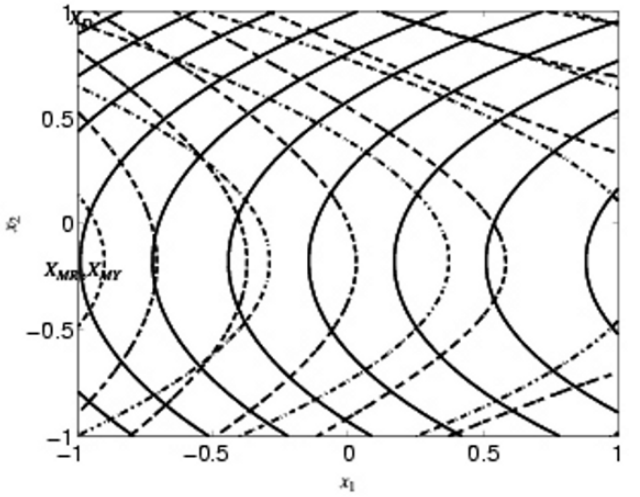

Fig 5. Contour plot of response surfaces for $\hat{C}_D$ (solid line), $\hat{C}_{MR}$ (dashed line) and $\hat{C}_{MY}$ (dashed-dotted line). Minimal values of $\hat{C}_D$, $\hat{C}_{MR}$ and $\hat{C}_{MY}$ are denoted with X_D, X_{MR} and X_{MY}, respectively.

2.4.2 Improvement of the model for the case with VGs

Table 4 Backward elimination of the polynomial response surface approximations for VG case.

	Removed terms	R^2	R_a^2
2nd order PRS for C_D	− − −	0.9231	0.8461
	β_{12}	0.9144	0.8573
	β_{22}	0.8824	0.8320
	Removed terms	R^2	R_a^2
2nd order PRS for C_L	− − −	0.9259	0.8517
	β_{11}	0.9259	0.8765
	β_{12}	0.9259	0.8941

The original RS was a second-order polynomial that was constructed over the design domain $6\,[\text{cm}] \le H \le 30\,[\text{cm}]$ and $24^o \le \alpha \le 46^o$. Ones the PRS

were constructed, it was found that the minimal value of $\hat{C}_D$ was at the edge of the design domain. Thus, two additional designs with $H = 38$ [cm] were added to the original six designs (black dots in Fig. 4). Also here t statistics were used to eliminate the regressors with insignificant or damaging influence onto the responses. Table 4 shows that R_a^2 for complete 2nd order PRS for $\hat{C}_D$ and $\hat{C}_L$ are 0.8461 and 0.8517, respectively. This was slightly improved to 0.8573 and 0.8941 for $\hat{C}_D$ and $\hat{C}_L$, respectively, using backward elimination procedure. The PRS models produced the optimal designs for both objective functions for vortex generator with maximal height and smallest angle (Fig. 6).

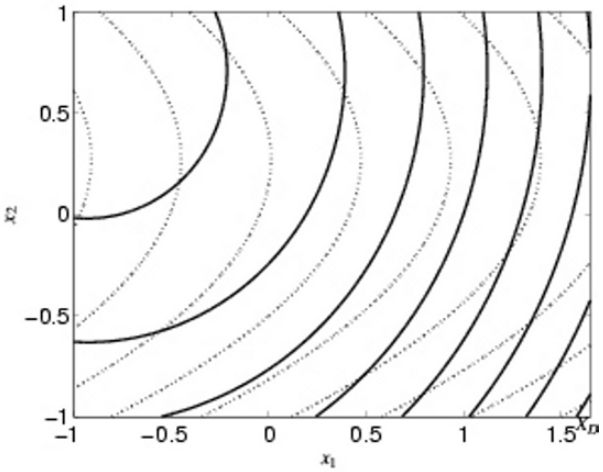

Fig 6. Contour plot of response surfaces for $\hat{C}_D$ (solid line) and $\hat{C}_L$ (dashed line) for VG case. Minimal values of $\hat{C}_D$ and $\hat{C}_L$ are denoted with X_D and X_L, respectively.

2.5 Validation of metamodels

Beside the measure of fit described above, another test in form of verification of the accuracy of the model prediction can be performed on the constructed metamodel in order to ensure its accuracy. This is done by constructing a new design that was used for the construction of the model and perform new computer experiment. The objective functions provided from this new simulation are then compared with the model prediction. For the purpose of validation of PRS approximations for the case of the train's front, flow around an additional train with $n = 4.015$ and $b = 3.52$ [m] was simulated. NS simulation of this new design resulted in following drag and moment coefficient: $C_D = 1.203$, $C_{MR} = 1.731$

and $C_{MY} = 7.892$ compared with responses $\hat{C}_D = 1.224$, $\hat{C}_{MR} = 1.675$ and $\hat{C}_{MY} = 7.542$ resulting from Eqs. 8-10. Thus the relative error between the NS simulated and the modeled objectives were 1.8%, 3.2% and 4.4% for the C_D, C_{MR} and C_{MY}, respectively. For the VG case, the design with maximal height and minimal angle was evaluated using NS simulation. This design point is located outside the DOE and the accuracy of the RS's approximation here is not expected to be large. The resulting C_D value was found to be 0.1068 compared with $\hat{C}_D = 0.1006$ resulting from PRS model. Thus the modelling error was approximately 5.8%.

3 Optimization Based on Metamodels

The multi-objective problem of the train's front resulted in both objectives with optimal values for the same design. For a short train used in the present paper a drag reduction of approximately 5% was achieved using the optimal design of VGs. However objectives were in conflict for VG case and this MOP was solved using an evolutionary multi-objective optimization procedure (so called real-coded genetic algorithm NSGA-II) by Deb *et al.* [3]. Running this genetic algorithm together with computer experiments (NS simulations) would be extremely computer demanding. However, since the metamodels for each objective are available in form of simple polynomial expressions, the evaluation of generic algorithm is fast and efficient. The objective of such an algorithm is to find solutions (in form of combinations of objectives) such that there is no other solution for which at least one objective has better value while values of remaining objectives are the same or better. Solutions obtained using this optimization procedure are called Pareto-optimal. The parameters chosen for the NSGA－II simulations are presented in Table 5.

Table 5 Parameters used for the NSGA－II simulation.

Population size	100
Generations	100
Crossover probability	0.9
Distribution parameter (for crossover)	20
Mutation probability	0.25
Distribution parameter (for mutation)	20

A population of hundred train designs were regenerated hundred times resulting in hundred Pareto-optimal solutions shown in Fig. 7a. Rolling and yawing moment coefficients tend to produce very similar optimal designs while drag

coefficient is in conflict to these two moment objectives. Figure 7a shows the Pareto optimal set of the three objectives. Note that the objectives on the axis are scaled due to relatively small changes in optimal designs. Pareto optimal solutions of two objectives in conflict $\hat{C}_D$ vs. $\hat{C}_{MR}$ presented in Fig. 7b show for example a reduction of 4% in drag by changing design results in an increase of rolling moment coefficient of 6%.

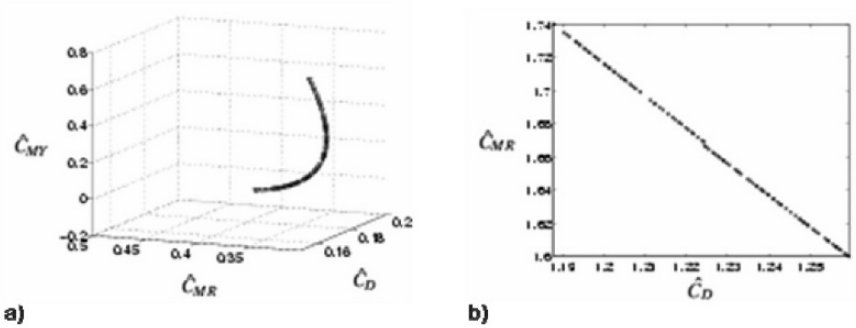

Fig. 7 a)Pareto optimal solutions for $(\hat{C}_D - 1.259)\times 10^4$, $(\hat{C}_{MR} - 1.599)\times 10^4$ and $(\hat{C}_{MY} - 6.917)\times 10^4$. b) Pareto optimal solutions for $\hat{C}_D$ vs. $\hat{C}_{MR}$.

4 Discussion

The present paper shows that optimization of train's aerodynamics can be done using simple polynomial response surfaces instead of complex NS simulations. Although only a first attempt is presented, a fairly good accuracy of objective functions was achieved with only second order PRSs. However, there are other metamodels available such as radial basis neural networks (RBNN) or Kriging models. It is reasonable to expect that these or some blend of these models will provide even better fit with the data and accuracy of the model than pure PRSs. Two optimization cases presented here illustrate the importance of choice of turbulence models in NS simulations on the optimization. Unfortunately the weakness of the Reynolds-Averaged Navier-Stokes simulations reflects on the optimization results. Besides, convergence problems often prevent reasonable fit of response surfaces with the data in DOE making them useless for the optimization purposes. On the other hand models such as standard $k-\varepsilon$ which almost always converge can produce inaccurate metamodel. In wait for a tremendous increase of computer power required for time-dependent NS simulations an appropriate trade-off between the accuracy and fit of metamodels with RANS data must be made. Making the optimization process automatic is of highest priority for putting the

suggested technique into production. Providing computational grids for designs in DOE is the Achilles heel of any such attempt. Hopefully new morphing and CAD tools will overcome this problem.

5 Acknowledgments

This work is financed by Banverket (Swedish National Rail Administration) under contract no.S05-3157/AL50 and it is a part of the project called Gröna Tåget (Eng. Green Train). FLUENT Sweden and Bombardier Transportation are supporting the project. Computer time at SNIC (Swedish National Infrastructure for Computing) resources at the Center for scientific computing at Chalmers (C3SE) is gratefully acknowledged. Several computational meshes used in simulations were made within student diploma projects [5,8].

References

1. Diedrichs B, Berg M, Stichel S and Krajnović S: (2007) Vehicle dynamics of a highspeed passenger car due to aerodynamics inside tunnels, I MECH E Part F Journal of Rail and Rapid Transit, Vol. 221, pp. 527-545
2. Chiu T and Squire L: (1992) An experimental study of the flow over a train in a crosswind at large yaw angles up to 90^0, Journal of Wind Engineering and Industrial Aerodynamics,45: pp. 47-74.
3. Deb K, Agrawal S, Pratap A and Mayarivan T: (2000) A fast and elitist multiobjective genetic algorithm for multi-objective optimization: NSGA-II, Parallel problem solving from nature VI conference, Paris, pp. 849-858.
4. Diedrichs B, Krajnović S and Berg M: (2008) On Tail Vibrations of Very High-Speed Trains Cruising Inside Tunnels, Engineering Applications of Computational Fluid Mechanics, 2(1):pp. 51-75.
5. Bjerklund E, Emilsson J, Hobroh E, Lenngren J, Norrgård C and Rynell A: (2007) Design of high-speed trains for cross-wind stability, Bachelor thesis (kandidatarbete), Departments of Applied Mechanics, Chalmers University of Technology, Gothenburg.
6. Hemida H, Krajnović S: (2006) Exploring the flow around a generic high-speed train under the influence of side winds using LES, Fourth International Symposium on Computational Wind Engineering, July 16-19, Yokohama, Japan.
7. Hemida H, Krajnović S and Davidson L: (2005) Large eddy simulations of the flow around a simplified high speed train under the influence of cross-wind. 17th AIAA Computational Dynamics Conference}, Toronto, Ontario, Canada.
8. Georgii J, Gustafsson O, Joelsson E, Martini H, Näsholm K and Ringius G: (2007) Drag reduction of high-speed trains using vortex generators, Bachelor thesis (kandidatarbete), Departments of Applied Mechanics, Chalmers University of Technology, Gothenburg.

Design Considerations for Maximizing Cooling Package Performance

Bhaskar Bhatnagar, Dan Schlesinger

Freightliner LLC, USA
bhaskarbhatnagar@freightliner.com

Abstract More stringent heavy vehicle emissions legislation demands considerably higher performance out of engine cooling systems. Presented is a study of various design parameters that can be used to maximize the cooling airflow for a Freightliner Class 8 truck. CFD analysis was used to analyze various fan shroud profiles, different fan immersions (overlap between the fan and fan shroud) and with two different engines. All of these design parameters lead to significantly different flow behavior inside the fan shroud and in the underhood region, in turn creating adverse or favorable pressure gradients. A series of isothermal CFD simulations are used to determine the effects of these flow characteristics on the radiator mass flow. For one of the simulation setup the predicted radiator coolant inlet temperature is compared to measured physical test data at different fan speeds. The methodology for the optimization of the cooling performance is outlined. It is shown that the presented simulation approach can provide accurate predictions of cooling airflow and coolant temperature.

Optimization and Correlation of a Class 8 Truck Cooling System

Clinton Lafferty, Kevin Horrigan, Ales Alajbegovic

Volvo Trucks North America, USA
clinton.lafferty@volvo.com

Abstract Development in engine technology to meet recent heavy vehicle emissions legislation has increased the demand on heavy vehicle cooling systems. The use of PowerFLOW®, a commercial computational fluid dynamics (CFD) software, allows a product development team to access a variety of cooling system improvements with no impact to the vehicle external appearance. This paper provides an overview of the PowerFLOW® modeling process and the results for several studies involving modifications to engine and cooling system parts. The design changes include the repositioning of the exhaust gas recirculation (EGR) cooler, changes to the fan diameter and position, and modifications to the exit shape of the shroud. Initial work focused on increasing cooling air mass flow and used a body force fan model with isothermal calculations. Results indicated only minimal changes with the EGR cooler repositioning, however, fan modifications resulted in a 13 percent cooling air massflow increase. The impact of the fan shroud exit shape on fan blade tip loss was computed with a multiple reference frame (MRF) fan model. Finally a detailed cooling system correlation study was performed involving a comparison to isothermal air mass flow rates and later thermal calculations involving heat exchangers modeled with PowerCOOL®.

Train Aerodynamics

Aerodynamic Improvements and Associated Energy Demand Reduction of Trains

Alexander Orellano and Stefan Sperling

Bombardier, Center of Competence for Aerodynamics and Thermodynamics, Germany, Alexander.orellano@de.transport.bombardier.com

Abstract The importance for developing energy efficient rail vehicles is increasing with rising energy prices and the vital necessity to reduce the CO_2 production to slow down the climate change. This study shows a comparison of different train types like regional and high-speed trains and provides estimation for improvements of the aerodynamic drag coefficient. Out of this estimation an assessment of the associated energy reduction is shown taking into account typical operational cycles with acceleration, constant speed and deceleration phases. Traditionally, aerodynamic improvements of high-speed trains were in the focus of the engineering community as the resistance to motion is increasing with the square of the velocity. However, this study reveals that it is necessary to consider regional and commuter applications equally. This transport sector is not only the one with the highest share in the market but exhibits also much higher potential for aerodynamic improvements then present day already optimized high-speed trains.

1 Introduction

In order to focus the engineers attention to the dominant and therefore relevant area related to energy demand reduction it is necessary to first get an overview of the energy fluxes and to fix the boundaries and the scope of the investigation. Figure 1 shows one specific example of the distribution of the traction energy demand of an electrical multiple unit covering the energy flux from the power supply substation up to a specific train within the line. A substantial portion of the energy provided by the substation to the line is already lost on the way to the train. The energy demanded by the train can be subdivided into a part which dissipates to heat and a part that is converted to kinetic energy due to the momentum gained by the accelerated mass of the train. The part of the energy dissipated to heat is marked with E_{Vd}. The most important contributors to this part are the aerodynamic drag and the losses of the traction system including the cooling devices. This energy is usually not used anymore and is released to the environment. Principally it

would be possible to convert these cooling losses back to electrical energy by an appropriate thermodynamic process like Clausius-Rankine or heat absorption process. Nevertheless, the efficiency cannot be higher then the Carnot process [1]. The temperature difference of the cooling liquid (usually water) to the environment ranges from 50 to 80 Kelvin which limits the theoretical efficiency of the thermodynamic process to be not greater then around 20 % which would lead to efficiencies around 10 to 15 % in a practical application. This fact prevents an economically justified operation of such a device for water cooling systems of trains. The part of the energy converted to kinetic energy can more easily be converted back to electrical power in conjunction with regenerative braking. This is common practice in most mainline applications. The rate of energy recovery during braking is dependent on the voltage, the relative number of driven axles and the capability of the substations control. The part of the kinetic energy which cannot be transferred back to the line is being dissipated in the brake resistor (E_{BR}). This analysis of the losses helps to determine the dominant terms of energy losses. However, when it comes to implementation of energy demand reduction technology it is important to analyse the decrease of energy demand related to the operational boundary conditions including speed profile, altitude profile and environmental temperatures. The losses can be divided in the following components:

- E_{VI} infrastructure losses
- E_{Vd} driving losses
- E_{Vb} braking losses
- E_{BR} brake resistor losses

The scope of the present investigation is to analyse the potential to reduce the driving losses of the train by reducing the aerodynamic drag of the train. It should be also noted that the analysis shown does not comprise the energy used for the auxiliaries of the train as e.g. the HVAC system. The energy demand for the HVAC system is extremely dependent on the application and on the external atmospheric boundary conditions and is not within the scope of the present investigation. The investigation presented here is thus restricted to the driving losses only.

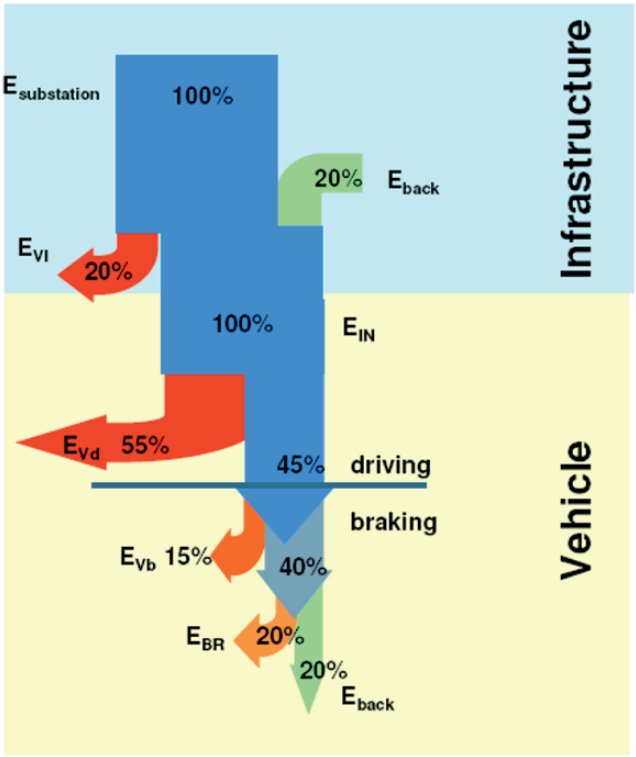

Fig. 1 Traction energy demand distribution.

2 Running Resistance

The total running resistance can be approximated by a quadratic approach, i.e. the Davis Formula [2]

$$R = a + b * v + c * v^2 + d + e \quad (1)$$

R[N] is the total running resistance in Newton
v[km/h] is the train speed
a[N], b[Nh/km], c[Nh2/km2] are the Davis coefficients
d[N] is the curve resistance and
e[N] is the slope resistance
The term *a* represents the mechanical rolling resistance. The term *b* is linearly dependent on the velocity and reflects the mechanical resistance and momentum losses due to air mass exchange of the train with the environment. The momentum

losses are mainly associated with the power needed to accelerate the air taken in to the speed of the train. The term c represents the classical aerodynamic drag which consists of the skin friction and the pressure drag. Typical contributors for the aerodynamic drag are [3]

- head and tail loss
- skin friction
- bogies
- protruding objects
- pantographs
- inter-car gaps
- ventilated brake
- underbelly friction

From an engineering point of view it is important to first determine the various contributions to the drag coefficient of the vehicle under investigation. The general train data for the regional and high-speed train considered within this study is given in Table 1.

Table 1 General data of investigated trains

	Regional train	High-speed train
Number of cars	4	8
Length	72 m	201 m
Width	2.93 m	2.95 m
Cross section area	10 m^2	10.25 m^2
Ground clearance	0.4 m	0.27 m
Total weight	128 t	470 t
Air volume rate	25000 m^3/h	169000 m^3/h
max. speed	160 km/h	330 km/h

2.1 Rolling Resistance

The velocity independent Davis coefficient a represents the force which is necessary to roll the train at zero speed on a track. An illustrative model for the A-coefficient refers to a small slope for the wheel to climb (see Fig. 2). The wheel and rail surfaces deform due to the axle load at the point of contact. Accordingly, the superstructure of the track deforms in a similar way. The magnitude of this deformation depends predominantly on the axle load and the properties of the involved material of the track and the wheel.

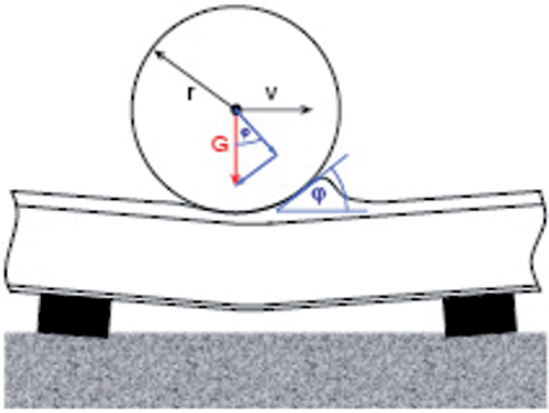

Fig. 2 Rolling resistance [3].

2.2 Momentum Resistance

The mechanical resistance scales linearly with the train velocity. The term is separated into two different parts; i.e the actual mechanical resistance (b_1) and the air momentum drag (b_2). The corresponding parts of the Davis formula read

$$b = b_1 + b_2. \tag{2}$$

The b_1-term supplements the rolling resistance with respect to modelling the wheel/tracksliding friction including brake and transmission drag, the resistance of friction bearings, friction inside gear units and suspension-drag contributions. b_1 depends on the specific track design and details of the suspension and transmission. The air-momentum drag coefficient b_2 is dependent on the following parameters: brake drag, transmission losses and air momentum drag. The air momentum drag is the energy required to accelerate the mass of air intake, e.g. cooling, air conditioning, etc. to the speed of the running train. Thus, b_2 exclusively hinges on the amount of exchanged air.

2.3 Aerodynamic Resistance

The coefficient for the aerodynamic drag is calculated as follows:

$$c_d = \frac{F_x}{0.5 * \quad * V^2 * A} \tag{3}$$

Where F_x is the force in driving direction, is the air density, V denotes the driving speed and A represents the reference area which is standardized to be $10m^2$ within the train aerodynamics community [4]. Note that the non-dimensional c_d value is not the same as the c value with dimensions within the Davis formula described above. The formula to derive the c_d value out of the Davis coefficient is

$$c_d = c_{Davis} * 2 * 3.6 * 3.6 / (\rho * A) \quad (4)$$

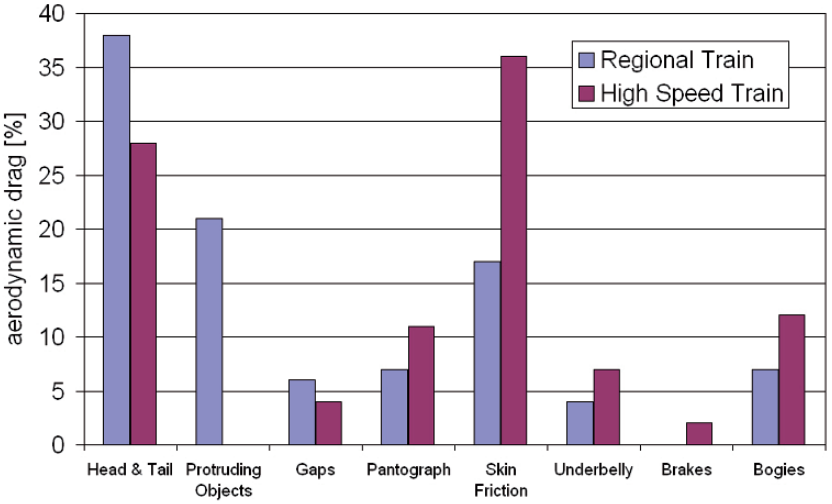

Fig. 3 Typical drag distribution for high-speed trains and regional trains.

Figure 3 gives a general overview of the specific contributions of the different components of a typical regional and high-speed train. The figures presented in the graph are highly dependent on the specific train under investigation. Nevertheless, a typical and electrical or Diesel multiple unit (see Fig. 4) exhibits objects, like HVAC, motor coolers, transformers, inverters and other equipment which are usually sticking out of the body shell and which are a major source of drag compared to a typical electrical multiple unit high-speed train with smooth surfaces and integrated components (see Fig. 5). The ratio between the surface of the train perpendicular to the flow direction, i.e. side walls, roof and underbelly, and the cross section area determines the relative importance of the skin friction. Thus, for high speed trains with approximately 200 m length it is the skin friction which dominates the drag. The drag of the regional train investigated here with 4 cars is dominated by the front and tail drag and the drag generated by the unshielded roof equipment. However, it should be noted that the drag value of one specific part of a train is highly influenced by the incoming flow and thus dependent on the surrounding flow which is influenced by near by objects. The engineering approach to derive the total drag by summarising the individual drag of different components is not taking into account this interrelationship.

Fig. 4 Talent II, modern electric multiple unit regional train.

Fig. 5 ICE3, electric multiple unit high-speed train.

3 Energy Demand for Typical Driving Cycles

3.1 Regional Traffic

The parameters of the regional train used in this study are listed in Table 1. To quantify the effect of reducing the aerodynamic coefficient on the energy consumption for regional traffic a driving cycle has been taken into account. This study focuses on Dortmund to Münster with 10 stations and 51 minutes journey time according to the time table of the German operator "Deutsche Bahn". Figure 6 shows the velocity of the train over the time. The total journey time is in our study 12 minutes shorter than the time table of the German operator "Deutsche Bahn" is telling. The station stopping time is in both cases the same (360 seconds). Therefore, the maximum velocity of the train used by the German operator "Deutsche Bahn" is not going up to 160 km/h.

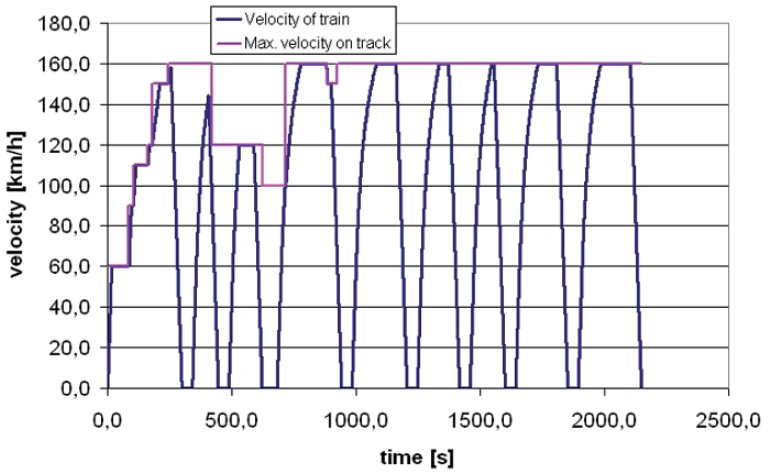

Fig. 6 Velocity profile of a Regional Train running up to 160 km/h.

However, the speed profile (see Fig. 6) shows a relatively short time where the train is running at maximum speed of 160 km/h which diminishes the importance of the aerodynamic drag and increases the relative importance of mass slightly related to the energy demand. Figure 7 shows the effect on the energy demand of the train dependent on the aerodynamic drag. A typical 70 m long regional train exhibits drag values around c_d =1.1. Furthermore, Fig. 7 shows the traction energy, regenerated energy and the total energy. The traction energy herein stands for the energy that can be metered between the line and the train. The regenerated energy

is the energy that can be fed back to the line while the train is braking. Therefore the train has to be equipped with electrical brakes. Last but not least, the total energy is the difference between the traction energy and the regenerated energy.

Figure 7 shows the impact of the aerodynamic drag on the energy demand of the regional train running on the reference line described above. It can be seen that approximately one third of the aerodynamic drag reduction in percentages can be saved in energy for the traction effort. Thus, the relative importance of reducing the drag of a regional train is lower compared to a high-speed application.

c_D	Traction energy [MWh]	Regenerated energy [MWh]	Total [MWh]	Difference [Mwh]	Difference [%]
130%	5022,072	1775,664	3246,408	327,9	10,1%
100%	4702,104	1783,584	2918,52	0,0	0,0%
70%	4379,76	1793,88	2585,88	-332,6	-12,9%

Fig. 7 Impact on the energy demand by varying the aerodynamic drag.

3.2 High-Speed Traffic

In order to quantify the effect of reducing the aerodynamic coefficient on the energy consumption a driving cycle has been taken into account with in a manner analogous to the regional train example above. This study focuses on Frankfurt to Köln (Cologne) with 6 stations and 83 minutes journey time according to the time table of the German operator "Deutsche Bahn". Despite the fact that this stretch is part of the high-speed line in Germany it should be noted that it exhibits a relatively high number of stops within a short distance. Therefore, the speed profile (see Fig. 8) shows a relatively short time where the train is running at maximum speed of 300 km/h. This is particularly important as the relative importance of the aerodynamic performance of the train related to energy demand is determined by the speed of the train and by the frequency of stops. The higher the top speed and the lower the number of stops the more important becomes the aerodynamic drag. Figure 9 shows the effect on the energy demand of the train dependent on the aerodynamic drag. A typical 200 m long high-speed train exhibits drag values around c_d = 1.1 [5]. On the right coordinate the impact on the journey time is also displayed. The journey time decreases with decreasing aerodynamic drag as the train is able to accelerate better with reduced drag.

Figure 10 shows the impact of the aerodynamic drag on the energy demand of the train running on the reference line described above. It can be seen that approximately half of the aerodynamic drag reduction in percentages can be saved in energy for the traction effort.

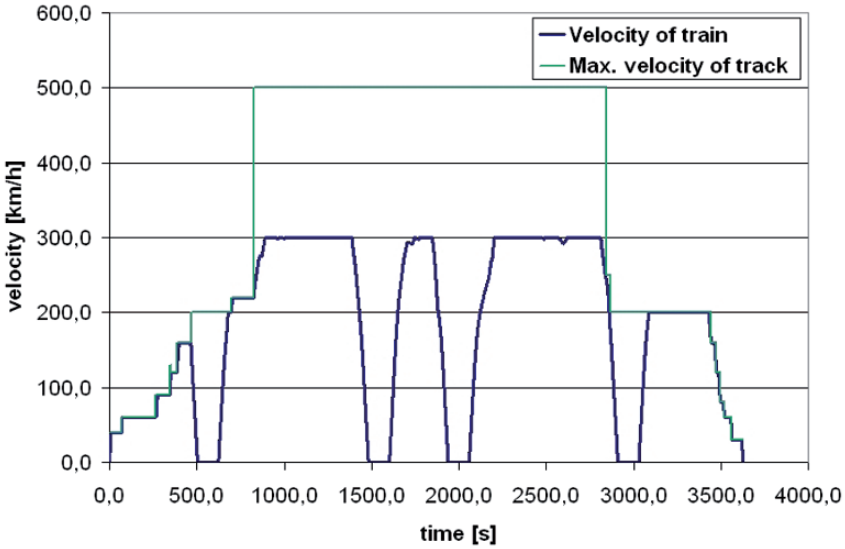

Fig. 8 Velocity profile of a High-Speed Train running up to 300 km/h.

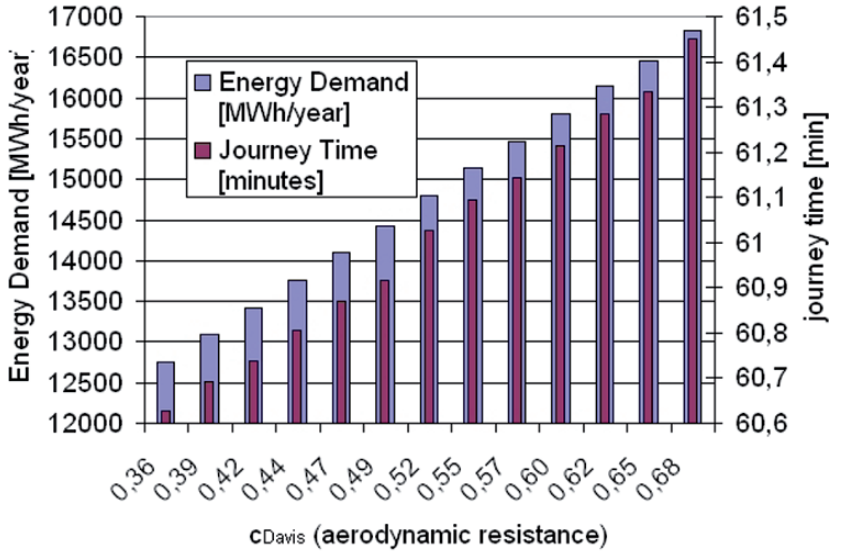

Fig. 9 Impact of the aerodynamic drag on the energy demand and the journey time.

c_D	Traction energy [MWh]	Regenerated energy [MWh]	Total [MWh]	Difference [Mwh]	Difference [%]
130%	25992,414	9163,638	16828,776	2025,4	12,0%
100%	24627,348	9823,95	14803,398	0,0	0,0%
70%	23242,896	10496,304	12746,592	-2056,8	-16,1%

Fig. 10 Impact on the energy demand by varying the aerodynamic drag

4 Potential for Reducing the Energy Demand by Drag Reduction

The potential for reducing the drag depends on the train type and on the vehicle chosen for reference. Nevertheless, the author will try to quantify the potential in terms of percentages of reduction of drag related to present day solutions that can be found on the track. The estimated drag reduction potential for a regional train is shown in Fig. 11. The biggest potential for improvements can be achieved by an optimisation of the head and the tail of the train. The tail drag can be reduced by reducing the longitudinal vortices which are produced at the tail of a regional train and by introducing a boat tailing shape in order to recover the pressure to certain extend. The longitudinal vortices can be reduced by either forcing a separation near to the position where they are produced (spoiler) or by keeping the pressure gradient in the circumferential direction as low as possible which can be achieved by a proper front shape. The potential to reduce the overall drag of a regional train is estimated to be around 20-25 %. This drag reduction would lead to an energy reduction of about 6-8 %. This in turn would lead to an energy saving of about 200 MWh/year and train. The assumption is that this train is running 17 hours per day on 360 days per year.

In terms of high-speed trains (see Fig. 12) the potential for improvement is not as big as for regional trains due to the fact that this type of trains has already received much attention from the aerodynamic community. Nevertheless, the highest potential is seen to be the head and tail and a proper design of the bogie cutout in conjunction with bogie fairings [6]. The potential for a reduction of the aerodynamic drag of a high-speed train is estimated to be around 14 %. This would lead to energy demand reduction of about 6-8 %. Thus, the potential to reduce the energy demand by improving the aerodynamics performance is the same for high-speed trains as for regional trains.

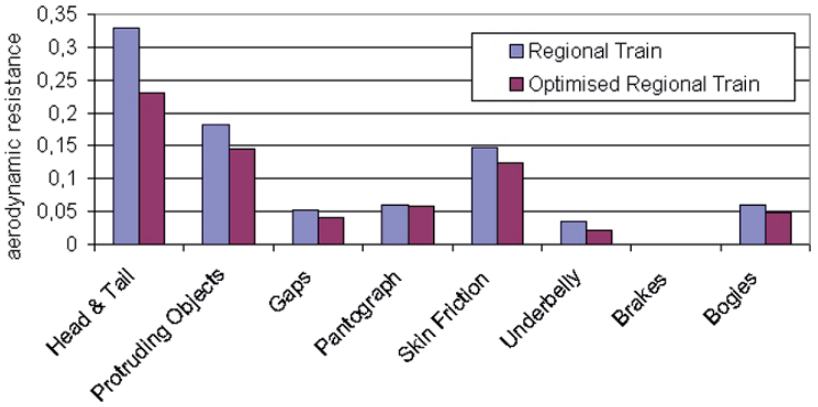

Fig. 11 Estimated potential for reducing the drag of a regional train

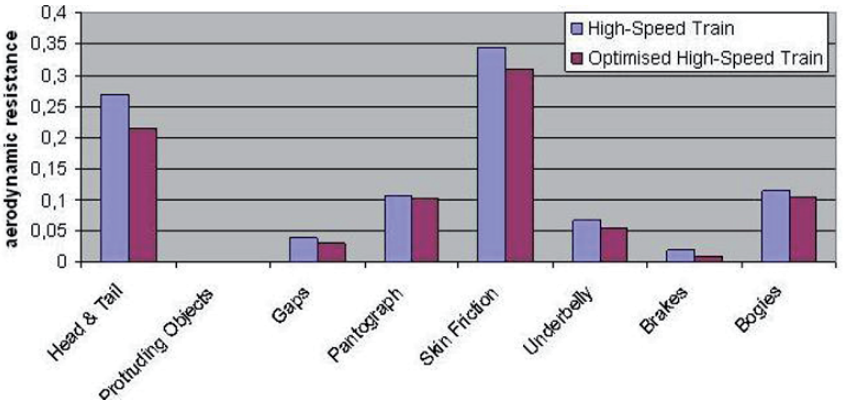

Fig. 12 Estimated potential for reducing the drag of a high-speed train

5 Conclusions

The present study shows that when it comes to energy reduction it is first important to know the distribution of the losses of the various components in order to focus the attention to the dominant losses. Secondly, it is important to define an operational cycle and proper boundary conditions in order to be able to simulate the effect of implementing technical measures on the averaged energy demand during a typical operational cycle. This study shows that a considerable amount of energy is being dissipated to heat and therefore lost due to the aerodynamic resistance of a train. Additionally, this study shows that aerodynamic drag is not only

important for high-speed train applications but that the reduction of aerodynamic drag is equally important for regional train applications. This is due to the fact that the potential for reducing the drag of a present day high-speed train is considerably lower then the potential of a reducing the aerodynamic drag of a present day regional train.

References

[1] H.D. Baehr, S. Kabelac, *Thermodynamik, Grundlagen und technische Anwendungen,* 13th ed. (Springer Verlag, 2006)

[2] Davis, W.L.: General Electric Review (1926) 3. T. Schill, *Rechnerbasierte Fahrwiderstandsprognose von Schienenfahrzeugen*, Student thesis (TU Berlin and Bombardier, 2004) 4. European Norm, EN 14067-4 Railway Applications. Aerodynamics. Requirements and test procedures for aerodynamics in open track, 2005 5. Peters, J.L.: Windkanaluntersuchungen zum Widerstandsverbesserungspotential von konstruktiv abgesicherten Drehgestellsch¨urzen und Dachgeräteverkleidungen am ICE

[3] Technical report, (Krauss Maffei Verkehrstechnik. August 1996) 6. Peters, J.L.: Aerodynamics of very high-speed trains and maglev vehicles: State of the art and future potential. Int. J. of vehicle design. Special Publication SP3, 308–341

[4] European Norm, EN 14067-4 Railway Applications. Aerodynamics. Requirements and test procedures for aerodynamics in open track, 2005

[5] Peters, J.L.: Windkanaluntersuchungen zum Widerstandsverbesserungspotential von konstruktiv abgesicherten Drehgestellschürzen und Dachgeräteverkleidungen am ICE 3. Technical report, (Krauss Maffei Verkehrstechnik. August 1996)

[6] Peters, J.L.: Aerodynamics of very high-speed trains and maglev vehicles: State of the art and future potential. Int. J. of vehicle design. Special Publication SP3, 308–341 (1983)

The use of Aeronautical Experimental Facilities and Measurement Techniques for the Aerodynamic Investigation of High Speed Trains

Andreas Dillmann

German Aerospace Center (DLR), Germany
andreas.dillmann@dlr.de

Abstract The development of future high speed trains is driven by commercial and ecological requirements which determine the increase of speed and payload while reducing weight and improving thermal and acoustical passenger comfort. To ensure the same level of safeness then for today's rolling stock, additional issues like Reynolds-Number and Mach-Number dependencies have to be explored. The influence of unsteady flow phenomena as well as the impact of the train's induced flow field on humans and infrastructure has to be investigated. For this purpose, special experimental facilities and techniques originally developed for aeronautical research proved to be extremely useful. For the investigation of viscous flow effects like separation and other boundary layer phenomena, a pressurized wind tunnel can realize high Reynolds numbers without entering the compressible flow regime. Validated results for the Göttingen high pressure wind tunnel show that it is possible to use extremely small models, down to a scale of 1:100, and to get good results if the accuracy of the model manufacturing process is high enough. A second possibility to increase the Reynolds number in a wind tunnel is to cool down the working fluid, thus increasing the Reynolds number up to a factor of 5.5. The main advantage of cryogenic wind tunnels is the possibility of independent adjustment of the Mach and Reynolds number. A third possibility to increase the Reynolds number is to change the working fluid of the facility, e.g. by using water instead of air. Advanced measurement techniques, which were originally developed for aeronautical research, allow a deep insight into the physical mechanisms governing the aerodynamic performance of high speed trains. A broad variety of experimental results is presented, showing that high Reynolds number facilities are in many cases an indispensable research tool for the aerodynamics of railroad vehicles.

Reduction of Skin-Friction Drag on a Generic Train Configuration

Sigfried Loose

German Aerospace Center (DLR), Germany
sigfried.loose@dlr.de

Abstract Wind-tunnel experiments were carried out to determine the drag-reduction potential of dimpled surfaces on a generic train model as well as the influence of the dimpled surface on the flow field. Forces and moments were measured with an external six component balance. The flow field investigation was done by use of particle image velocimetry (PIV). The measurements were executed over a wide range of Reynolds numbers in a cryogenic wind tunnel. The use of this wind tunnel allows the variation of Reynolds number while the Mach number remains constant and vice versa. The experiments were undertaken with a standard set up i.e.: the models consist of a complete end car and half mid car (Model scale 1:20); a fresh boundary layer on the ground realized by splitter plate; no force closure between mid car and end car. Two similar models were investigated. The first model was manufactured with a smooth, polished surface. The second model was similar to the first but with a dimpled surface. The dimples were circularly shaped and arranged in a certain pattern. The results of force measurements show for some configuration, depending on the Reynolds number, an overall drag reduction of more than 20%. In consideration of the fact that the total drag of the investigated configurations is mainly determined by friction drag this drag reduction can only come from a decrease of skin friction drag. To ensure that this interpretation is correct, pressure measurements were done in the intercarriage gap for all configurations. The influence of the dimpled surface on the flow field is directly visible at the leeward vortex system, which is resulting from the flow under yaw angles. All characteristic values of the vortex become weaker than for the non dimpled configuration.

Head Pressure Effects of Trains and Locomotives – Engineering Calculation Approaches for Homologation Purpose

Arnd Rueter

Siemens AG, Transportation Systems, Germany
arnd.rueter@siemens.com

Abstract The head pressure pulse and the head pressure drop of a train are the pressure signals measured during the passage of the first few meters of the train at a fixed position in open air or in a tunnel, respectively. Train pressure pulses are part of the pressure loading on objects (like other trains) and persons. A new train is admitted to operation if measured data statistically satisfies certain threshold values. Nowadays train homologation in Europe predominantly relies on measurements, yet appropriate prediction tools are needed during the engineering process. The described pressure effects are well reported in literature and calculation methods are available providing for adequate accuracy. The methods are reviewed, examples from engineering applications and comparisons to data from full scale measurements are presented. The prevalent flow features are discussed covering a typical range of vehicle shapes and operational conditions (regional to high speed). The use of CFD methods is evaluated. The modeling error is estimated and error mitigation is attempted. A virtual homologation approach is proposed. The open fields of the issue are outlined.

Numerical Analysis for Aerodynamics of High-Speed Trains Passing Tunnels

Jing Zhao, Renxian Li

National Key Laboratory of Traction Power, Southwest Jiaotong University, China
zhaojing_555@sina.com

Abstract High-speed trains running at 200~350km/h will be operated on Chinese high-speed railways after 2010. Some of the high-speed railways in China will be built in mountainous areas. Many tunnels have to be constructed for the railways. However, the tunnel aerodynamic effect of high-speed trains is not very clear, especially the aerodynamic influence when the train is running in or out of tunnels. Examples are the effect of air pressure impulse on the train window strength and on the ear films of passengers, the relationship between the tunnel section size and the aerodynamic force acted on the train body, the relationship between the buffer structure of the tunnel entrance and the intensity of air pressure impulse, and so on. Based on Reynolds average Navier-Storkes equations of viscous incompressible fluid, and on two equation turbulent models, the aerodynamic effect of high-speed train in tunnels was investigated by means of the technology of moving grids in computational fluid dynamics method. Flow fields of high-speed train for 4 running speeds (200, 250, 300, 350km/h), 3 sizes of tunnel sections and 2 kinds of buffer structures for tunnel entrance were calculated. The results show that the aerodynamic effect of the tunnel's blockage ratio is larger than that of train's speed when the tunnel section size is smaller than a finite blockage ratio; the buffer structure for a tunnel entrance may reduce the aerodynamic influence effectively. Based on the simulation results of the investigation, some suggestion values between tunnel blocking ratio and train running speed were presented.

Poster Session

A Study of the Influence of Aerodynamic Forces on a Human Body near a High-Speed Train

Renxian Li, Jing Zhao and Shu Zhang

School of Mechanical Engineering, Southwest Jiaotong University, Chengdu, P. R. China
rxli@swjtu.edu.cn

Abstract A study of the influence of aerodynamic force on human body near the high-speed train was completed by the means of the technology of moving grids in computational fluid dynamics method. 60 running situations, which includes 3 types of locomotive shape, 4 running speeds of train combining 5 distances from human body to the sidewall of the train (human-train distances), were simulated. The 4 running speeds are 200km/h, 250km/h, 300km/h and 350km/h. The 5 human-train distances are 1.0m, 1.5m, 2.0m, 2.5m and 3.5m. The study results show that the aerodynamic force acting on human body strongly affected by the shape of the passing train head. The aerodynamic force produced at 1.0m human-train distance by extremely blunt train head at 350km/h speed is 7 times more than that produced by a streamline train head at the same operating condition. With an increase of human-train distance, the differences among the aerodynamic forces produced by the different shape of train head decreases. The decrease is about a quadratic function of the human-train distance, and has nothing to do with train speed. The ratio of the maximum aerodynamic force produced by train head and that produced by train tail at a given human-train distance is about a constant and independent of train speed. The ratio of the maximum aerodynamic forces for any two different human-train distances produced by train head or train tail is about a constant and has nothing to do with train speed. The direction of the aerodynamic force acting on the human body is nearly the same in different running conditions independent of train head/tail shape. The direction of the aerodynamic force changes over 300 degrees when train head or train tail passes. Based on the calculation results, formulas for calculating the aerodynamic force acting on the human body and the maximum wind speed near the human body were presented. Safety distances for people walking or working near passing train were recommended.

1 Introduction

The operation of high-speed trains in the world provides a convenient, quick, safe and cheap way to travel for ordinary people in the high population density area. Since the first high-speed train was operated successfully in Japan in *1960s*, the high–speed trains of *200km/h* or faster have operated in Germany, France, Italy, United Kingdom and Sweden. The technology improvements in railway construction and railway vehicle manufacture make possible very high running speeds. In tests, the running speed of the French train *TGV* reaches *574km/h* while its operation speed is over *300km/h*. For the German high-speed train *ICE*, its test running speed is *406.9km/h* and its operating speed is over *250km/h*. Right now, there are many high-speed railways under construction in China and trains with running speeds over *200km/h* will be operated in the near future. According to the railway development program, about *12000* kilometers of high-speed railway will be built in the coming *15* years in China.

Many aerodynamic problems will be produced by the operation of high-speed trains, however. Some unfavorable influences on trains will emerge due to interaction of running train and surrounding air, such as aerodynamic drag and aerodynamic pressure waves acting on the train body caused by surrounding buildings. Many experimental and simulation studies have been done in this area[1~7]. There will also be adverse effects on the surrounding environment and persons near the railway due to induced air flow caused by passing trains. Most importantly, the air flow induced by high-speed trains (train wind) may impose some safety issues on people near high-speed railways.

Generally speaking, the strength of train wind will decrease with the distance increase between human body and trains, but what constitutes a safe distance for people to walk or work near high-speed railway? The standard of safety distance is different in different countries for high-speed trains. The average train wind velocity near the human body is used as a criterion to determine the safety distance in United Kingdom and Japan[8]. *9m/s* train wind velocity is used to determine platform safety distance in Japan. In the United Kingdom *25mph(≈11.1m/s)* train wind velocity is used to determine the platform safety distance and *38mph(≈16.9m/s)* train wind velocity is used to determine the safety distance for railway employees. Aerodynamic force is used as a criterion to decide the safety distance in Germany and in France[9]. The safety distance is defined as that for which a *100N* maximum allowed aerodynamic force acts on a human body. In the USA, the aerodynamic pressure acting on the ear drum (*0.2psi*) or train wind velocity about Beaufort number *7* is used to decide the safety distance.

In China, there is no corresponding standard for safety distance yet. Despite that it is a task of human safety engineering to draft the safety distance standard; it is an important prerequisite to understand the patterns of the aerodynamic forces acting on the human body as a function of train speed and distance between train and human before setting the standard.

The aerodynamic effect of train wind on the human body and surroundings is produced by the relative motion between the train, the air, and the surrounding objects. It is difficult to model this kind of flow field in wind tunnel because of the relative motion between the train and its surroundings. Real measurement around operating trains have been performed using instrumented human models by scientists of Japan, France and China[11~13]. These experiments were expensive and had many limitations, such as the condition of railways, maintaining the train velocity through the measurement point, the operation condition of test line and so on. Moreover, the measurement results exhibited dispersion in the survey data. Therefore, it is quite difficult to get accurate aerodynamic influence data using field measurements. Simulation by means of computational fluid dynamics is another method to study the vehicle aerodynamic problems. It has no limitation for train operating condition; it is convenient to compare the aerodynamic influence for different operating conditions and is less expensive than field experiments.

There are still some difficulties to simulating a flow field around bodies in relative motion. In early attempts, researchers first computed the wind field data near the train head using various CFD methods, and then estimated the force acting on a human body based on distribution of fluid velocity and pressure. Nevertheless, presence of the human body has an effect on the distribution of velocity and pressure of the train flow field. The moving train and human bodies should be simulated simultaneously and the relative motion between the train and human bodies should be simulated. In this paper, aerodynamic influence acting on human body near high-speed train was studied based on the moving mesh simulation method in CFD.

2 Methodology

2.1 Basic hypothesis

(1) Because Reynolds number of flow field around the high-speed train is larger than 10^6 due to the train running at high speed, the fluid is in turbulent state. The $k \sim \varepsilon$ two equation turbulent model has been used in the simulations.
(2) Train speed ranges *200~350km/h* in this study, and the flow velocity of induced air around the train is less than Mach *0.3*, so the flow is assumed to be incompressible.
(3) Some detail structures on vehicle body have been ignored to simplify the calculations, (e.g. pantograph, bogies, link section of carriages and the like).
(4) Shape of human body is too complicated to simulate. Some cylindrical bodies were used to model human bodies in this project following previous re-

search[14~16]. Height and diameter of the cylindrical body is set to *1.75m* and *0.45m* respectively. If these two size express height and shoulder width of human body, this cylindrical body simulates *90%* of Chinese adults.

2.2 Mathematical model

Based on Reynolds average Navier-Stokes equations of viscous incompressible fluid and *k*~ε two equations turbulent model, the flow field around train can be described as

$$u_{j,j} = 0 \tag{1}$$

$$\rho u_{j,t} + \rho u_j u_{i,j} = -p_{,i} + (\mu + \mu_t)(u_{i.jj} + u_{j,ij}) \tag{2}$$

$$\rho k_{,t} + \rho u_j k_{,j} = (\mu + \frac{\mu_t}{\sigma_k}) k_{,jj} + \mu_t G_k - \rho\varepsilon \tag{3}$$

$$\rho\varepsilon_{,t} + \rho u_j \varepsilon_{,j} = (\mu + \frac{\mu_t}{\sigma_\varepsilon})\varepsilon_{,jj} + c_1 \frac{\varepsilon}{k}\mu_t G_k - \rho c_2 \frac{\varepsilon^2}{k} \tag{4}$$

Where

$$G_k = (u_{i,j})^2 + u_{i,j}u_{j,i}\ , \qquad \mu_t = \rho c_\mu \frac{k^2}{\varepsilon}$$

u_j —— Velocity component of flow field (m/s);

p —— Pressure (Pa);

μ —— Dynamic viscosity coefficient (N·s/m^2);

ρ —— Density (kg/m^3);

μ_t —— Turbulent viscosity coefficient (N·s/m^2);

□ —— Turbulent kinetic energy (J/kg);

ε —— Dissipation rate of turbulent kinetic energy (J/kg);

$C_1, C_2, C_\mu, \sigma_k, \sigma_\varepsilon$ —— Constants，as *1.44, 1.92, 0.09, 1.0, 1.3*

The equations (1) to (4) were solved by finite volume method[18, 19].

2.3 Geometric model

The train is modeled as a *60m* long vehicle with same shape at the head and tail. Three cylindrical bodies, to model the human body, were put on one side of the train at the head and tail respectively. Three types of train head/tail shapes were modeled. Model 1 is a streamline head/tail shape; with a head/tail length of *8m*.

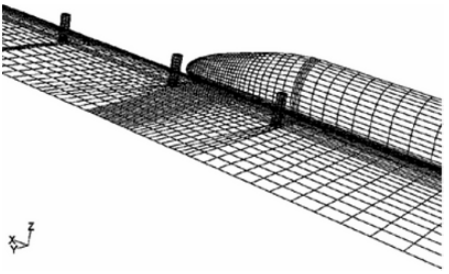

Fig. 1 A part of calculation mesh for model 1

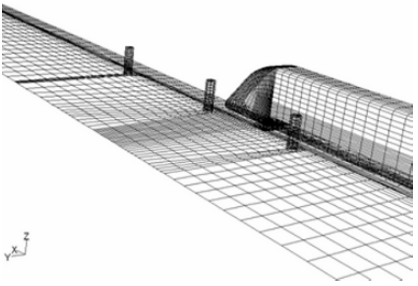

Fig. 2 A part of calculation mesh for model 2

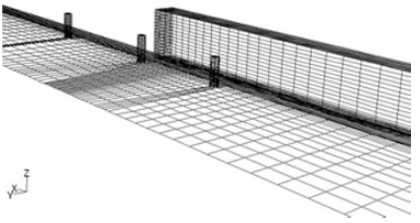

Fig. 3 A part of calculation mesh for model 3

Model 2 is a train with a fairly blunt head, with head/tail length of *3.9m*. Model 3 is an extremely blunt head train model having a length of *0m*. A part of the three train models calculation mesh is shown in Figs. 1 to 3 respectively. Length, width and height of the three train models were exact the same and are summarized below:

	Train length (*l*)	Train width *(b)*	Train height (*h*)	Length of changeable section at head/tail (*s*)
Model 1	60m	3.1m	3.7m	8.0m
Model 2	60m	3.1m	3.7m	3.9m
Model 3	60m	3.1m	3.7m	0.0m

3 Numerical calculation and result analysis

3.1 Calculation cases

In order to study the aerodynamic forces acting on a person near a high-speed railway, computational simulations of *4* train running speeds (*200km/h, 250km/h, 300km/h, and 350km/h*) and *5* human-train distances (*1.0m, 1.5m, 2.0m, 2.5m, and 3.5m*) were performed. 20 calculation cases were simulated for each train model for a total of cases simulated for the three train models. The effective moving distance of train relative to one cylindrical body was *33.75m* in each of the simulations. Mesh moving distance for each time step was *0.125m*. This means that *270* effective time steps were performed in each calculation case.

3.2 Simulation result analysis

3.2.1 Analysis of aerodynamic force acting on human body with different train shapes

Calculation result shown that there is a big effect for aerodynamic force acting on human body due to train wind produced by different train head/tail. Change tendency of aerodynamic force in horizontal direction produced by 3 model train head at *1.5m* human-train distance are shown in Figs. 4 to 6

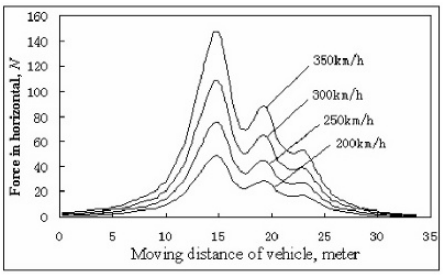

Fig. 4 Aerodynamic force acting on human body as train model 1 head passes

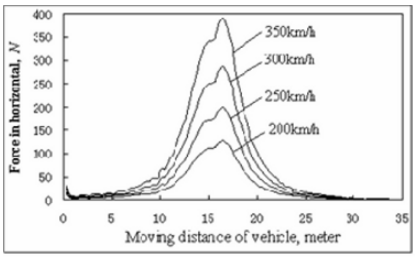

Fig.5 Aerodynamic force acting on human body as train model 2 head passes

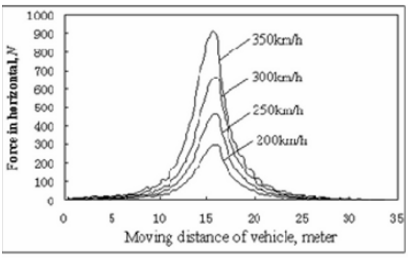

Fig.6 Aerodynamic force acting on human body as train model 3 head passes

Figures 4~6 show that, for the aerodynamic force acting on a human body produced by different train head shapes, not only there are big differences in value, but also there is a difference in the time over which the force acts. Comparing the change of aerodynamic force with different train head shapes, we find that the blunter the train head shape is, the larger the aerodynamic force acting on human body, and the shorter the acting time of the force. When different shapes of train tail pass, change in aerodynamic force is similar to the changes as train head passes. Figure 7~9 shown the change tendency of aerodynamic force produced by train tail of the 3 models at *2.5m* human-train distance.

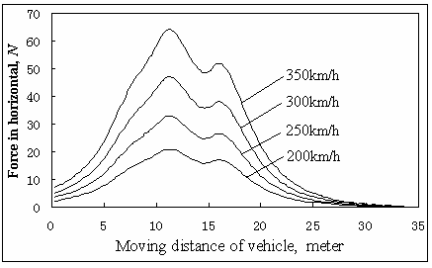

Fig. 7 Aerodynamic force acting on human body as train model 1 tail passes

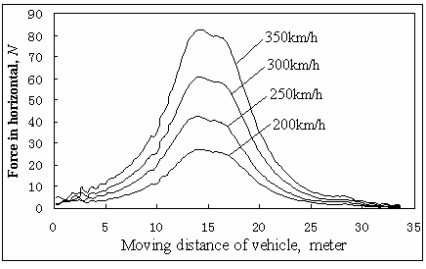

Fig.8 Aerodynamic force acting on human body as train model 2 tail passes

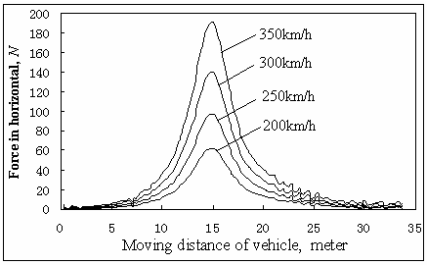

Fig.9 Aerodynamic force acting on human body as train model 3 tail passes

The maximum aerodynamic force acting on human body in all cases for the three models are listed in table 1. Keeping the train running speed and human-train distance constant, a ratio of the maximum aerodynamic force F_T produced by train-head wind and that F_W produced by train-tail wind are also listed in Table 1. The ratios of maximum forces produced by train head and by train tail in different human-train distances for each train model are listed in Table 2. Where $F_{T1.0m}$

means the maximum aerodynamic force produced by train-head wind at *1.0m* human-train distance. $F_{W1.0m}$ means that the maximum aerodynamic force produced by train-tail wind at the same distance. The others have similar meaning.

Table 1 The maximum aerodynamic force produced by train head/tail and their ratio

The maximum aerodynamic force and their ratio of train model 1												
v / d	200km/h			250km/h			300km/h			350km/h		
	F_T	F_{W0}	F_T/F_{W0}	F_T	F_{W0}	F_T/F_{W0}	F_T	F_{W0}	F_T/F_{W0}	F_T	F_{W0}	F_T/F_{W0}
1.0m	68.4	60.3	1.13	107.0	94.1	1.14	153.7	135.5	1.13	209.1	184.4	1.13
1.5m	48.3	38.2	1.26	75.5	59.6	1.27	108.7	85.8	1.27	147.9	116.8	1.27
2.0m	33.5	27.7	1.21	52.3	43.3	1.21	75.3	62.3	1.21	102.4	84.7	1.21
2.5m	24.4	21.0	1.16	38.1	32.8	1.16	54.9	47.2	1.16	74.6	64.2	1.16
3.5m	14.36	13.16	1.09	22.47	20.55	1.09	32.32	29.60	1.09	44.03	40.29	1.09
The maximum aerodynamic force and their ratio of train model 2												
1.0m	229.8	102.8	2.24	359.3	160.7	2.24	517.7	231.4	2.24	705.8	315.4	2.24
1.5m	127.2	61.3	2.07	198.9	96.2	2.07	286.5	138.8	2.06	390.5	189.6	2.06
2.0m	78.8	36.2	2.18	123.1	56.4	2.18	177.4	81.3	2.18	241.8	110.7	2.18
2.5m	53.1	27.0	1.97	83.0	42.2	1.97	119.5	60.7	1.97	160.7	82.7	1.94
3.5m	28.1	16.8	1.67	43.9	26.1	1.68	63.2	37.8	1.67	85.0	51.1	1.67
The maximum aerodynamic force and their ratio of train model 3												
1.0m	503.4	158.9	3.16	786.5	248.1	3.17	1132.	357.0	3.17	1533.0	483.8	3.17
1.5m	295.0	149.9	1.97	460.7	234.1	1.97	663.3	337.0	1.97	902.4	459.0	1.97
2.0m	180.3	94.6	1.91	281.1	147.7	1.90	404.7	212.6	1.90	551.9	289.2	1.91
2.5m	114.0	62.4	1.83	178.1	97.5	1.83	256.4	140.3	1.83	349.4	190.9	1.83
3.5m	63.9	34.0	1.88	99.8	53.2	1.88	143.7	76.5	1.88	195.8	104.0	1.88

Note: v – train running speed, d – human-train distance

Table 2 Ratio of the maximum forces in different human-train distances for three models

	Model 1, train head				Model 2, train head				Model 3, train head			
v / ratio	200 km/h	250 km/h	300 km/h	350 km/h	200 km/h	250 km/h	300 km/h	350 km/h	200 km/h	250 km/h	300 km/h	350 km/h
$F_{T1.0m}/F_{T1.5m}$	1.42	1.42	1.41	1.41	1.81	1.80	1.81	1.81	1.71	1.71	1.71	1.70
$F_{T1.5m}/F_{T2.0m}$	1.44	1.44	1.44	1.44	1.61	1.62	1.62	1.62	1.64	1.64	1.64	1.64
$F_{T2.0m}/F_{T2.5m}$	1.37	1.37	1.37	1.37	1.48	1.48	1.48	1.48	1.58	1.58	1.58	1.58
$F_{T2.5m}/F_{T3.5m}$	1.70	1.70	1.70	1.69	1.89	1.89	1.89	1.89	1.78	1.78	1.78	1.78
	Model 1, train tail				Model 2, train tail				Model 3, train tail			
$F_{W1.0m}/F_{W1.5m}$	1.58	1.58	1.58	1.58	1.68	1.67	1.67	1.66	1.06	1.06	1.06	1.05
$F_{W1.5m}/F_{W2.0m}$	1.38	1.38	1.38	1.38	1.70	1.70	1.71	1.71	1.58	1.58	1.59	1.59
$F_{W2.0m}/F_{W2.5m}$	1.32	1.32	1.32	1.32	1.34	1.34	1.34	1.34	1.52	1.51	1.52	1.51
$F_{W2.5m}/F_{W3.5m}$	1.60	1.60	1.59	1.59	1.61	1.62	1.61	1.62	1.84	1.83	1.83	1.84

By analyzing Table 1 and 2, we find an interesting phenomenon. The ratio of aerodynamic forces acting on a human body produced by train head wind over that produced by train tail wind at a given human-train distance for each train model is independent of train running speed. This phenomenon means that it is possible to infer a relationship for the force acting on a human body as a function of train running speed, distance from the train, and train head/tail shape.

3.2.2 Analysis of the direction of the aerodynamic force acting on human body

The change of the force direction in the horizontal plane acting on a human body for the different train models is almost the same. The change of the force direction produced by train head wind and by train tail wind in one calculation case for each train model is shown in figure 10 (a) and (b) respectively. From the figures we find that the force direction angles produced by train head wind and that by train tail wind for different train models changed over 300 degree. The force direction angle is the angle from the train running direction anticlockwise rotation to the aero-force direction.

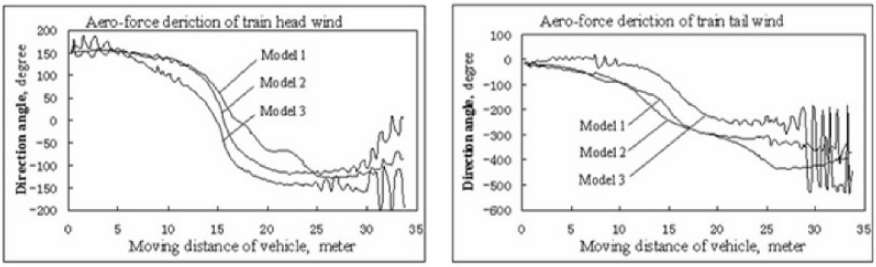

Fig. 10 Aerodynamic force direction change as various shape train head or train tail passes

3.3 Analysis of train wind velocity around human body near high-speed train

The maximum train wind velocity around human body in different calculation cases for train models 1, 2 and 3 are shown in Figs. 11-13 respectively. The wind velocity at human-train distance 0m is assumed to be equal to the train running speed. After summarizing all simulation results in 20 calculation cases for each train model, we find that the maximum wind velocity around human body is about a quadratic function of human–train distance when train running speed is held constant and the maximum wind velocity is about a linear function of train running speed when human-train distance is kept constant. According to these conclusions, we infer a relationship formula for the maximum wind velocity u around human body with train speed v and human-train distance d for each train model.

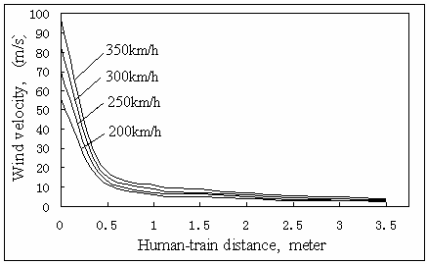

Fig. 11 Change of train wind velocity for model 1

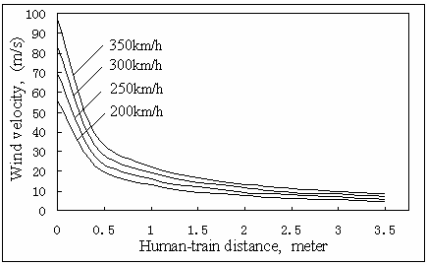

Fig.12 Change of train wind velocity for model 2

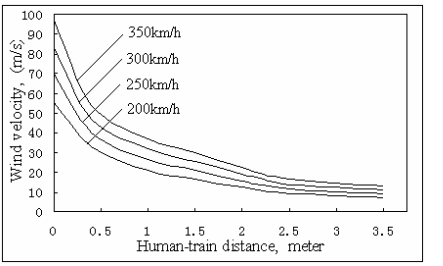

Fig. 13 Change of train wind velocity for model 3

Which are

$$u_{m1} = (1.2319)^{0.072v-4} \times (0.4575d^2 - 3.5496d + 9.1545) \quad (5)$$

$$u_{m2} = (1.1912)^{0.072v-4} \times (1.2549d^2 - 8.8644d + 20.7939) \quad (6)$$

$$u_{m3} = (1.2454)^{0.072v-4} \times (2.1907d^2 - 15.4286d + 34.2111) \quad (7)$$

where u_{mi} —— the maximum wind velocity around human body near model i *(m/s)*;

d —— human-train distance *(m)*;

v —— train running speed *(m/s)*;

$m1, m2, m3$ —— means model 1, model 2 and model 3 respectively.

Application range of the formulae (5) - (7) are $55.56 < v < 97.22 m/s$ and $1.0 < d < 3.5m$. The dimension of *m/s* used here for train running speed *v*. For reference, *55.56m/s* is equivalent to *200km/h* and *97.22m/s* is equivalent to *350km/h*. If the calculated train wind velocities are assumed to be correct values, the curve-fitting errors from formulae (5), (6) and (7) are less than 5%. For relationships between the train wind velocity and train head/tail shape, we were unable to infer accurate formulae from the current computational results.

4 Relationship among train wind force, train speed, human-train distance and train head/tail shapes

The aerodynamic force acting on human body produced by train wind is related to many factors, such as train running speed, human-train distance, train head/tail shapes, smoothness of train surface, relative height between human and train, temperature and moisture of ambient air and so on. But the main factors are three: train running speed, human-train distance and train head/tail shape. Of these three main factors, the train head/tail shape is the most complicated to describe. There are many geometric parameters to describe train head/tail shape even if

height and width of the train are kept constant. In order to simplify the analysis, we use only one geometric parameter, length of changeable section at train head/tail *S*, to describe the shape variation of train head/tail here. Thereupon, the aerodynamic force *F* acting on human body produced by train wind is a function of human-train distance *d*, train running speed *v* and the length of changeable section at the train head/tail, *S*. Based on the summary of the simulation results on maximum aerodynamic force in 60 calculation cases, include 3 train models, 4 train running speeds and 5 human-train distances, we infer the following relationship:

$$F_d = \alpha^{0.072v-4} \times (A \times S^2 - B \times S + C)$$
$$55.56 \le v \le 97.22 m/s, \quad 0 \le S \le 8m \tag{8}$$

where F —— human body aero-force produced by train wind in horizontal (*N*);

d —— human-train distance（*m*）;

v —— train running speed（*m/s*）;

S —— length of changeable section at train head/tail（*m*）;

α, A, B, C —— coefficients。

The human-train distance *d* as a subscript in formula (8) means that we use separate formula to describe the aerodynamic force for different human-train distance. The purpose is to guarantee precision of the formulae. The formulae for the aerodynamic force at each human-train distance as a function of train running speed and length of changeable section at train head/tail are:

$$F_{1.0} = (1.369)^{0.072v-4} \times (4.559S^2 - 95.7655S + 567.82) \tag{9}$$

$$F_{1.5} = (1.451)^{0.072v-4} \times (3.071S^2 - 56.526S + 305.735) \tag{10}$$

$$F_{2.0} = (1.452)^{0.072v-4} \times (1.927S^2 - 34.403S + 186.53) \tag{11}$$

$$F_{2.5} = (1.462)^{0.072v-4} \times (1.112S^2 - 20.389S + 116.896) \tag{12}$$

$$F_{3.5} = (1.487)^{0.072v-4} \times (0.775S^2 - 12.392S + 63.901) \tag{13}$$

If the computed aerodynamic forces are assumed to be correct values, formulae (9)-(13) have errors less than 5%. Formula (9) is accurate to 5% except for some points where the errors are as large as 10%. If allow the errors of the inferred formulae to be somewhat larger, it is possible to integrate formulae (9) ~ (13) to a single formula for calculating the human aerodynamic force. That is:

$$F = (1.656)^{2(3.5-d)} \times (1.4442)^{0.072v-4} \times (0.6863S^2 - 12.5392S + 69.064) \tag{14}$$

If the human aerodynamic force is calculated by formula (14), except for calculation error large than 20% in a few case points of train model 1, the calculation errors from formula (14) are less than 15%.

5 Conclusions and Suggestions

5.1 Conclusions

Based on Reynolds average Navier-Stokes equations of viscous incompressible fluid, and on $k \sim \varepsilon$ two equations turbulent model, the aerodynamic effects of train wind on human body near high-speed railway were investigated by finite volume method with moving mesh technology. From the numerical results of 60 calculation cases, the following findings can be gained:

(1) There is a big difference in the aerodynamic force acting on human body produced by different shapes of train head/tail. In running speed at *350km/h* and human-train distance of *1m*, the aerodynamic force produce by extremely blunt train head is 7 times more than that produced by a highly streamlined train head. The difference in the force decreases with the increase of human-train distance. The decrease pattern of the force difference is about a quadratic function with the distance and is independent of train running speed.

(2) For a single type of train head at a fixed human-train distance, the ratio of the maximum aerodynamic force produced by the train head over that produced by the train tail is nearly a constant and has nothing to do with train running speed. The ratio of the maximum aerodynamic forces produced by train head from different human-train distance is about a constant regardless of train running speed. The same situation appears around train tail.

(3) According to the conclusions mentioned above, formulae for calculating the aerodynamic force acting on human body produced by train wind may be inferred from the numerical results, listed in formulae (9) - (13). If the calculation precision of the formulae is reduced, it is possible to integrate formulae (9) - (13) into a unified formula for calculating the human aerodynamic force, which is given in formula (14).

(4) The change of the force direction acting on a human body in the horizontal plane in different calculation cases for each train model is almost the same. The change tendency of the force direction for different train models appears a similar type. The force direction angles produced by train head wind and that by train tail wind for different train models changed over 300 degree.

(5) In the numerical calculation range, the maximum wind velocity around human body is about a quadratic function of human–train distance for a given train running speed. The maximum wind velocity is about a linear function of train running speed when human-train distance is kept constant.

(6) According to conclusion (5), the maximum wind velocity u around human body as a function of train speed v and human-train distance d for each train model can be inferred, and are presented in formulae (5) - (7).

5.2 Suggestion of human safety distance

There are many shapes of heads/tails for high-speed trains in the world. The length of changeable section of these high-speed train head/tail is different each other. For example, the length for *E* system high-speed train head in Japan is more than *6m*, the head length of *TGV* in France is *5~7m*, *ICE* in Germany is *3~5m*, while for Chinese high speed trains it ranges from 2.7~*5.3m*. According to formulae (9) - (13), we can approximate the aerodynamic force acting on human body in the different train running speed based on the different head length. If the maximum aerodynamic force that a human can bear could be decided, the human safety distance could be obtained from these formulae. Based on *100N* aerodynamic force as human body bearing force, the safety distances for different train head lengths and different train running speeds are listed in Table 3.

Table 3 Suggestion of human safety distance based on *100N* criterion (*m*)

S(m) / *v(km/h)*	1	2	3	4	5	6	7	8
200	2.48	2.28	2.10	1.79	1.50	1.32	1.01	0.7*
250	3.16	2.82	2.46	2.21	1.92	1.54	1.39	1.09
300	3.7*	3.42	3.11	2.62	2.39	2.14	1.82	1.58
350	4.1*	3.9*	3.6*	3.35	3.03	2.66	2.34	2.11

Note: The data with * is estimate value from of the formula by extrapolation

The maximum wind velocity around a human body near a high-speed train for different train running speeds and human-train distances can also be obtained from formulae (5) - (7). Based on these formulae, it is possible to get the wind velocity around human body for different train head lengths. If the maximum wind velocity that a human can stand could be decided, the human safety distance can be obtained from the formulae. Based on *11m/s* velocity as human body limit, the safety distances for different train head lengths at different train running speeds are listed in Table 4.

Table 4 Suggestion of human safety distance based on *11m/s* criterion (*m*)

S(m) / *v(km/h)*	1	2	3	4	5	6	7	8
200	1.99	1.79	1.69	1.37	1.16	0.96*	0.75*	0.55*
250	2.46	2.24	1.97	1.72	1.46	1.21	0.96*	0.70*
300	3.12	2.76	2.41	2.07	1.75	1.45	1.15	0.85*
350	3.54*	3.17	2.81	2.46	2.11	1.77	1.42	1.07

Note: The data with * is estimate value from of the formula by extrapolation

From Tables 3 and 4 we can find that the safety distances calculated based on *11m/s* as criterion (United Kingdom) is less than that based on *100N* as criterion (Germany, France). If 9m/s is used as a criterion (Japan), we can get the fairly similar results.

Acknowledgments

Funding from doctoral education base (No. 20040613010) and from innovation engineering for university (No.705044) of Chinese Education Ministry is gratefully acknowledged. The thanks also give to funding of outstanding young scientist (No. 50525518) of China from NSFC.

References

1. Gawthorpe R G, Aerodynamics of trains in the open air [J] Railway Engineering International, 1978, 3: 7~12
2. Brockie N J W, Baker C J, Aerodynamic drag of high-speed trains [J] Journal of Wind Engineering and Industry Aerodynamics 1990, 34: 273-290.
3. Robert A M, Samuel H, Harvey S L, Measurement of aerodynamic pressures produced by passing trains [C] Proceedings of the 2002 ASME/IEEE joint rail conference, Washington DC, 2002, Apr.: 57~64
4. Samuel H, Martin S, High-speed passenger and intercity trains aerodynamic computer model [C] Proceedings of the 2000 international mechanical engineering congress & exposition, Orlando, Florida, 2000, Nov. 83~91
5. Joseph A S, Aerodynamics of high-speed trains [J] Annual review of fluid mechanics, 2001, 33: 371~414
6. Ben D, Mats B, Siniša K, Large eddy simulation of a typical European high-speed train inside tunnels [C] 2004 SAE world congress, SAE Paper 2004-01-0229, Detroit USA
7. Federal Railroad Administration of USA, Aerodynamic effects of high-speed trains [R] RR03-07, 2003, 7: 1~6
8. Federal Railroad Administration of USA, Aerodynamic effects of high-speed trains on people and property at stations in the Northeast Corridor [R] ORD-99/12, 1999, 12: 65~68
9. Federal Railroad Administration of USA, Assessment potential aerodynamic effects on personnel and equipment in proximity to high-speed train operations [R] DOT/FRA/ORD-99/11, 1999, 12: 25~32
10. Tezduyar T E, Finite Element Methods for Flow Problems with Moving Boundaries and Interfaces [J] Archives of Computational Methods in Engineering, 2001, 8: 83-13

11. Horie Toku, Hotoai Sokunan, Train Wind Surveying on Gongqi Test Railway Under the Nature Wind Condition, [R] Report of railway research, No. 1281, Tokyo, Railway society of Japan, 1983，10：29-33.
12. Houxiong Wang, Dezhao He, Heshou Xu, Aerodynamic characteristics of human body acted by train wind [C] Proceeding of the forth conferences on wind engineering and industrial aerodynamics of China, 1994，11：375~380
13. Montagne M S, Mesure du souffle provoque par le passage de la rame TGV 001 a grande vitesse, [C] Informations Techniques – SNCF-Equipment, Paris (1973), Nr, 12：60~62
14. Bo Lei, A study of high-speed train induced air flow and train passing pressure pulses in the open air [D] PhD dissertation of Southwest Jiaotong University, 1995：69~77 (in Chinese)
15. Neppert H, Sanderson R, Vorbeifahrt und ein- und beidseitigen säulernreihen und mauern sowie tunneleinfahrten [R] MBB-UH-22-73, 1973
16. Yasushi U, Motohiko Y, Aerodynamic force on circular cylinders of finite height [J] Journal of Wind Engineering and Industry Aerodynamic, 1994,51: 249~265
17. Autruffe M, Marty P, Aerodynamische untersuchungen an den schnelltriebzug TGV 001 der tranzösischen staatsbahn, [C] Z Leichtbau Verkehrsfahrz, 1975 Nr. 4: 70~73
18. Versteeg H K, Malalasekera W, An introduction to computational fluid dynamics [M] England, Longman Group Ltd 1995
19. Wenquan Tao，Numerical heat transfer [M] Xi'an Publish house of Xi'an Jiaotong University, 2001 (in Chinese)

Application of CFD to Rail Car and Locomotive Aerodynamics

James C. Paul[1], Richard W. Johnson[1], and Robert G. Yates[2]

[1] Airflow Sciences Corporation, 12190 Hubbard Street, Livonia, MI 48150, USA, jpaul@airflowsciences.com

[2] The Greenbrier Companies, 149 Saddle Oaks Court, Walnut Creek, CA 94596, USA, bob.yates@gbrx.com

Abstract CFD methods have been employed to solve a number of efficiency, safety and operational problems related to the aerodynamics of rail cars and locomotives. This paper reviews three case studies: 1) numerical models were employed to quantify the drag characteristics of two external railcar features; namely, well car side-posts and inter-platform gaps. The effects of various design modifications on train resistance and fuel usage were evaluated. 2) An operational safety issue facing railroad operators is wind-induced tip-over. A study was completed using CFD and wind tunnel tests to develop a database of tip-over tendencies for a variety of car types within the Norfolk Southern fleet. The use of this database in the development of a speed restricting system for the Sandusky Bay Bridge is also discussed. 3) Another safety issue involves the behavior of diesel exhaust plumes in the vicinity of locomotive cabs. Numerical simulations were performed for a variety of locomotives operating under a number of ambient conditions (wind speed, wind direction). The concentration of diesel exhaust at the operator cab window was quantified. Where appropriate, the studies provide information on the correlation of the CFD results with previously collected wind tunnel and field data.

Introduction

Railcar aerodynamic studies are typically undertaken to improve safety and increase fuel efficiency. A number of approaches are available to assist the engineer in developing improved designs, including numerical simulation, laboratory (wind tunnel) methods, and field tests.

Significant advances have been made in the development of 3-D CFD codes, including Reynolds-Averaged Navier-Stokes (RANS), Unsteady Reynolds-Averaged Navier-Stokes (URANS), Large Eddy Simulation (LES), Detached

Eddy Simulation (DES), Direct Numerical Simulation (DNS), spectral methods, vortex methods, and Lattice-Boltzmann methods [1, 2]. All of these have been applied to the evaluation of heavy vehicle aerodynamics [3, 4]. For the three studies presented below, appropriate tools were sought to provide practical engineering solutions within commercial timeframes and budgets. Because of the many configurations to be modeled, computationally-intensive methods such as LES, DES, and DNS could not be accommodated. Two 3-D RANS finite-volume simulation codes were selected: 1) a proprietary code, VISCOUS [5, 6], and 2) a commercial code, FLUENT [7]. The Reynolds stress tensor was addressed using the κ-ε equations [8, 9]. Although this method does not model detailed turbulent structures, it does predict average surface pressures and force differences with sufficient accuracy for rail car design and tipping moment determination [10]. The CFD simulations were supplemented with both wind tunnel and field tests.

Section I: Aerodynamic Drag Reduction

Studies aimed at reducing the tractive resistance of railroad trains have been performed since the advent of iron rails during the late 18th century [11]. Aerodynamic drag is a major contributor to locomotive power requirements, along with climbing resistance (gravity), frictional resistance (rolling, track, flange, bearing, suspension losses), and the force required for acceleration or deceleration. Measurements made using instrumented cars and coast-down methods indicate aerodynamic resistance can account for over 90% of the tractive effort at higher train speeds [12 through 19].

Review of Past Work

The earliest study of train aerodynamics reported in the literature involved small-scale wind tunnel tests performed during 1898 at Purdue University [20]. A significant amount of research on this topic was conducted during the 1920s and 1930s and is reviewed by Hoerner [21] and Tietjens [22]. Results of research on train resistance components are included in papers by Davis [23], Hay [24], Engdahl [25], and Paul [26]. Following the 1973-1974 OPEC oil embargo [27], many U.S. railroads and railroad equipment manufacturers initiated research programs to evaluate methods of reducing tractive resistance of freight trains [28 through 39]. A significant series of studies was supported by the Association of American Railroads during the 1980s [25, 40, 41, 42]. Airflow Sciences Corporation served as primary contractor for this program and has continued to conduct engineering analysis and design studies for a variety of railroads and rail car manufacturers [43

through 48]. Recent increases in fuel prices have once again generated interest in reducing train resistance.

Approach

During the current study, the aerodynamic performance of two types of well-type intermodal cars, each capable of transporting containers of varying lengths, were evaluated. Various design modifications aimed at reducing aerodynamic drag were modeled using RANS methods. Photos of the two well cars are shown in Figs. 1 and 2.

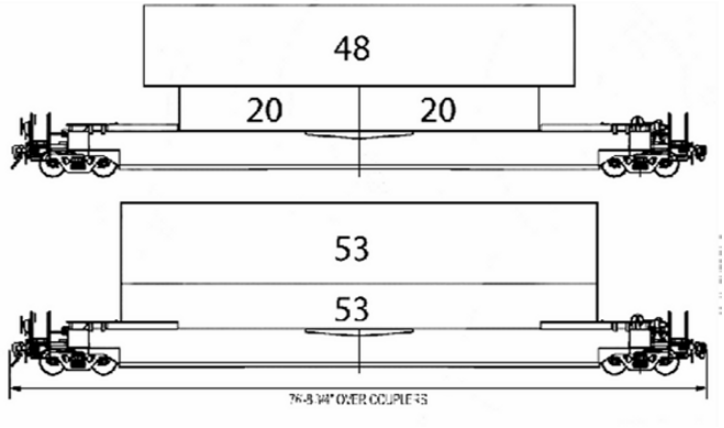

Fig. 1 Husky Stack Well-Type Intermodal Car. Schematic showing loading configuration with containers having lengths of 20', 48', and 53'

Two design features were modified to determine their effect on aerodynamic drag: 1) smooth sides versus exposed side posts, and 2) spacing between containers on adjacent cars. CFD models were coupled with an updated version of the AAR AERO program [42] to determine the drag area (see Equation 1) for various

container loads and car position-in-train. A fuel consumption calculation was performed to determine the influence of reduced drag on locomotive fuel consumption.

$$S_d = DragArea = C_d A \tag{1}$$

where C_d = drag coefficient of rail car at zero degrees yaw
and A = reference area (projected frontal area of rail car)

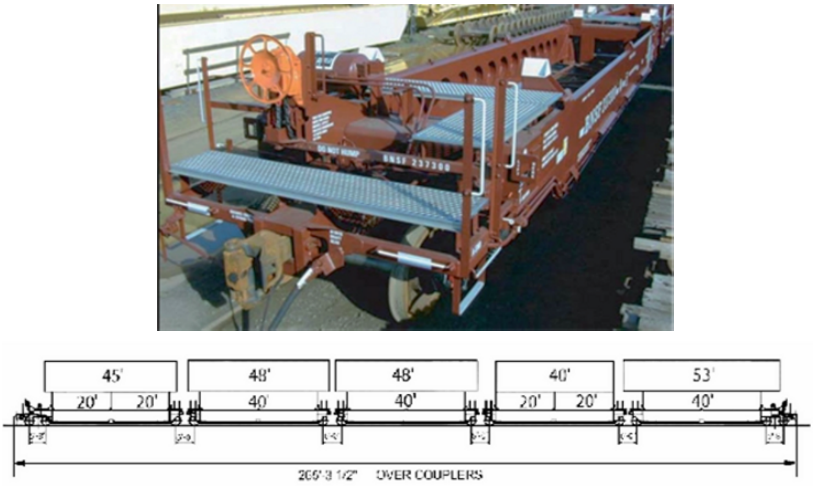

Fig. 2 Maxi-Stack Well-Type Intermodal Car. Schematic showing loading configuration with variety of container lengths.

Fuel consumption calculations are based on the equations developed by Paul, *et. al.* [26, pp. 8-9] [40, p.43]. Assuming the train is operating on straight, level track at constant speed, fuel consumption can be determined from a modified version of the Davis Equation [49]:

$$\begin{bmatrix}\text{Gallons of Fuel}\\ \text{Consumed per}\\ \text{1,000 miles}\end{bmatrix} = K\,(0.0015\,W + 0.00256\,S_d\,V^2 + C\,W) \tag{2}$$

where: K = Fuel consumed per distance traveled per unit of tractive resistance
= 0.2038 gallons/1,000 miles/lbf
S_d = Consist Drag Area (ft^2)
V = Train Speed (miles/hour)
W = Consist Weight (lbf)
C = Hill Factor = 0.0 for level routes and 0.0007 for hilly routes

The first two terms on the right side of Equation 2 represent resistance due to rolling friction and aerodynamic drag, respectively. The last term accounts for the effects of hill climbing. The constant, K, relating fuel consumed per distance traveled per unit of tractive resistance is based on locomotive operational data obtained by members of the Association of American Railroads. Similarly, constant C, the hill factor, is based on operational data for U.S. railroads.

Effects of Modifying Well Car Side Posts

Several researchers have evaluated the effects of modifying external structures on rail cars to reduce aerodynamic drag. Replacing exposed external ribs with smooth sides is particularly effective and offers the advantages of being low cost and easy to install. The table below provides a summary of several rib modification studies that were verified in the wind tunnel and during over-the-track test programs:

Table 1. Effects on Aerodynamic Drag of Rail Cars Due to Modification of Exposed External Ribs (Zero Degrees Yaw, Center Location in Train Consist)

Train Car Type	External Surface Configuration	Modification	Drag Reduction	Reference
Passenger Car	External Ribs and Structure	Smooth Side	6%	[21] pp. 12-10 to 12-11
ISO Container	External Ribs	Smooth Side	10%	[4] pp. 434-435
Hopper Car	External Ribs	Smooth Side	20%	[37] pp. 230-231
Gondola Car	External Ribs	Smooth Side	13%	[37] pp. 230-231
Well Type Intermodal	External Ribs on Trailers	Smooth Side	10%	[36] p. 214
Skeleton Type Intermodal	Platform Support Ribs	Shielded Ribs	15%	[36] p. 78
Gondola Car	External Ribs	Smooth Side	15%	[34] p. 101
Gondola Car	External Ribs	Shielded Ribcaps	17%	[39] p. 186
Open Top Hopper Car	External Ribs	Smooth Side	30%	[41] p. 105

The external ribs comprising the structure of rail cars, containers, and trailers are typically of a size that extends beyond the boundary layer. Flow enters the inter-rib spaces along the vehicle side surfaces and creates a high pressure condition

on the upstream side of each rib and a low pressure wake on the downstream side. Experiments have indicated this pressure distribution is essentially the same for each rib, except those located near the ends of the car, container, or trailer.

The original design of the well-type intermodal cars evaluated during the current study included exposed external side ribs along the side of the well as shown in Figs. 1 and 3. The high pressure on the upstream side and low pressure on the downstream side of each rib can be seen in the surface pressure plot of Fig. 3. Details of the flow at a mid-height horizontal plane for one of the exposed ribs are plotted in Fig. 4.

To reduce drag, a smooth, external surface was positioned at the outboard portion of the exposed side posts. This shielded the inter-rib cavities from the external flow as shown by the calculated pressure distribution in Fig. 5. The change in drag area between the exposed ribs and smooth side versions of the well car was calculated based on the surface pressure changes obtained from the numerical model. This ΔC_dA was referenced to the wind tunnel data using program AERO. The results are summarized in Table 2 for a single car loaded with various length containers. It is noted that drag reductions of 23% are obtained for the five-unit well car due to covering the exposed ribs with a smooth side. This result is similar to those presented in Table 1.

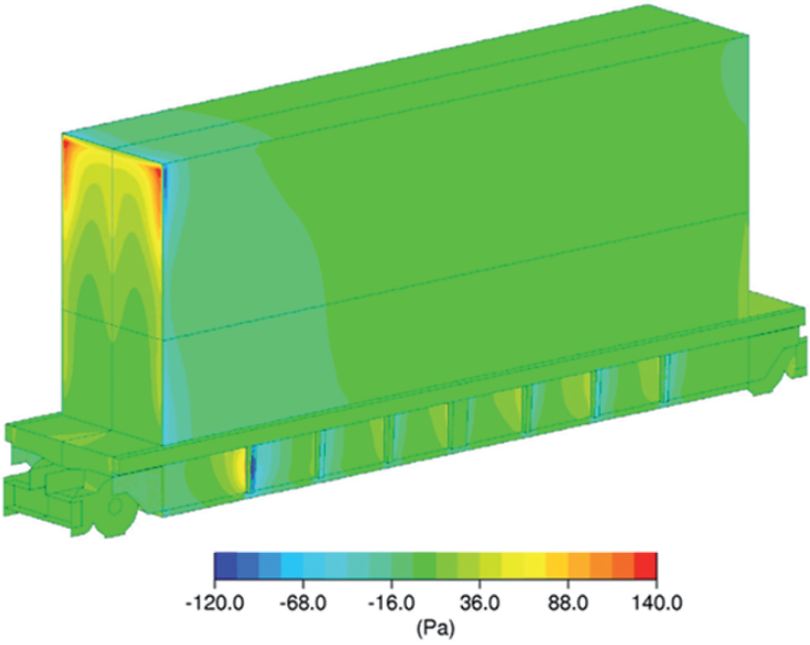

Fig. 3 Calculated Pressure Distribution on Well-Type Intermodal Car with Exposed Ribs (Side Posts), Train Direction is to the Left.

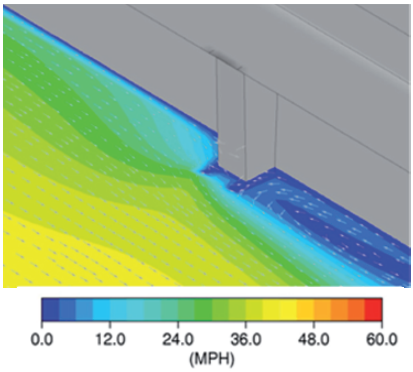

Fig. 4 Detail of Flow Near Well Car External Side Post at Mid-Height Horizontal Plane

Table 2 Drag Area Reduction for 5-Unit Well-Type Intermodal Car

Load Case	Drag Area (ft^2) Smooth Sides	Drag Area (ft^2) Exposed Side Posts
Two 40' long, 9.5' high containers stacked in the well	71.6	93.2
One 40' long, 8.5' high container in the well and one 40' long, 9.5' high container on top	70.6	92.3
Two 20' long, 8.5' high containers in the well and one 40' long, 8.5' high container on top	69.7	91.3

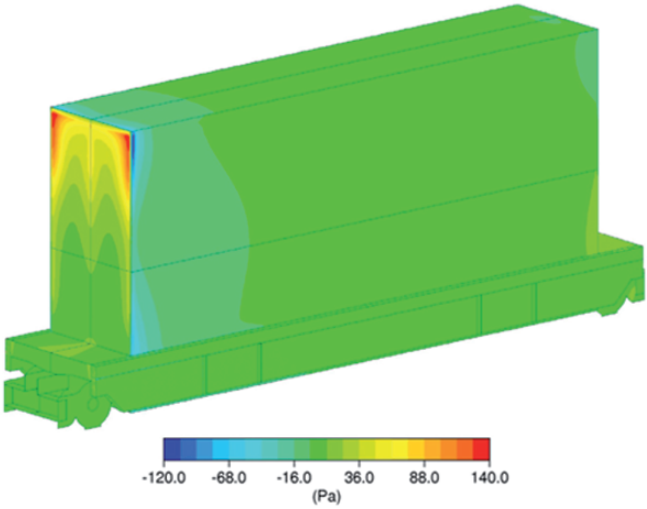

Fig. 5 Calculated Pressure Distribution on Well-Type Intermodal Car with Smooth Sides. Train Direction is to the Left.

Effects of Inter-Car Spacing

Many researchers have evaluated the effects of position-in-train and inter-car spacing on aerodynamic drag [21, 40, 41]. For the case of small gaps between adjacent cars, the flow appears to move smoothly from the rear of the upstream car to the front of the downstream car. The flow in the gap region is a trapped vortex that does not interact substantially with the free-stream. Adjacent cars with narrow inter-car gaps thus act as a single body. As gap distances increase, the drag approaches that of multiple, single bodies [41 p. 99]. This observation has been applied to open top bulk materials cars, such as hopper and gondola cars, where vertical baffles have been employed to provide multiple trapped flow regions, thus preventing high speed air from impacting forward-facing surfaces [41, 50, 51]. For well-type intermodal cars, of course, the gap distance is determined by the container lengths on adjacent cars. The maximum allowable gap is defined by the design of the car ends and couplers. Car manufacturers have proposed placing smaller containers (e.g. 20' ISO containers) on support structures located above the couplers to reduce inter-car gaps. Figure 6 shows the calculated velocity field along the train longitudinal centerline for both a standard well car and a modified well car equipped with spine containers in the region above the couplers. The simulations indicated the drag area of the well car decreased from 44.1 ft^2 to 38.1 ft^2 with the addition of the spine containers. However, the spine containers contributed 6.0 ft^2 of drag area, so no net gain was realized at zero degrees yaw [52].

The results of the various inter-car gap studies (both wind tunnel and CFD model results) were combined to produce the graph shown in Fig. 7. The baseline inter-car gap for the subject well cars is 61.5 inches. The graph provides an indication of the magnitude of the drag changes as the gap distance is increased or decreased from the baseline value. It is interesting to note that the baseline gap places the adjacent containers well into the regime where they are exhibiting the behavior of multiple, sequential bodies. By decreasing the gap from 61.5 inches to 40 inches, the drag can be decreased by 25%.

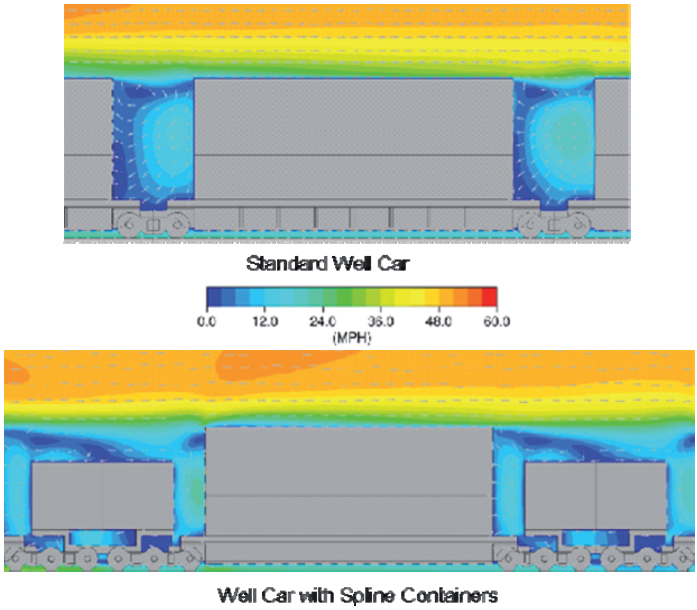

Fig. 6 Comparison of Centerline Flows for Standard and Spline-Type Well Cars

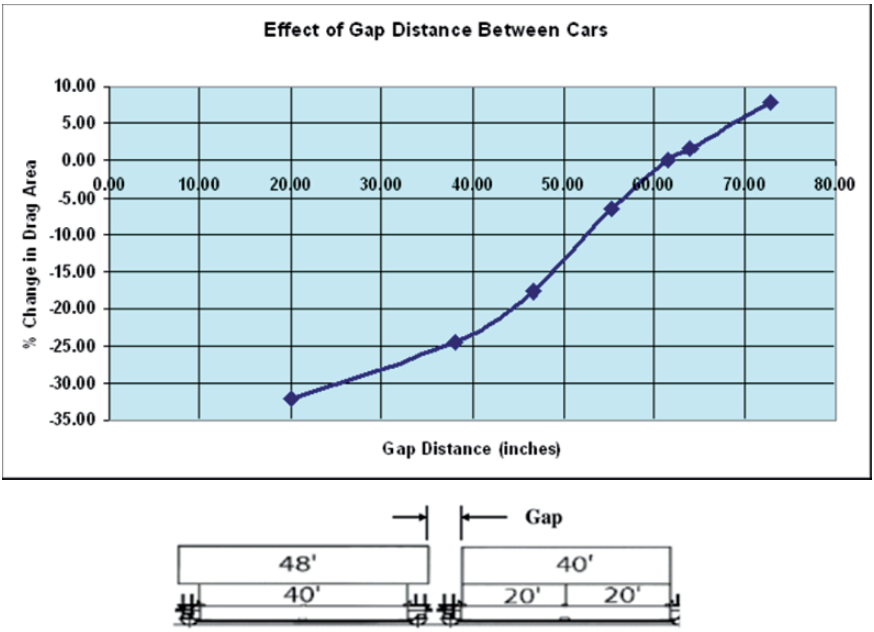

Fig. 7 Effect if Inter-Car Gap in Well Car Drag Area (Baseline Gap Distance is 61.5 Inches)

Results and Conclusions: Section I: Aerodynamic Drag Reduction

The calculated drag reductions resulting from 1) covering the exposed well ribs with smooth sides and 2) reducing the gap distance between adjacent cars were utilized to produce the fuel savings projections shown in Tables 3 and 4. For these comparisons, the following consist was assumed:

5 Locomotives, Twenty 5-Unit Well Cars (= 200 48' Containers)
Total Train Weight: 15,942,000 lbf

Table 3 Fuel Consumption: Gallons per 1,000 Miles: Well Car Intermodal Train with Exposed Ribs and Smooth Sides.

Configuration	Level Route			Hilly Route		
	40 MPH	50 MPH	60 MPH	40 MPH	50 MPH	60 MPH
Exposed Side Posts	6,785	7,860	9,175	9,059	10,135	11,449
Smooth Sides	6,287	7,082	8,053	8,561	9,356	10,328

Table 4 Fuel Consumption: Gallons per 1,000 Miles: Well Car Intermodal Train with Various Inter-Car Gaps.

Gap (inches)	Level Route			Hilly Route		
	40 MPH	50 MPH	60 MPH	40 MPH	50 MPH	60 MPH
61.5	6,785	7,860	9,175	9,059	10,135	11,449
55	6,661	7,666	8,895	8,935	9,940	11,169
47	6,450	7,337	8,421	8,725	9,612	10,696
20	6,173	6,904	7,798	8,447	9,179	10,072

Adding smooth sides to the well car improves fuel economy on level routes by 7.3% for low speeds up to 12% for high speeds. For hilly routes, fuel economy improvements vary from 5% at low speeds to 6% at high speeds. Reducing the inter-car gap also provides significant improvements in fuel economy. For level routes, reducing the inter-car gap from 61.5 inches to 47 inches reduces fuel usage by 5% at low speeds and 8% at high speeds. For hilly routes this reduction in gap distance improves fuel economy by 4% at low speeds and 7% at high speeds.

Section II: Wind Induced Tip-Over

Strong cross winds can lead to tip-over and derailment of train cars exhibiting large profiles and/or light weight, such as passenger coaches and intermodal equipment. The safety of railroad workers and the public is at risk during these events. The photo in Fig. 8 shows a tip-over accident that occurred during 2006 on the Kahnawake Bridge (Montreal, Quebec, Canada). Several other recent wind-related accidents, including those listed below, have led to engineering studies aimed at preventing their occurrence.

- 28 January 1987: Union Pacific Railroad: 4 empty containers blown from two TTX cars near Laramie, Wyoming; crosswind speeds measured to be 45 miles/hour.
- 24 March 1987: Union Pacific Railroad: 25 cars were derailed near Brule, Nebraska due to high winds, measured at 53 miles/hour.
- 11 November 1988: Consolidated Rail Corporation: 64 Road Railer intermodal cars derailed on the Sandusky Bay Causeway (Ohio) during high winds.
- 11 February 2003: Norfolk Southern Railway: train derailment on Sandusky Bay Causeway during high winds.

Cleanup costs can be significant and hence create an additional incentive for seeking an effective train speed restricting system aimed at reducing these events.

Photo Credit: http://www.citynoise.org, February 2006

Fig. 8 Freight Train Derailment: 18 February 2006, Montreal Quebec, Kahnawake Bridge, 67 mile/hour crosswinds.

Three primary goals were established for the current study:

- Develop railcar tipping moment (defined below) data base. This included gathering wind tunnel test data for high-population railcars and performing CFD simulations to gain additional insight into the aerodynamic conditions leading to tip-over events.
- Develop a real-time computer algorithm to signal appropriate train speed reductions during hazardous cross wind conditions.
- Select and locate wind sensors and configure and implement the train speed restricting system.

Review of Past Work

The wind tunnel studies funded by the Association of American Railroads included force measurements of a wide variety of cars and locomotives at yaw angles up to 90°. Much of this work is summarized by Furlong, *et. al.* [41]. These studies provide a large database of car side forces and rolling moments under crosswind conditions.

Matschke, *et. al.* [53] performed a risk assessment of cross winds on high speed trains to define countermeasures for safe railway operation. Andersson, *et. al.* [54] identified locations in Sweden prone to high winds and possible train overturning and performed a risk assessment for safe train operation. Experimental methods for measuring side forces and rolling moments for high-speed trains were developed by Sanquer, *et. al.* [55]. Pressure measurements on double-stack freight cars during train passing conditions were made by MacNeill, *et. al.* [56] and used for comparison with CFD simulations. The simulations were employed to define conditions under which double-stack container cars are subject to tip-over [57]. Hoppmann, *et. al.* [58] developed a wind prediction model as part of a railway safe operations system. Tipping effects on rail cars caused by jets emanating from tunnel pressure relief ducts were investigated by Polihonki, *et. al.* [59]. During 1988, Gielow, *et. al.* [60] conducted a series of wind tunnel tests using 16% scale models to determine the aerodynamic forces acting on a variety of rail cars, including intermodal and automobile transporters. The study culminated in development of a train-speed-restricting system to achieve safe operating conditions under high wind conditions along routes operated by Union Pacific Railroad. Additional evaluations on the tip-over behavior of autorack rail cars was performed by Airflow Sciences Corporation during 1998 [61]. Tipping moments were calculated as a function of train speed and cross wind speed and found to be less than half those of double-stack intermodal cars under the same cross wind conditions, primarily because of the higher pressures on the leeward side of the rounded-top autorack cars.

Approach and Speed Restricting System Description

The Sandusky Bay Causeway is located at the southwestern end of Lake Erie northwest of Sandusky, Ohio (see Fig. 9). Trains moving across the causeway are subject to the high winds that occur frequently in this region. Norfolk Southern Railway funded an engineering effort to develop a train speed restricting system with the goal of eliminating tip-over accidents at this location. The project was divided into several phases and concluded during 2006 with the implementation of

wind sensors located on the causeway, data acquisition hardware, and data analysis computers linked by the Norfolk Southern network [62].

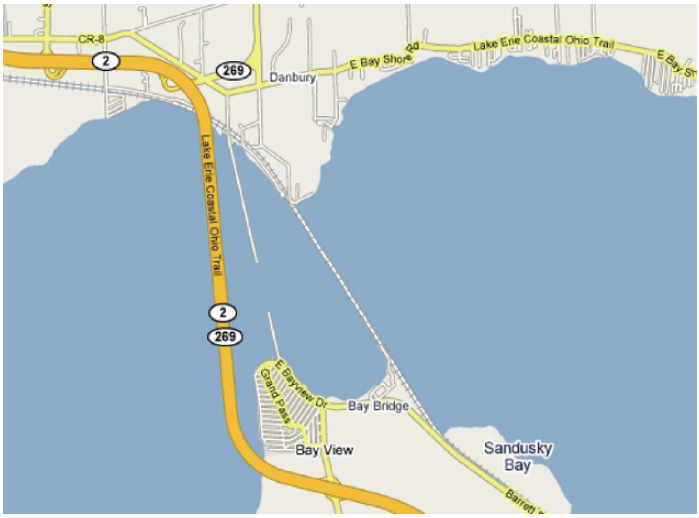

Fig. 9 Map Showing Sandusky Bay Causeway (*Map Credit: Google Maps)*

The main components of the Sandusky Bay Causeway Speed Restricting System are shown in the block diagram of Fig. 10.

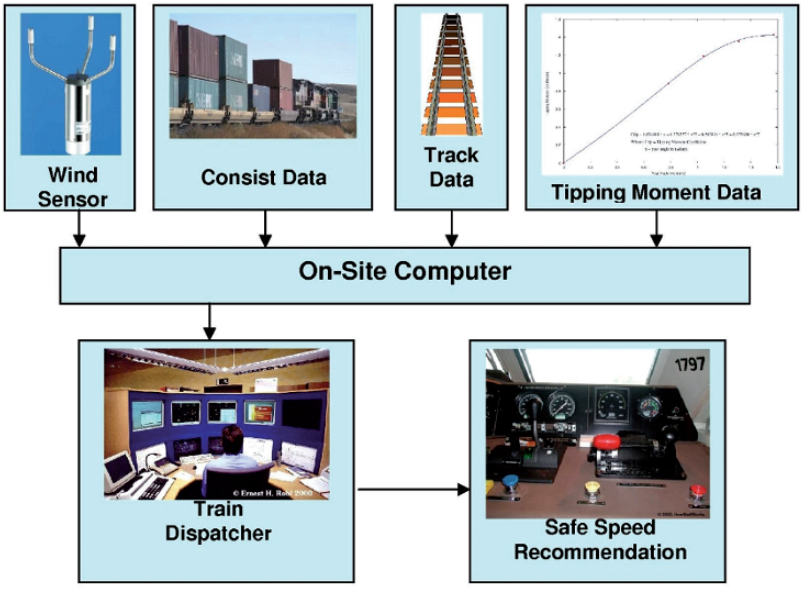

Fig. 10 Sandusky Bay Causeway Train Speed Restricting System Components

Tipping moment data were obtained from wind tunnel tests and CFD simulations. Data for the following car types were obtained from earlier wind tunnel tests [36, 37, 60, 63]. An example of the wind tunnel tipping moment coefficient plots is shown in Fig. 11. CFD models were constructed for each of the cars represented in the wind tunnel tests. Comparisons between forces and moments obtained from the CFD models compared favorably with those obtained during the wind tunnel tests. As noted earlier, the FLUENT RANS models provide good correlation with the average pressures on the leeward side of the vehicle, leading to good agreement with the measured rolling moments. Peters [64, p. 464] showed similarly good agreement between calculated tipping moments (using FLUENT) and wind tunnel data. Additional CFD models were developed to obtain tipping moments for car types not included in the original wind tunnel tests. Car types were selected from lists, provided by Norfolk Southern Railway, of representative freight train consists that traverse the Sandusky Bay Causeway. Rail cars aerodynamic characteristics obtained from the CFD models are listed in Table 5 and those obtained from earlier wind tunnel tests are listed in Table 6. Velocity profiles and pressure distributions for typical CFD models, in this case a 53' well-type intermodal car at 90° yaw, are shown in Figs. 12 and 13, respectively.

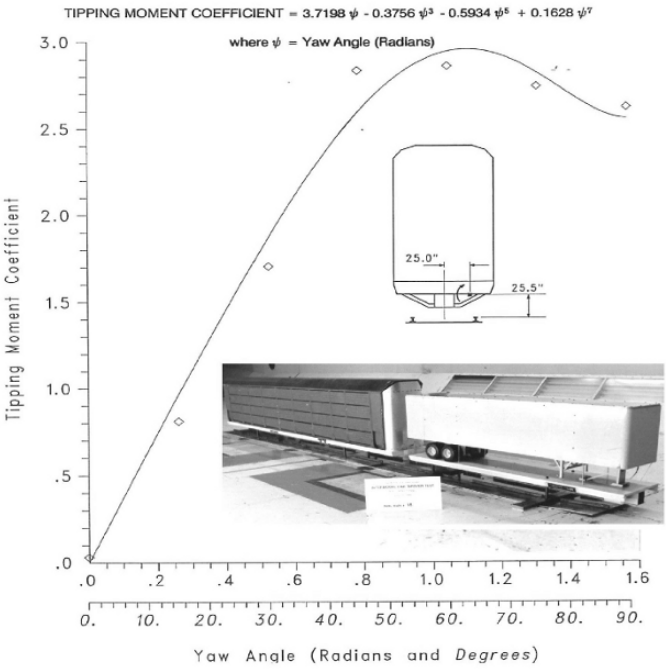

Fig. 11 Example Tipping Moment Plot Obtained from Wind Tunnel Test Data: Autorack Car.

Table 5 Rail Cars Evaluated Using CFD Models (C = Container)

Rail Car	Lading
BS177 Box Car	Empty
BS216 Box Car	Empty
BS89 Box Car	Empty
RoadRailer (53’ Trailer)	Empty
HS46 Hopper Car	Empty
H11D Hopper Car	Empty
G86 Gondola Car	Empty
53’ Well Car	53’ C on 53’ C

Table 6 Rail Cars Evaluated Using Wind Tunnel Models (C = Container, T = Trailer)

Rail Car	Lading
48’ Thrall Well Car	40’ C on 40’ C
48’ Thrall Well Car	53’ C on 48’ C
Gunderson Bulkhead Well Car	40’ C on 40’ C
Gunderson Bulkhead Well Car	40’ C on 40’ C
Gunderson Bulkhead Well Car	48’ C on 40’ C
Gunderson Bulkhead Well Car	48’ C on 40’ C
89’ Flat Car	Two 40’ T
89’ Flat Car	Two 45’ T
89’ Flat Car	One 40’ C
89’ Flat Car	Autorack

For each rail car, simulations were performed at yaw angles of 0°, 45°, 60°, 75°, and 90°, with 0° representing a pure headwind and 90° a pure cross wind condition. Forces and moments were computed for the center cars only for both the wind tunnel and CFD models. The upstream and downstream cars were included to provide an accurate representation of the flow field [50, pp. 151-152].

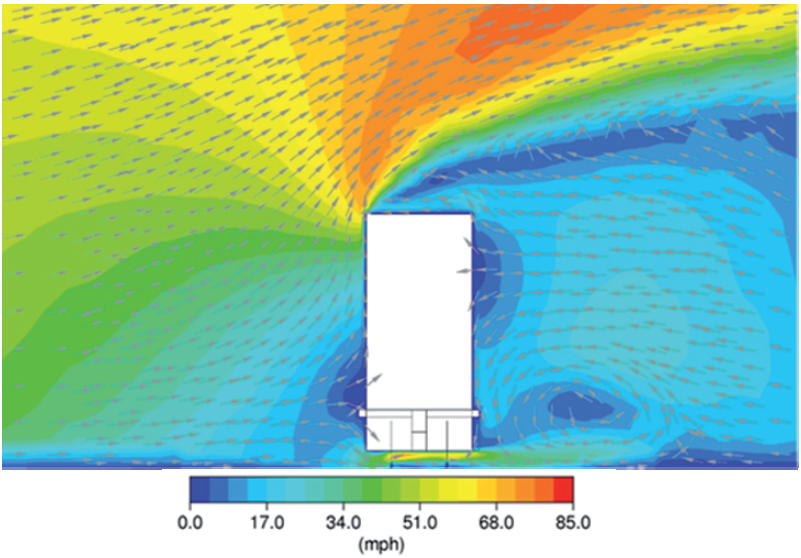

Fig. 12 Velocity Profile for 53' Well-Type Intermodal Car at 90° Yaw, Flow in Plane Perpendicular to Train Longitudinal Axis at Mid-Car Location.

Once the tipping moment relationships were established, 7th order polynomial curve fits were developed (see Fig. 11) and supplied as input to the train speed restricting algorithms.

A rail car will begin to rotate when the aerodynamic tipping moment exceeds the restoring moment. The restoring moment is taken as the weight of the railcar acting through the tipping arm. The aerodynamic tipping moment is taken as the weight of the rail car acting through the tipping arm, as illustrated in Figure 14. Note that dynamic effects are not included since they have been shown to be small compared to the wind forces and rail car weights.

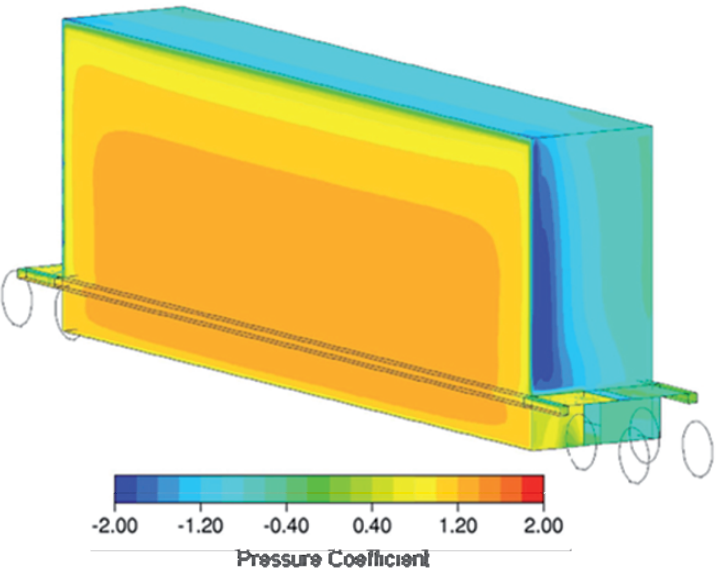

Fig. 13 Pressure Distribution, Windward Side, 53' Well-type Intermodal Car at 90° Yaw

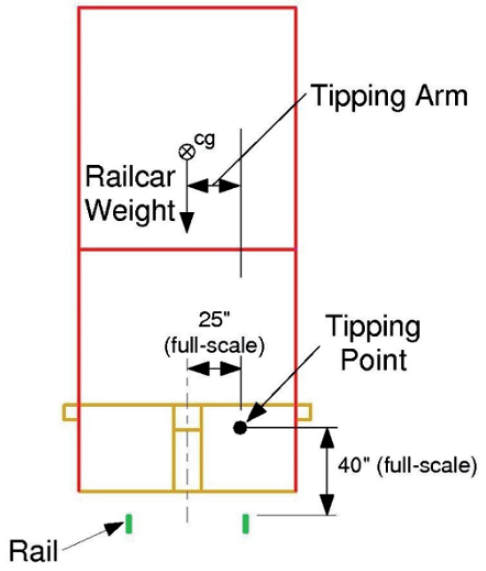

Fig. 14 Relationship Between Aerodynamic Tipping Moment and Restoring Moment

At the onset of tipping:

Restoring Moment = Aerodynamic Tipping Moment

$$W \cdot L = \tfrac{1}{2} \cdot \rho \cdot V^2 \cdot C_{tip} \cdot A_{ref} \cdot L_{ref} \tag{3}$$

where:

W = Light Weight of Railcar (Less Trucks) Plus Empty Containers or Trailers
L = Tipping Arm (Horizontal Distance between Railcar cg and Tipping Point)
ρ = Air Density
V = Wind Velocity Relative to Train
C_{tip} = Tipping Moment Coefficient
A_{ref} = Reference Area = 100 ft^2
L_{ref} = Reference Length = 50 ft

As noted above, C_{tip} is defined as a function of yaw angle (ψ) using a 7th order polynomial curve fit of the form:

$$C_{tip} = a \cdot \psi + b \cdot (\psi)^3 + c \cdot (\psi)^5 + d \cdot (\psi)^7 \tag{4}$$

The parameters a, b, c, d are the polynomial curve fit coefficients. Yaw angle and relative wind speed (V) are both functions of train speed (V_t), wind speed (V_w), and wind angle (θ) relative to the track. The sketch below shows the relationship between these variables.

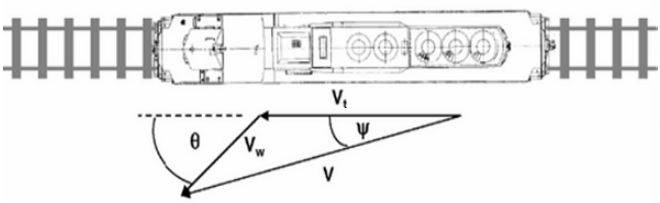

Thus, relative wind speed and yaw angle can be expressed as:

$$V^2 = (V_t + V_w \cdot \cos(\theta))^2 + (V_w \cdot \sin(\theta))^2$$
$$\psi = \tan^{-1}[V_w \cdot \sin(\theta) / (V_t + V_w \cdot \cos(\theta))] \tag{5}$$

Recall that the equation for safe train speed comes from a balance of the aerodynamic tipping moment and the restoring moment:

$$0 = W \cdot L - \tfrac{1}{2} \cdot \rho \cdot V^2 \cdot C_{tip} \cdot A_{ref} \cdot L_{ref} \tag{6}$$

Substituting the expressions for V and C_{tip} into the above equation yields the expression to be solved for safe train speed:

$$0 = W \cdot L - \tfrac{1}{2} \cdot \rho \cdot [(V_t + V_w \cdot \cos(\theta))^2 + (V_w \cdot \sin(\theta))^2] \cdot [a \cdot \psi + b \cdot (\psi)^3 + c \cdot (\psi)^5 + d \cdot (\psi)^7] \cdot A_{ref} \cdot L_{ref} \quad (7)$$

Because ψ is a function of V_t, numerical methods must be used to solve the above equation.

The weight used for each railcar is the light weight (less the truck weight) plus the empty weight of the appropriate container(s) or trailers. Unloaded weights are used in order to obtain the most conservative (lowest) tipping speeds for each railcar. The weight (W), and tipping arm (L), and tipping point for each rail car were included in the train speed restricting system database.

Wind data were obtained using an ultrasound-based anemometer located at the Causeway. The sensor was located 500 feet north of the bridge on the lake side to avoid interference by the bridge structure. The sensor is programmed to provide wind speed and direction at 5 second intervals.

Three separate computer algorithms work together to form the core of the Sandusky Bay speed restricting system. The names of these algorithms are SRS (acronym for Speed Restricting System), Wind, and Safespeed. Each performs a specific task in the computation and display of safe train speeds. Program SRS is installed on the Train Dispatcher's computer. Programs Wind and Safespeed are installed on the computer located at the Causeway. Program Wind acquires data from the anemometer and provides the information to Program Safespeed which, in turn, calculates the tipping speed for each rail car in the consist. These files are transferred to SRS for display on the Dispatcher's console.

Results and Conclusions, Section II: Wind-Induced Tip-Over

Wind tunnel and CFD investigations of a variety of freight cars were used to assemble a tipping moment data base for cross wind conditions. Each of the rail cars included in the data base exhibits a particular type of tip-over behavior as summarized in Table 7. These data served as the basis for development of a real-time speed restricting system for the Sandusky Bay Causeway. The system includes a set of computer algorithms for calculating safe train speeds based on wind data obtained from a site-mounted anemometer.

Table 7a Rail Car Tipping Characteristics, Car Parameters

Railcar	Tipping Point Relative to Centerline Top-of-Rail Position		Railcar Light Weight Including Trucks (lbs)	Unloaded Lading Weight (lbs)
	Horizontal Location (in.)	Vertical Location (in)		
BS177 Box Car	25	30	66,400	0
BS216 Box Car	25	30	77,400	0
BS 89 Box Car	25	30	111,800	0
53 Foot RoadRailer	28.25	0	-	15,800
HS46 Hopper Car	25	30	80,000	0
H11D Hopper Car	25	30	56,300	0
G86 Gondola Car	25	30	59,000	0
53 Foot Well Car	25	40	50,000	20,000
48 Foot Thrall Well Car	25	40	48,900	14,800
48 Foot Thrall Well Car	25	40	48,900	19,000
Gunderson Bulkhead Well Car	25	40	41,000	14,800
Gunderson Bulkhead Well Car	50.3	125.5	-	7,400
Gunderson Bulkhead Well Car	25	40	41,000	16,400
Gunderson Bulkhead Well Car	53.3	125.5	-	9,000
89 Foot Car	25	25.5	68,000	26,000
89 Foot Car	25	25.5	68,000	28,000
89 Foot Car	48	47.5	68,000	7,400
89 Foot Car	25	25.5	97,000	0

Table 7b Rail Car Tipping Characteristics, Manner of Tipping

Railcar	Total Weight of Tipping Railcar and Lading (lbs)	Manner of Tipping
BS177 Box Car	42400	Railcar tips off trucks
BS216 Box Car	53400	Railcar tips off trucks
BS 89 Box Car	87800	Railcar tips off trucks
53 Foot RoadRailer	27400	Combined trailer & trucks tip off rail
HS46 Hopper Car	56000	Railcar tips off trucks
H11D Hopper Car	32300	Railcar tips off trucks
G86 Gondola Car	35000	Railcar tips off trucks
53 Foot Well Car	46000	Combined trailer & trucks tip off rail
48 Foot Thrall Well Car	39700	Combined trailer & trucks tip off rail
48 Foot Thrall Well Car	43900	Combined trailer & trucks tip off rail
Gunderson Bulkhead Well Car	43800	Combined trailer & trucks tip off rail
Gunderson Bulkhead Well Car	7400	Top container tips off bottom container
Gunderson Bulkhead Well Car	45400	Combined trailer & trucks tip off rail
Gunderson Bulkhead Well Car	9000	Top container tips off bottom container
89 Foot Car	70000	Combined trailer & trucks tip off rail
89 Foot Car	72000	Combined trailer & trucks tip off rail
89 Foot Car	51400	Container blows off Railcar
89 Foot Car	73000	Railcar tips off trucks

Section III: Diesel Exhaust Plume Behavior

Many studies have indicated a relation between occupational exposure to diesel exhaust and diseases of the lung [65-68]. The relative risk (RR) for lung cancer, for example, among those classified as having been exposed to diesel exhaust, is approximately 1.2 to 1.5 times the risk in those classified as unexposed. Diesel exhaust emissions contain hundreds of chemical compounds, which are partly in the gaseous phase and partly in the particulate phase. Railroad locomotive operators have issued complaints regarding diesel exhaust entering the cab through open windows [69]. Most diesel particles are small enough (0.02 to 0.5 μm) to be transported deep into the lungs, where they pose the greatest hazard to human health [70, 71]. The goal of the current study is to evaluate the behavior of exhaust plumes issuing from diesel locomotives and quantify the levels of exhaust components at the operator cab window.

Review of Past Work

It is well known that separation zones on the leeward sides of large rectangular objects can entrain exhaust flows. To prevent "sick building" syndrome, for example, the American Society of Heating, Refrigeration, and Air Conditioning Engineers publishes guidelines for exhaust stack heights and intake vent locations for buildings and industrial facilities [72]. During wind tunnel tests completed for General Electric Transportation Systems during 1986 [73], smoke flow visualization methods were employed to assess the behavior of the simulated diesel engine exhaust plume for a locomotive. The study showed the plume was relatively unaffected by passive changes to the locomotive surface (strakes, baffles, vanes). As the photo in Fig. 15 shows, the exhaust is entrained within a strong vortex pattern on the leeward side of the locomotive that envelopes the operator's cab when the locomotive is operated with the long hood forward. It was shown that an auxiliary blower is effective at moving the plume above the operator's cab as shown in Fig. 16. Operating the locomotives with the short hood forward significantly reduces the concentration of the plume on the lead locomotive operator's cab.

Fig. 15 Diesel Exhaust Plume Behavior: 1/15-Scale Wind Tunnel Test, Yaw Angle = 10°, Long Hood Forward, Baseline Exhaust System

Fig. 16 Diesel Exhaust Plume Behavior, 1/15-Scale Wind Tunnel Test, Yaw Angle = 10°, Long Hood Forward, with Auxiliary Blower in Operation.

Approach

To quantify the concentration of exhaust at the locomotive operator's cab window, a significant research and simulation effort was required. The approach to performing this study is outlined below and shown schematically in Fig. 17.

Specific tasks included a) identification of typical switchyard and line-haul locomotives. Various references were employed, including the latest edition of *The Car and Locomotive Cyclopedia of American Practices*, locomotive manufacturer specifications, inventories of locomotives in various railroad fleets, and interviews with industry experts [74], b) assessment of U.S. track surveys and meteorological data, c) an evaluation of typical crosswind conditions (wind yaw angles) experienced within switchyards and line-haul operations, d) identification of typical locomotive throttle (notch) positions and train speeds for both switchyard and line-haul operations (these were used to calculate typical exhaust flow rates), e) diesel exhaust characteristics (flow rates, composition, and temperature) were obtained for a variety of locomotives, and f) other field test and wind tunnel test data relating to locomotive exhaust plume behavior were reviewed including field tests, wind tunnel tests, and CFD simulations. Concentrations of exhaust gas components and particulate matter at the leeward side windows of locomotives operating in both switchyard and line-haul conditions were identified for a range of operating conditions, based on the concentrations defined by the numerical models and the exhaust composition information obtained from the literature.

Full details of the exhaust concentration studies can be found in Paul and Linfield [75, 76]. A study of weather conditions [77] along a large number of railroad routes indicates that cross wind conditions occur during a majority of the time. Locomotives operating in cross wind conditions exhibit two distinct flow regions: 1) windward side of the vehicle, and 2) leeward side of the vehicle. Air flow patterns on the leeward side are characterized by large vortex formations and strong recirculating conditions. This recirculating, leeward-side wake acts to entrain gases emitted at the diesel engine exhaust stack.

To define effects of cross winds, both the track orientation and ambient wind patterns must be evaluated. During earlier studies [75, 76], specific track orientations were obtained from survey data and combined with historical wind records to determine the relative angle and speed of the air approaching the train. Analyses of train routes, train speeds, and ambient wind conditions indicate yaw angles vary from 5° to 69°. Lower yaw angles apply to higher train speeds and lower wind speeds. Higher yaw angles correspond to lower train speeds and higher wind speeds.

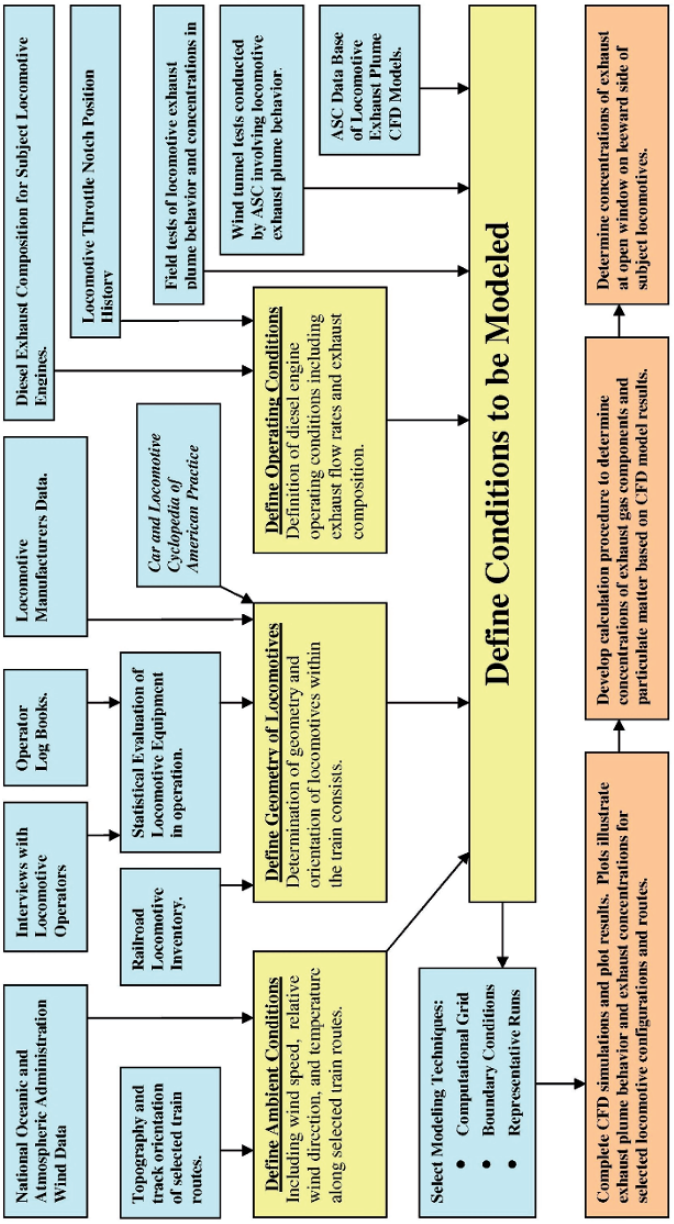

Fig. 17 Determination of Diesel Exhaust Plume Concentrations within Locomotive Cabs, Project Flow Chart.

A review of existing locomotive exhaust test data indicated flow rates are linearly proportional to engine horsepower [78]. Thus, for each throttle setting (also called "notch setting") used in the numerical simulations, the diesel exhaust flow rate can be scaled from available test data for similar 2-cycle engines. Test data available in the literature, such as that reported by Southwest Research Institute [79], were used to calculate exhaust gas temperatures and flow rates for a variety of locomotive models and manufacturers.

Exhaust gas composition was determined based on locomotive diesel engine test data reported in the literature (*Bosch Automotive Handbook* [80], Southwest Research Institute [81]). Exhaust gas components included in the current and previous studies were: 1) oxides of nitrogen (NO_x), 2) carbon monoxide (CO), 3) unburned hydrocarbons, 4) sulfur dioxide (SO_2), and 5) particulate matter. The exhaust composition for typical 2-cycle diesel engines is summarized in Table 8:

Table 8. Exhaust Composition for 2-Cycle Diesel Locomotive Engines

Exhaust Component	Low Value (g/bhp-hr)	High Value (g/bhp-hr)	Low Value (kg/bhp-sec)	High Value (kg/bhp-sec)
NO_x	10.01	16.11	2.78E-06	4.48E-06
CO	0.37	3.68	1.03E-07	1.02E-06
Unburned Hydrocarbons	0.20	0.45	5.56E-08	1.25E-07
SO_2	0.69	1.18	1.92E-07	3.28E-07
Particulate Matter	0.14	0.24	3.89E-08	6.67E-08

g/bhp-hr = grams per brake horsepower hour
kg/bhp-sec = kilograms per brake horsepower second

The mass fraction of diesel exhaust concentrations in the vicinity of a variety of locomotives has been calculated using the VISCOUS finite volume RANS code [5]. This code employs a staggered pressure-based solver over a Cartesian grid. The grid extended four train lengths forward of the locomotive, three train lengths aft of the trailing locomotive, 10 train heights above the locomotives and 5 train widths to each side. Initial models were evaluated using a range of grid sizes from fine to coarse in order to confirm grid independence. Boundary conditions, representing ambient wind conditions, were imposed at the outer edges of the computational domain. Additional boundary conditions relating to locomotive operation (exhaust flows, dynamic brake flows, electronics cooling flows, engine cooling system, etc.) were imposed at the appropriate geometric locations within the grid structure. The local concentrations of exhaust components were determined from the numerical simulation results (exhaust concentrations) and the exhaust components for 2-cycle diesel locomotive engines

In addition to ambient conditions (wind direction, speed, temperature), locomotive geometry, and operating conditions (exhaust flow rates, exhaust temperatures, throttle positions), field tests of locomotive exhaust plume behavior and exhaust component concentration measurements taken within cabs of operating locomotives were included in the analysis [82, 83, 84]. The models and field tests confirmed the characteristic windward/leeward side delineation of the flow field in the vicinity of operating locomotives operating under crosswind conditions. The strong recirculation region on the leeward side of the locomotive acts to entrain the gases emitted from the diesel engine exhaust and moves these gases along the longitudinal axis of the train.

Numerical simulations of diesel exhaust plume behavior were completed for seven locomotive types and 27 configurations (train orientation, wind speed, wind direction, exhaust flow rate). Three examples have been selected and are presented in Figs. 18 through 20. Each of these figures shows the calculated concentrations at various planes along the length of the train. The red colors correspond to regions having exhaust concentrations equal to the concentration at the stack outlet plane. Orange represents regions having exhaust concentrations equal to $1/10^{th}$ of the concentration at the stack exit. The yellow regions have concentrations equal to $1/100^{th}$ of the concentration at the stack exit, and so forth. The color scale is logarithmic, so the numbers represent concentration changes that vary by powers of 10.

The exhaust plume enters the wake on the leeward side and travels along this side of the train. Concentrations of exhaust components are higher in those wakes corresponding to higher train speeds and smaller yaw angles, such as those encountered in city-to-city runs (Figs. 19 and 20). Higher yaw angles, which occur at lower train speeds and higher cross wind speeds (Fig. 18), tend to enlarge the wake on the leeward side of the train and reduce the exhaust concentrations compared to those encountered at higher speeds where the wake tends to remain closer to the side of the train.

The numerical simulations indicate exhaust concentrations in the lead locomotive are highest for locomotives operated with the long hood forward. For switchyard operations (low speeds), exhaust concentrations in the lead locomotive increase with increasing yaw angles. For line-haul operations (high speeds), exhaust concentrations in the lead locomotive decrease with increasing yaw angles. Higher concentrations of exhaust occur at the leeward windows of the trailing locomotive for both the switchyard and line-haul operations.

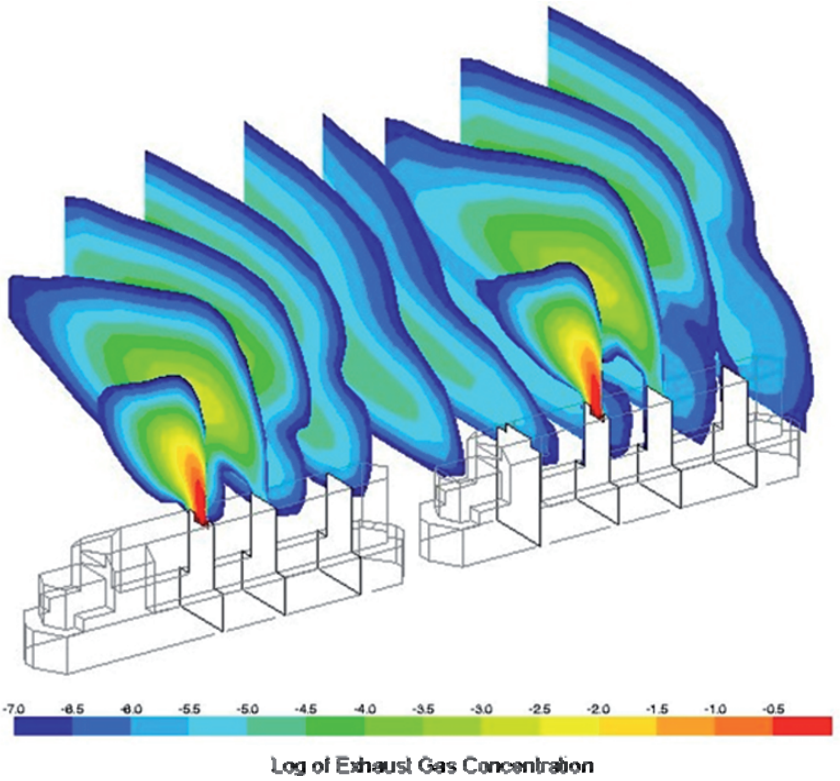

Fig. 18 Two GM EMD GP38 Locomotives, Both Oriented with Short Hood Forward, Throttle Position = Notch 8, Train Speed = 5 miles/hour, Wind Speed = 5 miles/hour (45° Yaw), Typical Low Speed (Switchyard) Operation. Train Direction: to the left; Crosswind: into the page.

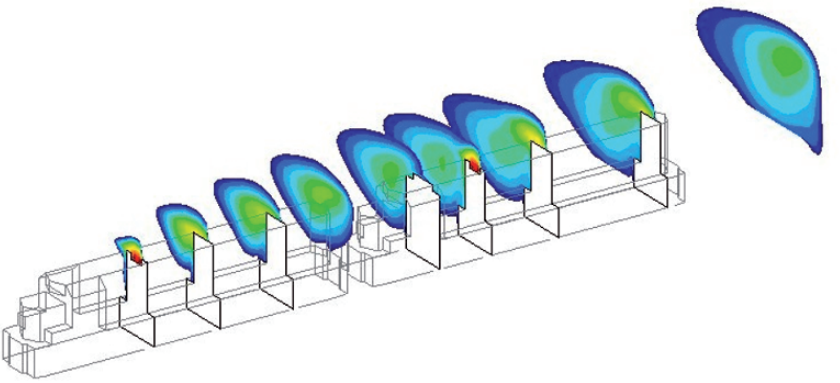

Fig. 19 Two GM EMD SD40 Locomotives, Both Oriented with Short Hood Forward, Throttle Position = Notch 5, Train Speed = 45 miles/hour, Wind Speed = 7 miles/hour (8.8° Yaw), Typical High Speed (Linehaul) Operation. Train Direction: to the left; Crosswind: into the page.

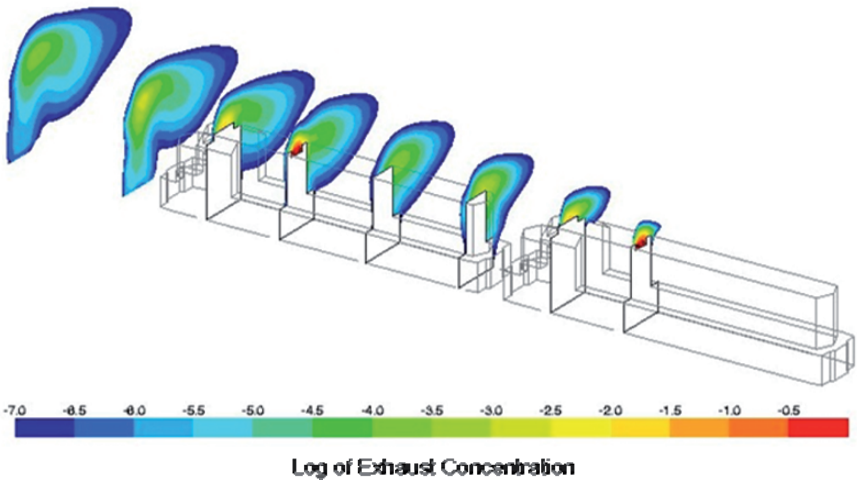

Fig. 20 Two GM EMD SD40 Locomotives, Both Oriented with Long Hood Forward, Throttle Position = Notch 5, Train Speed = 45 miles/hour, Wind Speed = 7 miles/hour (8.8° Yaw), Typical High-Sped (Linehaul) Operation. Train Direction: to the right; Crosswind: into the page.

Maximum exhaust concentrations for the lead locomotive occur for locomotives operating in line-haul service with the long hood forward and were as high as 0.008% of the concentration at the stack exit. Concentrations of exhaust at the leeward-side window of trailing locomotives were found to be relatively higher than that of the lead locomotive for either hood orientation.

Concentrations for both the gaseous components and the particulate matter present in the exhaust plume were calculated. Exhaust concentrations were obtained from the numerical simulations and component concentrations were defined using the calculation procedures. The diesel exhaust components of Table 8 can be converted to mass fractions for comparison to the results of the numerical models as shown in Table 9.

Table 9 Exhaust Flow Composition (Mass Fraction) for 2-Cycle, 12-Cylinder Diesel Engine as a Function of Throttle Position

Exhaust Gas Component	Throttle Notch 5 Flow Rate (grams/hr)	Throttle Notch 5 Flow Rate (kg/sec)	Throttle Notch 5 Mass Fraction*	Throttle Notch 8 Flow Rate (grams/hr)	Throttle Notch 8 Flow Rate (kg/sec)	Throttle Notch 8 Mass Fraction*
NO_x	25,584	0.0071	0.0027	47,133	0.0131	0.0038
CO	3,895	0.0011	0.0004	3,034	0.0008	0.0002
Hydrocarbons	595	0.0002	0.0001	1,375	0.0004	0.0001
SO_2	1,568	0.0004	0.0002	3,361	0.0009	0.0003
Particulate	348	0.0001	0.00004	697	0.0002	0.00006
0_2	(reported as mass fraction):		0.139	(reported as mass fraction):		0.119

* Component Mass Fraction = (component flow Rate kg/sec)/(Total Exhaust Flow Rate kg/sec)
Total Exhaust Flow Rate = 3.446 kg/sec (Notch 8) and 2.639 kg/sec (Notch 5)

Gaseous Components:

The molecular weight of the exhaust gas mixture at Notch Position 5 was calculated to be 28.875 [75]. Similarly, the molecular weight of the exhaust gas mixture at Notch Position 8 was determined to be 28.803. The following procedure was then applied to determine the mole fractions of each gaseous exhaust component at the leeward side windows for each of the simulated locomotives at both the leading and trailing positions.

A. For each of the selected simulations, obtain the mass fraction of exhaust present at the operator's cab leeward side window.
B. Determine the mass fraction of each exhaust component at the operator's cab window for each of the eight simulations and for both the leading and trailing locomotive (multiply component mass fraction by exhaust concentration at that location).
C. Calculate the mole fraction of the exhaust gas component.
D. Multiply the mole fraction by 1,000,000 to obtain the concentration for each component in ppmv.

The results for the gaseous component concentrations at the leeward-side window for the leading and trailing locomotives are shown in Tables 10 and 11, respectively.

Table 10a Calculated Exhaust Concentrations at the Leeward-Side Window of the Leading Locomotive, NO_x, CO, Hydrocarbons, SO_2.

Locomotive	Hood Forward	Yaw Angle	NO_x (ppmv)	CO (ppmv)	HCs (ppmv)	SO_2 (ppmv)
GP38	Short	45°	0.00000	0.00000	0.00000	0.00000
GP38	Short	21.8°	0.00000	0.00000	0.00000	0.00000
GP38	Long	45°	0.11646	0.00832	0.00830	0.00546
GP38	Long	21.8°	0.04037	0.00288	0.00288	0.00189
SD40	Short	49.7°	0.00000	0.00000	0.00000	0.00000
SD40	Short	8.84°	0.01252	0.00252	0.00126	0.00055
SD40	Long	49.7°	0.00621	0.00125	0.00062	0.00027
SD40	Long	8.84°	0.17326	0.03483	0.01738	0.00762

Table 10b Calculated Exhaust Concentrations at the Leeward-Side Window of the Leading Locomotive, O_2, CO_2, Aldehydes, and N_2.

Locomotive	Hood Forward	Yaw Angle	O_2 (ppmv)	CO_2 (ppmv)	Aldehydes	N_2 (ppmv)
GP38	Short	45°	0.00000	0.00000	0.00000	0.00000
GP38	Short	21.8°	0.00000	0.00000	0.00000	0.00000
GP38	Long	45°	4.33325	1.85280	0.00054	32.5184
GP38	Long	21.8°	1.50206	0.64225	0.00019	11.27201
SD40	Short	49.7°	0.00000	0.00000	0.00000	0.00000
SD40	Short	8.84°	0.76606	0.28042	0.00008	4.80206
SD40	Long	49.7°	0.38001	0.13911	0.00004	2.38212
SD40	Long	8.84°	10.5982	3.87951	0.00114	66.43475

It is noted that the concentrations in Tables 10 and 11 are for the exhaust components only. In other words, the oxygen and nitrogen components originate at the stack. Of course, oxygen and nitrogen from the surrounding air would also be present at these locations. Since the goal of the current study is to calculate the levels of exhaust components present at the operator's cab windows that originated in the engine, the concentrations of components present in the ambient air were not included.

Table 11a Calculated Exhaust Concentrations at the Leeward-Side Window of the Trailing Locomotive, NO_x, CO, Hydrocarbons, SO_2.

Locomotive	Hood Forward	Yaw Angle	NO_x (ppmv)	CO (ppmv)	HCs (ppmv)	SO_2 (ppmv)
GP38	Short	45°	0.04893	0.00349	0.00349	0.00229
GP38	Short	21.8°	0.06834	0.00488	0.00487	0.00320
GP38	Long	45°	1.44415	0.10314	0.10296	0.06765
GP38	Long	21.8°	0.30381	0.02170	0.02166	0.01423
SD40	Short	49.7°	0.36723	0.07383	0.03685	0.01614
SD40	Short	8.84°	10.4923	2.10936	1.05280	0.46116
SD40	Long	49.7°	1.06756	0.21462	0.10712	0.04692
SD40	Long	8.84°	9.59582	1.92914	0.96285	0.42175

Table 11b Calculated Exhaust Concentrations at the Leeward-Side Window of the Trailing Locomotive, O_2, CO_2, Aldehydes, and N_2.

Locomotive	Hood Forward	Yaw Angle	O_2 (ppmv)	CO_2 (ppmv)	Aldehydes	N_2 (ppmv)
GP38	Short	45°	1.82078	0.77852	0.00023	13.6638
GP38	Short	21.8°	2.54299	1.08732	0.00032	19.0835
GP38	Long	45°	53.7351	22.9759	0.00673	403.248
GP38	Long	21.8°	11.3044	4.83351	0.00142	84.8327
SD40	Short	49.7°	22.4631	8.22271	0.00241	140.810
SD40	Short	8.84°	641.808	234.937	0.06886	4,023.18
SD40	Long	49.7°	65.3021	23.9042	0.00701	409.347
SD40	Long	8.84°	586.971	214.864	0.06298	3,679.43

Particulate Matter:

Emissions and exposure guidelines for diesel particulate matter are generally given in units of mass per unit volume, typically, milligrams per cubic meter. As was done with the gaseous components, a calculation procedure was developed to determine the concentrations of diesel particulate at the leeward-side windows of the leading and trailing locomotives represented in the numerical simulations. The initial calculations involve determination of the total exhaust concentration at the locomotive window locations. The concentration of exhaust, in units of percent of total mass, at the leeward-side windows of both the leading and trailing locomotives can be taken from the computer simulations. If we multiply these concentrations by 1×10^6, we obtain the entries in Table 12, which are in units of parts per million based on mass.

Table 12 Concentrations of Exhaust at Cab Windows of Leading and Trailing Locomotives on a Mass Basis

Loco-Motive	Hood Forward	Yaw Angle	Train Speed (mph)	Concentration of Exhaust at Cab Window of Lead Locomotive (ppm_{mass})	Concentration of Exhaust at Cab Window of Trailing Locomotive (ppm_{mass})
GP38	Short	45°	5	0.000	16.994
GP38	Short	21.8°	5	0.000	23.734
GP38	Long	45°	5	40.448	501.519
GP38	Long	21.8°	5	14.019	105.506
SD40	Short	49.7°	5	0.000	179.038
SD40	Short	8.84°	45	6.106	5,115.433
SD40	Long	49.7°	5	3.029	520.481
SD40	Long	8.84°	45	84.471	4,678.365

To determine the mass flow rates of particulate, the following relationship is used:

$$Mdot_p = P_s \cdot HP \tag{8}$$

where:

$Mdot_p$ = Mass Flow Rate of Particulate (kg/sec)
P_s = Measured Particulate Emissions (kg/bhp-sec)
HP = Engine Power (bhp)

For the selected engine, throttle position Notch 5 corresponds to 1,463 horsepower and Notch Position 8 corresponds to 2,120 horsepower. Thus, the particulate flow rates at the exhaust stack for these two conditions are:

Table 13 Particulate Mass Flow Rates at Exit Plane of Diesel Engine Exhaust Stack

Loco-motive	Throttle Notch Setting	Engine Power (bhp)	Tested Emissions		Particulate Mass Flow	
			Low Value (kg/bhp-sec)	High Value (kg/bhp-sec)	Low Value (kg/sec)	High Value (kg/sec)
GP38	8	2,120	3.89×10^{-8}	6.67×10^{-8}	8.25×10^{-5}	1.41×10^{-4}
SD40	5	1,463	3.89×10^{-8}	6.67×10^{-8}	5.69×10^{-5}	9.76×10^{-5}

To calculate the particulate concentrations at the cab window locations, the following relationship was used:

$$\text{Particulate Concentration } (mg/m^3) = [(MF_e) \times (MFR_p / MFR_e)] \times [\rho_m] \times (10^6 \text{ mg/kg}) \tag{9}$$

where: MF_e = mass fraction of exhaust at leeward window location (from simulation)
MFR_p = mass flow rate of particulate at exhaust stack (kg/sec)

MFR_e = mass flow rate of exhaust (kg/sec)
ρ_m = density of air and exhaust gas mixture

The density of the air and exhaust gas mixture can be determined from the ideal gas law:

$$\rho_m = [(T_{ssc} + 273\ ^oC)/(T_w + 273\ ^oC)] \times [\rho_{ssc}] \quad (10)$$

where: T_{ssc} = Temperature (^oC) at sea level, standard conditions
T_w = Temperature at window location (^oC)
ρ_{ssc} = Density at sea level, standard conditions

The results of the particulate concentration analysis for both the leading and trailing locomotives and for the lower and upper value of measured particulates at the stack are presented in Tables 14 and 15.

Table 14 Particulate Concentrations at Cab Windows of Leading and Trailing Locomotives Based on Lower Value of Particulate Emissions at Stack.

Loco-Motive	Hood Forward	Yaw Angle	Train Speed (mph)	Concentration of Particulate at Cab Window of Lead Locomotive (mg/m^3)	Concentration of Particulate at Cab Window of Trailing Locomotive (mg/m^3)
GP38	Short	45°	5	0.0000	0.0005
GP38	Short	21.8°	5	0.0000	0.0007
GP38	Long	45°	5	0.0011	0.0142
GP38	Long	21.8°	5	0.0004	0.0030
SD40	Short	49.7°	5	0.0000	0.0046
SD40	Short	8.84°	45	0.0002	0.1303
SD40	Long	49.7°	5	0.0001	0.0133
SD40	Long	8.84°	45	0.0022	0.1192

Table 15 Particulate Concentrations at Cab Windows of Leading and Trailing Locomotives Based on Upper Value of Particulate Emissions at Stack.

Loco-Motive	Hood Forward	Yaw Angle	Train Speed (mph)	Concentration of Particulate at Cab Window of Lead Locomotive (mg/m^3)	Concentration of Particulate at Cab Window of Trailing Locomotive (mg/m^3)
GP38	Short	45°	5	0.0000	0.0008
GP38	Short	21.8°	5	0.0000	0.0012
GP38	Long	45°	5	0.0020	0.0244
GP38	Long	21.8°	5	0.0007	0.0051
SD40	Short	49.7°	5	0.0000	0.0078
SD40	Short	8.84°	45	0.0003	0.2234
SD40	Long	49.7°	5	0.0001	0.0228
SD40	Long	8.84°	45	0.0037	0.2044

Results and Conclusions, Section III: Diesel Exhaust Plume Behavior

Calculation procedures have been developed to determine the concentrations of diesel exhaust components, both gaseous and particle, at the leeward-side operator's cab window for both leading and trailing locomotives. Exhaust concentrations were obtained from CFD simulations and component concentrations were defined using the calculation procedures.

Calculations of the exhaust concentrations and exhaust components at the locomotive leeward-side windows showed several interesting results.

a) In switchyard and low-train-speed operations, exhaust concentrations at the trailing locomotive window are typically 10 to 800 times greater than those at the leading locomotive window when both locomotives have the same hood orientation.
b) In switchyard and low-train-speed operations, exhaust concentrations at the leeward-side window of the leading locomotive when operated with the long-hood-forward are between 3 and 30 times greater than those at the same location when the locomotive is operated with the short-hood-forward.
c) For line-haul operations, the recirculation zone on the leeward side of the locomotives is very strong and remains in closer proximity to the leeward side of the train. Exhaust concentrations at the leading locomotive cab leeward-side window with the locomotives oriented with the long-hood-forward are 14 times greater than those at the same location when the locomotives are oriented with the short hood forward. For the trailing locomotive, the exhaust concentrations at the leeward window are nearly equal for both the short-hood-forward and long-hood-forward orientations, again due to the strong vortex (recirculation zone) present in this area during high-speed operation.
d) The same trends were seen with the concentrations of particulate matter.
e) Because of the strong vortex pattern and high levels of turbulence on the leeward side of the locomotive, the diesel exhaust components are transported to the interior of the operator's cab through open windows. For high-speed line-haul operation, diesel exhaust components are present at the operator's cab window even when the locomotive is operated with the short-hood forward.

Conclusions and Suggestions for Future Research

CFD methods have been shown to be effective at evaluating the aerodynamics of rail cars and locomotives. The methods were employed to quantify the drag characteristics of external railcar features including well car side-posts and inter-platform gaps. Simulation results were coupled with wind tunnel tests to develop a database of tip-over tendencies for a variety of car types. Additionally, CFD models were developed for several locomotives operating under a number of ambient conditions (wind speed, wind direction). The concentration of diesel exhaust at the operator cab window was quantified. Correlations of the CFD results with previously collected wind tunnel and field data were performed for many of the simulations.

Additional research is suggested including: continued evaluation of rail car drag reduction designs using advanced CFD methods, additional wind tunnel and field tests to verify the various CFD models, and wind tunnel measurements of exhaust plume concentrations to verify simulation results.

Acknowledgments

This work was funded by the following organizations, which also approved release of the results: 1) Aerodynamic Drag Reduction: The Greenbrier Companies, 2) Wind-Induced Tip-Over: Norfolk Southern Railway Company, and 3) Diesel Exhaust Plume Behavior: Doffermyre Shields Canfield Knowles & Devine, LLP, and Romanucci & Blandin, LLC. Preparation of this paper was funded by Airflow Sciences Corporation.

References

[1] Anderson D., Tannehill J and Pletcher R, *Computational Fluid Dynamics and Heat Transfer*, Washington, Hemisphere Publishing Corporation, 1984.
[2] Wesseling P, *Principles of Computational Fluid Dynamics*, Heidelberg, Springer-Verlag, 2000.
[3] McCallen R, Browand F and Ross J (Editors), *The Aerodynamics of Heavy Vehicles: Trucks, Buses, and Trains,* New York, Springer-Verlag, 2004.
[4] Hucho W (Editor), *Aerodynamics of Road Vehicles*, Fourth Edition, Society of Automotive Engineer, Warrendale, Pennsylvania, 1998.
[5] Nelson R and Banka A, *VISCOUS Users Guide*, Livonia, Michigan, Airflow Sciences Corporation, 1993.
[6] Patankar S, *Numerical Heat Transfer and Fluid Flow*, New York, Hemisphere Publishing Corporation, 1980.
[7] *FLUENT 6.3 User's Manual,* Lebanon, New Hampshire, ANSYS, Inc., 2007.

[8] Launder B and Spalding D, *Mathematical Models of Turbulence*, New York, Academic Press, 1972.
[9] Launder B and Spalding D, "The Numerical Computation of Turbulent Flow", *Comp. Methods Appl. Mech. Eng.,* vol. 3, 1974, p. 269.
[10] Ahmed S, "Some Applications of RANS Methods", Section 15.6.3.2, Computational Fluid Dynamics, Chapter 15, *Aerodynamics of Road Vehicles*, Hucho, W. H. (Editor), Fourth Edition, Society of Automotive Engineer, Warrendale, Pennsylvania, 1998.
[11] Ellis H, *The Pictorial Encyclopedia of Railways*, New York, Hamlyn Publishing Corporation, 1968, pp. 12-30.
[12] Hammitt A, "Aerodynamic Forces on Freight Trains, Volume I – Wind Tunnel Test of Containers and Trailers on Flatcars", U. S. Department of Commerce, NTIS PB-264 304, December 1976.
[13] Joshi P, "Aerodynamic Forces on Freight Trains, Volume II – Full-Scale Aerodynamic Validation Tests of Trailer-On-A-Flat-Car (Series II)", U.S. Department of Commerce, NTIS PB-281 823, March 1978.
[14] Hammitt A, "Aerodynamic Forces on Freight Trains, Volume III – Correlation Report, Full Scale Trailers on Flat Cars and Comparison with Wind Tunnel Results", U.S. Department of Commerce, NTIS PB-288 137, September 1978.
[15] Hammitt A, "Aerodynamic Forces on Freight Trains, Volume IV – Wind Tunnel Tests of Freight Cars and New Trailer and Container Car Designs", U.S. Department of Commerce, NTIS PB80-174 899, June 1979.
[16] Hammitt A, "Aerodynamic Forces on Various Configurations of Railroad Cars for Carrying Trailers and Containers. Wind Tunnel Tests of Six Scale Model Configurations", U. S. Department of Commerce, NTIS PB80-174881, January 1979.
[17] Arnold G, "Synopsis, Full-Scale Aero-Drag-Measuring Gondola Car", Workshop on the Aerodynamic Drag of Trains, Derbyshire College of Higher Education, Derby, U.K., April 7-9, 1986.
[18] Gawthorp R, "Aerodynamics of Trains in the Open Air", *Railway Engineer International*, Volume 3, No. 3, May-June 1978, pp. 7-12.
[19] Dayman D, "Demonstration of the Coast-Down Technique for Determining Train Resistances", Final Report, Jet Propulsion Laboratory, Pasadena, California, Publication No. 83-85, October 1983.
[20] Goss W, "Atmosphere Resistance to the Motion of Railway Trains", *The Engineer*, 1898 (conducted at Purdue University).
[21] Hoerner S, "Efficiency of Railroad Trains", *Fluid Dynamic Drag*, Hoerner Fluid Dynamics, Brick Town, New Jersey, 1965, pp. 12-10 to 12-15.
[22] Tietjens O and Ripley K, "Air Resistance of High-Speed Trains and Interurban Cars", *Transactions ASME*, Vol. 54 (APM-54-23), 1932, pp. 235-251.
[23] Davis W, "The Traction Resistance of Electric Locomotives and Cars", *General Electric Review*, Vol. 29, October 1926, pp. 685-707.
[24] Hay W, *Railroad Engineering*, New York, John Wiley and Sons, 1982, pp. 69-89.
[25] Engdahl R, Gielow R and Paul J, "Train Resistance – Aerodynamics, Volume I of II, Intermodal Car Aerodynamics", Association of American Railroads, 1987.
[26] Paul J, Gielow R, Holmes A and Hickey P, "Reduction of Intermodal Car Aerodynamic Drag through Computerized Flow Simulation", American Society of Mechanical Engineers, Paper 83-RT-4, 1983.
[27] Arad U, *The 1973-1974 Arab Oil Embargo: Facts, Figures and Analysis*, Washington, D.C., Hudson Institute, 1974.
[28] Widjaja D, Scofield J, Holmes A and Gielow R, "An Application of Airflow Modeling Methods to the Santa Fe 10-Pack Fuel Foiler", Livonia, Michigan, Airflow Sciences Corporation Report R-80-004, 1 October 1980.

[29] MacFadyen A, Widjaja D, Holmes A, Paul J and Gielow R, "An Aerodynamic Drag Comparison of Streamlined and Conventional Locomotives Utilizing Numerical Airflow Simulation Methods", Livonia, Michigan, Airflow Sciences Corporation Report R-81-011, June 1981.
[30] Hickey P, MacFadyen A, Holmes A, Paul J and Gielow R, "An Aerodynamic Analysis of the Trailer Train Company 4-Runner Intermodal Car Using Numerical Flow Simulation Methods", Livonia, Michigan, Airflow Sciences Corporation Report R-82-005, 7 May 1982.
[31] Hickey P, Gielow R, Holmes A and Paul J, "Aerodynamic Drag Analysis of the Lo-Pac 2000 Intermodal Car", Livonia, Michigan, Airflow Sciences Corporation Report R-82-011, 15 September 1982.
[32] Gielow R, Holmes A and Paul J, "Aerodynamic Drag Analysis of the Ortner 100-Ton Rapid Discharge Car", Livonia, Michigan, Airflow Sciences Corporation Report R-82-014, 15 December 1982.
[33] Hickey P, Gielow R, Holmes A and Paul J, "Aerodynamic Modifications to the Budd Lo-Pac 2000 Intermodal Car", Livonia, Michigan, Airflow Sciences Corporation Report R-83-001, 31 January 1983.
[34] Hickey P, Holmes A, Paul J and Gielow R, "Aerodynamic Design Study of an Aluminum Gondola Car for Pullman Standard", Livonia, Michigan, Airflow Sciences Corporation Report R-83-005, 1 April 1983.
[35] Hickey P, Gielow R and Paul J, "An Aerodynamic Treatment Package for the Ortner Four Pocket Rapid Discharge Coal Car", Livonia, Michigan, Airflow Sciences Corporation Report R-83-013, 5 August 1983.
[36] Paul J, Smith T, Gielow M and Gielow R, " 3/10 Scale Wind Tunnel Test of Skeletonized and Well-Type Intermodal Rail Cars", Livonia, Michigan, Airflow Sciences Corporation Report R-83-019, 1 October 1983.
[37] Paul J, Nelson R, Groesbeck P, Polihonki D, Banka A, Keeler D and Gielow R, "3/10 Scale Hopper and Gondola Rail Car Wind Tunnel Test", Livonia, Michigan, Airflow Sciences Corporation Report R-84-019, 28 December 1984.
[38] Paul J and Gielow R, "Aerodynamic Enhancements of the Trailer Train Front Runner Single Platform Rail Car", Livonia, Michigan, Airflow Sciences Corporation Report R-84-009, 1 June 1984.
[39] Gielow R, Keeler D, Polihonki D, deJager D and Paul J, "16% Scale Gondola, Locomotive, and 89 Foot Car Wind Tunnel Test", Livonia, Michigan, Airflow Sciences Corporation Report R-85-011, 31 January 1986.
[40] Engdahl R, Gielow R and Paul J, "Train Resistance – Aerodynamics, Volume II of II, Open Top Car Applications", Association of American Railroads, 1987.
[41] Furlong C, Gielow M., Gielow R Paul J and Nelson R, "Results of Wind Tunnel and Full-Scale Tests Conducted from 1983 t 1987 in Support of The Association of American Railroad's Train Energy Program", Livonia, Michigan, Airflow Sciences Corporation Report Number R-88-010, 30 December 1988, AAR Report R-685.
[42] Furlong C, Gielow R, Paul J and Nelson R, "Aerodynamic Subroutine User's Guide, Train Aerodynamics Simulator", Livonia, Michigan, Airflow Sciences Corporation Report R-88-003, 15 July 1988.
[43] Polihonki D, Paul J and Banka A, "An Aerodynamic Optimization of the Front End Design for a Proposed Euroshuttle Train Double Deck Loader", Livonia, Michigan, Airflow Sciences Corporation Report R-90-003, 15 January 1990.
[44] Johnson R, "Fuel Consumption Analysis of Various Railcars", Livonia, Michigan, Airflow Sciences Corporation Report L-94-GB1-4, 12 September 1994.
[45] Johnson R, "Auto Hauler Fuel Consumption Analysis", Livonia, Michigan, Airflow Sciences Corporation Report L-98-GBC-1, 28 April 1998.
[46] Johnson R, "Wind Tunnel Results of a 16%-Scale Partitioned Gondola Car", Livonia, Michigan, Airflow Sciences Corporation Report L-04-ICE-1, 15 December 2004.

[47] Johnson R, "CFD Analysis of Smooth-Side (Husky-Stack 53) and Side Post 53 Foot Well Cars", Livonia, Michigan, Airflow Sciences Corporation Report L-06-GB5-3, 29 November 2006
[48] Johnson R, "Coal Car Aerodynamics", Livonia, Michigan, Airflow Sciences Corporation Reports L-06-BNS-1 and L-07-BNS-1, 5 December 2006 and 18 April 2007.
[49] Johnson R, "Maxi-X AP1 and Maxi-X MS Fuel Consumption Results", Livonia, Michigan, Airflow Sciences Corporation Report L-94-GBI-1, 24 June 1994.
[50] Watkins S, Saunders J and Kumar H, "Aerodynamic Drag Reduction of Goods Trains", *Journal of Wind Engineering and Industrial Aerodynamics"*, Vol. 40 (1992) pp. 147-178.
[51] Saunders J, Watkins S and Cassar R., "Vortex Optimisation of Slotted Tops and Cavities of Two Different Open Rail Wagons", *Journal of Wind Engineering and Industrial Aerodynamics*, Vol. 49 (1993), pp. 421-430.
[52] Johnson R, "CFD Analysis of Enhanced HS 40X US Well Car", Livonia, Michigan, Airflow Sciences Corporation Report L-07-GB3-1, 27 February 2007.
[53] Matschke G, Tielkes T, Deeg P and Schulte-Werning B, "Effects of Strong Cross Winds on High-Speed Trains – A Risk Assessment Approach", International Association for Probabilistic Safety Assessment and Management, PSAM5 Conference, Osaka, Japan, 27 November 2000.
[54] Andersson E, Haggstrom J, Sima M and Stichel S, "Assessment of Train-Overturning Risk Due to Strong Cross-Winds", Proceedings of the I MECH E Part F *Journal of Rail and Rapid Transit*, Volume 21 B, Number 3, 1 September 2004.
[55] Sanquer S, Barre C, Dufresne de Virel M and Cleon L, "Effects of Cross Winds on High-Speed Trains: Development of a New Experimental Methodology", *Journal of Wind Engineering and Industrial Aerodynamics*, Vol. 92, Issues 7-8, June 2004, pp. 535-545.
[56] MacNeill R, Holmes S and Lee H, "Measurement of the Aerodynamic Pressures Produced by Passing Trains", *Proceedings of the 2002 ASME/IEEE Joint Rail Conference*, Washington, DC, 23-25 April 2002.
[57] Holmes S, Toma E and Schroeder M, "High-Speed Passenger and Intercity Train Aerodynamic Computer Modeling", *Proceedings of ME2000*, The 2000 International Mechanical Engineering Congress & Exposition, Orlando, Florida, 5-10 November 2000.
[58] Hoppmann U, Koenig S, Tilkes T and Matschke G, "A Short-Term Strong Wind Prediction Model for Railway Application; Design and Verification", *Journal of Wind Engineering and Industrial Aerodynamics*, Vol. 90, 2002, pp. 1127-1134.
[59] Polihonki D, Paul J, Gielow R and Nelson R, "An Aerodynamic Evaluation of the Front End Design for a Bombardier Mass Transit Division Proposed Euroshuttle Train Double Deck Loader (DDL) Wagon, Livonia, Michigan, Airflow Sciences Corporation Report R-90-003, 15 January 1990.
[60] Gielow M, Polihonki D, Gielow R Paul J and Nelson R, "A Train-Speed-Restricting System to Achieve Safe Operations under High Wind Conditions Along Certain Union Pacific Routes", Livonia, Michigan, Airflow Sciences Corporation Report R-88-006, 26 August 1988.
[61] Johnson R, "Auto-Max Tip-Over Analysis", Livonia, Michigan, Airflow Sciences Corporation Report L-98-GB1-1, 12 August 1998.
[62] Johnson R and Nelson R, "Norfolk Southern Company Sandusky Bay Speed Restricting System", Livonia, Michigan, Airflow Sciences Corporation, Report R-06-NF1-1, 3 April 2006.
[63] Paul J, Groesbeck P, Gielow M, Keeler D, Banka A and Gielow R, "Southern Pacific Transportation Company 3/10 Scale Double-Stack Container Car Wind Tunnel Test", Livonia, Michigan, Airflow Sciences Corporation Report R-84-015, 4 October 1984.
[64] Peters J, "How to Reduce the Cross Wind Sensitivity of Trains", *The Aerodynamics of Heavy Vehicles: Trucks, Buses, and Trains,* McCallen, R., Browand, F., and Ross, J. (Editors), New York, Springer-Verlag, 2004, pp. 453-467.

[65] Bhatia R, Lopipero P and Smith A, "Diesel Exhaust Exposure and Lung Cancer", *Epidemiology*, Vol. 9 (1), January 1998, pp. 84-91.
[66] Nauss K, "Diesel Exhaust: A Critical Analysis of Emissions, Exposure, and Health Effects; Summary of a Health Effects Institute (HEI) Special Report: HEI Diesel Working Group", Cambridge, Massachusetts, DieselNet Technical Report, October 1997.
[67] Woskie S, Smith T, Hammond S, Schenker M, Garshick E and Speizer F, "Estimation of the Diesel Exposures of Railroad Workers: I. Current Exposures", *American Journal of Industrial Medicine*, Vol. 13, 1988, pp. 381-394.
[68] Woskie S, Smith T, Hammond S, Schenker M, Garshick E and Speizer F, "Estimation of the Diesel Exhaust Exposures of Railroad Workers: II. National and Historical Perspectives", *American Journal of Industrial Medicine*, Vol. 13, 1988, pp. 395-404.
[69] Correspondence, Brotherhood of Locomotive Engineers and Trainsmen, Cleveland, Ohio, 1986-1989.
[70] Liukonen L, Grogan J and Myers W, "Diesel Particulate Exposure to Railroad Train Crews", *American Industrial Hygiene Association Journal*, Vol. 63 (5), Sep.-Oct. 2002, pp. 610-616.
[71] "Diesel Engine Exhaust", *Health Hazard Advisory*, Hazard Evaluation System & Information Service, California Department of Health Services, Occupational Health Branch, November 2002.
[72] American Society of Heating, Refrigeration, and Air Conditioning Engineers (ASHRAE), *2007 ASHRAE Handbook*, Chapter 44, "Building Air Intake and Exhaust Design, Atlanta Georgia, 2007.
[73] Banka A, Gielow M., Paul J and Gielow R, "A Wind Tunnel Evaluation of Engine Exhaust Flow Patterns from a C39-8 Locomotive, Long Hood Forward", Livonia, Michigan, Airflow Sciences Corporation Report R-86-015, 26 September 1986.
[74] Ellsworth K, (Editor), and Houser F and Whitney D (Contributing Editors), *The Car and Locomotive Cyclopedia of American Practice*, Fourth Edition, Simmons-Boardman Publishing Corporation, Omaha, Nebraska, 1980.
[75] Paul J, Linfield K and Banka A, "Determination of Diesel Exhaust Plume Concentrations within Operator Cabs of Selected Locomotives", Livonia, Michigan, Airflow Sciences Corporation Report R-04-DS1-01, 3 December 2004.
[76] Paul J and Linfield K, "Assessment of Diesel Exhaust Plume Exposure Levels within Operator Cabs of Railroad Locomotives", Livonia, Michigan, Airflow Sciences Corporation Report R-06-RBL-01, 19 October 2006.
[77] National Climatic Data Center, Asheville, North Carolina, *Climatic Wind Data for the United States*, November 1998, for the time period 1930 through 1996. Refer to Web Site: www.ncdc.noaa.gov.
[78] Fritz S, Southwest Research Institute, "Locomotive Exhaust Emissions: Past Studies, Present Work, and Future Challenges", Presentation to the Society of Automotive Engineers, TC-9 Committee Meeting, Salt Lake City, Utah, January 1998.
[79] Fritz S, Southwest Research Institute, "Emissions Measurements – Locomotives", EPA Work Assignments 1-4 and 2-4, Contract No. 68-C2-0144, SwRI Report No. 5374-024, August 1995.
[80] Bauer H, Editor in Chief, *Bosch Automotive Handbook*, 4th Edition, 1996, Published by Robert Bosch GmbH, "Exhaust Emissions from Diesel Engines", pp. 530-531.
[81] Fritz S, Southwest Research Institute, "Diesel Fuel Effects on Locomotive Exhaust Emissions", 23rd CIMAC Congress, Paper No. 7A-05, May 2001.
[82] Video Tape (VHS Format) provided by General Electric Transportation Systems, GE WMM Loco Track Test on NS Smoke Ventilation", 17 August 1989.
[83] Whitaker L, "Diesel Exhaust Fume Study in GE C39-8 Cabs", Norfolk Southern Corporation, Mechanical Department, File 142.3, 22 August 1988.
[84] Beem D, "Diesel Fume Monitoring, Locomotive 3532", Norfolk Southern Corporation, File IH13, 13 September 1994.

Data Acquisition of a Tractor-Trailer Combination to Register Aerodynamic Performances

Gandert M.R. Van Raemdonck and Michel J.L. van Tooren

Faculty of Aerospace Engineering - Delft University of Technology - 2629HS Delft, The Netherlands
g.m.r.vanraemdonck@tudelft.nl

Abstract The design, production and verification of a data acquisition system to measure aerodynamic and mechanical characteristics of a tractor-trailer combination, operating in a real life environment, are presented. The main goal of this work is to derive a reference level of a truck with respect to its aerodynamic and mechanical performances. This way, if the truck is equipped with different aerodynamic aids, a correct comparison can be made between the aerodynamic drag reductions obtained by these devices. Also, a relation can be defined which links the aerodynamic drag reduction with fuel consumption savings. The acquisition system consists of an anemometer, which measures the wind speed and direction, and a two-axis inclination indicator, which is coupled to the FMS of the tractor via the CAN communication system and to the wipers to indicate if it is raining or not. The FMS of the tractor is measuring, for instance, the vehicle speed, the engine torque, the rpm, acceleration pedal position, cruise control, fuel rate, cargo weight and the like. All the measured data are registered on a hard disk and can be accessed through a simple USB connection. The processed data gives insight in the performance of the driver and in the aerodynamic behavior (C_D value of 0.430) as well as the mechanical characteristics (power required breakdown; 47% rolling resistance, 39% aerodynamic drag and 15% mechanical losses; average speed of 75 km/h; fuel consumption of 30 liters per 100 km) of the truck.

1 Introduction

The heavy duty transport industry which uses trucks to transport cargo is a very large business area since it is still the most used transport solution to deliver consumer goods. This fact manifests itself in an increasing amount of trucks on the road and in increased total fuel consumed, together with the related cost, for road transport. Due to the rising fuel prices it is crucial however, to find solutions

for this high fuel cost in order to stay competitive in this aggressive and fast changing market due to, for instance, the growth of the European Union. Generally there are two ways to reduce the fuel consumption of a vehicle. One can improve the efficiency of the available power which means an increase of the power delivered by the engine or, on the other hand, the required power that is needed to overcome the forces needs to be lowered. Considering the latter, it signifies achieving a reduction of fuel consumption by minimizing the weight of the vehicle and/or reducing its aerodynamic drag. Also the friction resistance of the tires is an important aspect with respect to the fuel consumption of road vehicles.

The reduction of fuel consumption of trucks by aerodynamic means has become an accepted practice in the last decades by mounting add-on devices for the tractor and the trailer. Also modifications of the main shape of the vehicle improved the aerodynamic efficiency in a positive way. Besides extensive wind tunnel testing, road testing of the aerodynamic devices is needed to convince the transportation market of the effectiveness of the aids. In this perspective a data acquisition system is designed, built and installed on a truck for the purpose of collecting data of the aerodynamic and mechanical performances of the vehicle and to register the behavior of the truck driver. The following collected parameters offer a complete overview of the performances: wind speed and direction, inclination and banking angle, vehicle speed, torque, rpm, vehicle weight, fuel consumption, distance traveled, cruise control activation, brake and acceleration pedal position.

The data acquisition system will be used to define a reference level of a particular truck, which is the starting point to compare different measured fuel economy improvements of several aerodynamic aids consistently. It also makes it possible to define a relation between the aerodynamic drag reduction and the fuel savings like M.J. Rose [1]. Previous road tests and investigations [2, 4, 3] have shown that the side wind is responsible for a small, but impossible to ignore, drag rise. In this respect it is important to consider a certain range of side winds during the design of vehicles and aerodynamic devices. Therefore the vehicle speed and wind direction are being measured and can be used as input data for numerical simulations and wind tunnel experiments.

The results which are discussed below are obtained from the installed data acquisitions system in a European tractor-trailer configuration of Jan de Rijk Transport (DAF XF95 type Space-cab with 3-axle trailer) which was transporting cargo all through West Europe in the period of February until July 2006. The registered data was downloaded weekly and processed with the aid of Matlab in order to get the desired output.

2 Sensors

WindSonic

The wind direction and speed is measured with the Windsonic [5], Fig.1, provided by Gill instruments. The WindSonic is a lightweight unit (0.5 kg) of robust construction, manufactured in a polycarbonate blend material which proved to installation and use without damage. The WindSonic measures the time taken for an ultrasonic pulse of sound to travel from the North transducer to the South transducer, and compares it with the time for a pulse from S to N transducer. In the same way the times are compared between West and East, and E to W transducers. The output of the WindSonic goes via a RS232 protocol and is picked up by a RS232 to CAN (Controller Area Network) device developed by Squarell Technology [6]. In order to guarantee the accuracy of the measurements it is important to know if it's raining. Therefore a sensor cable is connected to the engines of the windscreen wipers.

2-axis incline indicator

The second sensor mounted on the chassis of the truck is the two-axis incline indicator [7], which measures the pitching and banking angle, fig.1. The two-axis incline indicator has die cast aluminum housing with two integrated sensors for measuring inclinations along two axes. As well as the sensors, the box contains two independent signal conditioners, each with a 4-20mA, 2-wire output, and two separate voltage supply feeding of the corresponding current loop, one for each sensor. The two-axis incline indicator gives a range of 4 to 20 mA as output signal that corresponds to the calibrated range of angles. The Volt-mAmpere device of Squarell Technology receives the mA signals in a proper way.

Fleet Management System

Recent modern trucks are equipped with a Fleet Management System (FMS) which is a communication system with CANbus cable connections that measures and can register many variables amongst others engine power and torque, fuel consumption, velocity, rpm, vehicle weight, etc. according to the performance and the behavior of the truck and its driver. This data should enable us to create a blueprint of the circumstances of the surroundings and break up the total required

power in the different components. The sensors that are being used by the FMS to measure the truck related data are standard and already present on the truck.

3 Data Acquisition System

The desired data is logged with the aid of an ILogCan device developed by Squarell Technology. The ILogCan which is being used can store a total amount of 516MB and is linked simply with a USB-cable connected to a laptop to log the data. A special cable will link the ILogCan trough the FMS-plug to the CANbus communication system of the truck.

The total data acquisition system together with both the WindSonic and the 2-axis incline indicator are being installed in the cabin, on the roof of the cabin and onto the chassis of the truck behind the cabin of the DAF XF95. The different Squarell devices (RS323 to can, digital input device, V-mA device and ILogCan) are orderly assembled together into a waterproof electro box, Fig.1.

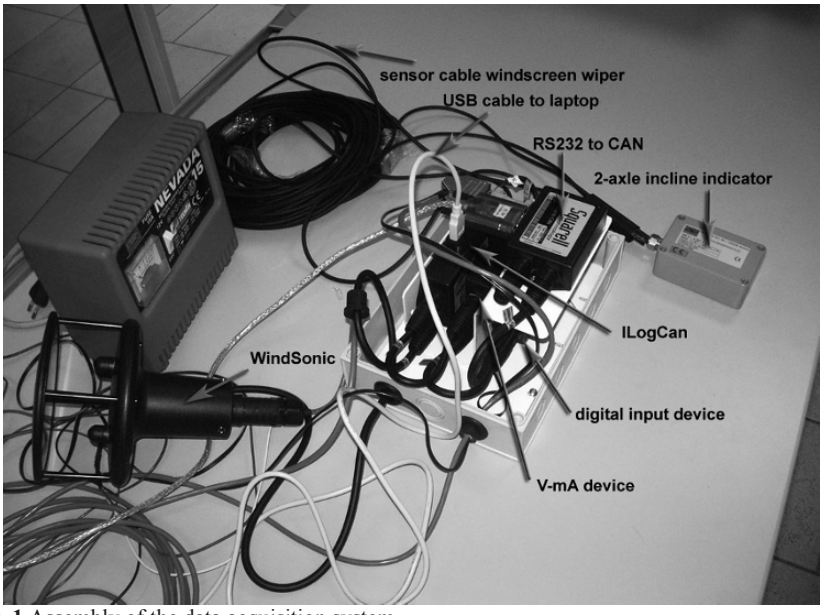

Fig. 1 Assembly of the data acquisition system.

The ILogCan is linked to the board computer of the truck through a special FMS to a DAF cable plugged in the CDM (Command Data Module) unit in the fuse box of the truck. The 12V power supply for the data acquisition system and the Wind- Sonic are also situated in this fuse box behind the passenger dashboard. A special bracket of stainless steel for the WindSonic is made to provide enough stiffness and is mounted in the symmetric plane just in front at the top roof of the

cabin. The two-axis incline indicator is fixed onto the chassis behind the cabin with a small stainless plate together with simple vibration dampers and bolts.

4 Results

The 500MB of data obtained by the measurement system is saved in four different text-files and are analyzed and processed with the aid of Matlab. The data acquisition system and the sensors were installed in the DAF XF95 at the beginning of February. Only the measurements from the 22th of May until the 28th of June 2006 will be discussed. The 28th of June was the last day of the measurements and the day the system was disassembled from the truck. To reduce the amount of working and memory time, the number of cells are reduced by taking an average over four measuring points, meaning that each value represents 2 seconds in time. With the aid of descriptive statistics and SPSS more general insight in the performance of the vehicle is possible. Besides the descriptive statistics possible relations between the different measured parameters are being investigated.

4.1 Descriptive Statistics

Vehicle velocity

Figure 2a shows the frequencies (number of measuring points during the test period) of the vehicle speed during the measuring period. The first thing that catches the eye is the large amount of time (in terms of percentage) when the vehicle is standing still. Also two different peaks at 80 km/h and 90 km/h are noticeable. Apparently the driver is driving at different maximum velocities in different countries. The average speed considering the whole data set is equal to 60 km/h while the average vehicle speed without the stops of the vehicle is 75 km/h. This second data set showed that 40% of the time the velocity was higher than 89 km/h.

Wind direction and wiper

Defining a range of wind directions is important for the wind tunnel tests to obtain a realistic representation of the real circumstances concerning the wind direction. The wind directions which are corresponding with the zero vehicle velocities are filtered out of the data set. A histogram of all the different measured wind directions (180° corresponds with straight ahead wind) during the described period can be seen in Fig.2b. The percentile table indicates that 30% of the total

number of occurring wind directions is centered around 178° and 179°. The range 170°-190° represents 88% of the total range of wind directions. The histogram tell us that more directions are measured which are coming from the left (direction lower than 180°). This statement is also supported by a skewness of 1,288 for the data set. The wipers were activated when it was raining during the registration period. Within rainy conditions the WindSonic is not measuring well. Only 4% of the testing period, it was raining, meaning that only 4% of the total data measured by the WindSonic and plot in the above figures is not reliable. This 4% is plausible due to the very hot weather between 22th of May and 28th of June 2006.

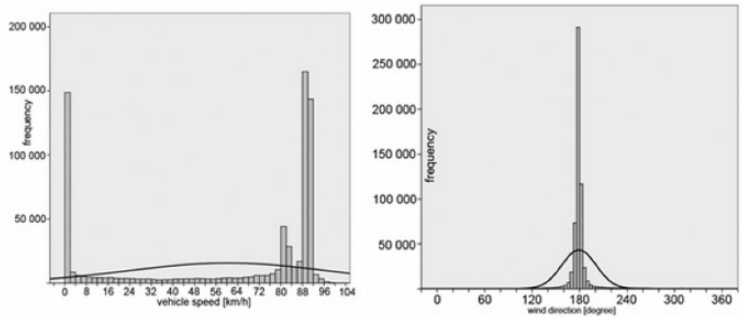

Fig. 2 (a) Overview of the measured vehicle velocities together with the mean; (b) Overview of the filtered wind directions together with the mean.

Acceleration pedal position, cruise control activation and brake switch

The behavior of the truck driver with respect to the acceleration pedal position is summarized in the next Fig.3a. Very remarkable is that during almost 75% of the time he does not touch the acceleration pedal. 8.6% of the rest of the time the driver is touching the pedal full throttle. Figure 3b tells us that 44.7% of the total time the driver has activated the cruise control. From the time the truck driver is not pushing down the acceleration pedal 6.7% he is braking to decelerate the vehicle.

Fuel rate and total fuel

The ratio between the total fuel used and the total distance traveled for the whole testing period is 0.3. In other words, 30 liters of diesel is consumed per 100 km traveled.

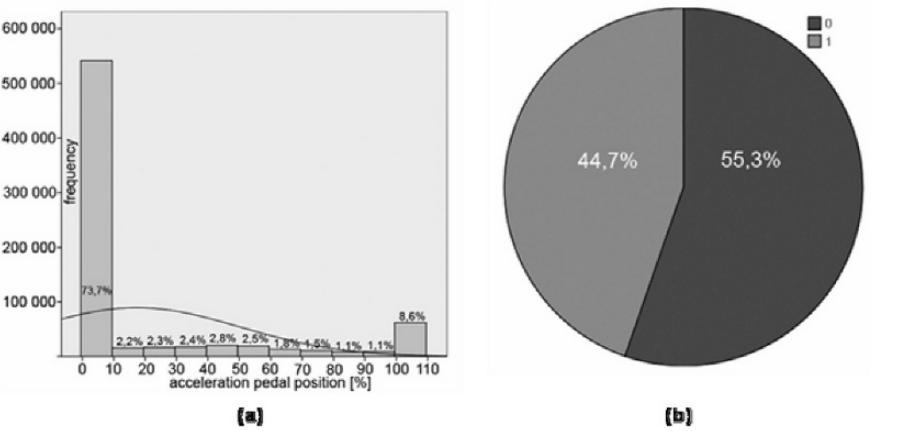

Fig. 3 (a) Overview of the acceleration pedal position together with the mean; (b) Indication of the cruise control activation.

4.2 Relations

Drag coefficient estimation

Equation.1 below describes the measured delivered power in relation to the different required power contributions to overcome the aerodynamic and friction forces and the total losses.

$$P_{req} = D_{aero} \cdot V + F_{friction} \cdot V + P_{losses} \quad (1)$$

P_{req} corresponds to the required power that is produced by the engine and is registered by the data acquisition system whereas $D_{aero} \cdot V$ is the aerodynamic force multiplied by the vehicle velocity. The friction force $F_{friction}$ originates from the friction between the wheels of the truck and the road. The friction force is dependent on the normal force N and the rolling resistance coefficient μ. The normal force N equals the weight m times the gravitational acceleration g. The weight m is composed out of the weight of the truck together with the trailer and the cargo.
Due to the absence of the required sensor to measure the cargo weight only a rough estimation could be made of the cargo weight. The rolling resistance coefficient depends mainly on the load, the inflation pressure; the speed and the remaining tire tread depth. A rolling coefficient of 0.0072 is suggested by Goodyear. The last variable in Eq.1 is the total power loss P_{losses} due to mechanical friction. If these total losses are known one can make an estimation of the drag coefficient of the truck with the aid of the measured delivered power and the calculated wheel

friction force. People of the DAF distribution center in Zwolle, The Netherlands provided a performance diagram of a DAF XF95 tractor which was equipped with the same engine (280kW/381hp) identical to the truck being used. This performance diagram can be seen in Fig.4a and is obtained by testing the particular tractor on a testing bench with a load of a half ton on the traction axis. The figure resembles the power delivered by the engine, the power measured at the wheels, the power loss (which is the difference between power engine and power loss) and finally the torque with respect to the engine revolutions per minute.

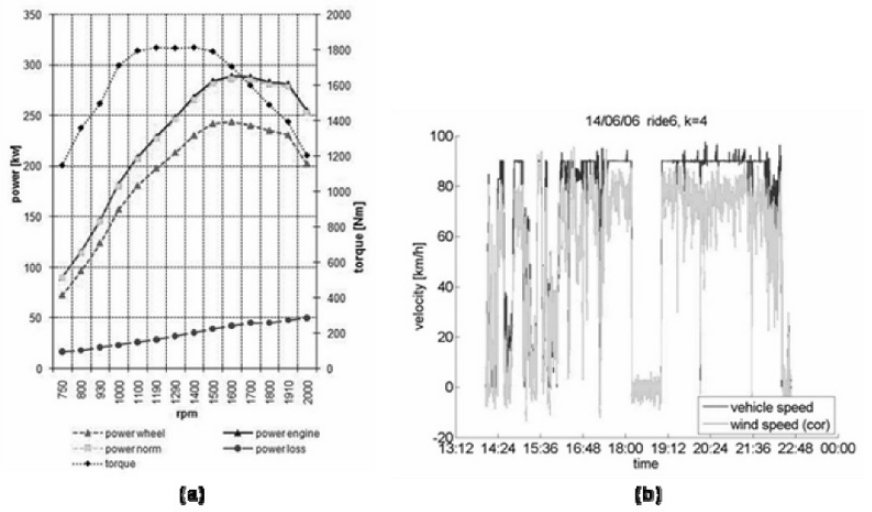

Fig. 4 (a) Engine performance diagram for a DAF XF95; (b) Estimated drag coefficient together with vehicle velocity.

With this data, a relation can be defined between the engine power and the power loss. This way the power due to total losses P_{loss} can be calculated with respect to the required power that is measured by the data acquisition system. In Fig.4b the estimated drag coefficient is plotted together with vehicle speed, the velocities below the 23m/s are filtered away in order to get the maximum constant velocity.

The average drag coefficient, based on a frontal area of 10.34m2, for the whole testing period of two months is 0.430. Within this estimation also the assumption is made that the vehicle does not generates downforce, which has an influence on the friction forces between the tires and the surface. Van Raemdonck [8] performed numerical simulations of a full scale symmetrical model of the same truck used during the data acquisition. A drag coefficient $C_D = 0.384$ was obtained after the numerical simulations. The difference between the estimated drag coefficient and the one simulated with the aid of computation fluid dynamics (CFD) is probably related to the fact that the model used during CFD was a simplified semi-model, not equipped with a radiator, no side-winds were simulated and the known short comings of the used turbulence model.

Power required contributions

All the different contributions in terms of percentage to the total power required P_{req} are known. Therefore it is possible to plot these contributions for a particular day, Fig.5a. At certain moments the total losses are reduced to zero, these are the moments when the truck driver releases the acceleration pedal position and the vehicle velocity drops. When the vehicle velocity is zero and the engine of the truck stays on, it is obvious that all power is lost to mechanical friction of the engine and axis.

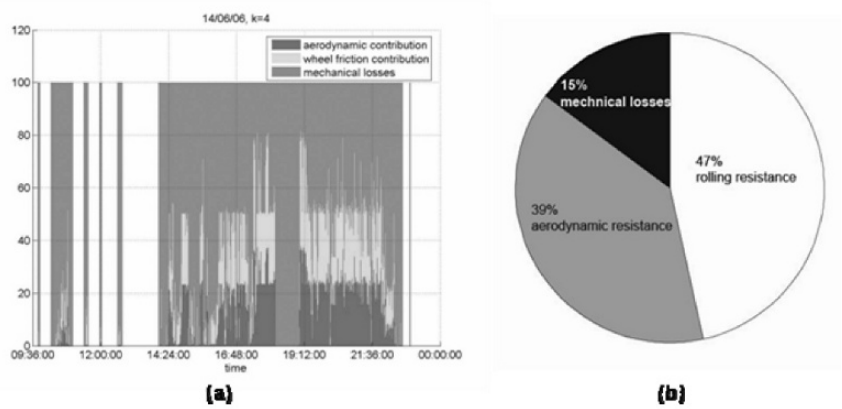

Fig. 5 (a) Overview of the different contributions with respect to the delivered power; (b) Average contributions for the whole testing period considering velocities higher than 23 m/s.

If the average for the whole testing period is calculated for the three different contributions, a summarizing pie-chart, Fig.5b, can be made. The figure illustrates that almost 15% of the delivered power is lost into the mechanical friction of the engine, the gearbox and the drive shafts. The rolling resistance is responsible for 47% of the total delivered power, while the aerodynamic forces consume 39%. Only the vehicle velocities which are equal or higher than 23m/s are considered.

Vehicle speed and wind velocity

It is interesting to compare both velocities, the vehicle speed registered by the FMS system of the truck and the wind velocity measured by the WindSonic. Figure 6a immediately shows that the wind speed is often lower than the vehicle velocity whereas the opposite is to be expected due to acceleration of the flow by the rounded cabin edge and by the roof deflector. A possible reason for this lower wind speed can be the fact that the bent flow, due to the presence of the cabin edge, separates when it comes along the front edge of the WindSonic and causes a wake and lower velocities in the horizontal measuring plane of the sensor. Therefore the WindSonic is being tested in the wind tunnel. It turned out that even for

major inclination angles up to 40 degrees no flow separation was occurring at the front edge of the Wind- Sonic and that the registered wind speeds and yaw angles were corresponding with speeds set through the wind tunnel. Numerical simulation of a full vehicle model of the cabin with roof and sun deflector together with the WindSonic can clarify the lower measured wind velocities. Another reason could be the fact that vehicle speed obtained through the FMS system is not correct. Unfortunately there was no access to the GPS data of the truck or a possibility of a short test run with the GPS of the truck at that moment to control the vehicle speed.

In order to prevent that the WindSonic is subject to an angle of incidence, the sensor should be placed far away from the front edge of the cabin edge. This is not possible for a truck due to practical and safety reasons and legislation.

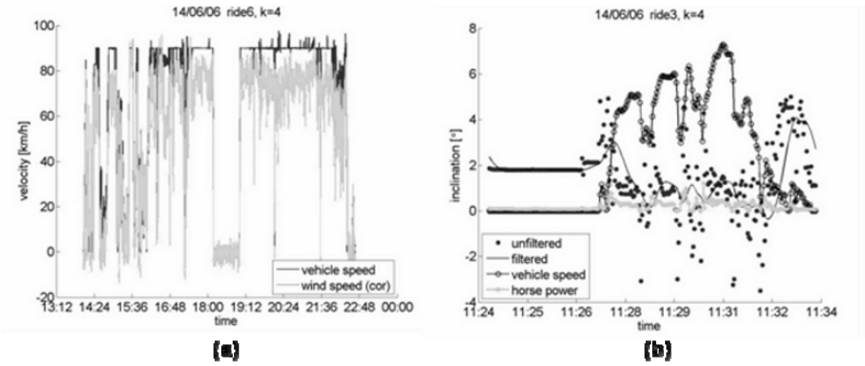

Fig. 6 (a) Vehicle speed and wind velocity; (b) Inclination angle together with the vehicle speed and horse power.

Inclination and banking

During the analysis of the data from the 2-axis incline indicator it turned out that the sensor was suffering from the vibrations induced by the truck and its engine. Even after manipulating the data by filtering, it was not possible to indicate whether the truck is driving up- or downhill. The sensor was then mounted on the chassis with rubber connections in order to dampen the vibrations as can be seen in Fig.6b and which was not very helpful. The figure indicates the inclination angle together with the vehicle speed and the horse power. The constant inclination angle is always corresponding with a zero vehicle speed and horse power. This once again states that the inclination (and banking) angle is suffering from the vibrations initiated by the engine. It is then advisable to use a less sensitive sensor to indicate inclination and banking angles.

5 Discussion and Conclusions

Within a testing period of six weeks an enormous amount of information was collected and processed with the aid of an extensive self-written Matlab code in order to be able to interpret all the different parameters and their relation to each other.

Unfortunately a closer investigation of the registered inclination and banking angle and the wind speed revealed that these sensors are not suitable for their initial purpose. This type of 2-axis incline indicator is too sensible for vibrations due to its build-up. An inclination indicator which is constructed with other, less vibrations sensitive principles to measure an angle should give better and more reliable results in future testing activities.

The position of the WindSonic is unfortunate because the sensor is suffering from the bent flow due to the rounded cabin top front edge. The flow investigation and calibration in the wind tunnel gave more insight in the results of the WindSonic and its behavior in an inclined flow: no flow separation was induced at the WindSonic front edge even at an inclined flow of 40°. Further numerical simulations are required to explain the lower measured wind velocities. It is also advisable to use a wind sensor that measures the wind velocity in all three directions. Another option is to use a wind velocity and direction sensor which is mounted on a beam in front of the vehicle. This way the WindSonic can be calibrated with respect to the extra (correct) measurements. It is advisable to check the velocity difference by comparing the vehicle speed registered by the FMS system with a corresponding GPS signal.

During the test period a reference level of the truck is defined which makes it possible to compare different aerodynamic devices and their corresponding fuel economy impact. Also more insight in the aerodynamic (C_D value of 0.430) and mechanical performances (the power required is split into 47% rolling resistance, 39% of aerodynamic drag and 15% mechanical losses; fuel consumption of 30 liters in 100 km; average speed of 75 km/h) is obtained as well as in the behavior of the truck driver and its surroundings (the wind direction range of ±10° is most occurring).

Acknowledgments

The authors would like to acknowledge the support from Jan de Rijk Transport, Kees Mulder Carrosserieën and Squarell Technology. Additional thanks to Rose McCallen, Fred Browand, Jim Ross and ECI for the organization of The Aerodynamics of Heavy Vehicles II conference.

References

[1] Rose M J (1987) Commercial Vehicle Economy - The Correlation Between Aerodynamic Drag and Fuel Consumption of a Typical Truck. J of Wind Eng Ind Aerodyn, 9:89-100.
[2] Harwell and Didcot (2001). Truck Aerodynamic Styling. ETSU, Oxfordshire. http://www.energysavingtrust.org.uk/uploads/documents/fleet/GPG308.pdf
[3] Wood R M, Bauer S X S (2003) Simple and Low-Cost Aerodynamic Drag Reduction Devices for Tractor-Trailer Trucks. SAE paper 2003-01-3377.
[4] Gilhaus A M, Renn V E (1986) Driving-Stability-Related Aerodynamic Forces and Their Interdependence-Results of Measurements on 3/8-Scale Basic Car Shapes. SAE Technical Paper 860211.
[5] Gill Instruments Ltd. http://www.gill.co.uk/products/anemometer/windsonic.htm
[6] Squarell Technology. http://www.squarell.com
[7] AE Sensors. http://www.aesensors.nl/pdf/Seika/SB2I e.pdf
[8] Van Raemdonck G M R (2006) Design of an Aerodynamic Aid for a Tractor-Trailer Combination. Master's thesis, Delft University of Technology, Faculty of Aerospace Engineering.

Automotive Testing in the DNW-LLF Wind Tunnel

Eddy Willemsen

German-Dutch Wind Tunnels (DNW), P.O. Box 175, 8300 AD Emmeloord, the Netherlands
eddy.willemsen@dnw.aero

Abstract The German Dutch Wind Tunnels is a foundation with the German Aerospace Center (DLR) and the Dutch National Aerospace Laboratory (NLR) as parent institutes. DNW operates ten aeronautical wind tunnels of DLR and NLR, located in Germany and the Netherlands. The main objective of the DNW organization is to provide the customer with a wide spectrum of wind tunnel test and simulation techniques, operated by one organization, providing the benefits of resource sharing, technology transfer, and coordinated research and development (R&D). The LLF is used for full-scale testing of trucks, buses, cars and alike. Heavy trucks are mounted in the 9.5m x 9.5m test section, whereby a wind speed of 60 m/s can be reached. The tested vehicle is connected to an external six-component balance with a resolution in drag measurement of 0.15N. In case of trucks, the front wheels and rear wheels are supported by air cushions. Flow visualization techniques (smoke, tufts, oil, laser light screen) are available, as well as PIV apparatus, pressure measurement equipment and an acoustic wall array for aerodynamic noise measurements. Smaller cars may also be tested with a moving ground plane of 10m long and 6.3m width. The belt has a maximum speed of 50 m/s. The poster will present an overview of the possibilities for automotive testing in the DNW-LLF wind tunnel.

Introduction

The German-Dutch Wind Tunnels (DNW) operates ten world class wind tunnels and one engine calibration facility of the German Aerospace Center (DLR) and the Dutch National Aerospace Laboratory (NLR). The main objective of the DNW organization is to provide its customers with a wide spectrum of wind tunnel test and simulation techniques, operated by one organization, providing the benefits of resource sharing, technology transfer, and coordinated research and development.

For a proper operation of the wind tunnels, it is of vital importance to keep the installations well maintained, but at the same time spend a sufficient amount of investment on the implementation of new measurement techniques. Over the years a continuous effort is made to offer customers the best quality of internal and external balances as well as electronically scanning pressure measurement systems, acoustic measurements, PIV technique and various flow visualization techniques.

Full-scale trucks and buses are tested in the LLF wind tunnel. Figure 1 shows a sketch of the layout of the LLF. This facility is located in the Netherlands, about 100 kilometers northeast from Amsterdam. At this site also a 37.5 percent scaled copy of the LLF is built. Figure 2 shows an aerial view of the testing site, where the two wind tunnels can be distinguished: the LST low in the middle and the large LLF in the upper right corner.

In fact, in the barn visible at the lower left corner a 10 percent pilot tunnel of the LLF is still operational and available and occasionally used for specific research concerning design matters of the LLF.

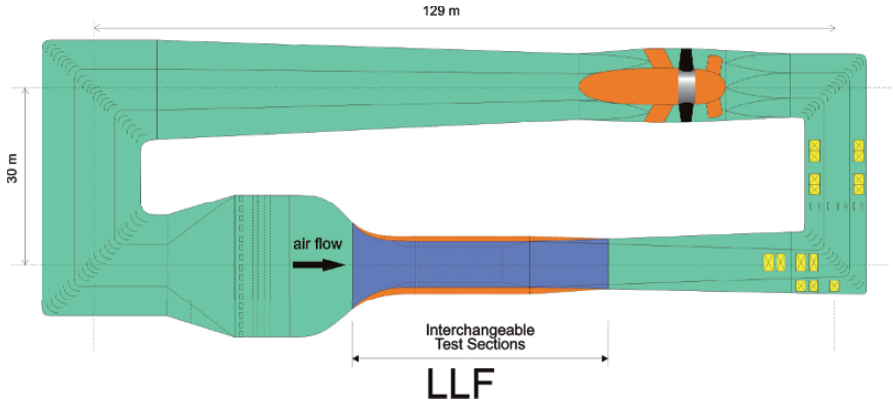

Fig. 1 Layout of the LLF

Test Setup

From the eleven different wind tunnels managed by DNW the largest wind tunnel LLF is suitable for full-scale testing of cars, buses and trucks.

The LLF is a closed loop atmospheric wind tunnel with interchangeable test sections of various dimensions. Large vehicles require the largest available test section of 9.5 m width and 9.5 m height. The cylindrical part of the test section is 20 m in length, succeeded by a transition part of 13 m in length between test section and a diffuser of 40 m length.

The 12.7 MW fan drive provides a maximum wind speed of 62 m/s. The flow quality is very good, with a turbulence level of less than 0.1 percent and velocity uniformity with less than 0.4 percent deviation from the centerline value.

Fig. 2 The LLF and LST wind tunnel

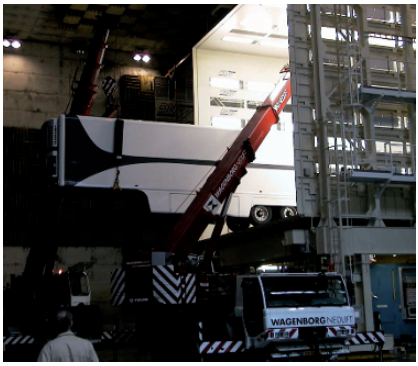

Fig. 3 Change of trailer

The drag is measured with the standard available external six-component platform balance, equipped with three horizontal and three vertical load cells. The horizontal load cells have a resolution of 0.15 N each, enabling accurate drag and side force measurements.

In the setup for trucks and buses, air cushions elements are mounted under the wheels to support the chassis. The height of these elements is kept very small in order to minimize the effect on the ground clearance. The air cushions are filled with pressurized air from a compressed air system. The vehicle is fixed by means of stiff struts to a supporting frame connected to the measuring part of the balance. The maximum yaw angle for an 18 m long truck is about 15°.

Figure 3 shows an action photo whereby the trailer is changed by means of two cranes during a test program.

Figure 4 shows a dimensional sketch of a truck mounted in the LLF test section at zero angle of yaw. The blockage is about 11 percent. In the 10 percent pilot tunnel of the LLF tests on models of a truck on four different scales were executed to determine a blockage correction specifically for trucks in the LLF.

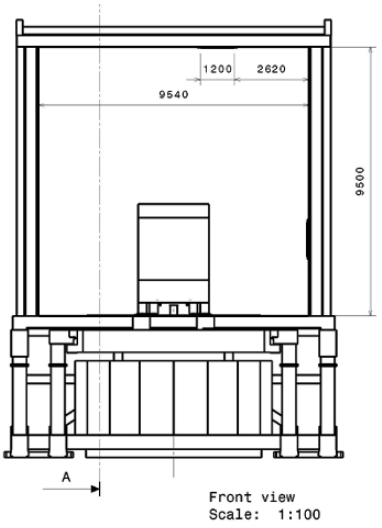

Fig. 4 Cross-sectional dimensions

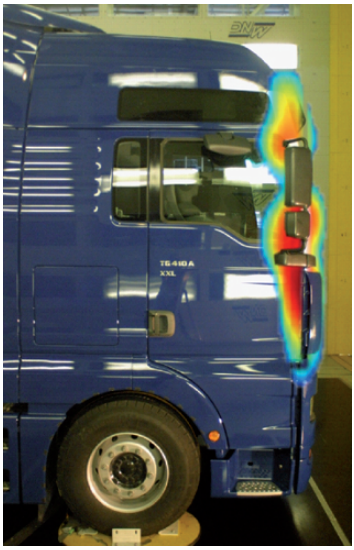

Fig.5 Acoustic test resluts

Test Equipment

At DNW all measuring techniques for aeronautical and aerospace testing are also available for tests on trucks, buses and the like.

The external balance provides the drag, side force and yawing moment.

Pressures can be measured with flat surface pressure taps, specially developed and manufactured for DNW.

Flow visualization can be realized with a hand-held smoke rod, with tufts, oil of different colors and laser light sheet.

Two microphone wall arrays may be used to measure the strength and location of acoustic sources. Figure 5 shows an example of test results, plotted in a side view photograph of a truck. The colors represent the strength of the sound production in the area of the side mirrors and corner vanes.

Beside standard testing techniques for trucks and buses DNW may also apply Particle Image Velocimetry or a traversing rake of eighteen five-hole pressure probes to obtain information about the flow field around the vehicle.

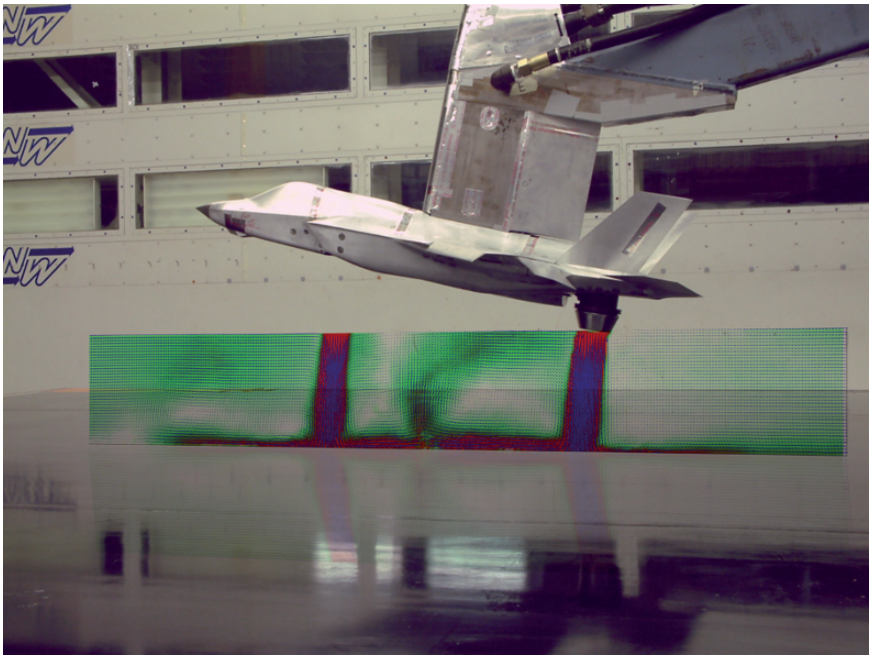

Fig. 6 Example of PIV results on a fighter aircraft

An Experimental Study of Tractor Base Bleed for Heavy Vehicle Aerodynamic Drag Reduction

Bruce Storms, Jason Ortega, Kambiz Salari

NASA Ames Research Center, USA
bruce.l.storms@nasa.gov

Abstract A significant contributor to heavy-vehicle aerodynamic drag is the tractor-trailer gap, especially when operating in a crosswind. At this condition, the freestream flow turns into the tractor-trailer gap, imparting a momentum exchange to the vehicle and subsequently increasing the aerodynamic drag. In common use today, tractor side-extenders provide significant drag reduction, but they are not without problems. Frequently damaged when the tractor pivots sharply with respect to the trailer, side extenders can incur additional costs for maintenance and repair. This issue can be alleviated by shortening extenders (thereby reducing their benefit) or devising an alternative drag-reduction concept. One such concept is tractor base bleed, in which air-flow is vented into the tractor-trailer gap through the back of the tractor. To study this concept, a wind-tunnel study was conducted for a generic 1:20-scale tractor-trailer configuration at width-based Reynolds number of 420,000. Delivered through a porous material embedded in the tractor base, the bleed flow was varied so as to generate velocities behind the tractor ranging from zero to 10% of the freestream velocity. Configurations were studied both with and without side extenders at two different tractor-trailer separation distances.

CFD, Numerical Methods and Application

Application of High Fidelity Numerical Simulations for Vehicle Aerodynamics

Parviz Moin

Stanford University, USA
moin@stanford.edu

Abstract Interest in the use of the large eddy simulation (LES) technique for computation of turbulent flows of industrial relevance has increased considerably. This is in part due to the availability of low cost, powerful supercomputers. Today, a computer cluster capable of one TFOPS sustained performance for a complex flow LES calculation costs about one hundred thousand dollars. Another reason for the increased interest in LES is the recent added capabilities for multi-physics and integrated flow simulations. As part of Stanford's DOE/ASC program, we have demonstrated and validated high fidelity simulations of multi-phase reacting turbulent flows in highly complex configurations in propulsion systems. The overarching problem in this program is simulation of flow through a complete jet engine, which is an extremely complex machine. LES computations of the entire engine flow are not feasible even with the most advanced supercomputers available. The Reynolds averaged Navier-Stokes (RANS) technique was used for the turbomachinery components and the combustor was simulated using LES. These simulations provided an early example of integrated simulations where different codes with different fidelity compute different portions of the system. A simulation environment had to be developed for the various codes to communicate with each other in an efficient and stable fashion. This integration technology and the associated science are suggested as the means for using LES in vehicle aerodynamics where Reynolds numbers are too high for high fidelity computation of the flow around the entire vehicle. LES can then be used in regions where RANS models are known to be inaccurate, and where LES provides access to flow quantities such as turbulent pressure fluctuations for predicting noise. Several examples of integrated simulations will be presented, including separation control for a high-lift system using synthetic jets.

Scale-Adaptive Simulation in the Context of Unsteady Flow Simulations

Florian Menter

ANSYS/Fluent/CFX, Germany
florian.menter@ansys.com

Abstract In the last decade, the spectrum of methodologies for the modeling of unsteady flows has significantly increased. Historically, the two choices were Unsteady Reynolds Averaged Navier-Stokes (URANS) and Large Eddy Simulation (LES) methods. Both have severe limitations with respect to their application to engineering flows. URANS, typically produces no turbulent spectral information, even in regions, where time and space resolution would be sufficient to do so, whereas LES requires very high grid counts for modeling of wall-bounded flows at moderate to high Reynolds numbers. CFD users therefore had little choice than to concentrate on steady state RANS solutions, even for applications, where it was clear that these models are not adequate. Detached Eddy Simulation (DES) as proposed by Spalart in 1997, lead to a shift in paradigm, as it combined the elements of RANS and LES in a way that allowed the simulation of unsteady detached flows with available computing power. More recent studies by Menter and Egorov, have however shown that the inability of classical URANS models to resolve turbulent structures is not an inherent shortcoming of the URANS approach, but only related to the way the scale equations have historically been derived. After re-visiting an exact scale equation that Rotta had developed in the 1950s, it became clear that an important term was omitted in all scale equations, which resulted in the inability of classical RANS models to resolve unsteady structures. Closer inspection of Rotta's equation shows that the second derivative of the velocity field should be included in the length scale equation. This so-called Scale-Adaptive Simulation (SAS) methodology behaves in many ways and for many applications similar to the DES formulation, but avoids some of the dangers of DES. On the other hand, it is not the goal of SAS to replace DES and it will be shown that both methods have their place in the spectrum of unsteady turbulence models. The paper will discuss the practical implications, but also the limitations of the SAS technology. Many results produced during the European research project DESIDER on external aerodynamic flow will be shown.

Computational Simulation of the GCM Tractor-Trailer Configuration

K. Sreenivas, B. Mitchell, S. Nichols, D. Hyams, D. Whitfield

University of Tennessee SimCenter at Chattanooga, Chattanooga, TN 37403, USA
kidambi-sreenivas@utc.edu

Abstract Aerodynamic simulations were carried out for the Generic Conventional Model, a 1/8th scale tractor-trailer model, that was tested in the NASA Ames 7'x10' tunnel. The computed forces are compared for the zero, ten and fourteen degree yaw cases while the pressure coefficients are compared to experimental data for the ten and fourteen degree cases. A DES version of the one-equation Menter SAS is used in these simulations. Overall forces as well as pressure distributions matched well for the fourteen degree case. For the ten degree case, the forces were in reasonable agreement while the pressure distributions indicated a need for tighter grid resolution as well as possibly advanced turbulence models.

Introduction

In 1997, fuel consumption among Class 8 trucks was 18 billion gallons [1]. At typical highway speeds (70 mph), 65% of the overall output of the engine is used for overcoming aerodynamic drag [2]. Consequently, a reduction in aerodynamic drag will result in substantial fuel savings. Given the large number of tractor/trailers on the road in the United States, this could translate into a significant reduction in domestic fuel consumption as well as a reduction in emissions that contribute to pollution.

The main contributors to the aerodynamic drag are the gap between tractor and trailer, the vehicle underbody and the base flow region of the trailer [3]. Significant flow structures exist in these regions and several experimental studies have been carried out to characterize them. One of the experimental studies used a 1/8th scale Ground Transportation System (GTS) model that consisted of simplified tractor trailer geometry with a cab-over-engine design and no tractor-trailer gap. This geometry was tested both at the Texas A&M University Low Speed Wind Tunnel [4]as well as the NASA Ames 7'x10' tunnel [5]and extensive data was collected for validation of computational simulations. Modifications to the GTS geometry to include a tractor trailer gap were incorporated in tests carried out at USC [6] and the influence of the gap on the overall flowfield assessed. Detailed

experimental studies were also carried out on a realistic tractor trailer combination, the Generic Conventional Model (GCM), in the NASA Ames 7'x10' as well as the 12' wind tunnel [7].

Computational studies aimed at evaluating the capabilities of current flow solvers for the prediction of heavy vehicle aerodynamics were carried out by a number of researchers [8]-[13]. Salari et al. [8] used the data from the GTS experiments and showed that with an appropriate choice of turbulence model, the overall drag coefficient could be predicted with reasonable accuracy. However, one of their key findings was that the details of the flow field, especially in the base flow region, were not being captured accurately. Pointer [9] used a commercial CFD flow solver to study the GCM model in the 7'x10' tunnel and the results indicated that the overall drag coefficient could be predicted with reasonable accuracy. However, no detailed flow field comparisons were presented. Maddox et al. [10] used another commercial CFD solver to simulate the flow around GTS model. They employed a detached eddy simulation (DES) approach and showed that an improvement in the predicted pressure (especially toward the base of the model) can be achieved. RANS simulations using the one-equation Spalart-Allmaras model and the two-equation Menter k-ω model were reported by Roy et al. [11]. LES simulations of a truncated GTS model were carried out by Ortega et al. [12]. Sreenivas et al. [13] simulated the flow field around the GTS model using an unstructured flow solver. They employed the DES version of the two-equation k-ε/k-ω turbulence model and showed that a single vortex structure that was observed experimentally could be reproduced by time-averaging an unsteady RANS simulation.

The present research effort focuses on *Tenasi*, a family of structured and unstructured flow solvers that have been developed at the University of Tennessee SimCenter at Chattanooga. The unstructured flow solver is used to simulate the flowfield around the GCM model inside the NASA 7'x10' tunnel at zero and ten degrees yaw. Results are presented comparing the axial and side forces as well as surface pressures with experimental data.

Numerical Approach

The governing equations solved by the *Tenasi* flow solver are the non-dimensional form of the Navier-Stokes equations in Cartesian coordinates. The variables appearing in the Navier-Stokes equations are nondimensionalized as follows: density ρ_r; velocity U_r; temperature T_r; pressure $\rho_r U_r^2$; length L_r; time $\frac{L_r}{U_r}$; energy and enthalpy h_r. This system of equations is closed by an equation of state the form $\rho = \rho(p,T)$. For a perfect gas with constant specific

heat, $h_r \equiv C_p T_r$, and it follows that $E_c = (\gamma - 1) M_r^2$ where $M_r = \frac{U_r}{c_r}$ is a reference Mach number and $c_r^2 = \gamma R T_r$ is the reference speed of sound. $\gamma = \frac{C_p}{C_v}$ is the ratio of specific heats, and R is the specific gas constant. The equation of state is then given by

$$p = \frac{\rho T}{\gamma M_r^2} = \frac{\rho c^2}{\gamma}; c^2 = \frac{T}{M_r^2}$$

The governing equations are discretized using a node-centered, finite-volume approach. A single parameter based preconditioner is employed so that the baseline *Tenasi* solver is applicable over a wide range of Mach numbers. The numerical fluxes are computed using high resolution fluxes based on Roe averaging and a Newton subiteration procedure is employed to ensure time accuracy. The linear system at each time step is solved using a Symmetric Gauss-Seidel algorithm. The details of the numerical algorithm are available in Sreenivas et al. [14].

Results

The results presented here include the GCM at zero, ten and fourteen degree yaw. These were three of the test cases chosen from the available experimental data. The simulations were carried out to include the NASA Ames 7'x10' tunnel as well as the GCM geometry. The reason for this was the experimental pressure coefficient was referenced to a specific location on the test section wall and including the tunnel was an easy way of comparing computed and experimental pressure distributions. The grids for all the cases were generated using a combination of Gridgen (for the tetrahedral portion) and HUGG [15] (for inserting the viscous layers). The characteristics of the grids used are detailed in **Table 1**.

Table 1 Grid Characteristics for the zero, ten and fourteen degree yaw cases for the GCM inside the 7'x10' Tunnel

Case	Nodes	Tetrahedral	Prism	Hex
0^o yaw	20,636,180	40,366,718	25,870,856	680,800
10^o yaw	18,937,191	41,828,550	23,253,152	0
14^o yaw	19,842,249	42,832,190	24,564,782	0

All the cases presented here at a Reynolds number of 1.15×10^6 (based on GCM model trailer width of 12.75 inches) and a tunnel test section Mach number of 0.15. Given the (relatively) high freestream Mach number that is present in the GCM experiments, a single parameter based preconditioned formulation is used to avoid any convergence difficulties associated with using a pure compressible flow solver. A quadratic reconstruction procedure was used to ensure higher order spatial accuracy while three Newton iterations were employed to ensure second order accuracy in time. The Menter SAS turbulence model in DES mode was used to model the effects of viscosity and the average y^+ for all the viscous surfaces were less than unity. A typical run consisted of running 5,000 time steps in a constant CFL mode (CFL of 25.0) followed by 20,000 time steps in a constant time step mode, with the non-dimensional time step being 10^{-3}. Each run required about 2 days of CPU time and utilized 200 cores.

The computed axial and side forces were compared to two sets of experimental data (Runs 43 and 75) and the comparisons are shown in Figs. 1 and 2. As can be seen from Fig. 1, there is an indication of large scale separation (indicated by an abrupt change in the axial force coefficient) in the experimental data between approximately 10^o and 12.5^o angles of yaw. Furthermore, the experimental data is asymmetric between positive and negative yaw angles and between the two runs. The computed axial force coefficient agrees well with experimental data for the zero and fourteen degree yaw cases. For the ten degree case, the computed axial force is lower than the experimental values. Correspondingly, the side forces are higher than the experimental values for the ten degree case (Fig. 2). This could be caused by separation occurring slightly earlier in the computations as compared to the experiment. Given the uncertainty in the experimental values at ten degree yaw, the overall agreement between the computed and experimental axial and side forces is good.

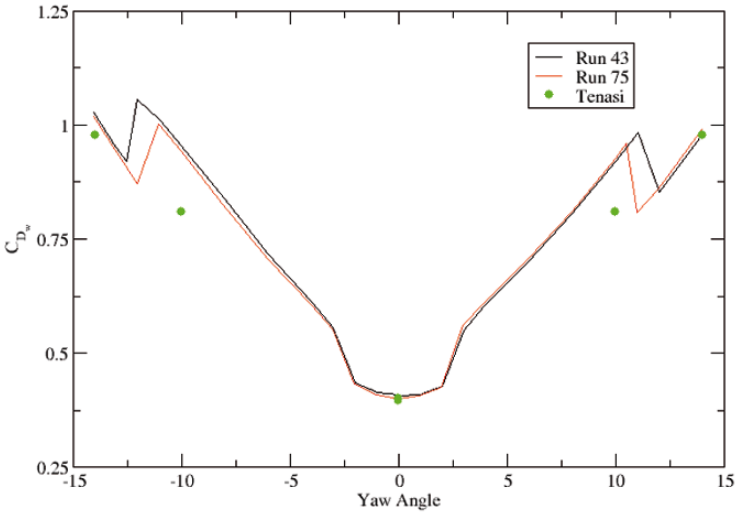

Fig. 1 Comparison of Axial Force Coefficient

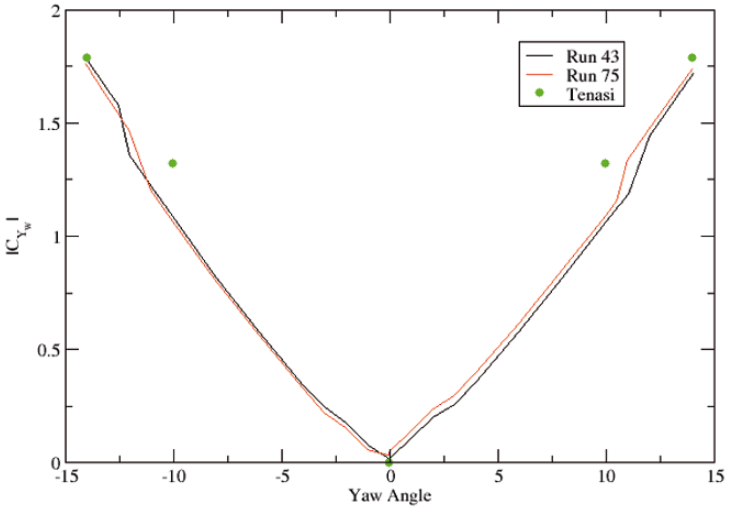

Fig. 2 Comparison of Side Force Coefficient

Detailed comparisons of surface pressure distributions are shown in Figs. 3 – 12 for the ten and fourteen degree yaw cases. The zero degree case results have been omitted for brevity. The experimental data shown in these graphs includes results from both the positive and negative yaw runs. The decision to include both sets of data was based on a couple of reasons:

(1) To get a measure of geometric asymmetry and experimental uncertainty: If the geometry and flow conditions were truly symmetric, then the values from the positive and negative yaw angles should be the same. Therefore any differences between the measured pressures would be an indication of geometric asymmetry and also provide a measure of experimental uncertainty.

(2) The instrumentation was not symmetric: The GCM model had more pressure taps on one side of the geometry relative to the other. Therefore, using data from both positive and negative yaw angles would enable an assessment of the computed solution.

Ten Degree Yaw

For the results presented here, the solutions were averaged over 1000 and 5000 time steps. The choice of time step in this particular instance was arbitrary; however, in a related study, an effort to define a convergence criterion for unsteady flows has been attempted with reasonable success [16]. This criterion was not employed in this study as it required the storage of considerable amount of data (on

the order of a terabyte). Figures 3 and 4 show a comparison of pressure distribution along the centerline of the tractor. As can be seen from the figures, the agreement is very good between the experimental data and computations. The effect of the choice in averaging period can be seen in both the plots. The 5000 time-step averaged solution appears to match the experimental data slightly better than the 1000 time-step averaged solution. There also appears to be a significant discrepancy between the experimental data around the x/w = 1.5 or so (close to the base of the tractor). The computations match the +10° yaw results very closely in this area. Overall, the computations seem to lie between the experimental data over the bulk of the centerline of the tractor.

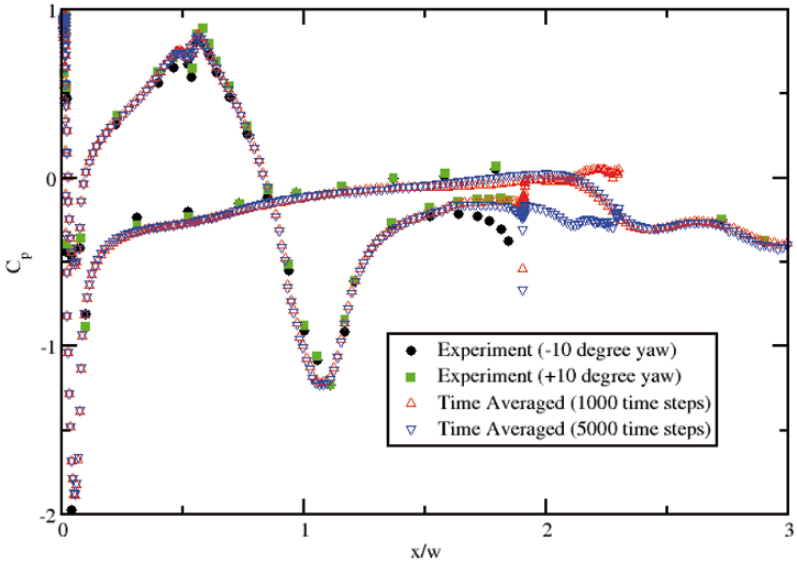

Fig. 3 Comparisons of Tractor Centerline Pressure Distribution along the x-axis for 10^{o} yaw

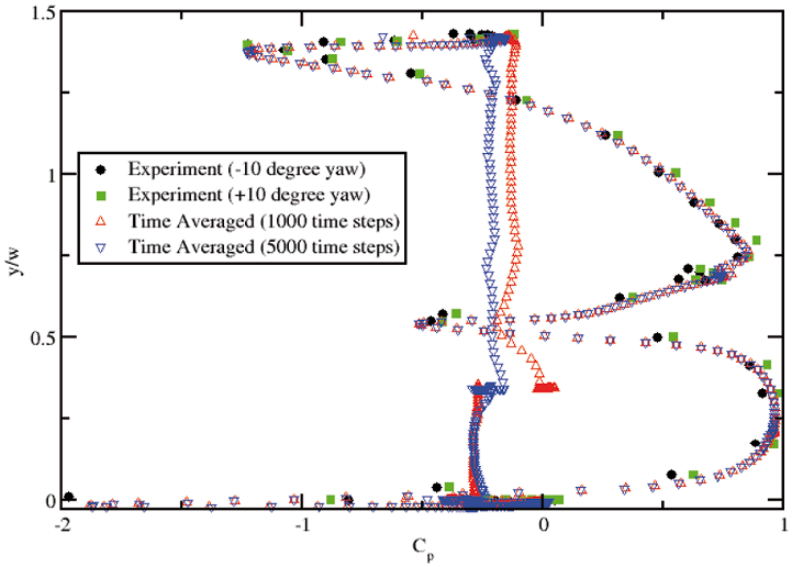

Fig. 4 Comparisons of Tractor Centerline Pressure Distribution along the y-axis for 10° yaw

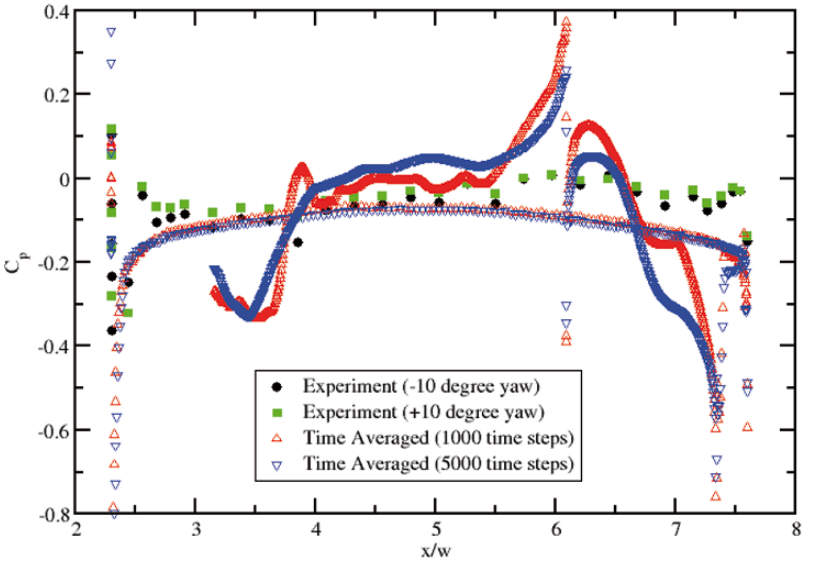

Fig. 5 Comparisons of Trailer Centerline Pressure Distribution (Top of trailer) for 10° yaw

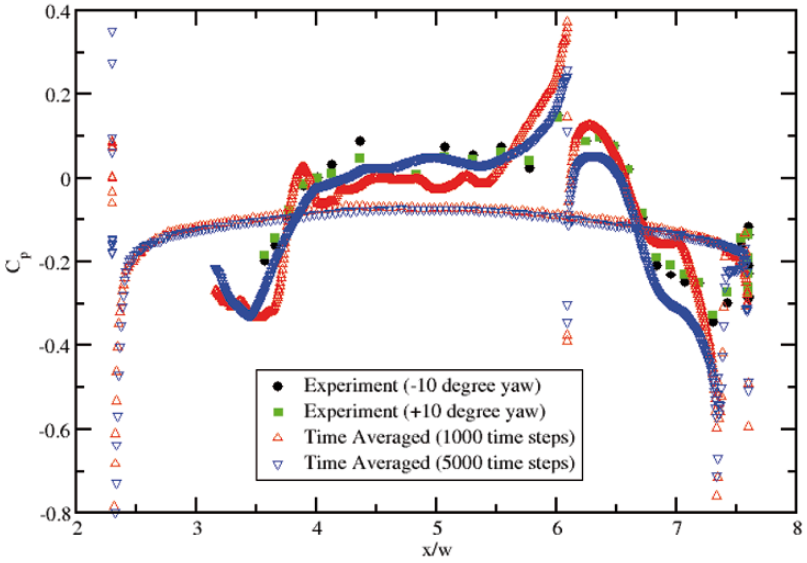

Fig. 6 Comparisons of Trailer Centerline Pressure Distribution (Bottom of trailer) for 10^{o} yaw

A comparison of the trailer centerline pressure distribution is shown in Figs. 5 and 6. The data is presented in two different graphs for clarity. The computational results are repeated between the figures, while only the top of the trailer data is shown in Fig. 5 and only the bottom of the trailer is shown in Fig.6. As can be seen from Fig. 5, the trend towards the base of the trailer is not captured correctly by the computed results. There is also no significant difference between the 1000 and 5000 time-step averaged solutions. It is possible that the base flow region has a very strong influence on the pressure distribution in the neighborhood of the trailer base. The comparison for the bottom of the trailer fares much better with the trend as well as the magnitude of the pressures being captured reasonably well (especially the 5000 time-step averaged solution).

The next comparison shown is for a line that is halfway up the side of the trailer (Fig. 7). As can be seen from the figure, the experimental data from the ±10° yaw provides a better picture of the overall pressure distribution on the trailer. The computations are reasonably close to the experimental data over the bulk of the trailer. The 5000 time-step averaged solution has smoothed out a lot of the fluctuations that are visible in the 1000 time-step averaged solution. The biggest discrepancy between the computed results and experimental data is at the front corner of the trailer. The experimental data seems to indicate a larger low pressure region (possibly caused by a large-scale vortex) while the computations indicate a much smaller low pressure region. Again, the 5000 time-step averaged solution compares much better to the experimental data than the 1000 time-step averaged solution. This discrepancy could account for some of the variation in the axial and side forces between the computed results and experimental data.

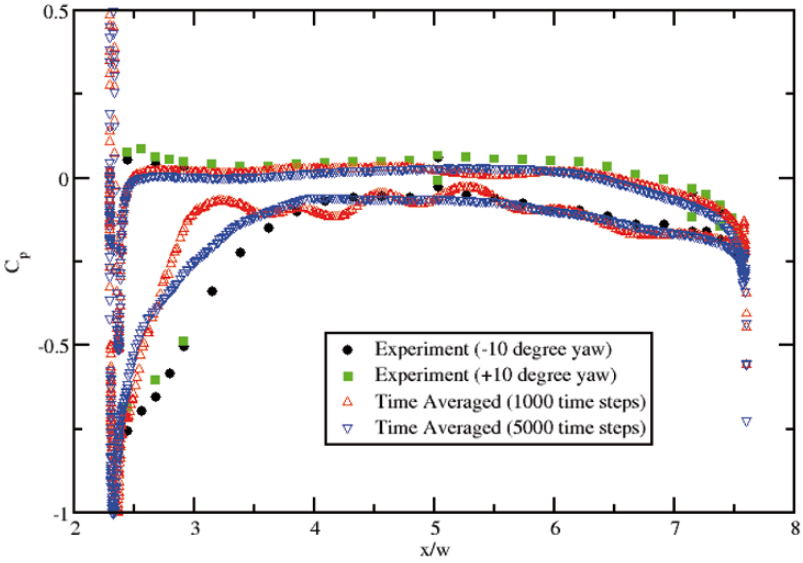

Fig. 7 Comparison of Trailer Pressure Distribution (y/w = 0.9137) for 10° yaw

Fourteen Degree Yaw

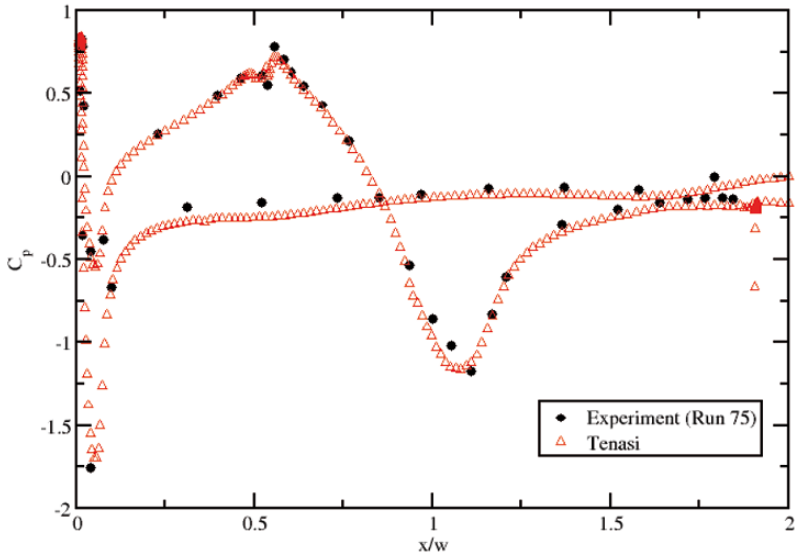

Fig. 8 Comparisons of Tractor Centerline Pressure Distribution along the x-axis for 14° yaw

An identical set of results is presented for the fourteen degree case as was done earlier for the ten degree case. This is done in an attempt to understand the similarities and differences between the solutions and also to shed light on the better agreement between the computed forces for the fourteen degree case as opposed to the ten degree case. Since the results for the ten degree case showed a better agreement between the 5000 time-step averaged solutions and experiment, only the 5000 time-step averaged results are presented for the fourteen degree case.

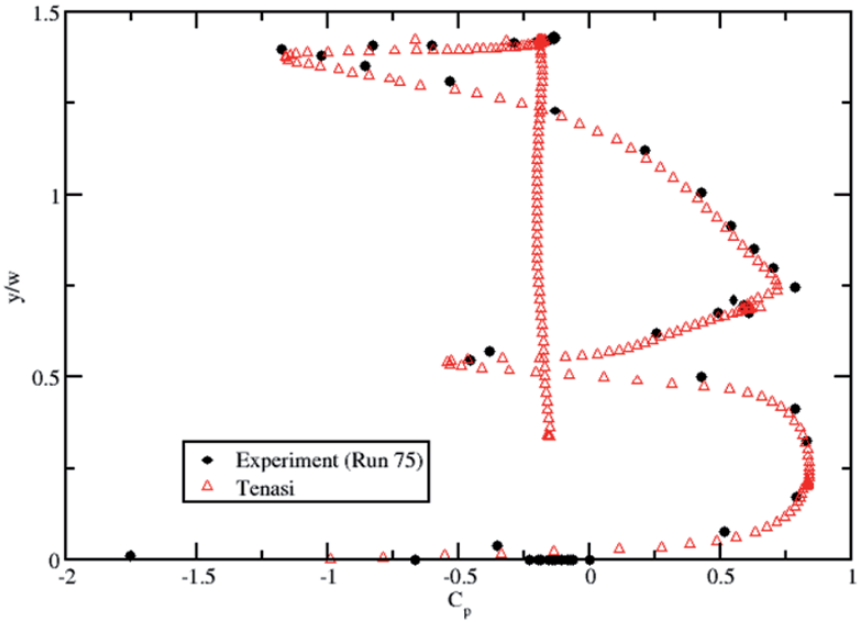

Fig. 9 Comparisons of Tractor Centerline Pressure Distribution along the y-axis for 14° yaw

The first sets of results are for the pressure distributions along the centerline of the cab and are shown in Figs. 8 and 9. The overall agreement in the pressure distribution is good and compares well with the agreement obtained for the ten degree case. The trailer centerline pressure distributions are compared in Figs. 10 and 11. As can be seen from these figures, the differences between the experimental data for the positive and negative yaw angles are quite evident with the computed data matching well with the -14° data over the front half of the trailer top surface (Fig. 10). The discrepancy in the pressure distribution over the back half of the top surface of the trailer is similar to that observed for the ten degree case; however, the magnitude here is much smaller than the ten degree case. The overall agreement over the bottom of the trailer centerline is similar to that obtained for the ten degree case.

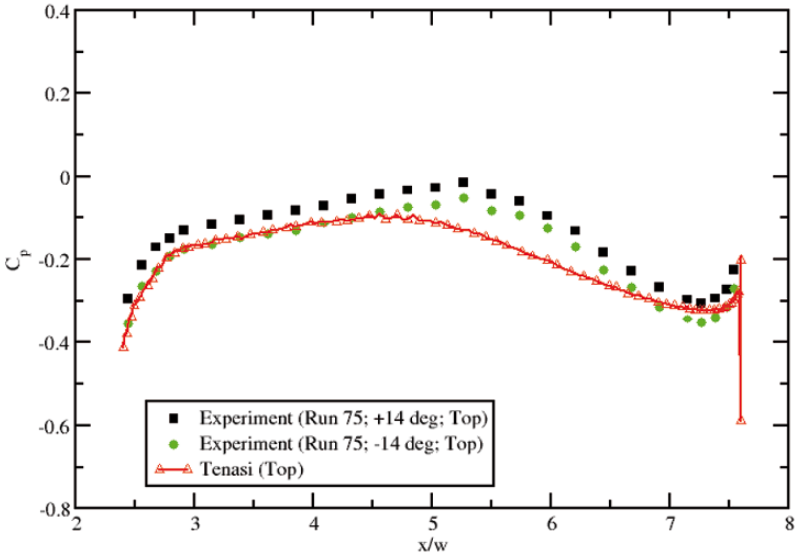

Fig. 10 Comparisons of Trailer Centerline Pressure Distribution (Top of trailer) for 14° yaw

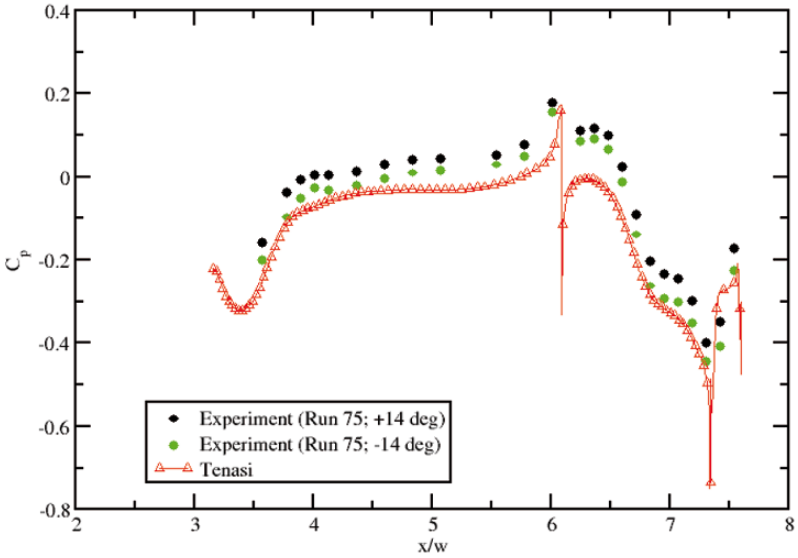

Fig. 11 Comparisons of Trailer Centerline Pressure Distribution (Bottom of trailer) for 14° yaw

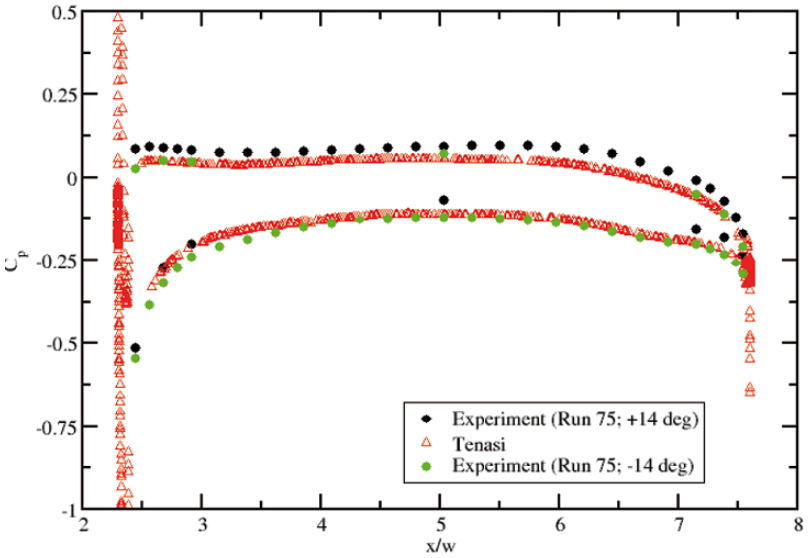

Fig. 12 Comparison of Trailer Pressure Distribution (y/w = 0.9137) for 14° yaw

The comparison of pressure distributions at the mid-plane (in the vertical direction) of the trailer are shown in Fig. 12. The overall agreement between the experimental data and computed results is good with the -14° data matching the computed results well. The biggest differences between the ten and fourteen degree cases can be seen by comparing Figs. 7 and 12. In the ten degree case (Fig. 7), the computed results are clearly not predicting the flow at the front of the trailer correctly while in the fourteen degree case (Fig. 12), there is good agreement everywhere. This could explain the differences in the agreement of the computed forces between the ten and fourteen degree cases.

Conclusions

Computed forces and pressure coefficient distributions were compared to experimental data for the GCM tractor-trailer configuration for ten and fourteen degrees yaw. Good agreement was obtained for the fourteen degree case while the ten degree case was in fair agreement with experimental data. The ten degree case pointed to the potential need for grid refinement in specific regions of the computational domain. It is also possible that the overall agreement for all the test cases could be improved by employing advanced turbulence models.

Acknowledgements

This work was supported in part by the US Department of Energy and the Oak Ridge National Laboratory through UT-Batelle contract number 4000035270 with Dr. W. Keith Kahl as technical monitor. This support is gratefully acknowledged. Thanks are also due to Dr. Rose McCallen, Dr. Jules Routbort and the late Dr. Sid Diamond for their generous guidance and encouragement. This work was also supported by the THEC Center of Excellence in Applied Computational Science and Engineering with Dr. Harry McDonald as technical monitor. Their support is greatly appreciated.

References

1 http://www.transportation.anl.gov/research/technology_analysis/truck_fuel_use.html
2 McCallen R, Couch R, Hsu J, Browand F, Hammache M, Leonard A, Brady M, Salari K, Rutledge W, Ross J, Storms B, Heineck J, Driver D, Bell J, and G Zilliac, "Progress in Reducing Aerodynamics Drag for Higher Efficiency of Heavy Duty Trucks(Class 7-8)," SAE Paper 1999-01-2238.
3 Cooper K, "Truck Aerodynamics Reborn – Lessons from the Past," SAE Paper 2003-01-3376, 2003.
4 Croll R, Gutierrez W, Hassan B, Suazo J and Riggins A, "Experimental Investigation of the Ground Transportation Systems (GTS) Project for Heavy Vehicle Drag Reduction," .SAE Paper 960907, February 1996.
5 Storms B, Ross J, Heineck J, Walker S, Driver D and Zilliac G, "An Experimental Study of the Ground Transportation System (GTS) Model in the NASA Ames 7-by 10-Ft Wind Tunnel," NASA/TM-2001-209621, February 2001.
6 Arcas D, Browand F and Hammache M, "Flow Structure in the Gap Between Two Bluff Bodies," AIAA Paper 2004-2250, June 2004.
7 Storms B, Satran D, Heineck J, Walker S, "A Summary of the Experimental Results for a Generic Tractor-Trailer in the Ames Research Center 7- by 10-Foot and 12-Foot Wind Tunnels," NASA TM-2006-213489, July 2006.
8 Salari K, Ortega J, and Castellucci P, "Computational Prediction of Aerodynamic Forces for a Simplified Integrated Tractor-Trailer Geometry", AIAA Paper 2004-2253, 34th AIAA Fluid Dynamics Conference and Exhibit, Portland, Oregon, June 2004.
9 Pointer D, "Evaluation of Commercial CFD Code Capabilities for Prediction of Heavy Vehicle Drag Coefficients," AIAA Paper 2004-2254, June 2004.
10 Maddox S, Squires K, Wurtzler K and J Forsythe, "Detached-Eddy Simulation of the Ground Transportation System," *The Aerodynamics of Heavy Vehicles: Trucks, Buses and Trains*, Springer, 2004, pp 89-104.
11 Roy C, Payne J, McWherter-Payne M and Salari K, "RANS Simulations of a Simplified Tractor/Trailer Geometry," *The Aerodynamics of Heavy Vehicles: Trucks, Buses and Trains*, Springer, 2004, pp 207-218.
12 Ortega J, Dunn T, McCallen R and Salari K, "Computational Simulation of Heavy Vehicle Trailer Wake," *The Aerodynamics of Heavy Vehicles: Trucks, Buses and Trains*, Springer, 2004, pp 219-233.

13 Sreenivas K, Pankajakshan R, Nichols D, Mitchell B, Taylor L and Whitfield D, "Aerodynamic Simulation of Heavy Trucks with Rotating Wheels," AIAA Paper 2006-1394, January 2006.
14 Sreenivas K, Hyams D, Nichols D, Mitchell B, Taylor L, Briley W and Whitfield D, "Development of an Unstructured Parallel Flow Solver for Arbitrary Mach Numbers," AIAA Paper No. 2005-0325, January 2005.
15 Karman S, "Unstructured Viscous Layer Insertion Using Linear-Elastic Smoothing," AIAA Paper 2006-0531, January 2006.
16 Pankajakshan R, Sreenivas K, Mitchell B and Whitfield D, "CFD Simulation of Class 8 Trucks," SAE Paper 2007-01-4293, October 2007.

Full-Scale Simulations of Drag Reduction Devices for Class 8 Trucks

Ramesh Pankajakshan, Brent Mitchell & David L. Whitfield

University of Tennessee SimCenter at Chattanooga, USA
ramesh-pankajakshan@utc.edu

Abstract Computational Fluid Dynamics (CFD) simulations were performed to evaluate drag reduction devices on a modified full-scale version of the Generic Conventional Model (GCM) geometry. All simulations were performed with a moving ground plane and rotating rear wheels. A trailer base flap simulation was performed for comparison with drag reduction data from wind tunnels and track and road tests. A front spoiler and three mud-flaps with modest drag reduction potential were evaluated in view of their higher probability of adoption by truck fleet operators.

Introduction

Aerodynamic drag accounts for approximately half the fuel consumption of a class 8 truck traveling at freeway speeds and even a 1% reduction in the drag value can yield cost savings significant enough to initiate adoption by large trucking companies. While a large number of effective drag reduction devices have been developed and are commercially available [1], uptake in the trucking industry has been relatively insignificant due to a veritable thicket of infrastructure, legislative, maintenance, staffing and aftermarket issues which have rendered them cost ineffective to a large section of trucking companies. A good example of such technology is the base flap which has seen slow adoption in spite of drag reductions in excess of 10%. While there clearly is the potential for substantial drag reduction in the base region of the trailer, any changes to this area of the truck have to be made in light of severe restrictions imposed by existing infrastructure and operational norms. The underbody of the truck offers an area with less potential but with the kind of restrictions which are more amenable to engineering solutions. Moreover, drag reduction devices which target consumables like mud flaps are more likely to be tried out and adopted since they often need to be changed due to wear and tear. The underbody is however by no means a *tabula rasa* on

which the aerodynamicist may impose his/her will. There are restrictions in terms of ground clearance and ease of access for maintenance and inspection which have been the bane of extant devices such as side skirts. There are also less obvious issues such as the effect of any drag devices on brake cooling flows as well as splash and spray.

Simulations

Flow Solver

Simulations were performed using the UT Tenasi flow solver [11] which is an Unsteady Reynolds Averaged Navier Stokes (unRANS)/Discrete Eddy Simulation (DES) code operating on unstructured grids with a finite volume node centered flux formulation. The incompressible solver used for slow speed flows uses the artificial compressibility approach of Chorin[2]. The 1-equation Menter SAS model in DES mode [8] was used for all the simulations. Integration was performed to the wall using grids generated to produces off-wall y+ values less than unity. The solver and grid generation approaches used in this work were validated using the Ground Transportation Systems (GTS) [3] and Generic Conventional Model (GCM) [13] experimental datasets. Pressure predictions were found to correlate well with experimental measurements over most of the geometry with the exception of the trailer base region [12].

Geometry and Grid Generation

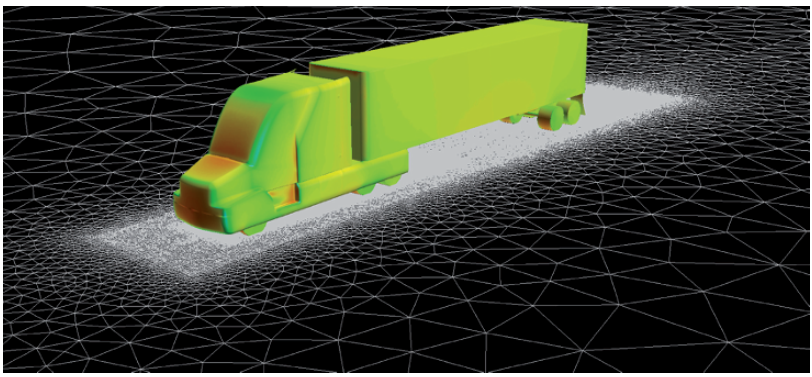

Fig. 1 GCM geometry and ground plane grid

A modified version of the GCM geometry (Fig. 1.) scaled for full-scale Reynolds numbers was chosen as the base geometry for the simulations in this study. The modifications include the addition of cab extenders and lowering of the geometry to allow the wheels to make contact with the ground plane. The support struts used for mounting the geometry in the wind-tunnel geometry were also removed. Fillets had to be introduced at the contact line between the wheel and the ground plane in order to facilitate the grid generation process.

The commercial grid generation package GridGen was used for generating a tetrahedral mesh for the GCM geometry. An in-house code called HUGG [6] was used to insert viscous layers. The off-wall spacings and growth parameters used were based on y+ constraints and experience gained in the course of the validation process. The grids used here have approximately 1.1 million surface elements on the GCM surface and 18 million control volumes in the field. Total time to solution for each case was 3 days on 200 processor cores (Intel Xeon 5160, 3.0 Ghz EM64T, 4MB cache, dual core).

Flow Conditions

The flow simulations were conducted at full-scale i.e. for a Reynolds number of 5.15 million based on a trailer width of 8.5 feet and a road speed of 65 mph. All simulations used a moving ground plane matching the road speed and rotating rear wheels on the trailer. Rotating wheels were incorporated into the simulation through a slip boundary condition which has been shown to work well for smooth wheels [10].

Wind-averaged drag simulations were conducted assuming a 7 mph crosswind at six (15, 45, 75, 105, 135 and 165 degrees) orientations with respect to the direction of travel of the truck. The wind-averaging procedure follows the method of Ingram [5] as described in [9] except that the drag forces are compared in the form of non-dimensional force coefficients calculated using the road speed as reference.

Results

Effect of Spinning Wheels

In order to evaluate the effect of spinning wheels on the drag of the truck, the 45 degree crosswind case with mud-flaps was rerun with the spinning wheel

boundary condition turned off. It was found that with stationary wheels, the drag increased by 5.4% over the spinning wheel case, with more than half the increment being due to an increase in the drag on the axle-wheel assembly as shown in Figure 2. Increased drag on the mud-flaps and trailer contributed to 27% and 15% of the total respectively.

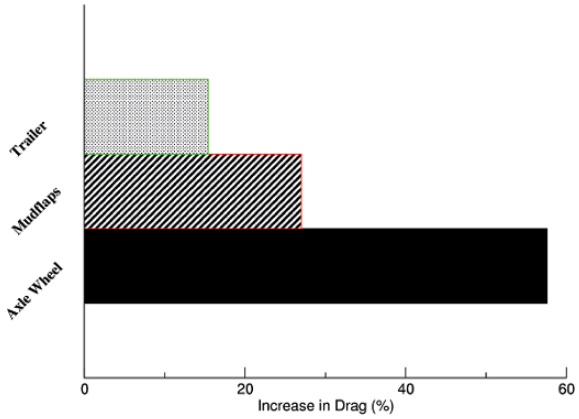

Fig. 2 Contributors to the drag increase caused by non-spinning wheels

Cab Extenders and Splitter Plates

The base GCM geometry which does not have cab extenders exhibits large drag increases in the presence of crosswinds. This effect can be almost totally mitigated by the addition of cab extenders or splitter plates on the front face of the trailer. Neither of these devices has any effect in the absence of crosswinds. Adding both devices provides no additional drag benefit. Since there are more trailers than tractors, cab extenders are probably the more economical option and they seem to have been universally adopted. The GCM model with cab extenders was chosen as the base model against which all drag reduction devices would be compared.

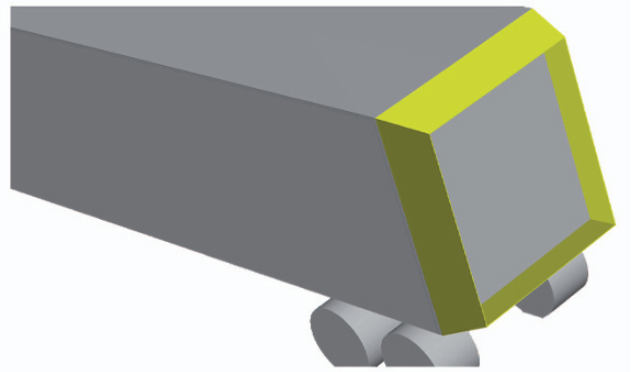

Fig. 3 Geometry of base flaps

Base Flaps

The base flaps consist of 4 panels inclined at an angle of 15 degrees to the axis of the truck as shown in Fig. 3. Each panel is one-quarter of the width of the trailer or approximately 2.1 feet. This device has been extensively studied by other researchers and a commercial product is available as well. This case was run to ensure that the drag reduction from this study was in qualitative agreement with the results in the literature. The computed wind-averaged drag reduction of 15% compares favorably with tunnel scale model tests (~14%) [13], track tests (~8.4%)[1] and road tests (~12% & ~20%)[7] with full trucks. The wind tunnel data was for the GCM geometry and is therefore in close agreement. The track and road tests were for actual class 8 trucks and the drag numbers are derived from fuel savings assuming that the percentage fuel saving was half the drag reduction percentage.

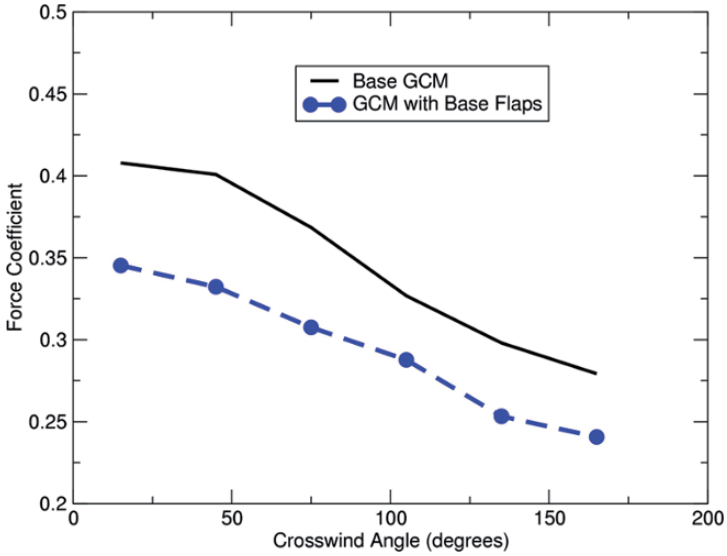

Fig. 4 Variation of axial force coefficient with crosswind angle

The drag force coefficients at the various crosswind angles are shown in Fig. 3. The effectiveness of the base flap was not particularly sensitive to the direction of the crosswind though it performs slightly better in head winds.

Front Spoiler

Front spoilers have been used in cars for a few decades to reduce underbody drag and improve cooling airflow but their effectiveness depends on careful sizing of the spoiler height [4]. The spoilers used in this study were approximately 3 inches in height and were located under the cab as shown in Fig.5.

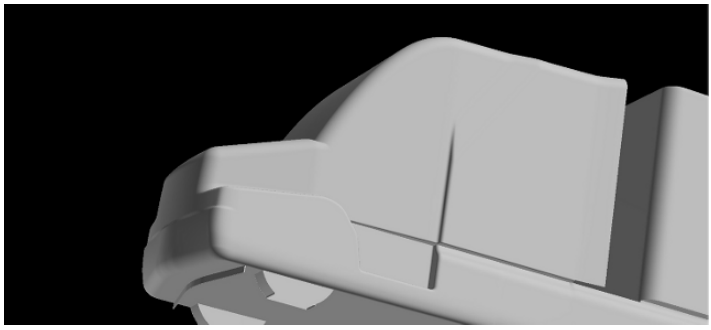

Fig. 5 Geometry and location of front spoiler

The front spoiler increased the wind-averaged drag on the GCM model by 0.2%. This implies that in an actual truck with front axles and other drag inducing components in the underbody region, the front spoiler could lead to small drag reductions. This is based on the fact that the drag increase due to the spoiler was 3.8% while it reduced drag on the rest of the truck by 3.6% even for a smooth underbody without front axles. Lowered velocities in the underbody region account for the reduced drag on the tractor and wheel assembly as well as a portion of the reduced drag on the trailer. The majority of the trailer drag reduction comes from lowering of the pressure on the front face of the trailer due to changes in flow over and around the tractor. The drag values at the various crosswind angles shown in Fig. 6b are also encouraging since the spoiler actually reduces drag when the truck is experiencing a head or tailwind. It might also be possible to modify the shape and/or height of the spoiler to reduce or eliminate the drag increase for non-parallel crosswinds. An accurate evaluation of this device will need simulations using a substantially more realistic truck model with underbody components and accurate capturing of the under-hood flow.

Fig. 6a Drag contributions of truck components

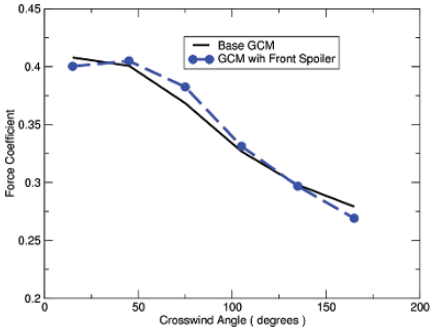

Fig.6b Variation of axial force coefficient with crosswind angle

Mud Flaps

Simulations were conducted to study the drag contribution of rear trailer mud flaps to the total drag and to look at ways in which this could be reduced. Full mud flaps which extend to the bottom of the trailer and half flaps that extend to the top the wheels as shown in Fig. 7a and Fig. 7b respectively were studied. Full flaps are usually used on trucks that transport shipping containers as well on “pup” trailers. Half flaps are more common and are usually installed on most dry freight trailers.

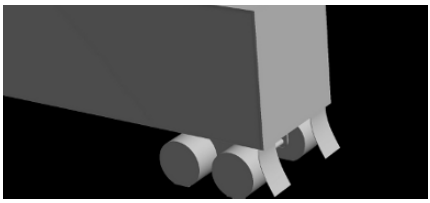

Fig.7a Geometry of full mud-flaps

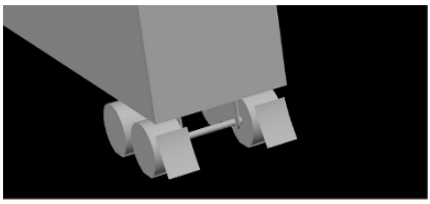

Fig.7b Geometry of half mud-flaps

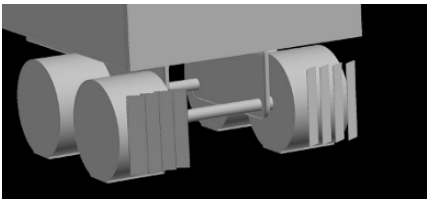

Fig.7c Geometry of half slats

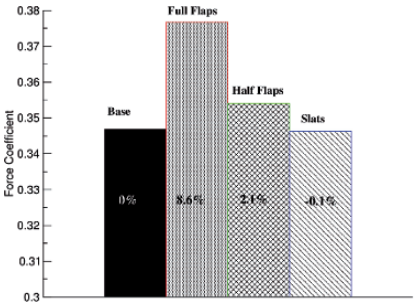

Fig.7d Drag force coefficients of trucks with various mud-flaps

The geometries of both flaps assume the presence of an anti-sail bracket with some curvature of the flaps beyond the device. A half slat (Fig. 7c) was studied as a possible low drag alternative for half flaps. The slats are inclined at an angle of 45 degrees to the flap plane and overlap each other to disallow straight flow through them. The wind-averaged drag value comparisons for the 3 components in Fig. 7d show that full flaps extract a heavy penalty by adding 8.6% to the drag while the half-flaps add only a modest 2.1%. The additional drag caused by half flaps can be completely eliminated by the use of half slats. Fig. 8a shows that the mud-flap and trailer account for 78% and 74% of the total drag increase while the wheel assembly experiences lower drag which accounts for 52% of the overall increase. The drag on the half-slats are almost identical to that on the base GCM for most crosswind angles as can be seen in Fig. 8b.

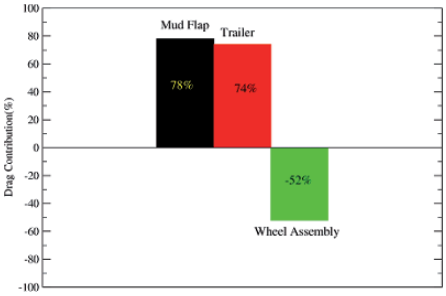

Fig. 8a Drag increase contributions for truck with full rear flaps

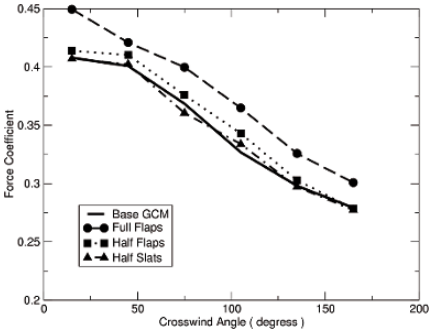

Fig. 8b Variation of drag with crosswind angle for truck with rear mud-flaps

Conclusions

The simulations with and without spinning wheels indicate that a more realistic treatment of the wheels in trucks is needed particularly when evaluating components in close proximity to the wheels. The question of whether a simple slip boundary condition based smooth wheel is sufficient to capture the change in flow characteristics caused by a real wheel with treaded tires and wheel holes cannot be answered without experimental studies and validation.

The base flap simulations demonstrate that the flow solver and grid resolution used in this study can produce a reasonable estimate of the relative magnitude of the drag reduction in the trailer base region in spite of the fact that validation studies show that CFD methods have a clear weakness in predicting flow features in this region. The implication is that a gross feature like the averaged pressure over the trailer back is being captured reasonably well while the smaller scale features are being missed. There is no guarantee that this is likely to be true for any and all devices that work in the base area and therefore simulations should be looked upon with skepticism in the absence of supporting experimental evidence.

The front spoiler simulation did not demonstrate any drag reduction for the GCM truck model. However the fact that the spoiler added only a negligible amount of drag indicates that the device is likely to reduce drag by a few percentage points for real truck with a significant amount of blockage in the underbody area.

A complete analysis of the mud-flaps would require the solution of a coupled fluid-structures problem downstream of a fully detailed rotating wheel. The current study has simplified the problem considerably in order to make it tractable and the results indicate that mud-flaps, particularly full flaps, are extracting a rather high toll in terms of their drag contribution. The half slat simulations indicate that simple changes to the mud flaps might be sufficient to mitigate their drag contributions. Other components in that area such as the rear impact guard, the

brake light panels and the license plate could be redesigned to perhaps yield small drag savings as well.

References

1. Browand F, Radovich C, & Boivin M (2005) Fuel Saving by Means of Flaps Attached to the Base of a Trailer: Field Test Results. SAE Paper 2005-01-1016.
2. Chorin AJ (1967) A Numerical Method for Solving Incompressible Viscous Flow Problems. J Comput Phys 2:12-26
3. Croll RH, Gutierrez WT, Hassan B, Suazo JE & Riggans AJ (1996) Experimental Investigations of the Ground Transportation Systems (GTS) Project for Heavy Vehicle Drag Reduction. SAE Paper 96-0907.
4. Hucho W-H (1998) Aerodynamics of Road Vehicles: From Fluid Mechanics to Vehicle Engineering, SAE International.
5. Ingram KC (1978) The Wind-Averaged Drag Coefficient Applied to Heavy Goods Vehicles. Transport and Road Research Laboratory Supplementary Report 392.
6. Karman S (2006) Unstructured Viscous Layer Insertion Using Linear-Elastic Smoothing. AIAA Paper 2006-0531.
7. McCallen R et al (2006) DOE's Effort to Reduce Truck Aerodynamic Drag through Joint Experiments and Computations. www.eere.energy.gov/vehiclesandfuels/pdfs/hvso_2006/02_mccallen.pdf
8. Nichols DS, Hyams DG, Sreenivas K., Mitchell B, Taylor LK & Whitfield DL (2006) Aerosol Propagation in an Urban Environment. AIAA Paper 2006-3726.
9. Ortega FM & Kambiz S (2004) An Experimental Study of Drag Reduction Devices for a Trailer Underbody and Base. AIAA Paper 2004-2252.
10. Pankajakshan R, Sreenivas K, Mitchell B & Whitfield DL (2007) CFD Simulations of Class8 Trucks. SAE Paper 2007-01-4293.
11. Sreenivas K, Hyams DG, Nichols DS, Mitchell B, Taylor LK, Briley WR, & Whitfield DL (2005) Development of an Unstructured Parallel Flow Solver for Arbitrary Mach Numbers. AIAA Paper 2005-0325.
12. Sreenivas K, Nichols DS, Hyams DG, Mitchell B, Sawyer S, Taylor LK & Whitfield DL (2007) Computational Simulation of Heavy Trucks. AIAA Paper 2007-1087.
13. Storms BL, Satran DR, Heineck JT, & Walker ST (2004) A Study of Reynolds Number Effects and Drag-Reduction Concepts on a Generic Tractor-Trailer. AIAA Paper 2004-2251.

Applicability of Commercial CFD Tools for Assessment of Heavy Vehicle Aerodynamic Characteristics

David Pointer, Tanju Sofu, Jimmy Chang, and David Weber

Argonne National Laboratory, 9700 S Cass Ave, Argonne, IL, 60439, USA.
David.Pointer@anl.gov

Abstract In preliminary validation studies, computational predictions from the commercial CFD codes Star-CD were compared with detailed velocity, pressure and force balance data from experiments completed in the 7 ft. by 10 ft. wind tunnel at NASA Ames using a Generic Conventional Model (GCM) that is representative of typical current-generation tractor-trailer geometries. Lessons learned from this validation study were then applied to the prediction of aerodynamic drag impacts associated with various changes to the GCM geometry, including the addition of trailer based drag reduction devices and modifications to the radiator and hood configuration. Add-on device studies have focused on ogive boat tails, with initial results indicating that a seven percent reduction in drag coefficient is easily achievable. Radiator and hood reconfiguration studies have focused on changing only the size of the radiator and angle of the hood components without changes to radii of curvature between the radiator grill and hood components. Initial results indicate that such changes lead to only modest changes in drag coefficient.

Introduction

With increasing worldwide concerns about higher air quality standards, greenhouse gas emissions and energy security, significant effort continues to be invested in the development of cleaner, more fuel efficient tractor trailer systems. Modern Class 8 tractor-trailers can have wind average drag coefficients as high as $C_D = 0.6$. At 70 miles per hour, as much of 65% of the total energy available for work that is expended by a typical heavy truck vehicle can be consumed in overcoming aerodynamic drag. Since the energy losses resulting from aerodynamic drag increase as vehicle speed increases, vehicles traveling at higher speeds expend even more energy in overcoming aerodynamic drag forces. A reduction in

the drag coefficient of such vehicles of 50% is not inconceivable and would result in a reduction in fuel use on the order of 25%. [1]

As part of the U.S. Department of Energy Office of FreedomCAR and Vehicle Technologies' Working Group on Aerodynamic Drag of Heavy Vehicles, Argonne National Laboratory is investigating the applicability of commercial Computational Fluid Dynamics (CFD) software for assessment of heavy vehicle aerodynamic characteristics as part of a computational simulation based design process for tractor-trailer systems. This work focuses on the assessment and application of tools and procedures for development and design of strategies or devices for reduction of aerodynamic drag related parasitic energy losses.

Methodology

Prior efforts [2,3,4] as part of the U.S. Department of Energy's Heavy Vehicle Aerodynamics Working Group have evaluated the applicability of commercial CFD software in heavy vehicle design, including assessments of the expected impact of grid resolution and structure on prediction accuracy, the impact of the RANS turbulence model formulation selected, and the impact of considering only half of a vehicle to reduce computational costs. The experience developed by this program provides generic advice for the application of a commercial finite-volume based CFD software package to the prediction of heavy vehicle aerodynamic drag coefficients. In this effort, the experience accumulated in the application of commercial CFD tools to heavy vehicles is applied to enable the quantification of the effects of changing the design of the vehicle. All computational simulations presented herein have used version 3.26 of the commercial CFD code Star-CD. [5]

All computational meshes were generated from CAD data using the automated meshing tools included with Star-CD. In the unstructured hybrid hexahedral/polyhedral computational meshes used in these studies, two separate parameters determine the local size of the mesh. A near-vehicle cell size defines the target cell size in the region immediately surrounding the vehicle surface, and a minimum cell size defines the minimum cell dimension which may be used to resolve curvature of the vehicle surface. Mesh sensitivity analyses included in earlier studies [2,3,4] examined the effects of changes in the near-vehicle cell size and minimum cell size parameters on the prediction of the drag coefficient.

Selection of Tractor Trailer Geometry

All studies presented herein are based on the Generic Conventional Model (GCM), developed by NASA Ames Research Center for scaled wind tunnel testing, is a generalized representation of a conventional aerodynamic U.S. tractor-trailer truck, as shown in Fig. 1. The 1/8th scale model is approximately 2.5 m long by 0.3 m wide by 0.5 m high. The studies contained herein consider experiments that were completed in the NASA Ames 7ft. by 10 ft. wind tunnel. Instrumentation included a force balance, 476 steady pressure transducers, 14 dynamic pressure transducers, and three-dimensional Particle Image Velocimetry (PIV). Data was collected at various Reynolds number values and yaw angles. [6]

Computational Requirements

Models are constructed using a 64-bit 2.8GHz Xeon Linux workstation with 8 GB of RAM. All simulations presented herein utilized the Beowulf cluster maintained by the Nuclear Engineering Division for performing engineering mechanics, fluid dynamics, and reactor engineering analyses. The cluster consists of three front-end (i.e., control) nodes and 100 compute nodes. Each of the 100 compute nodes has a 3.2 GHz Pentium IV processor with 2 GB of memory. The cluster's file server provides nearly 1 Terabyte of home file system space. All of the machines in the cluster are interconnected via Gigabit Ethernet. Typically, 10 computational nodes were used for each simulation.

All cases presented herein could be simulated to steady state convergence – defined by the reduction of the residual for each active equation below 10^{-4} and stabilization of the monitored value of the drag coefficient – with a turn around time of less than one day from the generation of the surface mesh to the completion of the simulation. The optical scan origin of the nominal CAD data makes modification of the geometry more difficult than would be expected for a geometry initially generated by a CAD package. Significant time and effort is required to ensure that all of the complex surfaces created from the optical scan maintain their numerous critical dimensions and connect at each edge to form a single closed volume.

Fig. 1 Generic Conventional Model Geometry

Brief Summary of Prior Validation and Sensitivity Results

Prior studies focused on establishing the validity of commercial CFD software for the prediction of the aerodynamic characteristics of a tractor-trailer vehicle. This previous effort included a mesh sensitivity study considering the effect of near vehicle cell size and minimum cell size on the accuracy of aerodynamic characteristics as well as the impact of turbulence model selection and the use of half vehicle versus full vehicle models. Additional studies have examined the ability to predict the impact of cross-winds on aerodynamic performance. [2,3,4]

Computational Mesh Sensitivity

A series of studies have been completed to evaluate sensitivity of the predictive accuracy to selection of the two primary characteristic dimensions of the generated computational mesh: the near vehicle cell size and the minimum cell size. To assess the impact of the near-vehicle cell size, a series of parametric simulations was completed specifying near-vehicle cell sizes between 6mm and 10 mm for the 1/8th scale GCM. Results, summarized in Table 1, indicate that the drag coefficient can be predicted with acceptable accuracy using a near vehicle cell size of 6 mm. Furthermore, coarser meshes using near vehicle cell sizes as large as 12 mm can likely be used for initial coarse evaluations and trending.

Based on these results, an additional study was completed to evaluate the impact of the minimum cell size. The default minimum cell size in the previous study was 1/8 the near-vehicle cell size. In this study the minimum cell size was reduced to determine whether the same computational accuracy observed in the 6mm case could be achieved using a smaller number of computational cells. When the minimum cell size in the 8 mm case was reduced from 1 mm to 0.5 mm, the accuracy of the drag coefficient prediction improved from 4.2 percent error to 1.0 percent error. This level accuracy was achieved using 30% fewer computa-

Table 1. Effects of Near-Vehicle Cell Size Parameter on Accuracy of Drag Coefficient Prediction.

Near-Vehicle Cell Size (mm)	Predicted Drag Coefficient	Error in Drag Coefficient
experiment	0.398	
16	0.449	12.0
12	0.441	10.3
10	0.418	4.9
8	0.415	4.2
6	0.405	1.7

Table 2. Results of evaluation of two-equation turbulence models for prediction of drag coefficients for the GCM geometry.

Turbulence Model	Predicted Drag Coefficient	Percent Error in Prediction
Experiment	0.398	--
High-Reynolds Number k-epsilon Model	0.402	1.0
Menter k-ω SST model	0.401	0.8
RNG model	0.389	2.3
Chen's model	0.3919	1.61
Quadratic model	0.3815	4.32

tional cells than in the most refined model in the near-vehicle cell size study. Further studies have shown that the further refinement of the near wall cells does not significantly improve the accuracy of the drag coefficient predictions.

Turbulence Model Effects

In all simulations completed for the computational mesh sensitivity studies, the high Reynolds number k-ε turbulence model was used in conjunction with a standard logarithmic wall function for the prediction of turbulent kinetic energy and eddy diffusivity. While the high Reynolds number k- ε turbulence model is a robust general purpose turbulence model, the strong adverse pressure gradients and large flow recirculation regions associated with the GCM geometry may limit the applicability of generic steady state RANS modeling strategies. Using the computational mesh with a near vehicle cell size of 8 mm and a near wall cell size limit of 0.5 mm, simulations of the aerodynamic characteristics of the GCM model were repeated using five steady RANS turbulence models and their associated wall functions: 1) the standard high-Reynolds number k-ε model with logarithmic wall function, 2) the Menter k-ω SST model, 3) the renormalization group (RNG) formulation of the k-ε model, 4) the Chen formulation of the k-ε model, and 5) the quadratic formulation of the k-ε model. Drag coefficients predicted using each of the selected steady-RANS turbulence models are shown in Table 2. The differences in the predicted drag coefficient are largely a result of localized discrepancies in the surface pressure coefficient predictions in the regions of separated flow, with the largest discrepancies appearing in the underbody region just behind the tractor.

Yaw Angle Effects

The effects of cross-winds on the vehicle performance are evaluated by rotating the model in the wind tunnel to introduce an effective yaw angle between the wind direction and the vehicle direction. In the wind tunnel experiments, yaw angles between 14 degrees and -14 degrees were considered. In the experiments, a low drag state is observed at low yaw angles. For yaw angles greater than 3 degrees a higher drag state was observed, where large flow separation zones begin to form along the leeward side of both the tractor and trailer, introducing significant turbulent instability into the flow field.

A series of simulations was completed to evaluate the effects of the computational mesh parameters on predictive accuracy at yaw angles greater than zero. Results of the mesh sensitivity study are summarized in Fig. 2. These studies show that the transition between the high and low drag state can be accurately captured using the methodology developed for the GCM at zero yaw angle. Furthermore, the studies demonstrate that the aerodynamic coefficients of the vehicle can be predicted within a few percent error when sufficient resolution is used near the vehicle surface.

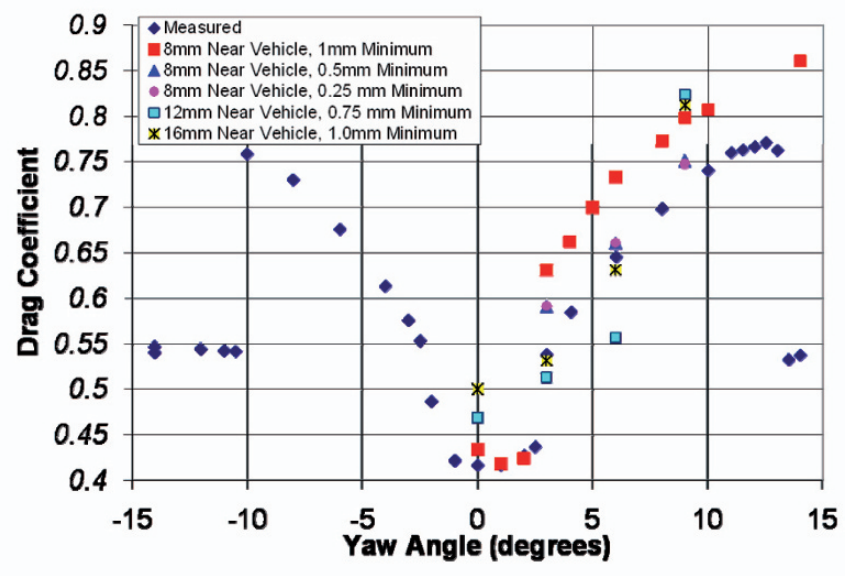

Fig. 2 Comparison of Drag Coefficient Predictions as a Function of Yaw Angle and Mesh Size Parameters.

Ogive Boat Tail Studies

A CAD geometry based on the GCM was developed with a representation of a commercially-marketed inflatable ogive boat tail device attached to the trailer, as shown in Fig. 3. Simulations using this geometry were completed using three different computational mesh configurations developed using the standard process outlined above. Results are summarized in Table 3. When compared with results for the standard configuration of the GCM using comparable mesh densities, a drag coefficient reduction of 7% is expected, which would correspond to a fuel savings of 3.5%. These predictions are consistent with claims based on wind tunnel and road tests by the company that markets the device.

Fig. 3 Modified GCM Geometry with Ogive Boat Tail

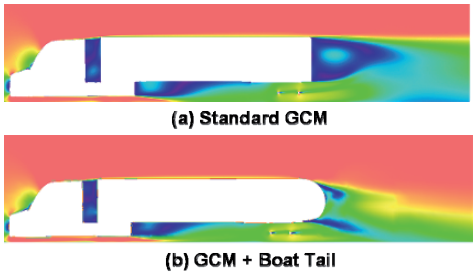

Fig. 4 Velocity Magnitude Predictions for the Standard GCM Geometry and for the Modified GCM Geometry with Ogive Boat Tail

The impact of the device on the wake behind the vehicle is quite dramatic, with the wake closing shortly behind the vehicle rather than many vehicle lengths downstream, as shown in the comparison between results with and without the device in Fig. 4. While this effect should improve driving conditions a vehicle length or more downstream from the rear of the tractor-trailer, as with most trailer boat tail devices, the more energetic turbulence in the reduced-length wake may negatively impact driving conditions for passenger cars near the rear of the vehicle.

Table 3 Summary of Drag Coefficient Predictions for the GCM Geometry with Ogive Boat Tail.

Near Vehicle Cell Size	Near Wall Cell Size	Drag Coefficient
12 mm	2 mm	0.4179
8 mm	1 mm	0.4116
8 mm	0.5 mm	0.3975

Radiator and Grille Modifications

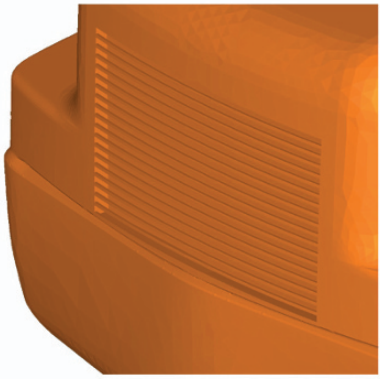

Fig. 5 Grill Geometry of the Modified Generic Conventional Model

In order to meet more restrictive EPA emissions requirements, manufacturers are likely to substantially redesign engine cooling packages to reject more of the engine heat that is currently carried away by the exhaust. An increase in radiator size is likely to result. In order to quantify the potential impact of this change on drag related parasitic energy losses, a series of modified GCM geometries have been developed with modified radiator or grille dimensions. To determine whether the flow of external air through the radiator and into the engine compartment must be modeled when considering tractor design changes, a series of simulations was completed in which an outlet condition is placed at or near the grill location. In these cases, air entering the engine compartment does not exit to rejoin the bulk flow, as if the vehicle contained a tank of infinite volume into which it was transferred. While not physically representative, this approach allows the effects of flow entering the radiator to be isolated from the effects of flow exiting the underhood region into the bulk flow around the vehicle.

The CAD description of the GCM surface was modified to include an open grill region as shown in Fig. 5. Flow then passes through this grill before exiting the model through an outlet condition placed roughly at the position of the radiator surface. Since flow velocities within the gap between the grill and radiator are very small and the pressure within the gap is much lower than the stagnation pressure, the impact of the inaccuracy of the force calculation at the outlet boundary on the total drag force calculation is expected to be minimal. With the modified geometry, consideration of flow into the radiator results in an increase in the vehicle drag coefficient of approximately 1 percent. Based on these results, it is assumed that the flow into the radiator can be neglected.

Radiator configuration effect studies have considered 4 sets of changes in configuration:

- Changes in grill/radiator height
- Changes in grill/radiator width
- Changes in grill/radiator surface area (aspect ratio maintained)
- Changes in grill/radiator tilt with respect to the vertical axis of the vehicle

In all cases, the GCM geometry is modified such that only the dimensions of the radiator and the angle of the top and side hood panels are changed. Although

the curved segments of the hood region have a complex geometry, the primary radius of curvature between the hood panels and between the top of the hood and the grill is maintained in all cases. A significant number of trial and error iterations between the CAD model and the CFD model were required for each geometric change to ensure that no defects were introduced by the modification of the CAD model which negatively impacted the ability to properly mesh the model or artificially introduced large changes in drag forces. All results presented herein are based on CAD surfaces which have been corrected through this procedure. These issues would almost certainly been avoided had a standard CAD model that was not based on an optical scan been used, since more of the surface construction information would have been recoverable in a standard CAD model.

The effects of changes in grill height on the aerodynamic characteristics of the GCM geometry were evaluated for a 10% reduction in grille height as well as 5% and 10% increases in grille height. To account for the effects of cross-winds on real highway vehicles, yaw angles of 0, 3 and 6 degrees were considered for each case. Predicted drag coefficients are compared with the values obtained for the nominal configuration, as shown in Fig. 6. All changes in drag coefficient observed fall within the expected accuracy of the simulation, which is +/- 1% for zero yaw and +/- 5% for higher yaw angles, and no significant impacts on drag-related parasitic losses can be expected to result from these design changes. The conclusion is supported by the surface pressure coefficient contours compared for the three variations and the nominal case in Fig. 7, which show that only the spatial distribution, not the integral sum, of the pressure force acting on the tractor is altered by this change in geometry.

The effects of changes in the width of the radiator and grill region on the aerodynamic characteristics of the GCM geometry were evaluated for both a 10% reduction and a 10% increase in the grill width. Yaw angles of 0, 3 and 6 degrees were again considered for each case. Predicted drag coefficients, shown in Fig. 8, exhibit even less variation that are observed for changes in height and are again within the expected error of the simulations. No significant change in drag force acting on the vehicle is expected as a consequence of small changes in the radiator width. Predicted surface pressure coefficient data, as shown in Fig. 9, again supports this conclusion.

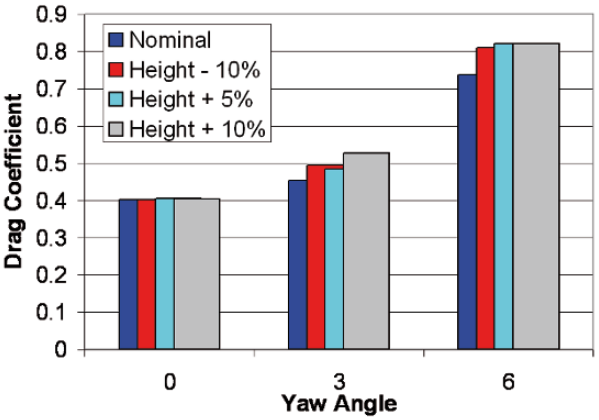

Fig. 6 Predicted Drag Coefficients for Changes in Radiator Height

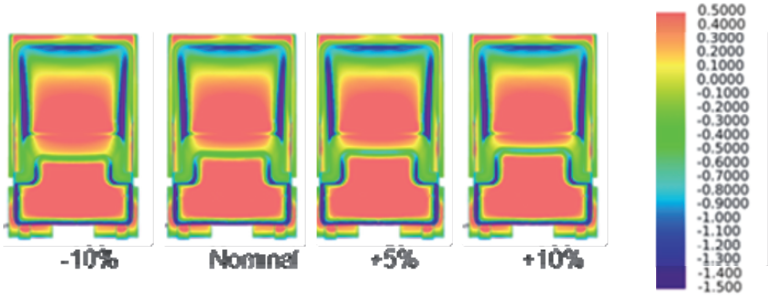

Fig. 7 Predicted Surface Pressure Coefficient Distributions for Changes in Radiator Height

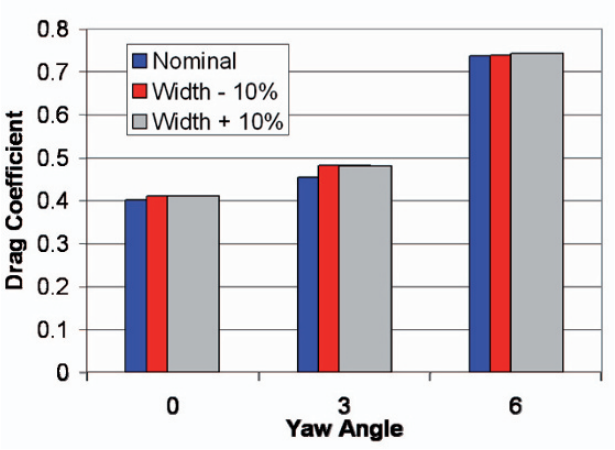

Fig. 8 Predicted Drag Coefficients for Changes in Radiator Width

Since the effects of changes in both height and width of the grill and radiator region where minimal, the effects of changing the total surface area of the radiator and grill region without changing the ratio of the height to the width was evaluated for only a 10% reduction in surface area. Yaw angles of 0, 3, and 6 degrees were again considered to account for cross wind effects. Predicted drag coefficients are shown alongside results for the nominal geometry in Fig. 10. No significant variation in the predicted drag coefficient is observed, and predicted surface pressure coefficient data, shown in Fig. 11, again confirms this conclusion.

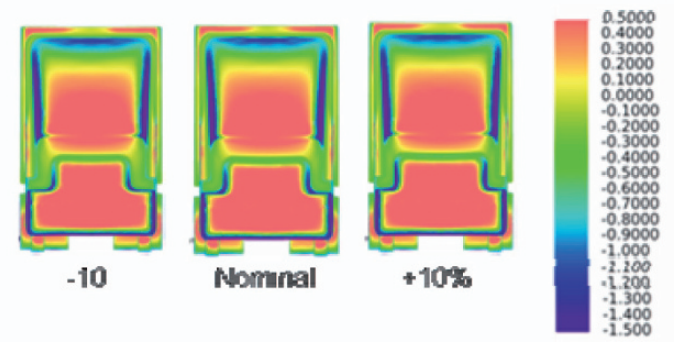

Fig. 9 Surface Pressure Coefficient Distributions for Changes in Radiator Width

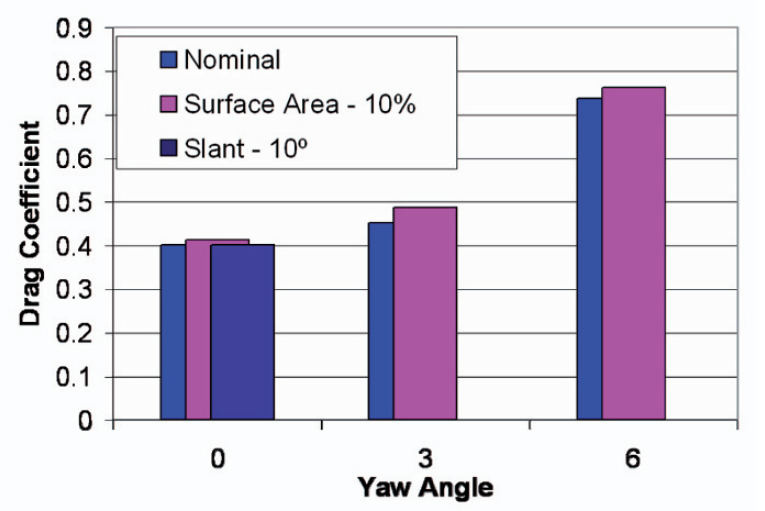

Fig. 10 Predicted Drag Coefficients for Changes in Radiator Surface Area and Radiator Tilt

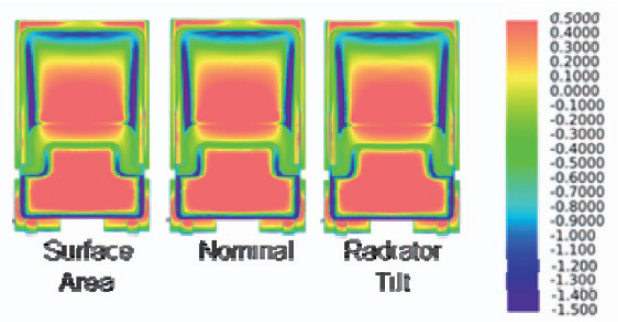

Fig. 11 Surface Pressure Coefficient Distributions for Changes in Radiator Surface Area and Radiator Tilt

In the final study, the effects of the tilt of the grill and radiator are investigated. The bottom of the grill/radiator region is held fixed and the top is tilted backward toward the rear of the vehicle until it is 10° from the vertical axis. Since the drag coefficient of this configuration at zero degrees is with 0.25 percent of the prediction for the nominal geometry, only this case was considered for this configuration. The surface pressure coefficient distribution, also shown in Fig. 11, again confirms this conclusion.

Conclusions

The purpose of this work was to evaluate the applicability of commercial CFD for the quantification of the effects of small and large geometric changes on the aerodynamic performance of a generic tractor-trailer configuration. Studies include the addition of an ogive boat tail to the base of the trailer and small modifications of the tractor's radiator and grille configuration. A nominal geometry based on the Generic Conventional Model was developed and the modified geometries were defined by altering the dimensions of the GCM using commercial CAD software. CFD models were developed using the commercial code Star-CD and the approach developed as part of the authors' prior contributions to the U.S. Department of Energy's Heavy Vehicle Aerodynamic Working Group.

Based on these results, the ogive boat tail concept appears to have the potential to reduce aerodynamic drag related parasitic energy losses and to improve fuel economy. Initial results indicate that small changes in radiator configuration offer neither a significant improvement in fuel economy when reducing the radiator size nor a significant penalty when increasing the radiator size – at least for reasonably aerodynamic vehicles. Small changes in radiator tilt also have a limited effect. These results do not, however, indicate that reductions in radiator size provide no benefit to all tractor trailer vehicles. For less aerodynamic tractors that do not al-

ready take advantage of the very significant benefits of corner rounding with relatively large radii of curvature, reductions in radiator size likely enable the development of new designs which do capitalize those benefits.

Acknowledgement

The submitted manuscript has been created by the University of Chicago as Operator of Argonne National Laboratory ("Argonne") under contract No. W-31-109-ENG-38 with the U.S. Department of Energy.

References

1. McCallen R et al, "DOE's Effort to Reduce Truck Aerodynamic Drag – Joint Experiments and Computations Lead to Smart Design," AIAA Fluid Dynamics Conference, AIAA, Portland, OR, 2004. UCRL-CONF-204819
2. David Pointer, Tanju Sofu, and David Weber, "Development of Guidelines for the Use of Commercial CFD in Tractor-Trailer Aerodynamic Design," 2005 SAE Commercial Vehicle Engineering Conference, Chicago, IL, November 2005. (SAE Paper No. 05CV-120).
3. David Pointer, "Evaluation of Commercial CFD Code Capabilities for Prediction of Heavy Vehicle Drag Coefficients," Proceedings of the 2004 AIAA Fluid Dynamics Conference and Exhibition, Portland, Oregon, June 2004. (AIAA-2004-2254)
4. David Pointer, Tanju Sofu, and David Weber, "Commercial CFD Code Validation for Heavy-Vehicle External Aerodynamics Simulation", in R McCallen, F Browand, and J Ross, eds., The Aerodynamics of Heavy Vehicles: Trucks, Buses and Trains, Berlin: Springer Verlag, 2004, pp 473-484.
5. Star-CD, CD-adapco group, Melville, NY.
6. Satran D, "An Experimental Study of the Generic Conventional Model (GCM) in the NASA Ames 7-by-10-Foot Wind Tunnel," United Engineering Foundation Conference on the Aerodynamics of Heavy Vehicles: Trucks, Buses, and Trains, United Engineering Foundation, New York, 2002.

Detached Eddy Simulations of a Simplified Tractor/Trailer Geometry

Christopher J. Roy[1] and Harshavardhan A. Ghuge[2]

[1] Aerospace and Ocean Engineering Department, Virginia Tech, 215 Randolph Hall, Blacksburg, Virginia, 24061-0203, cjroy@vt.edu

[2] Furnace Improvements, 1600 Highway 6 South, Ste. 480, Sugar Land, TX. 77478, Hghuge@heatflux.com

Abstract Detached Eddy Simulations (DES) are presented for the flow over simplified tractor/trailer geometry at zero degrees yaw angle. The simulations are conducted using a multi-block, structured computational fluid dynamics code. Coarse and fine grids of 3.8 million and 13.2 million cells, respectively, are used for the simulations. The analysis involves estimation of the period of initial flow transients as well as the period required to obtain statistical convergence, and suggests that prior DES studies for this case were not run long enough to ensure statistical independence. Time-averaged quantities compared with experimental data include vehicle drag, surface pressure and wake velocities. The drag coefficient predicted by the DES model matches closely with the experimental value; however, the DES model fails to accurately capture the details of the turbulent flow in the near wake of the trailer base. The simulations on the fine grid show significant improvement over the coarse grid results. Fourier analysis of the unsteady pressures in the base region suggests that the discrepancies in the near wake are/may be due to the improper transfer of turbulence information from the attached boundary layers (which are modeled with the Spalart-Allmaras RANS model) to the turbulent wake where LES-type modeling is used.

Introduction

Tractor-trailers are the prime means for transporting commodities across the US. At a common highway speed of 70 mph, 65% of the total engine output of a Class 8 tractor-trailer is consumed in overcoming the aerodynamic drag [1]. A reduction in the fuel consumption of these tractor-trailers even by a marginal amount can significantly reduce oil consumption and also generate less pollution. One of the ways to reduce the fuel consumption of a tractor-trailer is to reduce the overall aerodynamic drag.

The most common turbulence modeling approach for engineering applications involves solving the Reynolds-Averaged Navier-Stokes (RANS) equations [2]. The RANS equations model the effect of the turbulent eddies on the flow rather than resolving the eddies. Roy et al. [3] have performed RANS simulations on simplified tractor-trailer geometry at a zero degrees yaw angle using the baseline Menter k-ω model [4] and the Spalart-Allmaras one-equation model [5]. The flow over the front and sides of a tractor-trailer is mostly an attached boundary layer flow; however, there is massive separation in the near base region. Accurate prediction of the pressure in the near base region is important because the pressure in this region plays an important role in the pressure drag acting on the truck. The pressure drag is the major component of the overall aerodynamic drag acting on the tractor-trailer. The prediction of the pressure and velocity in the near base region made by Roy et al. [3] using RANS modeling is not in agreement with the experimental data due to the inability of the RANS models to accurately capture the near-wake three-dimensional vortical structure. Hence RANS modeling cannot be used for capturing the details of a massively separated flow which involves shedding of the vortices. To predict the details of the flow structure in the near wake region the turbulent eddies may need to be resolved. Large Eddy Simulation (LES) is the turbulence modeling technique in which the larger eddies are resolved and the effect of the smaller eddies is modeled using a sub-grid scale model. LES is computationally expensive but is generally more accurate compared to a RANS solution. The biggest drawback of LES is that it is cost prohibitive for modeling wall bounded high Reynolds number flows because of the fine mesh requirements of the model in the boundary layer. To overcome this drawback, the LES model was combined with the Spalart-Allmaras one-equation RANS model [5] to give a hybrid RANS/LES model called the Detached Eddy Simulation (DES) approach. DES was proposed by Spalart et al. [6], and Barone and Roy [7] have evaluated this model for simulation of turbulent wake flow applications. The DES model is used for simulating the flow over simplified tractor/trailer geometry in the current work.

Problem Formulation

A 1/8th scale simplified model of a class-8 tractor-trailer called the Ground Transportation System (GTS) was studied experimentally at the NASA Ames 7×10 ft wind tunnel [8]. Table 1 shows the dimensions of the model. The model is without any wheels and is supported by four posts. There is no tractor-trailer gap in the model, which helps to simplify the grid generation. The Reynolds number based on the trailer width (W = 0.3238 m) is approximately 2 million. The origin of the co-ordinate system is in the vertical symmetry plane and at the bottom of the front face of the GTS. The x-axis runs downstream. The y-axis is along the vertical direction and the z-axis runs spanwise towards the side wall. Surface

pressures, wake velocities (from PIV data) and coefficient of drag are used for comparison with the simulations in the present work. Figure 1 shows some of the PIV data planes located near the base of the GTS model which will be used for comparing the *u*- and *v*-velocity contours and streamlines. Table 2 shows the conditions of the wind tunnel during the experiment.

Table 1 Dimensions of the GTS

H	0.45 m
L	2.48 m
W	0.32 m

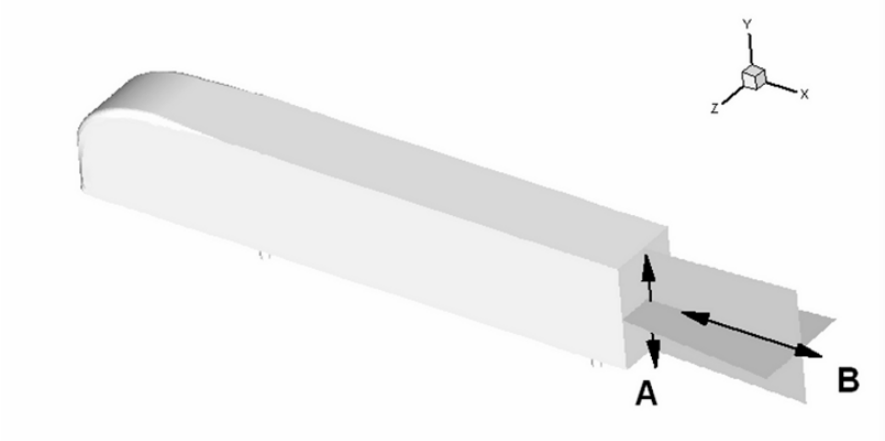

Fig. 1 PIV planes in the near base region

Table 2 Wind tunnel conditions

Parameter	Value
Re	2.02 million
V_∞	93.8 m/s
P_t	102,653.2 N/m^2
P_d	5266.82 N/m^2
T_t	285.76 K
	1.18 kg/m^3
P_{ref}	97,216. N/m^2
M_{ref}	0.279

Simulation Approach

The code used for the simulations was the Sandia Advanced Code for Compressible Aerothermodynamics Research and Analysis (SACCARA). It is a compressible flow solver used at Sandia National Laboratories and was originally developed from the INCA code [9][10] written by Amtec Engineering. It is used to solve the Navier-Stokes equations and the turbulence transport equations in finite-volume form. Code verification has been performed on the SACCARA code by code-to-code comparison with other Navier-Stokes codes [10] and with Direct Simulation Monte Carlo method [11]. The code uses a Lower-Upper Symmetric Gauss-Seidel scheme to solve the discretized equations. This scheme is based on the works of Yoon et al. [12] and Peery and Imlay [13] and has excellent scalability up to thousands of processors.

The SACCARA code uses a cell-centered finite volume approach. The code uses Yee's Symmetric Total Variation Diminishing (STVD) upwind scheme [14] for discretization of the convective terms in the Navier-Stokes equations. The scheme is modified to incorporate Harten's artificial compression switch (ACM) [15] to further reduce the dissipation, along with characteristic based filtering [14]. This modified STVD scheme uses the constant K to control the global numerical dissipation in the solution. The value of K varies from 0.03 to 2 and is problem dependent. For the current simulations, we employed $K = 0.2$. Harten's switch is used to reduce the numerical dissipation locally. The viscous terms were discretized using central differencing. A sub-iterative procedure is used to obtain second-order accuracy during the temporal discretization, where the summation of the discretized temporal derivative and the steady-state residual at the $n + 1$ time level is iterated until it reaches the specified tolerance value. Unless otherwise specified, for the coarse mesh the number of sub-iterations performed during each time step were $n_{It} = 4$, and for the fine mesh the number of sub-iterations performed during each time step were $n_{It} = 5$.

The destruction term in the Spalart-Allmaras one-equation model, when balanced with its production term, adjusts the eddy viscosity $\tilde{\upsilon}$ to scale it with the local strain rate S and the distance from the wall d, i.e., $\tilde{\upsilon} \propto Sd^2$ [6]. The Smagorinsky eddy viscosity model scales its subgrid scale eddy viscosity with S and grid spacing Δ i.e., $\tilde{\upsilon} \propto S\Delta^2$ [6]. Spalart modified the Spalart-Allmaras one-equation model in which the distance from the wall d is replaced by $\tilde{d}$

$$\tilde{d} = \min(d, C_{DES}\Delta)$$

where Δ is maximum mesh spacing in the three coordinate directions

$$\Delta = \max(\Delta x, \Delta y, \Delta z)$$

and C_{DES} is the constant proposed by Spalart and is equal to 0.65 [6]. Away from the wall, $d > \Delta$ i.e., $\tilde{d}$ becomes equal to $C_{DES}\Delta$ and the model is modified to give Smagorinsky's subgrid LES model. Near the wall $d < \Delta$ and the model behaves as the Spalart-Allmaras one-equation model. The DES model is thus a combination of the Spalart-Allmaras one equation model and Smagorinsky's subgrid-scale LES model.

The simulations were performed over a domain that included a significant portion of the wind tunnel test section with the GTS model insertion location consistent with the experiment. A coarse mesh having 3.8 million cells and a fine mesh having 13.2 million cells were used to perform the study. Figure 2 shows the coarse mesh around the base of the GTS in the vertical symmetry plane. The grids were generated such that the highest value of the wall y^+ term is 1.4 from the coarse mesh. The structured mesh employed used point to point connectivity at the interface of two blocks. Both the grids were decomposed and solved using 86 processors.

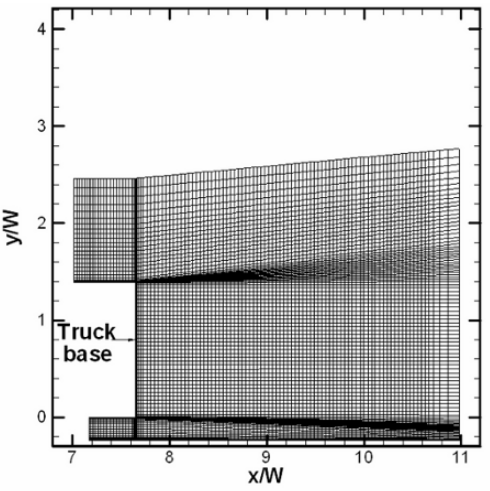

Fig. 2 Coarse mesh near the base of the GTS (z/W = 0)

The inflow boundary employs stagnation values for pressure P_t = 102,653 N/m^2 and temperature T_t = 285.76 K and enforces inflow normal to the boundary. The outflow boundary used a fixed static pressure of P = 97,700 N/m^2. The back pressure was chosen so that the tunnel wall reference pressure (P_{ref}) located at x/W = 4.47, y/W = 2.588 and z/W = -4.7 matched with the experiment. The reference pressure is used in the calculation of the pressure coefficient and drag coefficient.

$$C_p = \frac{P - P_{ref}}{P_t - P_{ref}} \qquad \text{and} \qquad C_D = \frac{D}{(P_t - P_{ref})(WH)}$$

Table 3 compares average reference pressure values from the coarse and fine mesh with the experimental value. Slip wall conditions were applied to the top and side walls of the wind tunnel to save the computational cost, while the floor of the wind tunnel, the GTS surface and the support posts employ no-slip velocity conditions and assume an adiabatic wall. The freestream dynamic eddy viscosity is set at $\mu_t = 1\times10^{-5}$ N/m^2. Solid wall boundary condition for the turbulence model can be found in [16].

Table 3 Comparison of reference pressure (P_{ref}) from the experiment and time-averaged reference pressure (P_{ref}) from simulations

Experiment	Coarse Mesh	Fine Mesh
97,336 N/m^2	97,295 N/m^2	97,249 N/m^2

Time has been non-dimensionalized by a reference time scale τ defined as

$$\tau = W / V_\infty = 0.0034 s$$

where V_∞, the freestream velocity is equal to 93.8 m/s. The coarse mesh simulations were performed using a non-dimensional time step $\Delta\tau_s = 1.16\times10^{-3}$ ($\Delta t_s = 4\times10^{-6}$ s) and the fine mesh simulations were performed using a non-dimensional time step of $\Delta\tau_s = 2.32\times10^{-3}$ (i.e., $\Delta t_s = 8\times10^{-6}$ s). Table 4 gives the characteristic length scales for the fine and coarse meshes (note that the length scales are non-dimensionalized by the width of the trailer).

Table 4 Characteristic length scales

Mesh	Δ_{wall}	Δ_{wake}	Points across the wake (considering maximum grid spacing)
Coarse	6.17×10^{-5}	0.038	26
Fine	3.08×10^{-5}	0.026	38

Numerical Accuracy

DES is a simulation of an unsteady flow i.e., it yields a time-accurate solution. To assess the mean properties of the flow the data from the simulations have to be averaged over some time window. The size of the time window is determined by performing a statistical convergence analysis. The statistical convergence analysis performed during this research involved averaging the data from the unsteady solution over different time windows. The time windows used for averaging the data are shown in Fig. 3. This figure shows pressure signal from the simulations located in the base of the GTS ($x/W = 0.64$, $y/W = 0.63$ and $z/W = -0.46$). The signal is plotted against non-dimensional time τ. It is assumed that the largest time window shown in the figure is wide enough to give statistically converged results. Also, computation of a bigger time window will increase the computational cost. The

width of this window is $\Delta\tau_w = 270$ ($\Delta t_w = 0.91$ s). Time-averaged velocity profiles corresponding to the time windows shown in Fig. 3 were used for this analysis. The line B shown in Fig. 1 is the location where the velocity profiles were computed respectively. These locations are in the turbulent wake of the flow over the GTS. Figure 4 compares the differences between the various u/V_{ref} velocity profiles corresponding to the smaller time windows shown in Fig. 3 and the u/V_{ref} velocity profile corresponding to the biggest time window. The velocity profiles corresponding to time windows having starting time $\tau_{start} = 394$ and beyond have minimal difference with respect to the corresponding profile from the biggest window. An upper and lower limit is placed on the results from the smaller time windows. These limits are equal to the maximum difference between the variable calculated from the corresponding smaller time window and the variable obtained from biggest time window/best available solution. This analysis suggested that the smallest possible time window giving results close to the statistically converged values is the window corresponding to $\tau_{start} = 394$, $\tau_{end} = 571$ (i.e., $\Delta\tau_w = 177$ or $\Delta t_w \approx 0.612$ s). Any window which is smaller than this is not wide enough to give results close to the converged values. Hence all the comparison with the experimental data is made by time averaging the data from the simulations over a period of $\Delta t_w = 0.612$ s. Unaune et al. [17] and Maddox et al. [18] have reported the statistical convergence period of $\Delta t_w \approx 0.35$ s and 0.27 s, respectively.

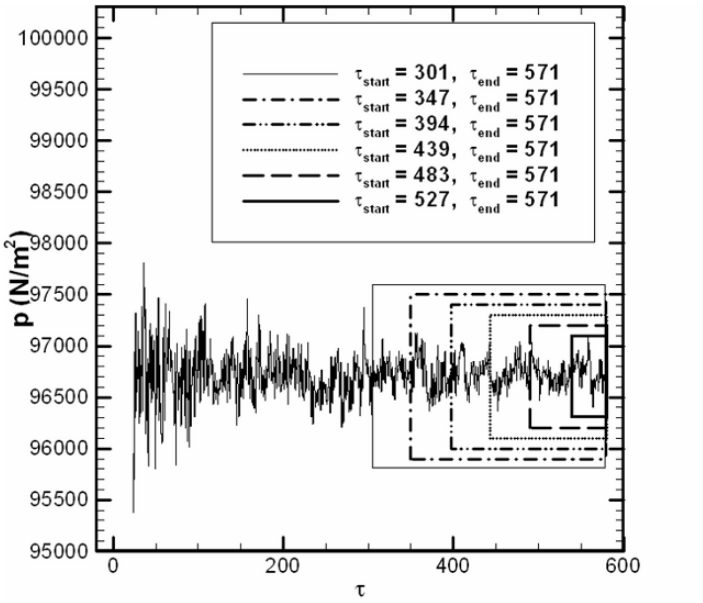

Fig. 3 Time windows for statistical convergence

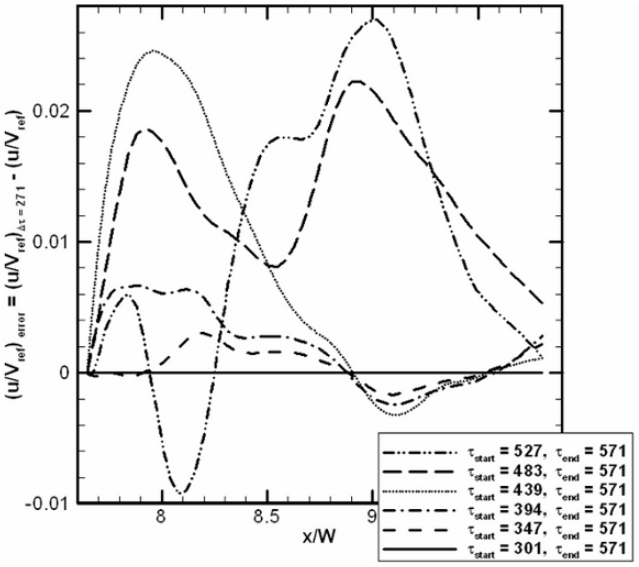

Fig. 4. Error in axial velocity relative to largest window: coarse mesh ($K = 0.2$)

The simulations are initialized with freestream values of velocity, pressure and temperature. The flow over the GTS during some initial time period oscillates because of the waves generated due to sudden exposure of the GTS to the freestream flow. These oscillations are called the initial transients. The large pressure oscillations seen in Fig. 5 near $\tau = 0$ are the initial transients in the flow. As the flow over the GTS settles the initial transients diminish. The data collected during the initial transient period should be neglected. Therefore the time period of existence of initial transients has to be calculated. For calculating the period of initial transients the pressure profiles along the line A shown in Fig. 1 was time averaged over a window with $\Delta\tau_w = 177$. $\Delta\tau_w = 177$ is the time window required to achieve statistically converged results which was determined in the previous section. The time window was slid along the time axis as shown in Fig. 5. Figure 6 compares the differences between C_p profiles corresponding to the various earlier time windows shown in Fig. 5 and the C_p profile from the window farthest along the time axis. It is assumed that the window farthest along the time axis is far enough from $\tau = 0$ and does not involve any initial transients. Pressure and velocity profiles corresponding to time windows having starting time $\tau_{start} = 301$ and beyond have minimal difference with respect to the corresponding profiles from the farthest window. This suggests the existence of initial transients up to $\tau =$ 301, i.e., t = 0.92 s. The data collected after this period has marginal effect of the initial transients and can be used for comparison with the experiment. This will be done by considering an upper and lower limit over the time-averaged data from the simulations denoting the effect of the initial transients. Initial transience period

predicted by Unaune et al. [17] is 0.2 s which is significantly less than that predicted here.

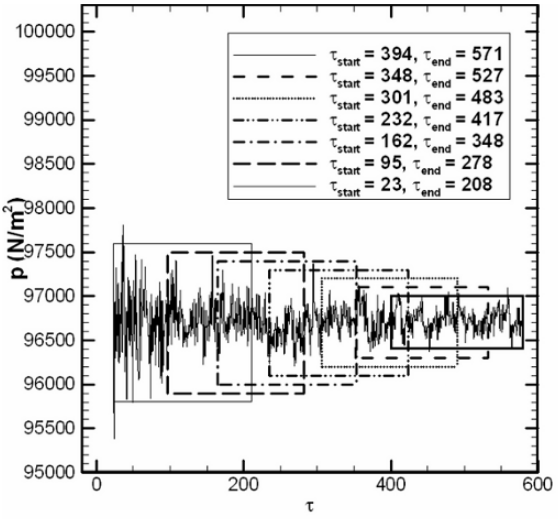

Fig. 5 Time windows for estimating initial transients

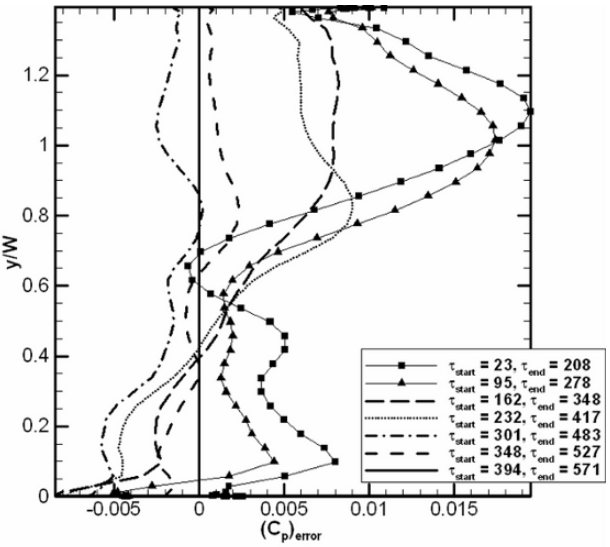

Fig. 6 Cp profile error relative to final time window: coarse mesh ($K = 0.2$)

The maximum uncertainty due to the effect of insufficient statistical convergence, presence of initial transients, temporal discretization (see Ref. [19]) and

insufficient iterative convergence (see Ref. [19]) was calculated for the pressure and velocity of the flow. Table 5 gives the values of the uncertainty from these sources. The total uncertainty was calculated using an analogy to experimental uncertainty propagation techniques using the formula

$$U_T = \sqrt{U_1^2 + U_2^2 + U_3^2 + U_4^2} \ .$$

Table 5 Maxiumum uncertainty bounds

Source of uncertainty	*Cp*	*u/Vref*	*v/Vref*	*w/Vref*
Initial transients (U_1)	0.006	0.01557	0.01524	0.0212
Statistical convergence (U_2)	0.0047	0.00665	0.01103	0.01396
Number of sub-iterations (U_3)	0.007	0.01915	0.015	0.02296
Time step (U_4)	0.0175	0.05116	0.0430	0.00564
Total uncertainty (U_T)	0.028	0.0572	0.0493	0.0346

The effect of mesh size is studied by comparing results from the coarse and the fine meshes. Figure 7 compares the u/V_{ref} velocity contours and streamlines from the coarse and fine mesh in the vertical streamwise plane (shown in Fig. 1). Figure 7 (top) shows that the coarse mesh simulations predict the upper vortex dominant over the lower vortex. The fine mesh results shown in Fig. 7 (bottom) show the vortices are almost equal in size. Figure 8 compares the pressure coefficient along the line A in Fig. 1. The coarse mesh pressure profile shows a bulge in the negative direction in the upper half of the trailer base due to the dominant upper vortex in the coarse mesh. The fine mesh pressure profile is almost a flat curve due to equal size of the upper and lower vortices (Fig. 7, bottom). It should be noted that the $\Delta\tau_s$ and n_{It} values used for the fine and coarse mesh simulations are different. However the effect of $\Delta\tau_s$ and n_{It} on the results from the simulations is relatively small when compared to the effect of the mesh size. The fine mesh results, which are expected to be more accurate, are now compared with the experiment.

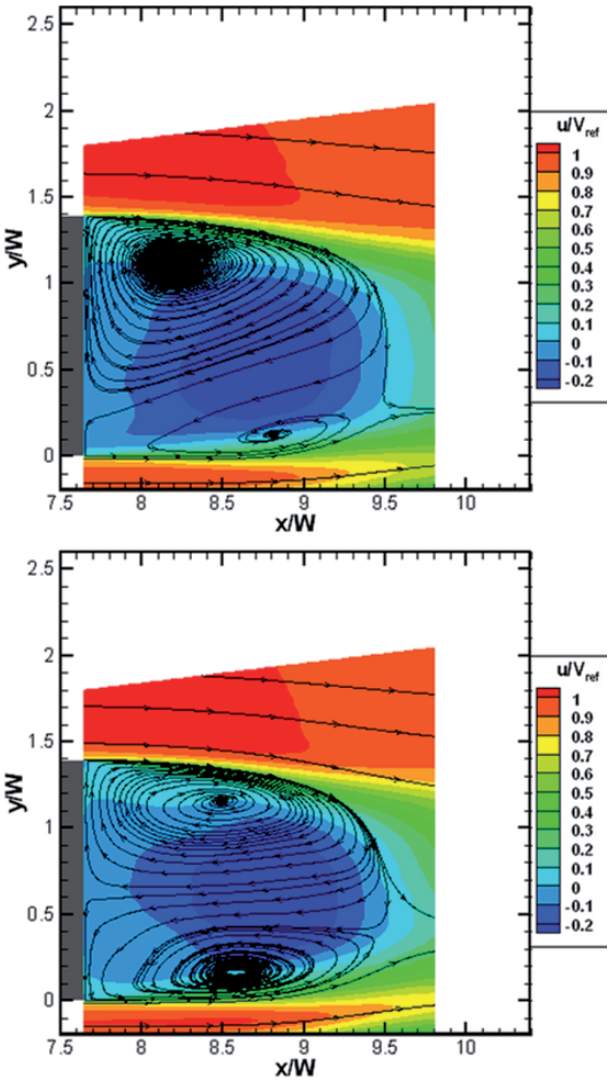

Fig. 7 Axial velocity contours and streamlines for the coarse mesh (top) and fine mesh (bottom)

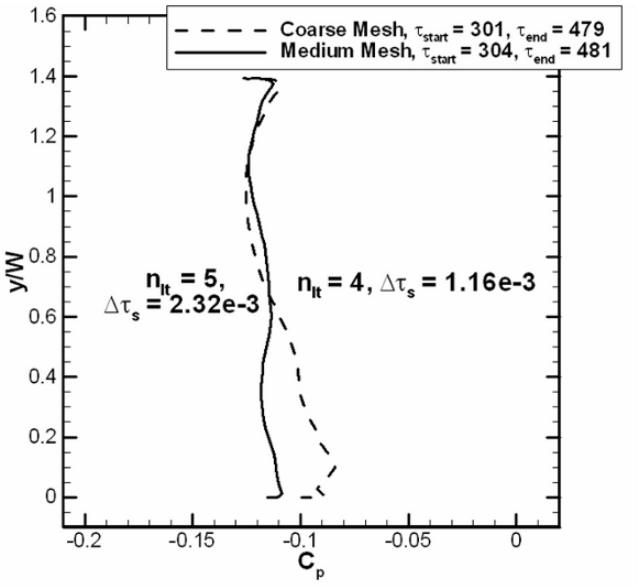

Fig. 8 Effect of mesh size on the base pressure distribution

Results and Discussion

Figures 9a and 9b compare the u/V_{ref} velocity contours and streamlines in the vertical streamwise plane (vertical plane in Fig. 1) from the experiment and fine mesh simulations. The experimental data shows the lower vortex located much closer to the base of the GTS model and at a higher location than the simulations. The upper vortex is not seen in the experimental PIV window but the nature of the streamlines in the window suggests that it may be located near the upper right corner of the window. The distribution of the vortices in the fine mesh simulations is more symmetric as seen in Fig. 9b. Figure 9c shows the u/V_{ref} velocity contours and streamlines in the vertical streamwise plane from the RANS modeling performed by Roy et al. [3]. The figure shows very similar structure of the upper and lower vortices when compared to the DES simulations. However the vortices from the RANS modeling are closer to the base of the GTS model than the results from DES simulations. This difference in location of the vortices from the experiment and the simulations gives a major difference in the pressure distribution on the base of the GTS model obtained from the experiment and the simulations (to be discussed later).

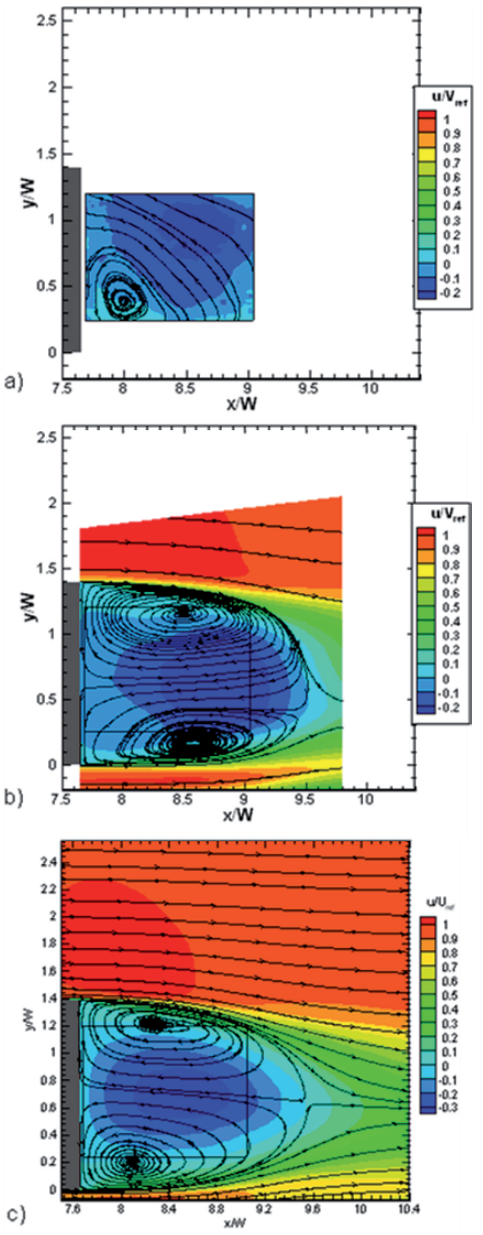

Fig. 9 Axial velocity contours and streamlines for a) experiment [8], b) fine mesh DES, and c) RANS computations [3]

Figsures 10a, b and c compare the u/V_{ref}, v/V_{ref} and w/V_{ref} velocity profiles, respectively, from the experiment and the simulations. These profiles are plotted along the line B shown in the base of the GTS model in Fig. 1. The uncertainty bounds on the profiles from the simulations are obtained from Table 5. Out of the two PIV data sets one was obtained from the vertical streamwise PIV data plane (vertical plane in Fig. 1) and the other data set is obtained from horizontal streamwise PIV data plane at $y/W = 0.696$ (horizontal plane in Fig. 1). The difference in the experimental data sets may be the result of errors in the PIV measurements. Figure 10a shows that the recovery of the u-velocity from the experiment starts earlier than the simulations. Figure 10b shows the v-velocity profiles from the experiment has a completely different trend than the profile from the simulations. Figure 10c shows a comparison of the w-velocity. Since these profiles are in the $z/W = 0$ plane i.e., the vertical symmetry plane of the GTS the w-velocity should ideally be zero in this plane and we see the same in the profiles from the simulations and the experiment.

Figure 11a compares the pressure distribution plotted along the line A in the base of the GTS as shown in Fig. 1. It should be noted that in Fig. 11a the pressure profiles are plotted on a magnified C_p scale, so that even though it appears that the profile from the DES simulations and the profile from the RANS modeling performed by Roy et al. [3] do not match with the experimental data, the overall range of the pressure predicted by the computational models match with the range of the experimental pressure values. The plot shows that the profile from the DES simulations is almost a flat curve but the RANS model shows the opposite trend of pressure distribution to that seen in the experiment. The uncertainty bound on the profile from DES simulations is obtained from Table **5**. Figure 11b compares the pressure distribution along the top and bottom surfaces of the GTS in the $z/W = 0$ plane from the experiment and the simulations. The top and bottom surfaces are in the attached boundary layer flow region where the DES model does a good job of the matching with the experimental data.

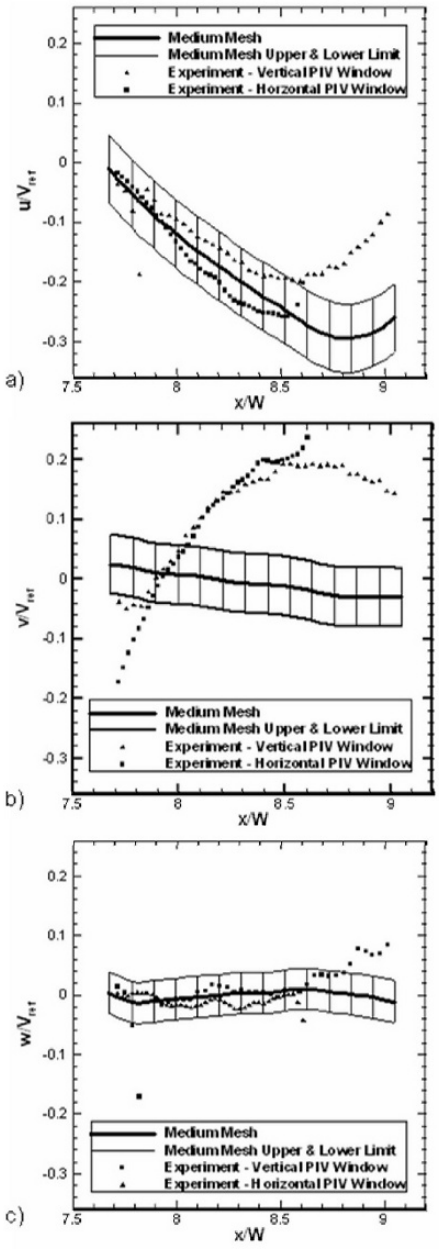

Fig. 10 Comparison of velocity profiles from experiment and DES simulations along the axial line in the wake a) u/Vref, b) v/Vref and c) w/Vref

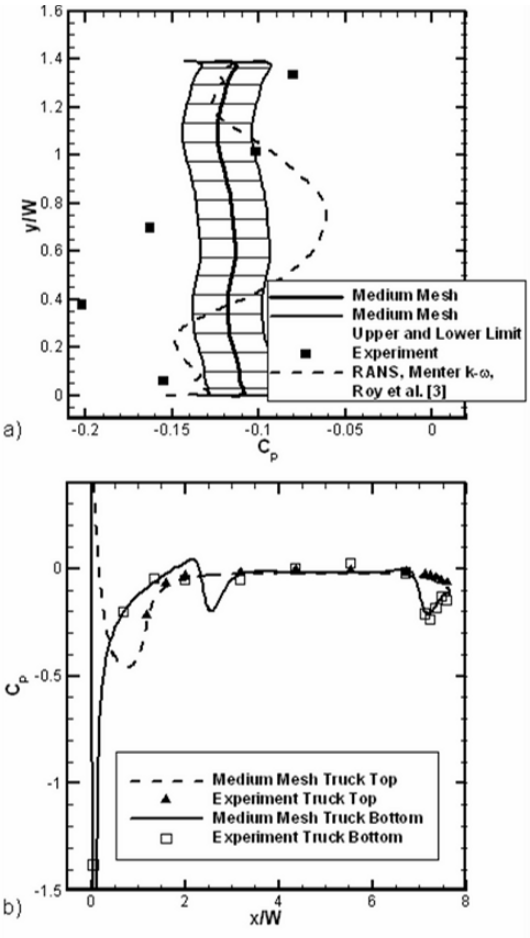

Fig. 11 Pressure coefficient profiles for a) the trailer base and b) the top and bottom of the GTS

Table 6 compares the drag coefficient from the simulations with the experimental data. The table shows that the DES simulations of the fine mesh, coarse mesh and the DES by Unaune et al. [17] do a very good job of predicting the drag. The reason for the high value of error in the drag predicted by Maddox et al. [18] is not known. RANS models overpredict the drag value by a large amount as compared to the DES simulations.

Table 6 Drag coefficient

Source	C_D	% error w.r.t. experiment
Experiment	0.249	0%
Coarse mesh DES (3.8M cells)	0.2565	+3 %
Fine mesh DES (13.2M cells)	0.2439	-2 %
Unaune et al. [17]DES (13.8M cells)	0.253	+1.6%
Maddox et al. [18]DES (6M cells)	0.279	+12%
Roy et al. RANS Menter k-ω (20M cells)	0.298	-19%
Roy et al. RANS Spalart-Allmaras (20M cells)	0.413	+65%

In the experiment a high-frequency pressure transducer is located on the base of the GTS model (x/W = 7.647, y/W = 0.63 and z/W = -0.46). The power spectra for the unsteady pressure signal is obtained by performing a fast Fourier transformation (FFT) of the normalized unsteady pressure signal from the experiment and the simulations. FFT is an efficient way to perform a discrete Fourier transform of a signal. It converts the signal from the time domain into the frequency domain. This power spectrum serves the purpose of giving an idea about the frequency of the turbulent structures in the region near the base of the GTS model. The frequency corresponding to the peak in the power spectra is the frequency containing the most turbulent energy. Although not shown, the power spectra obtained from the experiment shows a peak frequency at nearly 24Hz. The power spectra from the simulations show three peaks at approximately 80 Hz, 110 Hz and 130 Hz. Also some peaks are seen in the range of 10 to 30 Hz which appear to roughly correspond to the dominant frequency found in the experiment. Animations of the turbulent flow in the wake were performed and they showed the flapping of the shear layers which separate from the attached boundary layers on the top and bottom surfaces of the GTS in the LES region in the wake. The peaks in the simulation power spectra appear to correspond to the large-scale unsteadiness of the shear layers observed in the animations. We surmise that the presence of the additional peaks in the power spectra from the DES simulations (which are not found in the experiment) is due to the inability of the RANS boundary layer to properly transfer turbulence fluctuation information into the shear layer in the LES region. This is an acknowledged short-coming of the DES method and may in fact be responsible for the inability of the DES method to reproduce the wake structure seen in the experiments.

Conclusions

The estimated initial transient period ($t \approx 1$ s) and the time period required for achieving statistical convergence ($t \approx 0.61$ s) should provide guidance for future simulations. The drag value predicted by the simulations agrees with the experimental value. The pressure values predicted by the DES in the attached boundary layer regions also matches with the experiment. The range of the pressure values predicted by the DES simulations in the base of the GTS model agrees with the range of the values of pressure from the experiment. The actual pressure profile in the base region, however, does not match with the experimental data. The pressure profile from the DES simulations however gives much better prediction than RANS modeling [3]. The prediction of the location of the vortices near the base of the model does not match with the experimental data. Here the DES model fails to accurately capture the details of the turbulent flow in the near base region. The failure of the current DES simulations to predict wake details appear to be related to one of the main drawbacks of the hybrid RANS/LES methods, namely that there is no mechanism to transfer turbulence fluctuation information from the RANS region (i.e., the boundary layer) to the LES region (i.e., the wake). Hence when the shear layers separated from the surface of the trailer enter the wake region governed by the LES model, there is no way to convert the large, modeled eddy viscosity into large-scale turbulent fluctuations required for the LES model. Research on the transfer of information from the modeled turbulence obtained from RANS equations in the boundary layer to the LES model in the separated region should improve the predictions of the wake flow details given by DES on coarser grids.

References

[1] MacCallen R, Salari K, Ortega J, Browand F, Hammache M, Hsu T, Leonard A, Chatelain P, Rubel M, Roy C, DeChant L, Hassan B, Heineck J, Yaste D, Storms B, Englar R and Pointer D, 2004, "DOE's Effort to Reduce Truck Aerodynamic Drag - Joint Experiments and Computations Lead to Smart Design," 34th AIAA Fluid Dynamics Conference, June 28 - July 1, Portland, OR.

[2] Wilcox D,1998, Turbulence Modeling for CFD, 2nd Ed., DCW Industries, Inc., La Canada, CA.

[3] Roy C, Payne J and Payne M, 2006 "RANS Simulations of a Simplified Tractor/Trailer Geometry," Journal of Fluids Engineering, Vol. 128, pp. 1083-1089.

[4] Menter F, 1994, "Two-equation Eddy-viscosity Turbulence Models for Engineering Applications" AIAA Journal, Vol. 32, pp. 269-289.

[5] Spalart P and Allmaras S, 1994, "A One-Equation Turbulence Model for Aerodynamic Flows," La Recherche Aerospatiale, 1, pp. 5-21.
[6] Spalart P, Jou W, Strelets M and Allmaras S, 1997, "Comments on the Feasibility of LES for Wings and on a Hybrid RANS/LES Approach," Advances in DNS/LES, Columbus, OH, Greyden Press.
[7] Roy C, DeChant L, Payne J and Blottner F, 2003 "Bluff-Body Flow simulations Using Hybrid RANS/LES," AIAA 2003-3889.
[8] Storms B, Ross J, Heineck J, Walker S, Driver D and Zilliac G, 2001, "An Experimental Study of the Ground Transportation System (GTS) Model in the NASA Ames 7- by 10-Ft Wind Tunnel," NASA/TM-2001-209621.
[9] INCA User's Manual, Version 2.0, 1995, Amtec Engineering, Inc., Bellevue, WA.
[10] Payne J and Walker M, 1995 "Verification of Computational Aerodynamic Predictions for Complex Hypersonic Vehicles using the INCA Code," AIAA Paper 95-0762.
[11] Roy C, McWherter-Payne M and Oberkampf W, 2003, "Verification and Validation for Laminar Hypersonic Flowfields Part 1: Verification," AIAA Journal, 41 (10), pp. 1934-1943.
[12] Yoon S and Jameson A, 1987 "An LU-SSOR Scheme for the Euler and Navier-Stokes Equations," AIAA Paper 87-0600.
[13] Peery K and Imlay S, 1986 "An Efficient Implicit Method for Solving Viscous Multi-Stream Nozzle/Afterbody Flow Fields," AIAA Paper 86-1380.
[14] Yee H, Sandham N and Djomehri M, 1998 "Low-dissipative High-Order Shock-Capturing Methods Using Characteristic-Based Filters," Journal of Computational Physics, Vol. 150, pp. 199-238.
[15] Harten A, 1984 "On Class of High Resolution Total-Variation-Stable Schemes," SIAM Journal of Numerical Analysis, Vol. 21, No. 1, pp. 1-23.
[16] Roy C and Blottner F, 2003 "Methodology for Turbulence Model Validation: Application to Hypersonic Flows," Journal of Spacecrafts and Rockets, Vol. 40, No. 3. pp. 313-325.
[17] Unaune S, Sovani S and Kim S, 2005, "Aerodynamics of a Generic Ground Transportation System: Detached Eddy Simulations," SAE Technical Papers, 2005-01-0548.
[18] Maddox S, Squires K, Wurtzler K and Forsythe J, 2004, "Detached-Eddy Simulation of the Ground Transportation System," The Aerodynamics of Heavy Vehicles: Trucks, Buses and Trains, R McCallen, F Browand, and J Ross, Eds., Springer, Berlin, Germany, pp. 89-106.
[19] Ghuge H, "Detached Eddy Simulations of a Simplified Tractor-Trailer Geometry," Masters Thesis, Auburn University, May 2007.

A Hybrid RANS/LES Turbulence Model for use in the Simulation of Turbulent Separated Flows

Kambiz Salari, Paul Castellucci

Lawrence Livermore National Lab, USA
salari1@llnl.gov

Abstract Currently, there exists a lack of confidence in the computational simulation of turbulent separated flows at large Reynolds numbers. The most accurate methods available are too computationally costly for use in engineering applications. Using concepts borrowed from large-eddy simulation (LES), a two-equation Reynolds-averaged Navier-Stokes (RANS) turbulence model is modified to simulate the turbulent wakes behind bluff bodies. This modification involves the computation of one additional scalar field, adding very little to the overall computational cost. When properly inserted in the baseline RANS model, this modification mimics LES in the separated wake, yet reverts to the unmodified form near no-slip surfaces. In this manner, superior predictive capability may be achieved without the additional cost of fine spatial resolution associated with LES near solid boundaries. Simulations using several modified and baseline RANS models are benchmarked against both LES and experimental data for a circular cylinder wake at Reynolds number 3900. These results reveal substantial improvements using the modified system and appear to drive the baseline wake solution toward that of LES, as intended. Further results include the simulation of the turbulent wake created by the Ground Transportation System (GTS), a simplified tractor-trailer geometry studied extensively by the Department of Energy for use in turbulence model validation.

Vehicle and Tire Spray and Vehicle Interaction

Spray from Commercial Vehicles: A Method of Evaluation and Results from Road Tests

Simon Watkins

School of Aerospace, Mechanical and Manufacturing Engineering, RMIT University, Melbourne, Australia
simon@rmit.edu.au

Abstract An accurate and repeatable measurement of truck-induced spray is required to develop and test spray-reducing devices. Such a system is described, based on a sequence of CCD-captured video images of a black and white chequerboard which was partially obscured by spray from a passing test truck. Images were analyzed to reveal the contrast changes, from which spray densities were inferred. Results of on-road trials are described and it was found that none of the tested wheel-mounted systems offered any statistically significant reduction in spray. Supporting track and wind-tunnel tests documented the flow vectors close to the truck; for an unmodified vehicle and when fitted with sideskirts and a cab-mounted add-on aerodynamic device. It was concluded from the flow field studies that the problem of vision impairment for a passing motorist would be significantly reduced when sideskirts and (for vehicles hauling a high load) correctly-matched cab roof deflectors were fitted. This offers the trucking industry the combined advantages of drag and spray reduction.

1. Introduction

Trucks traveling on wet roads are known to present a nuisance to other road users; particularly when attempting overtaking maneuvers. Whilst some contention exists over the extent of danger this poses, it is clearly of annoyance to other road users and known to be a source of cleaning costs to the trucking industry [1].

There have been many attempts to retrofit several types of commercial vehicles, including buses, with devices designed to ameliorate the spray via inserts or other changes or treatment to the mudguards. These have included fabric materials, bristles and specially shaped inserts which all try to catch splash and spray in order to avoid the vision impairment associated with lateral passage of spray into the area of passing vehicles. However, analyzing the effectiveness of these devices

has proved difficult and unreliable and in 2000 a report to the USA Congress [2] concluded that there was “significant interest in splash and spray suppression by government and the private sector”. It also found that “technologies that purport to reduce splash and spray cannot be shown to translate into real world visibility improvements for drivers” and that when reviewing work in Europe “there are no data that show devices that are approved under their laboratory test result in better visibility on vehicles on the road”.

There have been several experiments conducted in Australia which have provided insights into methods to repeatably document vision impairment and to quantify the influences of mudguard treatment and the influence of aerodynamics on the movement of the spray. Other attempts to counter the lack of a reliable method and to investigate the influence of devices include [3, 4, 5, 6]. These have generally involved the use of video acquisition and analysis techniques to quantify truck-induced spray, although other laser-based methods have been used, prior to the advent of relatively low cost PCs and CCD cameras.

The video-based spray-measuring system described herein was developed at RMIT University, on behalf of the Australian Federal Office of Road Safety. From the conception of the project it was decided that the system should represent what an overtaking motorist would experience as closely as possible. This system and some typical results are described here with an overview of some supporting flow field studies.

2. Spray-Measuring System

The spray-measuring system uses the change in contrast of recorded video images to determine the density of spray. Whilst it was considered that the measurement of brightness could have a use in the measurements, a series of laboratory tests, where spray was generated in the laboratory and videoed under a range of different conditions [7] demonstrated the undesirable influence of brightness on the results. Clearly for any road or track tests this would prove problematic since the changing light (including the influence of clouds shading direct sunlight) would be an unwanted variable. The choice of contrast as the defining variable was based on the fact that objects, such as other motor vehicles, are seen by the human eye due to their contrast with the surrounding background. The laboratory tests also indicated that the use of contrast variation, as opposed to changes in image brightness, for determining spray density produced more repeatable results under a wider range of lighting conditions. The use of a contrast-based system therefore allows for better correlation of results from different test sessions than is possible with a brightness-based system. This has the advantage that testing can be conducted at different times, under different lighting conditions, while maintaining confidence in the repeatability of results.

In order to measure the change in contrast due to spray, chequered target boards were used. These target boards consisted of a grid of alternating black-and-white squares. An image of each board was taken immediately prior to the boards being obscured by spray and the contrast of each grid square in this 'control' image defined as 100% contrast. A series of images was then recorded with the target boards partially obscured with spray and the contrast of each grid square again calculated. The change in contrast of each grid square was then calculated as a percentage of the contrast of the control image, thus giving a relative value which can be compared to other results taken under different conditions.

2.1 Hardware

The main hardware components of the spray-measuring system were a pair of CCD cameras, associated video capture cards and the two chequered target boards. The CCD cameras had manually adjustable iris and shutter speed so that they did not automatically correct for the increased image brightness when spray is present. The video capture cards were installed in PCs and set to capture video at a rate of 12.5 frames-per-second at a resolution of 192x144 pixels. The images were 8-bit (256 level) greyscale. Each video sequence recorded contained 100 frames (8 seconds of video), of which approximately half were used for analysis in determining the effectiveness of the spray-reducing devices.

The target boards measured 3.2m horizontally and 2.4m vertically. Each board had been divided into a black-and-white chequered grid of 195mm squares (192 squares on each board). Vertical boarders of 40mm and horizontal boarders of 30mm surrounded the chequered region to prevent light diffusing around the target boards into the recorded region.

2.2 Software

Video capture was performed with software supplied with the video capture boards. After a video sequence was captured, it was converted into a series of bi-mapped images. As with the captured video, these images were 8-bit greyscale.

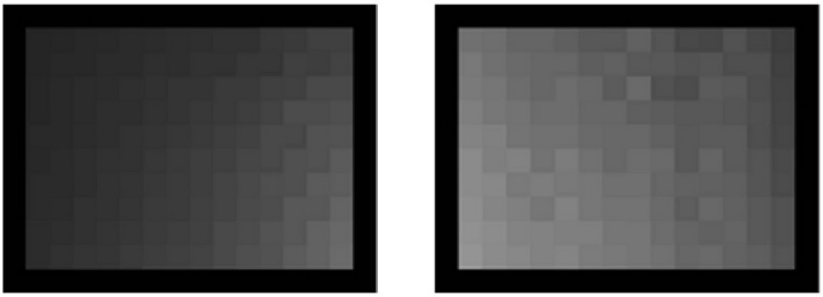

Fig. 1 Examples of time-averaged contrast change images (left and right-hand sides of a passing truck)

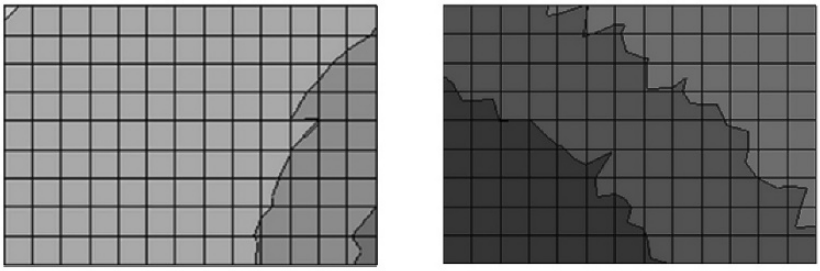

Fig. 2 Examples of spray-density contour plots (left and right-hand sides, corresponding to the images in Fig. 1)

Custom software was written for the analysis of the video images. The analysis relied on the change in image contrast due to spray obscuring the target boards. The first image of each sequence was taken as the control image and the analysis software assigned each grid square in the control image a contrast value of 100%, after calculating an absolute value of contrast. Here contrast is defined as the ratio of the brightness of the centre square to the average brightness of the squares above, below, left and right of the centre square.

Subsequent images were compared relative to the control image and the percentage difference in contrast of each grid square, relative to the corresponding square of the control image, was taken as the change in contrast for that square. The average change in contrast for each square over the series of images was also calculated to form an image of time-averaged contrast change (an example of the time-average contrast change, for the left and right-hand sides of the vehicle, is shown in Fig. 1, where the white regions indicate areas of decreased contrast). From the averaged image, the overall change in contrast of the image was calculated and topographical plots were formed to show the density distribution of spray. An example spray-density contour plot is shown in Fig. 2. As images were recorded from each side of the test vehicle simultaneously, an average of the left and right-hand sides of the vehicle was also calculated. The average of the two sides was used for comparisons between different test runs and vehicle configurations as the effects of varying wind conditions was shown to be greatly reduced.

Results were processed immediately after each run to provide rapid feedback as to the effectiveness of a spray-reducing device.

After the initial analysis of results, it was observed that the results were being influenced by the 'shake' of the cameras as the test vehicle passed. As the location of the grid squares were moving relative to the boundaries of the images, this generated apparent changes in contrast. To overcome this problem, two routines were added to the software. The first routine located the boundaries of each individual square from the control image while the second routine 'tracked' the grid squares as they moved with camera shake - a form of digital image-stabilization. With the implementation of these two routines, it was found that the results were considerably more repeatable.

3. Testing Of Spray-Reducing Devices

3.1 Test Track

Testing was conducted at the Anglesea Complex Proving Ground, in Victoria, Australia. A 3.2km oval track at the Complex was employed for the tests as it incorporates a 200m section of wetted track and allowed the test vehicle to maintain a steady 100km/h though the test section. In the test section, the track surface is fine-grade asphalt and there is a downhill gradient of 1-in-200 in the direction of travel and a cross-slope of 1-in-75 from right-to-left. Surface wetting was obtained from a series of sprinkler heads spaced at 5m intervals along the high (right) side of the track. The sprinkler flow rates were independently variable and were set to provide the maximum flow rate without impinging on the test vehicle as it passed. All of the sprinkler heads rotated through 120° to provide a reasonably even coverage of water. The sprinklers were operated for 30 minutes before testing to allow the water distribution to stabilize and then run continuously for the remainder of testing. Due to slight undulations of the track surface, the water depth varied from <1mm to 3mm in the test section. A short duration after each run ensured the track was repeatably saturated.

3.2 Test Procedure

An overview of test layout and procedure can be seen in Figs. 3 and 4. The cameras were mounted on tripods at a height of 1m (similar to the eye level of a

driver seated in a conventional car) and laterally aligned with the centre of the corresponding target board. The target boards were mounted with their lower edges 800mm above the track surface with a distance of 3.5m between the two boards, allowing a clearance of 500mm between the extremities of the 2.5m wide test vehicle as it passed between them. The target boards were placed at the end of the wetted section of track with the cameras placed 75m from the target boards. This left approximately 125m of wetted track for the complete wetting of the underside of the test vehicle before it passed the cameras.

Recording of the video images was triggered by an infra-red relay switch 20m before the truck passed the cameras.

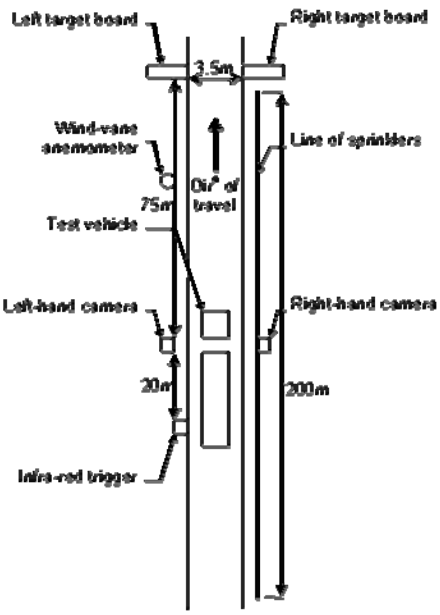

Fig. 3 Test overview

3.3 Test Vehicle

All tests were conducted with a Freightliner FL106, conventional-cab, tandem-axle tractor unit and a Lucar 4.0m, tandem-axle box trailer. The test vehicle is shown in Fig. 4.

Fig. 4 Test vehicle and track

3.4 Spray-Reducing Devices

Three configurations were tested. 'Configuration A' was the baseline configuration of the truck, as supplied for testing. This configuration included mudguards fitted to the drive wheels and untextured rubber mudflaps fitted behind all wheels. 'Configuration B' was the same as the baseline configuration but with the fitment of commercially-available textured mudflaps to the drive and trailer wheels (necessitating the removal of the untextured flaps). 'Configuration C' was formed by the removal of all flaps and the drive-wheel mud-guards.

3.5 Test Method

Several recorded runs of each configuration were performed to determine the repeatability of the results. The vehicle speed was held at a constant (and speed governed) 100km/h through the test section. Video capture was triggered 20m before the truck passed the cameras and continued for 8 seconds, at the end of which the truck was 125m past the target boards. This allowed the first image of each video sequence to be used as the control image and the build-up and dissipation of spray to be recorded. At regular intervals throughout the day, ambient temperature and humidity readings were taken. Wind speed and wind direction were also measured for each run.

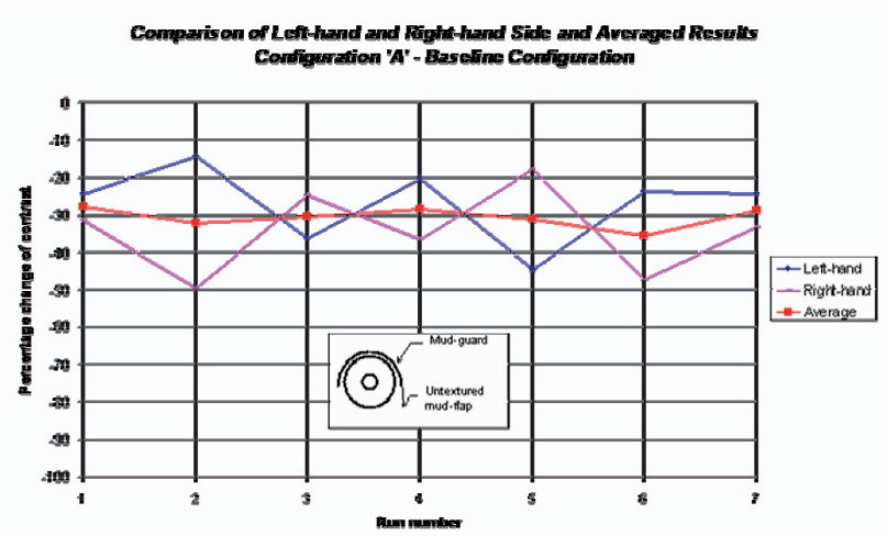

Fig. 5 Results of Configuration ‘A’

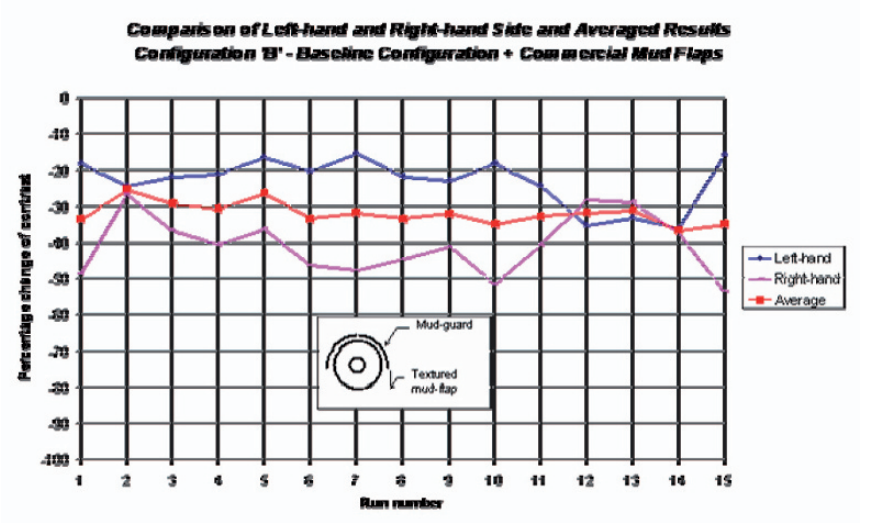

Fig. 6 Results of Configuration ‘B’

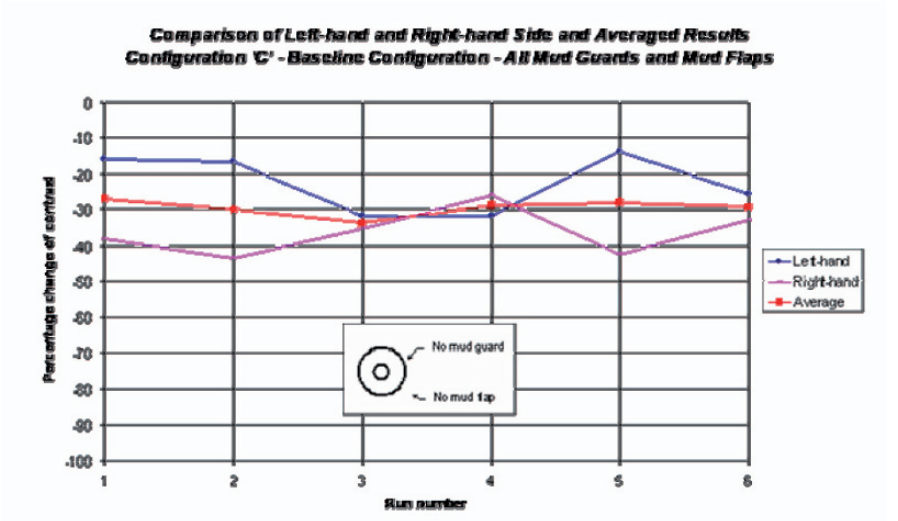

Fig. 7 Results of Configuration 'C'

3.6 Results and Discussion

The repeatability of results with varying ambient conditions was found to be very good. It was also found that the averaging of the left and right-hand side results proved very effective in reducing the effects of varying wind direction and wind speed, although it should be noted that winds were light (<10km/h) and wind direction was relatively constant. No significant changes in ambient temperature or humidity were recorded.

The graphs of Fig. 5 to 7 show the results for each of the three configurations tested. Each graph shows the percentage change in contrast due to spray for the left and right-hand sides of the truck and the average change in contrast of both sides for a number of runs. The graphs show that while the results from the left and right sides varying considerably, the averaged results remain relatively consistent. This is particularly evident with Configuration A - the percentage of spray recorded on the left and right hand sides varied considerably but the average of the two sides remained almost constant at a change in contrast of -30%.

This is further evidenced from Table 1, which gives a summary of the results. Values given are the calculated mean percentage change in contrast, the population standard deviation from the mean, 95% confidence intervals from the mean and the 95% confidence intervals as a percentage of the mean value. These values are given for the left-hand side of the truck, the right-hand side of the truck and the average of the left and right hand sides of the truck.

From the 95% confidence intervals it can be seen that it is advantageous to measure the spray from both sides of the truck simultaneously and average the

results. Referring to Configuration A, the 95% confidence intervals for the left and right hand sides are 7.1 and 7.9 (or 26.3% and 22.9% of the means) respectively. However, the 95% confidence interval for the averaged result is 1.9, or 6.1% of the mean value. The results for the other configurations tested also show similar patterns.

The results also indicated that there was very little variation in the quantity of measured spray between each configuration. As the differences in results are all within the 95% confidence intervals, no conclusions can be made as to which configuration performed best. These results were also confirmed by spectators during testing and by subsequent viewing of video tape recorded during the testing.

Figure 7 shows a plot of the typical variation of spray density against the test vehicle distance from the camera. At a distance of 0m, the front of the truck is level with the camera, at 75m the front of the truck is level with the target boards and at 200m the truck is 125m past the target boards. If looked at from right-to-left, the graph is an indication of the variation in visibility that a motorist can expect to see when approaching a truck and then overtaking that truck. Initially, there is a steady increase in the spray density, the rate of which increases as the back of the truck is approached. After passing the trailer wheels the spray density begins to decrease but there is a slight increase in density as the drive wheels are passed. Beyond this point there is a rapid decrease in spray density until the truck is completely passed. (The reduction in contrast near a distance of 80m is believed to be due to the target boards and the influence they have on the flow field and the truck passes by them.).

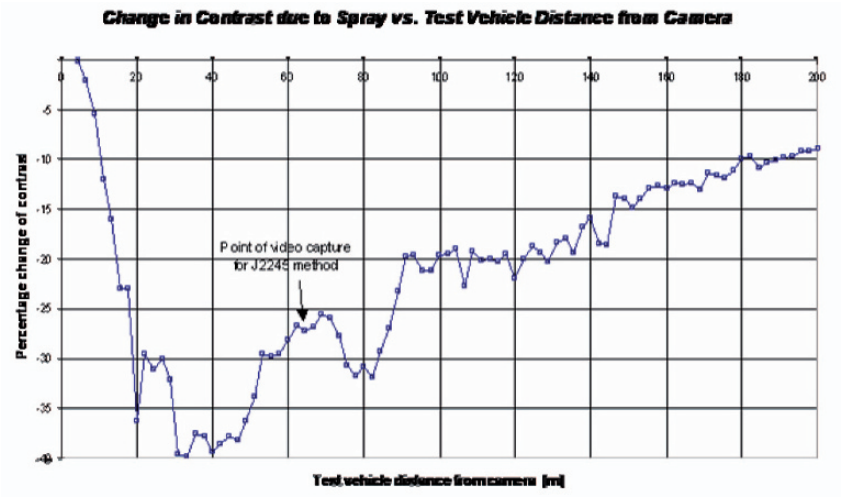

Fig. 8 Typical variation of change in contrast due to spray with test vehicle distance from camera

Table 1 Summary of results

Configuration 'A'			
	Left	Right	Ave
Mean %ADC	-26.8	-34.4	-30.6
StdDev	9.5	10.6	2.5
95% Confidence	7.1	7.9	1.9
(95% CI/Mean)*100	26.3	22.9	6.1
Configuration 'B'			
	Left	Right	Ave
Mean %ADC	-23.0	-40.6	-31.8
StdDev	6.5	8.1	2.9
95% Confidence	3.3	4.1	1.5
(95% CI/Mean)*100	14.3	10.1	4.6
Configuration 'C'			
	Left	Right	Ave
Mean %ADC	-22.5	-36.3	-29.4
StdDev	7.5	5.9	2.1
95% Confidence	6.0	4.7	1.7
(95% CI/Mean)*100	26.7	13.1	5.7

3.7 Comparisons of Technique with Recommended Practices

A Society of Automotive Engineers (SAE) standard exists for spray measurements – J2245 [8]. There is one main difference between the spray-measuring system described here and [8] - the J2245 method records four frames of video at 30 frames-per-second when the front of the truck is 10.67m (35ft) from the target boards, whereas the method described here records 100 frames of video at 12.5 frames-per-second. The J2245 method therefore provides an average over a very short period of time (4/30ths of a second). This has one main advantage over a longer recording period. The short time period means that the results are relatively instantaneous and are therefore not greatly effected by the camera 'seeing' different regions of the spray cloud as the camera-to-truck distances changes over the time of recording (although this does simulate what a passing motorist will see). However, as Fig. 8 shows, the density of spray changes rapidly in the region where the four frames are recorded (10.67m before the target boards or about the 65m mark). Therefore, small variations in the point of recording can produce significant variations in results. Also, the spray clouds being measured are highly turbulent and time-variant. From a study of video recorded during testing, it is believed that the period of oscillation of the spray clouds can be as long as one second. This indicates that several seconds of video needs to be analyzed for good statistical significance of results. Doing so should also reduce the number of runs required to attain the same degree of repeatability.

There are other minor differences between the two methods (such as the distance from cameras to target boards, the calculation of grid square contrast values and vehicle speed in the test section) but none of these are expected to have a significant influence on the differences in results.

4. Flow Field Measurement – An Overview

As supporting documentation to the spray work, flowfield mapping was undertaken utilizing dynamically calibrated "Cobra" probes which could provide information on the time-average and transient flow fields around commercial vehicles. Details of the probe systems can be found in [9] and they were found to be suited to use during on-road and wind-tunnel testing, particularly the ability to measure the local pressure in a turbulent flow field away from a solid surface. In the outdoor environment, the much improved durability and long-term stability compared to alternative methods (such as hot-wires or laser-Doppler systems) was considered very beneficial. The on-road tests were performed by driving the truck (with various modifications, including full side skirting almost down to the road surface) past banks of probes. The tunnel tests involved 3-component traverses around and under a one-tenth model of the truck. For each measurement point, the following data were recorded: u, v and w components of velocity; static pressure; reference dynamic pressure; temperature; and barometric pressure. As the time history of each variable was recorded, the turbulence intensities and Reynolds stresses were also calculated at each point. Details of the test methods and results for track and wind-tunnel environments can be found in [10]. A selected result that illustrates the influence of the flow changes associated with aerodynamic modifications is shown in Fig 9. Here the velocity vectors relative to the moving vehicle are plotted (i.e. the magnitude of the freestream velocity has been removed from each point to allow for comparison with the on-road pass-by measurements) and are nondimensionalised by the freestream velocity. These measurements were for a horizontal plane that was equivalent to 250mm (in full scale) above the road surface.

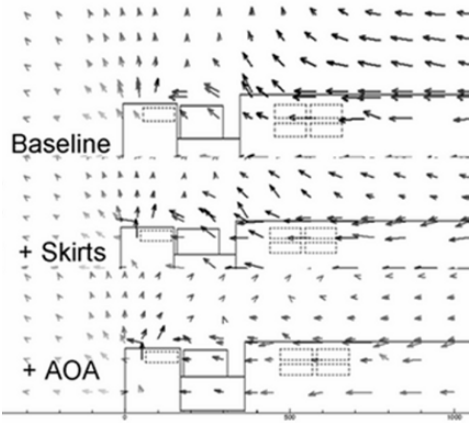

Fig. 9 Velocity vectors, resolved in the horizontal plane and relative to a moving vehicle, at equivalent road elevation of 250mm, adapted from [10]. Data taken from a one-tenth scale model of the full-size truck.

5. Discussion

The rapidly changing velocity field alongside trucks is apparent and highlights the need for instrumentation with a high frequency response when utilizing the pass-by method of testing. From the track tests [10] the addition of skirts was noted to reduce the local pressure alongside the truck and to also reduce the velocity in the same area. This reduction and modification in the velocity is seen in the tunnel results above and most noticeable is the reduction in lateral air velocity components in the area between the rear of the cab and the front of the trailer face when a cabin mounted add-on aerodynamic device (AOA) was fitted. This flow modification when (correctly matched) AOAs are used on trucks hauling relatively high loads is considered to offer significant benefits. From the track work it was seen to prevent the spray from being 'carried along' with the truck. From a combination of the tunnel and track work, the reduction in lateral flow emanating from the drive wheels could clearly be seen to reduce the spray in this region.

Although not part of the spray testing program it is instructive to consider Fig. 10. This aerial photograph shows a "road train" on a dry dirt road in the Northern Territory of Australia. Whilst the vehicle has no aerodynamic device and a quite different cabin to the vehicle in the spray tests, the visualization by the dust clouds offers insight into the flow field.

Fig. 10 Dust flow visualization from a cattle road train

Several features are evident. The flow to either side of the vehicle is not symmetrical – in either a transient or time-averaged manner. It appears that there is a

slight crosswind component of the atmospheric wind causing a significantly larger wake on the leeward side of the vehicle. This emphasizes the need for averaging even on days of relatively low winds. Secondly some of the flow below the stagnation point on the trailer front face is deflected down and into the gap between the cabin rear and the trailer, where some flow emerges laterally in the vicinity of the drive wheels – this is evidenced as the dust-free flow in this area. Prior work has established that the drive wheels are a major source of spray and the lateral flow at this point will cause the spray from the drive wheels to be laterally deflected across the areas to the left and right of the truck and into the line of sight of the passing motorist.

5. Conclusions and Recommendations

The spray-measuring system has been shown to be able to repeatably measure truck-induced spray. Although there were no major variations in ambient conditions during testing, the results indicate that the system effectively averages results to reduce the effects of varying ambient conditions, particularly cross-winds.

The results obtained from track testing include a measure of the overall spray cloud density, a picture of the distribution of spray within the viewable area and an indication of the variation of spray density as would be seen by a passing motorist. The spray-measuring system could also be used to measure the extent of other particle clouds, such as diesel or industrial exhaust smoke, with minor modification.

The road and tunnel flow field measurements enabled new insights into the low-level flow field which is considered to be an important “driver” for the spray generated by trucks on wet roads. In particular it was noted that the lateral flow was considerable when there was no AOA cabin-mounted aerodynamic device for a truck hauling a high load (but less so when trailer skirts were fitted). The work demonstrated the correct use of cabin devices can reduce the displacement of spray laterally and into the potential path of any passing vehicle. It has also been shown on several occasions that both the skirts and cabin-mounted devices reduce drag of trucks via wind-tunnel and road tests [e.g. 12]. Thus the use of correctly matched cabin-mounted devices will not only reduce drag; they will also reduce the lateral flow that drives spray from wet roads into the areas of concern for passing motorists. This offers the trucking community an added bonus that will result in enhanced opinions from the passing motorists.

6. Acknowledgments

The authors would like to thank the following companies and individuals, without whom this program could not have been undertaken: Mercedes-Benz Australia, Australia Post, Drs. Garry Zimmer and Juliette Milbank and Mr Tim Paton. The financial support and encouragement of Mr. Keith Seyer of the Federal Office of Road Safety and Mr. Brian Wells of the Australian Automobile Association is gratefully acknowledged.

7. References

1. C Baughan, B Hedges and J Field, "A National Survey of Lorry Nuisance", TRRL Report SR 774, Transport and Road Research Laboratory, 1983.
2. Anon, "Update on Status of Spray Suppression Technology for Large Trucks", Report US to Congress, March 2000. Available from: http://www-nrd.nhtsa.dot.gov/PDF/nrd-12/SplashSpray.pdf
3. Dumas and Lemay, "Splash and Spray Measurements and Control: Recent Progress in Quebec", in Proc. The Aerodynamics of Heavy Vehicles; Trucks, Buses and Trains, Springer 2004, ISBN-10: 3540220887.
4. C Baughan, "Water Spray from Road Vehicles: Measuring the Effectiveness of Spray Reductions," Proc. Vision in Vehicles - III, A.G. Gale et al, ed., Elsevier Science Publishers B.V., pp. 275-282, 1991.
5. J Scheltens and A Luyombya, "Spray Cloud Measurement System Based on Computer Analysis of Video Images", SAE Technical Paper 872277, 1987
6. C Gorte, R Joyner, K Pedersen and C McConnell, "The MVMA Investigation Into the Complexities of Heavy Truck Splash and Spray Problem", Proc. 10th International Technical Conference on Experimental Safety Vehicles, U.S. Dept. of Commerce National Technical Information Service, pp. 848-863, 1985.
7. Puclin A, "Quantitative Truck Spray Measurements", Masters by Research Thesis, RMIT University, Melbourne, Australia, 1997.
8. Anon, "Recommended Practice for Splash and Spray Evaluation - SAE J2245", SAE Handbook 1995, pp. 28.01-28.08, 1995.
9. Watkins S, Mousley P and Hooper J, "Measurement of Fluctuating Flows Using Multi-Hole Probes", Proc. 9th Int. Cong. on Sound and Vibration, University of Southern Florida and NASA, July 2003. Details of the instrumentation can also be found at: http://www.turbulentflow.com.au

10. Mousley P and Watkins S, “A Method of Flow Measurement about Full-Scale and Model-Scale Vehicles”, SAE Technical Paper 2000-01-0871 also in SAE Transactions – Journal of Passenger Cars, 2000, ISBN 0-7680-0574-4.
11. Saunders J, Watkins S, Hoffmann P and Buckley F, “Tractor-Trailer Aerodynamic Devices; Fuel Saving Predictions and Comparison of On-Road and Wind Tunnel Tests”, SAE Technical Paper 850286, from International Congress of the Society of Automotive Engineers America, Detroit, February 1985.

Experiments on Spray from a Rolling Tire

Charles Radovich and Dennis Plocher

Department of Aerospace & Mechanical Engineering
University of Southern California, Los Angeles, CA 90089
radovich@alumni.usc.edu, plocher@usc.edu

Abstract A novel laboratory apparatus has been built to understand the key mechanisms behind spray emerging from a rolling tire. Water leaving the tire from a single circumferential groove is analyzed using high-speed imaging. Visualizations reveal the formation of thin sheets of water connecting the roadway and the tire that eventually break into a droplet field. It is proposed that sheet breakup is the result of hydrodynamic instability. There is a preferred wavelength for disturbances on the sheet. After breakup, this preferred wavelength is preserved in slender ribs (or ligaments) that continue downstream until they disintegrate into droplets. Weber numbers based on the water density, tire circumferential speed and groove width vary in the range 1,900 – 60,300. The transition from sheet to spray is accelerated with increasing Weber number. Farther downstream, it is shown that droplet size and velocity distributions can be quantified as a function of Weber number.

1 Introduction

Tires moving through standing water create splash and spray which can decrease visibility and prove hazardous for other vehicles. Spray is defined here as water that has been forced through the tread pattern in the tire patch (contact patch between the tire and the pavement), thus, "processed" by the tire.

Our visualizations show that tires produce water spray as a result of the formation and breakup of thin sheets of fluid. An example spray image is shown in Fig. 1.1, taken using a laser sheet for illumination (~10 nanoseconds exposure time). The tire on top (in the image) has a single rectangular circumferential groove 11 mm wide by 5.6 mm deep. The bottom tire has no groove. The peripheral speed of the tires is about 12 m/s, and the volume flow of water delivered upstream of the tire contact patch is just sufficient to fill the circumferential groove.

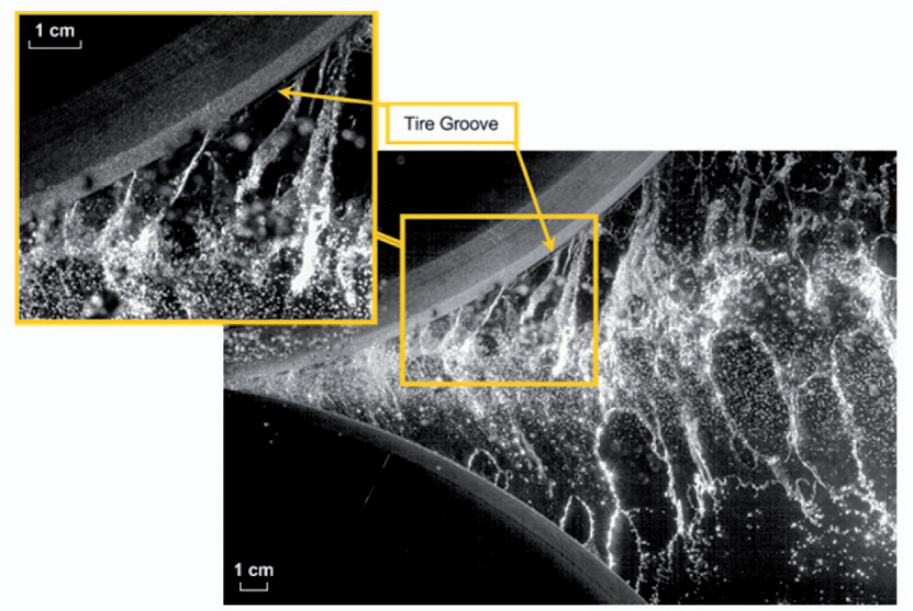

Fig. 1.1 Spray image using laser sheet illumination (~10 ns pulse time)

The laser illuminated image contains bright, irregular regions containing water that has left the circumferential groove. These irregular regions appear attached to the tires by ligaments and by thin sheets of water occupying the regions between the ligaments. There are breaks in the sheets and the smallest droplets appear to form along these rupture boundaries. Referring to the water leaving the circumferential groove as the central "jet," the droplet formation process appears to be the combination of the instability and breakup of this central jet and the breakup or tearing of the thin sheets connecting the central jet to the tires.

Downstream from the contact patch, the spray ultimately disintegrates into a droplet field. Information on the distribution of sizes and velocities of these droplets is desired. This paper details the steps taken towards imaging and analyzing the spray immediately leaving the contact patch and the droplet field farther downstream. In brief, droplet size estimates come from counting the number of pixels a droplet occupies in an image. After determining the size distribution, images are "filtered" for specific size ranges and digital particle image velocimetry (DPIV) is used to estimate droplet velocities as a function of droplet diameter.

2 Description of the Experiment

2.1 Justification for the two-tire geometry in the laboratory

In order to correctly model a tire rolling over a wet road, the physics of the tire patch must be understood. There are two reference frames applicable, as shown in Fig. 2.1. In the first reference frame, an observer watches a tire roll along the wet pavement at a velocity U_{truck}. In the second reference frame, the observer rides with the rotating tire and sees water coming at the tire with velocity U_{truck}. Now, using the principle of symmetry, a second tire represents the road, as shown in
Fig. 2.2. This principle of symmetry and a reference frame riding with the car is used to model the tire/water interaction in the laboratory.

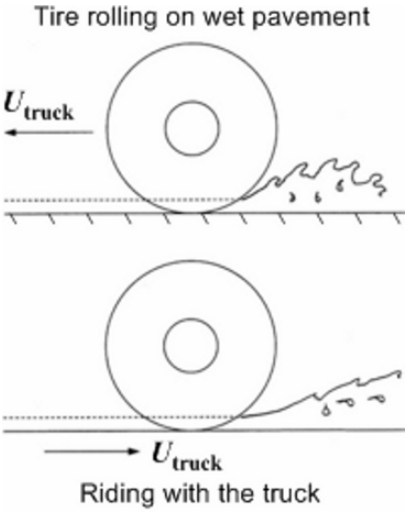

Fig. 2.1 Two reference frames for a tire rolling over wet pavement

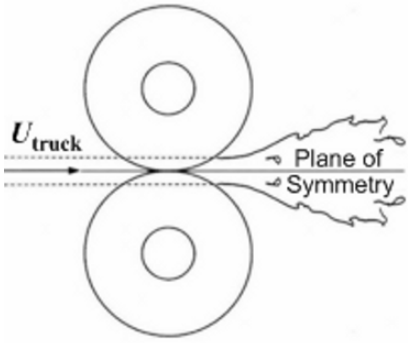

Fig. 2.2 Using principle of symmetry, a second tire represents the pavement

2.2 The Tire Spray Simulator

The apparatus for studying tire spray is shown in Fig. 2.3. It consists of two rotating tires pressed together to form a tire patch, a system to deliver water at the peripheral speed of the tires and a means for visualizing spray coming from the tire patch.

Two wheels are suspended by swinging arms with tires touching. The tires (P-175/70 R13) are pressed together to form the contact patch and are held in place by a spring-shock that is positioned using a stepper-motor-controlled lead screw. A Sensotech load cell measures the force between the tires. The left-most wheel in Fig. 2.3 rotates by means of a chain drive and a Leeson DC electric motor and motor-controller. The tire to the right is driven by contact at the tire patch.

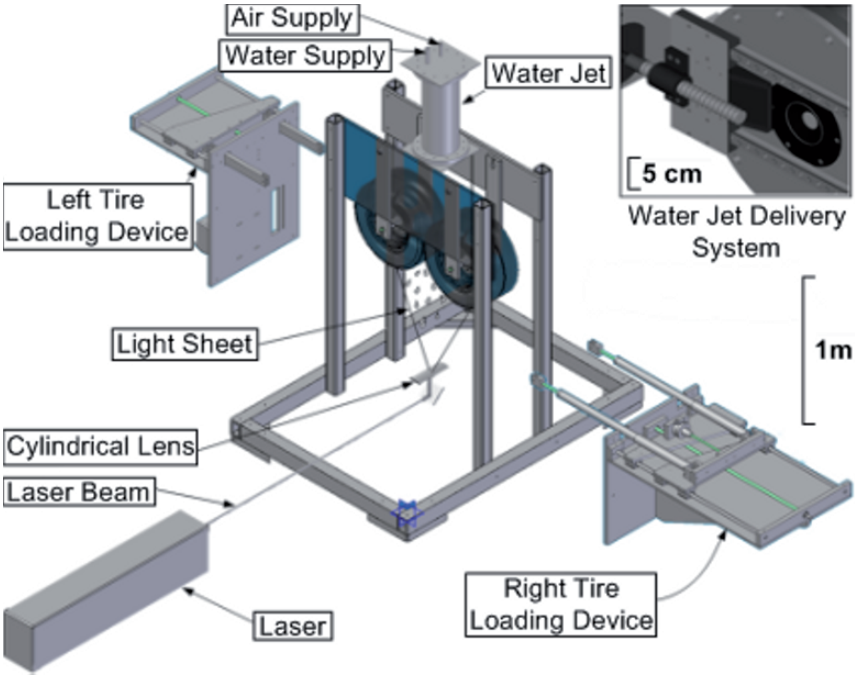

Fig. 2.3 The tire spray simulator

Wheel speed can be set in the range 3 m/s – 25 m/s. Precise wheel speed is measured by counting time intervals between pulses produced by a (stationary) Hall-effect pick-up and a toothed ring mounted on each wheel hub. The measured circumference of the grooved (*g*) and non-grooved (*s*) tires was $C_g = 1778 \pm 5$ mm and $C_s = 1810 \pm 5$ mm. Since the uncertainty in the time interval is on the order of microseconds, error in the estimate of tire speed, $\Delta U/U$, comes from uncertainty in knowledge of the tire circumference and is of the order 3×10^{-3} or less.

Visualizations of the tire spray are captured using a video camera set to record at 1600 fps and 5 μs exposure time. Recorded images are 400 by 1260 pixels in resolution. The spray field can be illuminated using either a laser sheet or backlighting. Laser sheet illumination allows for sharp, detailed images; however, pixel intensity information is often lost due to camera saturation as a result of specular reflection of light from the water surface. A more suitable means for imaging, and the method used for the remaining results in this paper, is backlighting.

Figure 2.4 displays a side view of the experimental setup showing the orientation of the camera, tires, frosted (diffusive) glass and light source.

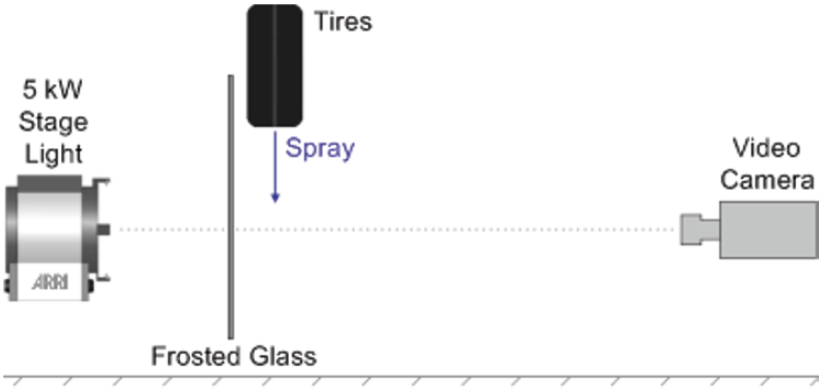

Fig. 2.4 Experimental setup for backlight imaging

2.3 Droplet Size Calibration

A series of calibration images were taken to verify that droplets of various sizes could be identified at all locations in the image field. A syringe pump, fit with a 21G hypodermic needle, delivered a single water droplet of a known size to the image field. A variation in droplet sizes was simulated by moving the camera farther from (or closer to) the free falling droplet. For each image of a droplet, a background image was recorded just before the droplet entered the field of view. This background image is used to account for and to correct any non-uniformities in the backlighting. Figure 2.5 shows an image of the prescribed droplet paired with its background image.

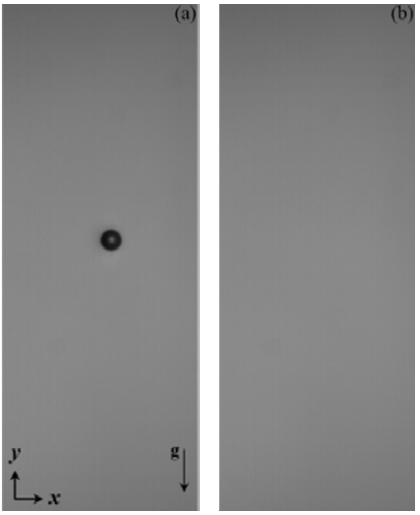

Fig. 2.5 (a) Image of a freefalling water droplet (D = 2.84 mm), (b) Background image, taken just before the droplet entered the field of view

Figure 2.6a shows a surface map of the image intensities recorded for a single droplet. Intensity values are expressed as a fraction of the average background intensity. The curvature of the surface is evidence of a non-uniformly lit background. In order to correct for this gradient, a linear gain correction matrix, $G(i,j)$, based on the background image was calculated and applied to the original intensity map $I'(i,j)$. Indices i and j refer to each pixel in the image field. Figure 2.6b shows the gain corrected intensity map $I_c(i,j)$. The final image used for analysis, $I(i,j)$, is obtained by subtracting the average background intensity from I_c and performing an inversion of the intensity map; Figure 2.6c. Equation Set 1 outlines the gain correction procedure.

$$\begin{aligned} G(i,j) &= \overline{BG}./BG(i,j) \\ I_c(i,j) &= G(i,j).*I'(i,j) \\ I(i,j) &= -1.*\left(I_c(i,j) - \overline{BG}\right) \end{aligned} \tag{1}$$

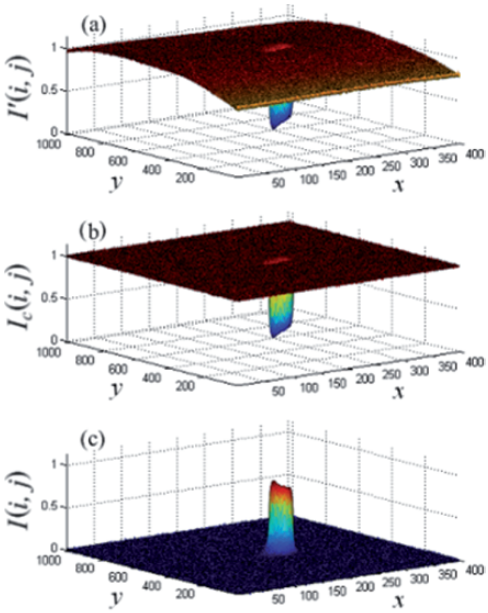

Fig. 2.6 Image intensity maps for (a) the raw image, (b) gain corrected image, (c) gain corrected and inverted image used for analysis

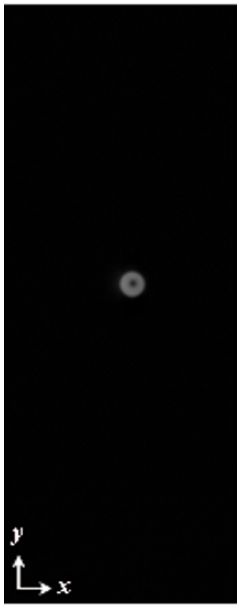

Fig. 2.7 Gain corrected and inverted image of a water droplet

An example of a gain corrected and inverted image is shown in Fig. 2.7. This figure has a single droplet near the center of the camera field of view. Backlighting transmitted through the droplet contributes to the dark spot in the center of the inverted droplet image (seen as a bright spot in Fig. 2.5a). Droplets can pass through any part of the image during a tire spray experiment. In order to verify that droplets are identifiable at all locations in the image, the calibration procedure was repeated for droplets located at the top and bottom of the image field.

The ability to resolve droplets of various sizes was also verified. The presence of smaller (larger) droplets was simulated by using the same 21G syringe pump and moving the camera farther away from (closer to) the apparatus. At each camera location, the prescribed droplet occupied a certain number of pixels. Observed droplet sizes ranged from 55 to 1380 pixels in area.

Figure 2.8 shows the intensity surface maps for four different droplet sizes at the top, center and bottom of the image field. This figure is a composite surface map with each droplet coming from a separate test. The presence of a droplet creates an intensity "mountain" with a broad base and narrow peak. The number of pixels retained in this mountain leads to the droplet size estimate. The black plane represents a cutoff threshold that determines which pixels to keep or to discard. Pixels with an intensity value at or above the threshold will be retained. Increasing or decreasing the threshold value will change the number of preserved pixels and subsequently alter the droplet size estimate.

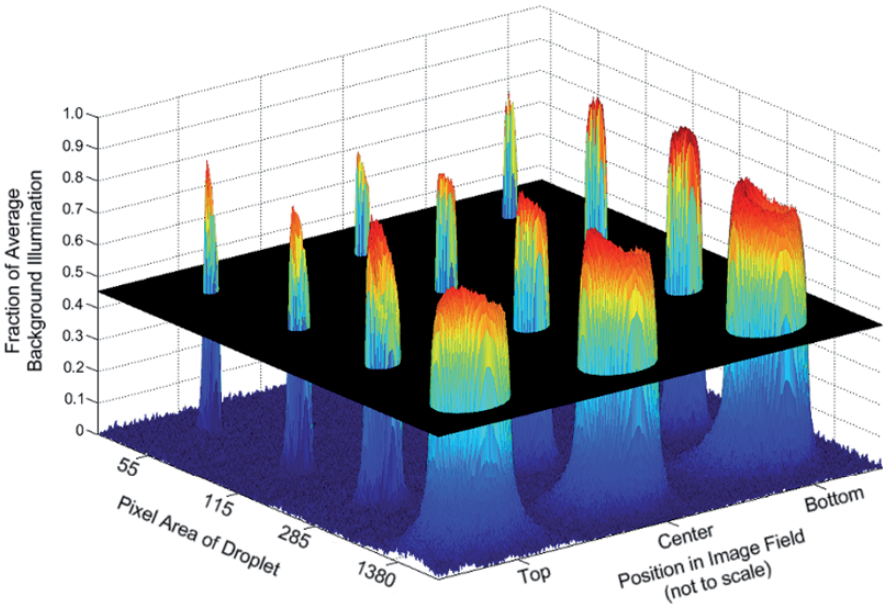

Fig. 2.8 Image intensity maps of four droplet sizes at the top, center and bottom of an image

Figure 2.9 illustrates the steps taken to estimate droplet size by counting the number of pixels a droplet occupies. Gray-scale images are reduced to black and white (binary) images after applying a threshold; Figure 2.9a. Pixels that are preserved are turned white (1) and everything else is set to black (0). Large droplets often allow a partial amount of light to transmit through, resulting in a "hole" at the center of the droplet. If a hole exists, it must be filled before counting pixels and determining the droplet size; Figure 2.9b. Once all droplets have been filled, the remaining pixels can be counted; Figure 2.9c.

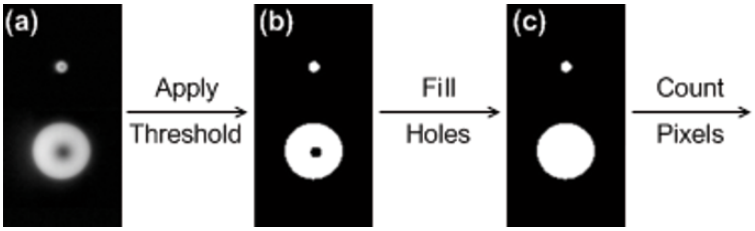

Fig. 2.9 Image processing used to determine the size of a droplet

Figure 2.10 shows the effect on the droplet diameter estimate when various threshold values are used. The abscissa represents the droplet area in terms of pixels; the ordinate is the estimated diameter calculated using $D = \sqrt{(4A/\ )}$ and the

appropriate mm/pixel factor for each camera location tested. The size of the droplet is 2.84 ± 0.09 mm in diameter, based on the average weight measured for a series of droplets. The experimental results provided in this figure clarify what threshold value is needed to estimate a droplet diameter within 5%, and to what extent various droplet sizes can be resolved with a single exposure. There is an increased sensitivity to minor changes in the threshold value for smaller droplets since these images have fewer pixels compared to the larger droplets. For all droplet sizes tested, an accurate estimate of the diameter was achieved using a threshold value equal to 45% of the average background illumination.

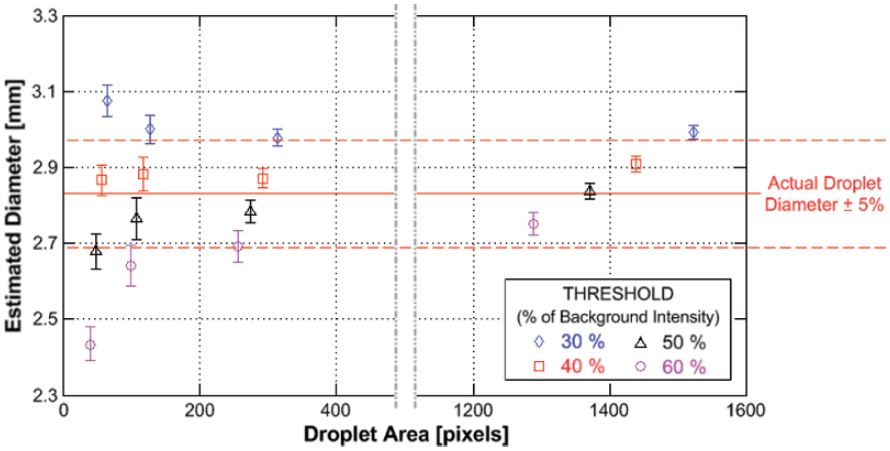

Fig. 2.10 Droplet diameter estimates for several droplet sizes and various threshold values

It was also observed that, in the spray plane, droplet images have a high contrast ratio compared to images outside of the focal plane. During the initial water delivery, spray may fall outside of the contact patch or create water spots on the frosted glass plate. These artifacts are undesirable for analysis as they are outside of the spray plane (the region downstream of the contact patch where the camera is focused). Therefore, applying an intensity cutoff threshold to the image retains pixels within and discards artifacts away from the region of interest. Previous works by Marmottant and Villermaux [1] and by Eastwood *et al* [2] illustrate a similar effort towards droplet detection and sizing.

3 Results

3.1 Sheet Formation and Break-Up

The Weber number is the most important parameter governing the formation of the water sheet and subsequent decay into a droplet field. This quantity is a ratio of the distorting force associated with fluid inertia to the (largely) restoring effect of surface tension (Equation 2). The Weber number is defined using the width of the tire groove (h = 11 mm), the density of water (ρ = 998 kg/m^3), the speed of the water jet (U) and surface tension for water against air (σ = 0.073 N/m).

$$We = \frac{\rho h U^2}{\sigma} \tag{2}$$

A backlit image of the spray field produced at U = 6 m/s (We = 5,400) is shown in Fig. 3.1; the direction of flow is from left to right. The upper tire has a single circumferential groove; the lower tire has a buffed smooth surface. The field of view in this image is approximately 26.1 by 8.3 cm with the end of the contact patch visible on the left edge. Fluid leaving the contact patch remains attached to both tires and forms a thin sheet as the tires separate. The thickness of the sheet was not measured directly, however, it is estimated to be on the order of <1 mm. There are waves on the sheet that appear as dark rib structures. These ribs exhibit a periodic nature, suggesting a natural instability in the fluid flow. The sheet ultimately breaks up into a droplet field as it moves away from the contact patch.

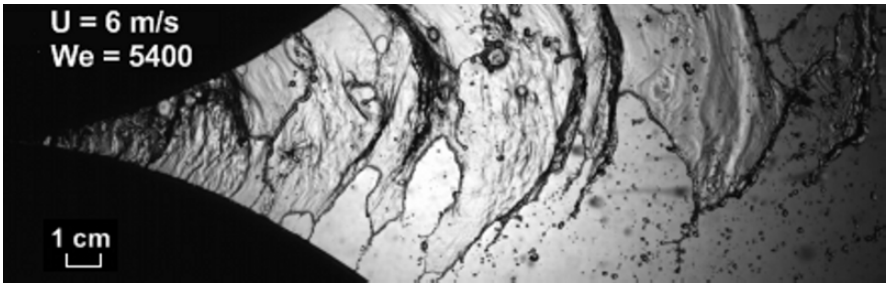

Fig. 3.1 Tire spray pattern at U = 6 m/s, We = 5,400

The development of the liquid sheet is sketched in Fig. 3.2, as it would appear at several cross planes looking upstream. The water passes through the tire patch

inside the groove. At the downstream end of the tire patch the treads begin to move apart following the arc of the rotating tires, with the water exiting the tire patch as a jet attached to the groove on one side and to the smooth tire on the other side. The groove begins to drain and air flows in to fill the developing void. Sheets connect the jet to the smooth tire and to the water remaining in the groove. The jet takes on a sinuous shape (instability) as can be seen at the extreme left in Fig. 3.1. Farther downstream, the sheet begins to separate from the surfaces of the tires. As breaks appear in the sheet, the sinuous jet forms into slender ribs (ligaments) orientated cross-stream to the flow.

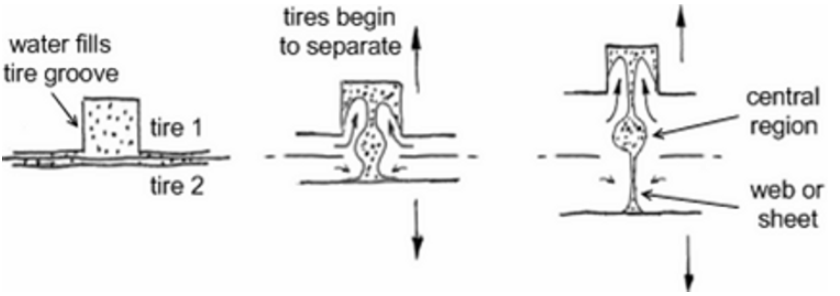

Fig. 3.2 Expected behavior of water as it leaves the tire groove at the contact patch

Eventually, ribs and sheets become a droplet field having a distribution of droplet sizes. At places where the sheet is thinnest, small droplets form along the edges of breaks and holes in the sheet. Where the broken sheet is thicker, the water within the contracting sheet is incorporated into the rib structure. Larger droplets are produced with the break-up of the periodic rib structure.

The spray patterns produced from a rolling tire are dependent on the Weber number. As described by Lefebvre [3], the development of a liquid sheet into a droplet field is governed by the fluid properties and initial velocity of the flow. Given that the groove width and properties of water are fixed, specific Weber numbers are achieved through changes in the tire speed (and jet velocity). Figure 3.3 shows images taken at We = 1,900 and 48,900. At low Weber number (Fig. 3.3a), the flow field is heavily influenced by surface tension as edges of the broken sheet are rapidly pulled in towards the rib structures and little or no sheet remains. The majority of the droplet field at low We results from the break-up of the rib structures, thus, larger droplet sizes are expected. At higher Weber number (Fig. 3.3b), the flow is driven by the fluid inertia and more liquid remains in the sheets. The breakup of these thin sheets tends to produce smaller droplets.

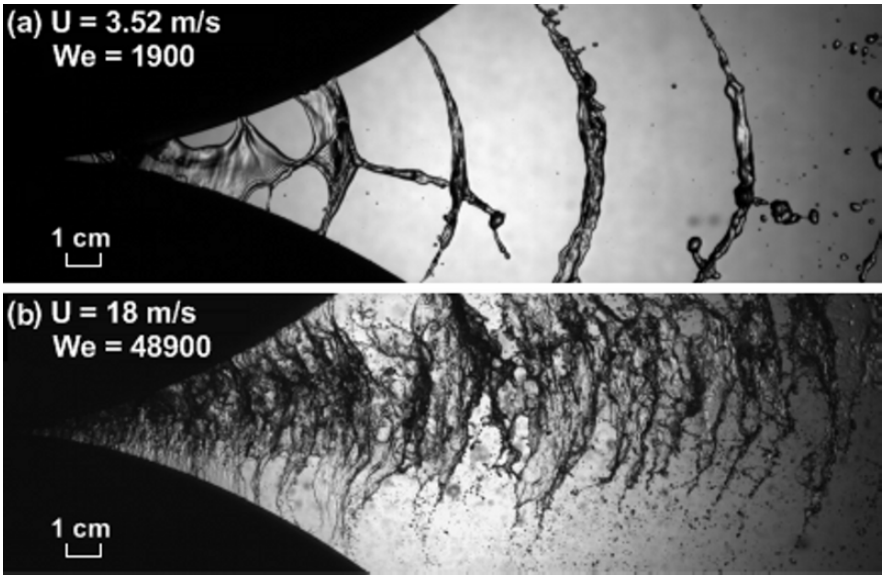

Fig. 3.3 Spray pattern variation with Weber number

3.2 Droplet Field Size and Velocity Estimates

Figure 3.4a is a single image from the video showing a portion of the droplet field produced by tires rotating at $U = 6$ m/s. The direction of flow in these images is from top to bottom. The center of the image field is one meter downstream from the end of the contact patch and the field of view is approximately 13 by 4 cm. Figure 3.4a reveals various droplet sizes as well as several "fuzzy" spots due to spray that fell outside of the contact patch at the start of the experiment. Figure 3.4b shows the gain corrected and thresholded image with only droplets in the spray plane remaining.

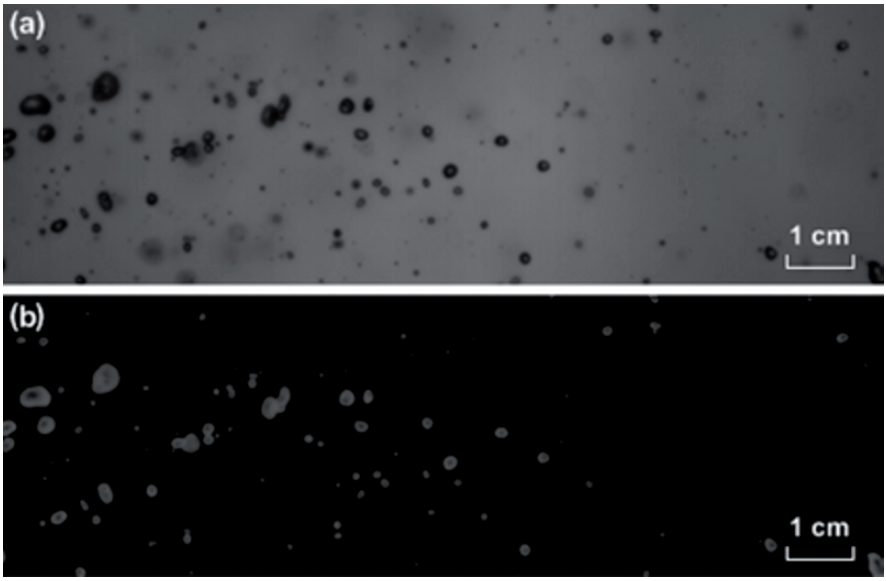

Fig. 3.4 Droplet field at U = 6 m/s, We = 5,400: (a) raw image, (b) gain corrected and thresholded image

Figure 3.5 displays the distribution of sizes for the droplets detected in this video frame. A total of fifty-eight (58) droplets were detected, ranging from 0.8 to 4.4 mm in diameter. This distribution is derived from the single image presented in Fig. 3.4. Statistically more reliable distributions can be built up by adding contributions from multiple (hundreds of) frames.

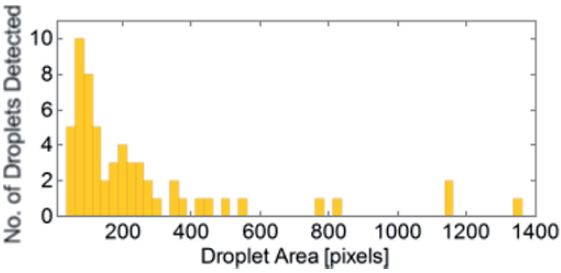

Fig. 3.5 Distribution of droplet sizes

Given a distribution of droplet diameters, images can be "filtered" for specific droplet sizes and DPIV performed to estimate droplet velocities as a function of diameter. Figure 3.6 represents a filtered version of Fig. 3.4b with only droplets from 1.65 to 2.33 mm in diameter shown. This image and a successive image taken 625 μs later were processed using DPIV to obtain the velocity vectors for each droplet in this size range. The DPIV process tracks the motion of a droplet by

cross-correlating the two images. What makes this application of DPIV different from the standard technique is that only regions adjacent to particle centroids in the first image are interrogated in the second image. This greatly increases the efficiency of the DPIV algorithm. Typical particle displacements in the image pairs are on the order of forty pixels. The velocity estimate for droplets in this size range was 6.85 ± 0.5 m/s. The two droplets presented without a velocity vector had moved out of the image view before the second image was recorded.

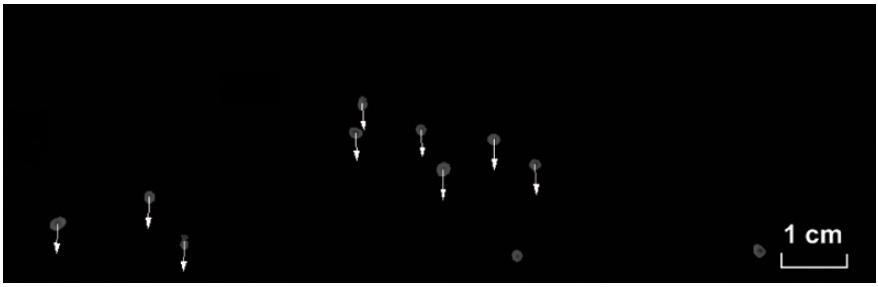

Fig. 3.6 $U = 6$ m/s spray field, filtered for droplets between 1.65 and 2.33 mm in diameter

The DPIV process was repeated for a smaller set of droplets with diameters between 1.16 and 1.65 mm. The estimated velocity for this size range was 6.15 ± 0.3 m/s. The spatial location, with respect to the contact patch centerline, and velocity vectors for these two droplet diameter ranges is presented in Fig. 3.7. A divergence away from the contact patch centerline is evident by the direction of the velocity vectors. This behavior is due to the tendency of water to attach to the surface of a tire and the ability of a tire to carry water laterally away from the plane of symmetry.

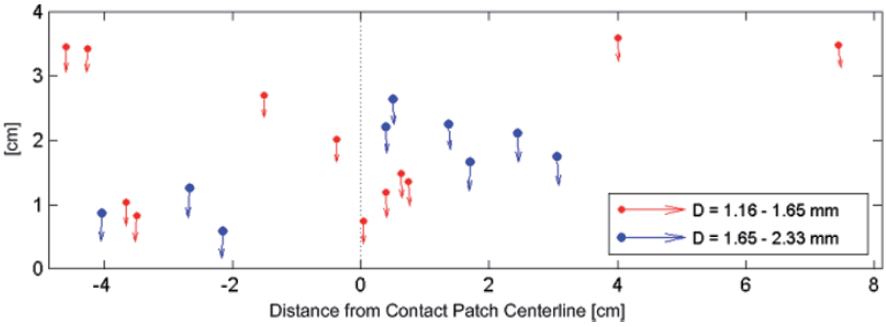

Fig. 3.7 A demonstration of DPIV results for two droplet size ranges

4 Conclusions

The operation of a tire spray simulator has been demonstrated. Video of the developing spray was captured in the region just downstream of the tire patch. From this video the flow was qualitatively described as a jet exiting the tire patch that spreads out into a sheet which spans the distance between the two tires. The sheet, thickened by the central jet, is unstable and forms sinuous waves that break into a cross-stream rib structure. Ultimately, the entire flow disintegrates into a droplet field.

A technique for isolating and measuring the size and velocity of individual droplets has been developed and calibrated. The ability to detect droplet sizes a factor of 5 different in diameter using a single exposure was demonstrated, with the lower limit of detection approaching 50 pixels in area. It is possible that this lower limit can be further relaxed.

Acknowledgments The authors would like to acknowledge the continued financial support from the Michelin Americas Research & Development Corporation as well as the production of tires for the experiment. Support from the Department of Energy (DOE) is also acknowledged. Additional thanks to Rose McCallen, Fred Browand, Jim Ross and ECI for the organization of The Aerodynamics of Heavy Vehicles II conference.

References

[1] Marmottant P, Villermaux E, On Spray Formation, *J. Fluid Mech.*, 2004, Vol. 498, pp. 73-111.

[2] Eastwood C D, Armi L and Lasheras J C, The Breakup of Immiscible Fluids in Turbulent Flows, *J. Fluid Mech.*, 2004, Vol. 502, pp. 309-333.

[3] Lefebvre A, *Atomization and Sprays (Combustion: An International Series)*, CRC, 1988.

Computational Simulation of the Flow Field of a Filter System inside Self-Ventilated Road Tunnels due to Heavy Vehicle Traffic

Florian Iser[1] and Raimund A. Almbauer[2]

[1] The Virtual Vehicle Competence Center, Area 2, Inffeldgasse 21a, 8010 Graz, Austria, e-mail: florian.iser@v2c2.at

[2] Institute for Internal Combustion Engines and Thermodynamics, Graz University of Technology, Inffeldgasse 25, 8010 Graz, Austria, e-mail: almbauer@vkmb.tugraz.at

Abstract This paper combines heavy vehicle aerodynamics with environmental considerations. The problem of air pollution in urban environments is strongly connected to the emissions of local traffic. Moreover, by-pass road tunnels in densely populated areas use often longitudinal ventilation systems, which produce high concentrations at the outlet portal. An EU-LIFE project started to investigate the potential and the feasibility of combining dust filters with standard noise protection systems. As part of the project one application deals with the reduction of pollutant emissions from road tunnel portals. For the investigation of the effectiveness of these filters, simulations of a simplified heavy vehicle shape were conducted using Computational Fluid Dynamics (CFD). The first part of this paper deals with the validation of the CFD tool. Therefore, the Ground Transportation System (GTS) in the NASA Ames 7 feet by 10 feet wind tunnel was simulated and the results were compared to measurements. The second part covers the considerations of the flow field induced by heavy vehicle traffic within a highway road tunnel equipped with filters. As a result, the amount of the volume flow through the filters for one complete heavy vehicle cycle is displayed.

1 Introduction

Many cities in the world face poor air quality in their urban environments. Especially the European Union supports activities to reduce the amount of very fine particles, named particulate matter. The smaller the particles are the higher is the risk of serious impact on human organs. Therefore the World Healthy Organization (WHO), the European Union (EU), and federal governments released limits for the maximum concentration of particles smaller than 10 μm (PM10) in diameter.

For the member states of the European Union an exceedance of the daily mean threshold value of 50 µg/m³ of less than 35 days per year is allowed at the present time. The European Acid Deposition model system (EURAD) [5] predicts the concentration of PM10 over Europe. Especially, on winter days, large areas of Europe exceeded the daily mean limit. For example, the city of Klagenfurt which is located in the south of Austria, exceeded the daily mean limit on 80 days during the winter season between October and March. That means, nearly every second day the concentration of PM10 exceeded the threshold values.

On the other hand, the issue of noise pollution from traffic is becoming more important. In the year 2006, more than EUR 85 million was invested in Austria to build noise protection walls near highways. Currently, about 430 km of the 2060 km long Austrian highway network is provided with noise barriers. Furthermore, 20 % to 30 % of the total costs for new highway constructions are invested into noise protection systems [1].

The Virtual Vehicle Competence Center and the Graz University of Technology started a project together with five other partners to investigate the feasibility to reduce the PM10 concentration from traffic sources where they originate. The Sound and Particle Absorbing System (SPAS) should be able to combine the functions of a standard noise barrier with an integrated dust filter near streets. This paper deals with the road tunnel application of the SPAS elements. The target is to reduce the PM10 emissions at the tunnel outlet portal with no additional effort than the flow energy of the traffic.

1.1 PM10 Sources of Klagenfurt

Based on a previous project, named KAPA GS, accomplished by the Graz University of Technology and regional partners in 2005, the primary sources of PM10 emissions for the city of Klagenfurt were determined. As a result, 52 % of the PM10 emissions are generated by local traffic. However, only one-third of the traffic emissions are exhaust emissions whereas the remaining two-third are non-exhaust emissions like brake wear, tire wear, street wear, and resuspension.

1.2 Road Tunnel Situation

Inside a road tunnel higher concentrations of pollutants occur because of a reduced dilution with fresh air compared to non-tunnel situations. Especially for self-ventilated road tunnels which have no intermediate air exchange all traffic emissions are transported to the outlet portal. Results of different dispersion

models by Oettl et al. [7, 8] shows the high concentration of polluted air in the environment due to emissions at the tunnel end. Even for ventilated road tunnels dispersion of traffic pollutants is a big issue.

An advantage for the CFD calculation of a road tunnel is the constant and well known boundary conditions. The geometry data of the tunnel cross-section is known, the traffic speed is nearly constant and after a few hundred meters, inside the tunnel climate influences are strongly reduced. Even under snowy conditions the tunnel end is usually try. Nevertheless, there are also two critical points concerning the tunnel application which have to be mentioned. One is the clearance issue of the tunnel geometry. Every additional mounted device must be within the clearance pro-file. The second point is the various safety regulations. The SPAS elements must fulfill all fire-retarding requirements as well as all durability considerations.

The moving traffic inside an unidirectional road tunnel generates a vehicle-induced constant velocity. The force contributed by each vehicle depends on the size, its blockage ratio [4] and various other parameters such as traffic frequencies and pressure difference at the tunnel portals. The SPAS filters for this tunnel consideration are intended to be placed at each side wall and additionally on the tunnel ceiling. To provide enough space for the flow, a distance of 100 mm was considered between the filters backside and the tunnel walls. This configuration was investigated and the volume flow through each filter was calculated. Moreover, a volume rate per unit length was derived with a constant traffic speed of 23 m/s.

To obtain validated CFD settings, the following chapter describes the preceded calculation with the GTS. Later in Section 3, the CFD setup was transferred to the real tunnel geometry with an adapted GTS. Finally, the volume flow values for the SPAS filters were evaluated.

2 Preceded CFD Calculations

This section describes the CFD calculations which were conducted prior to the tunnel application. The target was to validate the CFD calculation for a similar geometrical setup with wind tunnel measurements. Furthermore, this preceded CFD simulation validates the simulation method, especially concerning the mesh and turbulence modeling.

2.1 Problem Formulation

For the use of a generic shape for heavy vehicles the Ground Transportation System (GTS) was chosen which was introduced by Gutierrenz et al. [2]. The GTS shape is a simplified tractor-trailer configuration using a cab-over tractor design. A 1/8 scale model of the GTS was measured at the NASA Ames 7 feet by 10 feet wind tunnel [13]. All length parameters are non-dimensionalized by the trailer width w = 0.3238 m. To reach a Reynolds number that is comparable to the full size case, high velocities inside the test section of more than 90 m/s were necessary to obtain Re = 2,000,000. However, Mach numbers of about 0.28 demand compressible flow simulation. The basis for the CFD validation presented herein was the NASA experiment at run 7 point 9.

2.2 Numerical Setup

All CFD calculations were conducted with CD-adapco's STAR-CCM+ V2. This new developed commercial code offers a fully integrated automatic mesh tool which provides a surface wrapper and a hybrid mesh generator. For the GTS calculations a trimmed mesh was deployed which is an unstructured hexahedral mesh with trimmed cells near the wall. To make it comparable with CFD calculations of Roy et al. [11] and to avoid validation issues concerning the wall treatment, the boundary layer was fully resolved. Hence, the non-dimensional wall distance was $y^+ \leq 0.5$. Menters BSL k-ω turbulence model was used, because this configuration delivered the best results for the GTS model, as already published by various authors [9, 11, 12]. Refinement regions were provided at the trailer base and in the gap between the GTS bottom and the wind tunnel floor. For the wall boundaries a number of 30 prism cells parallel to the surface were employed. Furthermore, the mesh size on the GTS surface varied from 2 mm up to 8 mm. These mesh settings lead to an overall number of 21.8 million cells. Finally, the boundary setup for the calculation including the GTS is shown in Fig. 2.1.

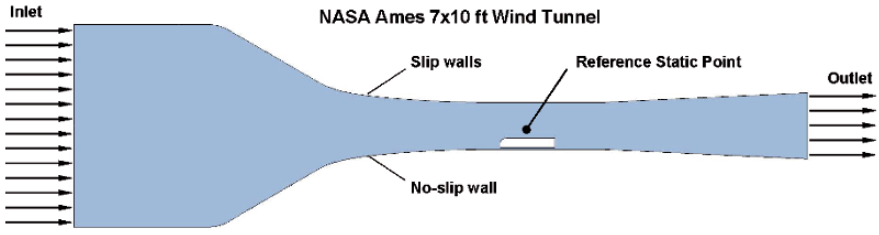

Fig. 2.1 Boundary setup for the NASA Ames wind tunnel including the GTS

2.3 Results

The first consideration was to validate the boundary layer profile of the floor for an empty wind tunnel configuration. Figure 2.2 compares the profile of the CFD calculation with the ones based on the NASA experimental data of run 404. The CFD calculation provided a very similar profile compared to measured data and is used for further investigations.

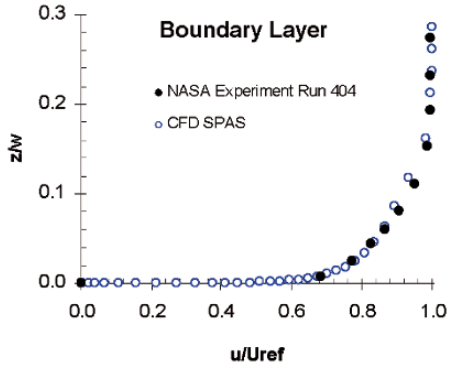

Fig. 2.2 Comparison of measured and calculated boundary profile for an empty NASA Ames wind tunnel

The GTS calculations were run in parallel on an Opteron cluster using 24 CPUs. The first detailed discussion of the results is dealing with the pressure distribution on the surface. Furthermore, Fig. 2.3 gives the surface pressure results for the front and base region of the GTS. It can be seen that the distribution on the front end conforms to measurements. However, at the trailer base, only the pressure level is predicted correctly but not the pressure distribution.

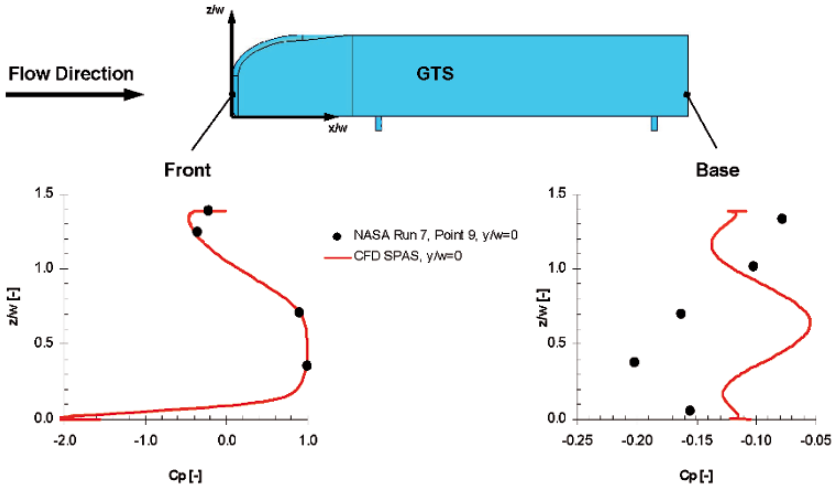

Fig. 2.3 Comparison of measured and calculated surface pressures on the front and base of the GTS

To evaluate the reason for this characteristic, streamlines were calculated and compared to particle image velocimetry (PIV) measurements which were also contributed by the NASA experiment. The trailer wake in the horizontal cut shows a similar profile between the CFD results and the PIV data (Fig. 2.4). Nevertheless, the vertical cut displays the reason for the surface pressure discrepancy. So, the shape of the trailer wake could not be predicted in a sufficient way by the turbulence model. These findings were already discussed by Roy et al. [11].

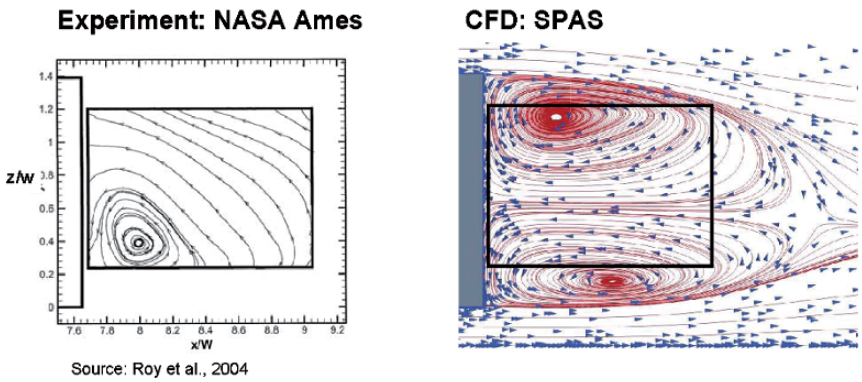

Fig. 2.4 Comparison of measured [10] and calculated streamlines for the horizontal cross-section in the middle of the GTS base

The integration of the surface pressure field results in the drag coefficient C_D. As a result, the drag coefficient for the GTS without the four posts was calculated

to C_D = 0.237, which is 5.4 % below the measurement value. Table 2.1 compares the experimental data with the different CFD results.

Table 2.1 Drag coefficient for the GTS from various sources

	C_D	Error	Source
NASA Ames experiment	0.250 ± 0.01		[11]
Menters k-ω	0.237	5.4 %	
Menters k-ω (Roy et al.)	0.298 ± 0.06	19.2 %	[13]

This presented CFD setup was used for the prediction of the flow field around SPAS filters inside the road tunnel, which is described in the following chapter.

3 Road Tunnel Application

This section deals with the application of the SPAS elements in a road tunnel and with the transformation of the CFD setup for a predictive task. The first section deals with the provided heavy vehicle shape, whereas the following sections describe the tunnel setup and the CFD calculations, respectively.

3.1 Ground Transportation System for the EU

The use of a generic heavy vehicle shape is reasonable because of the cab-over design of European truck manufactures. To meet the requirements of the European legislation, the overall heavy vehicle length is limited to 16.5 m, with a width of 2.5 m, and a height of 4 m. The original GTS's width is 2.6 m, so it was scaled down to 2.5 m and automatically the height of 3.96 m was reached. However, the overall length was too long; therefore a section of the trailer was cut out to obtain the 16.5 m in total length. This modified shape is referred in this paper as the EU-GTS for obvious reasons.

3.2 Road Tunnel Setup

The chosen road tunnel, named according to the nearest village Lendorf, is located at the highway A2 in the area of the city of Klagenfurt. The shape of the tunnel cross-section is rectangular and the total length is about 800 m. The detailed tunnel information is summed up in Table 3.1. The tunnel is self-ventilated

and therefore high pollution concentrations, including PM10, can be expected at the tunnel outlet portal. Figure 3.1 shows the arrangement of the EU-GTS inside the tunnel. The coordinate system is equal to the preceded GTS calculation described in Section 2. To avoid interactions of the tunnel portal because of the changing geometry, the calculated section does not include any tunnel end.

Table 3.1 Detailed information for the road tunnel Lendorf

Caption	Value
Daily traffic (for each direction, counted 2003)	15,500 vehicles
Cars-to-heavy vehicles ratio (fleet composition, counted 2003)	83 % to 17 %
Total tunnel length	800 m
Tunnel cross-sectional area	47.5 m²
Longitudinal velocity (measured in similar tunnels)	7 m/s
Exhaust PM10 emission for the fleet	0.026 g/km
Non-exhaust PM10 emission for the fleet	0.052 g/km

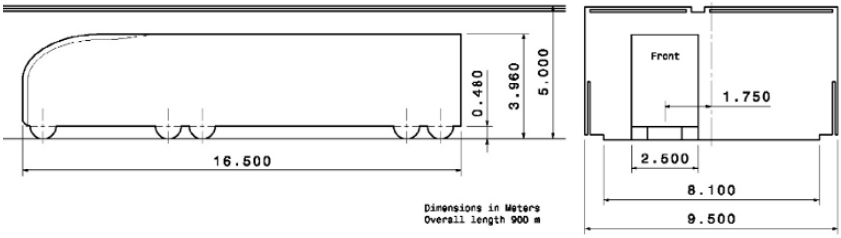

Fig. 3.1 Arrangement of the EU-GTS inside the road tunnel Lendorf

3.3 Computational Setup

The computational domain was very similar to those of the GTS in the NASA Ames wind tunnel. However, the tunnel walls were set as no-slip walls and additional refinements were necessary to obtain a higher resolution between the SPAS filters and the tunnel walls. As described in section 3.1 the EU-GTS required the same refinement regions as the GTS which is known from the preceded simulation.

Nevertheless, some additional settings were taken embedding the SPAS filter material:

- Porosities for the SPAS filters cells
- Translational Moving Reference Frame (MRF) for the SPAS filters cells
- Higher inlet turbulence due to traffic inside the tunnel
- Incompressible flow
- Modified cell sizes

The porosity values for the filters were measured at the Virtual Vehicle's own wind tunnel. Several materials were investigated to obtain a low pressure loss. To consider the stationary CFD simulation, the EU-GTS stands still and the tunnel walls are moved with a surface velocity of the vehicle speed. However, due to the porosity values, the filter cells themselves allow only a flow direction normal to the surface (y-axis) and therefore they need an additional reference velocity component (x-axis). These settings were made with a translational MRF approach. Furthermore, all end faces of the four filters were connected with the starting faces by using a periodic boundary condition.

For the amount of turbulence at the tunnel inlet the investigation of Lindener et al. [6] shows turbulent intensities and turbulent length scales for heavy traffic on highways. These measurements were taken from non-tunnel situations and provide a guide value. In the work of Hall [3], who dealt with gas dispersion in road tunnels, the turbulence intensity and the length scale were given within 10 % and 10 % of the tunnel diameter, respectively. As a result, a turbulence intensity I = 10 % and a turbulent length scale L = 0.5 m were set for the road tunnel simulation.

The full-scale CFD simulation with a vehicle speed of 23 m/s allowed the application of the incompressible flow assumption. In order to consider a wind speed of 7 m/s in the longitudinal direction of the tunnel due to traffic drag, the intake flow velocity was reduced to 16 m/s to generate a resulting vehicle speed of 23 m/s for the simulation. Thus, the longitudinal velocity generates a boundary layer on the walls. Therefore, all wall boundaries are resolved by 30 parallel cell layers. To provide similar y^+-values for the EU-GTS as for the GTS, the cell sizes were adjusted. For example, the wall distance for first boundary layer near the surface was set to 0.016 mm. The modifications of the mesh lead to 22.7 million cells and a y^+ of approximately 0.8 for the EU-GTS surface, which was important to fulfill the requirements of the low-y^+ turbulence model.

3.4 Results

The simulation of the EU-GTS inside the road tunnel shows the impact of the high blockage ratio. The calculation was run on 26 CPUs in parallel for 178 hours. In fact, a convergent solution was reached within 6500 iterations. Again, the drag coefficient for the EU-GTS without the posts was calculated to C_D = 0.293 for this road tunnel setup. Because of the missing reference point, a direct comparison of the surface pressure distribution between the GTS and the EU-GTS was not possible.

All length values presented in this section are non-dimensionalized with the EU-GTS width W = 2.5 m. In Fig. 3.2 to 3.4, three cross-sections along the x-axis provide an understanding of the interaction between the flow field and the EU-GTS even far away from the vehicle shape. The cuts at x/W = 0.10, x/W = 1.50, and x/W = 6.68 display the positions at the front of the EU-GTS, in the middle of the trailer, and immediately behind the rear end, respectively. As a result, the tangential velocity magnitude v_t represents the displacement due to the EU-GTS body. Furthermore, the position of the SPAS filters can be adopted due to these results.

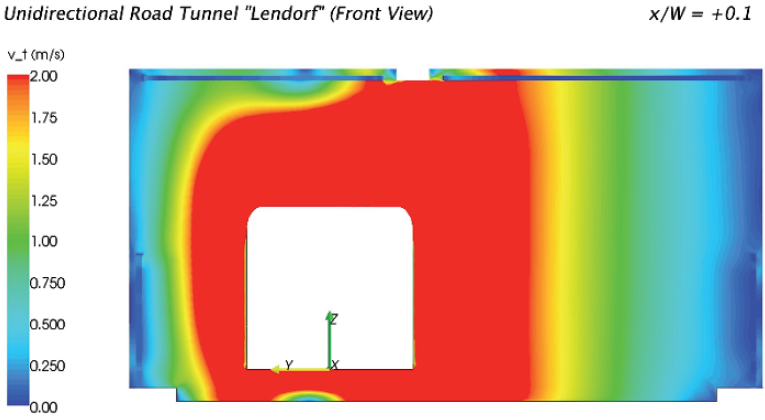

Fig. 3.2 Tangential velocity magnitude of a vertical plane cut at x/W = 0.1 at the EU-GTS front

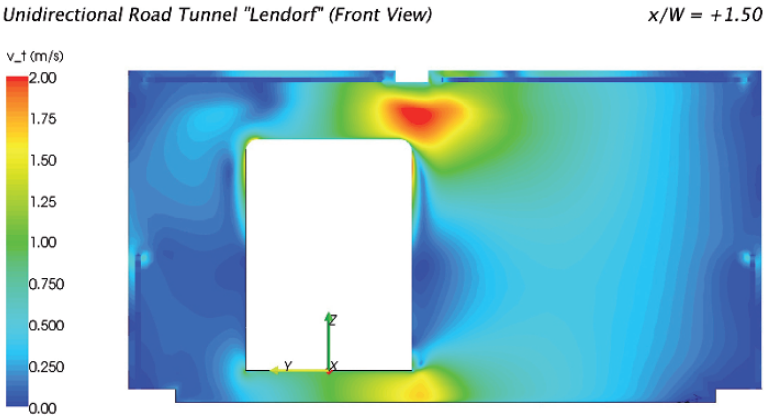

Fig. 3.3 Tangential velocity magnitude of a vertical plane cut at x/W = 1.5 at the middle of trailer

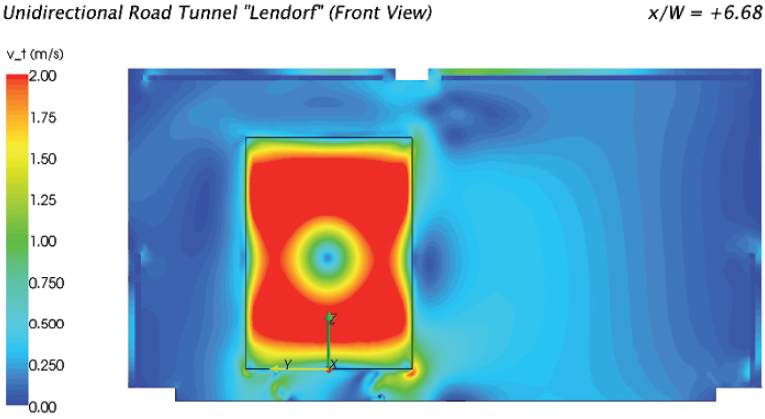

Fig. 3.4 Tangential velocity magnitude of a vertical plane cut at x/W = 6.68 immediately behind the trailer base

Figure 3.5 shows the velocity v_y which is normal to the SPAS filter surface on a horizontal line. This line is drawn at a height of $z/W = 0.4$ inside the SPAS filter cells of filter A. The velocity v_y begins and ends at rest; therefore one complete heavy vehicle cycle is captured by the plot. However, v_y depends strongly on the z/W-position.

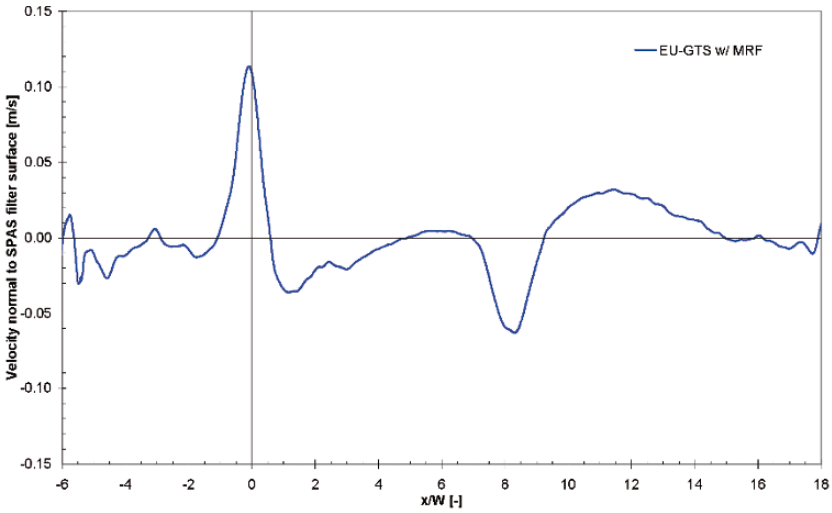

Fig. 3.5 Velocity v_y normal through SPAS filter A on a line-probe at z/W = 0.4

For the prediction of the entire volume flow through the SPAS filters, the product of filter area and v_y have to be integrated. Furthermore, the volume flow was separated into forward and backward direction to obtain an in-flow and out-flow value. The notation of all four SPAS filters as well as the directions for in- and out-flows are shown in Fig. 3.6. To obtain the volume for 1 m length of all four SPAS filters, the volume flow must be multiplied by the time per meter length, which is the reciprocal value of the vehicle speed (Table 3.2). These calculated values are valid for only one EU-GTS and must be multiplied with the heavy vehicle traffic.

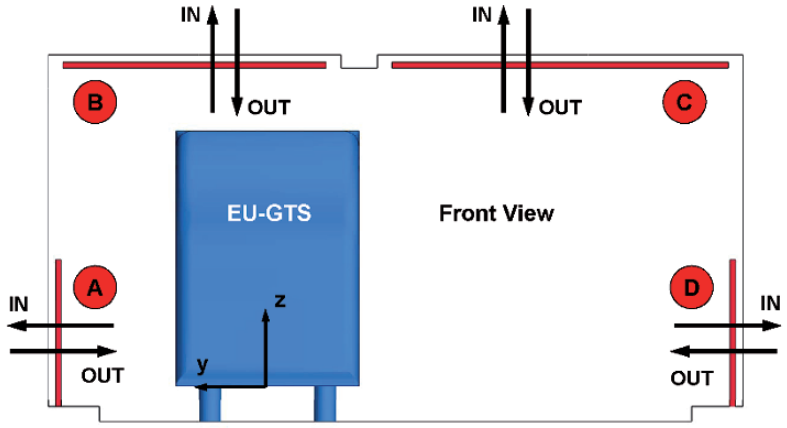

Fig. 3.6 SPAS filter caption and in-flow, out-flow definition

Table 3.2 Volume flow and volume per unit length through the SPAS filters

SPAS Filter	V'_{in} (m³/s)	V'_{out} (m³/s)	V_{in}/l (m³/m)	V_{out}/l (m³/m)
A	1.454	1.257	0.0632	0.0546
B	1.185	0.106	0.0515	0.0046
C	2.983	1.224	0.1297	0.0532
D	1.488	1.096	0.0647	0.0476

4 Conclusions and Outlook

Local traffic contributes a significant part to bad air quality in cities. The target of the EU-LIFE SPAS project is a reduction of traffic emissions where they originate, and in case of a road tunnel this is at their outlet portals. Therefore, filters were investigated to evaluation the volume flow which can be later used to estimate the effectiveness of dust filtration systems.

To obtain the flow field around such SPAS filter elements, a simplified shape of a European-like heavy vehicle was primarily simulated inside the NASA Ames wind tunnel to validate the CFD-code and the appropriate settings. Then these findings were transferred to a self-ventilated road tunnel, where the SPAS filters were mounted on the tunnel walls as well as on the ceiling. As a result, the volume per length which flows through the SPAS filters delivered an order of magnitude for the further filtration effort, especially PM10.

Further CFD simulations will be dealing with the influence of the exact position of heavy vehicles driving through road tunnels. A previous parameter study, which was made under different conditions, provided a strong non-linear influence of the distance between the heavy vehicle and the tunnel wall. Moreover, detailed models of European heavy vehicles will result in more complex flow fields inside a road tunnel and will help to obtain a better understanding of the flow mechanisms.

Acknowledgments

The authors would like to thank Bruce Storms from NASA Ames for the very helpful data of the experimental investigation of the GTS in the NASA Ames wind tunnel. This project is funded by the European Commission as part of the EU-LIFE project.

References

[1] Autobahnen- und Schnellstraßen-Finanzierungs-Aktiengesellschaft: Annual Report of the ASFINAG Group (2006)
[2] Gutierrez W, Hassan B, Croll R, Rutledge W: Aerodynamics Overview of the Ground Transportation Systems (GTS) Project for Heavy Vehicle Drag Reduction. SAE Paper (960906 SP-1145) (1996)
[3] Hall R: Modelling of Dense Gas Dispersion in Tunnels. Contract research report 359/2001, HSE -Health and Safety Executive (2001)
[4] Hucho W (ed.): Aerodynamics of Road Vehicles, 4th edn. SAE, Warrendale (1998)
[5] Langmann B, Graf H: The Chemistry of the Polluted Atmosphere Over Europe: Simulations and Sensitivity Studies with a Regional Chemistry-Transport-Model. Atmospheric Environment 31(19), 3239–3257 (1997)
[6] Lindener N, Miehling H, Cogotti A, Cogotti F, Maffei M: Aeroacoustic Measurements in Turbulent Flow on the Road and in the Wind Tunnel. In: J. Wiedemann (ed.) Progress in Vehicle Aerodynamics and Thermal Management V, pp. 193–211. FKFS -Research Institute of Automotive Engineering and Vehicle Engines Stuttgart (2007)
[7] Oettl D, Sturm P, Almbauer R, Okamoto S, Horiuchi K: Dispersion from Road Tunnel Portals: Comparison of two Different Modelling Approaches. Atmospheric Environment 37, 5165–5175 (2003)
[8] Oettl D, Sturm P, Bacher M, Pretterhofer G, Almbauer R: A Simple Model for the Dispersion of Pollutants from a Road Tunnel Portal. Atmospheric Environment 36, 2943– 2953 (2002)
[9] Pointer W, Sofu T, Weber D: Development of Guidelines for the Use of Commercial CFD in Tractor-Trailer Aerodynamic Design. SAE (SAE 2005-01-3513) (2005)
[10] Roy C, Payne J, McWherter-Payne M, Salari K: RANS Simulations of a Simplified Tractor/Trailer Geometry. In: R. McCallen, F. Browand, J. Ross (eds.) Lecture Notes in Applied and Computational Mechanics -The Aerodynamics of Heavy Vehicles: Trucks, Buses, and Trains, vol. 19, pp. 207–218. Springer (2004)
[11] Roy C, Payne J, McWherter-Payne M: RANS Simulations of a Simplified Tractor/Trailer Geometry. Journal of Fluids Engineering 128, 1083–1089 (2006)
[12] Salari K, Ortega J, Castellucci P: Computational Prediction of Aerodynamic Forces for a Simplified Integrated Tractor-Trailer Geometry. AIAA Paper (AIAA-2004-2253) (2004)
[13] Storms B, Ross J, Heineck J, Walker S, Driver D, Zilliac G: An Experimental Study of the Ground Transportation System (GTS) Model in the NASA Ames 7-by 10-Ft Wind Tunnel. NASA-TM (2001-209621) (2001)

Experiments and Calculations Relevant to Aerodynamic Effects during Highway Passing Maneuvers

B. Basara[1], S. Girimaji[2], S. Jakirlic[3], F. Aldudak[3] and M. Schrefl[4]

[1] AVL List GmbH AVL List GmbH, Hans List Platz 1, 8020 Graz, Austria
[2] Aerospace Engineering Department, Texas A&M University, TX 77843, USA
[3] Fluid Mechanics and Aerodynamics, Darmstadt University of Technology, Germany
[4] BMW AG, Aerodynamics, Munich, Germany
branislav.basara@avl.com

Abstract Aerodynamic effects during highway passing maneuvers are still not well documented. To better understand these effects, a 40% car-truck overtaking process has been carried out in the BMW wind tunnel. As a first step, the car aerodynamics has been measured without the truck to establish the reference pressure distribution for subsequent tests. The overtaking process has been approximated by fixing the truck model at eight stationary positions relative to the car model. This approximates the overtaking process as a quasi-stationary process. The reference calculations are performed with a new variant of $\overline{v^2} - f$ model, the so-called ζ-f model (Hanjalic et al., 2004). Furthermore, the calculations are also performed by using recently proposed Partially-averaged Navier Stokes (PANS) model (Girimaji et al., 2003, Girimaji and Hamid, 2005) in order to capture unsteady effects more correctly compared with the unsteady RANS. Because of its extensive reference database, the well-known Ahmed body benchmark (25 degrees) was computationally investigated as an introductory case with respect to the comparative assessment of the RANS and PANS approaches. A validation procedure for the PANS method is then conducted by computing the single passenger car (40% BMW model).

Introduction

There are a number of publications in the field of the external car aerodynamics, e.g. Baxendele et al. (1996), Makowsky and Kim (2000), Basara et al. (2001) etc. However, we will highlight only two, which are the most relevant for the work presented here. In the work of Basara and Tibaut (2002), the error of the steady state approach for the flows where transient effects are important, was analyzed. And in the work of Khalighi et al. (2001), the $\overline{v^2}-f$ (Durbin, 1991) was successfully used to predict the unsteady wake behind a bluff body.

This complementary experimental and computational study focuses on turbulence model validation in such a complex flow situation. The model applied relies on the elliptic relaxation (ER) concept providing a continuous modification of the homogeneous pressure-strain process as the wall is approached to satisfy the wall conditions, thus avoiding the need for any wall topography parameter. This model approach represents a further contribution towards more robust use of advanced closure models. The variable ζ represents the ratio $\overline{v^2}/k$ ($\overline{v^2}$ is a scalar property in the Durbins $\overline{v^2}-f$ model, which reduces to the wall-normal stress in the near-wall region) providing more convenient formulation of the equation for ζ and especially of the wall boundary conditions for the elliptic function *f*. This model is used in conjunction with the so-called universal wall treatment. The latter method blends the integration up to the wall (exact boundary conditions) with the wall functions, enabling well-defined boundary conditions irrespective of the position of the wall-closest computational node. This method is especially attractive for computations of industrial flows in complex domains where higher grid flexibility, i.e. weaker sensitivity against grid non-uniformities in the near wall regions, featured by different mean flow and turbulence phenomena (flow acceleration/deceleration, streamline curvature effects, separation, etc.), is desirable. All simulations were performed by using the commercial CFD software package AVL FIRE v8.5 (2006).

The corresponding wind tunnel tests were performed in the full scale wind tunnel of the BMW Group in Munich. Both, tests on 1:2.5 scale models and on a full-scale cars were performed. Despite geometrical differences, the data obtained for both car configurations can be used for mutual comparison. The aerodynamic effects during highway passing maneuvers are still not completely understood. To better understand these effects, a 40% overtaking process has been planned in the BMW wind tunnel, Fig. 2. As a first step, the car aerodynamics has been measured without the truck to gain the reference pressure distribution for subsequent tests, Fig. 1. This simplification to a 40% model is acceptable and no significant discrepancies to full scale pressure field are to be expected. This is in accordance with Széchényi (2004), Yamamoto et al. (1996). This simplified configuration has been chosen to be capable to extend the measurements in a second step to overtaking processes which have been approximated by eight stationary relative positions. By doing so the unsteady overtaking process has been simplified to a set of

stationary process. In the present work only the flow past a single passenger car configuration (40% model) was considered.

Experimental Details

The 40%-model was equipped with 54 surface-mounted pressure tabs: 13 pressure tabs were mounted on each car-side; 14 on bonnet, roof and trunk, see Figs. 1-3 for their distribution at the car surface. In addition, the stagnation point pressure has been acquired. The pressure tabs were wired to the car interior and connected to a 64-channel PSI pressure module to measure the surface pressure distribution in reference to the plenum pressure. The car model was a foam model. Tests have been performed at a velocity of 140 km/h, resulting in a Reynolds-number of $9x10^5$.

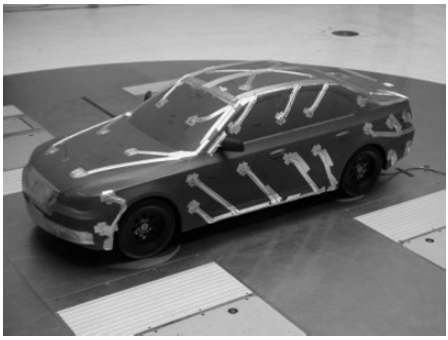

Fig. 1 Wind tunnel configuration

Fig. 2 Wind tunnel configuration in the case of overtaking process

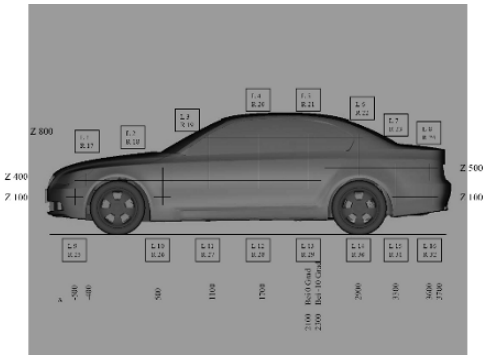

Fig. 3 Pressure tabs distribution at the side surface

Computational Model

The flow field is modeled by the Reynolds-Averaged Navier Stokes equations coupled with the eddy-viscosity $\zeta - f$ model equations. The continuity and momentum equations may be written as:

$$\frac{\partial}{\partial x_j}(\rho U_j) = 0 \tag{1}$$

$$\frac{\partial}{\partial t}(\rho U_i) + \frac{\partial}{\partial x_j}(\rho U_i U_j) = -\frac{\partial p}{\partial x_i} + \frac{\partial}{\partial x_j}(\tau_{ij} - \rho\overline{u_i u_j}) \tag{2}$$

where ρ is the fluid density, U_i is the mean-velocity vector, p is the static pressure, t is time and τ_{ij} denotes the mean viscous stress tensor:

$$\tau_{ij} = 2\mu S_{ij} \tag{3}$$

In the above, μ is the dynamic viscosity and the mean strain rate tensor S_{ij} is given as:

$$S_{ij} = \frac{1}{2}\left(\frac{\partial U_i}{\partial x_j} + \frac{\partial U_j}{\partial x_i}\right) \tag{4}$$

The last term in Equation (2) $(-\rho\overline{u_i u_j})$ is the unknown Reynolds stress tensor which is obtained from the constitutive relation analogous to Equation (3) (Bousinessq's analogy):

$$-\rho\overline{u_i u_j} = 2\rho\nu_t S_{ij} - \frac{2}{3}\rho k\delta_{ij} \tag{5}$$

where μ_t is the turbulent viscosity, δ_{ij} is the Kronecker delta and $k = 0.5\overline{u_i u_i}$ represents the turbulent kinetic energy. In the $\zeta - f$ (Hanjalic et al. 2004) model the eddy-viscosity is defined as:

$$\nu_t = C_\mu \zeta k\tau \tag{6}$$

where ζ is the velocity scale ratio obtained from the following equation:

$$\frac{D\zeta}{Dt} = f - \frac{\zeta}{k}P_k + \frac{\partial}{\partial x_j}\left[\left(\nu + \frac{\nu_t}{\sigma_\zeta}\right)\frac{\partial\zeta}{\partial x_j}\right] \tag{7}$$

The time scale τ is given as

$$\tau = \max\left[\min\left(\frac{k}{\varepsilon}, \frac{a}{\sqrt{6}C_\mu S\zeta}\right), C_\tau\left(\frac{\nu}{\varepsilon}\right)^{1/2}\right] \tag{8}$$

The coefficients appearing in Equations (6) and (8) take the values $\alpha = 0.6$, $C_\mu = 0.22$ and $C_\tau = 6.0$. The complete model is given by following equations:

$$\frac{Dk}{Dt} = (P_k - \varepsilon) + \frac{\partial}{\partial x_j}\left[\left(\nu + \frac{\nu_t}{\sigma_k}\right)\frac{\partial k}{\partial x_j}\right] \tag{9}$$

$$\frac{D\varepsilon}{Dt} = \frac{C_{\varepsilon 1}P_k - C_{\varepsilon 2}\varepsilon}{\tau} + \frac{\partial}{\partial x_j}\left[\left(\nu + \frac{\nu_t}{\sigma_\varepsilon}\right)\frac{\partial\varepsilon}{\partial x_j}\right] \tag{10}$$

In above equations, the production of k is given as:

$$P_k = -\overline{u_i u_j}\frac{\partial U_i}{\partial x_j} \tag{11}$$

These equations are solved in conjunction with an equation for the elliptic rellaxation function f which is formulated by using the pressure-strain model of Speziale, Sarkar and Gatski (1991) and given as:

$$L^2\nabla^2 f - f = \frac{1}{\tau}\left(c_1 + C_2'\frac{P_k}{\varepsilon}\right)\left(\zeta - \frac{2}{3}\right) - \left(\frac{C_4}{3} - C_5\right)\frac{P_k}{k} \tag{12}$$

where f goes to zero at the wall: $f_{wall} = \lim_{y\to 0} \frac{-2\nu\zeta}{y^2}$ and the length scale L is obtained from:

$$L = C_L \max\left(\min\left(\frac{k^{3/2}}{\varepsilon}, \frac{k^{1/2}}{\sqrt{6} C_\mu S \zeta} \right), C_\eta \left(\frac{\nu^3}{\varepsilon} \right)^{1/4} \right) \tag{13}$$

Hanjalic et al. (2004) neglected the last term in Eq. (12) due to small values of $\left(C_4/3 - C_5\right) \approx 0.008$, and they also decreased $C_2^{'}$ from the original SSG value 0.9 to 0.65 in order to take into account the discrepancy in the definition of ε in the log-law region. The $\zeta - f$ model is very robust and more accurate than the simpler two-equation eddy viscosity models (Hanjalic et al., 2004). Nevertheless, the model is usable for a relatively coarse mesh next to the wall but again the cell next to the wall should reach a non-dimensional wall distance y^+ as a maximum less than 3. The largest error is introduced when the first computational cell fails in the buffer region, e.g. $5 \le y^+ < 30$. Some authors have combined the integration up to the wall with wall functions. These smoothing functions which blend two formulations together are known as automatic wall treatment, hybrid or compound wall treatment, etc. Popovac and Hanjalic (2005) proposed the blending formula for the quantities specified at the cell P next to the wall as

$$\phi_P = \phi_\nu e^{-\Gamma} + \phi_t e^{-1/\Gamma} \tag{14}$$

where 'ν' is the viscous and 't' the fully turbulent value of the variables: wall shear stress, production and dissipation of the turbulence kinetic energy. Their compound wall treatment was introduced under the name "Hybrid Wall Treatment" in AVL FIRE due to some simplifications of the original approach. The original compound wall treatment of Popovac & Hanjalic (2005) includes the tangential pressure gradient and convection, but here, the simplest approach is used which includes the standard wall function. Another departure from the original formulation is in the calculation of the dissipation rate as proposed by Basara (2006).

The Partially-Averaged Navier-Stokes (PANS) approach is a recently proposed method by Girimaji et al. (2003), which changes seamlessly from RANS to the direct numerical solution of the Navier-Stokes equations (DNS) as the unresolved-to-total ratios of kinetic energy and dissipation are varied. There are two variants of the PANS model derived up to now, one based on the k-ε formulation and another based on the k-ω formulation (Lakshmipathy & Girimaji, 2006). We have used here the first formulation where the unresolved kinetic energy and dissipation

equations are systematically derived from the k-ε model. The model equations for the unresolved kinetic energy k_u and the unresolved dissipation ε_u are given as

$$\frac{Dk_u}{Dt} = (P_u - \varepsilon_u) + \frac{\partial}{\partial x_j}\left[\left(\nu + \frac{\nu_u}{\sigma_{ku}}\right)\frac{\partial k_u}{\partial x_j}\right] \tag{15}$$

$$\frac{D\varepsilon_u}{Dt} = C_{\varepsilon 1} P_u \frac{\varepsilon_u}{k_u} - C^*_{\varepsilon 2}\frac{\varepsilon_u^2}{k_u} + \frac{\partial}{\partial x_j}\left[\left(\nu + \frac{\nu_u}{\sigma_{\varepsilon u}}\right)\frac{\partial \varepsilon_u}{\partial x_j}\right] \tag{16}$$

where the eddy viscosity of unresolved scales is equal to

$$\nu_u = c_\mu \frac{k_u^2}{\varepsilon_u} \tag{17}$$

The model coefficients are

$$C^*_{\varepsilon 2} = C_{\varepsilon 1+}\frac{f_k}{f_\varepsilon}(C_{\varepsilon 2} - C_{\varepsilon 1});\ \ \sigma_{k,\varepsilon u} = \sigma_{k,\varepsilon}\frac{f_k^2}{f_\varepsilon} \tag{18}$$

The parameter which determines the unresolved-to-total kinetic energy ratio f_k is defined based on the grid spacing, following Girimaji & Hamid (2005), thus

$$f_k = \frac{1}{c_\mu}\left(\frac{\Delta}{\Lambda}\right)^{2/3} \tag{19}$$

where Δ is the grid cell dimension and Λ is the Taylor scale of turbulence. The PANS asymptotic behaviour goes smoothly from RANS to DNS with decreasing f_k. In the work presented here, the parameter f_k is implemented in the computational procedure as a dynamic parameter, changing at each point at the end of every time step, and then it is used as a fixed value at the same location during the next time step.

Results and Discussion

The first case used for comparisons is the Ahmed Body (Ahmed, 1984), a three-dimensional idealized vehicle model which represents the key benchmark for validation of the turbulence models regarding external car aerodynamics. This case allows investigation of the back slant effect on the overall drag force. At a certain angle of the slant, a vortex breakdown phenomenon appears causing the sudden pressure drop acting on the model. The case with the back slant angle of 25° is calculated here as this is the angle at which all RANS models fail to correctly predict. Predicted streamlines with the ζ-f model are shown in Fig. 4.

The ζ-f model predicts the complete rear part in the separation region starting near the top edge. There is also no separation at the front part as shown in some latest measurements, see Lienhart et al. (2002), and Spohn and Gillieron (2002).

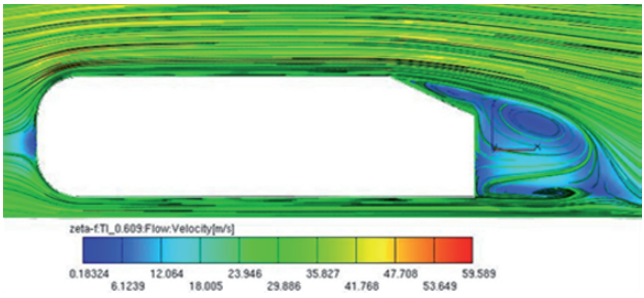

Fig. 4 Predicted streamlines by the ζ-f model

In the calculations performed with the PANS, the flow attaches to the slant again as reported by measurements. The PANS also captures the separation at the front part of the body as shown in Fig. 5. The selected velocity profiles for comparisons with the measurements are placed at the middle plane on the slant of the body at x=-0.183, -0.103 and -0.003m respectively as sketched in Fig. 6. Both the streamwise and normal velocity components are not captured well with the ζ-f model at all chosen locations. On the other hand, the PANS predicted all profiles very close to the measured values as shown in Fig. 7. It is important to note that the same computational mesh consisted of 8 million cells (an unstructured mesh with hexahedral, tetrahedral and prismatic elements) was used for all calculations.

The same procedure was repeated for the BMW model, but this time using 4 million computational cells following work of Basara et al. (2007). In that work, the computational domain was meshed with two grids containing 2.85 million and 4 million hexahedral cells. Coarser grids, comprising 1.3 and 2.5 million, cells were also tested. The region around the car body was refined for the y^+-values of the wall-nearest grid cells. This was achieved by combining blocks of structured meshes connected with arbitrary interfaces. The finest grid provided y^+-values in the range of 10-30, while for other meshes y^+-values were in the range of 20-60 and above (as shown in the work of Basara et al. 2007). The grid was optimized in order to allow future calculations including the truck model on relatively small mesh sizes. Fig. 8 shows the instantaneous vorticity as calculated by using PANS. This relatively coarse mesh, considering mesh requirements for the Large Eddy Simulation, was again fine enough that the dynamic parameter f_k depart from the RANS value 1, so the strong transient motion at the end of the model, was captured. The first comparisons with the measurements were made for the time averaged pressure coefficient C_P at the center plane of the model. At the mid part of

the model, the calculated pressure coefficient is over-predicted on the upper side, see Fig. 9. But in general, there is a good agreement with the measured data. Comparing the predicted and measured pressure coefficients on the side of the car, Z= 0.28, as shown in Fig. 9, it is again clear that the main differences appear in the description of the transient wake behind the model. Nevertheless, this was the main reason to introduce PANS method in the calculations of the passing maneuvers where the transient effects might have an important role, see Fig. 10.

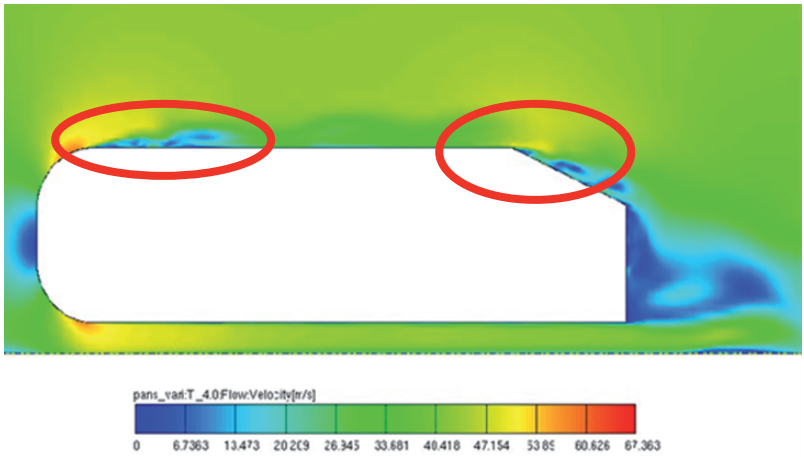

Fig. 5 Instantaneous velocity magnitude as predicted by PANS

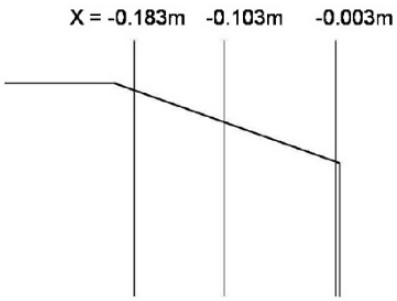

Fig. 6 Selected positions for the comparisons of velocity profiles

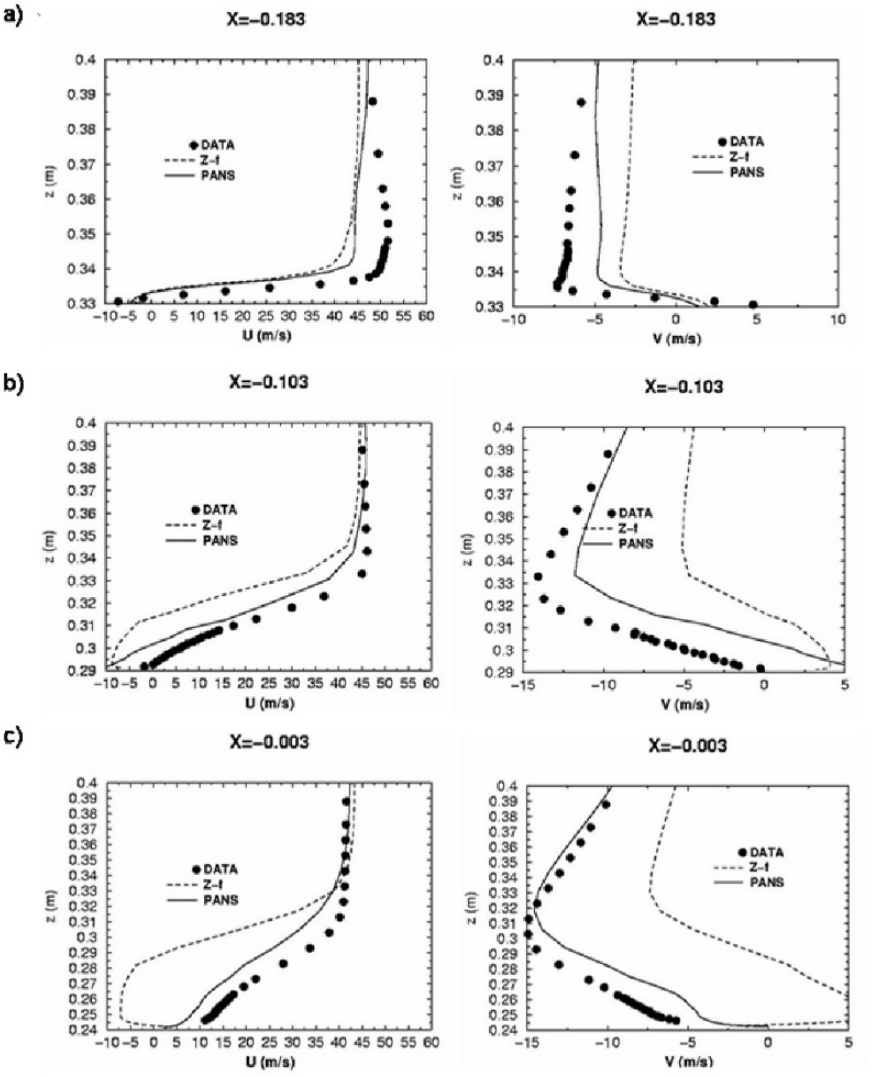

Fig. 7 Predicted mean and normal velocity components as predicted by the ζ-f model and the PANS: (a) -0.183m; (b) -0.103m; and (c) -0.003m

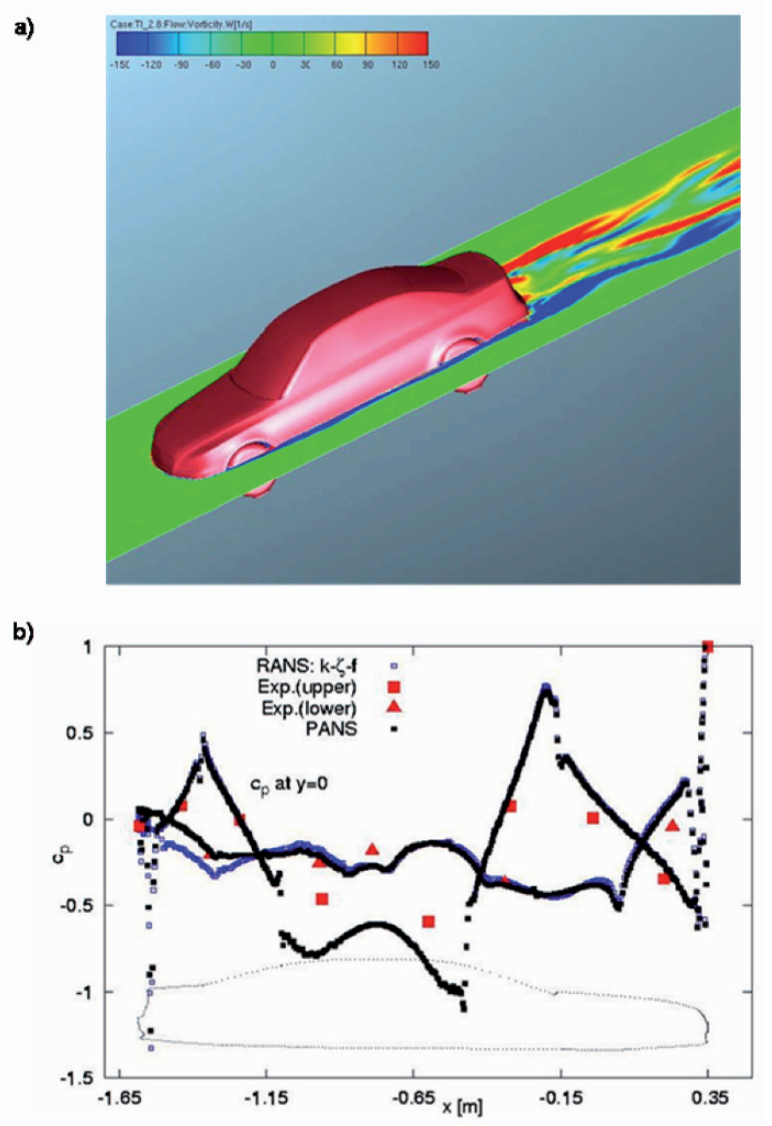

Fig. 8 Predicted an instantaneous vorticity (a) and a mean pressure coefficient at the center plane of the model (b)

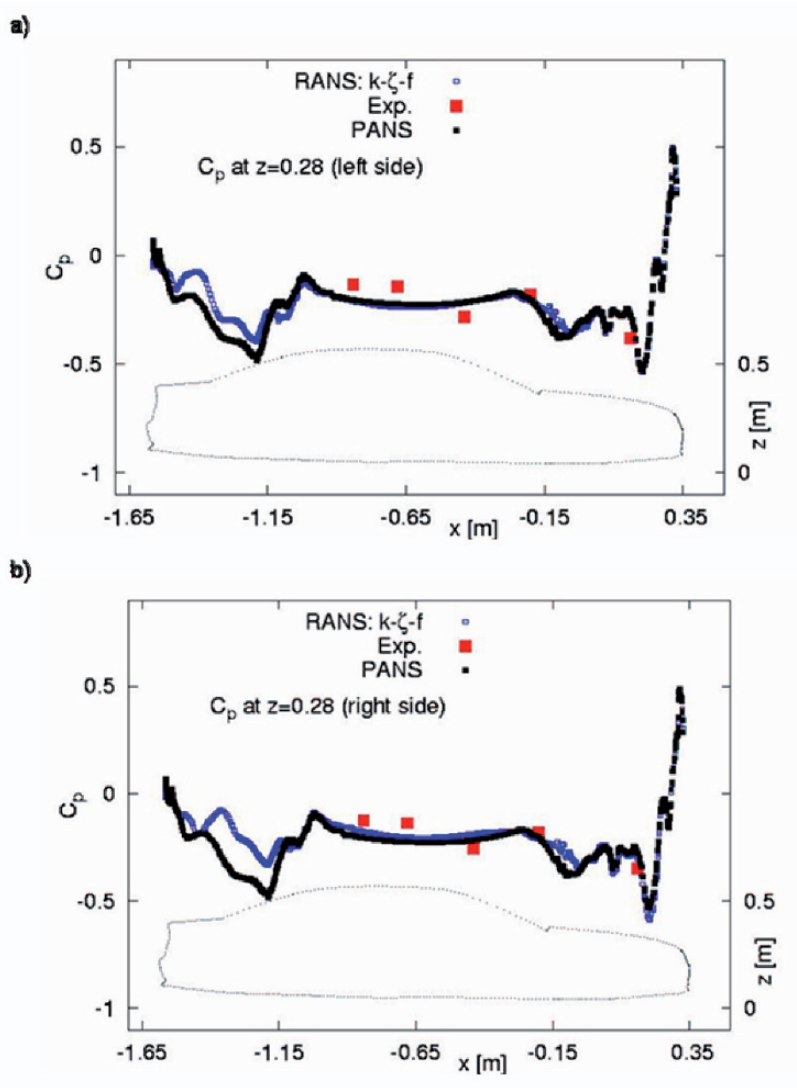

Fig. **9** Predicted pressure coefficient at the side plane z=0.28: (a) right side and (b) left side

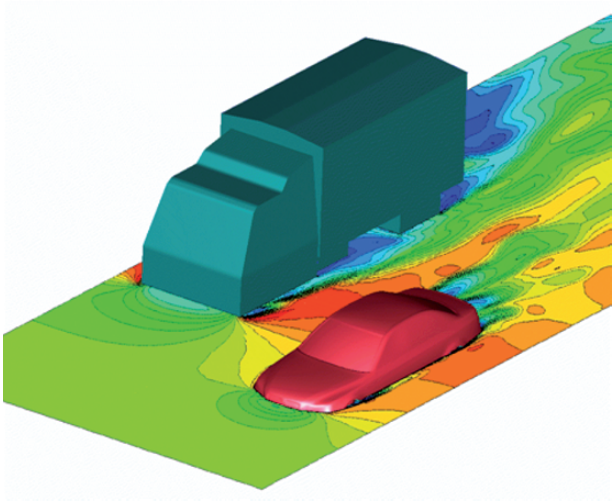

Fig. **10** A simulated passing maneuver showing contours of velocity magnitude

Conclusions

Potential of a recently proposed near-wall ζ-f turbulence model as well as the novel PANS approach for predicting the unsteady flow and associated turbulence around a 40%-scaled BMW car configuration including wheels were illustrated. PANS calculations were superior over the unsteady RANS calculations for the Ahmed Body, and therefore it is expected that this might bring an important difference for the simulation of transient passing maneuvers. A dynamic update of the PANS key parameter, the unresolved-to-total kinetic energy ratio, seems to be the promising approach to improve results on employed computational meshes. However, the both of the methods, exhibited good agreement with available experimental database for three-dimensional wall pressure mapping covering the car surface. The future work will include the simulation of the passing maneuvers with static meshes following presented measurements but also with moving meshes needed for the comparisons with the recent road measurements.

References

AVL AST (2006) FIRE Manual 8.5. AVL List GmbH. Graz.

Basara B (2006): An Eddy Viscosity Transport Model Based on Elliptic Relaxation Approach, AIAA J., Vol. 44, pp. 1686-1690.

Basara B, Przulj V and Tibaut P (2001): On the calculation of external aerodynamics: Industrial Benchmarks,. SAE 2001-01-0701.

Basara B and Tibaut P (2002): Time dependent vs. steady state calculations of external aerodynamics, Proc. of the Aerodynamics of Heavy Vehicles: Trucks, Buses and Trains, Lecture Notes in Applied and Computational Mechanics, Vol. 19, pp. 107-119, Springer.

Basara B, Aldudak F, Jakirlic S, Tropea C, Schrefl M, Mayer J and Hanjalic K (2007): Experimental investigations and computations of unsteady flow past a real car using a robust elliptic relaxation closure with a universal wall treatment", SAE 2007-01-0104.

Baxendele A, Graysmith J, Howell J and Hayness T (1996): The CFD Investigation of Flow Separation over a Simple Vehicle Model, Proc, RaeS Vehicle Aerodynamics Conference, Loughborough University, U.K.

Durbin P (1991): Near-Wall Turbulence Closure Modelling Without Damping Functions, Theoret. Comput. Fluid Dynamic., Vol. 3, pp. 1-13.

Girimaji S, Srinivasan R and Jeong E (2003): PANS Turbulence Models For Seamless Transition Between RANS And LES: Fixed Point Analysis And Preliminary Results. Int. 4th ASME_JSME Joint Engineering Conference, Honolulu, Hawaii, FEDSM2003-45336.

Girimaji S and Abdul-Hamid K (2005): Partially –Averaged Navier-Stokes Model For Turbulence: Implementation And Validation. AIAA Aerospace Sciences Meeting and Exhibit, Reno, Nevada, 2005-0502.

Hanjalic K, Popovac M, Hadziabdic M (2004): A robust near-wall elliptic-relaxation eddy-viscosity turbulence model for, Int. J. of Heat and Fluid Flow, 25, 1047-1051.

Khalighi B, Zhang S, Koromilas C, Balkanyi S, Bernal P, Iaccarino G and Moin P (2001): Experimental and computational study of unsteady wake flow behind a bluff body with a drag reduction device, SAE 2001-01-1042.

Lakshmipathy S and Girimaji S (2006): Partially-Averaged Navier-Stokes Method for Turbulent Flows: k-ε model Implementation, AIAA Aerospace Sciences Meeting and Exhibit, Reno, Nevada, 2006-119.

Lienhart H and Becker S (2003): Flow and Turbulent Structure in the Wake of a Simplified Car Model. SAE 2003-01-0656.

Makowsky F and Kim S (2000): Advances in External-Aero Simulation of Ground Vehicles Using the Steady RANS Equations, SAE 2000-01-0484, Detroit.

Popovac M, Hanjalic K (2005): Compound Wall Treatment for RANS Computation of Complex Turbulent Flows, Third MIT Conf. On Comp. Fluid and Solid Mech., edited by K.Bathe, Vol. 1, Elsevier, 802-806.

Speziale C, Sarkar S, Gatski T (1991): Modeling the Pressure-Strain Correlation of Turbulence: An Invariant Dynamical Systems Approach, J. Fluid Mech., Vol. 227, pp. 245-272.

Széchényi E (2004): The Overtaking Process of Vehicles, Progress in Vehicle Aerodynamics III-Unsteady Flow Effects.

Spohn A and Gillieron P (2002): Flow separations generated by a simplified geometry of an automotive vehicle. IUTAM Symposium, Touluse, France, 227, 245-272.

Yamamoto S (1996): Aerodynamic Influence of a Passenger Vehicle on the Stability of the Other Vehicles, JSAE9730074.

Drag Reduction

Design & Test Techniques for Drag Reduction at Swift Engineering – A Racecar Manufactures Perspective

Mark Page

Swift Engineering, USA
mpage@swiftengineering.com

Abstract Swift Engineering designs and builds high performance racecars and aircrafts. Techniques developed in this fast paced environment are relevant to transport industry. Experimental and analytical design example will be presented.

Summary of Full-Scale Wind Tunnel Tests of Aerodynamic Drag-Reducing Devices for Tractor-Trailers

Jason Leuschen and Kevin R. Cooper

National Research Council, Ottawa, Canada
jason.leuschen@nrc.ca

Introduction

The National Research Council of Canada (NRC) has completed an evaluation of several prototype and commercially-available drag reduction devices for Class-8 tractor-trailer combinations. The evaluation focused on potential reductions in fuel consumption based on the results of full-scale wind-tunnel tests. The following is a summary of the results more fully presented in SAE 2006-01-3456.

Three primary devices have been evaluated, with the combination able to reduce fuel consumption by approximately 6,667 liters (1,761 US gal) annually, based on 130,000 km (81,000 miles) traveled per tractor at a speed of 100 km/hr (62 mi/hr).

Test program Summary

The test program was run in March 2006 in the 9-meter wind tunnel of the NRC, located in Ottawa, Canada. This is a closed-wall, closed-return, atmospheric wind tunnel having a test section that is 9.14 m high, 9.14 m wide and 22.5 m long. It has a maximum speed of 200 km/h (120 mi/h) and a turbulence level of 0.5 percent.

The tractor drive wheels sat on pads attached to the main balance below the tunnel floor. The front tractor wheels and the trailer bogey were floated on low-profile air bearings to allow the balance to measure the wind-axis drag and side forces, and to permit the turntable to rotate up to a yaw angle of at least 13°. Both forces are necessary to compute the body-axis drag.

The installation used in this test is seen in Fig. 1. The tractor under test was a Volvo VN 660 provided by Robert Transport Inc. of Quebec, Canada. The trailer could be configured to be either 8.5 m (28 ft) or 12.2 m (40 ft) long by removing a section of the body. The kingpin was set for a 1.14 m (45 inch) gap between the front face of the trailer and the rear face of the cab. The side corners at the front of the trailer are rounded with a 127 mm (5 inch) radius but the top edge is square.

Fig. 1 Volvo VN 660 and 28-ft. Trailer in the NRC 9m x 9m wind tunnel

Discussion of results

The data presented in this paper are given as the wind-averaged drag coefficient at 29.6 m/s (107 km/h, 65 mi/h). The procedure for the calculation of the wind averaged drag coefficient comes from [6] and is summarized in [1].

Based on the change in wind-averaged drag, the expected fuel-savings is calculated from,

$$\Delta\mu(V_t) = 4.25x10^{-4} V_t^2 \Delta\overline{C_D}(V_t) A \text{ L/100 km} \qquad (1)$$

Where A was 10.9 m^2 (the value used in calculating the drag coefficients) and V_t was taken as 100 km/h (62 MPH). The constant in equation (1) is based on a transmission efficiency of 0.85, an air density of 1.225 kg/m^3 and an average

specific fuel consumption of 0.275 liters/kW-h (0.042 US gal/hp-h) and a unit conversion factor of 1.072.

It is possible to calculate the annual fuel savings realized by installing these aerodynamic devices for an average fleet. Average annual distances covered by heavy trucks are now in the range of 200,000 km (125,000 mi), but only a portion of this distance is covered at cruise speed. For the purposes of this paper, the distance covered at cruising speed will be assumed to be 130,000 km (81,000 mi). This will result in a conservative estimate of fuel-savings because these devices continue to provide fuel savings at lower speeds, which has been neglected here. Thus, the annual fuel saving is 1,300 times that for the 100 km distance given in equation (1).

The standard vehicle components that were evaluated are shown in Figs. 2 and 3. The drag and resulting annual fuel consumption changes are summarized in Table 1.

Table 1 Tractor Component Drag and Fuel Increments

	$\Delta\overline{C_D}(100\,\text{kph})$	Annual fuel savings (L)
OEM side mirrors	-0.016	-938
OEM bug deflector	-0.015	-903
OEM fender mirrors	-0.010	-588
engine cooling inlets blocked	0.000	0
sun visor w/ roof deflector	0.001	54
hub caps (truck & trailer)	0.002	120
deer bumper	0.002	120
wrap-around splash guards	0.005	292
prototype roof deflector filler	0.014	825
fifth wheel forward 254 mm	0.016	982
OEM tank and cab skirts	0.027	1,596
OEM side extenders	0.042	2,499
OEM roof deflector	0.072	4,318

Fig. 2 Common components whose drag effects were measured

Fig. 3 Common components whose drag effects were measured

It can be seen that many components produce noteworthy drag and fuel changes. In particular, the bug deflector raises fuel consumption and the mirrors are also an area worth study. Mirrors have been singled out since they are a large source of drag that are dictated by current safety regulations. It would be possible to eliminate mirror drag if regulations were changed to allow video cameras to replace mirrors as the means of providing rearward vision. The price of the video system would be covered by fuel savings, and the cameras may increase safety by offering a larger field of view with infra-red capabilities that can penetrate fog, rain or darkness.

All of the other components are beneficial, especially the standard cab-roof fairing, cab side extenders and tank skirts, which form the current aerodynamic package. The sun visor was an OEM product, its design obviously having been developed in conjunction with the roof deflector, so it actually produced a small drag reduction. This may not be the case if the sun visor is used with trucks without a roof deflector.

Eliminating the cooling flow, by covering the front grille and the lower intake in the front bumper, had a negligible effect on drag. This has been observed in several full- and model-scale tests of modern tractors.

Prototype hub caps consisting of solid metal disks on the outside wheels of the trailer and tractor showed a negligible change in drag. Recall that this test was performed with fixed wheels and the effects of wheel rotation on the results are unknown. Furthermore, these disks could be expected to have a harmful effect on brake cooling.

Another prototype considered was a panel to fill the large cut-out on top of the roof deflector that provides space for the trailer during sharp cornering maneuvers. The fuel savings from this panel are significant and it is envisioned that a simple, lightweight, flexible panel should be able to provide this function at low cost.

Finally, the effect of reducing the tractor-trailer gap was studied. There are operational issues to be addressed in doing this, such as axle weights, ride quality and turn clearance, but the potential savings are significant for no capital cost. The expected change in drag depends upon the original gap size. In this case, the gap was reduced from 1.14m (45 in) to 0.89m (35 in). If the original gap were larger or smaller than 1.14m, the drag reduction may be smaller or larger, respectively, than that measured here. A related note is that the optimum angle of the tractor roof deflector is partly a function of the gap size. Thus, a significant change in gap size should be accompanied by a re-optimization of the roof deflector. In previous studies an overall drag increase has been observed after significantly reducing the gap without adjusting the roof deflector, likely because the airflow is underdeflected and strikes the trailer which is now closer.

The results presented in Table 1 are application specific and will only apply strictly to the particular model of tractor and component tested. Nevertheless, the results are useful as guidelines to the expected magnitudes in similar applications. As an example, the deer bumper showed a slight reduction in drag, a surprising result considering its large form. This shows that a properly designed and positioned deer bumper can provide a drag reduction.

The new components that were evaluated are shown in Figs. 4 and 5 and aerodynamic drag and fuel results are summarized in Table 2.

Table 2 Performance of new add-on components

	$\overline{\Delta C_D}(100\,\text{kph})$	Annual fuel savings (L)
base drag reduction		
Transtex Composite folding rear trailer deflector	0.0506	3,047
Aerovolution inflatable rear trailer fairing	0.0438	2,638
Trailer vortex strakes	-0.0195	-1,174
trailer leading edge fairings		
Freight Wing NXT Leading Edge Fairing wo/ roof deflector	0.0369	2,222
Manac prototype trailer leading edge fairing	0.0335	2,015
Freight Wing NXT Leading Edge Fairing w/ roof deflector	-0.0019	-114
underbody drag reduction		
Freight Wing Belly Fairing (low rider)*	0.0478	2,879
Laydon Composites main and rear skirts*	0.0391	2,355
Laydon Composites main skirts*	0.0376	2,264
Freight Wing Belly Fairing*	0.0367	2,210
Francis Cardolle trailer bogey fairing	0.0145	872
Francis Cardolle trailer wheel fairings	0.0078	470
gap sealing		
Laydon Composite trailer nose fairing	0.0135	813
Volvo cab side extender extensions	0.0123	741
Labyrinthine truck-trailer gap seal	0.0018	110

* Modified to fit a 40-foot trailer.

The large region of separated flow at the rear of a van-style trailer is the largest untreated source of drag on a modern tractor trailer. Not surprisingly, this is the area where the greatest reductions in drag were found. Two devices were tested in this area, the inflatable Aerovolution and triple-panel Transtex boattails. Each device addresses the issues of access to the trailer doors, though in different manners, while producing significant reductions in drag. These devices would be complementary to trailer skirts, and vice versa, and the choice between them comes down to non-aerodynamic issues.

The vortex generators at the rear of the trailer increased overall drag. The measured base pressure did not change, so the extra drag must be tare drag on the angle sections. They were made from 51mm x 51mm aluminum angle, 914 mm long, installed six per side on the trailer, 30° nose up from the horizontal. Four were mounted on the roof in an asymmetrical arrangement about the trailer centerline.

As has been seen before [2], a fairing on the front top face of the trailer provides little additional benefit when a cab-roof deflector is present. However, if a

roof deflector is not present, a leading-edge fairing can provide significant fuel savings, although only about half as much as a full roof deflector. This may be a consideration for trucks that often operate without a van trailer, for instance switching between flatbeds and vans, when a fixed roof deflector may increase the drag with a flatbed.

Both brands of trailer skirts tested showed similar drag reductions to each other and to those previously reported [1, 2]. The rear skirts, behind the trailer bogeys, showed no reduction in drag, although they may be effective when paired with a boat-tail [2]. It should be noted that the skirts were not installed as prescribed by the manufacturers. Ground clearance was approximately 100 mm (4 in) greater than normal due to the air bearings, which would decrease the drag reduction. The trailer was 12.2 m (40 ft) in length instead of the typical lengths of greater than 14.6 m (48 ft) that the skirts are designed for.

A lower skirt provides better performance, as shown in [1]. Previously [1,2], skirts had been tested on an 8.5 m long trailer with results close to those measured with the 12.2 m trailer presented here. Thus, it is expected that trailer length is not a critical parameter since most of the drag reduction comes from sheltering the trailer bogey.

A fairing on the trailer bogey was less effective than the skirts. This suggests that the skirts may also reduce the drag on the rough underbody of the trailer. It would be interesting to cover the trailer floor ribs to verify this.

The labyrinthine gap seal provided almost no drag reduction. The seal was made up of six 305 mm deep 17 mm thick plywood panels that were 2.44 m (8 ft) high. It would appear that they did not significantly block the gap flow, and only served to move the trailer front face closer to the tractor. The Laydon Composites Nose fairing provides a modest drag reduction and would be useful in situations where complete gap closure is not possible. Fully closing the gap is clearly the target to aim for, although partial closure through additional cab-extender extensions is simple and still beneficial.

Fig. 4 New add-on components

Fig. 5 New add-on components

The results obtained for the production devices were sensibly like those found in the development tests. The combination of: tractor-mounted gap sealing with the largest available side extenders, trailer side skirts and trailer boat-tailing combine to provide a total drag reduction of $\Delta\overline{C_D}(107) \approx 0.111$. Payback periods will vary based on fleet statistics, but the savings for any particular operation mode can be calculated with the data in Tables 1 and 2 using Equation (1). The critical parameters are fuel cost, device cost, annual cruise mileage and cruise

speed. Keep in mind that while fuel savings will increase with speed, overall consumption will increase by a greater amount.

Conclusions

Full-scale wind tunnel measurements were made on new production add-on devices meant to reduce the aerodynamic drag of Class-8 tractor-trailers beyond that provided by the current aerodynamic package. They consisted of devices to reduce the tractor-trailer-gap drag, to reduce trailer underbody and bogey drag, and to reduce trailer base drag.

Simple estimates of fuel consumption at steady speed on a flat road indicated annual fuel savings of 6,667 liters (1,761 US gallons). This estimate was predicated on a cruising speed of 100 km/h (62 mi/h) and 130,000km (81,0000 miles) traveled annually at this speed.

Acknowledgments

The National Research Council of Canada greatly appreciates the financial support of Natural Resources Canada in this study. It also appreciates the support of Transport Robert Inc and the suppliers of the new hardware. Finally, The NRC thanks its colleagues involved in the US DOE-sponsored aerodynamic drag reduction programs for the moral and intellectual support that they have generously provided.

References

1. Cooper K – Truck Aerodynamics Reborn – Lessons from the Past. SAE Truck and Bus Conference and Exposition, SAE 2003-01-3376, Houston, TX, Nov. 2003.
2. Cooper K & Leuschen J – Model and Full-Scale Wind Tunnel Tests of Second-Generation Aerodynamic Fuel Saving Devices for Tractor-Trailers. SAE 2005-01-3512. SAE Commercial Vehicle Engineering Conference, Chicago, IL, USA, Oct. 2005.

3. Cooper K (ed.) – Wind Tunnel Wall Corrections for Automotive Shapes in Closed-Jet Wind Tunnels. Society of Automotive Engineers Special Publication SAE SP-1176, Warrendale, MI, USA, Feb. 1996.
4. Leuschen J & Cooper K - Full-Scale Wind Tunnel Tests of Production and Prototype, Second-Generation Aerodynamic Drag-Reducing Devices for Tractor-Trailers. SAE 2006-01-3456.
5. Wood R & Bauer S – Simple and Low-Cost Aerodynamic Drag Reduction Devices for Tractor-Trailer Trucks. SAE 2003-01-3377, SAE Truck and Bus Conference and Exposition, Houston, TX, USA, Nov. 2003.
6. Cooper K (ed.) – SAE Wind Tunnel Test Procedure for Trucks and Buses. SAE Recommended Practice J1252, Aug. 1979.

A Fleet Operator's Perspective on Commercial Vehicle Drag Reduction

Réjean Laflamme

Robert Transport, Canada
rlaflamme@robert.ca

Abstract The research establishment has proven the potential fuel-savings for many devices/modifications for commercial trucks, however many of these developments remain in limited use. The primary reason that these substantial fuel-savings are not being realized is that fleet operators have chosen not to adopt them in their current form. Why have roof fairings been accepted while trailer skirts haven't? The reasoning behind the selection is logical, and often not obvious, so to succeed the development community must understand the environment of the fleet operator and respond with appropriate technology. This paper will address the considerations of a typical fleet operator when evaluating new technologies. A discussion and examples of the following issues will be given:

1. Introduction to Robert Transport: size of fleet, typical equipment, types of cargo, description of routes.
2. Operating Costs: a. Cost of installation, maintenance and operation in terms of cash and lost productivity.
   b. Weight of the device vs. cargo when the amount of paying cargo is limited by weight not volume.
   c. How do we measure the savings from the device? Track tests are expensive and relatively inaccurate and fleet tests can be statistically irrelevant.
3. Operating Procedures: How compatible are the devices with current roads, shipping yards and loading facilities?
4. Human Resources: There is a shortage of qualified drivers so it can be difficult to retain drivers if the technology adds to the driver's workload, is unpleasant or adversely affects driver comfort.
5. Reliability: The cost of unplanned downtime is significant, so the technology is expected to operate reliably, for 10 years or longer, in a variety of harsh conditions including extreme temperatures, wind, road salt, dust. Another consideration is resilience to damage caused by the drivers.
6. Safety: Visibility and crash worthiness.

Class 8 Vehicle Fuel Savings using Sealed Single and Dual Open Aft Cavities

Kenneth D. Visser, Kevin Grover

Clarkson University, USA
visser@clarkson.edu

Abstract Over-the-road tests have been conducted to evaluate and optimize sealed single and dual open aft cavity geometries for drag reduction on Class 8 tractor-trailers. Several tractor-trailer combinations and methods were used over various routes in northern New York. Additional testing on the most promising geometries was carried out by Volvo Technology of America, Inc. at the Transportation Research Center Inc. in Ohio according to the Recommended Practice J1321 Joint TMC/SAE Fuel Consumption Test Procedure - Type II. An over-the-road improvement of 0.63 mpg was observed in the back to back runs in New York, which corresponds to an estimated fuel savings of about 10% for present day class 8 loaded tractor-trailers. Reported results from the SAE test indicated a fuel savings of 3.9% to 4.7% which is estimated to be approximately 0.46 to 0.57 mpg based on the as tested empty tractor-trailer configurations. The optimal geometry for the sealed aft cavity was found to be 15 deg inset on the side top panels, and a 7 deg inset on the bottom. It was observed during the New York tests that a noticeable shift in the data occurred over time, attributed to the warming of the fuel during the test, and this underscores the necessity for back to back run testing.

A Novel Approach to Heavy Vehicle Drag Reduction

Alec Wong[1], Kevin Horrigan[2]

[1] Kenworth Truck Company, USA
[2] EXA Corporation, USA
alec.wong@paccar.com

Abstract The recent volatility of fuel prices and the potential of explicit CO_2 emission control regulations have caused aerodynamic performance to become a critical component of heavy vehicle development. The use of traditional computational fluid dynamics (CFD) simulation for aerodynamic drag prediction on fully complex production geometries has not been adopted for a number of key reasons: the high level of expertise required, simulation time-to-completion, and accuracy versus experiment. This paper demonstrates that the proprietary, Lattice-Boltzmann based simulation method of EXA Corporation delivers valuable results on fully complex geometry, allowing aerodynamic optimization in the concept and design phase. Included is an overview of the simulation method and results for two fully detailed open grille Kenworth models: the T603 and T2000. Comparisons are made to full scale drag meter testing. Additional results are provided for several trailer drag reduction devices including a full gap seal, side skirts, boat tail, and wake boards. Advanced post-processing of the simulation results is used to study transient flow structures and highlight the physics involved with the drag reduction of these devices.

European Truck Aerodynamics – A Comparison Between Conventional and CoE Truck Aerodynamics and a Look into Future Trends and Possibilities

Linus Hjelm and Björn Bergqvist

Volvo 3P, Sweden
linus.hjelm@volvo.com

Abstract The aerodynamic situation for trucks on the European market differs from that in North America on a number of points. Perhaps the most significant difference is that in Europe trucks are of the CoE configuration (Cab over Engine) and in North America trucks are of the conventional type with a hood. Another major difference is that trucks in Europe are speed limited to 90 km/h (56 mph) which of course means that aerodynamics as a whole has less of an impact there. These differences are primarily dictated by different legislations, which in turn have a lot of different side effects. This paper will high-light some of the differences and their impact on aerodynamics, as well as taking a look at possible future ideas such as: extended front or short nose, ride height adjustments, convoy driving, etc.

1 Introduction

Historically most trucks have been of the conventional type. But with the increasing need to make transportation more effective, maximizing load at the expense of space for the driver, has predominantly in Europe, resulted in trucks with the Cab placed on top of the engine (CoE). All these constraints are regulated by legislations. These legislations are, and have been, very different in European compared to in North America. (There are differences in other parts of the world but those will not be considered here).

Of all different legislations it is the ones concerning the length, height, width, weight which has had the biggest impact on the over all shape of the trucks, and hence the aerodynamics. But there are also differences in culture, infrastructure and geography which have contributed in making the detailed design of trucks on the two continents different.

2 Length

The regulation which has most impact on the over all design is the one regarding the length of the vehicle. In Europe all lengths, depending on truck-trailer combination and depending on country, are measured from the most forward point to the most rearward point of the whole vehicle. In North America length regulation does not restrict the total over all length in the same way (see Fig. 1). This is the reason why, in Europe the cabs are of the more compact so called CoE type and in North America they are of the conventional type with a hood. A conventional truck is aerodynamically better than a CoE. For example the difference between a CoE Volvo and a conventional Volvo is of the order of around 0.05 in C_D.

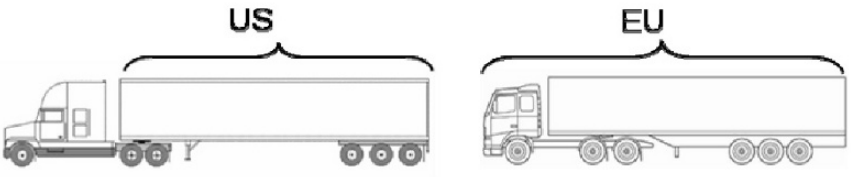

Fig. 1 Different ways of measuring length

When it comes to the cab shape itself this constraint has meant that for a truck OEM in Europe you are left with a fairly limited number of parameters you can work with, for example: Windscreen rake, corner radii, wedge angle, roof shape, underside. And the freedom to work with these parameters is very limited. On one hand you have the length and width regulations and on the other hand you have a constantly increasing need for interior volume and packaging space for all components inside.

Normally there is little extra room to work with on the lower part of the front when it comes to shape, as it is very packed with cooling unit, head lamps, washer liquid bottles etc. All European trucks are also fitted with so called dirt deflectors on the lower corners. If these dirt deflectors are aerodynamically beneficial or not depends on both the design of the detail itself as well as on the design of the cab in this area.

The main priority is to ensure enough corner radius to make the flow stay attached. The part on the lower part of the truck which allows for the biggest room for modifications is probably the bumper/spoiler/underside.

The area where there is still a little bit more freedom to work with is the roof shape and windscreen angle, in other words, the top of the cab. The trend however is that the cab sizes, the height of the cabs, are getting higher and higher, due to increasing need for interior volume. Even here there will be less and less to work with.

As conventional trucks are less restricted in lengths there is more room for design changes on them compared to a CoE truck.

Another indirect effect of the different type of length legislations is the size of the gap between the back wall of the cab and the front face of the semitrailer. Due to the over all length regulation this is kept to a minimum in Europe to ensure as much loading capacity as possible, while still maintaining full mobility between cab and trailer. In North America these gaps are usually much bigger, sometimes up to three/four times bigger. And not surprisingly big gaps have a major negative impact on the C_D-value (see Fig. 2).

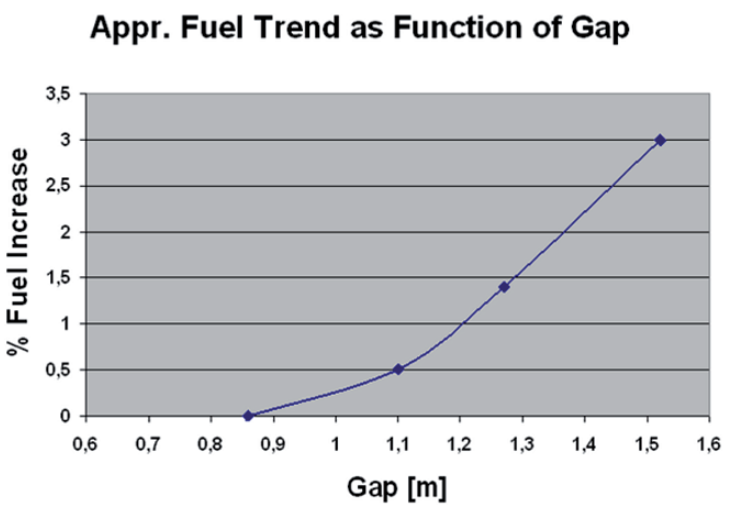

Fig. 2 Importance of gap for fuel economy. Tested on a Volvo VN ½-scale model truck + trailer during tests in the Volvo wind tunnel (PVT) in Gothenburg

3 Height

In Europe there are a lot more variations in the total height regulation, from country to country than in North America, and it can differ with as much as 1 m. This has led to that adjustable roof fairings are more or less standard on all European trucks. An adjustable roof fairing requires roof fairing setting instructions. In Fig. 3 one example of such a setting instruction can be seen. The user measure the distance between the rear wall of the cab and the front wall of the trailer (G), and the vertical distance between the top of the trailer and the top of the cab (H=H1-H2). These numbers are then put in the table, and the appropriate fixing in the adjustment details can be found.

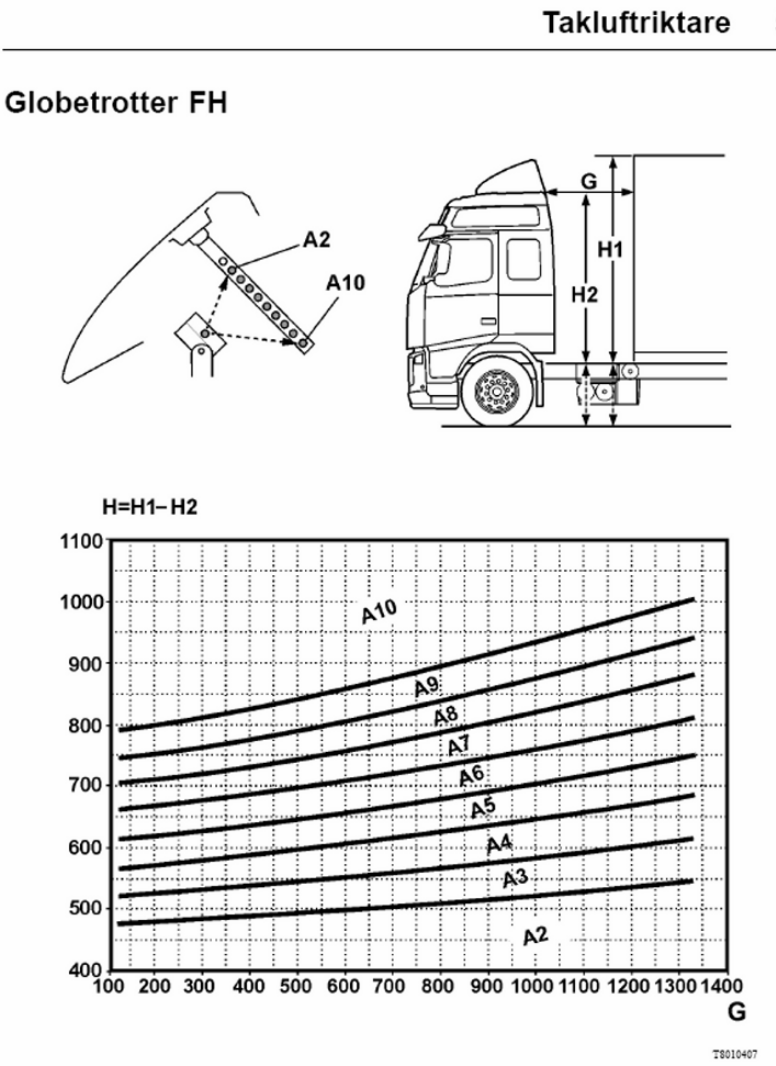

Fig. 3 Roof fairing setting instruction. Example from the Driver Handbook [1]

4 Width

There is one standard over all width in North America, 2.59 m. In Europe there are three; 2.50, 2.55 and 2.60 m depending on country and on type of transport. In

Europe the width of the cabs are made as close to 2.50 m wide as possible in order to maximize the interior volume. In North America the cabs are usually made a bit narrower to ensure easy ingress and egress to the cab.

5 Speed

One regulation which has a big impact on aerodynamics, but perhaps not so much on the actual design of the trucks is the speed. In Europe trucks are electronically limited to 90 km/h (56 mph), whereas in North America considerably higher speeds are common. During our tests the drag becomes Reynolds number independent at just over 4*10^6, equivalent to a speed around 70 km/h (see Fig. 4).

The higher speeds in North America means that aerodynamics account for a larger part on the over all fuel consumption and the over all cost for the truck owners.

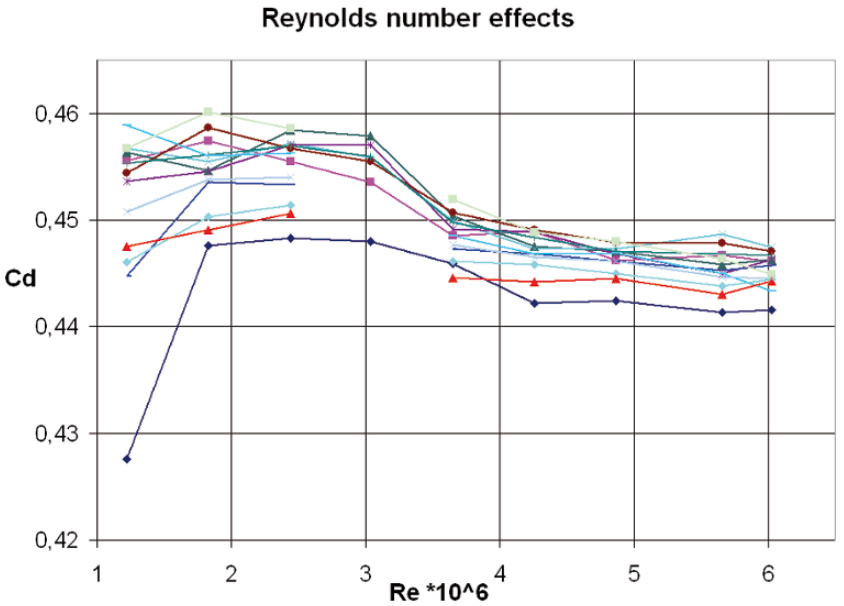

Fig. 4 Reynolds number effects. Each line corresponds to a different ½-scale model truck configuration tested at different speeds in order to investigate the Reynolds number effects. Reference length is the square root of the projected frontal area

6 Trailer

It's not only the tractors that are different, so are the trailers. The vertical corner radii are well rounded in North America while they have sharp or angled corners in Europe. But because the gap is smaller in Europe the side fairings on the cabs can be fitted fairly well with the trailer so they somewhat reduce the bad effect of having sharp corners.

The underside of the trailers are usually quite different, in North America the undersides are usually flat and "empty" whereas in Europe they have beams and are also usually fitted with tool boxes, spare wheels etc. And for safety reasons trucks in Europe have to have under run protections around all sides of the vehicle, even on the trailers. These things help to reduce the C_D because they all act a bit like chassis fairings on the trailer.

7 Future

The C_D for a CoE truck-semitrailer combination today is somewhere around 0.6 – 0.65. Unfortunately this number will not decrease much unless the legislation and trucking/truck transport business change. The aerodynamic evolution is getting closer and closer to the flat part of the development curve when it comes to basic cab shape for CoE – trailer combination. In Fig. 5 the aerodynamic development of a number of different CoE Volvo truck models from the seventies up until today can be seen.

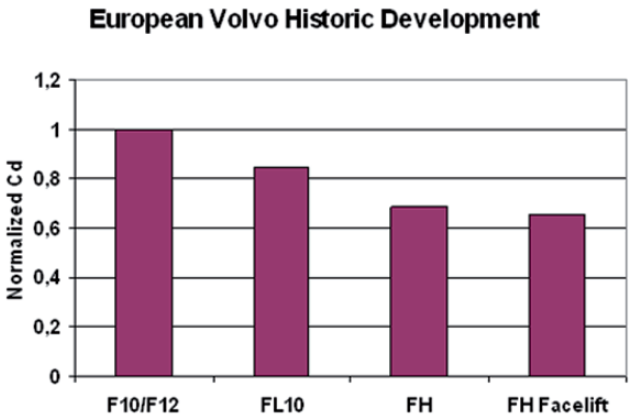

Fig. 5 Aerodynamic development of CoE Volvo trucks. F10/F12 is a model from the seventies and the FH is the current model

Once a good cab shape is achieved, and roof fairings, side fairings and chassis fairings are fitted, the easy gains have been achieved.

In order to reach significant improvements the trailers have to be worked with, or ultimately, treat a tractor trailer combination as one unit.

However there are still some potential areas on the cab and perhaps the most interesting one is the so called; Crash zone, or Soft nose, on CoE (see Fig. 6). Due to safety reasons, discussions have been going on in Europe about introducing an extension of the front face below the wind shield of around 300 mm. This should act as a deformation zone to protect or to minimize injuries to pedestrians, bicyclists and other traffic. Such a “nose” could of course provide a chance to design the front of the truck more aerodynamically efficient. Some initial tests have shown that there seems to be a non negligible potential. The main problem for introducing this seems to have more to do with administration than with anything technical. To define the technical specifications for a deformation zone, and to avoid that this extra volume is not used to package “hard” things is the problem.

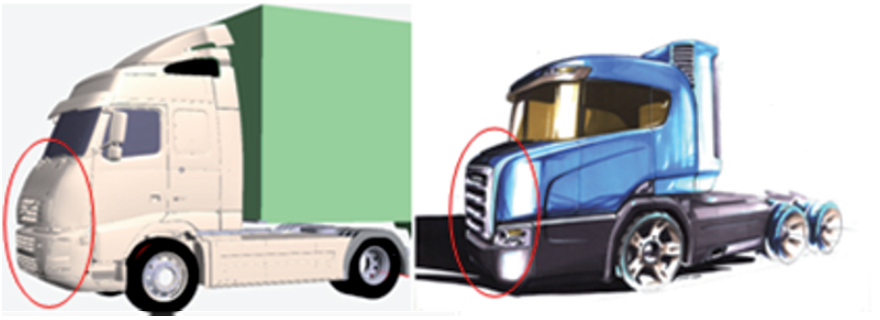

Fig. 6 Examples of “Crash nose" or “Soft nose”. Front face of the truck below the windshield extended approximately 300 mm forward.

The mirrors are another potential area for improvements. It is clear that it would be beneficial if they could be replaced by cameras. However, in some cases where flow separations occur at the A-pillar, the mirrors work as guiding vanes, directing the flow around the A-pillar so that the net drag of the truck actually decreases when the mirrors are added. In order to get a good benefit from replacing the mirrors with cameras, the cab has to be designed in such a way that separations are avoided at the A-pillars.

In North America the length legislations has recently changed to allow for another 2 or 4 feet of extra length at the rear of the trailer in order to make it possible to put add-on devices there. This extra length is to be used for fuel saving reasons only, not to store extra cargo. This of course opens a big potential for reducing the C_D. But the problem is that such a device easily gets in conflict with the rear door openings. Therefore a device like that needs to be made practical for the user, if it is ever going to be used.

Another feature on trucks, which have a big impact on aerodynamics, are the gaps between the bodies of tractor-semitrailer combinations and rigid-trailer combinations, which are necessary for the vehicle to be able to maneuver.

In fact, the usages for trucks are very different between when they are driving slowly/standing still, and when they are driving fast. It could be said that they have two modes; One when driving slow/standing still (when all the flexibility to maneuver in confined spaces is needed, during loading/unloading, and often good ground clearance is needed for curbs or when driving on and of ferries). The second mode is when driving at high speed (on a road when only a very small maneuverability is needed, and if the road is even and smooth very little ground clearance is needed). One idea could therefore be to make use of this and in some ways alter the shape/configuration between these two modes at a predefined speed for example.

One example is to have a coupling which can be shortened once you are on a motorway to decrease the gap between the different bodies in order to reduce the drag contribution from such gaps (see Fig. 7).

Fig. 7 Adjustable length of coupling

Another example could be the ride height of the vehicle; it could be lowered once you have reached a certain speed (see Fig. 8). You do not drive very fast on a bad or uneven road. This requires that the truck is equipped with air suspension on all axels, which only a limited number of trucks have today.

Fig. 8 Adjustable ride height

Inflatable gap-fillings between the rear wall of the cab and front face of the trailer is another idea. Iveco has shown that, as well as an inflatable boat tailing on one of their concept trucks [2, 3].

More and more trucks today are equipped with ACC (Adaptive Cruise Control), which makes it technically possible to drive very close behind another truck in order to make use of the aerodynamic benefits of moving in a close convoy. But to make that a reality the safety aspects have to be solved.

8 Conclusions

No doubt there is a huge potential to reduce the C_D on trucks. That has been shown by countless tests and simulations as well as by a number of concept trucks over the years. But in order to make a reality out of that, the trailers have to be worked with in one way or another.

That the trailers stand for a majority of the drag of a truck on the road is common knowledge. During the years a lot of resources have been spent on finding devices, shapes and solutions which will work aerodynamically. So the main problem is not how to make a truck more aerodynamically efficient, because we have good knowledge of that today, the real challenge lies in finding practical, robust, economic, low maintenance and not to forget, aesthetic solutions which will work in real life situations.

In order for that to be a reality, truck OEM:s, trailer OEM:s as well as the end customers need to find ways to cooperate more closely.

Acknowledgments

Michael Sorrells, Volvo 3P

References

1. “Driver Handbook”, Volvo Trucks Corporation, 2007.
2. http://195.200.115.136/Textbase/work/2007/vehicle/Durelli.pdf
3. http://www.roadtransport.com/Articles/2008/01/31/129674/15-better-mpg-with-transport-concept.html

Advanced Experimental Methods for the Analysis and Aerodynamic Design of Heavy Vehicles

Mike Camosy, Andre Brown, Henri Kowalczyk, Gaylord Couthier

Auto Research Center, USA
mcamosy@arcindy.com

Abstract Extensive knowledge exists in the testing of 1/8th scale, Class 8 tractor trailer models within fixed floor wind tunnels. This size of model has proven to correlate well with in a Reynolds number ranging between 1M and 6M. Prior testing is well documented on a Generic Conventional Model (GCM) in the NASA AMES 7x10ft and 12ft wind tunnels. Within this prior research into Heavy Vehicle Aerodynamics, it has been identified on numerous occasions that improved accuracy will allow for greater understanding of the flow field structure in the underbody and internal flow regions. The aim of this paper is to summarize the new research conducted at the Auto Research Center (ARC), a 50% rolling road scale wind tunnel facility in Indianapolis, Indiana. ARC has tested a rolling road 1/8th scale tractor trailer at 50m/s constant dynamic (approximately 1M Re). The model features fully articulated suspension & axle systems, engine bay detail for internal flow simulation, realistic radiator blockage, and an automated model motion system capable of controlling the model in roll, heave, pitch & yaw. To remain consistent with the previous testing conducted by NASA AMES, a replica of the GCM tractor and trailer shapes were used for the upper aerodynamic surfaces. The test objectives initially included a demonstration of correlation between the ARC and NASA wind tunnels with the rolling road switched off. This baseline is then compared to data obtained with the rolling road on, allowing the impact of 18 rotating wheels & tires on the flow structure to be visualized and analyzed. Further studies are presented on the effects of improved detail in the underbody regions, and on the effects of internal & cooling flows as applied to the GCM model. Future work at ARC will use detailed cab bodywork for analysis of specific OEM tractors & trailers.

Author Index